

**Active Interface Engineered Oxygen Electrocatalysts
for
Electrochemical Energy Applications**

by

Mr. Narugopal Manna

10CC16A26001

A thesis submitted to the
Academy of Scientific & Innovative Research
for the award of the degree of
DOCTOR of PHILOSOPHY
in
SCIENCE

Under the supervision of
Dr. Sreekumar Kurungot



CSIR-National Chemical Laboratory, Pune



Academy of Scientific & Innovative Research

AcSIR Headquarters, CSIR-HRDC campus

Sector 19, Kamla Nehru Nagar,

Ghaziabad, U.P. -201 002, India

May 2022

CERTIFICATE

This is to certify that the work incorporated in this Ph.D. thesis entitled “Active Interface Engineered Oxygen Electrocatalysts for Electrochemical Energy Applications” submitted by Mr. Narugopal Manna to the Academy of Scientific and Innovative Research (AcSIR) in partial fulfillment of the requirements for the award of the Degree of Doctor of Philosophy in Science, embodies original research work under my guidance. We further certify that this work has not been submitted to any other University or Institution in part or full for the award of any degree or diploma. Research material(s) obtained from other source(s) and used in this research work has/have been duly acknowledged in the thesis. Image(s), illustration(s), figure(s), table(s) etc., used in the thesis from other source(s), have also been duly cited and acknowledged.



Narugopal Manna

(Student)

Name with date

(31.05.2022)



Dr. Sreekumar Kurungot

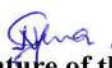
(Supervisor)

Name with date

(31.05.2022)

STATEMENTS OF ACADEMIC INTEGRITY


I, **Mr. Narugopal Manna**, a Ph.D. student of the Academy of Scientific and Innovative Research (AcSIR) with Registration No. 10CC16A26001 hereby undertake that, the thesis entitled “**Active Interface Engineered Oxygen Electrocatalysts for Electrochemical Energy Applications**” has been prepared by me and that the document reports original work carried out by me and is free of any plagiarism in compliance with the UGC Regulations on “*Promotion of Academic Integrity and Prevention of Plagiarism in Higher Educational Institutions (2018)*” and the CSIR Guidelines for “*Ethics in Research and in Governance (2020)*”.


Signature of the Student

Date: 31.05.2022

Place: Pune

It is hereby certified that the work done by the student, under my supervision, is plagiarism-free in accordance with the UGC Regulations on “*Promotion of Academic Integrity and Prevention of Plagiarism in Higher Educational Institutions (2018)*” and the CSIR Guidelines for “*Ethics in Research and in Governance (2020)*”.


Signature of the Supervisor

Name: Dr. Sreekumar Kurungot

Date: 31.05.2022

Place: Pune

Acknowledgments

At this moment of completing my doctoral thesis, I take this opportunity to thank everyone who has directly or indirectly given input and support throughout the timeline of my Ph.D. journey at CSIR-NCL, Pune.

I express my deep and sincere gratitude to my research advisor Dr. Sreekumar Kurungot, for his constant advice and support throughout my Ph.D. Journey. He has always given me space and freedom while keeping me on track, which transformed me into an independent researcher. He has spent valuable time at his maximum to discuss my work progress on a monthly, weekly, and occasionally daily basis. That helps me a lot to finish the project on time. He has taught me a lot, not just in the field of research, but also in terms of time management. His lab's culture of weekly literature and work presentations allows me to learn and interact with the other members of the group through scientific conversations. I want to thank him again for providing an amazing research environment and all of the necessary research facilities during my time at CSIR-NCL.

I am thankful to Dr. Ashish K. Lele (Director, CSIR-NCL), and Prof. Ashwini K. Nangia (Former Director, CSIR-NCL) for providing the opportunity to work in this esteemed laboratory and to make use of the facilities of this laboratory. I am grateful to Dr. T.G. Ajithkumar (Chair of the Physical and Materials Chemistry Division), and Dr. BLV. Prasad (Former Chair of the Physical and Materials Chemistry Division), for providing the infrastructures in the division.

I thank my doctoral advisory committee members Dr. BLV Prasad, Dr. Paresh Dhepe, and Dr. H. V. Thulasiram, for their support, timely assessment, and valuable suggestions, comments, and fruitful discussions during the DAC meetings. The suggestions and discussions have helped me to improve the quality of the work.

I would like to thank student academic office (SAO) staff, Chairman Dr. C.P. Vinod, former AcSIR Coordinator Dr. Mahesh J. Kulkarni, and current AcSIR Coordinator Dr. Santosh Mhaske, Mr. Purushothaman, Mrs. Purnima Khole, Ms. Komal, Mrs. Vaishali, Mrs. Poornima, and Mr. Santosh, for timely processing my Ph.D. related documents.

I also thank Dr. E Balaraman, Dr. Pankaj Podder, Dr. Sayan Bagchi, and Dr. Arup Rath for their excellent lectures during the coursework. I am profoundly thankful to the CMC division at CSIR-NCL for ensuring the smooth execution of sample characterization, which is one of the essential parts of my research work. I would like to thank Mr. Gholap, Dr. Selvaraj, Dr. Vinod, Mr. Shrinivas Deo, Mrs. Rupali, Mr. Venkitesh, Mr. Thushar, Mrs. Sheethal, Mr. Chetan, and Ms. Medha, for the valuable help in the characterization of various samples and effective scientific discussions. Thanks to Mrs. Sunita Barve and Mr. Gati K. Nayak for the effective library facilities for accessing the various journals and the support provided in the plagiarism checking.

My senior Dr. Santosh K. Singh needs a special mention. The suggestions and support provided by him from the beginning of my research life are remarkable. He helped me with the manuscript writing during several phases of my doctorate studies.

I am grateful to my former labmates Dr. Harshitha B. A., Dr. Santosh Singh, Dr. Roby Soni, Dr. Varchaswal Kashyap, Dr. Vidyanand V., Dr. Pranav K.G., Dr. Rajith I.V., Dr. Siddheshwar Bhange, Dr. Nadeema Ayasha and Dr. Meena Ghosh for their mentoring and care during my days at CSIR-NCL. I want to give thanks and appreciation to my current labmates Sachin, Geeta, Ajmal, Swati, Maria, Priyanka, Sidharth, Mayank, Athira B, Athira Y, and Sachin Patil, for their support and for providing a beautiful friendly atmosphere in the lab. Thanks to the former and current post-docs in the lab, Dr. Raji, Dr. Gaurav, Dr. Debasree, Dr. Shilpa, and Dr. Vandana. I want to share my special gratitude to Dr. Anupam Biswas and Dr. Janardan Kundu for the collaboration. I am always grateful to Dr. Arun Torris, for his time to help me with the tomography analysis.

A special thanks to my close friends Soma, Milan, and Sujata, who take care of me as a family member during the lockdown when I was seriously affected by health issues due to an accident.

I always cherish the beautiful moments spent at the beginning of my Ph.D. with my dear friends Himdari, Sanjukta, Pronay, Suvenduda, Basuda, Srinjini, Kaushik, Vikash, and Pavan, during my stay at CSIR-NCL, which was pleasant and eventful. I appreciate all of the Bengali students at CSIR-NCL Tapas da, Tamal da, Subrata da, Sutanu da, Piyali di, Rupa di, Shaibal da, Debu da, Abhijit da, Sayantan da, Subhrasis da, Nirsad, Asish, Abdul, Tubai, Srijan, Biplab, Debtirtha, Rahul, Sushmita, and Twinkle with whom I have spent quality time in various Bengali programs and occasional events at NCL. I am delighted to have met and befriended many other interesting people from all over India at CSIR-NCL. During my stay at NCL, I was involved in other activities such as sports and various event management, where I met so many fantastic friends Ravi, Sheena, Tripathi, Ajit, Mahendra Wagh, Rashid, Pinka, Mahendra Pauer, Himanshu, Dr. Srikant, and many others. I would like to thank the cooks of HoR-4, GJ, and New Hostels, specially Sujit and Chottu for providing good Bengali dishes.

Above all, I would like to thank my family; I couldn't even finish it without their selfless support. There are no words to express how grateful I am to maa and baba for their hardships and struggles in educating me. I attribute everything to them. Thank you for always being there for me. I want to thank my siblings Sibani, and Bandana, for being such supportive and encouraging sisters. I am glad to dedicate this thesis to my family.

Though many have not been mentioned here, their support and affection are with me.

Narugopal Manna

List of Abbreviations

ADT	Accelerated Durability Test
BET	Brunauer–Emmett–Teller
CNT	Carbon Nanotube
CA	Chronoamperometry
CP	Chronopotentiometry
CE	Counter Electrode
CV	Cyclic Voltammetry
C_{dl}	Double-layer Capacitance
DOE	Department of Energy
EDAX	Energy Dispersive X-ray Analysis
ECSA	Electrochemical Surface Area
EIS	Electrochemical Impedance spectroscopy
FESEM	Field Emission Scanning Electron Microscope
GC	Glassy Carbon
Gr	Graphene
HRTEM	High Resolution Transmission Electron Microscopy
IPA	Isopropyl Alcohol
K-L	Koutecky-Levich
LSV	Linear Sweep Voltammetry
MEA	Membrane Electrolyte Assembly

MWCNT	Multi-walled Carbon Nanotubes
NEGF	Nitrogen-doped Entangled Graphene Framework
OCV	Open Circuit Voltage
ORR	Oxygen Reduction Reaction
OER	Oxygen Evolution Reaction
PAFC	Phosphoric Acid Fuel Cell
PBI	Polybenzimidazole
PEMFC	Polymer Electrolyte Membrane Fuel Cell
PGM	Platinum Group Metal
pNEGF	Nitrogen-doped Porous Entangled Graphene Framework
PTFE	Polytetrafluoroethylene
RE	Reference Electrode
RHE	Reversible Hydrogen Electrode
RDE	Rotating Disc Electrode
RRDE	Rotating Ring Disk Electrode
RZAB	Rechargeable Zinc-air battery
SAED	Selected Area Electron Diffraction
SEM	Scanning Electron Microscopy
SWCNT	Single-walled Carbon Nanotube
TEM	Transmission Electron Microscope
TGA	Thermogravimetric Analysis

TBP	Triple Phase Boundary
WE	Working Electrode
WS	Water Splitting
XRD	X-ray Diffraction
ZAB	Zinc-air Battery
1D	One Dimensional
2D	Two Dimensional
3D	Three Dimensional

Preface.....1-5

Chapter 1

Introduction: Oxygen Electrocatalysts for the Electrochemical Energy Applications 6-48

1.1. Introduction 7-8

1.2. Hydrogen Energy: Water Splitting, Fuel Cells, and Metal-Air Batteries 8-9

1.3. Electrochemical Water Splitting 9

 1.3.1. Water Splitting Mechanism 10-11

1.4. Fuel Cells 11-15

 1.4.1. Polymer Exchange Membrane Fuel Cell (PEMFC) 12-13

 1.4.2. PEMFC Mechanism 13-14

 1.4.3. I-V Characteristics of the Fuel Cells 14-15

1.5. Metal-Air Battery (MAB) 15-20

 1.5.1. Zn-Air Battery 17

 1.5.2. Primary ZAB 17

 1.5.3. Mechanical Rechargeable ZAB 17

 1.5.4. Secondary ZAB (Rechargeable) 17-18

 1.5.5. liquid-state-ZAB 18

 1.5.6. Solid-state Rechargeable ZAB 18

 1.5.7. Mechanism in RZAB Overall Reaction 18-19

 1.5.8. Bifunctional Oxygen Activity at the Air-cathode Interface of ZAB 19-20

1.6. Oxygen Electrochemistry (ORR & OER) 20-24

 1.6.1. Oxygen Evolution Reaction (OER) 20-21

 1.6.2. State-of-the-art OER Catalysts 21

 1.6.3. Oxygen Reduction Reaction (ORR) 21-22

 1.6.4. State-of-the-art ORR Catalysts 22-24

 1.6.5. Bifunctional Active Sites for ORR and OER 24-39

1.7. Fundamentals of Catalytic Active Site Designing for ORR and OER 24-25

 1.7.1. Noble Metal-based Catalysts 25-26

 1.7.2. Pt-based Catalysts for ORR 26-27

1.7.3. Non-noble Metal-based Electrocatalysts	27-28
1.7.4. Transition Metal Oxides (TMO), Hydroxides, and Layered Double Hydroxide (LDH) (LDH)	28
1.7.5. Structure, Composition, and Morphology Controlled Oxides, Hydroxides, and LDH	28-29
1.7.6. Transition Metal Oxides	29
1.7.7. Spinel Oxides	29
1.7.8. Transition Metal (oxy) hydroxides (TMH)	29-30
1.7.9. Layered double hydroxides (LDH)	30-31
1.7.10. Role of Carbon Nano-Structures	31-32
1.7.11. Fullerenes	32
1.7.12. Carbon Nanotubes (CNTs)	32-33
1.7.13. Graphene	33-34
1.7.14. Heteroatom Doped Graphene	34-35
1.7.15. Influences of the Morphologies of Heteroatom-doped Carbon Support	35
1.7.16. Layered Double Hydroxides Supported Carbon	36
1.7.17. Spinel Oxide Supported Carbon	36-39
1.8. Conclusions, Scope, and Objectives of the Thesis	39-42
1.9. References	42-48

Chapter 2

NiFe Layered Double Hydroxide-Decorated N-Doped Entangled-Graphene Framework: A Robust Water Oxidation Electrocatalyst 49-74

Framework: A Robust Water Oxidation Electrocatalyst

2.1. Introduction	50-51
2.2. Experimental	51-55
2.2.1. Materials	51
2.2.2. Synthesis of Graphene Oxide (GO)	51-52
2.2.3. Synthesis of Nitrogen-doped Entangled Graphene (NEGF)	52
2.2.4. Synthesis of NiFe-LDH Supported Nitrogen-doped Entangled Graphene (NiFe-LDH/NEGF)	52
2.2.5. Synthesis of Unsupported NiFe-LDH	52-53
2.2.6. Synthesis of Ni(OH) ₂ /NEGF	53

2.2.7. Synthesis of NiFe-LDH/NEGF (w/o)	53
2.2.8. Synthesis of NiFe-LDH/EGF	53
2.2.9. Material Characterization	53-54
2.2.10. Electrochemical Studies	54-55
2.3. Results and Discussion	55-70
2.3.1. FESEM Analysis	56--57
2.3.2. TEM Analysis	57-58
2.3.3. EDX Analysis	58
2.3.4. Surface Area Analysis	58-59
2.3.5. XRD Analysis	59-60
2.3.6. Raman Analysis	60-61
2.8.7. TGA Analysis	61-63
2.8.8. XPS Analysis	63-65
2.8.9. Electrochemical Analysis	65-70
2.4. Conclusions	70-71
2.5. References	71-74

Chapter 3

Zinc-Air Battery Catalyzed by Co₃O₄ Nanorod-Supported N-doped Entangled Graphene for Oxygen Reduction Reaction	75-106
3.1. Introduction	76-78
3.2. Experimental Section	78-84
3.2.1. Materials	78
3.2.2. Synthesis of Graphene Oxide (GO)	78-79
3.2.3. Synthesis of Co ₃ O ₄ Supported N-doped Entangled 3D Graphene (Co ₃ O ₄ /NEGF)	79
3.2.4. Physical Characterization	80-82
3.2.5. Rotating Disk Electrode (RDE) Study	82-83
3.2.6. Rotating Ring Disk Electrode Study	83
3.2.7. Zinc-Air Battery (ZAB) Fabrication and Testing	83
3.2.8. The Hg/HgO Reference Electrode Calibration and Conversion to RHE	84

3.3. Results and Discussion	84-101
3.3.1. FESEM Analysis	85-86
3.3.2. Micro-Computed Tomography Analysis	86
3.3.3. TEM Analysis	87-88
3.3.4. HRTEM Analysis	88
3.3.5. XRD Analysis	89
3.3.6. Raman Analysis	90
3.3.7. Surface Area Analysis	90-92
3.3.8. TGA Analysis	92
3.3.9. XPS Analysis	93-94
3.3.10. Electrochemical Analysis	94-101
3.4. Conclusions	101-102
3.5. Reference	102-106

Chapter 4

Air-Cathode Interface-Engineered Electrocatalyst for Solid-State Rechargeable Zinc-Air Battery	107-137
4.1. Introduction	108-110
4.2. Experimental Section	110-113
4.2.1. Materials	110
4.2.2. Synthesis of Graphene Oxide (GO)	110
4.2.3. Synthesis of MnCo ₂ O ₄ -Supported N-doped Entangled 3D Graphene (MnCo ₂ O ₄ /NEGF)	110-111
4.2.4. Physical Characterization	111-112
4.2.5. Rotating Ring Disk Electrode Study	112
4.2.6. The Hg/HgO Reference Electrode Calibration and Conversion to RHE	112-113
4.2.7. Preparation of the Gel Electrolytes	113
4.2.8. Assembly and Testing of the Solid-State ZAB Device	113
4.3. Results and Discussion	113-132
4.3.1. FESEM Analysis	116
4.3.2. Micro-Computed Tomography Analysis	116

4.3.3. TEM and HRTEM Analyses	117-119
4.3.4. Surface Area Analysis	119
4.3.5. Thermogravimetric Analysis	119
4.3.6. XRD Analysis	119-120
4.3.7. XPS Analysis	120-122
4.3.8. Raman Analysis	122-123
4.3.9. Electrochemical Analysis	123-132
4.4. Conclusions	132
4.5. References	133-137

Chapter 5

Microwave-Induced Micro-Porous Graphene supported Pt₃Co alloy as an Improved Mass Active and Durable ORR catalysts	138-165
5.1. Introduction	139-141
5.2. Experimental Section	141-144
5.2.1. Materials	141
5.2.2. Synthesis of Graphene Oxide (GO)	141
5.2.3. Synthesis of Nitrogen-Doped Entangled Graphene (NEGF)	141-142
5.2.4. Synthesis of Nitrogen-Doped Porous Entangled Graphene (pNEGF)	142
5.2.5. Synthesis of Pt ₃ Co Supported N-doped Entangled 3D Graphene (Pt ₃ Co/pNEGF)	142
5.2.6. Physical Characterization	142-143
5.2.7. Rotating Disk Electrode Study (RDE)	143
5.2.8. Rotating Ring Disk Electrode Study (RRDE)	143-144
5.2.9. The Ag/AgCl Reference Electrode Calibration and Conversion to RHE	144
5.3. Results and Discussion	144-159
5.3.1. FESEM Analysis	145-146
5.3.2. Micro-Computed Tomography Analysis	147-148
5.3.3. HRTEM Analyse	148-149
5.5.4 Surface Area Analysis	149-150
5.3.5. Raman Analysis	151

5.3.6. XRD Analysis	151
5.3.7. XPS Analysis	152-153
5.3.8 Thermogravimetric Analysis	154
5.3.9 Electrochemical Analysis	154-159
5.4. Conclusion	159
5.5. References	160-165

Chapter 6

Summary & Future Perspectives	166-173
6.1. Summary	166-172
6.2. Future Prospects	172-173
Abstract	174
List of Patents and Publications	175-177
Erratum	178

1. Introduction: The growing population and the digitization era drive up the global energy demand, which is expected to rise even faster in the coming years. A significant amount of energy is currently being produced from the fossil fuels such as petroleum, natural gas, coal, and so on. However, these energy sources are not enough to fulfill the requirement of the world population. In addition, environmental pollution is a significant issue associated with the fossil fuel-based energy sources. To avoid the harmful effects of the fossil fuels on the environment and to ensure a safe and healthy future, the non-renewable energy sources must be replaced with the appropriate renewable technologies. Based on the current scenario, even though the research on the renewable energy (wind, tidal, solar, geothermal, etc.) is being well-progressed to tackle this issue, due to the intermittency of such renewable resources, alternative electrochemical energy storage and energy conversion technologies are urgently needed to effectively bridge the technological gaps. The electrochemical water splitting, fuel cells, and rechargeable zinc-air batteries (RZABs) have been identified as the major electrochemical energy technologies that can suit to catering the diverse practical needs in terms of energy efficiency.

2. Statement of the problem: The development and commercialization of such devices (water splitting, fuel cells, and RZABs) have been affected by the issues related to the performance and cost of operation and system. The two electrode reactions that occur in the case of water electrolysis are the hydrogen evolution reaction (HER) and the oxygen evolution reaction (OER) at the cathode and anode, respectively. Similarly, the hydrogen oxidation reaction (HOR) at the anode and the oxygen reduction reaction (ORR) at the cathode are the involved primary reactions in a hydrogen fuel cell. In addition, OER and ORR are the primary reactions that occur at the cathode of an RZAB during the charging and discharging processes, respectively. It is known that ORR and OER are the two prominent electrode processes that determine the efficiency of the electrochemical devices which deal with such reactions. However, the oxygen reactions (ORR/OER) suffer from sluggish kinetics, which significantly suppress the overall performance of the respective electrochemical energy devices. Hence, improved performance and durable ORR/OER catalysts are highly desirable. Over the last decade, substantial progress has been made to improve the performance and durability of the various electrochemical energy devices by introducing electrocatalysts with better activity characteristics for facilitating the desired reactions. To design an electrocatalyst, mostly two approaches are being adopted: (i) increasing the intrinsic activity of the catalyst by controlling the structure, morphology, and composition of the electrocatalyst, and (ii) increasing the number of the active sites with the help of suitable support morphologies and composition-controlled electrocatalyst systems.

3. Objectives: A survey of the existing electrocatalysts for many of the above-mentioned applications reveals that most of the catalysts are based on 1-dimensional (1D) and 2-dimensional (2D) conducting carbon supports. A major drawback of such materials is the inability to deliver the full activity in the electrodes due to the reasons such as aggregation of the particles and pore-blocking during the processes

involved in the electrode fabrication. This leads to a lowering of the electrochemical active surface area (ECSA) and mass transfer issues by concomitantly increasing the overpotentials associated with the electrode reactions. To overcome these issues associated with the ORR/OER electrocatalysts, the present dissertation explores various strategies for active interface engineering, mainly by developing electrocatalysts with 3-dimensional (3D) morphologies. These 3D structured electrocatalysts are expected to better retain their morphological features and, thereby, the intrinsic activity characteristics during the process involved in the conversion of the catalysts to the electrodes. The main objectives of the works covered in the thesis are as follows:

1. Modulating the surface area and porosity characteristics of the electrocatalysts for ORR/OER applications by developing catalysts based on 3D graphene supports with an aim to improve the mass transport properties of the gaseous reactants and products released during the electrochemical process along with better electrode-electrolyte interface formation.
2. To gain additional performance enhancement from the 3D graphene scaffolds as substrates for catalysts by inducing nitrogen doping into the graphene framework by which efficient anchoring sites for the dispersion of the desired active sites can be achieved.
3. To increase the structural integrity of the electrocatalysts under the drastic electrochemical environments by employing more corrosion resistant 3D graphene-based electrocatalysts and, thereby ensure better long-term performance under a range pH conditions.
4. To develop various 3D graphene-based electrocatalysts by decorating active components such as layered double hydroxids, and spinel metal oxide nanoparticles to explore possibilities for achieving better catalysts with modulated performance characteristics for OER and ORR.
5. To improve the mass transfer properties of the 3D support by inducing microporosity which helps for dispersing small-sized platinum-cobalt alloy (Pt₃Co) nanoparticles, leading to improved ORR performance in acidic conditions.

4. Methodology: The present dissertation explores various strategies for the active interface engineering by developing electrocatalysts with 3D morphologies for ORR and OER applications. The outcome of the individual chapters is highlighted below.

Chapter 1 introduces the importance of the electrochemical energy technologies such as electrochemical water splitting, rechargeable ZAB, and PEMFC, along with detailed discussions on their working principles. This chapter covers the reaction mechanisms associated with the individual electrochemical reactions in each case and the important role of the oxygen electrocatalysts in deciding the overall device performance. Furthermore, the chapter also includes a concise *state-of-the-art* survey of the development of the 3D carbon-supported platinum and platinum-free electrocatalysts for ORR and OER applications. The obtained activity and the major drawbacks associated with the existing electrocatalysts developed by various research findings are described systematically. Further, this

chapter also discusses the general strategies adopted to improve the activity of the electrocatalyst materials and their generally adopted synthesis methodologies.

Chapter 2 describes the preparation of nitrogen-doped entangled graphene framework (NEGF) decorated with the nickel-iron layered double hydroxide (NiFe-LDH) nanostructures by an *in-situ* solvothermal method followed by freeze-drying (NiFe-LDH/NEGF). NiFe-LDH is known as an active catalyst for the electrochemical OER process. The layered structure of LDH allows the intercalation of water and anions during the electrochemical OER process and, therefore, displays bulk redox activity. The primary activity degradation factors for NiFe-LDH include insufficient electronic conductivity, poor active center exposure, and hindered reaction species transport. By keeping all these performance-constraining factors under consideration, in the present case of the work, by anchoring the NiFe-LDH over NEGF, improved performance could be achieved on NiFe-LDH/NEGF. Through this rational designing strategy, the NEGF acted as a useful active support by tuning the electronic structure and distribution of NiFe-LDH along with its role as a substrate to provide an open and exposed catalytic architecture. The freeze-drying method helped to prevent the restacking of the graphene sheets. The incorporation of NEGF has significantly reduced the overpotential for the electrochemical oxygen evolution reaction (OER) in 1 M KOH solution. This corresponds to an overpotential reduction from 340 mV for NiFe-LDH to 290 mV for NiFe-LDH/NEGF to reach the benchmark current density of 10 mA cm⁻².

Chapter 3 deals with the development of Co₃O₄ nanorod bearing NEGF (Co₃O₄/NEGF) as a versatile noble metal-free ORR electrocatalyst and its application as an air-electrode in the primary zinc-air battery (ZAB). In a ZAB, the discharge process involves ORR at the cathode, and the slow kinetics of the process lowers the efficiency of the system performance, especially in the case of precious metal-free electrocatalysts. The spinel structures of the cobalt oxides are being explored as electrocatalysts, including for ORR applications, where the mixed valency of Co in Co₃O₄ (*i.e.*, Co²⁺ and Co³⁺) plays a vital role in the fcc crystal structure. The mixed valency of cobalt helps in establishing a better electron transport mechanism and, thereby, towards preferable electrochemical activity. Further, to improve the intrinsic ORR characteristics, recently, the shape and size-controlled design of the metal oxide-based catalysts has also been executed. Among them, the nanorods of the cobalt oxide have become an interesting class of 1D morphology that helps to facilitate rapid charge transport and also assures adequate diffusion of the reactants. However, the cobalt oxide-based electrodes suffer from the limitation of their poor electronic conductivity. Hence, to utilize the full potential of Co₃O₄ nanorods by effectively tackling the issues related to conductivity and mass transfer, this chapter highlights the efforts made in the direction of developing and demonstrating Co₃O₄/NEGF, which consists of Co₃O₄ nanorods uniformly distributed over nitrogen-doped entangled porous 3D-graphene (NEGF), as a potential ORR electrocatalyst. The synthesis of the catalyst involves a sequential pathway involving hydrothermal treatment followed by freeze-drying to build the desired structural architecture of the

catalyst. The catalyst is found to be displaying promising ORR activity during the validation both under the single-electrode testing and as an air-electrode in ZAB. In 0.1 M KOH solution, Co₃O₄/NEGF displays only 60 mV onset potential shift compared to the *state-of-the-art* Pt/C catalyst. The hydrothermal treatment and freeze-drying processes are found to be playing vital roles in tuning the morphological and structural features of the catalyst. Apart from its favorable contribution towards ORR, the doped nitrogen helps to facilitate efficient dispersion of the oxide nanorods on the graphene. The ZAB fabricated by employing Co₃O₄/NEGF as the cathode catalyst is thus found to be an efficient competitor for the system based on the Pt/C cathode.

Chapter 4 introduces a bimetallic manganese-cobalt-based spinel oxide (MnCo₂O₄) supported NEGF (MnCo₂O₄/NEGF) as an efficient bifunctional electrocatalyst for facilitating both ORR and OER, and, thereby, as a versatile air-electrode material for rechargeable zinc-air battery (RZAB) application. An all-solid-state RZAB could be demonstrated by employing MnCo₂O₄/NEGF as the air-cathode since the 3D morphology of the catalyst helped to achieve an effective interface with the electrolyte. The work covered in this chapter includes discussions on the strategies adopted for tuning the intrinsic bi-functional activity of the spinel structure of MnCo₂O₄ concerning morphology and composition. The binary or ternary transition metal spinel oxides possess interesting bi-functional oxygen activity. The presence of a second metal with different charges alters the d-band centers and changes the electronic properties of the spinel oxides, thereby helping towards better bi-functional oxygen redox activity. By accommodating this active species on NEGF, an efficient catalyst system with features favoring effective active “triple-phase boundary (TPB)” could be developed. The chapter discusses the interesting ORR and OER activity characteristics displayed by the system, followed by the practical demonstration of the catalyst as an air-electrode in an RZAB. The cell displayed a maximum peak power density of 202 mW cm⁻², which is significantly higher as compared to the one based on the Pt/C+RuO₂ standard catalyst pair (124 mW cm⁻²). The all-solid-state device displayed a charge-discharge voltage with a low voltage gap of 0.70 V at 10 mA cm⁻² and a small increment of 86 mV after 50 h.

The catalytic materials based on non-noble metal-supported NEGF developed as per the details given in **Chapters 2, 3, and 4** displayed high electrocatalytic ORR and OER activity under basic conditions with long term durability. Considering the interesting stable morphology of the mesoporous structure of the NEGF system, further incorporating microporosity in the system (pNEGF) will be beneficial in further tuning the electrode requirements. In addition to the need for better catalysts as replacements for the *state-of-the-art* Pt/C for PEM fuel cells (PEMFCs) with the ability to function under acidic pH conditions, the material has been further explored for this application by using pNEGF as a substrate for dispersing Pt-Co alloy based (Pt₃Co) nanoparticles. Accordingly, **Chapter 5** deals with the results pertaining to the development and demonstration of the microporous structure of 3D graphene-supported-platinum cobalt alloy (Pt₃Co/pNEGF) as an ORR electrocatalyst with the ability to function

better under acidic conditions. Microwave treatment of NEGF creates the 3D porous carbon support (pNEGF) with a large pore volume and dense micro/mesoporous surfaces. The carbon support porosity, within micro- and mesopore range, has a significant impact on achieving the distribution of the small-sized alloy nanoparticles as well as an efficient mass transfer process. Alloying Pt with Co slightly reduces the Pt metal loading without affecting the ORR activity. In addition, the presence of an early transition metal to Pt could alter the Pt-Pt interatomic distance, resulting in a down-shift of the d-band center and changing the electronic structures of active Pt sites for ORR. The performance of the catalyst could be evaluated to understand the activity characteristics and the structural advantages, and an assessment has been done concerning the key performance indicators in comparison with the characteristics of the commercial Pt/C catalyst. Pt₃Co/pNEGF and 40 % Pt/C in 0.1 M HClO₄ display the ORR onset potentials of 0.99 and 1.0 V *vs.* RHE, respectively. The mass activities calculated from the ORR polarization curves reveal 1.5 times higher activity for Pt₃Co/pNEGF compared to its counterpart Pt/C system.

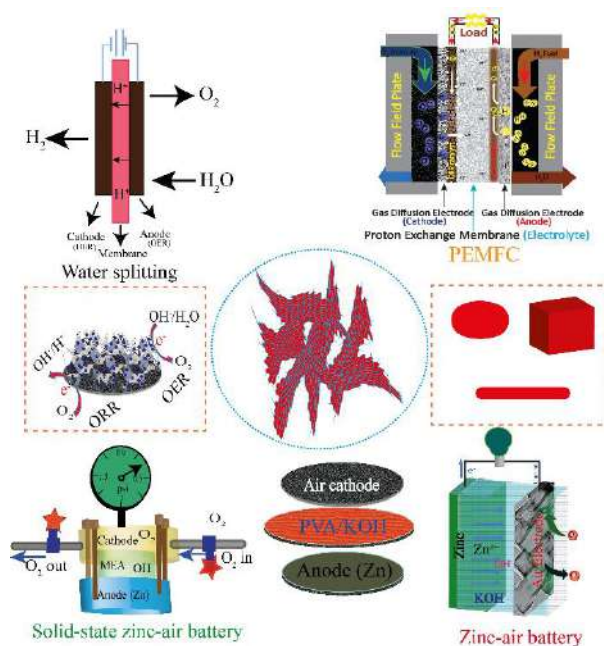
5. Summary: Chapter 6 summarises the key findings and conclusions of each working chapter of the thesis. The developed N-doped 3D graphene (NEGF) acts as a high surface area porous support for the dispersion of double hydroxides and spinel oxides. In addition, the developed microporous structure of the N-doped porous 3D graphene (pNEGF) acts as the ideal support for the dispersion of the small-sized Pt₃Co nanoparticles. Furthermore, the doped nitrogen acts as the anchoring site for the uniform dispersion of the nanoparticles. The N-doped 3D graphene exhibits mesoporosity and microporosity which significantly accelerates the mass transfer of the gaseous reactant/products. The nitrogen-doped 3D supported Pt, and Pt-free catalysts show significant performance in terms of the activity as well as durability under the optimized reaction conditions. Thus, the findings of the thesis reflect how targeted rational designing strategies can help to effectively address some of the pertinent issues associated with the existing ORR/OER electrocatalysts in terms of the performance, durability, and cost.

6. Future perspectives: Chapter-6 also covers the future scope of the thesis work, where the prospects of the materials and findings as captured in the various chapters are highlighted, considering the application potentials in the related fields.

Chapter-1

Oxygen Electrocatalysts for Electrochemical Energy Applications

This chapter briefly covers the global energy consumption scenario and the importance of the electrochemical energy devices, followed by the development of the electrocatalysts for the oxygen redox processes. This chapter includes a concise description of the structure, major components, working principles, and challenges associated with electrochemical water-splitting (WS), rechargeable zinc-air batteries (RZABs), and polymer electrolyte membrane fuel cells (PEMFCs). In continuation, the role played by the oxygen evolution reaction (OER), and the oxygen reduction reaction (ORR) in determining the overall performance of the respective electrochemical energy devices has been discussed. The effect of variation in pH on the ORR and OER processes and their respective mechanisms have also been studied. Further, a focused discussion of the RZAB by highlighting the existing challenges in the bifunctional oxygen activity (ORR/OER) at the air-electrode interface has been provided. The various strategies adopted for improving the bifunctional activity at the air cathode of RZAB are also included in this section. Moreover, a discussion on the current status of the electrocatalysts targeted for OER and ORR applications as well as for the bifunctional processes (ORR/OER) based on the noble and non-noble metal systems are included. Furthermore, the important role played by the support for the catalytic active site tuning and in the overall performance modulation has been discussed. The development of the carbon supports and their morphological importance have been discussed elaborately, followed by the role played by the heteroatom doping as well as the porosity towards the active site modulation. Afterward, the structural importance of the support and especially the three-dimensional (3D) structures of the graphitic carbon morphology are included. Following that, the prospective benefits and the drawbacks of each of these material types are discussed in detail. Finally, at the end of the thesis, the objective and scope of the current thesis are listed.



1.1. Introduction:

Globally, climate change is the central issue that the planet is facing, among the other associated problems.¹ Energy research is the major backbone to dealing with the current global issues such as global warming and environmental carbon footprint.² Currently, coal (30 %), oil (30%), and natural gas (24%) are being used as the major sources of energy in various power sectors to fulfill the global energy demand.² The worldwide increasing population and gradually changing human lifestyle in the era of industrialization demand more energy in the various sectors.³ Furthermore, the reserved fossil fuel sources cannot meet the future energy demand.² In addition, the carbon-based fuel-burning directly emits CO₂, NO₂, SO₂, etc., into the atmosphere, impacting the environment as well as the carbon footprint resulting in the global warming.³ To address these issues, carbon-neutral and efficient energy technologies are required to achieve a more sustainable society.³ Significant research progress has been made

on renewable energies (**Figure-1.1**), such as solar, wind, tidal waves, geothermal energy, and nuclear power as alternatives to the fossil fuels.²

Due to the geographical limitations hindering the commercialization of these renewable energy technologies, a proper amalgamation of the energy conversion and storage devices is required to resolve the existing issues.⁵ In this context, the electrochemical energy technologies such as water electrolyzers, fuel cells, and batteries which have the potential to replace the traditional energy systems have come to the forefront.⁵ Hydrogen (H₂) is considered as a promising carbon-neutral fuel to be used in the electrochemical technologies and can replace the carbon-based

fossil fuel energy technologies.⁶ As the Earth consists of 75 % of water, extracting hydrogen power from water can alter the clean energy scenario.⁶ Therefore, research on hydrogen production through the water-splitting process has gained considerable attention globally.⁶ Complementary to the water-splitting technology, the hydrogen fuel cell resides as a hydrogen energy-transform technology, which transforms H₂ and O₂ into the water as a clean product and produces electrical energy.⁷ Despite the many benefits of the fuel cells, batteries are a good



Figure-1.1. The major contributors of the available renewable energy sources (Reprinted with permission, Copyright © 2021 Research, Invention, and Innovation Congress: Innovation Electricals and Electronics (RI2C)).

partner for storing energy.⁷ Therefore, these three kinds of electrochemical energy technologies are mainly considered to resolve the clean energy issues.

1.2. Hydrogen Energy: Water Splitting, Fuel Cells, and Metal-air Batteries:

Hydrogen is considered as a carbon-free energy carrier to fulfill the need of future clean energy technological demand.⁶ The specific energy density of hydrogen is about 140 KJ g^{-1} , which is significantly higher than the existing fuels such as natural gas and petroleum-based products.⁵ Moreover, the increasing market share and the high price of the petroleum products also increase the demand for an alternative, cheap and sustainable solution.⁶ Although the hydrogen production rate is globally increased dramatically, 96 % of the hydrogen is being produced by the combustion of the fossil fuels.⁶ Thus, a significant amount of hydrogen produced through the steam reforming process largely contributes to CO_2 production.⁶ Therefore, the involvement of an alternative and clean way of hydrogen production is essentially needed to deal with the issues mentioned above.⁷ In the same line, the electrochemical water splitting is

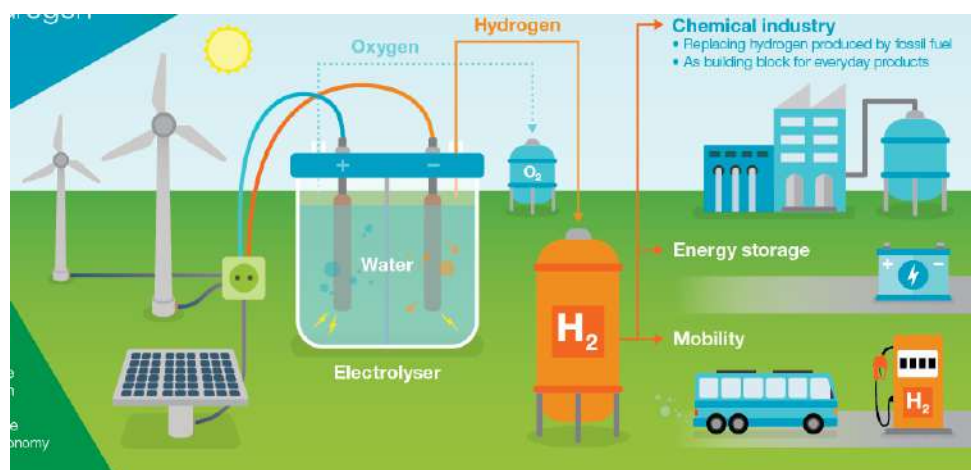


Figure-1.2. Hydrogen energy cycle involving water splitting, fuel cells, and metal-air battery (Reprinted with permission, Copyright © 2020, Elsevier, License Number: 5314871194164).

a currently growing field of research as a sustainable way of hydrogen generation that could provide an alternative solution to the climate change issues.⁴ Thus, the strategic development of an economical and efficient way of electrochemical water splitting technology for clean hydrogen production can meet the future clean energy demand.⁶ In the water-splitting device, the electrochemical redox processes occur at the cathode and the anode resulting in the production of hydrogen and oxygen, respectively.⁶ Further, in the complementary fuel cell devices, the hydrogen can be used as a green fuel, where the stored chemical energy in the

hydrogen is transformed into electrical energy.⁸ Additionally, the battery helps to store the chemical energy, and during the discharging process, that chemical energy converts into electrical energy.⁸ Hence, an effective combination of the water electrolyzer, fuel cells, and metal-air batteries can change the clean energy global market.⁸ Considering this, the focus of the thesis includes a brief description of the working principles of these energy devices; in line with this, the next part discusses the catalyst development for water splitting, PEMFCs, and metal-air batteries.

1.3. Electrochemical water splitting: The term "water splitting" refers to the chemical process in which water is split into O_2 and H_2 *via* the electrochemical redox processes. The water electrolysis is recognized as one of the most effective methods of producing clean H_2 . It utilizes renewable feedstock water and generates O_2 as a by-product in addition to H_2 . Due to the technological and economic constraints, the water electrolysis accounts for only 4% of the total

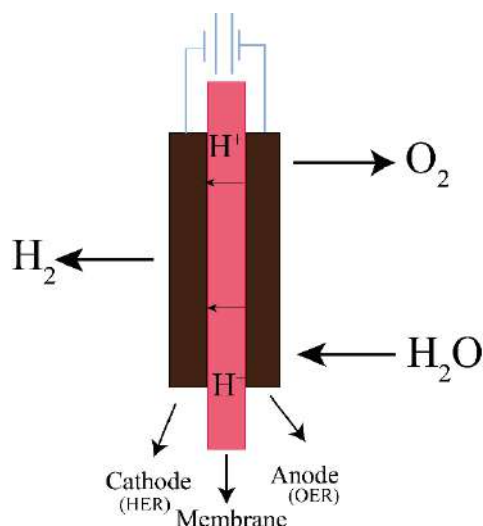


Figure 1.3. A schematic representation of the processes involved in the polymer electrolyte membrane (PEM) water electrolyzer.

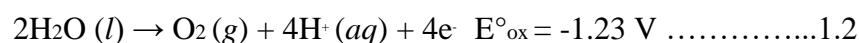
global H_2 production.⁵ The electrochemical water-splitting technology has been considered as a much more efficient process than the other water-splitting technologies available for the green hydrogen production. **Figure 1.3** illustrates a water electrolyzer consisting of an anode and cathode with the electrodes separated by a solid membrane. The electrical insulating membrane manages the ion transport between the two electrodes, separating the product gases formed during the electrochemical process.⁶ Mainly two kinds of solid membranes are being used for the electrolyzer, namely, the anion exchange membrane (AEM) and the proton exchange membrane (PEM).

1.3.1. Water splitting mechanism: The water electrolyzer is the most environmentally friendly technique for producing green H₂. The water electrolyzer is preferred over the other types of the H₂ generation technologies because of its lower operating temperature (30-80 °C), purity of the hydrogen output, and higher efficiency.⁹ Depending on the electrolytes (acidic and basic) in which the electrolysis process occurs, the water-splitting reaction can be described mainly in two ways. In acidic and alkaline electrolytes, the calculated thermodynamic potential for the electrochemical water electrolysis is 1.23 V.⁹ In reality, the potential shifts to a greater value than the calculated thermodynamic potential due to the higher potential required to overcome the activation energy barriers for the OER and HER electrode processes. The higher overpotential affects the overall efficiency of the water electrolysis process.

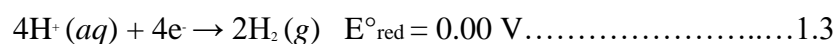
Overall reaction⁹:



Anode (water oxidation):



Cathode (water reduction):



In the PEM electrolyzer, the water electrolysis involves an external electric field passing to the anode where water dissociates through the redox process and forms O₂ and proton with the release of electrons.⁹ This electron passes to the cathode *via* the external circuit, and the proton transfers to the cathode through the proton exchange membrane, where the water molecules reduce and liberate H₂. The proton is reduced to hydrogen gas at the cathode *via* the four-electron (4e⁻) process. According to the optimum faradaic efficiency, the amount of the H₂ produced is twice that of O₂. The OER process is found to be a 4e⁻ oxidation process that occurs at a higher overpotential than the two-electron (2e⁻) process of the hydrogen evolution. Hence, the overall water splitting process efficiency depends on the OER process. To improve the water splitting efficiency in the water electrolyzer process, the overpotential for OER must be reduced. Therefore, the development of an electrocatalyst to accelerate the OER kinetics at the anode is an appropriate way to resolve the overpotential. To address the electrode overpotential, the usage of the precious materials-based OER electrocatalysts raises the overall cost of the

system. As a result, highly efficient, low-cost catalysts for OER are critical for the long-term development of the water electrolyzers for the H₂ production.

1.4. Fuel Cells: The fuel cells are electrochemical energy conversion devices that convert the stored chemical energy in a fuel into electrical energy through electrochemical reactions.¹⁰ In general, small organic molecules such as formic acid, methanol and ethanol, along with clean hydrogen are being used as the fuel in fuel cells. Sir William Grove is known as the "Father of the Fuel Cell". The fuel cells offer a lot of potential for increased energy conversion, and their ecologically friendly construction and operation make them more viable in the energy market.¹¹

Table-1.1: The classification of the different types of fuel cells (Reprinted with permission, Copyright © 2004, American Chemical Society).

		Low-Temperature Fuel Cell		High-Temperature Fuel Cell		
		Alkaline Fuel Cell (AFC)	Direct Methanol Fuel Cell (DMFC)	Polymer Electrolyte Membrane Fuel Cell (PEMFC)	PAFC Phosphoric Acid Fuel Cell	MCFC Molten Carbon Fuel Cell
Electrolyte	Caustic Potash Solution	Proton - Conducting Membrane	Proton/hydroxyl ion Conducting Membrane	Concentrated Phosphoric Acid	Molten Carbonate	Ceramic
Fuel	Hydrogen	Methanol	Hydrogen	Hydrogen	Natural gas, Coal	Natural gas, Coal
Temperature Range	<100°C	<100°C	<160°C	200°C	650°C	1000°C
Power Range	Watts/Kilowatts	Watts/Kilowatts	Watts/Kilowatts	Kilowatts	Kilowatts/Megawatts	Kilowatts/Megawatts
Applications	Outer space	Vehicles, small appliances	Vehicles, domestic supply,	Power plants, power stations	Power plants, combined heat and power	Power plants

The fuel cells are being employed in commercial, industrial, and residential structures, as well as in distant or inaccessible places, for primary and backup power applications.¹¹ They also power the hydrogen fueled vehicles such as automobiles, submarines motorcycles, boats, and buses. NASA's space projects were the first to deploy the commercial fuel cells to power satellites and space capsules.¹² The efficiency-wise, fuel cells reside in a better position than that of the combustion engines. The fuel in a fuel cell is not burnt like in an internal combustion engine. In addition, the fuel cells will not cause major greenhouse emissions. Moreover, the fuel cells have no moving parts which help to their long lifespan. The fuel cell generates power as long as the fuel and the oxidant are supplied at the anode and cathode, respectively.

The anode electrode oxidizes the fuel in the fuel cell, whereas, the cathode electrode reduces the oxidant. The electrolyte is a critical part of a fuel cell because it separates the two electrodes, cathode, and anode, to make a complete device and transports ions from one electrode to the other.¹³ There are various types of fuel cells, each with its own method of operation and electrolyte. The fundamental operation of all the fuel cells is based on the same notion, which can be easily illustrated. However, to fabricate the fuel cells for practical applications, the cost, efficiency, and dependability issues must be effectively overcome. Different types of fuel cells with varying sizes and forms are popular in this context to achieve improved efficiency. The electrolytes employed in each type of the fuel cell determine its efficiency and operating temperature. The electrolytes utilized in the fuel cells include molten carbonate, alkali, phosphoric acid, solid oxides, and polymer electrolyte membranes (PEM). The very first three electrolytes are liquids, while the last two are solids. The circulation of the electrolytes through the device in the liquid fuel cells necessitates using additional elements to manage the electrolyte movement. In comparison to the others, each form of the fuel cell has its own set of benefits and downsides. The various types of the fuel cells available are classified in **Table 1.1**. In the case of a hydrogen fuel cell, the products are only water and heat; this guarantees zero contribution to the global warming by controlling the release of any greenhouse gases into the environment.¹⁴

1.4.1. Polymer Electrolytes Membrane (PEM) Fuel Cells (PEMFCs): Polymer electrolyte membrane fuel cells (PEMFCs) are well-recognized among the various kinds of the fuel cells due to their higher output efficiency.¹⁵ Catalyst coated over the gas diffusion electrode (GDL) is used as the cathode and anode which are separated by the polymer electrolyte membrane (PEM). Depending on the nature of the ion transport and the molecular structure, the membrane can conduct proton (H^+) or hydroxyl ion (OH^-).¹⁶ The hydroxyl ion conduction is

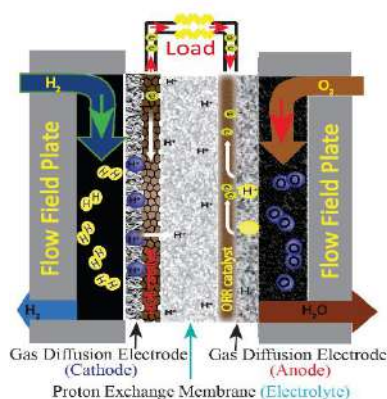


Figure 1.4. Schematic illustration of the Proton Exchange Membrane Fuel Cell (PEMFC).

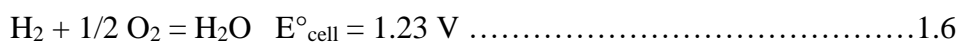
required in alkaline membrane fuel cell (AMFC) and proton ion conduction is needed in acidic membrane fuel cell (PEMFC) application. Furthermore, PEMFCs are divided into the low-temperature PEMFCs (LT-PEMFCs) and the high-temperature PEMFCs (HT-PEMFCs) based on the operating temperature. The LT-PEMFC is being considered the most suitable for the transportation purposes, which has a larger market share in the transport sector.¹⁷ **Figure 1.4** depicts a schematic illustration of the PEMFC, representing the three major parts of the fuel cell, *viz.*, the cathode, anode, and proton exchange membrane. The electrolyte plays a key function in preferentially carrying the protons generated at the anode without passing any oxygen and hydrogen molecules between the electrodes.

1.4.2. PEMFC Mechanism:

The primary reaction (HOR/ORR) of a typical PEMFC occurs at the catalyst coated electrode surface.⁵ At the anode, the hydrogen oxidizes and produces protons (H^+), which migrate to the cathode through the proton exchange membrane electrolyte.^{16,17} Because the membrane is electrically insulating, the electrons emitted during HOR at the anode travel to the cathode *via* the external circuit.



At the cathode, the 4 protons and 4 electrons react with the fuel (O_2) to produce water and electricity. Water and heat are produced as the by-products of the overall reaction.



The electrochemical ORR process occurs at a higher potential (1.23 V) than the theoretical hydrogen oxidation potential (0.0 V), making the ORR kinetics slower than HOR.¹⁷ The slow ORR kinetics is responsible for the significant loss of performance in the fuel cells. ORR occurs through a multi-electron process, so a slow electron transfer rate at the cathode leads to higher overpotential in the overall performance of PEMFCs. This limiting factor could alter by the suitable electrocatalysts design for the ORR catalysts.

1.4.3. I-V Characteristic of the Fuel Cells: Despite the ORR performance at the PEMFC cathode, the current (I) - voltage (V) polarisation plot is a critical piece of information for understanding and evaluating the fuel cell performance.^{15,18} The integral parts of

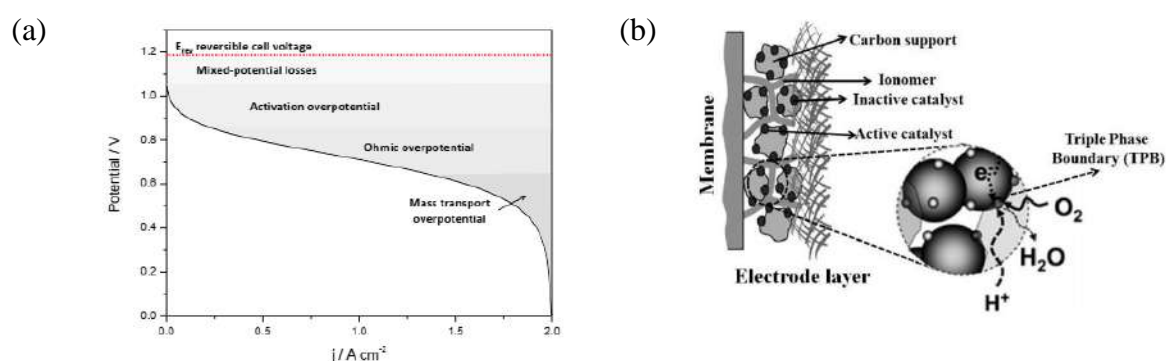


Figure 1.5. (a) A typical fuel cell current (I) – voltage (V) polarisation plot; (b) representation of the triple-phase engineered fuel cell electrode (Reprinted with permission, Copyright © 2021, Springer Nature).

the PEMFC are the current collector, porous gas diffusion electrode, gaskets, sub gaskets, an electrolyte, and bipolar plates. Each of the components plays a significant role in the overall performance of the PEMFC. The three active portions of a typical fuel cell polarization curve (**Figure 1.5a**) are as follows: 1) activation overpotential - a region that is heavily reliant on the intrinsic properties of electrocatalysts, 2) ohmic resistance polarisation and 3) mass transport resistance. The complete behavior of the polarization plot is controlled by the membrane electrode assembly (MEA) properties.^{16, 18} An MEA comprises two electrodes and a solid membrane sandwiched between them. Despite the properties of the catalysts, an MEA performance is also controlled by the other parameters such as operating temperature, oxidant partial pressure, relative humidity, etc.¹⁸ The polarisation region in which the ohmic resistance and the concentration components contribute to the mass transfer properties affects the overall performance in the polarization plot. The thermodynamic efficiency of PEMFC can be enhanced by optimizing the fuel pressure, temperature control, and water management.

However, in order to improve the PEMFC efficiency, the voltage drops caused by the ohmic, activation, and concentration overpotentials must be addressed. The cathodic side involving the ORR process has a maximum contribution to the activation polarisation. The occurrence of several sorts of internal resistance contributions in the cell is blamed for the ohmic loss. This includes resistance caused by the membrane that separates the electrodes, contact issues with the cell's components, and resistance from the electrode sides caused by the presence of electronic insulating components, such as a binder and other additives. The active centers' mass transport constraints cause the third polarisation loss. This is mostly due to the fuel and oxidant transporting at a slower rate than required on the catalyst surface. The leading cause for this is the presence of excess binders, which can block the active centers and limit the gas reactant transport to the active sites.¹⁷ Additionally, the generated water on the catalyst's surface can impede oxygen transport to the active centers. Therefore, the ORR active site tuning with the 'triple-phase-boundary' (TPB) engineering is critical for improving the accessible ORR catalytic centers of the reactant gases in PEMFCs.¹⁸ TPB is created when a catalyst, an ionomer, and the reactant gases are combined efficiently. The schematic representation of TPB is shown in **Figure 1.5b**. The proper production of the TPB formation unit balances the electron transport through the catalyst, the ionic transport through the ionomer, and the reactant gas movement at the electrodes. Typically, the catalyst ink is made by dispersing the catalyst and ionomer in the correct ratio in a certain solvent (for example, isopropyl alcohol). This would allow the ionomer to make good contact with the catalyst, allowing for more effective TPB production. Therefore, designing the ORR electrocatalysts with improved mass activity and suitable TPB formation units is an essential criterion for enhancing the overall performance of the fuel cells.

1.5. Metal-Air Battery (MAB):

As previously mentioned, the metal-air batteries (MABs) are possible energy technologies projected to play critical roles as a partner of the fuel cells in various future energy storage applications. The working principle of the MABs is the same as the fuel cells; as an alternative to the hydrogen which is used as the fuel in the fuel cell, an appropriate metal will be used as a fuel in the MABs.¹⁹ A typical MAB is shown in **Figure 1.6**, where a series of metals such as Na, K, Li, Zn, Mn, Al, etc., are being used as the anode. In the case of a rechargeable MAB (RMAB), a bifunctional (ORR/OER) active catalyst coated-gas diffusion layer (GDL) will be

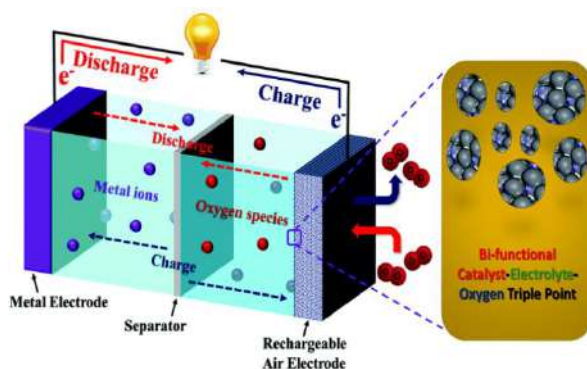


Figure 1.6. A schematic illustration of a typical metal-air battery (Reprinted with permission, Copyright © 2010 John Wiley and Sons, License Number: 5314760230016).

used as an air cathode.¹⁶ In the air-electrode, ORR and OER take place, respectively, during the discharging and charging process of the RMAB device.²⁰

Abraham *et al.* demonstrated a rechargeable Li-air battery in 1996 as the first MAB.¹⁹ The Li⁺ conducting polymer as a separator, lithium metal as an anode, and a carbon composite as a cathode were used to make the battery.²⁰ Furthermore, the work has been progressed on the other metals instead of Li, such as Na, K, etc.²¹ Since the alkali metals (Li, Na, and K) are explosive in aqueous solution, non-aqueous organic solvents/polymers have been used as the electrolytes to keep the electrodes safely connected.²¹ As evidenced by the recent reports, consistent efforts have been devoted to developing RMABs in non-aqueous systems.^{22,23} Importantly, the efficiency of a MAB depends on the oxygen electrokinetics (ORR/OER) at the air cathode.^{24,25} Poor oxygen solubility and slow kinetics of ORR/OER in non-aqueous MABs prevent the further commercialization of this alkali metal-based air battery system.^{22,23} Considering the safety and air cathode kinetics in the non-aqueous systems, the alkaline earth metal (Mg), transition metal (Zn, Fe, and Mn), and non-transition metal (Al) based anodes in the aqueous battery systems are well-considered in the MAB field.^{23,24} Among them, the Zn-

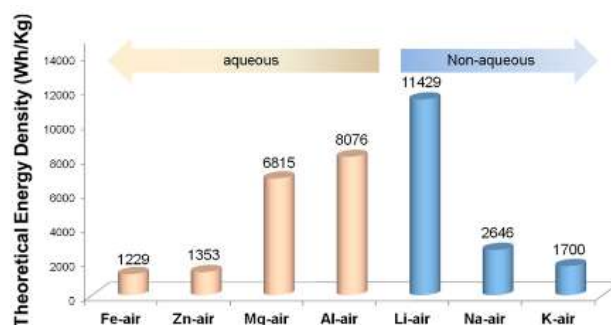


Figure 1.7. The theoretical energy densities corresponding to the different types of the metal-air batteries (MABs) (Reprinted with permission, Copyright © 2010, American Chemical Society).

air battery (ZAB) is considered a promising one, as it has high specific and gravimetric energy densities.²⁵

1.5.1. Zn-Air Battery:

In comparison to the conventional lithium-ion (250-300 Wh/kg), lead-acid (150-200 Wh/kg), and other metal-air batteries, Zn-Air batteries (ZABs) offer the highest theoretical energy density (1100 Wh/kg) (**Figure 1.7**).²⁶ Furthermore, the great natural availability of zinc, ease of mining, and nontoxicity are the considerable advantages of the ZAB systems.²⁷ The zinc electrode with a high surface area is often used as an anode in these systems to fulfill the high power requirements.²⁸ The cathode component of ZAB is necessary for highly active and durable air electrocatalysts to facilitate ORR and OER.²⁹⁻³² The basic structure of a ZAB is depicted schematically in **Figure 1.6**. It comprises an alkaline electrolyte in a liquid system or membrane as a separator in a solid system, a negative zinc electrode as an anode, and a positive air electrode as a cathode. Furthermore, based on the electrolytes (liquid/solid) and the function of the air cathode (discharging/charging), ZAB is further classified into various forms.

1.5.2. Primary ZAB (non-rechargeable): Primary ZAB consists of an air electrode coated with catalysts that only take part in the ORR process. Therefore, after the complete discharge process, the cell needs to replace with fresh catalysts. During the initial period of the ZAB development, primary ZAB devices were in general used for various purposes such as marker lights, oceanographic research, railway signals, etc.; Manganese dioxide is used in hybrid cell cathodes to enable high peak currents in primary ZAB.²

1.5.3. Mechanical rechargeable ZAB: Based on the demand for the rechargeable ZAB, the primary ZAB was mechanically researched for various applications by replacing the Zn anode. During the discharge process, the Zn anode has more chances of oxidation and forming ZnO surface layer, which inhibits the further discharge process. Therefore, by using the air cathode with higher durability, and also by mechanically changing the anode (Zn) and electrolyte, the primary ZAB can be effectively converted into a mechanically rechargeable ZAB system.³⁷

1.5.4. Secondary ZAB (Rechargeable): Although mechanical rechargeable ZAB is widely applied to various stationary applications, it is quite tricky for compact cell fabrication. Therefore, RZAB fabrication with a bifunctional oxygen catalyst (ORR and OER) coated with a gas diffusion layer (GDL) is considered an advanced solution to fabricate an electrically

rechargeable ZAB. A sound electrically recharged system could have a low material cost and higher specific energy.²⁸

1.5.5. liquid-state-ZAB: For stationary applications with a larger power unit, utilizing a liquid-state ZAB has an ample opportunity as it is quite simple to assemble. In a liquid-state ZAB, a zinc foil will be used as an anode with the catalyst-coated GDL as the cathode, and these will be dipped into a concentrated alkaline (KOH) solution. Although it has great advantages in terms of ease in fabrication and cost, it has significant disadvantages as well. The water-based electrolyte that catalyzes the zinc precipitation must be carefully managed in the RZAB based on an aqueous electrolyte. Dendrite production and limited solubility of oxygen in high concentrated electrolytes challenge the liquid-state ZAB system.²⁹

1.5.6. Solid-state rechargeable ZAB: The application of the solid-state batteries in various sectors is gradually increasing. Most importantly, the transport sector is looking for devices that will be free of liquid systems.³⁰ Keeping this in mind, work on the solid-state RZABs significantly progressed. In this system, the zinc serves as the anode, an ORR/OER bifunctional catalyst-coated GDL acts as the cathode, and a gel electrolyte serves both as the solid electrolyte and separator for the two electrodes.³¹ The gel electrolyte has a significant role in fabricating a solid-state ZAB system to keep the system hydrated.³² Additionally, the designing of the ORR and OER catalysts and their electrodes with effective “triple-phase boundary (TPB)” formation at the air cathode interface of the RZAB is an important part of the research.³²⁻³⁶ Details of the rechargeable ZAB mechanism are given below.

1.5.7. Mechanism in RZAB overall reaction:

The performance of a RZAB directly depends on the bifunctional oxygen redox activity (ORR and OER) at the air-electrode.³² In the ZAB, during the discharge process, the atmospheric oxygen diffuses into the porous cathode where the ORR catalyst promotes oxygen reduction to hydroxyl ion (OH⁻) formation in the alkaline condition. The generated OH⁻ ions at the cathode migrate to the anode and react with Zn to form Zn(OH)₄²⁻, which further transformed to ZnO. The overall reaction of ZAB during the discharge process involves the reaction of zinc with O₂ to form ZnO.³⁴

Discharge:

Cathode: $O_2 + 2H_2O + 4e^- \rightarrow 4OH^-$ 1.7



Recharge:

Anode:



Cathode:



During the charging, ZnO dissociates through the electrochemical process and forms Zn and O₂. So, the overall process of Zn-air battery efficiency depends on ORR at the time of the discharging cycle and OER at the time of the charging process at the air cathode.³⁶

1.5.8. Bifunctional oxygen activity at the ZAB air-cathode interface: Above stated equations indicate that the efficiency of RZAB is controlled by the ORR/OER kinetics at the air cathode.³²⁻³⁶ The rechargeable ability of ZAB is hindered by the irreversibility of the stable ZnO formed at the anode during the discharge process.³³ Therefore, a higher charging voltage is required to electrically decompose the ZnO, which suppresses the energy efficiency of ZAB significantly. Additionally, the mass transfer properties of the catalysts significantly affect the overall performance of RZAB.³⁵ Hence, to overcome the ORR and OER kinetics at the RZAB air cathode, suitable designing of OER/ORR catalyst, as well as air cathode interface engineering with improved mass transfer properties, is essentially needed. The active bifunctional catalyst

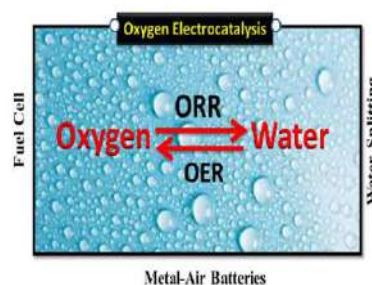


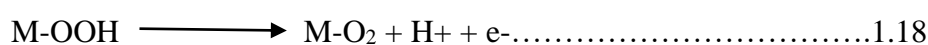
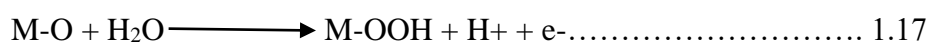
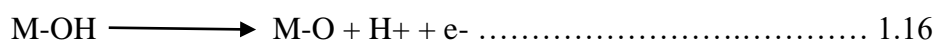
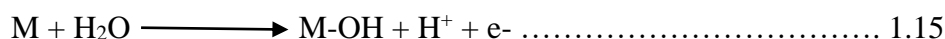
Figure-1.8. The figure shows the relevance of oxygen electrochemistry in the potential green energy-related technologies (Reprinted with permission, Copyright © 2010, John Wiley and Sons, License Number: 5314760230016).

(ORR/OER) having an effective triple-phase boundary (TPB) unit helps to make a better interface with the air cathode.³²⁻³⁶

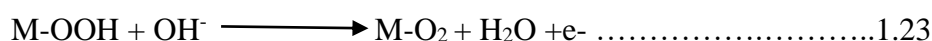
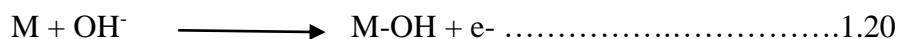
1.6. Oxygen Electrochemistry (ORR & OER): The efficiency of the above-mentioned electrochemical energy devices (water splitting, PEMFC and RZAB) is controlled by either OER (water splitting), ORR (PEMFC), or both ORR and OER (Rechargeable ZAB) (**Figure 1.8**). A slow oxygen electro kinetics suppresses the overall efficiency of the respective device performance. Therefore, the oxygen electrokinetics is the rate-determining step in measuring the overall device performance. Hence, the ORR and OER processes involve several elementary steps; it generally proceeds through the $4e^-/4H^+$ process. One is bond breaking (ORR), and the other is the bond-making (OER) process.^{35,35} Details about the ORR and OER processes and their elementary steps are explained below.

1.6.1. Oxygen Evolution Reaction (OER): OER is an important electrochemical reaction at the anode of the water-splitting process and in the zinc-air battery air cathode charging process. In both the systems, the reaction occurs on the surface of the electrocatalyst through a multistep $4e^-$ redox reaction.^{6,36} Depending on the electrolytes, the OER process goes through various stages are given below:

Acidic media:



Alkaline media:





Therefore, designing a suitable electrocatalyst with multiple adsorption sites for the various

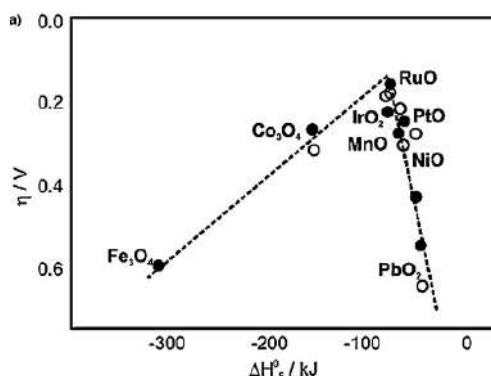


Figure 1.9. The oxygen evolution reaction activity as a function of the oxygen binding energy is depicted in a volcano graphic (Reprinted with permission Copyright © 2013, John Wiley and Sons, License Number: 5314761062922).

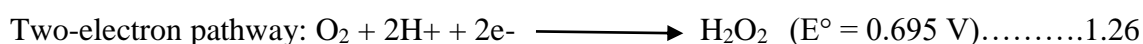
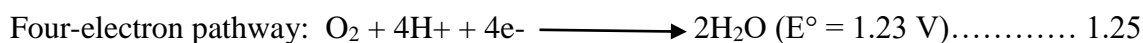
intermediates species is essential to control the electrochemical OER process.

1.6.2. State-of-the-art OER catalysts: Electrochemical OER is a $4e^-$ redox process that occurs on the metal surface through the adsorption and desorption process of the reactants, products, and various intermediates.³⁸ Figure 1.9 presented a volcano plot for the OER active catalyst. The figure shows that RuO_2 and IrO_2 reside on the top of the plot and ascribe to a lower overpotential for OER with optimum adsorption and desorption energy compared to the other transition metal oxides.³⁹ In acidic and alkaline mediums, the precious-group metal-based catalysts, such as IrO_2 and RuO_2 , are currently the benchmark catalysts for ORR and OER.³⁹⁻⁴⁴ However, researchers are working to produce low-cost electrocatalysts based on easily available active materials for scale-up applications because of their high cost and scarcity. As a result, developing a non-precious metal-based OER catalyst for water electrolysis and ZAB applications is very much desirable.

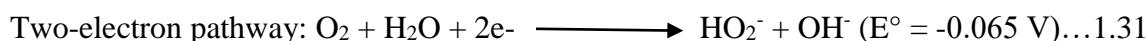
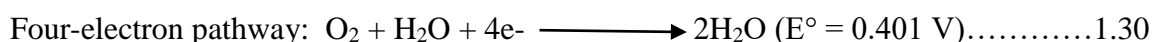
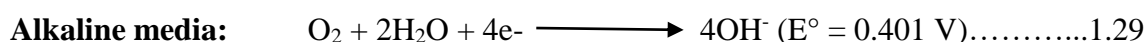
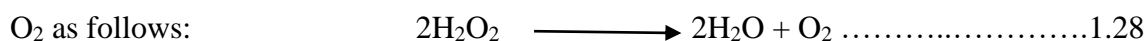
1.6.3. Oxygen Reduction Reaction (ORR): ORR is the important reaction that occurs at the cathode of PEMFC and the charging process of RZAB air cathode in acidic and alkaline conditions, respectively.^{8, 45} The electrochemical ORR process in the acidic as well as in basic medium goes through the $4e^-$ and $2e^-$ processes: 1) The $4e^-$ path, in which the oxygen molecule is reduced straight to H_2O , and 2) the $(2+2)e^-$ path, in which the O_2 molecule is reduced first to H_2O_2 and then to H_2O .⁴⁰ The reaction route is thought to be determined by the type of the

active site and the mode of interaction of the O₂ molecule with the active site.⁴⁶⁻⁴⁸ The ORR is deficient in the 2e⁻ route, which reduces the overall efficiency. Furthermore, the H₂O₂ produced poses a stability problem in the catalyst and membrane.

Acidic media:



The alternate decomposition of the H₂O₂ produced in (1.26) leads to the formation of H₂O and



The ORR process is kinetically slow due to high thermodynamic reduction potential around 1.23 V.⁶ The sluggish kinetics of ORR is attributed to the higher binding energy of the O=O bond (498 kJ/mol) that must be cleaved at lower potential during the ORR reaction.⁴⁸ To improve the kinetics of ORR, the activation energy of the reaction should be reduced.⁴⁹ The activation energy of ORR can be reduced by designing the electrocatalysts and by reducing the electrode potential.⁵⁶ The potential difference between the electrode (E) and the equilibrium (E_{eq}, 1.23 V for the ORR) of a reaction is known as the overpotential η (Equation 1.3).⁴⁹

$$\eta = E - E_{\text{eq}} \dots\dots\dots 1.33$$

A suitable catalyst design for the ORR process is targeted to lower the overpotential, which will improve the overall efficiency.

1.6.4. State-of-the-art ORR catalysts:

The higher binding energy of oxygen molecules requires electrocatalytic active sites to break the O=O bond. Currently, Pt-supported carbon is the best active catalyst for the electrochemical

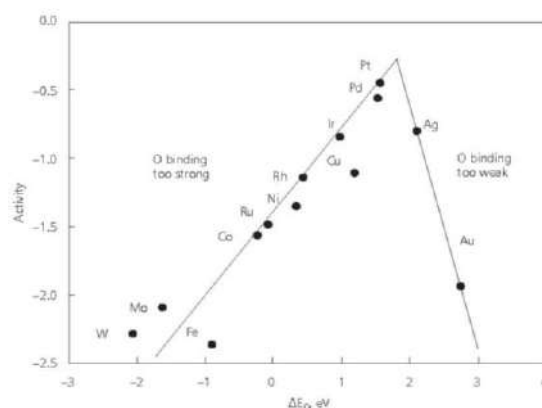
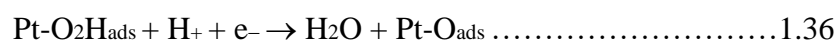


Figure 1.10. The volcano plot indicating the oxygen reduction activity as a function of oxygen binding energy (Reprinted with permission Copyright © 2013, John Wiley and Sons, License Number 5314761062922).

ORR process.⁵⁰ **Figure 1.10** displays the volcano plot, suggesting a theoretical calculation of the ORR activity vs. the adsorption-desorption energy (ΔE_0) of oxygen over the range of metal centers. Among the other metal active sites, Pt resides on the higher active sites of the volcano plot with an optimum value of the adsorption-desorption energy compared to the other noble and non-noble metal-based systems.⁵¹ It is also noted that the other noble metal-based systems (e.g., Pd, Ir, Cu, Ag) lie almost near to the Pt in the volcano plot. Further, the evidence-based studies suggested that the ORR process on the Pt surface occurs in two ways, one is the associative, and another is the dissociative mechanism. Hence, the mechanism reveals that the ORR process goes through several intermediate steps; the different intermediates have a set of thermodynamic energy of adsorption and desorption.⁵² Although Pt is the best active catalyst for ORR, the Pt-based electrocatalysts still suffer from a large overpotential of about 230 mV (corresponding to an electrode potential of about 1.0 V).⁵² Furthermore, scarcity and the high cost of Pt forced us to focus on reducing the Pt loading in the fuel cell cathodes.

Associative mechanism



Dissociative mechanism

1.6.5. Bifunctional active sites for ORR and OER: The performance of the RZAB depends on the bifunctional oxygen electrochemistry (ORR and OER) at the air cathode.³¹⁻³³ Although noble metal-based catalysts are used as an active site for ORR (Pt), and OER (IrO₂ and RuO₂),

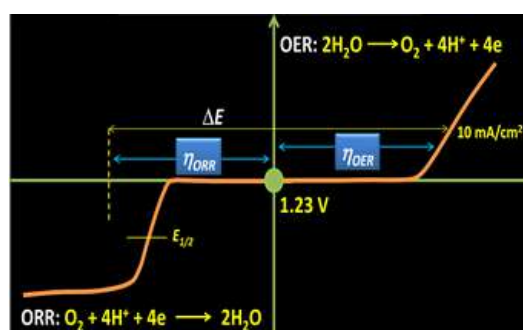


Figure-1.11. The plot representing the bifunctional oxygen redox activity as a function of the potential (Reprinted with permission, Copyright © 2019, John Wiley and Sons, License Number: 5314761402335).

they make a poor choice as the bifunctional electrocatalysts due to their high selectivity for a particular reaction (ORR or OER).^{40,41,51} An ideal bifunctional catalyst should have better ORR and OER activity.^{30,31} The bifunctional activity of the catalysts is measured with the energy difference (ΔE) between the potential reaching the current density of 10 mA cm^{-2} for the OER process and the half-wave ($E_{1/2}$) potential for the ORR process (**Figure 1.11**). The lower gap ΔE value signifies the higher efficiency of the bifunctional activity of the electrocatalyst. As per the literature report, the non-noble metal-based transition metal systems are widely reported as bifunctional oxygen electrocatalysts.

1.7. Fundamentals of the Catalytically Active Site Designing for ORR and OER: The catalysts are the substrates, which alter the kinetics of the chemical reactions by changing the chemical reaction pathway. The ORR and OER processes both occur on the surface of the electrode in water splitting; similarly, RZAB and PEMFC require the catalysts to accelerate the respective electrochemical processes. Several factors influence the ORR and OER reaction kinetics, such as adsorption of the reactant (O_2/OH^-) on the catalyst, structure, bonding nature,

and energy barrier. Hence, the adsorption/desorption characteristics and the nature of the chemical reaction (disproportionation) play important roles in the oxygen redox processes. As the ORR and OER processes go through several intermediate steps which are sensitive to the surface properties, modulation of the catalysts' surface to tune the ORR/OER active sites is an important area of research. To design the electrocatalysts, mostly two strategies are being adopted as shown in **Figure 1.12**.⁵² One is increasing the intrinsic activity by controlling the structure, morphology, and composition of the electrocatalyst's active sites. Another is increasing the number of the active sites with the help of the support structures and morphology-control along with the modulation of the active site's shape, size, and composition. As increasing the intrinsic activity of the active sites has a drawback for large-scale productions with a greater reproducibility, the second method of increasing the number of the active sites is widely being considered a practically feasible option. In the same way, lots of work has been done previously to control the structure, morphology, and surface property tuning of the active sites and support systems to improve the electrochemical ORR and OER processes. Accordingly, the work has been progressed on the noble and non-noble metal systems following the above-mentioned strategies to enhance the ORR and OER performance and durability. The following few sections in this chapter will discuss the progress made in the direction of the catalyst design, mainly targeted on the noble metal and non-noble metal-based systems for the ORR and OER applications.⁵² These include the Pt-based alloys and the low-cost, non-noble metal-based catalysts, such as transition metal-based oxides, hydroxides, and layered double hydroxide-based systems. Moreover, the issues with the low conductivity and long-term durability are further addressed by using suitable carbon supports. Hence, the progress made in the direction of shape, size, morphology, and compositional tuning of the active sites, and carbon support morphology modulation are also briefly discussed.

1.7.1. Noble Metal-based Catalysts: The above discussion and the volcano plot reveal that Pt is the best active catalyst for the electrochemical ORR. Similarly, the Ir and Ru-based catalysts are studied for the OER reaction.^{31,51} Furthermore, their utility is limited due to several reasons such as cost, availability, and stability. However, the use of the noble metal catalysts cannot be completely avoided due to the absence of alternative non-noble metal-based catalysts which are active and stable in acidic conditions. Therefore, a significant effort is still being given to the development of low-cost and durable electrocatalysts based on Pt by adopting strategies

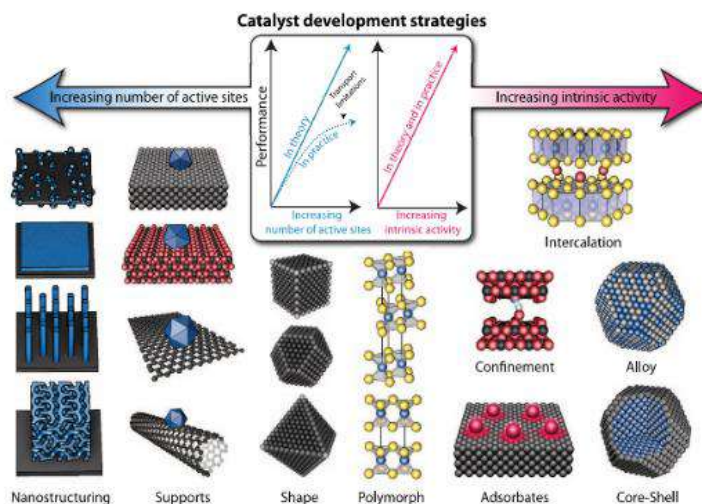


Figure 1.12. The figure indicating the various design strategies involved in developing the electrocatalysts (Reprinted with permission, Copyright © 2017, Science).

such as alloying and core-shell structuring of Pt with suitable non-noble metal transition metal systems.

1.7.2. Pt-Based Catalysts for ORR: In the last few decades, much research has been done on the development of various Pt-alloy-based and core-shell structured catalysts to improve the ORR activity and durability.⁵³ The alloying of Pt with non-noble transition metals (Fe, Co, Ni) enhances the stability of the Pt-based catalysts by avoiding the metal dissolution and oxide formation on the surface of Pt under the electrochemical environments. Furthermore, the studies reveal the relationship between the electronic structure modification after the Pt-alloy formation with the non-noble transition metals with a corresponding activity enhancement towards ORR. When Pt is alloyed with non-noble metal-based transition metals, the 5d orbital vacancy of the Pt changes due to charge transfer from the electron-rich transition metal, resulting in a decrease in the Pt-Pt interatomic distance.⁵⁴⁻⁵⁶ The Pt atoms with increased d-band vacancy have more ability to accept the 2p electrons donated by O₂, resulting in effective adsorption of the O₂ molecule over the Pt surface. The lattice re-construction in the alloy provides improved oxygen adsorption sites which significantly accelerates the ORR reaction kinetics.⁵⁷⁻⁵⁹ Furthermore, the Pt-alloy structure with various compositions also substantially changes the ORR activity. In a report by Stamenkovic *et al.*⁶⁰, the Pt-Co/C, Pt-Cr/C, and Pt-Fe/C type bimetallic catalysts are active toward ORR. Among these, the Pt-Co/C system is found to be more ORR active than the Pt-Fe/C and Pt-Cr/C systems. This result suggested that the choice of the transition metal for the alloy formation as well as the reaction condition has

an impact on the ORR activity. Moreover, the specific composition in the alloy also significantly affects the overall ORR activity. The same research group also investigated various Pt₃M alloys (M = Fe, Co, Ni, V, and Ti) for ORR with skeleton and skin structures.⁶¹ The Pt skeleton structure shows different activity than the Pt skin structure in the prepared alloy

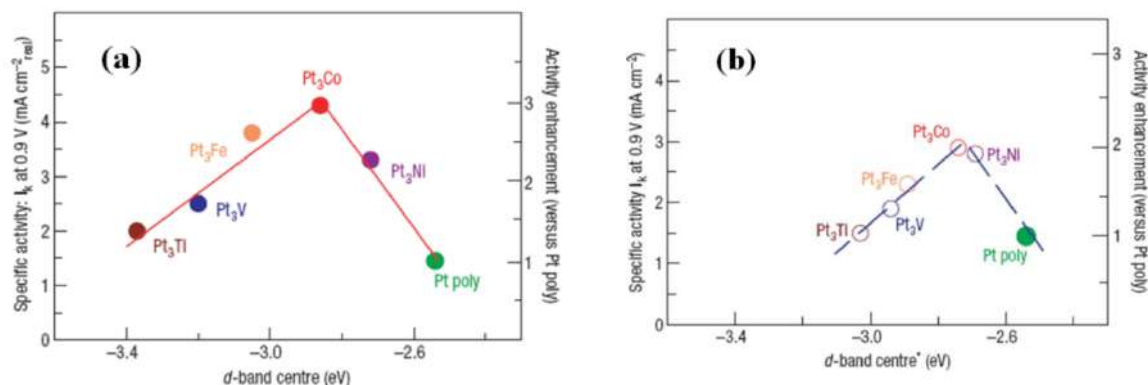


Figure 1.13. Comparable ORR specific activity of catalysts in 0.1 M HClO₄ solution, with changing the d-spacing with various transition metals in platinum alloy structure: (a) Pt-skin and (b) Pt-skeleton surface (Reprinted with permission Copyright © 2007, Nature, License Number: 5314830032578).

catalyst systems. Pt₃Co skin structure of the alloy exhibits approximately three times higher ORR activity than Pt (**Figure 1.13a-b**). These findings suggested that, to obtain an improved ORR active catalyst, the adsorption and desorption energies of the ORR reaction intermediate species on the Pt surface should be balanced against the surface coverage of the blocking oxygenated species. In addition, the carbon substrate acts as a support to overcome the particle agglomeration during the electrochemical performance measurement. However, the highly corrosive operating environment of PEMFCs catalyzes the carbon support corrosion, which results in the agglomeration of the Pt nanoparticles. Therefore, the ORR catalytic activity decreases with time, which significantly affects the overall ORR performance in the PEMFC device. An alternative carbon supporting material is required to meet this problem, having higher resistance to corrosion in the PEMFC environment.

1.7.3. Non-Noble Metal-based Electrocatalysts: The noble metal-based catalysts are active materials for ORR and OER, but their utility is limited due to many reasons such as cost, availability, and stability. Considering this fact, several non-noble transition metals, including Fe, Co, Mn, Ni, Cu, and Cr, have been investigated as potential active centers as an alternative to the noble metal-based ORR and OER electrocatalysts in alkaline conditions.^{46,49} The next

part of the thesis will include a discussion on the progress made in the development of the noble metal-free catalysts, mainly based on transition metal oxides, hydroxides, and layer double hydroxides towards ORR and OER.

1.7.4. Transition metal oxides (TMO), Hydroxide, and Layered double hydroxide (LDH):

Transition metal oxides, hydroxides, and layered double hydroxides have gained considerable attention as non-noble metal-based electrocatalysts due to their low cost, ease in synthesis, and sufficient durability.⁶²⁻⁶⁵ Furthermore, the size, shape, and morphological tuning of such catalyst systems could modulate the ORR, OER, or the bifunctional activity (ORR and OER).⁶⁶ Several reports on the ORR and OER activity catalysts have been published to date, focusing on the transition metal-based electrocatalysts (e.g., nickel, cobalt, manganese, and iron), including single transition metal oxides, metal (oxy) hydroxides, and double-layer hybrids.⁶² The next part of this thesis focuses on providing a discussion on the various strategies adopted for enhancing the catalytic activities by controlling the structural aspects and compositions.⁶⁶ Even though the benefits of the transition metal oxides, hydroxides, and layered double hydroxides have been explored for ORR and OER in alkaline solution, these materials suffer from poor electronic conductivity. Hence, compositing these materials with nano carbons as substrates is a smart and effective way of overcoming the limitation related to conductivity.

1.7.5. Structure, Composition, and Morphology Controlled oxides, hydroxides, and LDH:

The current research on the metal oxides, hydroxides, and LDHs mainly focuses on tuning the intrinsic activity with modulation in the structure, morphology, and composition.⁶⁶ Among the various structures of the oxides reported such as spinel oxides, perovskite, and rutile structure of oxides, the spinel oxides have been mostly explored for the ORR and OER applications. Similarly, the hydroxides and LDHs have emerged as potential candidates with the unique structure of the hydroxides making them useful as multifunctional materials. They are easy to synthesize, and their 2D lamellar open interlayer structure significantly contributes to the interlayer ion exchangeability. Furthermore, engineering the nanostructure morphology (e.g., nanostructure or pore structure) of the metal oxides, hydroxides, and LDH for ORR and OER helps to control the intrinsic activity for improving the electrocatalytic performance based on efficiency and durability. In some cases, the nanostructured catalysts are suitably combined with other transition metals, and thus formed binary or ternary metal composites are found to possess significantly improved catalytic performance compared to the single metal counterparts.⁶⁷⁻⁷¹ The next section of the thesis includes a brief review of the role of the possible

systems that can be explored as cost-effective alternative catalysts for ORR and OER applications.

1.7.6. Transition Metal oxides (TMO): Although electrons always fill the s-shells of the positive metallic ions, the d-shells may not be filled in transition-metal oxides (TMOs). This unique electronic structure of the metal oxides brings various characteristic properties, including high dielectric constants, a wide range of tunable bandgaps, good electrical characteristics, etc.⁶⁴ Additionally, the bandgap and electronic structure-activity of the TMO could be tuned by controlling the shape, size, and composition, which further significantly alter their chemical and physical properties.²⁸ In addition, TMOs possess various electronic states that act in a ferromagnetic, ferrimagnetic, and semiconductive nature. Hence, the oxides of the transition metals are being considered as fascinating functional materials. Furthermore, the poor conductivity of the metal oxides could be overcome by using a conductive carbon support for their dispersion.⁶⁷ The earth-abundant elements (Mn, Ni, Co, Ti, Mo, and so on) form the most common oxides, such as Co_3O_4 , CoO , and MnO_2 , which have been extensively studied as excellent candidates for ORR applications.⁶⁴ Several strategies have been adopted in recent times for the development of the TMO-based electrocatalysts for ORR applications in alkaline media.

1.7.7. Spinel oxides: Based on the current advancement of metal oxide structures, the spinel structure of the metal oxides has special attention due to its better electronic properties in the presence of the different oxidation states of the metal centers.⁶⁵⁻⁶⁸ The spinel oxides have attracted attention towards oxygen electrocatalysis due to their ease of synthesis, low cost, and tuneable composition. The general formula for the spinel-type metal oxides is AB_2O_4 , where A represents a transition metal ion having the +2 oxidation state which resides in a tetrahedral site and B is a transition metal ion having the +3 oxidation state residing in an octahedral site.⁶⁸⁻⁷⁰ In a spinel oxide structure, A and B sites are occupied by the same element (e.g., Co_3O_4), or they can be occupied by different elements (e.g., MnCo_2O_4).⁷¹⁻⁷⁵ The spinel oxides have displayed interesting electrochemical activity and durability in alkaline media.

1.7.8. Transition Metal (oxy) hydroxides (TMH): The transition metal (oxy) hydroxides (TMH) are considered to be a promising active material for electrochemical OER applications. TMH are low-cost materials with larger specific surface area, significant stability in alkaline media, and distinct electron distribution. Even though research on TMH has been well progressed, so far it is known to be displaying promising OER activity in alkaline media.³⁶

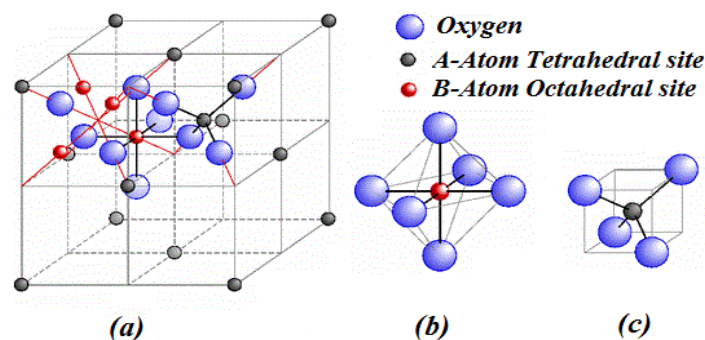


Figure 1.14. The figure representing the structure of the spinel oxide and the distribution of the A and B cations in the system (Reprinted with permission, Copyright © 2020, Springer Nature, License Number: 5314830455417).

Furthermore, the OER activity gets enhanced by incorporating species such as Fe, Co, Ni, or Cu in the system. However, the main concern of adopting this strategy is the long-term stability of these binary metal centers in water splitting devices with high concentrated pH conditions. Therefore, further research has been carried out on TMH by compositing with carbon supports, which improves the conductivity, resulting in improved performance in terms of activity as well as durably.

1.7.9. Layered double hydroxides (LDH): LDHs are the class of 2D materials, consisting of a layer structure where two positively charged brucite-like host layers are sandwiched by anions and solvent molecules (**Figure 1.15**), where the anions balance the excess positive charge. The brucite layers in LDHs are composed of bivalent metal cations (such as Co^{2+} , Ni^{2+} , Zn^{2+} , and Fe^{2+}) with a percentage of the metal ions substituted by isomorphous trivalent metal cations (such as Fe^{3+} , Al^{3+} , Mn^{3+} , or Ga^{3+}).^{62,63} In the MO_6 configuration, all of these metal ions are octahedrally coordinated by hydroxyl groups. In the presence of the trivalent metal cations, the layer structure of the hydroxide acquires an extra positive charge. To balance this excess positive charge, several inorganic or organic anions (e.g., CO_3^{2-} , Cl , NO_3 ,

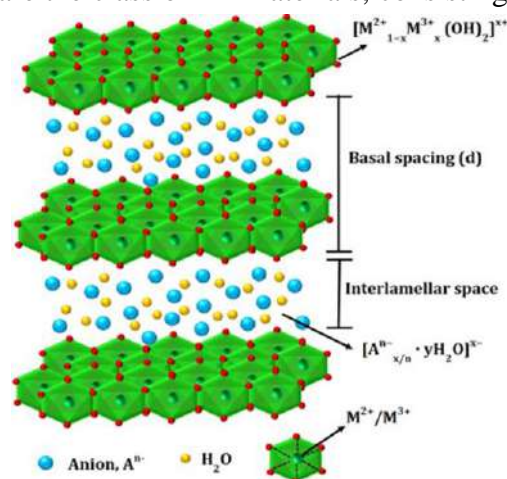


Figure 1.15. Structure of the layered double hydroxide (LDH) (Reprinted with permission, Copyright © 2021, Multidisciplinary Digital Publishing Institute).

and SO_4^{2-}) are instantly intercalated. Thus, a standard molecular formula of LDH is $[\text{M}_{2+1}^x\text{M}_{3+x}(\text{OH})_2][\text{A}_n]_x/nz\text{H}_2\text{O}$, where M^{2+} and M^{3+} denote the divalent and trivalent metal cations, respectively, A_n denotes the filled interlayer anions, and x represents the range of 0.2 to 0.4. It is worth noting that LDHs can also comprise M^+ and M^{4+} cations. The special structural features of LDH resulted in the unique ability to display OER type electrocatalytic activity. Among the various LDHs reported, the NiFe-based LDHs are well-known for their OER activity in the electrochemical water-splitting applications.

1.7.10. Role of Carbon Nano-Structures: Although the active site modulation (spinel oxides, LDH, alloy structure) is showing improved OER and ORR performance, in most cases, the active sites are decorated on a variety

of carbon support morphologies. The selection of the carbon morphology significantly affects the overall activity and durability of the electrocatalysts.⁷⁶⁻⁸⁰ High electrical conductivity is one of the most notable features of the carbon. They are used for various applications due to their mechanical stability and distinctive morphological properties. Carbon is the building block of the organic chemistry family. Various allotropes of carbon, such as graphite, fullerenes, and carbon nanotubes have gained significant attention in various fields

of applications.⁷⁷ The discovery of Buckminster fullerenes and one-dimensional carbon nanotubes (CNTs) shows a new direction in the research of carbon-based nanomaterials. Furthermore, the discovery of graphene (Gr), which is a single layer of graphite, has gained significant progress in the energy-based technology research. Moreover, the nanostructures of carbon with distinctive surface modification and morphological tuning with controlled electrical, optical, and mechanical features are considered to be very effective in improving the energy conversion and storage characteristics. Moreover, the unique properties of fullerenes, graphene, and carbon nanotubes (CNTs) gained significant attention in the field of developing

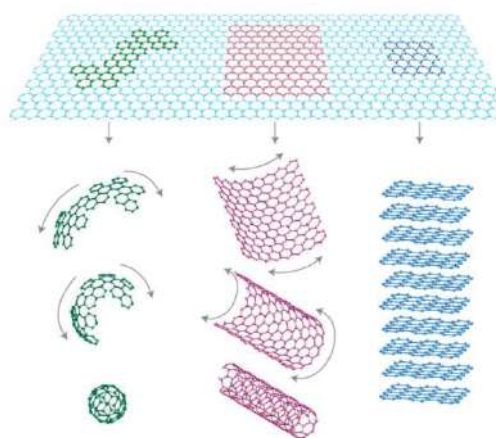


Figure 1.16. The figure highlights the importance of graphene as the mother of all the other graphitic forms of carbon, including the 0D fullerene, 1D SWCNT, and 3D graphite. (Reprinted with permission, Copyright © 2018, John Wiley and Sons, License Number: 5314831024409).

high-performance energy conversion and storage devices.⁷⁸ The next part will discuss more on the specific forms of the nanocarbons which have gained ample space in the development of electrocatalysts for energy applications.

1.7.11. Fullerenes: The discovery of fullerene is widely regarded as a watershed moment in materials chemistry. Fullerene is made up of sixty (C_{60}) or seventy (C_{70}) carbon atoms bonded



Figure 1.17. The pictorial representation of the buckminsterfullerene (Reprinted with permission, Copyright © 2012, John Wiley and Sons, License Number: 5314780410622).

together in pentagons and hexagons to form spherical cages that resemble the soccer ball patches (**Figure 1.17**). There have been several attempts to utilize fullerenes as an advanced carbon material for extending their utility in the energy storage and conversion device applications. With ultra-low Pt loading, metallofullerenes have been proposed as suitable ORR catalysts for the fuel cell applications. Fullerene-Pt nanoparticle assemblies were also attempted, which were formed by joining and separating fullerene and Pt nanoparticles.⁷⁸ Using molecular layers of C_{60} as a linker system, various Pt nanoparticles were immobilized on a gold electrode. Following CO treatment, these assemblies were active for methanol oxidation.

1.7.12. Carbon Nanotubes (CNTs): After Iijima's ground-breaking breakthrough in 1991 with the discovery of the needle-like tubes of carbon known as carbon nanotubes (CNTs), the material chemistry world has taken on a new shape. CNTs drew the attention of many researchers due to their unique electrochemical capabilities. CNTs are classified based on the Number of layers arranged in the tubular form, which are single-walled carbon nanotubes (SWCNTs) and multi-walled carbon nanotubes (MWCNTs).⁷⁸ CNT has emerged as a promising support material for lowering the amount of Pt in the Pt-based catalysts for the fuel cell applications. Furthermore, doping of heteroatoms into the carbon structure of CNTs (*i.e.*,

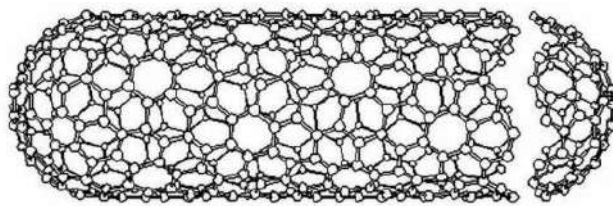


Figure 1.18. The representation of the structure of the carbon nanotube (Reprinted with permission, Copyright © 2012, John Wiley and Sons, License Number: 5314780410622).

N, B, and P) has recently been used to substitute Pt and to explore the possibilities of developing non-Pt electrocatalysts for fuel cells.⁷⁸ The helicity and diameter of the CNTs are commonly acknowledged as the controlling criteria for both the metallic and semiconducting properties. CNTs have a hollow core, which is intriguing, as are their unusual metallic and semiconducting properties. CNTs are also resistant to the formation of complexes.

1.7.13. Graphene: Graphene is the latest member of the carbon family. Graphene has the 2D structure of single-atom-thick carbon nanosheets and has been considered as an important class of materials used for various applications, including energy conversion and storage technologies. Graphene is a honeycomb crystal structure made up of the sp^2 -bonded one-atom-thick planar sheets of carbon atoms.⁷⁹ In 2004, Konstantin Novoselov and Andre Geim

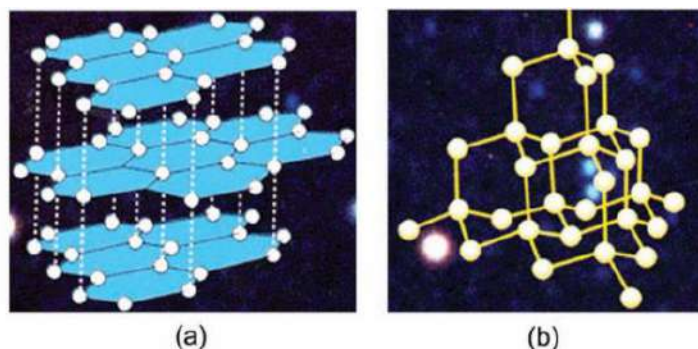


Figure 1.19. The structural representations of the graphene (Reprinted with permission, Copyright © 2012, John Wiley and Sons, License Number: 5314780410622).

developed graphene by continuously dividing graphite crystals into smaller and smaller parts with sticky tape until individual atomic planes were created. In 2010, they received the Nobel Prize in Physics.⁸⁰ Afterward, the research on graphene has gradually increased. As previously stated, graphene is the latest carbon allotrope to be recognized as the most exciting chemical in the field of energy research. **Figure 1.19** shows the 2D structure of the graphene consisting of more than one layer. The electrical properties of graphene are derived from its electronic

configuration. Graphene has high stretchability, making it excellent for flexible conductors. Moreover, the increased surface area originated from the 2D structure of graphene, compared to the other carbon morphologies, as well as high electronic conductivity makes it an interesting carbon support material for the ORR and OER applications.⁸⁰ Furthermore, heteroatom doping into graphene is found to be altering its electrical properties. The graphene-based products generally have significantly improved electrochemically active surface area due to the intrinsically high surface area of the substrate and better exposure of the active sites.

1.7.14. Heteroatom doped graphene: Graphene is a 2-dimensional (2D) sheet of carbon network, where most of the carbon is connected through the symmetric sp^2 carbon centers. Doping graphene with a heteroatom creates a difference in the electronegativity and this leads to a positive charge density on the neighboring carbon atoms.⁸⁰ The heteroatom doped asymmetric carbon centers are helpful to the growth of the active sites as well as for facilitating chemisorption of the reactants and intermediates during the electrochemical processes. The graphitic materials doped with nitrogen have recently made a massive impact in the world of energy applications. The doping of the foreign atoms modifies the host's basic electrical and mechanical properties, making them ideal catalysts for the energy applications. **Figure 1.20** shows that, among the various doped heteroatoms, the doping with nitrogen considerably changes the electronic properties of the graphitic carbon system. Furthermore, based on spectroscopic investigation, the doped nitrogen is classified as graphitic, pyridinic, pyrrolic, quaternary nitrogen, and N-oxides.

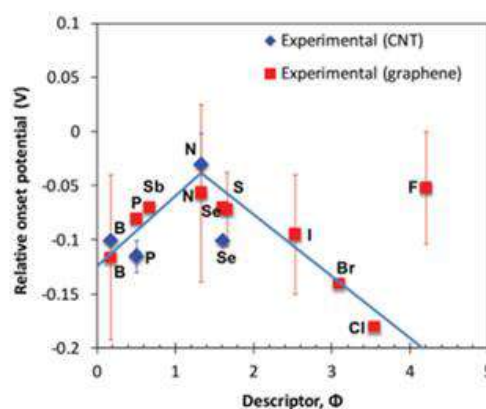


Figure 1.20. For carbon materials doped with p-block elements, the relative E_{onset} to that of a Pt/C catalyst was evaluated as a function of the descriptor. (Copyright © 2015, John Wiley and Sons, License Number: 5314780760854).

The pyridinic nitrogen refers to the nitrogen that is bound to the two sp^2 carbons in the six-membered pyridinic ring. The pyrrolic nitrogen has similar coordination in a five-membered ring. The graphitic nitrogen is produced by substituting the carbon inside the aromatic ring. The nitrogen coordinated with the three sp^3 carbon atoms is referred to as the quaternary nitrogen.⁷⁹ **Figure 1.21** depicts the types of the doped states of the nitrogen in the graphene framework. The doped nitrogen into the graphene matrix makes the N-doped graphene more

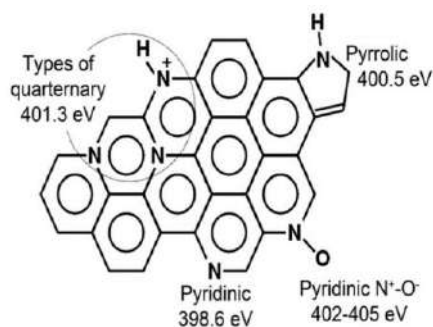


Figure 1.21. Showing the presence of four types of doped nitrogen into the graphene structure (Reprinted with permission, Copyright © 2015, John Wiley and Sons, License Number: 5314780760854).

tunable with respect to the chemical and physical properties of the system. Therefore, the N-doped graphene system has gained the interest of the researchers as an effective substrate with great possibilities in the energy applications. Additionally, the N-doping of the graphene support makes the system active toward ORR. In this direction, significant research has been done and important correlations could be derived related to the amount of the dopant level and the ORR activity, implying that the doped nitrogen may have an important role in deciding the catalytic activity.

1.7.15. Influences of the Morphologies of Heteroatom-doped Carbon Support: As previously stated, the strategies focused on increasing the number density of the active sites are widely accepted for improving the performances of the catalysts for the electrochemical energy application. Therefore, the size, shape, and morphological modulations of the active sites along with the right structural alterations of the support materials have received enormous attention. The incorporation of a carbon support with a significant porosity could potentially increase the density of the active sites. Considering this advantage, it can be stated that, the morphology and porosity have considerable importance towards the electrochemical performance improvement. Hence, the heteroatom-doped and porous structured graphene materials with more customized morphologies have been projected as potential substrates for the designing of high-performing catalysts for the oxygen electrochemistry applications.

1.7.16. Layered Double Hydroxides Supported Carbon: Nickel (Ni) is a common first-row transition metal with high ductility and corrosion resistance. In the early twentieth century, the oxides of Ni were discovered to have OER electrocatalytic activity in alkaline solution. The most important observation was that the nickel (Ni) is always found to be mixed with a lower quantity of Fe on the earth ore components. The presence of the Fe impurities in nickel

hydroxide ($\text{Ni}(\text{OH})_2$) significantly alters the OER performance in alkaline media. Afterward, this interesting discovery got the attention of many researchers. To find the correlation between the Fe percentage in the $\text{Ni}(\text{OH})_2$ structure and OER activity, many studies were performed. In addition, recently the Ni and Fe-based advanced structures such as nickel-iron layered double hydroxides (NiFe-LDH) have been explored as active and durable OER electrocatalysts. Furthermore, the lower conductivity of NiFe-LDH and durability could be overcome by adding a suitable carbon additive, which serves as the substrate for the growth and dispersion of the LDH moieties. In this direction, Magesh *et al.* reported NiFe/RGO, which outperforms the bare NiFe and reference IrO_2 in terms of OER with a lower benchmark over potential value of 0.245 V. Similarly, Sasaki *et al.*, reported exfoliated NiFe-LDH nanosheets supported on two different forms of graphene, *viz.*, graphene oxide (GO), and reduced graphene oxide (rGO).⁴⁰ The morphological alterations of NiFe-LDH incurred in the system resulted in an improved OER performance. Furthermore, with respect to the two morphologies of the graphene substrates, a difference in the electrochemical OER performance has been observed, which reveals the importance of the right morphology of the selected substrate for the catalytically active sites.

1.7.17. Spinel Oxide Supported Carbon: Spinel structures of oxides have been studied extensively for their highly efficient ORR catalytic activity. The spinel structure of Co_3O_4 is the most widely recognized as a promising ORR active catalyst. In the spinel structure of cobalt oxides, cobalt exists in two different oxidation states (Co^{2+} and Co^{3+}) and resides in the tetrahedral and octahedral sites, respectively.^{66–68} The cobalt ions in different oxidation states significantly alter the electron transport mechanism, which directly affects the electrocatalytic ORR activity. Furthermore, the surface adsorption characteristics and electronic structure modulations occur with alterations of the morphologies of the spinel oxides. For the reasons stated above, the morphology modification has proven to be an effective strategy for increasing the ORR activity. Hence, Co_3O_4 can be tuned into a variety of morphologies, such as nanospheres, nanotubes, and nanosheets, which change the surface electronic properties and thereby improve the ORR performance. Furthermore, combining Co_3O_4 with carbon materials has been proven to be a quick way to boost its catalytic activity.⁶⁹ Zhao *et al.* recently reported mesoporous Co_3O_4 nanowires with improved electrocatalytic activity.⁸¹ **Figure 1.22** represents the comparative electrochemical performance of the different Co_3O_4 -graphene composites. The mesoporous spinel oxide-supported on reduced graphene (rm- Co_3O_4 /3DG) shows a significantly higher onset potential of 0.93 V (*vs.* RHE), which is comparable to the *state-of-*

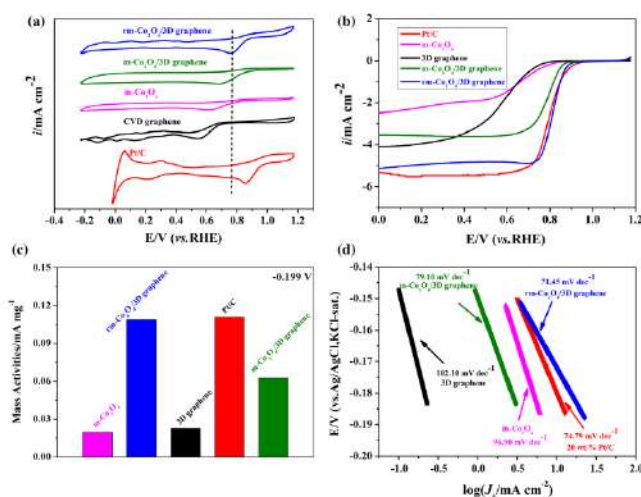


Figure 1.22. (a) The comparative cyclic voltammograms of m-Co₃O₄, 3D graphene, m-Co₃O₄/3DG and rm-Co₃O₄/3DG, and 20 wt% Pt/C electrocatalysts in O₂-saturated 0.1 M KOH aqueous solution; (b) comparative linear sweep voltammograms recorded for m-Co₃O₄, 3D graphene, m-Co₃O₄/3DG and rm-Co₃O₄/3DG, and 20 wt% Pt/C electrocatalysts in O₂-saturated 0.1 M KOH solution at the working electrode rotation rate of 1600 rpm with a scan rate of 5 mV s⁻¹; (c) comparable mass activity m-Co₃O₄, 3D graphene, m-Co₃O₄/3DG, rm-Co₃O₄/3DG, and 20 wt% Pt/C at 0.199 V; (d) the Tafel slopes derived from the LSV profiles; (d) the mass activities estimated for the catalysts (Reprinted with permission from reference 86 © 2020, Springer Nature, License Number: 5314840225171).

the-art Pt/C (0.97 V vs. RHE). Furthermore, the half-wave potential of rm-Co₃O₄/3DG is shown as 0.84 V (vs. RHE). In addition, the mass activity of the reduced graphene oxide-supported catalyst (rm-Co₃O₄/3DG) is higher than the graphene oxide-supported mesoporous Co₃O₄. This reveals the important role played by the reduced graphene structure in favorably altering the catalytic activity in the composites.⁹⁹ Another report from the Tian-Yi Ma group deals with the synthesis of various morphologies of the Co₃O₄ nanocrystals (**Figure 1.23**) such as the nanocube (NC), nanotruncated octahedron (NTO), and nanopolyhedron (NP).⁸² Furthermore, the nanocrystals were decorated on nitrogen-doped reduced graphene oxide (N-rGO) to overcome the conductivity and stability issues. Also, the electrochemical performance measurements of the catalysts revealed the morphology-dependent bifunctional electrocatalytic (ORR and OER) activity of the systems. In addition, to the morphological tuning of the spinel structure of the cobalt oxide, further compositional tuning with other metals also improves the bifunctional oxygen electrocatalytic activity. The bimetallic spinel structures of the oxides have advantages over the single metal spinel oxides in terms of the electrochemical ORR and OER electrocatalysts for the ORR and OER applications. The cobalt manganese spinel-type oxides are a class of materials that several researchers have extensively studied. As the cobalt oxide

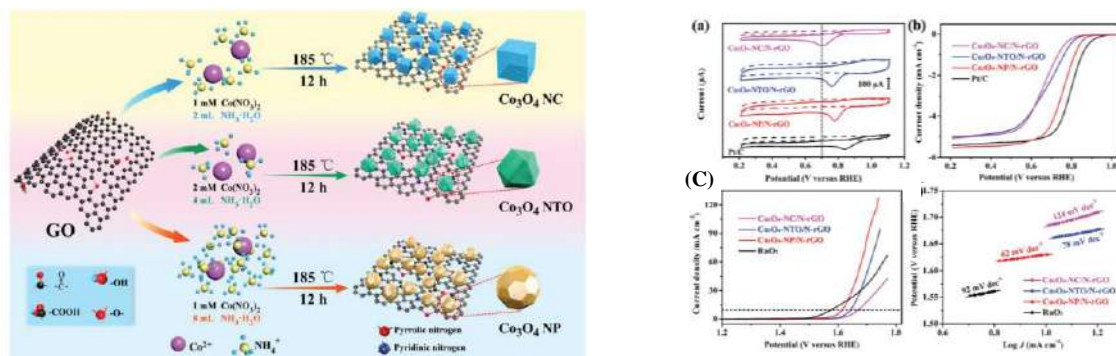


Figure 1.23. Some strategies adopted for the morphology-controlled synthesis of the cobalt oxide-supported nanocomposites ($\text{Co}_3\text{O}_4\text{-NC/N-rGO}$, $\text{Co}_3\text{O}_4\text{-NTO/N-rGO}$, and $\text{Co}_3\text{O}_4\text{-NP/N-rGO}$), followed by their evaluation towards oxygen electrocatalysis (Reprinted with permission from reference 87, Copyright © 2017, John Wiley and Sons, License Number: 5314840424314).

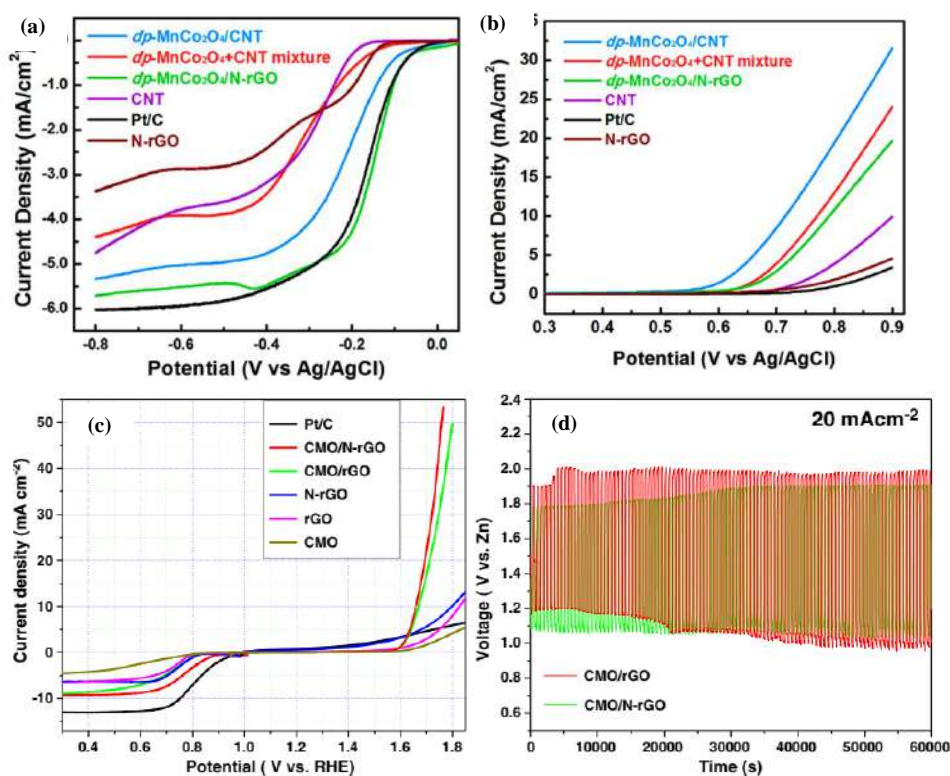


Figure 1.24. The ORR (a) and OER (b) activities of the commercial Pt/C, rGO, N-rGO, CMO, CMO/rGO, and CMO/N-rGO (O_2 -saturated 0.1 M KOH at a scan rate of 5 mVs^{-1}); (c) the comparative LSVs revealing the bifunctional (ORR and OER) activity of Pt/C, rGO, N-rGO, CMO, CMO/rGO and CMO/N-rGO; (d) the voltage vs time curves of Zn-air battery recorded at a current density of 20 mA cm^{-2} (Reprinted with permission from reference 88, Copyright © 2014, American Chemical Society).

is a well-developed spinel oxide, incorporating Mn into the cobalt oxide lattice helps to create more number of the active sites which are responsible for both OER and ORR. A report by Liu *et al* reveals the preparation of a dual-phase spinel structure of MnCo_2O_4 (dp- MnCo_2O_4) nanocrystals supported over the nitrogen-doped reduced graphene oxide and carbon nanotubes (CNTs), resulting in high-performance. (Figure 1.24)⁸³ The synergistic interaction between the spinel structure of the bimetallic oxide (dp- MnCo_2O_4) and carbon nanotubes effectively improves the bifunctional ORR and OER activities. The dp- $\text{MnCo}_2\text{O}_4/\text{N-rGO}$ hybrid catalyst shows comparable ORR activity and significantly improved OER performance compared to the commercial Pt/C. Furthermore, to know the important role played by the support, they have compared the electrocatalytic OER and OER performances with two different support systems, *viz.*, CNT and nitrogen-doped reduced graphene oxide (N-rGO). The catalyst (dp- $\text{MnCo}_2\text{O}_4/\text{N-rGO}$) shows improved ORR performance than dp- $\text{MnCo}_2\text{O}_4/\text{CNT}$. Moreover, the OER performance of dp- $\text{MnCo}_2\text{O}_4/\text{N-rGO}$ is lower than that of dp- $\text{MnCo}_2\text{O}_4/\text{CNT}$. Furthermore, the bifunctional activity (ORR and OER) of dp- $\text{MnCo}_2\text{O}_4/\text{N-rGO}$ is higher than that on dp- $\text{MnCo}_2\text{O}_4/\text{CNT}$, revealing the advantage of N-rGO as a support over CNT. This result suggested that the morphology of the support plays a significant role in deciding the performance of the catalysts towards oxygen electrochemistry. In the case of the N-rGO support, the presence of porosity favors efficient mass transport and provides more accessible active sites.

1.8. Conclusions, Scope, and Objectives of the Thesis: In summary, the introductory chapter of the present thesis includes a brief overview of the recent energy scenario and the importance of the electrochemical energy technologies. It is obvious that a multi-directional strategy is required to build economically viable electrochemical energy generation and storage systems for prospective applications. Commercialization of fuel cells, metal-air batteries, and water electrolyzers rely on the effectiveness of the oxygen electrochemistry (ORR/OER). Therefore, the electrocatalysts with demand-specific active sites for ORR and OER reside on the top priority, as they decide the PEMFC (ORR) and water splitting (OER) performance. Similarly, to make the zinc-air batteries more economically successful, the appealing property of the rechargeability should be added. This is possible if the air electrodes of RZAB can handle both ORR (discharging) and OER (charging) processes at low overpotential. The high cost and lower durability of the noble metal-based catalysts for ORR (Pt) and OER (IrO_2 and RuO_2) remains the main obstacle to commercializing such electrochemical energy devices. Furthermore, the poor bifunctional activity of such catalysts hinders the use of rechargeable

ZAB air cathode. Hence, the low-cost, efficient, and durable electrocatalyst development for ORR, OER, and both (ORR + OER) is necessary to manufacture affordable devices for commercialization. Therefore, research on low-Pt and Pt-free catalyst synthesis with shape, size, and morphology modulated mono and multimetallic moieties on the support has great scope. However, the inability to fully utilize the active sites in the reaction interphase suppresses the efficiency of the catalysts in device performance. This necessitates solutions based on microstructure engineering of the catalyst support for extending the active "triple-phase boundary (TPB)" unit. Therefore, the active reaction site tuning with surface morphology modification could facilitate ORR and OER under various energy applications.

The key scope of the present thesis is to overcome these issues associated with the ORR/OER electrocatalysts. Surface and porosity modifications of the 3D morphologies of graphene can be carried out to improve the electrode kinetics in the electrochemical energy devices such as water electrolyzers, PEMFCs, and metal-air batteries. The 3D structure of graphene can be used as a support to achieve better intrinsic activities, electrical conductivity, and porosity of the catalysts. Furthermore, heteroatom doping over the carbon support can be utilized as an effective strategy for improving the active site dispersion characteristics. The developed heteroatom-doped 3D structures of graphene support could be used as suitable supports for developing low-cost and durable electrocatalysts based on layered double hydroxides and spinel structured metal oxides for OER and ORR applications. In addition, to improve the bifunctional oxygen catalytic activity (ORR/OER), the metal centers in the spinel oxides can be stoichiometrically replaced with other metal species. Furthermore, to get the ORR performance in an acidic medium with a low Pt-based system, Pt-based alloy moieties can be suitably decorated over the same 3D support for PEMFC applications. These strategically designed active sites for ORR and OER over the 3D graphene support can improve the activity as well as mass transport properties with better feasibilities for establishing the active triple-phase boundaries (TPB) both with the liquid and solid electrolytes.

The main objectives of the works covered in the thesis are as follows:

1. To modulate the surface area and porosity characteristics of the electrocatalysts for ORR/OER applications by developing the catalysts based on the 3D graphene supports intending to improve the mass transport properties of the gaseous reactants and products released during the electrochemical processes. This strategy is expected to also help to achieve better electrode-electrolyte interface formation.

2. It is also decided to explore the possibilities to impart additional performance enhancement from the 3D graphene scaffolds as substrates for catalysts by inducing nitrogen doping into the graphene framework by which efficient anchoring sites for the dispersion of the desired active sites can be achieved.
3. To develop various 3D graphene-based electrocatalysts by decorating active components such as layered double hydroxides, spinel metal oxide nanoparticles, and Pt-alloy nanoparticles to explore possibilities for achieving better catalysts with modulated performance characteristics for OER and ORR and also to achieve an efficient catalyst that can display ORR+OER bifunctional activity. The key requirements such as structural integrity, reactant utilization, performance, and durability need to be addressed while selecting the catalyst designing strategies for the specific applications.
4. One of the specific objectives is to design a cost-effective OER electrocatalyst based on nitrogen-doped entangled graphene framework (NEGF) bearing the nickel-iron layered double hydroxide (NiFe-LDH) nanostructures through a process that prevents restacking of the graphene sheets (NiFe-LDH/NEGF). The incorporation of NEGF is expected to improve the effective utilization of the active sites and thus reduce the overpotential for OER.
5. To explore the possibility of developing a Pt-free ORR electrocatalyst for ZAB applications based on the Co_3O_4 spinel structure by a strategy involving both shape controlling of the spinel oxide nanoparticles and their simultaneous dispersion on NEGF ($\text{Co}_3\text{O}_4/\text{NEGF}$). This is expected to reap the dual benefits of fine-tuning the intrinsic activity of the active sites towards ORR and forming a process-friendly catalyst texture.
6. The study also intends to impart ORR/OER bifunctional characteristics to the abovementioned $\text{Co}_3\text{O}_4/\text{NEGF}$ catalyst by stoichiometrically incorporating a species such as Mn into the Co_3O_4 spinel lattice to form a bimetallic spinel oxide supported NEGF ($\text{MnCo}_2\text{O}_4/\text{NEGF}$) catalyst. With the bifunctional feature and the favorable structural attributes originating from the NEGF texture, demonstration of an all-solid-state RZAB is targeted by employing $\text{MnCo}_2\text{O}_4/\text{NEGF}$ as the air-cathode in the cell.
7. To validate the possibility of developing a process-friendly catalyst for ORR in PEMFC applications by creating the active sites of Pt-Co alloy nanoparticles on NEGF ($\text{Pt}_3\text{Co}/\text{pNEGF}$) to function better under acidic conditions. The possibility of additional

creation of porosity for oxygen enrichment also is another objective for this specific application. The carbon support porosity, within the micro-and mesopore range, has a significant impact on achieving the distribution of the small-sized alloy nanoparticles as well as improving the mass transfer characteristics.

1.9. References:

1. Oladokun, M. G.; Odesola, I. A., Household Energy Consumption and Carbon Emissions for Sustainable Cities—A Critical Review of Modelling Approaches. *International Journal of Sustainable Built Environment* 2015, 4, 231-247.
2. S.Chu, A.Majumdar, Opportunities and challenges for a sustainable energy future, *Nature*, 2012, 488, 294-303.
3. Budde-Meiwes, H.; Drillkens, J.; Lunz, B.; Muennix, J.; Rothgang, S.; Kowal, J.; Sauer, D. U. A review of current automotive battery technology and future prospects. *Proceedings of the Institution of Mechanical Engineers, Part D: Journal of Automobile Engineering* 2013, 227, 761-776.
4. Gür, T. M. Review of electrical energy storage technologies, materials and systems: challenges and prospects for large-scale grid storage. *Energy & Environmental Science* 2018, 11, 2696-2767.
5. Dresselhaus, M.S. and I.L. Thomas, Alternative Energy Technologies. *Nature*, 2001, 332-337.
6. Crabtree, G.W., M.S. Dresselhaus, and M.V. Buchanan, The Hydrogen Economy. *Physics Today*, 2004, 57, 39-44.
7. Ahuja, V. and R. Green, Carbon dioxide removal from the air for alkaline fuel cells operating with liquid-hydrogen-A synergistic advantage. *International Journal of Hydrogen Energy*, 1998, 23, 131-137.
8. Kirubakaran, A.; Jain, S.; Nema, R. K., A Review on Fuel Cell Technologies and Power Electronic Interface. *Renewable Sustainable Energy Rev.* 2009, 13, 2430-2440.
9. X. Li, X. Hao, A. Abudula, G. Guan, Nanostructured catalysts for electrochemical water splitting: current state and prospects, *J. Mater. Chem. A*, 2016, 11973-12000.
10. Birss, V.I., A. Damjanovic, and P.G. Hudson, Oxygen Evolution at Platinum-Electrodes in Alkaline-Solutions Mechanism of the Reaction. *Journal of the Electrochemical Society*, 1986, 133, 1621-1625
11. Rosli, R. E.; Sulong, A. B.; Daud, W. R. W.; Zulkifley, M. A.; Husaini, T.; Rosli, M. I.; Majlan, E. H.; Haque, M. A., A Review of High-temperature Proton Exchange Membrane Fuel Cell (HT-PEMFC) system. *Int. J. Hydrogen Energy* 2017, 42, 9293-9314.
12. D. P. Wilkinson, Proton exchange membrane fuel cells: materials properties and performance. Boca Raton, FL: CRC Press/Taylor & Francis, 2010, ISBN 9781439806647.

13. D. P. Wilkinson, Proton exchange membrane fuel cells: materials properties and performance. Boca Raton, FL: CRC Press/Taylor & Francis, 2010, ISBN: 978-1-4398-0664-7.
14. O. S. Burheim, H. Su, S. Pasupathi, J. G. Pharoah, and B. G. Pollet, "Thermal conductivity and temperature profiles of the microporous layers used for the polymer electrolyte membrane fuel cell," *International Journal of Hydrogen Energy*, vol. 2013, 38, 8437-8447.
15. U. Pasaogullari and C. Y. Wang, "Two-phase transport and the role of microporous layer in polymer electrolyte fuel cells," *Electrochimica Acta*, 2004, 12, 4359-4369.
16. A. M. Kannan, L. Cindrella, and L. Munukutla, "Functionally graded nano-porous gas diffusion layer for proton exchange membrane fuel cells under low relative humidity conditions," *Electrochimica Acta*, vol.2008, 53, 2416-2422.
17. Kraysberg, A.; Ein-Eli, Y., Review of Advanced Materials for Proton Exchange Membrane Fuel Cells. *Energy & Fuels* 2014, 28, 7303-7330.
18. Omasta, T. J.; Park, A. M.; LaManna, J. M.; Zhang, Y.; Peng, X.; Wang, L.; Jacobson, D. L.; Varcoe, J. R.; Hussey, D. S.; Pivovar, B. S.; Mustain, W. E., Beyond Catalysis and Membranes: Visualizing and Solving the Challenge of Electrode Water Accumulation and Flooding in AEMFCs. *Energy Environ. Sci.* 2018, 11, 551-558.
19. Lee, J.-S.; Tai Kim, S.; Cao, R.; Choi, N.-S.; Liu, M.; Lee, K. T.; Cho, J., Metal-Air batteries with High Energy Density: Li–Air versus Zn–Air. *Adv. Energy Mater.* 2011, 1, 34-50.
20. Laoire, C. O.; Mukerjee, S.; Abraham, K. M.; Plichta, E. J.; Hendrickson, M. A., Elucidating the Mechanism of Oxygen Reduction for Lithium-Air Battery Applications. *J. Phys. Chem. C* 2009, 113, 20127-20134.
21. Zhang, X.; Wang, X.-G.; Xie, Z.; Zhou, Z., Recent Progress in Rechargeable Alkali Metal–air Batteries. *Green Energy & Environment* 2016, 1, 4-17.
22. Yi, J.; Liu, X.; Guo, S.; Zhu, K.; Xue, H.; Zhou, H., Novel Stable Gel Polymer Electrolyte: Toward a High Safety and Long Life Li–Air Battery. *ACS Appl. Mater. Interfaces* 2015, 7, 23798-23804.
23. Li, Y.; Lu, J., Metal-Air Batteries: Will They Be the Future Electrochemical Energy Storage Device of Choice? *ACS Energy Letters* 2017, 2, 1370-1377.
24. Gu, P.; Zheng, M.; Zhao, Q.; Xiao, X.; Xue, H.; Pang, H., Rechargeable zinc–air batteries: a promising way to green energy. *Journal of Materials Chemistry A* 2017, 5 (17), 7651-7666.
25. Li, Y.; Gong, M.; Liang, Y.; Feng, J.; Kim, J.-E.; Wang, H.; Hong, G.; Zhang, B.; Dai, H., Advanced Zinc-air Batteries Based on High-performance Hybrid Electrocatalysts. *Nat. Commun.* 2013, 4, 1805
26. Li, Y.; Dai, H., Recent Advances in Zinc-air Batteries. *Chem. Soc. Rev.* 2014, 43, 5257-5275.

27. Li, Y.; Gong, M.; Liang, Y.; Feng, J.; Kim, J. E.; Wang, H.; Hong, G.; Zhang, B.; Dai, H. Advanced Zinc-Air Batteries Based on High-Performance Hybrid Electrocatalysts. *Nat. Commun* 2013, 4, 1–7.
28. Fu, J.; Cano, Z. P.; Park, M. G.; Yu, A.; Fowler, M.; Chen, Z., Electrically Rechargeable Zinc-Air Batteries: Progress, Challenges, and Perspectives. *Adv. Mater.* 2017, 29, n/a-n/a.
29. Zhou, H.; Wang, Y.; Li, H.; He, P., The Development of a New Type of Rechargeable Batteries Based on Hybrid Electrolytes. *ChemSusChem* 2010, 3, 1009-1019.
30. Li, Y.; Gong, M.; Liang, Y.; Feng, J.; Kim, J. E.; Wang, H.; Hong, G.; Zhang, B.; Dai, H., Advanced zinc-air batteries based on high-performance hybrid electrocatalysts. *Nat Commun* 2013, 4, 1805-1810.
31. Cheng, F.; Chen, J., Metal-air batteries: from oxygen reduction electrochemistry to cathode catalysts. *Chem Soc Rev* 2012, 41, 2172-92.
32. Yu, J.; Li, B. Q.; Zhao, C. X.; Liu, J. N.; Zhang, Q., Asymmetric Air Cathode Design for Enhanced Interfacial Electrocatalytic Reactions in High-Performance Zinc-Air Batteries. *Adv Mater* 2020, 32, 8488-8492.
33. Wang, X. X.; Yang, X.; Liu, H.; Han, T.; Hu, J.; Li, H.; Wu, G., Air Electrodes for Flexible and Rechargeable Zn–Air Batteries. *Small Structures* 2021, 3, 10-12.
34. Pan, J.; Xu, Y. Y.; Yang, H.; Dong, Z.; Liu, H.; Xia, B. Y., Advanced Architectures and Relatives of Air Electrodes in Zn-Air Batteries. *Adv Sci (Weinh)* 2018, 5 (4), 1700691.
35. Chai, G.-L.; Qiu, K.; Qiao, M.; Titirici, M.-M.; Shang, C.; Guo, Z., Active sites engineering leads to exceptional ORR and OER bifunctionality in P,N Co-doped graphene frameworks. *Energy & Environmental Science* 2017, 10 (5), 1186-1195.
36. Han, C.; Li, W.; Liu, H.-K.; Dou, S.; Wang, J., Design strategies for developing non-precious metal-based bi-functional catalysts for alkaline electrolyte based zinc-air batteries. *Materials Horizons* 2019, 6 (9), 1812-1827.
37. Pseudo-Boehmite AlOOH supported NGr Composite-Based Air Electrode for Mechanically Rechargeable Zn-Air Battery Applications, Kharabe P. G; Manna, N.; Ayasha, N.; Singh, S. K.; Mehta, S; Nair, A; Joshi, K; Kurungot, S. *Journal of Materials Chemistry A.*, 2022, 10, 10014–10025.
38. X. Li, X. Hao, A. Abudula, G. Guan, Nanostructured catalysts for electrochemical water splitting: current state and prospects, *J. Mater. Chem. A*, 2016, 11973-12000.
39. C. C. McCrory, S. Jung, J. C. Peters, T. F. Jaramillo, Benchmarking Heterogeneous Electrocatalysts for the Oxygen Evolution Reaction, *JACS*, 2013, 135, 16977-87.
40. Li, Y.; Zhao, M.; Zhao, Y.; Song, L.; Zhang, Z., FeNi Layered Double-Hydroxide Nanosheets on a 3D Carbon Network as an Efficient Electrocatalyst for the Oxygen Evolution Reaction. *Particle & Particle Systems Characterization* 2016, 33, 158-166.

41. Lee, Y., J. Suntivich, K.J. May, E.E. Perry, and Y. Shao-Horn, Synthesis and Activities of Rutile IrO₂ and RuO₂ Nanoparticles for Oxygen Evolution in Acid and Alkaline Solutions. *Journal of Physical Chemistry Letters*, 2012. 3, 399-404.
42. Gao, M.R., W.C. Sheng, Z.B. Zhuang, Q.R. Fang, S. Gu, J. Jiang, and Y.S. Yan, Efficient Water Oxidation Using Nanostructured alpha-Nickel-Hydroxide as an Electrocatalyst. *Journal of the American Chemical Society*, 2014. 136, 7077-7084.
43. Wen, T.C. and C.C. Hu, Hydrogen and Oxygen Evolutions on Ru-Ir Binary Oxides. *Journal of the Electrochemical Society*, 1992. 139, 2158-2163.
44. Forgie, R., G. Bugosh, K.C. Neyerlin, Z.C. Liu, and P. Strasser, Bimetallic Ru Electrocatalysts for the OER and Electrolytic Water Splitting in Acidic Media. *Electrochemical and Solid-State Letters*, 2010. 13, 36-39.
45. Zhou, R.; Zheng, Y.; Jaroniec, M.; Qiao, S.-Z., Determination of the Electron Transfer Number for the Oxygen Reduction Reaction: From Theory to Experiment. *ACS Catal.* 2016, 6, 4720-4728.
46. Shimizu, K.; Sepunaru, L.; Compton, R. G., Innovative Catalyst Design for the Oxygen Reduction Reaction for Fuel cells. *Chem. Sci.* 2016, 7, 3364-3369.
47. Shao, M.; Chang, Q.; Dodelet, J.-P.; Chenitz, R., Recent Advances in Electrocatalysts for Oxygen Reduction Reaction. *Chem. Rev.* 2016, 116, 3594-3657.
48. Jiao, Y.; Zheng, Y.; Jaroniec, M.; Qiao, S. Z., Origin of the Electrocatalytic Oxygen Reduction Activity of Graphene-Based Catalysts: A Roadmap to Achieve the Best Performance. *J. Am. Chem. Soc.* 2014, 136, 4394-4403.
49. Ge, X.; Sumboja, A.; Wu, D.; An, T.; Li, B.; Goh, F. W. T.; Hor, T. S. A.; Zong, Y.; Liu, Z., Oxygen Reduction in Alkaline Media: From Mechanisms to Recent Advances of Catalysts. *ACS Catal.* 2015, 5, 4643-4667.
50. Wang, D.-W.; Su, D., Heterogeneous Nanocarbon Materials for Oxygen Reduction Reaction. *Energy Environ. Sci.* 2014, 7, 576-591.
51. Liu, S.; White, M. G.; Liu, P., Mechanism of Oxygen Reduction Reaction on Pt (111) in Alkaline Solution: Importance of Chemisorbed Water on Surface. *J. Phys. Chem. C* 2016, 120, 15288-15298.
52. Wei, Z. SEHJAKOB K. F.; Dickens, K. N. N. and Thomas Jaramillo, F. Combining theory and experiment in electrocatalysis: Insights into materials design, 2017, 355, 6321-6325
53. Čolić, V.; Bandarenka, A. S., Pt Alloy Electrocatalysts for the Oxygen Reduction Reaction: From Model Surfaces to Nanostructured Systems. *ACS Catal.* 2016, 5378-5385.
54. Guo, S.; Li, D.; Zhu, H.; Zhang, S.; Markovic, N. M.; Stamenkovic, V. R.; Sun, S., FePt and CoPt Nanowires as Efficient Catalysts for the Oxygen Reduction Reaction. *Angew. Chem. Int. Ed.* 2013, 52, 3465-3468.

55. Nie, Y.; Li, L.; Wei, Z., Recent Advancements in Pt and Pt-free Catalysts for Oxygen Reduction Reaction. *Chem. Soc. Rev.* 2015, 44, 2168-2201.
56. Stephens, I. E. L.; Bondarenko, A. S.; Gronbjerg, U.; Rossmeisl, J.; Chorkendorff, I., Understanding the Electrocatalysis of Oxygen Reduction on Platinum and Its Alloys. *Energy Environ. Sci.* 2012, 5, 6744-6762.
57. Liu, Z.; Lei, Y.; Wang, G. First-Principles Computation of Surface Segregation in L10 CoPt Magnetic Nanoparticles. *J. Phys.: Condens. Matter* 2016, 28, 266002.
58. Sun, X.; Jia, Z. Y.; Huang, Y. H.; Harrell, J. W.; Nikles, D. E.; Sun, K.; Wang, L. M. Synthesis and Magnetic Properties of CoPt Nanoparticles. *J. Appl. Phys.* 2004, 95, 6747.
59. Karipoth, P.; Joseyphus, R. J. Evolution of High Coercivity in CoPt Nanoparticles Through Nitrogen Assisted Annealing. *J. Supercond. Novel Magn.* 2014, 27, 2123–2130
60. Stamenkovic, V. R.; Mun, B. S.; Mayrhofer, K. J. J.; Ross, P. N.; Markovic, N. M., Effect of Surface Composition on Electronic Structure, Stability, and Electrocatalytic Properties of Pt Transition Metal Alloys: Pt-Skin versus Pt-Skeleton Surfaces. *J. Am. Chem. Soc.* 2006, 128, 8813-8819.
61. Stamenkovic, V. R.; Mun, B. S.; Arenz, M.; Mayrhofer, K. J. J.; Lucas, C. A.; Wang, G.; Ross, P. N.; Markovic, N. M., Trends in Electrocatalysis on Extended and Nanoscale Pt Bimetallic Alloy Surfaces. *Nat. Mater.* 2007, 6, 241-247.
62. Zhang, Y., B. Cui, O. Derr, Z.B. Yao, Z.T. Qin, X.Y. Deng, J.B. Li, and H. Lin, Hierarchical Cobalt-Based Hydroxide Microspheres for Water Oxidation. *Nanoscale*, 2014. 6, 3376-3383.
63. Gao, M.R., W.C. Sheng, Z.B. Zhuang, Q.R. Fang, S. Gu, J. Jiang, and Y.S. Yan, Efficient Water Oxidation Using Nanostructured alpha-Nickel-Hydroxide as an Electrocatalyst. *Journal of the American Chemical Society*, 2014. 136, 7077-7084.
64. Wang, Y.; Li, J.; Wei, Z. Transition-Metal-Oxide-Based Catalysts for the Oxygen Reduction Reaction. *J. Mater Chem. A* 2018, 6, 8194–8209.
65. J. Suntivich, H. A. Gasteiger, N. Yabuuchi, H. Nakanishi, J. B. Goodenough, and Y. Shao-Horn, "Design principles for oxygen-reduction activity on perovskite oxide catalysts for fuel cells and metal-air batteries," *Nature Chemistry*, vol. 3, 546-550, 2011.
66. Singh, S. K.; Dhavale, V. M.; Kurungot, S. Surface-Tuned Co₃O₄ Nanoparticles Dispersed on Nitrogen-Doped Graphene as an Efficient Cathode Electrocatalyst for Mechanical Rechargeable Zinc–Air Battery Application. *ACS Appl. Mater. Interfaces* 2015, 7, 21138–21149.
67. Singh, S. K.; Dhavale, V. M.; Kurungot, S. Low Surface Energy Plane Exposed Co₃O₄ Nanocubes Supported on Nitrogen-Doped Graphene as an Electrocatalyst for Efficient Water Oxidation. *ACS Appl. Mater. Interfaces* 2015, 7, 442–451.

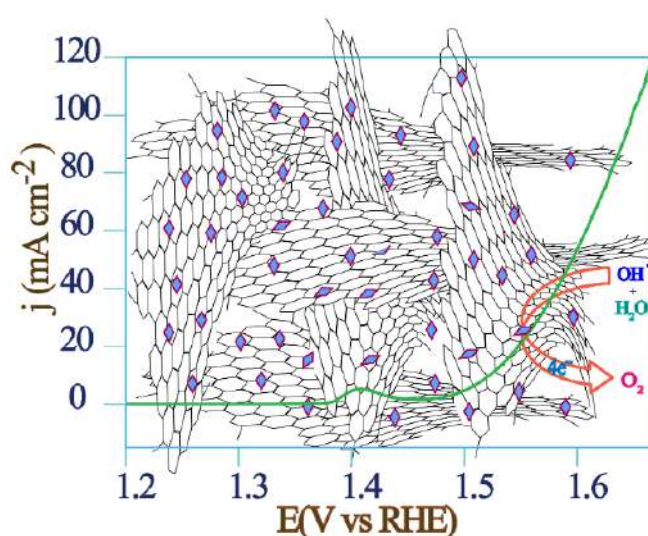
68. Ma, T. Y.; Zheng, Y.; Dai, S.; Jaroniec, M.; Qiao, S. Z., Mesoporous MnCo_2O_4 with abundant Vacancy Defects as High-performance Oxygen Reduction Catalysts. *J. Mater. Chem. A* 2014, 2, 8676-8682.
69. Zhu, H.; Zhang, S.; Huang, Y.-X.; Wu, L.; Sun, S., Monodisperse $\text{M}_x\text{Fe}_{3-x}\text{O}_4$ (M = Fe, Cu, Co, Mn) Nanoparticles and Their Electrocatalysis for Oxygen Reduction Reaction. *Nano Lett.* 2013, 13, 2947-2951.
70. Ning, R.; Tian, J.; Asiri, A. M.; Qusti, A. H.; Al-Youbi, A. O.; Sun, X., Spinel CuCo_2O_4 Nanoparticles Supported on N-Doped Reduced Graphene Oxide: A Highly Active and Stable Hybrid Electrocatalyst for the Oxygen Reduction Reaction. *Langmuir* 2013, 29, 13146-13151.
71. Ge, X.; Liu, Y.; Goh, F. W. T.; Hor, T. S. A.; Zong, Y.; Xiao, P.; Zhang, Z.; Lim, S. H.; Li, B.; Wang, X.; Liu, Z., Dual-Phase Spinel MnCo_2O_4 and Spinel MnCo_2O_4 /Nanocarbon Hybrids for Electrocatalytic Oxygen Reduction and Evolution. *ACS Appl. Mater. Interfaces* 2014, 6, 12684-12691.
72. Bian, W.; Yang, Z.; Strasser, P.; Yang, R., A CoFe_2O_4 /Graphene Nanohybrid as an Efficient Bi-functional Electrocatalyst for Oxygen Reduction and Oxygen Evolution. *J. Power Sources* 2014, 250, 196-203.
73. Liang, Y.; Wang, H.; Zhou, J.; Li, Y.; Wang, J.; Regier, T.; Dai, H., Covalent Hybrid of Spinel Manganese–Cobalt Oxide and Graphene as Advanced Oxygen Reduction Electrocatalysts. *J. Am. Chem. Soc.* 2012, 134, 3517-3523.
74. Zhao, Q.; Yan, Z.; Chen, C.; Chen, J., Spinels: Controlled Preparation, Oxygen Reduction/Evolution Reaction Application, and Beyond. *Chem Rev* 2017, 117 (15), 10121-10211.
75. Su, H.; Wang, X.-T.; Hu, J.-X.; Ouyang, T.; Xiao, K.; Liu, Z.-Q., Co–Mn spinel supported self-catalysis induced N-doped carbon nanotubes with high efficiency electron transport channels for zinc–air batteries. *Journal of Materials Chemistry A* 2019, 7 (39), 22307-22313.
76. Zhao, H.; Sun, C.; Jin, Z.; Wang, D.; Yan, X.; Chen, Z. G.; Zhu, G.; Yao, X., Carbon for Oxygen Reduction Reaction: A Defect Mechanism. *J. Mater. Chem. A* 2015.
77. Zhang, J.; Xia, Z.; Dai, L., Carbon-Based Electrocatalysts for Advanced Energy Conversion and Storage. *Science Advances* 2015, 1.
78. Castanheira, L.; Silva, W. O.; Lima, F. H. B.; Crisci, A.; Dubau, L.; Maillard, F., Carbon Corrosion in Proton-Exchange Membrane Fuel Cells: Effect of the Carbon Structure, the Degradation Protocol, and the Gas Atmosphere. *ACS Catal.* 2015, 5, 2184-2194.
79. Tan, H.; Tang, J.; Henzie, J.; Li, Y.; Xu, X.; Chen, T.; Wang, Z.; Wang, J.; Ide, Y.; Bando, Y.; Yamauchi, Y., Assembly of Hollow Carbon Nanospheres on Graphene Nanosheets and Creation of Iron-Nitrogen-Doped Porous Carbon for Oxygen Reduction. *ACS Nano* 2018, 10, 780-786.

80. Lv, Q.; Si, W.; He, J.; Sun, L.; Zhang, C.; Wang, N.; Yang, Z.; Li, X.; Wang, X.; Deng, W.; Long, Y.; Huang, C.; Li, Y., Selectively Nitrogen-doped Carbon Materials as Superior Metal-free Catalysts for Oxygen Reduction. *Nature Communications* 2018, 9, 3376.
81. Liu, Y., Zhan, F., Zhao, N. *et al.* Reduced mesoporous Co_3O_4 nanowires grown on 3D graphene as efficient catalysts for oxygen reduction and binder-free electrodes in aluminum-air batteries. *J Mater Sci* 56, 3861–3873 (2021).
82. Xiaopeng Han, Guowei He, Yu He, Jinfeng Zhang, Xuerong Zheng, Lanlan Li, Cheng Zhong, Wenbin Hu, Yida Deng, Tian-Yi Ma Engineering Catalytic Active Sites on Cobalt Oxide Surface for Enhanced Oxygen Electrocatalysis *Adv. Energy Mater.* 2018, 8, 1702222.
83. Xiaoming G.; Yayuan L. F. W.; Thomas G. T. S.; Andy H.; Yun Z.; Peng X.; Zheng Z.; Suo H. L.; Bing L.; Xin W.; and Zhaolin L.; Dual-Phase Spinel MnCo_2O_4 and Spinel MnCo_2O_4 /Nanocarbon Hybrids for Electrocatalytic Oxygen Reduction and Evolution *ACS Appl. Mater. Interfaces* 2014, 6, 15, 12684–12691.

Chapter 2

NiFe Layered double hydroxide-Decorated N-Doped Entangled-Graphene Framework: A Robust Water Oxidation Electrocatalyst

Three Dimensional (3D) porous carbon materials are highly desirable for electrochemical applications owing to their high surface area and porosity. Uniformly distributed porosity in the 3D architecture of the carbon support materials allows the reactant molecules to access more numbers of electrochemical active centres, and such morphologies also help for the simultaneous removal of the product formed during the electrochemical reactions. To explore these advantages, we have prepared nitrogen-doped entangled graphene framework (NEGF) decorated with the NiFe-Layered Double Hydroxide (NiFe-LDH) nanostructures (NiFe-LDH/NEGF) by an *in-situ* solvothermal method followed by freeze-drying at high vacuum pressure and low-temperature conditions. The freeze-drying method helped to prevent the restacking of the graphene sheets and the formation of high surface area NEGF supported NiFe-LDH. The incorporation of NEGF has significantly reduced the overpotential for the electrochemical oxygen evolution reaction (OER) in 1 M KOH solution. This corresponds to an overpotential reduction from 340 mV for NiFe-LDH to 290 mV for NiFe-LDH/NEGF to reach the benchmark current density of 10 mA cm^{-2} . The preparation of the catalyst is conceived through a low-temperature scalable process.



Content of this chapter is published in the following article: DOI: 10.1039/C9NA00808J

Nanoscale Adv., 2020, 2, 1709-1717

Reproduced with permission from Royal Society of Chemistry

2.1. Introduction:

Owing to the increased energy demand and environmental concerns, it is an urgent need to focus on alternative carbon-free fuels.¹ In this respect, fuel cell has emerged as a promising alternative technology to the conventional heat engines.² However, being an electrochemical energy conversion device, its sustainability as well as eco-friendly nature is directly dependent on the source of the fuel, *e.g.*, H₂ (having the highest gravimetric energy density, *i.e.*, 140 MJ/Kg).³ Among the various ways of H₂ generation, water splitting can be the sustainable resource of H₂.⁴ Electrochemical water splitting involves two half-cell reactions, *i.e.*, cathodic hydrogen evolution reaction (HER) and the anodic oxygen evolution reaction (OER). However, owing to the four proton-coupled four electron-transfer reactions, OER is thermodynamically unfavourable, limiting the overall energy efficiency of these vital electrochemical areas.⁵ Currently, precious-group metal-based, *i.e.*, IrO₂- and RuO₂-based, catalysts are the benchmark both in the acidic and alkaline medium for OER.⁶ However, their high cost and scarcity have triggered research toward the development of low-cost and readily available active materials for scale-up utilizations.⁷ In the last few years, various earth-abundant transition metal (Mn, Fe, Co, and Ni) -based oxides, hydroxides, and alloys have been explored as promising alternatives to catalyze OER in alkaline medium.⁸⁻¹⁰ For instance, Sumboja *et al.*⁸ designed NiMn layered double hydroxide as an efficient OER electrocatalyst. In another report, Kang *et al.*¹¹ demonstrated the activity of NiFe-oxide toward the water oxidation reaction. Despite satisfactory performances, these support-free catalysts suffer from active centre agglomeration and poor electronic conductivity issues, affecting their long-term stability.¹¹⁻¹⁴ A way out to the conductivity issue is to modulate the electronic structure by *in situ* anchoring of these transition metal oxides/hydroxides over cost-effective conducting supports.^{15,16} Among the various cost-effective conducting supports, carbon-based materials with electrochemically favourable characteristics, *i.e.*, high electronic conductivity and surface area, have emerged as universal choices in the electrocatalysis field.^{15,16} For instance, in a recent report, Zhan *et al.*¹⁷ achieved improved activity as well as stability by anchoring the OER-active NiFe layered double hydroxides over nitrogen-doped graphene. Similarly, Chandrasekaran *et al.*¹⁸ also reported improved OER performance by anchoring NiFe layer double hydroxide over reduced graphene oxide.

Though two-dimensional (2D) graphene and one-dimensional (1D) carbon nanotubes have emerged as convincing OER-catalyst supports, their in-depth micro-architecture has come out to be the proficiency-limiting factor.¹⁶ For instance, theoretically, graphene provides a surface area of as high as $\sim 2630 \text{ m}^2 \text{ g}^{-1}$ as well as outstanding electrical conductivity.^{19,20} However, practically, the well-known restacking issue of the graphene layers affects its surface area as well as electronic conductivity to a large extent.²¹ Besides,

CNTs suffer from the low surface area, restricting sufficient active material loading as well as their detachment during the reaction.^{20,21} Hence, tuning the micro-architectural characteristics of the catalyst-support is a key contributor to increase the active centre loading as well as accessibility to tune the overall performance.²² Among several potential candidates, three-dimensional entangled-graphene frameworks (3D-EGF), having a high surface area as well as electronic conductivity, is gaining enormous attention as the conducting support.^{22,23} In spite of that, 3D-EGF with a hierarchical porous structure also serves as a promising substrate to accommodate a huge number of exposed active materials to facilitate the seamless diffusion of the electrocatalytic reaction species.²⁴⁻²⁶ Recently, several methods have been adopted for the designing of the 3D graphene, including hard and soft-template-based methods²⁷, freeze-drying method³⁰, microporous template-based CVD method^{28,30}, and a nonporous metal-based CVD method.^{28,29}

Among all these methods, the freeze-drying is found to be quite appealing as it generates plenty of homogeneous porosity, as well as the process leads to the higher mechanical strength of the interconnected graphene network.^{27,32,33} The primary activity degradation factors in the catalyst systems based on the conventional support morphologies include insufficient electronic conductivity, poor active center exposure, and hindered reaction species transport. By keeping all these performance-constraining factors in mind, herein, a catalyst designing strategy has been introduced by involving the anchoring of the nano-sized NiFe-layered double hydroxide (NiFe-LDH) over N-doped entangled graphene framework (NEGF) with an expectation that the modified morphology of the catalyst will help to overcome the existing challenges involved in the water oxidation reaction. The rationally designed NEGF acted as a useful active substrate to tune the electronic structure and the NiFe-LDH distribution, along with providing an architecture comprised of open and exposed catalytic systems.

2.2. Experimental:

2.2.1. Materials:

Nickel acetate hexahydrate [Ni(OAc)₂·6H₂O], iron acetate hexahydrate [Fe(OAc)₂·6H₂O], ammonium hydroxide (NH₄OH), graphite, and potassium permanganate (KMnO₄) were purchased from Sigma-Aldrich. Phosphoric acid (H₃PO₄) and sulphuric acid (H₂SO₄) were purchased from Thomas Baker. The entire chemical reagents were used as such without any further purification.

2.2.2. Synthesis of Graphene Oxide (GO):

Improved Hummer's method was employed for synthesizing graphene oxide (GO)¹. In brief, 3 g of graphite powder and 18 g of KMnO₄ were well mixed by using a mortar and pestle. After complete mixing, the

powder was slowly added to the flask containing a solution mixture of $\text{H}_3\text{PO}_4:\text{H}_2\text{SO}_4$ (1:9) at 0 °C. After complete transfer of the solid combination, the temperature of the solution was increased slowly up to 60 °C and was kept for 12 h at a constant temperature. After completion of the reaction, the solution mixture was held for a few hours with regular rotation to reach the temperature at room temperature. The obtained reaction mixture was slowly poured into ice-cooled water containing 3% H_2O_2 , which leads to a yellowish solution. It was then washed several times with distilled water followed by centrifugation at 10000 rpm. The obtained solid residue was further washed with 30% HCl for the removal of any metal impurities. This was again washed with plenty of water to neutralize the acidic pH. Finally, a dark chocolate-colored highly viscous solution was obtained, which was further washed with ether and kept in an oven for drying at 40 °C.

2.2.3. Synthesis of Nitrogen-doped Entangled Graphene (NEGF):

60 mg of GO was dispersed in 20 ml (3:1) of an aqueous solution of ammonia (30% v/v) *via* water-bath sonication and overnight stirring. The complete solution was transferred into a Teflon-lined autoclave and the mixture was kept for 12 h at 180 °C. After complete cooling to room temperature, the sample was washed by water for 5-6 times to remove the excess ammonia, followed by freeze-drying to prepare the nitrogen-doped entangled graphene framework (NEGF).

2.2.4. Synthesis of NiFe-LDH Supported Nitrogen-doped entangled graphene (NiFe-LDH/NEGF):

60 mg of the as-prepared GO was added to 20 ml (3:1) of an aqueous solution of ammonia (30% v/v), *via* water-bath sonication and overnight stirring. After the complete dispersion of GO, $\text{Ni}(\text{OAc})_2 \cdot 4\text{H}_2\text{O}$ and $\text{Fe}(\text{OAc})_2 \cdot 4\text{H}_2\text{O}$ were added to the solution and the mixture was kept stirring for another 6 h. After complete mixing of the metal ions, the reaction mixture was transferred into a Teflon-lined autoclave and heated at 180 °C for 12 h. Subsequently, the autoclave was allowed to cool down naturally and the sample was washed by water for 5-6 times to remove the excess ammonia. This was further subjected to freeze-drying for 10 h at -52 °C under high vacuum pressure. After the completion of the freeze-drying process, the sample was collected, which adopted a flaky kind of structure.

2.2.5. Synthesis of unsupported NiFe-LDH:

Synthesis of NiFe-LDH was done by adding nickel acetate and iron acetate salt into 20 ml (3:1) of aqueous solution of ammonia (30% v/v), and the mixture was thereafter kept for 6 h with constant stirring. After complete mixing, the solution was transferred into a Teflon-lined autoclave and the system was kept for 12

h at 180 °C. After complete cooling to room temperature, the sample was washed with water 5-6 times to remove the excess ammonia. The final sample was dried in an oven at 60 °C and collected.

2.2.6. Synthesis of Ni(OH)₂/NEGF:

Synthesis of Ni(OH)₂/NEGF has been done in the same way as NiFe-LDH/NEGF, except for the addition of iron acetate. 60 mg of GO was dispersed in 20 ml (3:1) of an aqueous solution of ammonia (30% v/v) *via* water-bath sonication and overnight stirring. After complete dispersion of GO, nickel acetate was added to the solution and the mixture was kept for 6 h with constant stirring. After complete mixing, the solution was transferred into a Teflon-lined autoclave and heated for 12 h at 180 °C. After complete cooling to room temperature, the sample was washed with water 5-6 times to remove the excess ammonia, followed by freeze-drying to prepare Ni(OH)₂/NEGF.

2.2.7. Synthesis of NiFe-LDH/NEGF (w/o):

To comparatively study the effect of freeze-drying and doped nitrogen atom on the carbon support, we have synthesized NiFe-LDH over the nitrogen-doped graphene without freeze-drying, which is named as NiFe-LDH/NEGF (w/o). The process involved for the synthesis of NiFe-LDH/NEGF (w/o) is the same as that adopted for NiFe-LDH/NEGF, except that, instead of using freeze-drying, the sample was dried by filtration after hydrothermal treatment for 12 h at 180 °C.

2.2.8. Synthesis of NiFe-LDH/EGF:

Instead of ammonia, only water was used to study the effect of nitrogen-doping, and the sample is named as NiFe-LDH/EGF. The synthesis process of NiFe-LDH/EGF is the same as that of NiFe-LDH/NEGF, except that, instead of using ammonia solution, only water was used as the solvent, followed by solvothermal treatment of the mixture for 12 h at 180 °C and applying the freeze-dried method.

2.2.9 Material Characterization:

The morphological investigation was performed using field emission scanning electron microscopy (FESEM) and transmission electron microscopy (TEM) methods. FESEM analysis was performed by FEI Nova Nano SEM 450 FESEM microscope. TEM images were recorded on a Tecnai T-20 instrument at an accelerating voltage of 200 kV. The TEM sample was prepared by drop coating of the well-dispersed sample in isopropyl alcohol (1 mg of sample in 5 ml solvent) on a carbon-coated 200 mesh copper grid. The sample-coated TEM grid was dried for 1 h under an IR-lamp. The as-synthesized sample's crystallinity was measured by the powder X-ray diffraction (PXRD) analysis. The XRD measurement was performed on a Rigaku Smart Lab diffractometer with Cu K α radiation ($\lambda = 1.5406 \text{ \AA}$) with a scan rate of 5° min^{-1} in

the 2θ range of 5 to 80° . X-ray photoelectron spectroscopy (XPS) was performed using a fully integrated, monochromated small spot X-ray photoelectron spectrometer (XPS) system. It is specified with the 180° double focussing hemispherical analyzer-128-channel detector and micro-focused Al $K\alpha$ as X-ray monochromator source. Thermal stability of the material and the metal composite loading over the carbon were analyzed using an SDT Q600 DSC-TDA thermo-gravimetric (TG) instrument in the temperature range of RT (Room Temperature)- 900°C at a constant heating rate of $10^\circ\text{C min}^{-1}$ in an oxygen atmosphere. Raman spectral investigations were carried out using a 632 nm green laser (NRS 1500W) on an HR 800 RAMAN spectrometer. N_2 adsorption-desorption isotherm experiments were performed on a Quantachrome Quadrasorb automatic volumetric instrument to analyze the surface area and pore volume of the samples.

2.2.10. Electrochemical Studies:

The electrochemical data were acquired with the help of a set of electrochemical techniques, including linear sweep voltammetry (LSV) using a rotating disc electrode (RDE) made of glassy carbon (0.0706 cm^2) connected to the Pine Instrument. A three-electrode electrochemical cell was used with an SP-300 model Bio Logic potentiostat. Hg/HgO was employed as the reference electrode, and graphite rod (Alfa Aesar, 99.99%) was used as a counter electrode. For OER performance comparison, we included the electrochemical activity profiling of 20% RuO_2/C . RuO_2/C was prepared from commercial RuO_2 hydrate by adopting the procedure reported by Thomas Audichon *et al.*² The heat-treated RuO_2 was mixed with Vulcan carbon in the composition ratio of 1:4 to get 20% RuO_2/C . The catalyst slurry was prepared by mixing the catalyst (5 mg) in 1 mL isopropyl alcohol-water (3:2) solution and 40 μL of Nafion solution (5 wt%, Sigma-Aldrich) using water-bath sonication for approximately 1 h. After well mixing, the catalyst slurry was coated on the surface of the working electrode, which was polished with 0.3 μm alumina slurry in DI-water followed by cleaning with DI-water and acetone. 2.5 μL of the ink was drop coated on the surface of the RDE (0.0706 cm^2) electrode. After coating the material on the electrode surface, the electrode was dried under an IR-lamp for 1 h. A catalyst-coated dry electrode was prepared for the electrochemical study. An aqueous solution of 1 M KOH (de-aerated with nitrogen gas) was used as an electrolyte for the RDE experiments. All the electrode potentials were first converted into the reversible hydrogen electrode (RHE) through an RHE calibration experiment, which was done previously in our lab³, and for 1 M KOH, $E(\text{RHE}) = E(\text{Hg/HgO}) + 0.917\text{ V}$. All the RDE experiments were carried out at a constant rotating rate of 1600 rpm in order to maintain a uniform ionic concentration of the reactant as well as to prevent accumulation of the products, *i.e.*, O_2 bubbles over the electrode surface. The linear sweep voltammetry

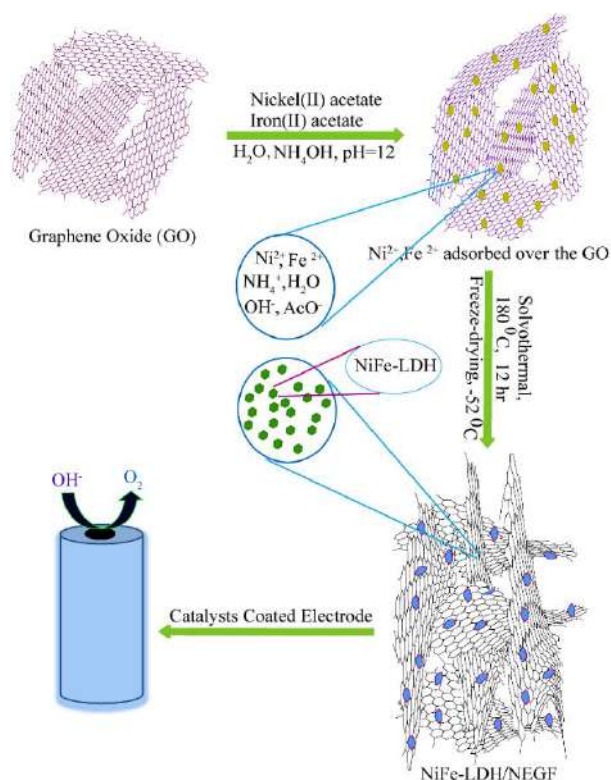


Figure 2.1. Schematic representation for the synthesis of NiFe-LDH-anchored N-doped 3D entangled graphene framework (NiFe-LDH/NEGF) and its application as an efficient OER electrocatalyst. (Reprinted (adapted) with permission from *Nanoscale Adv.*, 2020, 2, 1709. Copyright (2020) Royal Society of Chemistry).

data was corrected with 65% iR -compensation, where i and R indicate the current measured and the ohmic resistance employed between the working and reference electrode, respectively. Current densities were normalized by the known value of electrode surface area, and the reaction overpotential was determined using the equation: $\eta = [E(\text{RHE}) - 1.23] \text{ V}$. The Faradaic impedance was measured using the PEIS technique (Potentiostatic Electrochemical Impedance Spectroscopy) by using a SP-300 Biologic test station in the Faradaic region at 1.57 V vs. RHE covering the 100 kHz - 0.1 Hz frequency range with 10 mV amplitude of sinusoidal potential perturbation as followed by J.F.C. Boodts *et al.*⁴ to study the Faradaic impedance of oxygen evolution reaction. All the impedance values are normalized with the electrode area of 0.0706 cm².

2.3. Results and Discussion

The preparation procedure for the homogeneously distributed NiFe-LDH over NEGF involves two steps, as illustrated in **Figure 2.1**. The reaction mixture was first treated solvothermally followed by lyophilization under high vacuum and low temperature (-52 °C) conditions. The adopted lyophilization process helped to prevent the graphene sheet-restacking at these experimental conditions, generating an entangled graphene

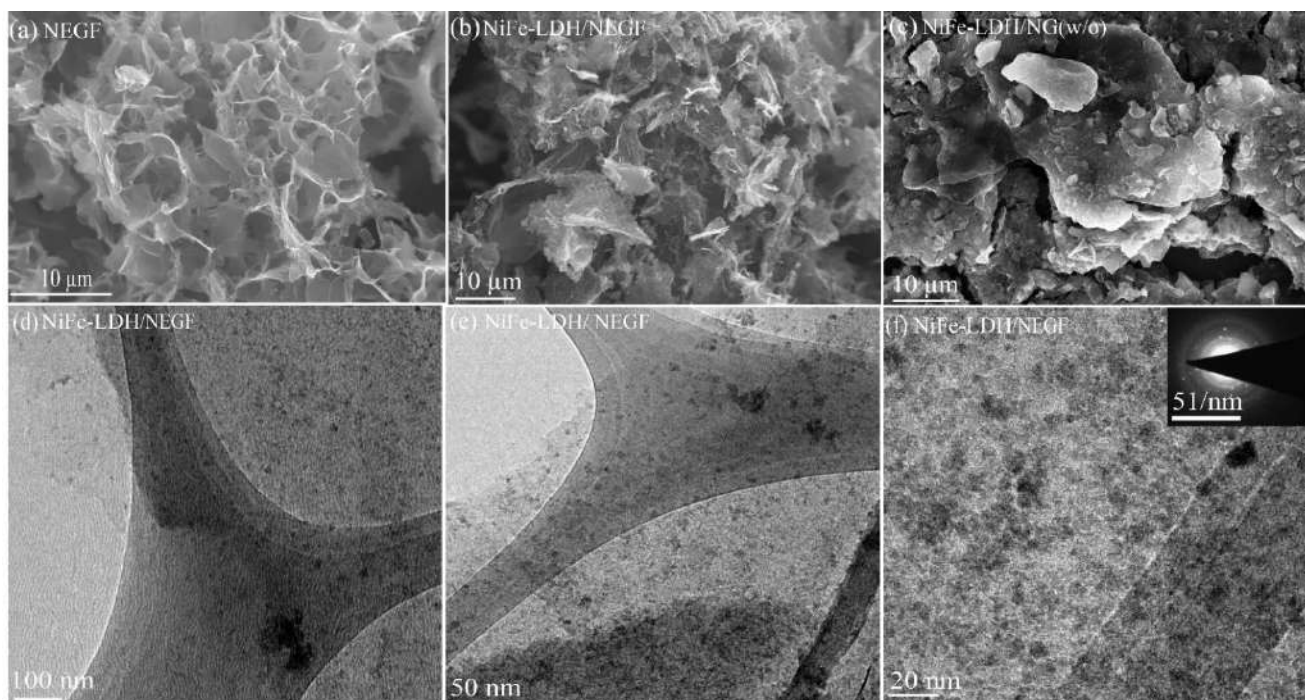


Figure 2.2. FESEM images of (a) NEGF; (b) NiFe-LDH/NEGF; (c) NiFe-LDH/NEGF (w/o); (d), (e), and (f) are the TEM images of NiFe-LDH/NEGF recorded at different magnifications. (Reprinted (adapted) with permission from *Nanoscale Adv.*, 2020, 2, 1709. Copyright (2020) Royal Society of Chemistry).

framework by crosslinking of the graphene sheets.²⁹ The interesting role played by ammonium ion is that it helps in the strengthening of the graphene hydrogel along with nitrogen doping at a temperature of as low as just 180 °C in the solvothermal conditions.³⁴ Ammonium hydroxide enhances the interaction between two graphene sheets by its alkaline hydroxyl groups and ammonium ions.

2.3.1. FESEM Analysis:

The formation of hierarchical NEGF was first examined through field-emission scanning electron microscopy (FESEM). **Figure 2.2a** represents the FESEM image of NEGF, displaying a 3D entangled network formulated with randomly oriented graphene nanosheets. Such an entangled 3D framework not only prevented the agglomeration of the graphene nanosheets but it also provided high surface area as well as porosity to the matrix. It, henceforth, facilitated the easy migration of reactants and gaseous products released during the electrochemical reactions.^{24,25} Such a type of interconnected graphene framework is also retained during the *in situ* loading of the active material, *i.e.*, NiFe-LDH, as depicted in **Figure 2.2b**. **Figure 2.2c** shows the FESEM image of the NiFe-LDH-anchored nitrogen-doped graphene without the

freeze-drying step, presenting ill-defined agglomerated morphology with thick and stacked graphene patches. Hence, FESEM analysis supports the role of lyophilization to prevent the restacking of the

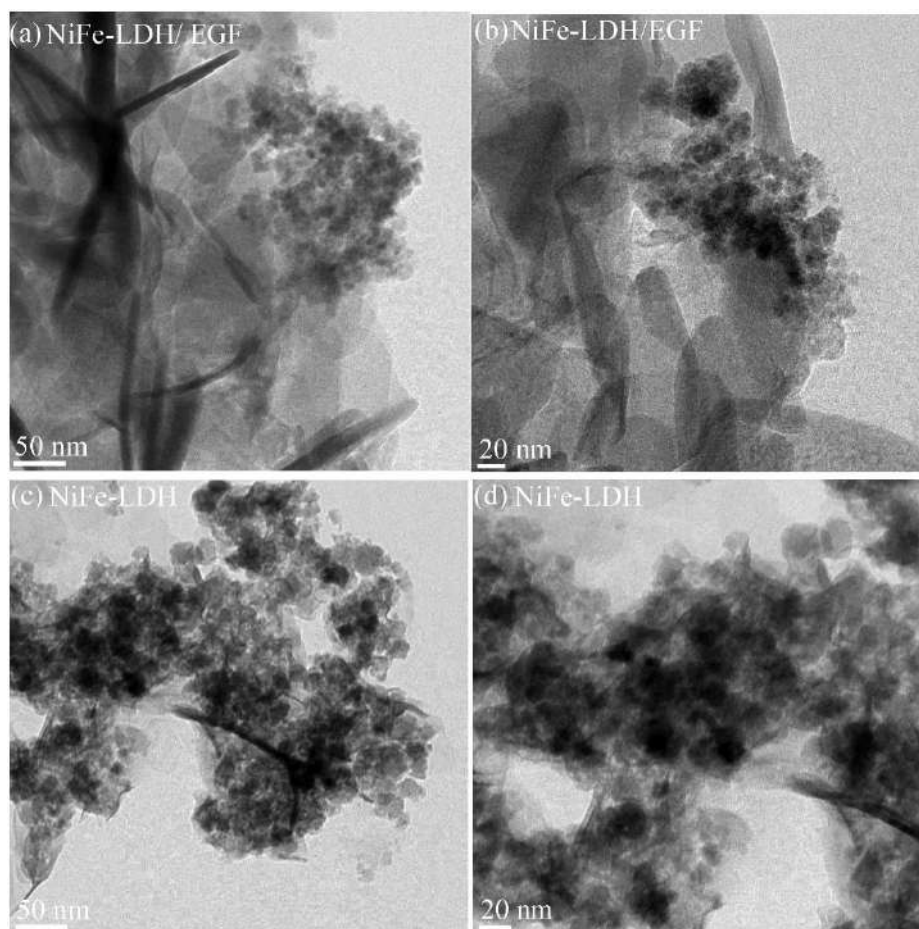


Figure 2.3. TEM images of the samples: (a) and (b) are the images of NiFe-LDH/EGF; (c) and (d) are the images of the unsupported NiFe-LDH. (Reprinted (adapted) with permission from *Nanoscale Adv.*, 2020, 2, 1709. Copyright (2020) Royal Society of Chemistry).

graphene nanosheets, assisted by the water removal at the high vacuum and low-temperature conditions.

2.3.2. TEM Analysis:

Next, to FESEM, transmission electron microscopy (TEM) analysis was performed to find out the size and distribution of the decorated NiFe-LDH over the graphene sheets. **Figures 2.2d** and **2.2e** represent the TEM images of NiFe-LDH/NEGF recorded at different magnifications. The TEM analysis revealed a homogenous distribution of the layered double hydroxide nanostructures over NEGF. The further magnified TEM image presented in **Figure 2.2f** depicts that the anchored LDH nanostructures are ill-resolved and amorphous in nature. The amorphous nature of the anchored NiFe-LDH is further supported

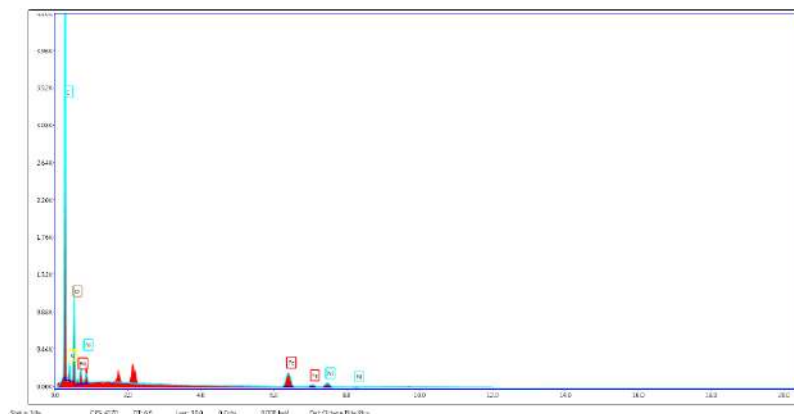


Figure 2.4. EDS pattern of the NiFe-LDH/NEGF. (Reprinted (adapted) with permission from Nanoscale Adv., 2020, 2, 1709 Copyright (2020) Royal Society of Chemistry).

by the diffused ring pattern in selected area electron diffraction (SAED) analysis (inset of **Figure 2.2f**). The role of N-doping toward facilitating the homogenous distribution of the metal hydroxides over NEGF is also studied by comparatively analyzing the TEM images of NiFe-LDH-anchored N-doped and un-doped entangled graphene framework (EGF). **Figures 2.3a** and **2.3b** represent the TEM images of NiFe-LDH-supported un-doped EGF, depicting the larger agglomerates of NiFe-LDH over the support sheets. This finding shows the crucial role played by N- doping to create plenty of metal anchoring sites along with the tuning of the size of LDH nanostructures as well as in avoiding their agglomeration.³⁴ Further, to study the need of support for decorating discrete active LDH nanostructures, TEM analysis was extended to a support-free NiFe-LDH system. The comparative study showed that, in the absence of any substrate, LDH depicts more chances of agglomeration and acquiring a bulky morphology (**Figure 2.3c** and **2.3d**). We have further extracted the weight % and atomic % of the various species present in the sample and the corresponding data is presented in **Figure 2.4**. The respective elemental composition is shown in **Table 2.1**.

2.3.4. BET Analysis:

The BET analysis of NiFe-LDH/NEGF evidenced the essential role played by freeze-drying toward maintaining a highly porous and exposed surface of the catalyst. It is reflected both through the surface area obtained, *i.e.*, 328 m²/g, as well as porosity from the pore size distribution profile giving the distribution of pores in the range of 2 to 5 nm (**Figure 2.5a**). These results further guarantee the individual graphene sheets acquired into the bulk structure. Of note, the surface area of NEGF is found to be higher than that of NiFe-

LDH/NEGF (547 m²/g vs 328 m²/g), which is obvious owing to the blockage and covering of some of the pores of NEGF through the as-grown NiFe-LDH nanostructures. As depicted in **Figure 2.5a**,

Table 2.1. EDS data corresponding to NiFe-LDH/NEGF. (Reprinted (adapted) with permission from Nanoscale Adv., 2020, 2, 1709. Copyright (2020) Royal Society of Chemistry).

Element	Weight %	Atomic %
C K	52.13	64.08
N K	10.21	10.76
O K	23.25	21.45
FeK	6.95	1.84
NiK	7.46	1.88

NiFe-LDH/NEGF shows the higher cumulative area in the pore size range of 2 to 5 nm, suggesting the mesoporous nature of NiFe-LDH/NEG. However, the pore-size distribution profile of NiFe-LDH/NG (w/o) showed diminished intensity in the above-mentioned pore-size region, supporting the role of freeze-drying to make an open and exposed catalyst framework. Pore size distribution analysis is also extended on NEGF, presenting a similar pore size distribution profile to that of NiFe-LDH/NEGF (**Figure 2.5a**). To make a better understanding of the contribution of different parameters towards catalytic performance, BET isotherms for all the samples are recorded and the corresponding data is presented in **Figure 2.6a**. Furthermore, the pore size distribution profile for NEGF shown in **Figure 2.6b** reveals the presence of a similar distribution of porosity.

2.3.5. XRD analysis:

To identify the phase and crystallinity of the as-synthesized samples, X-ray diffraction (XRD) analysis has been performed. **Figure 2.5b** consists of the comparative XRD patterns for NEGF and NiFe-LDH/NEGF. PXRD pattern for NEGF shows an intense peak at the 2θ value of 26° , corresponding to the (002) diffraction peak of the reduced graphene oxide.²⁶ PXRD pattern of NiFe-LDH/NEGF shows a comparatively intense and prominent (001) plane, matching well with the JCPDS Card No. 040-0215. NiFe-LDH/NEGF also shows a broad and intense (002) plane of NEGF, attributing to the anchoring of NiFe-LDH over NEGF. To study the role of Fe incorporation in the Ni-hydroxide crystal structure, the growth of nickel hydroxide over the nitrogen-doped entangled graphene (NEGF) has been realized in the same reaction conditions and has been abbreviated as α -Ni(OH)₂/NEGF. Comparative PXRD patterns of α -Ni(OH)₂/NEGF and NiFe-

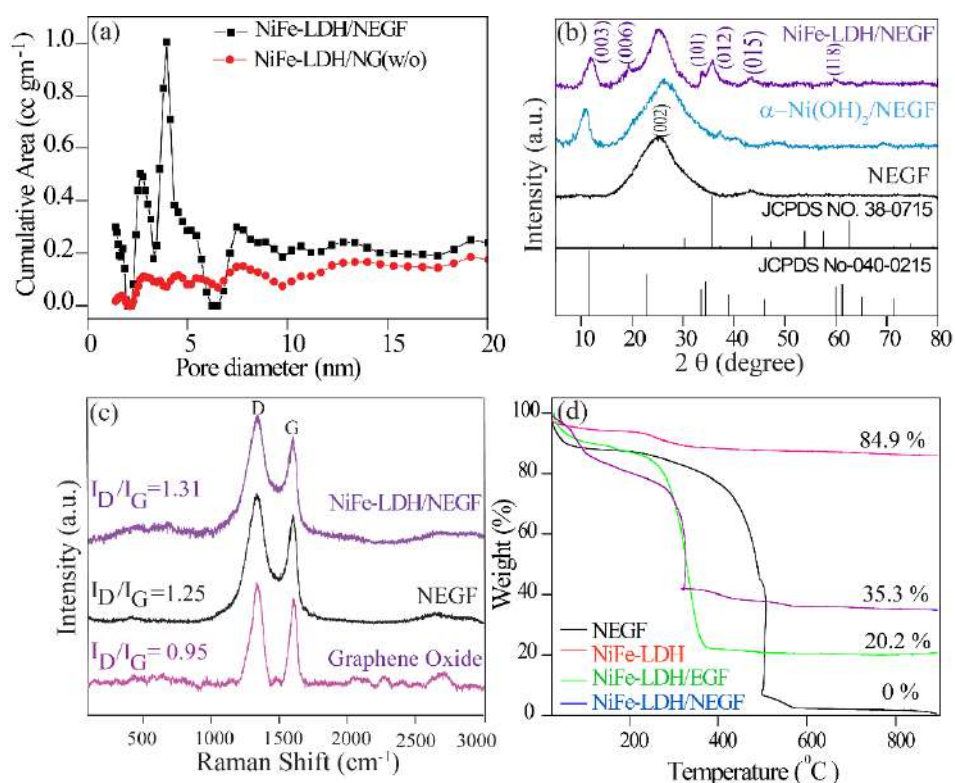


Figure-2.5. Comparative physical characterizations of the as-prepared catalysts: (a) pore-size distribution profiles of NEGF and NiFe-LDH/NEGF; (b) PXRD patterns of NEGF, α -Ni(OH)₂, and NiFe-LDH/NEGF; (c) Raman spectra of GO, NEGF, and NiFe-LDH/NEGF and (d) TGA profiles. (Reprinted (adapted) with permission from *Nanoscale Adv.*, 2020, 2, 1709. Copyright (2020) Royal Society of Chemistry).

LDH/NEGF suggested the increased order of the hydroxide layers after the Fe incorporation into the α -Ni(OH)₂ crystal structure owing to the poor intensity of the hydroxide peaks in the former case.^{36,37}

2.3.5. Raman analysis:

Next, to the crystal phase identification, Raman analysis was conducted to investigate the graphitization and defect extent in the microstructure of the synthesized graphene-based materials. **Figure 2.5c** comprises the comparative Raman spectra of GO, NEGF, and NiFe-LDH/NEGF. The spectra show that the typical peaks for all the samples are located in the range of 1300 and 1600 cm⁻¹, which is due to the stock phonon interaction of the carbon materials created by the laser excitation.³⁶ In all the comparative samples, the intense peak at 1320 cm⁻¹ is due to the defective (D) nature of the carbon, including disorders in bonding, heteroatom doping, and vacancy in the carbon lattice.³⁷ As shown in **Figure 2.5c**, another intense peak

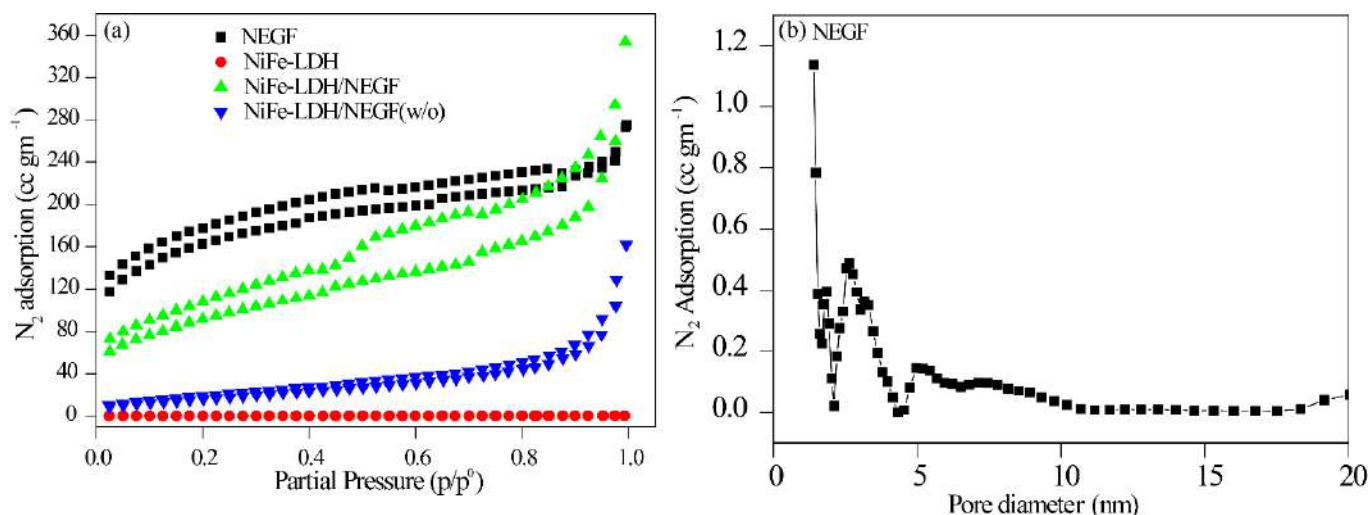


Figure 2.6. BET analysis of NEGF: (a) comparative BET isotherms of NEGF, NiFe-LDH, NiFe-LDH/NEGF, and NiFe-LDH/NEGF (w/o); and (b) pore size distribution profile. (Reprinted (adapted) with permission from *Nanoscale Adv.*, 2020, 2, 1709. Copyright (2020) Royal Society of Chemistry).

appeared in the range of 1580 to 1600 cm^{-1} is attributed to the graphitic nature of the carbon,³⁸ indicating ordered lattice structure from the vibration of the Csp^2 in the plane.³⁹ The intensity ratio of the defective carbon peak to the graphitic carbon peak, *i.e.*, I_D/I_G ratio, helps to find out the extent of defects/disorders and graphitization extent in the carbon-based materials.^{34,39} The I_D/I_G values for NEGF (1.31) and NiFe-LDH/NEGF (1.25) are higher than that of GO (0.95), suggesting the GO reduction to reduced graphene oxide (rGO) during the hydrothermal treatment. Besides, higher intensity of the defective carbon for NEGF and NiFe-LDH/NEGF is demonstrating a decrease in the average size of the sp^2 domains due to the removal of the oxygen-containing functional groups and doping of nitrogen (N) atom over the carbon atom.^{34,41} Higher defect and disorders over the carbon support help to generate plenty of nucleation sites for the nanoparticle growth, their controlled homogeneity, and size distribution.⁴¹

2.3.7. TGA analysis:

After confirming the highly open, and entangled graphene framework characteristics of NEGF along with the good active material dispersion over it, thermogravimetric analysis (TGA) was employed to get the idea of total active material loading over NEGF. TGA was carried out by annealing the sample from 25 to $900\text{ }^\circ\text{C}$ with a scan rate of $5\text{ }^\circ\text{C}$ per minute in an oxygen atmosphere. **Figure 2.5d** represents the TGA curves for NEGF, NiFe-LDH, NiFe-LDH/NEGF, and NiFe-LDH/EGF. For all the compared samples, an initial weight loss was observed near around 100 - $150\text{ }^\circ\text{C}$, owing to the evaporation of physisorbed water molecules. NEGF contains only a composite of nitrogen, oxygen, and major content of carbon, which starts

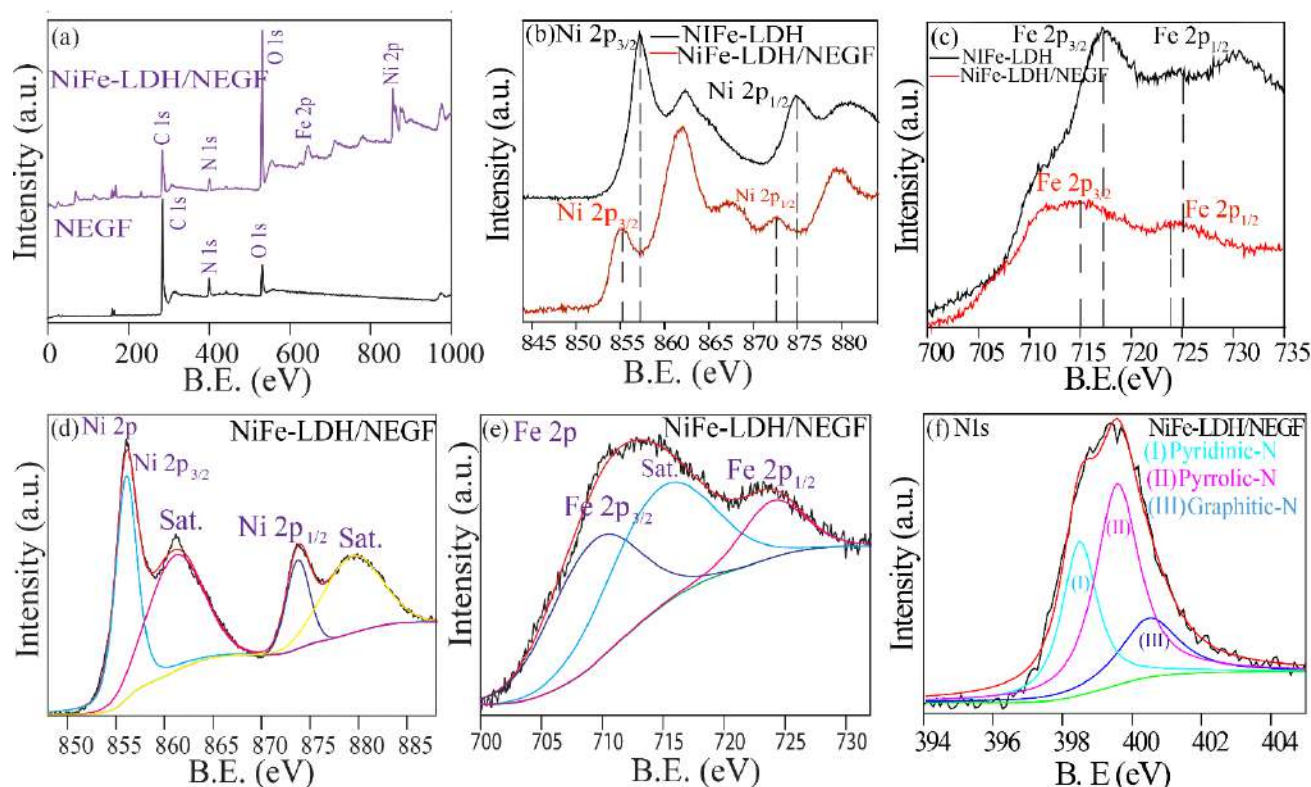


Figure-2.7. XPS analysis: (a) XPS survey scan spectra of NEGF and NiFe-LDH/NEGF; (b) XPS spectra of Fe 2p in NiFe-LDH and NiFe-LDH/NEGF; (c) XPS spectra of Ni 2p in NiFe-LDH and NiFe-LDH/NEGF; (b), (c) and (d) are the high-resolution deconvoluted spectra of Ni 2p, Fe 2p and N 1s of NiFe-LDH/NEGF, respectively. (Reprinted (adapted) with permission from *Nanoscale Adv.*, 2020, 2, 1709. Copyright (2020) Royal Society of Chemistry).

burning at around 400 °C, and at near 500 °C, complete calcination is observed in the oxygen atmosphere. This complete conversion of carbon and nitrogen to mixed oxide products fly off, so the rest of the sample weight becomes zero. In the case of NiFe-LDH, no such major weight loss was observed. However, in the other two supported systems, *i.e.*, NiFe-LDH/NEGF and NiFe-LDH/EGF, reasonable water loss is encountered owing to the presence of LDH and porous carbon having larger accessibility for a physisorbed water molecule. In the two later samples, major weight loss in the temperature region of 350 to 500 °C might be because of the oxidation of carbon. As it is already illustrated in the Raman analysis section that, nitrogen doping over the carbon surface helps to create plenty of metal-binding sites, which increases the metal support interactions.⁴⁴ This can be further supported by the TGA data. As visible from **Figure 2.5d** NiFe-LDH/NEGF shows comparatively higher active material loading (~35%) than that of NiFe-LDH/EGF (~20%). This strongly anchored and higher active material loading may help toward improving the electrocatalytic activity and durability.⁴²

2.3.8. XPS analysis:

The electronic structure tuning of all the surface elements, *i.e.*, N-doping over the carbon support, binding energy change due to the catalyst support interactions, and formation of NiFe-LDH, is thoroughly analysed by employing X-ray photoelectron spectroscopy (XPS) measurements. **Figure 2.7a** represents the survey spectra of NEGF and NiFe-LDH/NEGF, affirming the presence of Ni, Fe, O, N, and C in NiFe-LDH/NEGF and N, O, and C in NEGF. In both the cases, the common elements C, O, and N are having binding energy values located at around ~ 284.8 , ~ 531.5 , and ~ 400.5 eV, respectively.^{43,44,45} In the case of NiFe-LDH/NEGF, two new peaks are present at ~ 710.8 and ~ 855.6 eV, corresponding to the elements Fe and Ni, respectively.^{46,47,48} From **Figure 2.7a.**, it is apparent that the surface composition of carbon and nitrogen is decreased in NiFe-LDH/NEGF, which is due to the coverage of NiFe-LDH over the nitrogen-doped carbon. However, the O1s peak is found to intensify after the NiFe-LDH loading, basically coming from the hydroxide moieties as well as intercalated carbonate and water species.^{40,41,42} To know the electronic interaction of NEGF and NiFe-LDH, the binding energy value for Ni 2p and Fe 2p has been compared (**Figures 2.7b** and **2.7c**). There is a strong interaction between supported NiFe-LDH and the doped-N of the graphene. Due to the electronegativity difference between the doped-N and NiFe, there will be electron transfer between these two entities. The comparable XPS spectra of NiFe-LDH and NiFe-LDH/NEGF shown in **Figure 2.7b** and **2.7c** clearly show a shift in the binding energy of the metals, evidencing the electron transfer from the doped nitrogen to the metal, which is responsible for the reduction in B.E. These core level spectra were deconvoluted to study their chemical state in the LDH-system. **Figure 2.7d** represents the deconvoluted Ni 2p spectrum of NiFe-LDH/NEGF, depicting the two main spin-orbit doublets of Ni, *i.e.*, Ni 2p_{3/2} (873.3 eV) and Ni 2p_{1/2} (855.6 eV) along with two bands. The binding energy value of these two doublets suggests the +2 oxidation state of Ni in the NiFe-LDH system.^{48, 49} **Figure 2.7e** represents the deconvoluted XPS spectra of NiFe-LDH/NEGF in the Fe 2p core level. It exhibits two prominent spin-orbit doublets located at 710.9 and 725.1 eV corresponding to Fe 2p_{3/2} and Fe 2p_{1/2} splitting for Fe³⁺ oxidation state, respectively.^[50,51] Hence, deconvolution as well as binding energy assignment of the different spin states of Ni and Fe core-level spectra has helped to find out the oxidation states of the two elements in LDH. Further, high-resolution XPS of NEGF and NiFe-LDH/NEGF are comparatively analyzed in the C 1s, O 1s, and N 1s core regions (**Figure 2.8** and **Figure 2.7f**). Various chemical states of carbon, *i.e.*, C-C, C=C (284 eV), C-O (286 eV), and C-N/C=N (400 eV), with different binding energy values owing to the unique chemical environment of carbon as marked in the respectively (**Figure 2.8a** and **2.8b**).^{43,44} The C 1s spectrum of NiFe-LDH/NEGF showed an additional CO₃²⁻ anion peak at 289.8 eV, indirectly illustrating the growth of layer double hydroxide over NEGF.^{46,47,48} Subsequently,

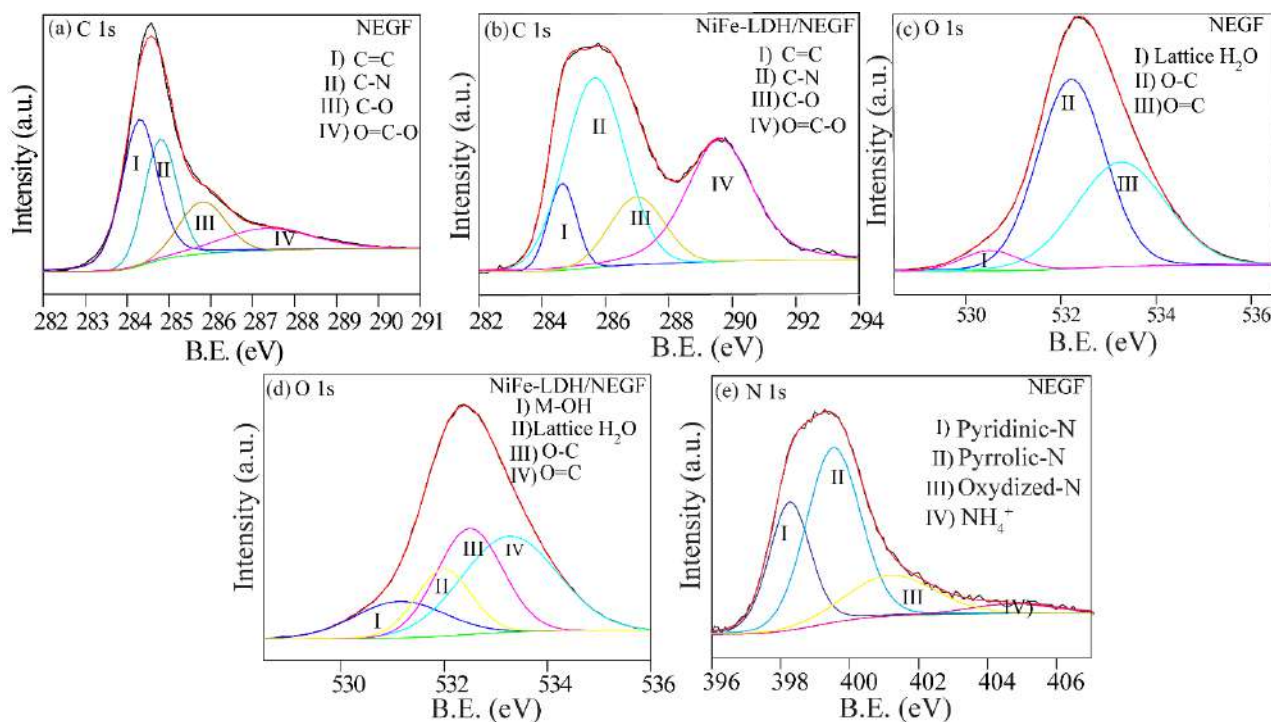


Figure 2.8. XPS analysis: (a) C 1s spectra of NEGF; (b) C 1s spectra of NiFe-LDH/NEGF; (c) O 1s spectra of NiFe-LDH/NEGF; (d) O 1s spectra of NEGF and (e) N 1s spectra of NiFe-LDH/NEGF. (Reprinted (adapted) with permission from *Nanoscale Adv.*, 2020, 2, 1709. Copyright (2020) Royal Society of Chemistry).

deconvoluted O1s core level spectrum was comparatively examined for both NEGF and NiFe-LDH/NEGF as given in **Figures 2.8c and 2.8d**. In NEGF, oxygen binds with carbon in the form of C-O, C=O, and epoxy group formation. However, in case of NiFe-LDH/NEGF, O 1s spectra show quite good disparity owing to the surface rich layer of the double hydroxide (LDH), having oxygen coordinated in the form of Ni(OOH), Fe-OH, Ni-OH, and in the carbonate or lattice H₂O form. Deconvoluted N 1s spectra of NEGF and NiFe-LDH/NEGF are also examined to know the types of nitrogen present in the graphene matrix along with their total percentage in **Figures 2.8e and 2.7f**. The N 1s spectrum of NEGF (**Figure 2.8e**) identifies a higher percentage (42.4%) of pyrrolic-N (399.7 eV) and almost similar percentage (41.6%) of pyridinic-N (398.6 eV) along with a lower quantity (15.9%) of quaternary-N (400.5 eV). Further, the N 1s spectrum of NiFe-LDH/NEGF is also deconvoluted to find out any change in the XPS spectrum after the NiFe-LDH loading over NEGF. **Figure 2.7f** depicts the deconvoluted N 1s spectrum locating all the deconvoluted peaks which are present in NEGF, suggesting the N-doping in graphene matrix remains the same during

the *in situ* loading of NiFe-LDH. Thus, deconvoluted XPS of C 1s, O 1s, and N 1s clearly conclude the solvothermal-assisted reduced graphene oxide formation as well as layer double hydroxide growth.

2.3.9. Electrochemical Analysis:

All the employed physical characterization techniques conclude the formation as well as favorable characteristics of NiFe-LDH/NEGF to catalyze the water oxidation reaction. The study was extended subsequently to understand the electrocatalytic performance characteristics of the catalyst. The dedicated electrochemical analyses were carried out by employing various techniques, *e.g.*, electrochemical surface area (ECSA) measurement, linear sweep voltammetry (LSV) and chronoamperometry. All the analyses were carried out using Hg/HgO as a reference electrode in 1 M KOH, which was further calibrated to RHE using the standard calibration method.⁴⁹ All the polarization curves were recorded after an ohmic potential drop (*iR*-drop) compensation by 65%. Comparative ECSA values were first examined to find out the accessible active center density of the various employed catalysts. For platinum-free systems, double-layer capacitance (C_{dl}) in the non-Faradaic region is the reasonable parameter to measure the ECSA.⁵⁰ **Figures 2.9 and 2.10a** show the higher double-layer capacitance (C_{dl}) values possessed by NiFe-LDH/NEGF (7.9 mF cm^{-2}), as compared to that of the other two samples, *i.e.*, for NiFe-LDH/NG (w/o) (3.7 mF cm^{-2}) and NiFe-LDH (1.0 mF cm^{-2}). It suggests higher charge accumulation as well as electrolyte infiltration on the highly exposed and open texture of the catalyst system (NiFe-LDH/NEGF).

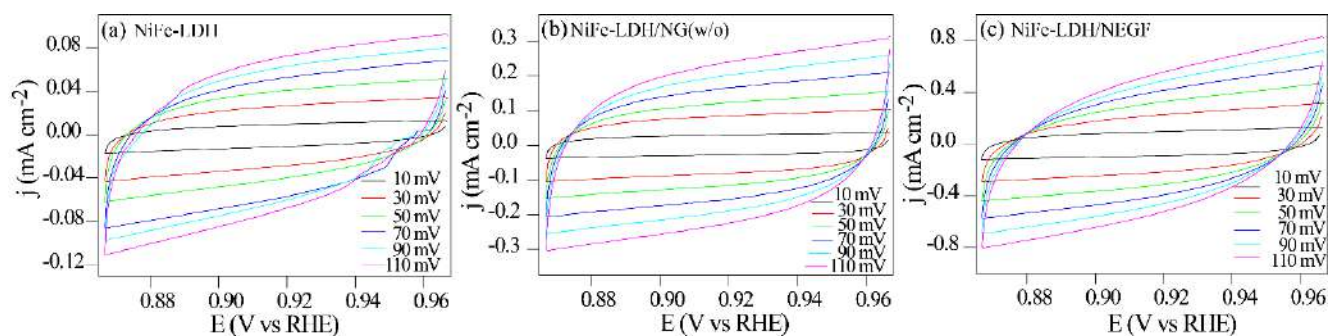


Figure 2.9. ECSA measurement through electrochemical double-layer charge capacitance (C_{dl}) measurement by recording CV in the non-Faradic region at different scan rates of 10 to 110 mV/s: (a) NiFe-LDH; (b) NiFe-LDH/NEGF (w/o), and (c) NiFe-LDH/NEGF. (Reprinted (adapted) with permission from Nanoscale Adv., 2020, 2, 1709. Copyright (2020) Royal Society of Chemistry).

Figure 2.10b represents the polarization curves recorded for oxygen evolution reaction (OER). The overpotential observed at a current density of 10 mA cm^{-2} for NiFe-LDH/NEGF (290 mV) is lower than that of NiFe-LDH (350 mV), NiFe-LDH/NG (w/o) (340 mV), and 20% RuO₂/C (310 mV). Higher

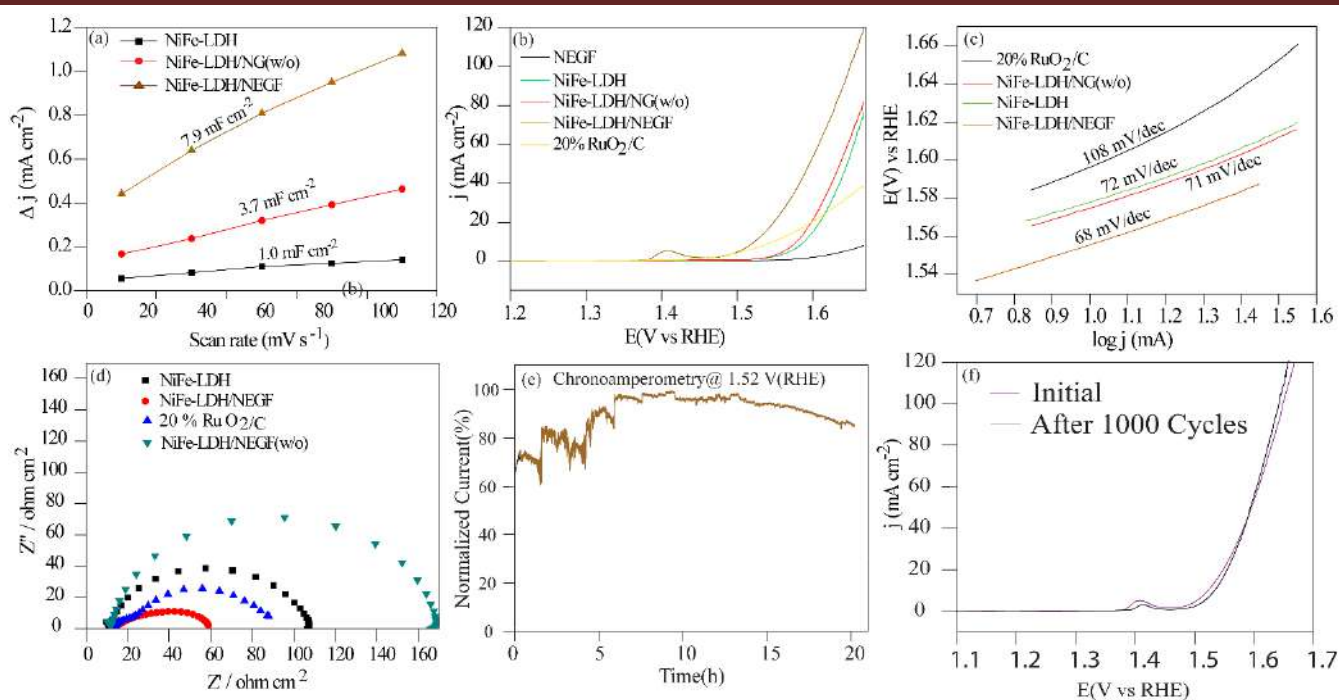


Figure-2.10. Electrochemical analysis of the as-synthesized catalysts in 1 M KOH: (a) comparative plots of the scan rate dependent double-layer capacitive current density (C_{dl}) at 0.91 V vs. RHE; (b) the OER polarization curves recorded at 10 mV s^{-1} scan rate and 1600 rpm of the working electrode; (c) Tafel plots; (d) Nyquist plots recorded on NiFe-LDH, NiFe-LDH/NEGF, 20 % RuO_2/C and NiFe-LDH/NEGF(w/o) at an applied potential of 1.57 V in the AC frequency range between 100 kHz and 0.1 Hz; (e) chronoamperometric stability test for NiFe-LDH/NEGF; (f) LSV plots recorded over NiFe-LDH/NEGF before and after the 1000 CV cycles. (Reprinted (adapted) with permission from *Nanoscale Adv.*, 2020, 2, 1709. Copyright (2020) Royal Society of Chemistry).

Table 2.2. Comparison of the OER activity data of the present work. (Reprinted (adapted) with permission from *Nanoscale Adv.*, 2020, 2, 1709. Copyright (2020) Royal Society of Chemistry).

Electrocatalysts	Overpotential (mV)	Double Layer Capacitance (C_{dl})	Tafel Slop (mV dec^{-1})
NiFe-LDH	350 mV	1.1 mF cm^{-2}	72
NiFe-LDH/NG(w/o)	340 mV	3.9 mF cm^{-2}	71
NiFe-LDH/NEGF	290 mV	8.8 mF cm^{-2}	68
20% RuO_2/C	310 mV	-	108
NiFe-LDH/EGF	370 mV	-	-

electrocatalytic activity of NiFe-LDH/NEGF toward OER, as compared to that of NiFe-LDH, clearly reveals the effect of NEGF support to distribute the active NiFe-LDH homogenously by alleviating the active center agglomeration. Moreover, the effect of freeze-drying is also reflected in the polarization

plots, representing the poor activity of the sample without freeze-drying (*i.e.*, NiFe-LDH/NG (w/o)). All the catalysts composed of Ni have a characteristic oxidation peak just before starting the OER process; however, due to higher OER current in the LSVs, these peaks are not prominently visible. However, after zooming in the oxidative region, these peaks can be visualized prominently as shown in **Figure 2.11b**. The oxidation peak at 1.4 V is derived from the oxy hydroxyl formation of the NiFe active sites. This peak is coming mostly in the Ni-based systems. When Ni is mixed with Fe, the intensity of the peak is enhanced by the redox-active metal centers. As the conductivity as well as activity of the NiFe system becomes low during oxy hydroxyl ion formation, the current generated will not become that much significant. In the case of the carbon-supported systems *viz.* NiFe-LDH/NG (w/o) and NiFe-LDH/NEGF, the intensity of the peak increases. In the case of the system without freeze-drying, NiFe-LDH/NG (w/o), the activity is too low compared to NiFe-LDH/NEGF. Hence, the peak at 1.4 V for NiFe-LDH/NG (w/o) system is not a prominent one. On the other hand, in the case of NiFe-LDH/NEGF, the activity is high, and so the intensity of the peak at 1.4 V when all the synergy works well for this system. Since, in the case of NiFe-LDH/NG (w/o), the self-assembly texture gets collapsed and thus restricts the active center accessibility.

Further, the role of N- doping for designing a robust catalyst can also be studied by comparatively analyzing the OER activity for NiFe-LDH/NEGF and NiFe-LDH/EGF (w/o). **Figure 2.11a** represents the lower performance of NiFe-LDH/EGF (370 mV) as compared to that of NiFe-LDH/NEGF (290 mV). The reason for such a performance variation substantiates the role of nitrogen doping, which provides better interaction of the active material with support as well as its better active material dispersion property. Hence, N-doping helps to improve the electrocatalytic activity by controlling the particle size as well as facilitating higher catalytic active center loading. **Table 2.2** and **Table 2.3** summarize the performance of the various employed catalysts and comparable performance with previously reported catalysts.

Kinetics for the adsorption of the reactant and intermediates as well as desorption of the product, *i.e.*, O₂ over the catalytic site, can be examined by Tafel analysis. A lower Tafel slope defines faster reaction kinetics, low overpotential, and higher kinetic current density. The Tafel slope was obtained by plotting the log of current density ($\log j$) *vs.* potential (V) in the OER potential range. The comparative Tafel plots for NiFe-LDH/NEGF (68 mV/dec), NiFe-LDH (72 mV/dec), NiFe-LDH/NEGF (w/o) (72 mV/dec) and 20% RuO₂/C (68 mV/dec) are shown in **Figure 2.10c**. The lower Tafel value for NiFe-LDH/NEGF indicates better OER kinetics as compared to that of the other catalysts. To further determine the kinetics of the electron transport in various employed catalysts, the Faradaic impedance analysis at a particular potential (1.57 V) was performed. N-doping in graphitic carbon matrix is expected to give better electrochemical

Table 2.3. Comparison of the OER activity data of the present work with the different works published in the literature (Reprinted (adapted) with permission from *Nanoscale Adv.*, 2020, 2, 1709. Copyright (2020) Royal Society of Chemistry).

Sr. No.	Electrocatalyst	Over potential (mV)	Electrolyte	Tafel slop (mV/dec.)	Ref.
1.	NiFe LDH/oGSH hybrid	350	0.1 M KOH	54	4
2.	NiFe LDH/C (Vulcan XC-72R)	360	0.1 M KOH	51	5
3.	NiFe LDH/CNT hybrid	308	0.1 M KOH	35	6
4.	NiFeOx fim	336	1.0 M KOH	30	7
5.	NiFe LDH	302	1.0 M KOH	40	8
6.	Ni-Fe	331	1.0 M KOH	58	9
7.	NiFe-LDH/NEGF	290	1.0 M KOH	68	This Work

activity compared to the system without nitrogen doping due to electronic structure modulation of the catalysts. Electrochemical impedance measurement data in **Figure 2.11c** clearly displays a smaller charge transfer resistance (R_{ct}) for NiFe-LDH/NEGF. This result stands out as a direct evidence of faster charge transfer during the catalytic OER process. The comparative Nyquist plots given in **Figure 2.10d** show the lowest charge-transfer resistance ($R_{ct} = 46 \text{ ohm cm}^2$) in the case of NiFe-LDH/NEGF as compared to RuO_2 ($R_{ct} = 86 \text{ ohm cm}^2$), NiFe-LDH ($R_{ct} = 107 \text{ ohm cm}^2$), NiFe-LDH/NEGF ($R_{ct} = 159 \text{ ohm cm}^2$). The lower R_{ct} value indicates better electronic transport throughout the catalyst system owing to a better interaction of NiFe-LDH with the N-doped entangled framework of graphene.

The durability of the catalyst is another vital parameter to define its robustness, basically its lifetime. The durability of the catalyst was measured by performing chronoamperometry and cycling durability. A chronoamperometric test was performed at a constant potential (a potential needed to achieve a current density of 10 mA cm^{-2}) with a continuous rotation of the working electrode at 1600 rpm. **Figure 2.11e** represents quite good stability of the designed catalyst with nearly 80% performance retention even after 20 h of continuous performance. **Figure 2.11f** depicts the LSV plots before and after the 1000 CV stability cycles, further supporting the higher durability of the designed catalyst. A slight increment in the current density after the cycle durability is basically due to the exposure of more and more catalytic active centers during the electrochemical cycling. Such good durability of the catalyst is attributed to the better interaction of the N-doped entangled graphene with NiFe-LDH.

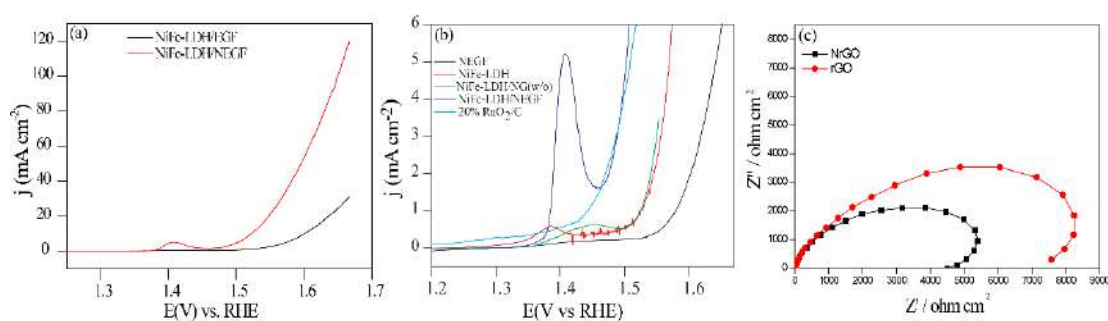


Figure-2.11. (a) Comparative OER polarization curves of NiFe-LDH/NEGF and NiFe-LDH/EGF. The OER polarization curves were recorded at 10 mV s^{-1} scan rate and 1600 rpm of the working electrode; (b) comparative OER polarization curves of NEGF, NiFe-LDH, NiFe-LDH/NEGF, NiFe-LDH/NGr (w/o) and RuO_2 by zooming in the oxidative region; (c) Nyquist plots recorded on rGO and NrGO at an applied potential of 1.57 V in the AC frequency range between 100 kHz and 0.1 Hz. (Reprinted (adapted) with permission from *Nanoscale Adv.*, 2020, 2, 1709. Copyright (2020) Royal Society of Chemistry).

2.4. Conclusions

In this work, a solvothermal treatment followed by the freeze-drying method is proposed for the synthesis of NiFe-LDH on the surface of the nitrogen-doped entangled graphene framework (NEGF). In the presence of ammonium hydroxide, the formation of layered double hydroxide and nitrogen doping on the graphitic carbon skeleton is realized in a single step. Further, freeze-drying helped to maintain the stable, interconnected structure of the graphene sheets, leading to the formation of the entangled structure of graphene. The establishment of high surface area N-doped entangled graphene supported NiFe-LDH has been confirmed by FESEM, TEM, XRD, and BET surface area measurements. High surface area and well-maintained porous graphene have shown higher accessibility of gaseous reactants and electrolytes. Homogeneously distributed NiFe-LDH over nitrogen-doped graphene displayed excellent performance for the oxygen evolution reaction. This promising OER catalytic activity can be ascribed to the following reasons: (1) the uniform distribution of the NiFe-LDH nanostructure in the presence of the anchoring sites on NEGF, (2) the synergistic effect of the bimetallic double hydroxide layer and N-doped graphene, and (3) homogeneous distribution of the pores over the N-doped graphene. The catalyst also exhibited outstanding stability even after 20 h of continuous operation.

2.5. References

1. S.Chu, A.Majumdar, Opportunities and challenges for a sustainable energy future, *Nature*, 2012, **488**, 294-303.
2. Chu, S., Cui, Y. & Liu, N. The path towards sustainable energy. *Nature Mater.* 2016, **16**, 16-22
3. J. O'M. Bockris, Response: Hydrogen and Power, *Science*, 1972, **176**, 1323-1323.
4. Mallouk, T. Divide and conquer. *Nat. Chem.*, 2013, **5**, 362-363.
5. M. Görlin, P. Chernev, J. F. d. Araújo, T. Reier, S. Dresp, B. Paul, R. krahnert, H.Dau, and P. Strasser, Parameterization of Water Electrooxidation Catalyzed by Metal Oxides Using Fourier Transformed Alternating Current Voltammetry, *J. Am. Chem. Soc.*, 2016, **138**, 5603-14.
6. Y. Lee, J. Suntivich, K. J. May, E. E. Perry, Y. Shao-Horn, Synthesis and Activities of Rutile IrO₂ and RuO₂ Nanoparticles for Oxygen Evolution in Acid and Alkaline Solutions, *J Phys Chem Lett*, 2012, **3**, 399-404.
7. C. C.McCrory, S.Jung, J.C. Peters, T. F.Jaramillo, Benchmarking Heterogeneous Electrocatalysts for the Oxygen Evolution Reaction, *JACS*, 2013, **135**, 16977-87.
8. A. Sumboja, J. Chen, Y. Zong, P.S. Lee, Z. Liu, NiMn layered double hydroxides as efficient electrocatalysts for the oxygen evolution reaction and their application in rechargeable Zn–air batteries, *Nanoscale*, 2017, **9**, 774-780.
9. S. K. Singh, D. Kumar, V. M. Dhavale, S. Pal, S. Kurungot, Strategic Preparation of Efficient and Durable NiCo Alloy Supported N-Doped Porous Graphene as an Oxygen Evolution Electrocatalyst: A Theoretical and Experimental Investigation, *Advanced Materials Interfaces*, 2016, **3**, 1600532.
10. Q. Wang, L. Shang, R. Shi, X. Zhang Y. Zhao, G. I. N.Waterhouse, L. Z. Wu, C.H.Tung, T. Zhang, Zinc-Air Batteries: NiFe Layered Double Hydroxide Nanoparticles on Co,N-Codoped Carbon Nanoframes as Efficient Bifunctional Catalysts for Rechargeable Zinc–Air Batteries, *Advanced Energy Materials*, 2017, 1700467.
11. B. K.Kang, M. H. Woo, J. Lee, Y. H. Song, Z. Wang, Y.Guo, D. H.Yoon, Mesoporous Ni–Fe oxide multi-composite hollow nanocages for efficient electrocatalytic water oxidation reactions, *Journal of Materials Chemistry A*, 2017, **5**, 4320–4324.
12. X. Li, X. Hao, A. Abudula, G. Guan, Nanostructured catalysts for electrochemical water splitting: current state and prospects, *J. Mater. Chem. A*, 2016, 11973-12000.
13. F. Dionigi, P. Strasser, NiFe-Based (Oxy)hydroxide Catalysts for Oxygen Evolution Reaction in Non-Acidic Electrolytes, *Advanced Energy Materials*, 2016, **6**, 1600621.
14. S. Chen, S.S. Thind, A. Chen, Plasmon-enhanced solar water splitting with metal oxide nanostructures: A brief overview of recent trends, *Electrochemistry Communications*, 2016, **63**, 10-17.
15. N.Chandrasekaran, S. Muthusamy, Binderless, Free-Standing Porous Interconnects of Ni–Fe Alloy Decorated Reduced Graphene Oxide for Oxygen Evolution Reaction, *Langmuir*, 2017, **33**, 2-10.
16. Y. Li, H. He, W. Fu, C. Mu, X. Z Tang, Z. Liu, D. Chi, X. Hu, A robust and luminescent covalent organic framework as a highly sensitive and selective sensor for the detection of Cu²⁺ ions, *Chem Commun* 2016, **52**, 1439-42.
17. T. Zhan, X. Liu, S. Lu, W. Hou, Quaternary Bimetallic Phosphosulphide Nanosheets Derived from Prussian

Blue Analogues: Origin of the Ultra-high Activity for Oxygen Evolution, *Applied Catalysis B: Environmental*, 2017, **205**, 551-558.

18. N. Chandrasekaran, S.Muthusamy, Core/Shell NiFe Nanoalloy with a Discrete N-doped Graphitic Carbon Cover for Enhanced Water Oxidation, *Langmuir*, 2017, **3**, 2-10.

19. Q. Quan, X. Lin, N. Zhang, Y. J.Xu, Graphene and its derivatives as versatile templates for materials synthesis and functional applications, *Nanoscale*, 2017, **9**, 2398-2416.

20. Y. Zhu, S. Murali, W. Cai, X. Li, J. W. Suk, J. R. Potts, R. S. Ruoff, Graphene and Graphene Oxide: Synthesis, Properties, and Applications, *Adv Mater*, 2010, **22**, 3906-24.

21. W.Ng, Y. Yang, K. van der Veen, G. Rothenberg, N.Yan, Enhancing the performance of 3D porous N-doped carbon in oxygen reduction reaction and supercapacitor via boosting the meso-macropore interconnectivity using the “exsolved” dual-template, *Carbon*, 2018, **129**, 293-300.

22. X. Tang, Y. Zeng, L. Cao, L. Yang, Z. Wang, D. Fang, Y. Gao, Z. Shao, B. Yi, Anchoring ultrafine Pt nanoparticles on the 3D hierarchical self-assembly of graphene/functionalized carbon black as a highly efficient oxygen reduction catalyst for PEMFCs, *Journal of Materials Chemistry A*, 2018, **6**, 15074-15082.

23. S. Chen, J. Duan, M. Jaroniec, S. Z. Qiao, Three-dimensional N-doped graphene hydrogel/NiCo double hydroxide electrocatalysts for highly efficient oxygen evolution, *Angew Chem* 2013, **52**, 13567-70.

24. Z. S.Wu, S. Yang, Y.Sun, K.Parvez, X. Feng, K. Mullen, *J Am Chem Soc*, 2012, **134**, 9082-5.

25. C. Zhu, H. Li, S. Fu, D. Du, Y. Lin, One-pot fabrication of N-doped graphene supported dandelion-like PtRu nanocrystals as efficient and robust electrocatalysts towards formic acid oxidation, *Chem Soc Rev*, 2016, **45**, 517-31.

26. Y. Ma, L. Sun, W. Huang, L. Zhang, J. Zhao, Q. Fan, W. Huang, In Situ Synthesis of Metal Nanoparticles on Single-Layer Graphene Oxide and Reduced Graphene Oxide Surfaces, *The Journal of Physical Chemistry C*, 2011, **115**, 24592-24597.

27. Y. Ito, Y. Tanabe, K. Sugawara, M. Koshino, T. Takahashi, K. Tanigaki, H. Aoki, M. Chen, Three-dimensional porous graphene networks expand graphene-based electronic device applications, *Phys Chem Chem Phys*, 2018, **20**, 6024-6033.

28. Q. Shi, Y. Cha, Y. Song, J. Lee, I. Zhu, C. Li, X.Song, M. K. Du, D. Lin, Y. 3D graphene-based hybrid materials: synthesis and applications in energy storage and conversion, *Nanoscale*, 2016, **8**, 15414-47.

29. L. Zhang, T. Wu, H. Na, C. Pan, X. Xu, G. Huang, Y. Liu, J. Gao, L. Zhang, Facile Fabrication of Superhydrophobic Sponge with Selective Absorption and Collection of Oil from Water, *Industrial & Engineering Chemistry Research*, 2016, **55**, 6553-62.

30. A. Kong, A. Kong, X. Zhu, Z. Han, Y. Yu, Y. Zhang, B. Dong, Y. Shan, Highly Efficient Oxygen Reduction Catalysts by Rational Synthesis of Nanoconfined Maghemite in a Nitrogen-Doped Graphene Framework, *ACS Catalysis*, 2014, **4**, 1793-1800.

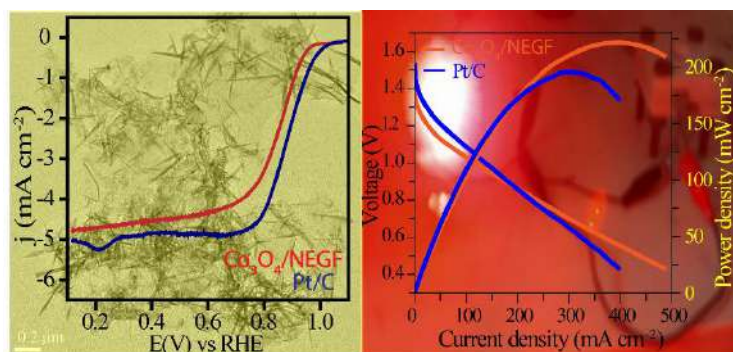
31. L. Jiang, Z. Fan, Design of advanced porous graphene materials: from graphene nanomesh to 3D architectures, *Nanoscale*, 2014, **6**, 1922-45.
32. X. Zhang, Z.Sui, B. Xu, S. Yue, Y. Luo, W. Zhan, B. Liu, Mechanically strong and highly conductive graphene aerogel and its use as electrodes for electrochemical power sources, *Journal of Materials Chemistry*, 2011, **21**, 6494.
33. S. H. Lee, H. W. Kim, J. O.Hwang, W. J. Lee, J. Kwon, C. W. Bielawski, R.S. Ruoff, S. O. Kim, S.H. Lee, Three-Dimensional Self-Assembly of Graphene Oxide Platelets into Mechanically Flexible Macroporous Carbon Films *Angew Chem Int*, 2010, **49**, 10084-8.
34. S. Kabir, K. Artyushkova, A. Serov, P. Atanassov, S. Kabir, Role of Nitrogen Moieties in N-Doped 3D-Graphene Nanosheets for Oxygen Electroreduction in Acidic and Alkaline Media, *ACS Appl Mater Interfaces*, 2018, **10**, 11623-11632.
35. R.Karunagaran, C.Coghlan, C.Shearer, D.Tran, K.Gulat, T.T.Tung, C.Doonan, D. Losic, Revitalized interest in vanadium pentoxide as cathode material for lithium-ion batteries and beyond, *Materials*, 2018, **11**, 205.
36. N.Ayasha, V. M. Dhavale, and S. Kurungot, NiZn double hydroxide nanosheet-anchored nitrogen-doped graphene enriched with the γ -NiOOH phase as an activity modulated water oxidation electrocatalyst, *Nanoscale*, 2017, **9**, 12590.
37. M.Gao, W.Sheng, Z.Zhuang, Q.Fang, S.Gu, J. Jiang, Y. Yan, Efficient Water Oxidation Using Nanostructured α -Nickel-Hydroxide as an Electrocatalyst, *J Am Chem Soc*, 2014, **136**, 7077-84.
38. Singh, S. K. Dhavale, V. M. Kurungot, S. Low Surface Energy Plane Exposed Co₃O₄ Nanocubes Supported on Nitrogen-Doped Graphene as an Electrocatalyst for Efficient Water Oxidation, *ACS Appl Mater Interfaces*, 2015, **7**, 442-51.
39. I.S. Amiin, J.Zhang, Z. Kou, X. Liu, O. K. Asare, H.Zhou, K.Cheng,H. Zhang, L. Mai, M. Pan, S.Mu, Self-Organized 3D Porous Graphene Dual-Doped with Biomass-Sponsored Nitrogen and Sulfur for Oxygen Reduction and Evolution, *ACS Appl Mater Interfaces* 2016, **8**, 29408-29418.
40. Nadeema, Ayasha. Walko, Priyanka S. Devi, R. Nandini. Kurungot, Sreekumar. Alkaline Water Electrolysis by NiZn-Double Hydroxide-Derived Porous Nickel Selenide-Nitrogen-Doped Graphene Composite, *ACS Appl. Energy Mater.* 2018, **1**, 5500–5510.
41. Y. Cao, S. Mao, M. Li, Y.Chen, Y. Wang, Metal/Porous Carbon Composites for Heterogeneous Catalysis: Old Catalysts with Improved Performance Promoted by N-Doping, *ACS Catal.* 2017, **7**, 8090–8112.
42. S. K. Singh, V. M. Dhavale, S.Kurungot, Low Surface Energy Plane Exposed Co₃O₄ Nanocubes Supported on Nitrogen-Doped Graphene as an Electrocatalyst for Efficient Water Oxidation, *ACS Appl Mater Interfaces*, 2015, **7**, 21138-49.
43. S.K.Singh, V.Kashyap, N. Manna, S.N Bhange,.R.Soni, R. Boukherroub, S.Szunerits, S.Kurungot, Efficient and Durable Oxygen Reduction Electrocatalyst Based on CoMn Alloy Oxide Nanoparticles Supported Over N-Doped Porous Graphene, *ACS Catalysis* 2017, **7**, 6700-6710.

44. Xiang, Q. Liu, Y.Zou, X. Hu, B. Qiang, Y.Yu, D. Yin, W. Chen, C. Hydrothermal Synthesis of a New Kind of N-Doped Graphene Gel-like Hybrid As an Enhanced ORR Electrocatalyst, *ACS Appl. Mater. Interfaces* 2018, **10**, 10842-10850.
45. S. N. Bhange, S.M. Unni, S. Kurungot, Nitrogen and sulphur co-doped crumbled graphene for the oxygen reduction reaction with improved activity and stability in acidic medium, *J. Mater. Chem. A*, 2016, **4**, 6014-6020.
46. C. Xie, Y. Wang, K. Hu, L. Tao, X. Huang, J.Huo, S. Wang, In situ confined synthesis of molybdenum oxide decorated nickel-iron alloy nanosheets from MoO_4^{2-} intercalated layered double hydroxides for the oxygen evolution reaction, *J. Mater. Chem. A*, 2017, **5**, 87-91.
47. Singh, S. K. Dhavale, V. M. Kurungot, S. Low Surface Energy Plane Exposed Co_3O_4 Nanocubes Supported on Nitrogen-Doped Graphene as an Electrocatalyst for Efficient Water Oxidation, *ACS Appl Mater Interfaces*, 2015, **7**, 442-51.
48. Mullangi, D. Dhavale, V. Shalini, S. Nandi, S. Collins, S. Woo, T. Kurungot, S. Vaidhyanathan, R. Low-Overpotential Electrocatalytic Water Splitting with Noble-Metal-Free Nanoparticles Supported in a sp^3 N-Rich Flexible COF, *Advanced Energy Materials* 2016, **6**, 1600110.
49. Gangadharan, P.K. Unni, S M. Kumar, N. Ghosh, P.Kurungot, S. Nitrogen-Doped Graphene with a Three-Dimensional Architecture Assisted by Carbon Nitride Tetrapods as an Efficient Metal-Free Electrocatalyst for Hydrogen Evolution, *ChemElectroChem*, 2017, **4**, 2643-2652.
50. V. A. Alves, L. A. da Silva, and J. F. C. Boodts, Surface characterization of $\text{IrO}_2/\text{TiO}_2/\text{CeO}_2$ oxide electrodes and Faradaic impedance investigation of the oxygen evolution reaction from alkaline solution, *Electrochimica Acta*, 1998, **44**, 1525-1534.
51. V. Kashyap, S. Kurungot, zirconium-Substituted Cobalt Ferrite Nanoparticle Supported N-doped Reduced Graphene Oxide as an Efficient Bifunctional Electrocatalyst for Rechargeable Zn–Air Battery, *ACS Catal.* 2018, **8**, 3715,–3726.
52. V. M. Dhavale, S. S. Gaikwad, L. George, R. N. Devi, S. Kurungot, Nanocrystalline Fe– Fe_2O_3 particle-deposited N-doped graphene as an activity-modulated Pt-free electrocatalyst for oxygen reduction reaction, *Nanoscale*, 2014, **6**, 13179-87.

Chapter-3

Zinc-Air Battery Catalyzed by Co_3O_4 Nanorod-Supported N-doped Entangled Graphene for Oxygen Reduction Reaction

The work reported in this chapter deals with the development of an efficient non-Pt electrocatalyst for electrochemical oxygen reduction reaction (ORR) through a sequential pathway involving hydrothermal treatment followed by freeze-drying to build the desired structural architecture of the catalyst. The designed catalyst ($\text{Co}_3\text{O}_4/\text{NEGF}$), which contains the Co_3O_4 nanorods anchored on the surface of the 3D structured N-doped graphene, was found to be displaying higher ORR activity during single-electrode testing and demonstration



of a Zn-air battery (ZAB) system. Under the hydrothermal treatment at $180\text{ }^\circ\text{C}$ in the presence of ammonia, nitrogen got doped into the carbon framework of the graphene, which subsequently formed a self-assembled entangled 3D structure of graphene after freeze-drying. The hydrothermal treatment and freeze-drying processes are found to be playing vital roles in tuning the morphological and structural features of the catalyst. The doped nitrogen, apart from its favorable contribution towards ORR, helps to facilitate efficient dispersion of the oxide nanorods on graphene. $\text{Co}_3\text{O}_4/\text{NEGF}$ displayed remarkable ORR activity in 0.1 M KOH solution, as evident from the 60 mV onset potential shift compared to the state-of-the-art Pt/C catalyst and the Tafel slope value of 74 mV dec^{-1} vs. 68 mV dec^{-1} for Pt/C. The ZAB fabricated by employing $\text{Co}_3\text{O}_4/\text{NEGF}$ as the cathode catalyst was found to be an efficient competitor for the system based on the Pt/C cathode. This high-performance has been credited to the controlled interplay of the governing factors such as the interfacial interactions leading to the efficient dispersion of the metal oxide nanorods, increased catalyst surface area, the cooperative effect arising from the defects present in the N-doped porous 3D-graphene, and the synergetic interactions operating in the system.

Content of this chapter is published in the following article: DOI: 10.1021/acsaem.1c00210

ACS Appl. Energy Mater. 2021, 4, 5, 4570-4580.

Reproduced with permission from American Chemical Society.

3.1. Introduction:

The strategic designing of cost-effective advanced electrocatalysts with better electrocatalytic performance for the oxygen reduction reaction (ORR) has become immensely important for realizing alkaline electrolyte membrane fuel cells (AEMFCs) and metal-air batteries (MABs) as competitive candidates in the energy market.^{1,2} However, the sluggish ORR kinetics at the cathode is considered as a significant limiting factor in achieving the enhanced efficiency of energy conversion from these classes of energy devices.³ Platinum nanoparticle-supported carbon (Pt/C) materials are primarily used as the electrocatalysts for promoting ORR in real systems, which are still suffering from high cost and low stability under the operating conditions.⁴ Normally, the ORR process is known to be slow; even though the ORR kinetics can be improved by increasing the Pt/C catalyst loading, this cannot be taken as a practical solution owing to the exorbitant cost of the Pt catalysts.⁴ Besides, the less availability of Pt (37 ppb in Earth's crust) and its expensiveness (US\$32.4 g⁻¹ as the 2019 average price) have triggered the scientific community to make progressive works on increasing the efficiency of the Pt-based catalysts or the development of highly efficient low-Pt/Pt-free catalysts.^{5,6} However, most of the reported low-Pt/Pt-free systems are unable to evolve as viable alternatives to the state-of-the-art Pt systems owing to the reasons such as complicated synthesis chemistry, stability issues, and unreliable performance characteristics.^{6,7} Therefore, the industries are still compelled to depend on the Pt catalysts all the while indulging in the active R&D efforts for developing reliable and high performing low-cost Pt-free ORR catalysts.⁸

Among the various non-Pt systems explored for ORR, extensive studies have been done in the last few decades focused on the non-precious transition metal-based oxides and hydroxides.⁹ Among the various transition metal (Fe, Co, Mn, Ni) systems, the oxides of cobalt received enormous attention as ORR electrocatalysts due to their favorable electronic structure.^{10,11,12,13} Based on the current advances in the cobalt oxides, spinel and perovskite structures of cobalt oxides are being explored for the electrochemical device applications in recent times.³ Among these, the spinel structured cobalt oxides have gained particular interest toward the electrocatalytic applications.³ The spinel structure mixed valency of Co in Co₃O₄ (*i.e.*, Co²⁺ and Co³⁺) plays a vital role in the fcc crystal structure.^{14,15} Moreover, in the normal spinel structure (AB₂O₄) of the Co₃O₄, the mixed valency cations are distributed in the octahedral and tetrahedral sites. In Co₃O₄, 1/8 of the tetrahedral A sites and 1/2 of the octahedral sites are occupied by the

Co^{2+} and Co^{3+} ions, respectively.^{14, 15} The mixed valency of cobalt helps in establishing a better electron transport mechanism and thereby towards preferable electrochemical activity.¹⁶ Furthermore, as a means to improve the intrinsic ORR characteristics, recently, shape and size-controlled designing of the metal oxide-based catalysts also has been executed as a strategy, and interesting performance fine-tuning could be realized.^{12, 13, 14, 22} Considering the fact that the shape and size-controlled modifications of the cobalt oxide nanoparticles help in achieving the promising electronic enhancement, these strategies are being adopted for designing alternative catalysts improved catalytic performance and durability.^{17, 18, 19} Previously, various shape- and size-controlled cobalt oxide morphologies (cubic²⁰, truncated octahedron²⁰, polyhedron²⁰ and nanorod²¹) have been reported for the electrocatalytic ORR processes.⁵ Among them, the nanorods of cobalt oxide have become an interesting class of 1D morphology that helps to facilitate rapid charge transport and adequate diffusion of the reactants.^{22, 21} However, the cobalt oxide-based electrodes suffer from the limitation of their poor electronic conductivity, which detrimentally affects their prospects to serve as potential electrocatalysts.^{24, 25} The incorporation of conducting carbon support to the cobalt oxides has been adopted as a viable strategy to overcome the conductivity-related limitations of these classes of the systems.^{23, 25, 26}

Despite the promises the nanorods of Co_3O_4 offer as an effective ORR catalyst, these morphologies need to be dispersed on a carbon substrate to tackle the issues related to conductivity and aggregation simultaneously.²⁵ Among the various carbon supports, graphitic carbons show the optimum activity as well as durability. There are few previous reports suggesting the synthesis of different cobalt oxide nanoparticle-based systems supported over nitrogen-doped graphitic carbon formed through various high/low-temperature *in-situ/ex-situ* methods. Jasinski, *et. al*⁴² reported the ORR activity of a cobalt-based Metal-N-C catalyst prepared by pyrolysis of cobalt phthalocyanine along with separate metal, nitrogen, and carbon precursors. Although the activity and durability of such catalysts have been improved with time, identifying the active-site structure still lagged due to the lack of crystallographic order of the metal atoms and the simultaneous presence of crystalline metal phases.⁴² Hence, the high-temperature methods which control the structural and morphological features of the metal centers and carbon substrate are not preferably feasible.⁴² Considering the low-temperature method, anchoring of the active catalytic sites (metal oxides) on 2D graphene (Gr) has been emerged as a promising strategy due to the interesting features of Gr and the desirable morphological features of the Gr-based composites. For example, Gr offers a theoretical surface area of as high as $\sim 2630 \text{ m}^2 \text{ g}^{-1}$ as well as excellent electrical conductivity.²⁶

^{27, 28, 40, 41} However, practically, their electrocatalytic surface area (ECSA) is affected by the Gr layers due to a well-known restacking issue.²⁹ The conventional approaches for constructing the interfaces between the two different components have followed the method of epitaxial growth under solution conditions in which the substrate's crystal surface and the epitaxial interfaces should be precisely controlled.^{30,31} Nevertheless, these approaches suffer from tedious multi-stage processes, substantial waste of metal species, and low yields, which ultimately hinder the large-scale production of the systems.³¹

Hence, looking at the difficulties in the synthesis of Co₃O₄ nanorods along with their proper dispersion on the Gr support, in this chapter, an easy and scalable procedure is reported, which involves dispersion of the Co₃O₄ nanorods on nitrogen-doped entangled porous 3D-graphene (NEGF) by utilizing the electronegativity difference of the doped-N to act as efficient anchoring sites for the metal oxide nanoparticles.³² The rationally designed NEGF functioned as an anchoring-cum-active substrate, which ensured both homogeneous distribution of the Co₃O₄ nanorods and favorable modulation towards ORR. We have introduced a sequential pathway involving hydrothermal treatment followed by freeze-drying to build the desired structural architecture of the catalyst containing the Co₃O₄ nanorod anchored on NEGF (Co₃O₄/NEGF). The realistic validation of the catalyst as a versatile cathode for the Zn-air battery could be subsequently performed, which is found to be competing well with a similar system based on the Pt/C catalyst.

3.2. Experimental Section:

3.2.1. Materials: Cobalt acetate tetrahydrate [Co(OAc)₂·4H₂O], potassium permanganate (KMnO₄), graphite, and ammonium hydroxide (NH₄OH) were purchased from Sigma-Aldrich. Phosphoric acid (H₃PO₄) and sulphuric acid (H₂SO₄) were procured from Thomas Baker. All the chemicals were used as such without any further purification.⁶

3.2.2. Synthesis of Graphene Oxide (GO): For the synthesis of graphene oxide (GO), improved Hummer's method was employed.³³ In brevity, 3 g of graphite powder and 18 g of KMnO₄ were well mixed by using a mortar and pestle. After proper mixing, the resulting powder was slowly added to the flask containing a solution of H₃PO₄:H₂SO₄ (1:9) under the ice bath environment. After complete transfer of the solid combination, the temperature of the reaction mixture was increased slowly up to 60 °C and kept on stirring for 12 h at a constant temperature. After completing the reaction, the mixture was held for

a few hours with continuous rotation to cool down to room temperature. The resulting reaction mixture was slowly poured into ice-cooled water containing 3% of H₂O₂, which became a yellowish solution. Furthermore, the obtained solution was washed several times with a copious amount of distilled water, followed by centrifugation at 10000 rpm. The obtained solid residue was further washed with 30% HCl to remove any metal impurities, followed by washing with plenty of water to neutralize the acidic pH and wash off the impurities. Finally, the collected dark chocolate-colored, highly viscous solution was washed with ethanol and diethyl ether and kept in an oven for drying at 40 °C to get the GO powder.

3.2.3. Synthesis of Co₃O₄ Supported N-doped Entangled 3D Graphene (Co₃O₄/NEGF): For the synthesis of the active catalytic material, 90 mg of the as-prepared GO was added to 30 ml of an aqueous solution of ammonia (30% v/v) by maintaining the ratio of 3:1 *via* overnight stirring and water-bath sonication. Co(OAc)₂.4H₂O was added to the solution after the full dispersion of GO, and the mixture was kept on stirring for another 6 h. Initially, at a low concentration of ammonia, the cobalt ions react with ammonia and form Co(NH₃)₆²⁺, which leads to the change of the color of the solution from pink to green (see the color change of the solution in **Figure 3.1**). Further changing the pH of the solution in the presence of air causes the oxidation of Co(NH₃)₆²⁺ to Co(NH₃)₆³⁺. However, when the concentration of the hydroxyl ions becomes higher, the Co³⁺ ions react with the hydroxyl ions (as the solubility product of Co(OH)₃ = 1 x 10⁻⁴³), resulting in the formation of Co(OH)₃.²⁰ The well-mixed reaction mixture was transferred into a Teflon-lined autoclave, and the system was kept for 12 h at 180 °C, Co(OH)₃ helps to grow the nanorod structure of Co₃O₄ during the hydrothermal treatment.²⁰ After completing the reaction, the mixture was allowed to cool down to room temperature naturally, followed by washing the obtained materials with a copious amount of water to eliminate the excess ammonia. The resulting sample was also vacuum freeze-dried at -52 °C for 10 h. After the freeze-drying process, the powder sample was collected, which adopted a flaky and light texture, and the sample has been designated as Co₃O₄/NEGF. The employed method is a simple and fast process that is promising for scaling up to larger applications. For comparing the catalytic activity during the electrochemical investigations, control samples like N-doped entangled graphene (NEGF) and Co₃O₄ nanorods were synthesized by using the same methods without adding any metal precursor and graphene oxide, respectively.

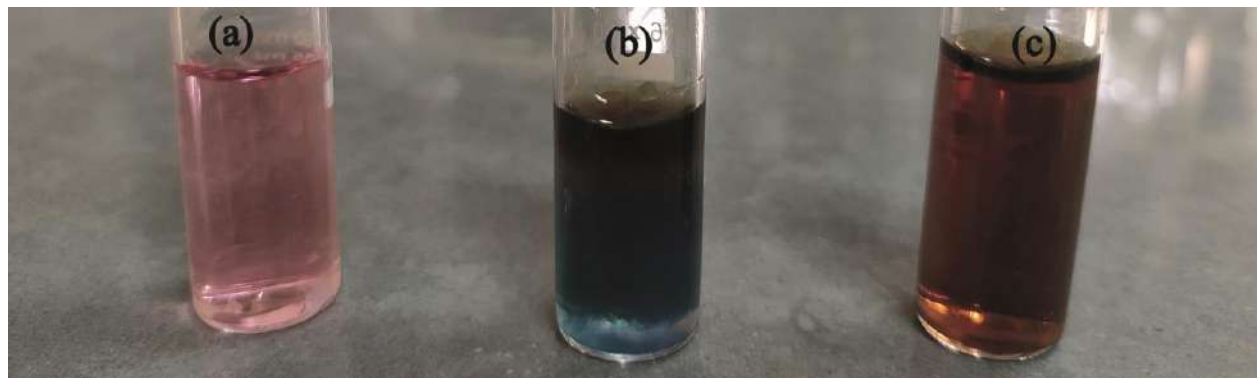


Figure 3.1. The digital photographs of the colored solutions with different amounts of ammonia added in the air atmosphere: (a) 0 mL, (b) 1 mL, and (c) 2 mL. The color of the solution gradually changes from pink to green to almost dark on increasing the concentration of NH_4OH . The oxygen from the air can oxidize $\text{Co}(\text{NH}_3)_6^{2+}$ to $\text{Co}(\text{NH}_3)_6^{3+}$ turning the solution almost black in color, while the green suspension is due to the formation of layered $\text{Co}(\text{OH})_2$.⁸ Thus, the different concentration of the added NH_4OH leads to the different states of the precursor solution, eventually, affecting the morphologies of the obtained Co_3O_4 nanorod after the hydrothermal treatment. (Reprinted (adapted) with permission from ACS Appl. Energy Mater. 2021, 4, 5, 4570-4580. Copyright (2021) American Chemical Society).

3.2.4. Physical Characterization: The structural properties (morphology, shape, and size), surface composition, surface properties, thermal stability, and physical interactions between the metal oxide nanoparticles and the support of the synthesized catalysts were investigated with the help of HRTEM, TEM, ESEM, FESEM, Raman spectroscopy, XPS, XRD, TGA and BET measurements.¹ The FESEM analyses were carried out by FEI Nova Nano SEM 450 FESEM microscopes, and TEM images were recorded on a Tecnai T-20 instrument at an accelerating voltage of 200 kV. FESEM samples were prepared by the thin coating of isopropyl alcohol (IPA) dispersed sample (5 mg of sample in 5 mg IPA) on a silicon wafer. This sample was dried for 1 h under an IR lamp. The HAADF-STEM mapping was performed using FEI, TECNAI G2 F20 TEM instrument (conditions: accelerated voltage = 200 kV; resolution = 0.17 nm). The HRTEM images were recorded using a JEOL JEM F-200 HRTEM instrument with a point-to-point resolution of 0.19 nm. The samples for TEM and HRTEM were prepared by drop coating the well-dispersed sample in isopropyl alcohol (1.0 mg of the sample in 5 mL solvent) on a carbon-coated 200 mesh copper grid. The sample-coated TEM grid was dried for 1 h under an IR lamp. The elemental inspection was done by using SEM-EDS with a Quanta 200 3D FEI instrument connected with

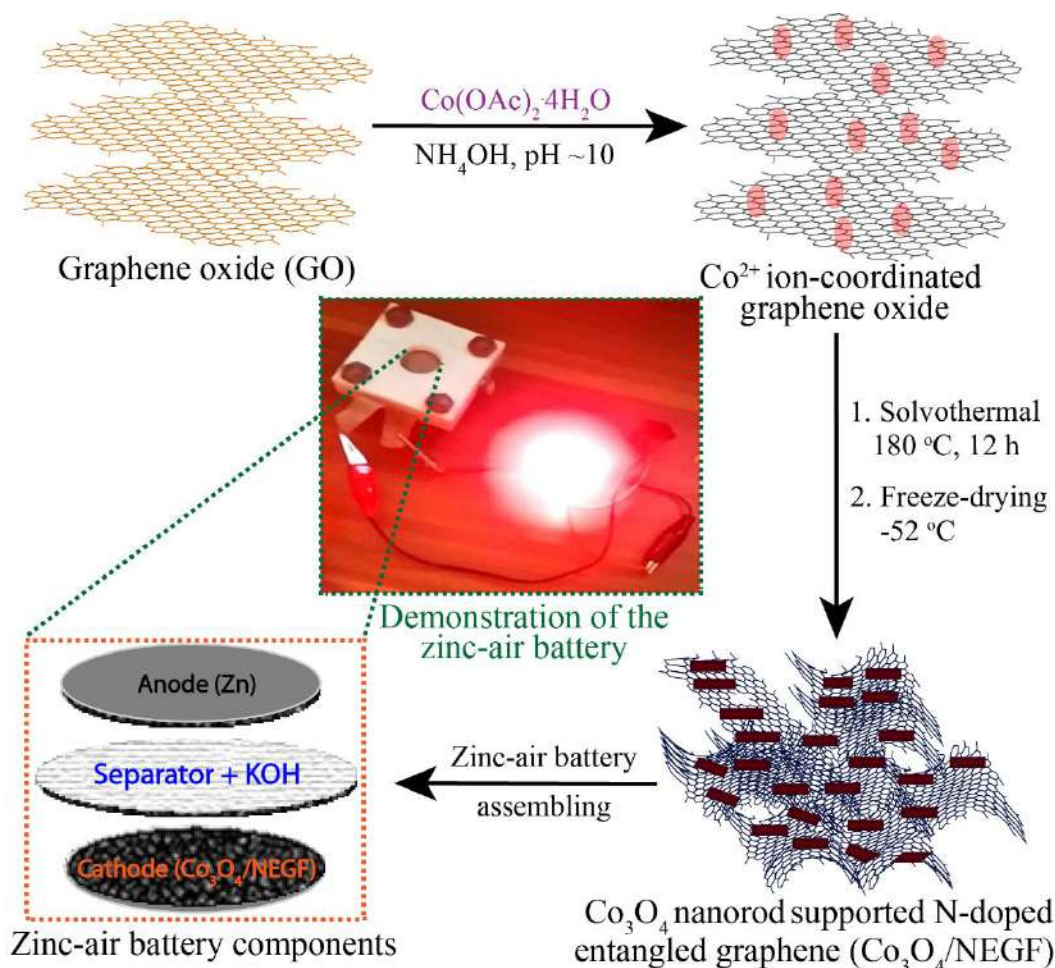


Figure 3.2. Schematic presentation of the stepwise synthesis strategy developed to obtain the $\text{Co}_3\text{O}_4/\text{NEGF}$ catalyst followed by fabrication and demonstration of the Zn-air battery. (Reprinted (adapted) with permission from ACS Appl. Energy Mater. 2021, 4, 5, 4570-4580. Copyright (2021) American Chemical Society).

the TEAMTM EDS analysis system. Powder X-ray diffraction (PXRD) analysis was done to check the crystallinity of the as-synthesized samples. The XRD measurement was carried out on a Rigaku Smart Lab diffractometer with Cu $\text{K}\alpha$ radiation ($\lambda = 1.5406\text{ \AA}$) with a scan rate of 5° min^{-1} in the 2θ range of 5 to 80° . The thermal stability of the catalyst and metal composite loading over the carbon was measured using an SDT Q600 DSC-TDA thermo-gravimetric (TG) instrument in the temperature range of Room Temperature to $900\text{ }^\circ\text{C}$ at a constant heating rate of $10\text{ }^\circ\text{C min}^{-1}$ under an oxygen atmosphere. The XPS measurement was performed using a fully integrated, monochromatic small spot XPS system. It is

specified with an X-ray monochromator source by the 180° double-focusing hemispherical analyzer-128-channel detector and micro-focused Al K α . Raman spectral evaluation was carried out using a 632 nm green laser (NRS 1500W) on an HR 800 RAMAN spectrometer. Nitrogen (N₂) adsorption-desorption isotherm experiments were performed on a Quantachrome-Quadrachrome automatic volumetric instrument to analyze the surface area and pore volume of the samples. GO, NEGF and Co₃O₄/NEGF were imaged using X-ray microtomography (Xradia 510 Versa X-ray Microscope, Zeiss, Pleasanton, CA, USA) to study their internal structure and morphology. Samples were loaded into the sample holder and held in between the assembly of the X-ray source and the detector. The assembly of the detector was composed of a scintillator, an objective lens, and a CCD camera. The X-ray source has been ramped up to 7 W and 80 kV. The tomographic image procurement was completed by obtaining 3201 projections over 360° rotation, with one second of X-ray exposure time per projection. Pixel size was 4.0 microns, for every sample, for imaging a sample volume of approx. 4x4 mm in size. Reference images were also collected and averaged without adding any samples in the beam. To generate the two-dimensional (2D) virtual cross-sections (transverse sections) of the samples, the filtered back-projection algorithm was used for the reconstruction of the projections. Dragonfly Pro (Version 3.6) was used as an image processing software, to generate volume-rendered three-dimensional (3D) images of the samples.²

3.2.5. Rotating Disk Electrode (RDE) Study: The electrochemical analysis was done by performing hydrodynamic method, using a rotating disc electrode (RDE) made of glassy carbon (0.0706 cm²) with a couple of experimental electrochemical techniques such as cyclic voltammetry (CV) and linear sweep voltammetry (LSV) using a Pine instrument for the rotation of the electrodes. A set-up of a three-electrode electrochemical cell was used with an SP-300 model BioLogic potentiostat. The Hg/HgO as the reference electrode and a graphite rod (Alfa Aesar, 99.99%) as a counter electrode were employed for the electrochemical analyses. For the comparison of the ORR performance of the prepared catalyst, we included the electrochemical activity of 20% Pt/C. The catalyst slurry was prepared by mixing the catalyst (5 mg) in 1 mL isopropyl alcohol-water (3:2) solution and 40 μ L of Nafion solution (5 wt%, Sigma-Aldrich) using a water-bath sonication for approximately 1 h. After well mixing, the catalysts slurry was coated on the surface of the working electrode by drop-casting, which was polished with 0.3 μ m alumina slurry in DI-water followed by cleaning with DI-water and acetone. A 10 μ L of the ink was drop-coated on the surface of the RDE electrode; the electrode was then dried under an IR-lamp for 1 h. To check the electrochemical performance, the experiment was carried out in an aqueous solution of 0.1 M KOH. All

the experimental electrode potentials were converted into the reversible hydrogen electrode (RHE) through an RHE calibration experiment, which was previously done in our lab.

3.2.6. Rotating Ring Disk Electrode Study: For the RRDE analysis of the prepared catalysts, a rotating ring disk electrode (RRDE) built of glassy carbon (0.196 cm²) coated with the catalyst was used. The testing was done in 0.1 M KOH solution by scanning the voltage at the rate of 10 mV s⁻¹ while keeping the ring electrode at a constant potential of 0.40 V vs. Hg/HgO. The H₂O₂ collection efficiency (N) at the ring was determined with a K₃Fe(CN)₆ solution, which is found to be 0.37.³ The calculation of H₂O₂% and the number of electron transfer (n) during ORR was carried out by following the equations below:

$$\% \text{ peroxide} = (200 \times I_R \times N) / (I_D + I_R / N)$$

$$n = 4 \times I_D / (I_D + I_R / N)$$

where, I_D = Faradaic current at the disk,

I_R = Faradaic current at the ring,

N = H₂O₂ collection efficiency of the ring electrode.

All the experiments were carried out at room temperature.

3.2.7. Zinc-Air Battery (ZAB) Fabrication and Testing: ZAB was fabricated by using Zn powder and Co₃O₄/NEGF as the anode and cathode electrodes, respectively, by employing an in-house-built electrochemical cell. The catalyst slurry for the coating over the GDL was prepared by sonicating Co₃O₄/NEGF for 1 h in isopropyl alcohol and water mixture. Subsequently, 10 wt% of Nafion solution was added to the above sonicated solution, and the mixture was maintained for 1 h additional sonication. In order to achieve a catalyst loading of 1.0 mg/cm² (electrode area = 1.0 cm²), the resulting catalyst slurry was brush-coated on a carbon gas diffusion layer (GDL) and dried at 60 °C for 12 h. In addition, as an anode, Zn powder was used. Finally, the ZAB was assembled by pairing the anode and cathode using the Celgard[®] membrane soaked in 6.0 M KOH as a separator. The ZAB setup was subsequently tested at room temperature using a multichannel VMP-3 model Bio-Logic potentiostat/galvanostat. The battery was analyzed by steady-state polarisation at a scan rate of 5 mV/s.

3.2.8. The Hg/HgO reference electrode calibration and conversion to RHE:

The Hg/HgO electrode was calibrated by using the same method as reported in our previous report⁵ using a conventional 3-electrode system employing a platinum RDE electrode as the working electrode (WE), graphite rod as the counter electrode (CE), and Hg/HgO as the reference electrode (RE) under H₂-saturated 0.1 M KOH solution as an electrolyte. The linear sweep voltammogram (LSV) was recorded at a scan rate of 0.50 mV/s. The potential when the current crosses the zero point during the LSV measurement was taken as the thermodynamic potential for the hydrogen electrode reactions. The potential at the zero current was found to be at -0.8722 V. Hence, for the conversion of the voltage recorded with respect to Hg/HgO to the RHE scale, the following equation is used:

$$E \text{ (RHE)} = E \text{ (Hg/HgO)} + 0.8722 \text{ V} \dots\dots\dots 1$$

3.3. Result and Discussions:

The stepwise procedure involved in the synthesis of Co₃O₄/NEGF and its application as the cathode material for the zinc-air battery fabrication is presented in **Figure 3.2**. The hydrothermal treatment was performed after facilitating the anchoring of cobalt (Co²⁺) and ammonium (NH₄⁺) ions on the surface of GO. The adsorption of the positively charged ions over GO is enabled due to the electronegativity difference of the oxy/carboxy functional groups present on GO. The GO anchored with the Co²⁺ ions was subjected to the hydrothermal treatment at 180 °C, which facilitates the *in-situ* formation and dispersion of the Co₃O₄ nanorods on N-doped reduced graphene oxide. This was followed by the freeze-drying process to establish the self-assembled structure of the metal oxide nanorods bearing N-doped entangled 3D graphene (Co₃O₄/NEGF). In the process, the negatively charged GO surface interacts with the positively charged metal ions and thus mobilizes their adsorption during the continuous stirring at room temperature. As the hydrothermal process proceeds at high temperature and pressure, the metal ions gradually get nucleated, resulting in the formation of the Co₃O₄ nanorods anchored over the N-doped reduced graphene oxide. The crucial freeze-drying step adopted subsequent to the hydrothermal process helps to establish the 3D interconnected morphology (Co₃O₄/NEGF), ensuring high surface area and accessible porous architecture to the catalyst. With the help of field emission scanning electron microscopy (FESEM), X-ray micro-computed tomography (micro-CT), high-resolution transmission

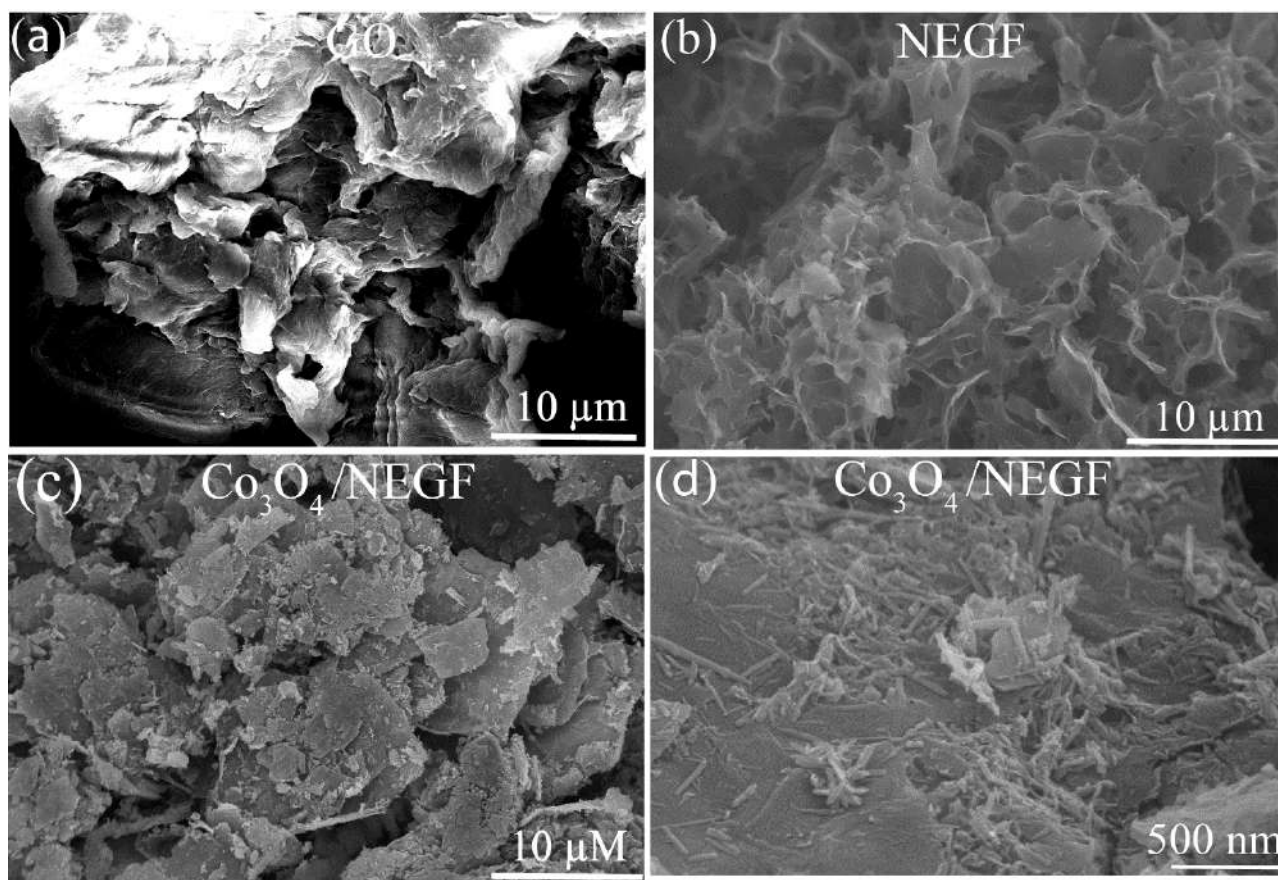


Figure 3.3. (a) The FESEM images of GO showing the stacked nature of the sheets in their pristine form; (b) and (c) the FESEM images of NEGF and Co₃O₄/NEGF, respectively, displaying the porous architecture of the entangled 3D graphene sheets; (d) FESEM images of the Co₃O₄/NEGF representing the uniform distribution of the Co₃O₄ nanorods over NEGF; (Reprinted (adapted) with permission from ACS Appl. Energy Mater. 2021, 4, 5, 4570-4580. Copyright (2021) American Chemical Society).

electron microscopy (HRTEM), and electron energy loss spectroscopy (EELS) studies, a detailed structural analysis of the prepared catalyst was carried out.

3.3.1. FESEM Analysis:

As mentioned before, the freeze-drying step induces porosity in the entangled reduced graphene oxide, which could be evidenced in the FESEM images presented in **Figure 3.3**. **Figure 3.3a** represents the FESEM images of the pristine GO, which is displaying the presence of stacked graphene sheets. However,

the role of the adopted freeze-drying process to accomplish the 3D interconnected nature of NEGF in bare NEGF and $\text{Co}_3\text{O}_4/\text{NEGF}$ is evident in the FESEM images presented in **Figure 3.3b** and **3.3c**, respectively. The distribution of the Co_3O_4 nanorods is visible in the more focused view of the FESEM image presented in **Figure 3.3d**. This surface aligned growth points towards the influence of the oxy-functional groups of GO for facilitating the metal ion adsorption followed by the nucleation process to accomplish the well-distributed growth of the Co_3O_4 nanorods during the hydrothermal treatment. In addition, the FESEM imaging revealed the formation of a well-connected network of the nitrogen-doped graphene sheets, which has been originated from the self-assembling process under the reaction conditions.

3.3.2. Micro-Computed Tomography Analysis:

An X-ray micro-CT imaging technique has been employed to unveil the 3D microstructures of GO, NEGF, and $\text{Co}_3\text{O}_4/\text{NEGF}$ (**Figure 3.4a-d**). The 3D micro-CT image of GO presented in **Figure 3.4a** shows randomly oriented GO sheets, which also support the findings in the FESEM image of GO (**Figure 3.3a**), validating the presence of stacked graphene sheets in pristine GO. On the other hand, the 3D micro-CT image of the nitrogen-doped entangled graphene (NEGF) (**Figure 3.4b**) shows a haystack-like structure. This points towards the vital effect of the freeze-drying method towards the formation of a porous 3D structure. Further, advanced segmentation-based image analysis showed a significant amount of porosity (approximately 58%) in NEGF. The porous microstructure of NEGF has resulted in a higher surface area as compared to its precursor (GO). The 3D micro-CT image of $\text{Co}_3\text{O}_4/\text{NEGF}$ in **Figure 3.4c** also shows the 3D spatial distribution of the Co_3O_4 particles (**Figure 3.4c**, highlighted with blue circles) over the NEGF sheets. With the aid of a grey-scale histogram and mean intensity projection (MIP), Co_3O_4 particles present in the 3D micro-CT image of $\text{Co}_3\text{O}_4/\text{NEGF}$ are visualized separately in **Figure 3.4d**. The observed 3D micro-CT image shows the true spatial distribution of the Co_3O_4 particles over the NEGF sheets. Due to the limitations induced by the micro-CT resolution (1 micron), the shape of the Co_3O_4 particles is not resolved. $\text{Co}_3\text{O}_4/\text{NEGF}$ has approximately 48% porosity, which is 10% lower than its precursor (NEGF) and this reduction is attributed to the distribution of the metal oxide nanoparticles over NEGF. GO and $\text{Co}_3\text{O}_4/\text{NEGF}$ sheets showed an aspect ratio of 2:1 (length to width), as measured from their 2D micro-CT to their precursors (GO). Overall, the micro-CT images point towards the versatility of the catalyst synthesis steps in retaining the 3D structure of the products.

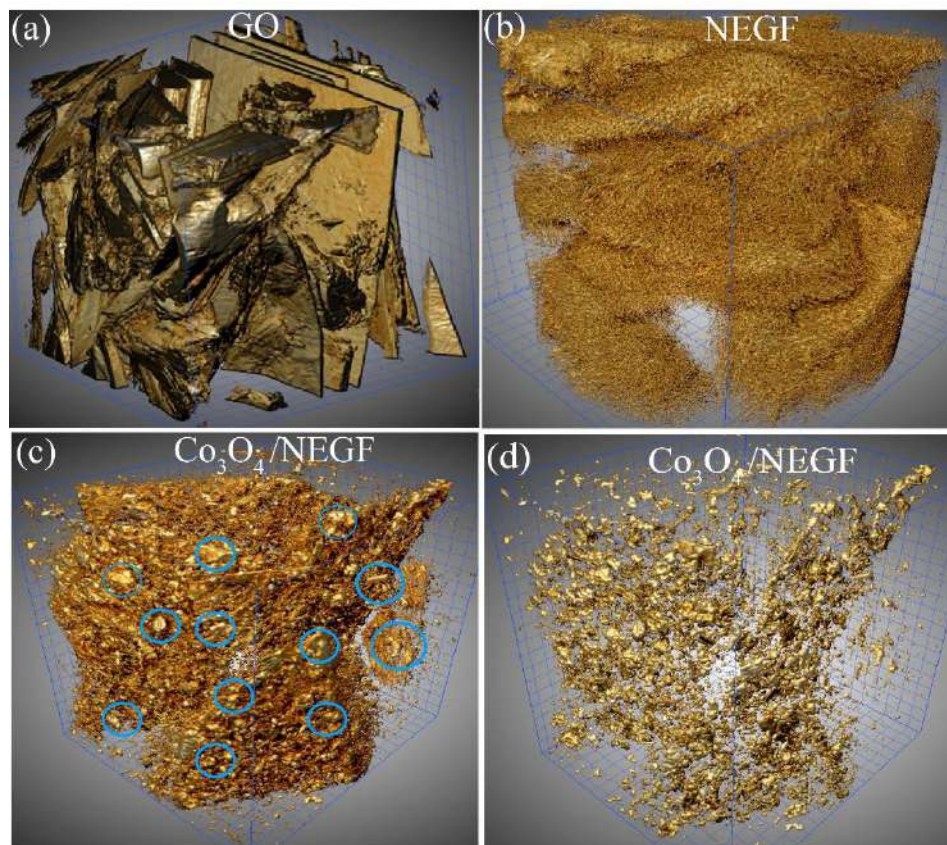


Figure 3.4. (a) the 3D micro-CT images of GO showing the randomly oriented stacks of individual GO sheets; (b) NEGF showing the micro porous 3D structure of the entangled graphene; (c) Co_3O_4 with the bright dots in the image representing the distribution of Co_3O_4 over the NEGF sheets, where few such dots are encircled for easy recognition (grid size is 100 microns); (d) 3D spatial visualization image of Co_3O_4 over the NEGF sheets. (Reprinted (adapted) with permission from ACS Appl. Energy Mater. 2021, 4, 5, 4570-4580. Copyright (2021) American Chemical Society).

3.3.3. TEM Analyses:

The TEM images of Co_3O_4 /NEGF are shown in **Figures 3.5a-d**. These images clearly depict the aligned distribution of the Co_3O_4 nanorods along the surface of NEGF. It should be noted that while some rods are clearly visible on the graphene surface (**Figure 3.5a** and **3.5b**), few others have a hazy appearance. The possible reason for the ambiguity in the visibility is that while the nanorods are distributed in the self-assembly structure of the entangled graphene, a significant amount would be lying towards the inner side of the graphene sheets, thereby partially masking them. The high magnification TEM images presented in **Figure 3.5c** and **d** clearly show the nanorod structure of Co_3O_4 . The nanorods are found to possess a

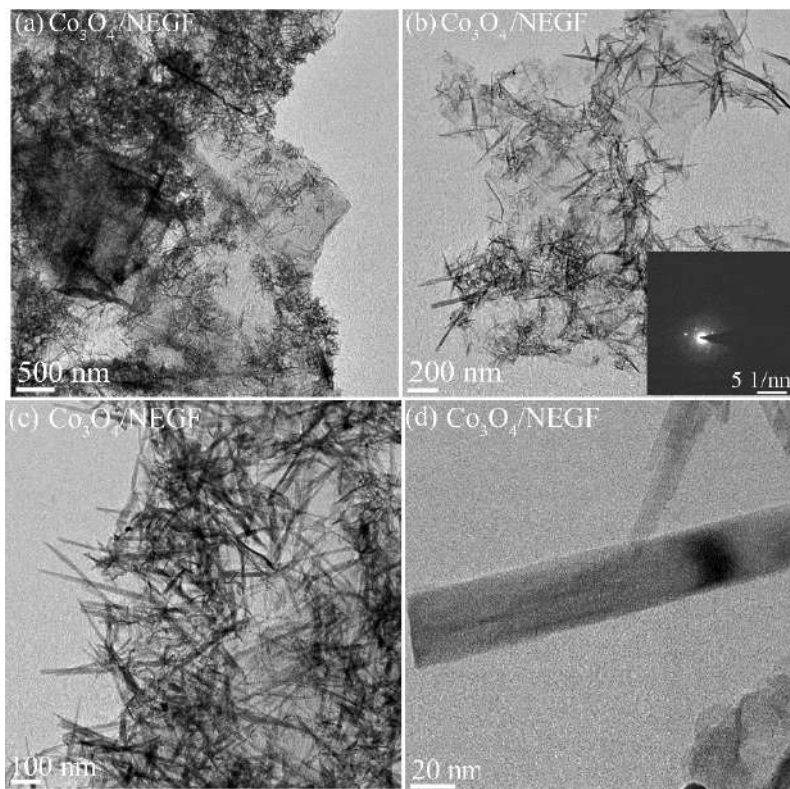


Figure 3.5. Transmission electron microscopy (TEM) images of $\text{Co}_3\text{O}_4/\text{NEGF}$: (a)-(b) TEM image of $\text{Co}_3\text{O}_4/\text{NEGF}$ displaying the distribution of the Co_3O_4 nanorods over the surface of the transparent sheets of NEGF (Inset of (b): SAED pattern showing the crystalline nature of Co_3O_4); (c) and (d) are the high magnification images representing the focused view of the nanorods of Co_3O_4 . (Reprinted (adapted) with permission from ACS Appl. Energy Mater. 2021, 4, 5, 4570-4580. Copyright (2021) American Chemical Society).

length of ~ 120 nm and a radius of ~ 5 nm. The selected area electron diffraction (SAED) pattern is shown in the inset of **Figure 3.5b**; the pattern displays a well-characterized diffraction ring corresponding to the polycrystalline nature of the Co_3O_4 nanorods.^{22,23} The observed diffraction rings are ascribed to the (002), (220), (400), (511), and (440) planes of the Co_3O_4 nanorods.^{22,23} **Figure 3.6a** represent the focused

3.3.4. HRTEM Analyses:

HRTEM images of a single Co_3O_4 nanorod recorded to perform the elemental mapping. The corresponding data presented in **Figure 3.6b-d** exhibit the presence and distribution of Co, O, C, and N, respectively, and this goes well with the expected composition of the catalyst.

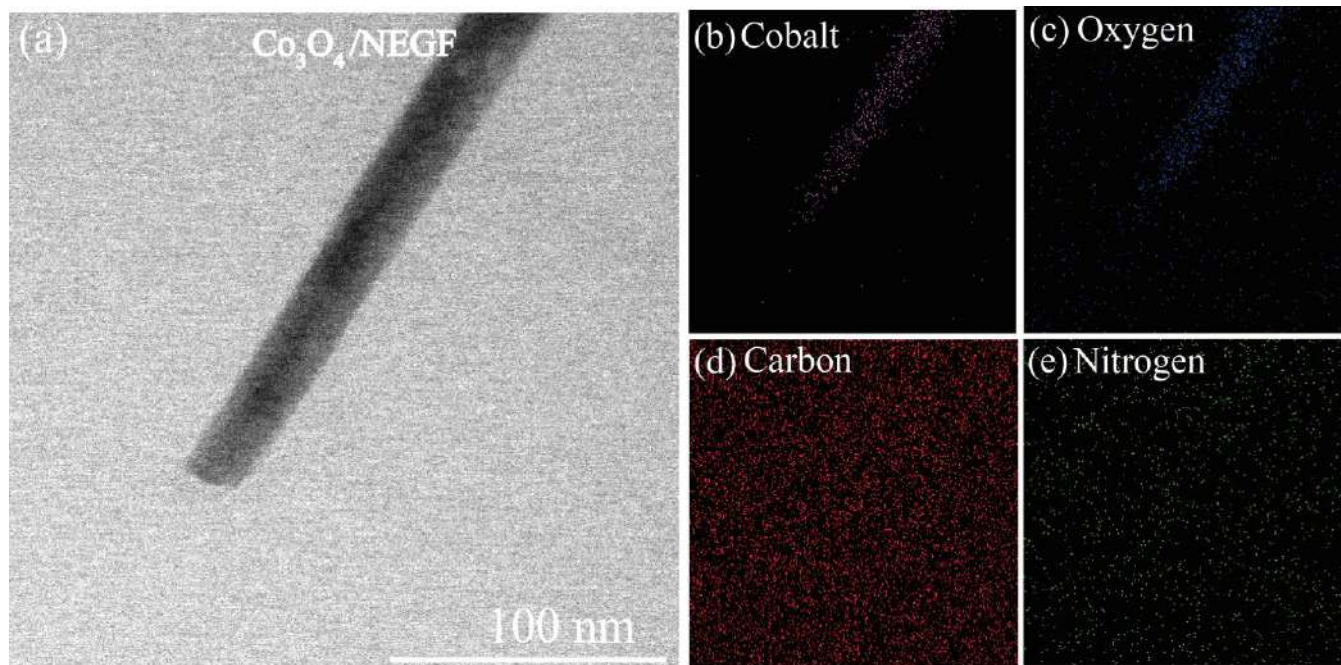


Figure 3.6. (a) HRTEM image of a single Co_3O_4 nanorod recorded for performing elemental mapping; (b)-(e) elemental analysis of $\text{Co}_3\text{O}_4/\text{NEGF}$ displaying the distribution of cobalt along the focused nanorod and oxygen, carbon, and nitrogen in the system. (Reprinted (adapted) with permission from ACS Appl. Energy Mater. 2021, 4, 5, 4570-4580. Copyright (2021) American Chemical Society).

3.3.5. XRD Analyses:

The XRD profile of NEGF (**Figure 3.7a**) displays the broad diffraction peaks at the 2θ values of 26 and 43° corresponding to the (002) and (100) graphitic diffraction plane, respectively, of the reduced graphene oxide.³⁷ The presence of metal impurities could be ruled out from the absence of any other diffraction peaks in the sample. The PXRD of $\text{Co}_3\text{O}_4/\text{NEGF}$ shows comparatively intense and prominent peaks corresponding to the (311) plane of Co_3O_4 , which matches well with the **JCPDS Card No: 00-042-1467**.^{25, 22, 23} The presence of these phases confirms the spinel structure possessed by the Co_3O_4 nanorods. As expected, $\text{Co}_3\text{O}_4/\text{NEGF}$ also shows the peak corresponding to the (002) plane of the NEGF substrate, which appears as a broad peak at the 2θ value of 24.5° . A small shift of the graphitic peak corresponding to the (002) plane in $\text{Co}_3\text{O}_4/\text{NEGF}$ towards a lower diffraction angle (**Figure 3.7a**) in comparison to the pristine NEGF has been observed. This is ascribed to the increased d-spacing of the graphene layers due to the insertion of the Co_3O_4 nanorods in between the graphene layers.³⁴

3.3.6. Raman Analyses:

The introduced defects in the porous N-doped 3D graphene support were further explored by Raman spectroscopy (**Figure 3.7b**). The D-band peak appeared to resemble the graphitic lattice vibration mode with the A_{1g} symmetry at a wavenumber of 1350 cm^{-1} , while the G-band peak at 1590 cm^{-1} corresponds to the E_{2g} symmetry graphitic lattice vibration mode.³⁵ It should be noted that the D-band in the Raman stands out as an indication of the introduced defects in the graphene framework, whereas the G-band describes the orderliness in the graphene.³⁵ In order to check the extent of the defects in the supported conducting carbon materials, the I_D/I_G ratio of the samples has been calculated, which are found to be 1.25 for the NEGF and 1.33 for $\text{Co}_3\text{O}_4/\text{NEGF}$. A more graphitic structure would be helpful for ensuing better electrocatalytic activity as well as durability. Further, incorporation of the defects creates nucleation sites for the metal oxide growth, leading to improved dispersion of the active sites and concomitantly high performance.²⁹ However, a considerably higher extent of defects can affect the stability of the carbon support. This points toward the need for an optimized level of graphitization and defects in the conducting support for ensuring improved overall catalytic performance as well as durability. The observed defect to the graphitic peak ratio in the case of NEGF ($I_D/I_G = 1.25$) is higher than that in the case of GO ($I_D/I_G = 1.0$). This shows that the defective sites are predominant in the case of NEGF as compared to GO. Furthermore, the Raman spectra analysis of Co_3O_4 (**Figure 3.7b**) shows the presence of the peaks at $400\text{--}600\text{ cm}^{-1}$, corresponding to the vibrations of the Co-O bond in a different plane of Co_3O_4 .¹⁴ A similar peak is observed in the case of $\text{Co}_3\text{O}_4/\text{NEGF}$; however, in this case, the peak intensity is slightly lower compared to the pristine Co_3O_4 , presumably due to the carbon support effect. However, the defective peak intensity is more prominent in $\text{Co}_3\text{O}_4/\text{NEGF}$ as compared to NEGF. The introduced higher defects in $\text{Co}_3\text{O}_4/\text{NEGF}$ compared to NEGF are due to metal oxide growth in the *in-situ* condition.⁵¹ The observed higher I_D/I_G ratio in the case of the metal oxide supported catalyst stands out as substantiating evidence towards the presence of comparatively high density of the defective sites in the system, which is found to be assisting the system in enhancing its catalytic activity.³⁶

3.3.7. Surface Area Analysis:

For further understanding of the role of freeze-drying towards improving the surface area of the catalyst as well as increasing the number of porous channels, BET surface area, and pore size distribution analyses

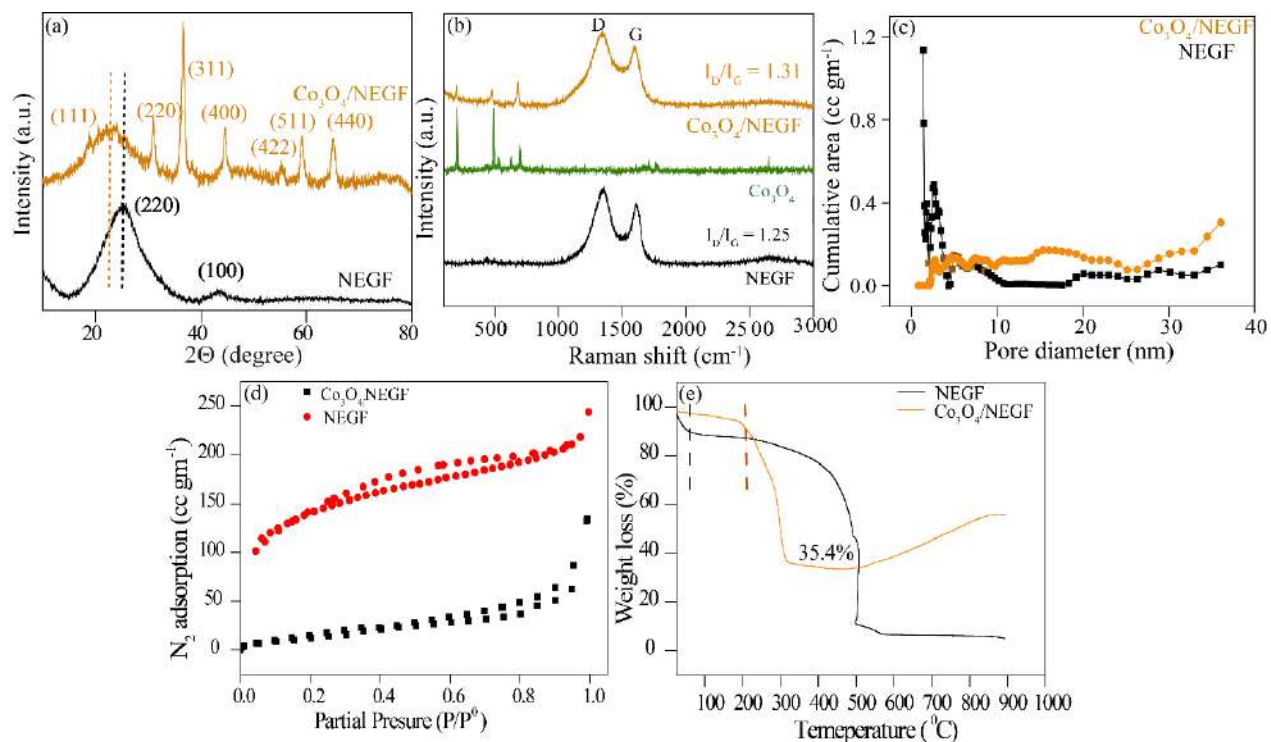


Figure 3.7. (a) Comparative PXRD patterns of NEGF and Co₃O₄/NEGF showing the diffraction planes corresponding to the spinel lattice of the Co₃O₄ nanorods; (b) Raman spectra of NEGF, Co₃O₄, and Co₃O₄/NEGF; (c) comparative pore-size distribution profiles of NEGF and Co₃O₄/NEGF showing the mesoporous nature of the prepared catalyst; (d) Comparative adsorption/desorption isotherms of nitrogen-doped entangled graphene framework (NEGF) and Co₃O₄/NEGF; (e) the comparative TGA profiles recorded for NEGF and Co₃O₄/NEGF under oxygen atmosphere. (Reprinted (adapted) with permission from ACS Appl. Energy Mater. 2021, 4, 5, 4570-4580. Copyright (2021) American Chemical Society).

have been performed (**Figure 3.7c** and **3.7d**). The pore size distribution profile in **Figure 3.7c** shows the pore distribution in the range of 2 to 5 nm in both NEGF and Co₃O₄/NEGF, but the former clearly showed a high-intensity pore distribution in the mesoporous size range of 2-7 nm. Additionally, NEGF shows a higher BET surface area of 450 m² g⁻¹, confirming the remarkably accessible and porous structure of the material as visualized from the FESEM images. However, the BET surface area of Co₃O₄/NEGF is found to be decreased substantially to 95 m² g⁻¹, suggesting the blockage of the pores and masking of the surface of the substrate in the presence of the dispersed metal oxide moieties. Both NEGF and Co₃O₄/NEGF showed Type-IV isotherms (**Figure 3.7d**).³⁷ The prepared Co₃O₄/NEGF catalyst contains almost 35 % of the cobalt oxide nanorods of dimension (120 nm in length and 12 nm in width) responsible for lowering

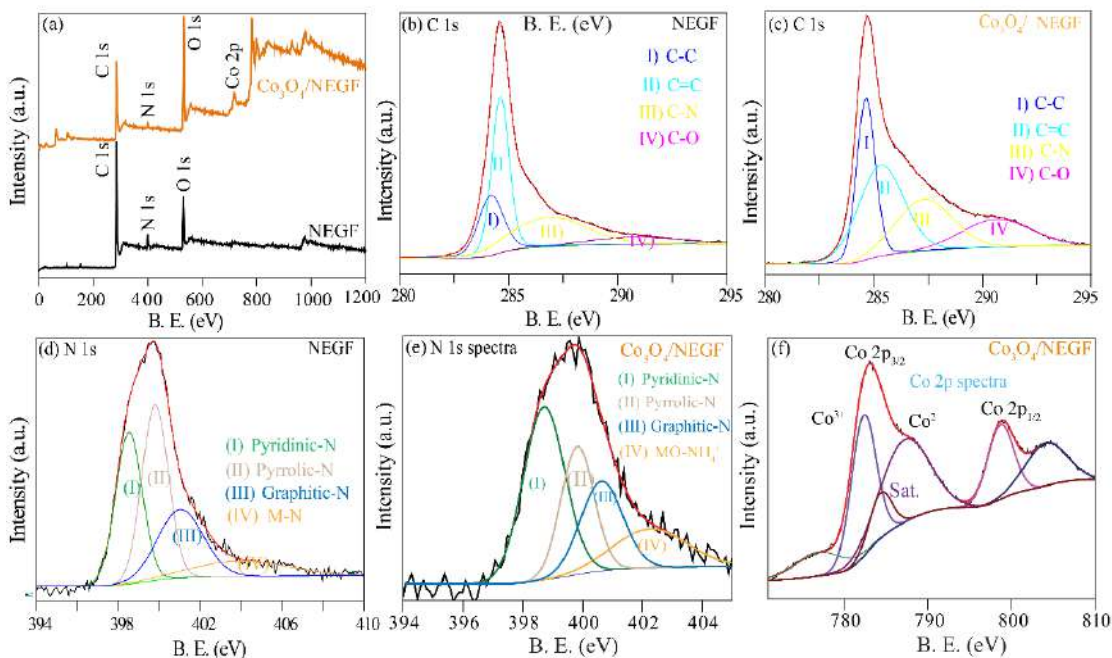


Figure 3.8. (a) Comparative the survey scan XPS spectra of NEGF and $\text{Co}_3\text{O}_4/\text{NEGF}$ confirming the presence of C, N, O, and Co in the respective systems; (b) and (c) C 1s spectra of NEGF, and $\text{Co}_3\text{O}_4/\text{NEGF}$; (d) and (e) N 1s spectra of NEGF $\text{Co}_3\text{O}_4/\text{NEGF}$; (f) the high-resolution deconvoluted XPS spectra of Co 2p states of $\text{Co}_3\text{O}_4/\text{NEGF}$. (Reprinted (adapted) with permission from ACS Appl. Energy Mater. 2021, 4, 5, 4570–4580. Copyright (2021) American Chemical Society).

the overall BET surface area. In this situation, the carbon surfaces loaded with Co_3O_4 entities are not being exposed completely to the adsorption of the gas molecules, which affects the total cumulative volume of $\text{Co}_3\text{O}_4/\text{NEGF}$ (**Figure 3.7d**). The defective sites and high porosity of the prepared catalyst are expected to allow seamless and fast diffusion of the reactants and electrolytes during electrocatalysis. This advantage is a determining factor in accomplishing the obtained higher electrocatalytic activity in the present case, as can be seen in a later section.

3.3.8. TGA Analysis:

The total metal oxide active site loading in $\text{Co}_3\text{O}_4/\text{NEGF}$ was determined by performing the thermogravimetric analysis (TGA). The measurement was performed by sampling from 25 to 900 °C at a scan rate of 5 °C per minute in the oxygen atmosphere. **Figure 3.7e** displays the TGA weight loss profiles for NEGF and $\text{Co}_3\text{O}_4/\text{NEGF}$, indicating a cobalt oxide loading of ~35.4 % in the case of the latter.⁶

3.3.9. XPS Analysis:

The insightful information on the nature of the surface moieties and the characteristics of the electronic interactions operating in the prepared system has been gained by employing X-ray photoelectron spectroscopy (XPS) measurements. **Figure 3.8a** shows the survey scan spectra of NEGF and $\text{Co}_3\text{O}_4/\text{NEGF}$, which confirm the presence of Co, O, N, and C in the systems from the characteristic binding energy peaks. In both the systems, C, O, and N appear as the common elements in the binding energy (BE) values at 284.8, 531.5, and 400.5 eV, respectively. The XPS peaks appeared between 0 to 200 eV correspond to the Si because the silicon wafer was employed as the support to the samples during the analysis. The observed two peaks at 100, and 150 eV correspond to the Si 2s and Si 2p states, respectively. The characteristic peak corresponding to Co in the case of $\text{Co}_3\text{O}_4/\text{NEGF}$ has appeared at the B.E. value of 784.2 eV.³⁸ The C and N peak intensities in $\text{Co}_3\text{O}_4/\text{NEGF}$ are found to be decreased due to Co_3O_4 coverage over NEGF. The comparative deconvoluted XPS spectra of NEGF and $\text{Co}_3\text{O}_4/\text{NEGF}$ are studied for gaining insightful information of C 1s, N 1s, O 1s, and Co 2p. The deconvoluted C 1s spectra of NEGF has displayed various peaks corresponding to C–C (283.5 eV), C=C (284 eV), C–N/C=N (287.5 eV), and C–O (291.5 eV), with different binding energy values due to the particular chemical environment of the carbon as shown in **Figure 3.8b**.³⁸ Similarly, the deconvoluted C 1s spectra of $\text{Co}_3\text{O}_4/\text{NEGF}$ has displayed the peaks corresponding to C–C (283.5), C=C (284), C–N/C=N (287.5 eV), and C–O (291.5), with similar binding energy and small change in the intensities due to the presence of Co_3O_4 as shown in **Figure 3.8c**. The peak intensities of the C–C and C–O bonds are higher than that of the C=C and C=N bonds in the case of $\text{Co}_3\text{O}_4/\text{NEGF}$ compared to NEGF due to the lower extent of graphitization in the presence of the Co_3O_4 nanorods. This observation is in accordance with the information gained from the Raman analysis. Deconvoluted N 1s spectra of NEGF, as shown in **Figure 3.8d**, displaying the pyridinic-N at 398.6 eV (32.9%) and the pyrrolic-N at 399.7 eV (41.6%) as the major moieties along with smaller proportions from the graphitic-N at 400.5 eV (19.3%) and NH_4^+ at 405.5 eV (15.9%). Furthermore, **Figure 3.8e** shows the deconvoluted N 1s spectra of $\text{Co}_3\text{O}_4/\text{NEGF}$. Deconvoluted peaks of $\text{Co}_3\text{O}_4/\text{NEGF}$ suggesting that the N-doping in the graphene matrix remains the same during the *in-situ* loading of Co_3O_4 along with the presence of the pyridinic-N at 398.6 eV (41.6%), pyrrolic-N at 399.7 eV (32.9%), graphitic-N at 400.5 eV (19.3%) and NH_4^+ at 402.5 eV (15.9%). The doped nitrogen in the graphene framework regulates metal oxide nanorods growth kinetics during the catalyst synthesis process. The Co 2p spectra of $\text{Co}_3\text{O}_4/\text{NEGF}$ showed two peaks (**Figure 3.8f**) at the BE values of 783.1 and 798.8 eV with a band

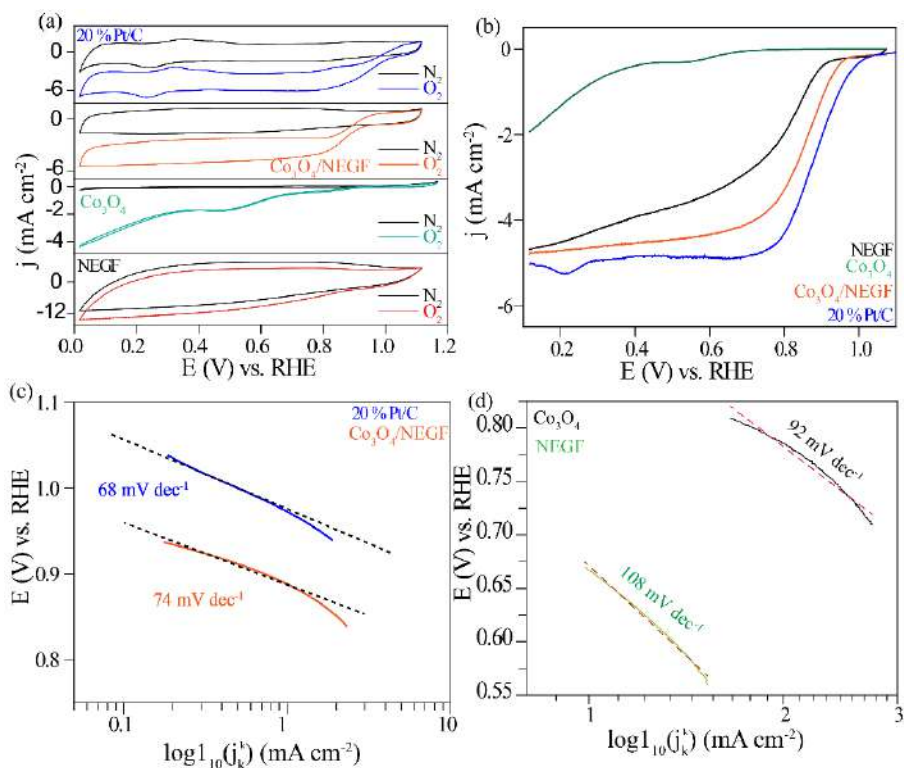


Figure 3.9. Electrocatalytic performance evaluation of $\text{Co}_3\text{O}_4/\text{NEGF}$ and the control samples (Co_3O_4 and NEGF) towards ORR in comparison to the state-of-the-art (Pt/C) catalyst: (a) comparative CV profiles recorded for NEGF, Co_3O_4 , $\text{Co}_3\text{O}_4/\text{NEGF}$, and Pt/C in N_2/O_2 saturated 0.1 M KOH at 900 RPM of the working electrode (WE); (b) LSV profiles of Pt/C, $\text{Co}_3\text{O}_4/\text{NEGF}$, Co_3O_4 , and NEGF recorded at an RPM of 1600 of the WE; (c) Tafel plots constructed for $\text{Co}_3\text{O}_4/\text{NEGF}$ and Pt/C; (d) Tafel plots constructed for Co_3O_4 and NEGF with the measured slopes of 92 and 108 mV dec^{-1} , respectively. (Reprinted (adapted) with permission from ACS Appl. Energy Mater. 2021, 4, 5, 4570-4580. Copyright (2021) American Chemical Society).

separation of ~ 15.7 eV. The peak separation of 15.7 eV is the characteristic feature of Co_3O_4 . These deconvoluted spectra show the two spin-spin coupling peaks for the peaks correspond to the $\text{Co } 2p_{3/2}$ and $\text{Co } 2p_{1/2}$ states of Co, thus point towards the existence of the +2 and +3 oxidation states, respectively, in the system.^{38, 39, 48}

3.3.10. Electrochemical Analysis:

The obtained catalyst was further explored for the electrochemical ORR performance by adopting a set of electrochemical techniques. The measurements were first recorded using Hg/HgO as the reference

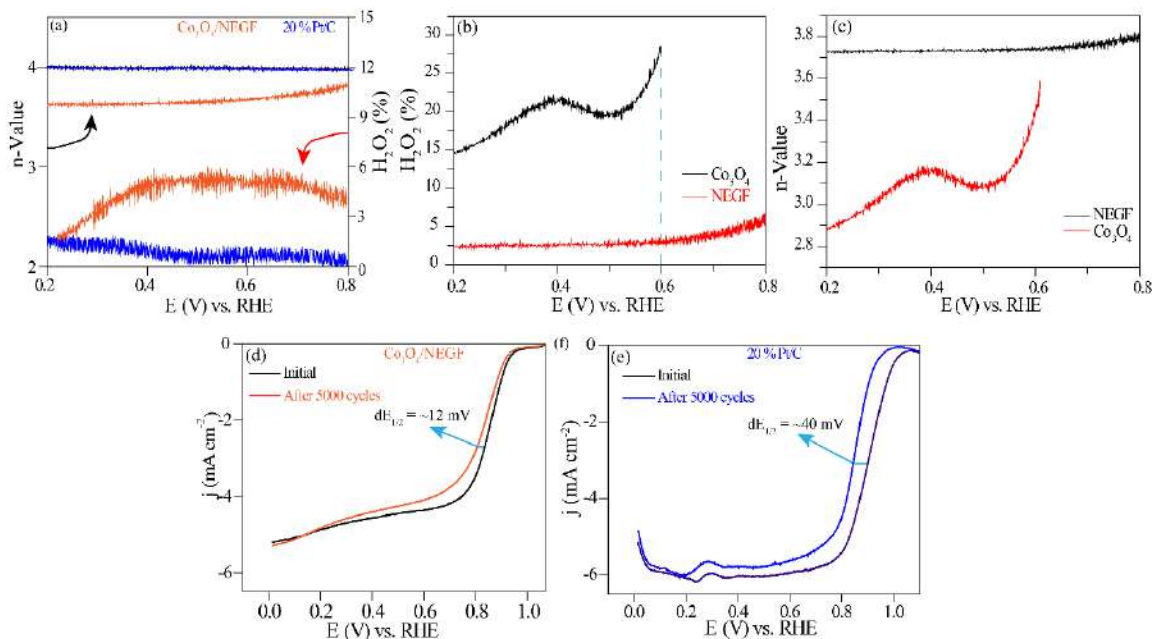


Figure 3.10. (a) RRDE analysis of Pt/C and $\text{Co}_3\text{O}_4/\text{NEGF}$ displaying the amount of H_2O_2 generated and the electron transfer number (n-value) corresponding to the ORR process; (b) RRDE analysis of NEGF and Co_3O_4 displaying the percentage of the generated H_2O_2 in the ORR process; (c) RRDE analysis of NEGF and Co_3O_4 displaying the electron transfer number (n-value); (d) and (e) the accelerated durability test (ADT) data of $\text{Co}_3\text{O}_4/\text{NEGF}$ and Pt/C, respectively. (Reprinted (adapted) with permission from ACS Appl. Energy Mater. 2021, 4, 5, 4570-4580. Copyright (2021) American Chemical Society).

electrode, and potentials were converted to the RHE scale. The cyclic voltammogram (CV) recorded for $\text{Co}_3\text{O}_4/\text{NEGF}$ under O_2 -saturated 0.1 M KOH electrolyte at a WE rotation speed of 900 rpm displays an ORR onset potential at 0.94 V vs. RHE, which is found to be only 60 mV lower compared to the onset potential of 1.00 V vs. RHE recorded for the state-of-the-art Pt/C catalyst (**Figure 3.9a**). On the other hand, a much larger shift of the onset potentials towards higher overpotential has been observed for NEGF (0.80 V vs. RHE) and Co_3O_4 (0.65 V vs. RHE) as shown in **Figure 3.9a**. The CV profile of NEGF follows a notable capacitive nature, which appears to be resulting from the high surface area acquired by the 3D graphene morphology resulting from the freeze-drying process.⁵⁰ To gain more precise information on the intrinsic activity characteristics of the systems towards ORR, the linear sweep voltammograms (LSVs) were recorded in the rotating disc electrode (RDE) mode. The LSVs were recorded under O_2 saturated conditions for $\text{Co}_3\text{O}_4/\text{NEGF}$, Co_3O_4 , NEGF, and Pt/C (**Figure 3.9b**) by maintaining the rotation speed of the WE at 1600 rpm and performing the voltage scan at the rate of 10 mV s^{-1} . The comparative LSV

profiles presented in **Figure 3.9b** clearly display the superior ORR performance achieved by $\text{Co}_3\text{O}_4/\text{NEGF}$ in comparison to the control samples, *viz.*, Co_3O_4 and NEGF. With an onset potential of 0.94 V *vs.* RHE (accounting only 60 mV overpotential compared to Pt/C) and a well-featured LSV profile, $\text{Co}_3\text{O}_4/\text{NEGF}$ could emerge as a potential contender as a non-Pt electrocatalyst for ORR. The half-wave potential ($E_{1/2}$) of $\text{Co}_3\text{O}_4/\text{NEGF}$ (0.80 V *vs.* RHE) is also found to be very close to that of Pt/C (0.90 V), which stands out as a quantitative indicator pointing towards the efficacy of the system to perform under the more demanding condition of reasonable current dragging. **Table 3.1** summarizes the values of the onset potential and $E_{1/2}$ for all the systems compared in this study. Associating the drastic difference in the ORR performance characteristics of Co_3O_4 and $\text{Co}_3\text{O}_4/\text{NEGF}$ towards ORR, it can be clearly understood the huge advantage incurred by the supported system through the cooperative and synergistic effects originated from the metal oxide-support interactions. The controlled interplay originated from the factors like the rough surface and nanorod morphology of Co_3O_4 , the 3D-morphology of the substrate

Table 3.1. The onset (E) and half-wave ($E_{1/2}$) potentials measured for the various catalysts. (Reprinted (adapted) with permission from ACS Appl. Energy Mater. 2021, 4, 5, 4570-4580. Copyright (2021) American Chemical Society).

Sample	Onset Potential E (V) <i>vs.</i> RHE	Half Wave Potential $E_{1/2}$ (V) <i>vs.</i> RHE
NEGF	0.80	0.69
Co_3O_4	0.65	0.54
$\text{Co}_3\text{O}_4/\text{NEGF}$	0.94	0.84
Pt/C	1.00	0.90

with its ability for ensuring seamless mass transport, and the modulations incurred through the electronic interactions in the dispersed state are emerging as the beneficial factors for $\text{Co}_3\text{O}_4/\text{NEGF}$.

Tafel slope is another important quantifiable parameter to understand the ORR kinetics. Tafel analysis has been performed for $\text{Co}_3\text{O}_4/\text{NEGF}$ and Pt/C by following the standard procedure (**Figure 3.9c**). $\text{Co}_3\text{O}_4/\text{NEGF}$ displays a Tafel slope of approximately 74 mV dec^{-1} , nearly comparable to 68 mV dec^{-1} measured for Pt/C. The observed Tafel slope values for NEGF and Co_3O_4 are 92 and 108 mV dec^{-1} , respectively (**Figure 3.9d**). The higher Tafel slope values of NEGF and Co_3O_4 compared to $\text{Co}_3\text{O}_4/\text{NEGF}$ suggest the slower ORR kinetics involved in the catalytic process over these systems.

A critical issue with the existing non-Pt electrocatalysts for ORR is the parallel involvement of the parasitic 2e- reduction process leading to the formation of H₂O₂ and the desired 4e- reduction resulting in the formation of H₂O. The limitation of this possibility has been ruled out in the present case by performing a rotating ring disc electrode (RRDE) analysis, which indicated an H₂O₂ yield of less than 6%. In the RRDE data presented in **Figure 3.10a** the peroxide species (HO₂⁻) generated during the ORR cycle was investigated and quantified. From **Figure 3.10a**, the H₂O₂ % is found to be remaining below 6%, with only marginal variations across the potential window for Co₃O₄/NEGF. The percentage of H₂O₂ generated in the case NEGF is around 3%, and that on Co₃O₄ is around 28% at 0.60 V with respect to RHE (**Figure 3.10b**). Although the percentage of H₂O₂ formation is higher in the individual electrocatalysts compared to the composite (Co₃O₄/NEGF), the relatively higher percentage of H₂O₂ formation in Co₃O₄ is due to the hindered electronic transport due to the lower conductivity of the metal oxide.⁵⁰ The obtained low H₂O₂ generation in the case of Co₃O₄/NEGF has been further substantiated from the calculated number of electrons (represented as ‘n-value’ in **Figure 3.10a**) of 3.75 in the case of Co₃O₄/NEGF (compared to 3.98 for Pt/C), which indicates the dominance of the water formation pathway (4e-transfer) in the reduction process. Furthermore, **Figure 3.10c** shows the n-value calculation for NEGF and Co₃O₄, which suggested that the n-value for NEGF is around 3.75 whereas that for Co₃O₄ is 3.6.

An accelerated durability test (ADT) of Co₃O₄/NEGF in comparison with Pt/C has been performed by subjecting the system under potential cycling between 1.2 and 0.80 V (RHE) at 100 mV s⁻¹ in O₂-saturated 0.1 M KOH condition. The purpose of this study was to understand the electrochemical stability of the system under corrosion-induced conditions, which can lead to catastrophic failure of the morphological features and result in concomitant variations in the key performance indicators. The ADT data corresponding to Co₃O₄/NEGF and Pt/C are presented in **Figure 3.10d** and **e**, respectively. As can be seen from the ADT profiles, Co₃O₄/NEGF could survive better under the triggered condition compared to its Pt/C counterpart, inferring to the better structural endurance possessed by the former. This can be quantitatively evaluated from the E_{1/2} value change of the systems subsequent to ADT, where the drop observed in the case of Co₃O₄/NEGF is only 12.2 mV compared to 40.5 mV incurred by Pt/C. It is known that the conventional carbon is prone to corrosion under the ORR conditions, which can lead to catalyst fouling, particle aggregation, and dissolution. While replacing the carbon with NEGF, the process enhances the binding interaction between the metal nanoparticles and graphene with the help of its functionalized and heteroatom incorporated binding centers.²⁸ The observed differences in the chemical

and physical properties of $\text{Co}_3\text{O}_4/\text{NEGF}$ before and after ADT is responsible for the minimal variation in $E_{1/2}$ of 12 mV which is very less in comparison to the Pt/C catalyst 40 mV (**Figure 3.10d, e**).

Post durability analysis of the $\text{Co}_3\text{O}_4/\text{NEGF}$ catalyst has been done by physical characterization of the pre-cycled sample. The TEM analysis of the pre-treated sample clearly shows the intact distribution of the Co_3O_4 nanorod as similar to the pristine $\text{Co}_3\text{O}_4/\text{NEGF}$ case. However, a surface roughness along with the thin layer formation over Co_3O_4 nanorods (**Figure 3.11a, b**) was evidenced, revealing the textural changes in the supported Co_3O_4 nanorods. The changes in the crystalline phase of $\text{Co}_3\text{O}_4/\text{NEGF}$ after ADT were observed by XRD analysis (**Figure 3.11c**). The XRD analysis reveals that the surface is covered with a thin layer of $\text{Co}(\text{OH})_2$ which was verified by the presence of the mixed-phase of Co_3O_4 and $\text{Co}(\text{OH})_2$ peaks.⁴⁶ The observed diffraction peaks are ascribed to the (002), (220), (400), (511), and (440) planes of the Co_3O_4 nanorods.^{20, 46} It is suppressing the more active (311) peak of Co_3O_4 after 5000 cycles with the concomitant formation of more active (100) peak for $\text{Co}(\text{OH})_2$.^{46, 47} In addition, the XPS analysis of the sample has further supported the presence of $\text{Co}(\text{OH})_2$ (**Figure 3.11d and e**).^{43, 48, 49} After the durability test, further deconvoluted Co 2p spectra analysis suggested the change in the electronic state as evidenced from the change in the Co peak position (**Figure 3.11e**).^{48, 49} The deconvoluted XPS spectra of Co_3O_4 after ADT evidenced the presence of three different forms of Co-ions.

Hence, in the longer run, the in-house catalyst is expected to outperform the Pt/C system both in terms of performance and durability under a realistic system-level demonstration. The high intrinsic ORR activity displayed by $\text{Co}_3\text{O}_4/\text{NEGF}$ in the single-electrode mode could be further translated in terms of performance in the device level in a zinc-air battery (ZAB). As shown in **Figure 3.12a**, the ZAB consists of the ORR catalyst coated gas carbon diffusion layer (GDL) as the cathode, zinc powder as the anode, and 6 M KOH as the electrolyte. During the operation of the ZABs, diffused oxygen through the porous air cathode gets reduced to OH^- , which subsequently travels towards the anode through the electrolyte to facilitate oxidation of Zn to form its hydroxide and oxide. The released electron during the oxidation process of Zn flows through the outer circuit and establishes the flow of electric current.^{2, 44, 41} In the present case, the cells based on $\text{Co}_3\text{O}_4/\text{NEGF}$ and Pt/C are found to be displaying the open-circuit voltage(OCV) values of 1.31 and 1.40 V, respectively, which goes very well in line with the performance recorded during the half-cell mode of operation (**Figure 3.12b**). The performance of the demonstrated system is comparable to the ZAB systems reported in the literature (**Table 3.2**). The comparative steady-

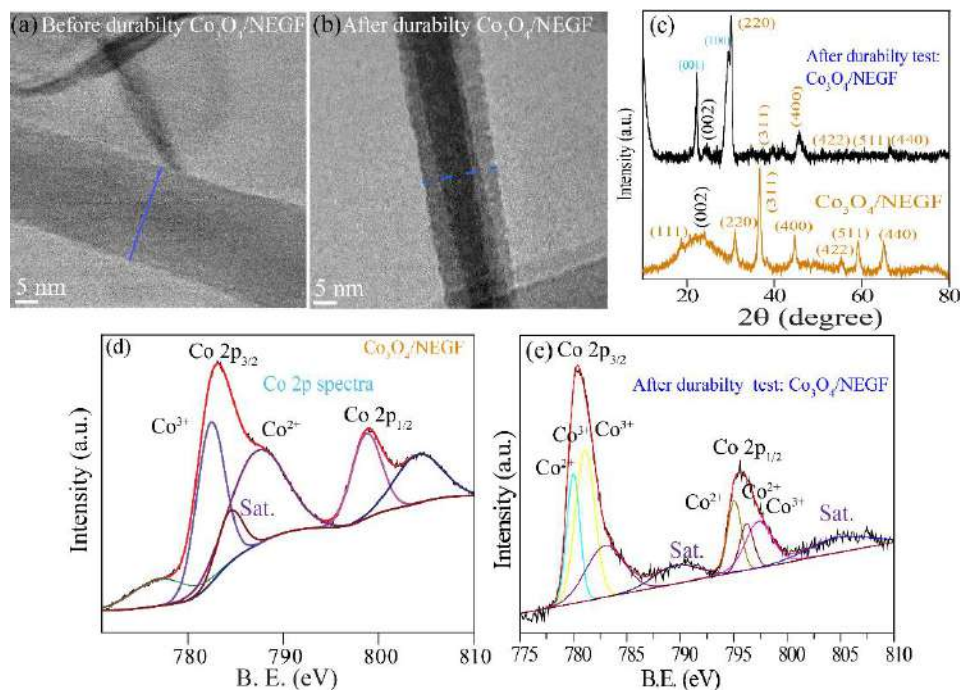


Figure 3.11. Post ADT analysis of the Co₃O₄/NEGF catalyst: (a) TEM image of Co₃O₄/NEGF before the electrochemical study, (b) TEM image of Co₃O₄/NEGF after ADT; (c) comparative XRD analysis of the sample Co₃O₄/NEGF before and after ADT showing the formation Co(OH)₂ layer over the Co₃O₄, (d) deconvoluted XPS spectra of the as prepared Co₃O₄/NEGF showing the peaks for Co²⁺ and Co³⁺ and (e) the deconvoluted XPS spectra of the electrocatalyst after ADT, showing the change in the binding energy of the Co and appearance of one extra peak of Co due to the presence of the Co-O bond in Co(OH)₂. (Reprinted (adapted) with permission from ACS Appl. Energy Mater. 2021, 4, 5, 4570-4580. Copyright (2021) American Chemical Society).

state cell polarization (**Figure 3.12b**) leads to maximum power densities (P_{\max}) of 190 and 210 mW cm⁻², respectively, for the ZABs based on Pt/C and Co₃O₄/NEGF as the cathode catalysts. It is interesting to note that, although the OCV for the cell based on Co₃O₄/NEGF is lower as compared to the counterpart system based on Pt/C, the performance of the former gradually picks up and outperforms the later. This is expected to be realized from the intrinsic advantage of Co₃O₄/NEGF as the ORR catalyst in terms of mass transport governed by the porous 3D architecture of NEGF. system based on Pt/C, the performance of the former gradually picks up and outperforms the later. This is expected to be realized from the intrinsic advantage of Co₃O₄/NEGF as the ORR catalyst in terms of mass transport governed by the porous 3D architecture of NEGF.

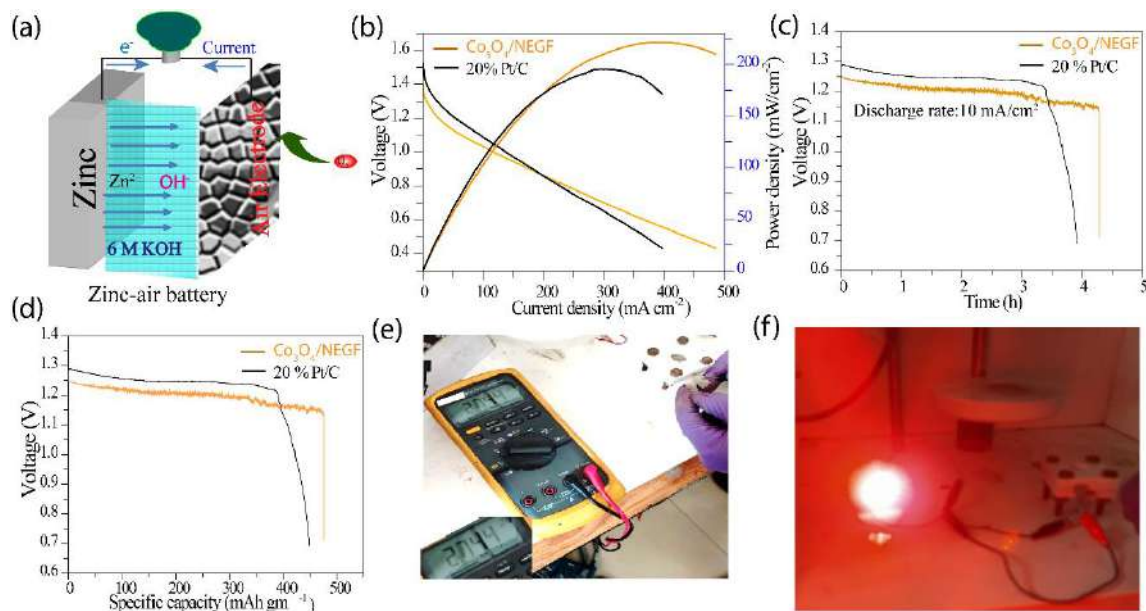


Figure 3.12. The zinc-air battery (ZAB) fabrication, performance evaluation, and demonstration: (a) schematic representation of the fabricated ZAB (cathode catalyst loading: 1.0 mg/cm²; anode: zinc powder; separator: Celgard® membrane soaked with 6M KOH); (b) polarization plots recorded on the ZABs fabricated by employing Co₃O₄/NEGF and Pt/C as the air electrodes; (c) long-term galvanostatic discharge curves of the ZABs with Co₃O₄/NEGF and Pt/C as the cathode catalysts until complete consumption of the anodic zinc powder; (d) galvanostatic discharge capacity of the battery after normalizing with the consumed amount of the zinc powder used for the fabrication of the ZABs; (e) demonstration of the assembled ZAB displaying the voltage of the two cells connected in series showing the voltage of 2.744 V as measured by using a multimeter; (f) digital photograph of the LED illuminated using the ZAB containing Co₃O₄/NEGF as the cathode catalyst. (Reprinted (adapted) with permission from ACS Appl. Energy Mater. 2021, 4, 5, 4570–4580. Copyright (2021) American Chemical Society).

Furthermore, the galvanostatic discharge curve recorded at 10 mA cm⁻² (**Figure 3.12c**) points towards the robustness of the in-house ZAB system. The discharge time for the ZABs based on Co₃O₄/NEGF and Pt/C is found to be nearly 4.5 h and 4 h, respectively. The voltage drop in the plateau region concerning the operation time is expected to result from the side reactions taking place over the surface of the Zn

Table 3.2. Comparison of the key performance indicators of the various ZABs reported in the literature with the reported system in this work. (Reprinted (adapted) with permission from ACS Appl. Energy Mater. 2021, 4, 5, 4570-4580. Copyright (2021) American Chemical Society).

Sr. No.	Electrocatalyst	Power density	Specific capacities (mAh/g _{m-Zn})	Current densities (mA/cm ²)	References
1.	CF-N-rGO-150	540 mW/cm ²	630 mAh/g _{m-Zn}	20 mA/cm ²	10
2.	CFZr(0.3)/N-rGO	-	727 mAh/g _{m-Zn}	20 mA/cm ²	11
3.	Co ₃ O ₄ -SP/NGr-24h	190 mW/cm ²	~590 mAh/g _{m-Zn}	10 mA/cm ²	12
4.	CoMn/pNGr(2:1)	230 mW/m ²	-	-	13
5.	Fe-N-PGC-800		731 mA h/g _{m-Zn}	100 mA/cm ²	14
6.	Co ₃ O ₄ /NEGF	210 mW/cm ²	490 mAh/g _{m-Zn}	10 mA/cm ²	This work

powder.^{22, 45, 46} The estimated specific capacity (**Figure 3.12d**) of the assembled ZAB based on Co₃O₄/NEGF is about 474 mAh/g_{m-Zn} compared to 445 mAh/g_{m-Zn} measured for the system based on Pt/C.

For the real-time demonstration of the fabricated ZAB, two ZAB devices based on Co₃O₄/NEGF cathode were connected in series, which result in an overall voltage of 2.744 V as measured using a multimeter device (**Figure 3.12e**). This device was subsequently employed to light an LED of 2 V, which resulted in steady illumination for a long time without any interruption (**Figure 3.12f**). Thus, overall, a close matching and promising performance could be ensured during the demonstration of the ZAB based on the in-house catalyst for facilitating ORR in the cathode, which justified our findings of the performance mapping of the material-specific intrinsic activity of Co₃O₄/NEGF through the single-electrode studies.

3.4. Conclusions:

In summary, a prospective non-noble metal-based ORR electrocatalyst derived by the dispersion of Co₃O₄ nanorods on 3D structured nitrogen-doped entangled graphene (NEGF), designated as Co₃O₄/NEGF, was achieved by employing a simple and scalable hydrothermal method followed by freeze-drying. As a catalyst, Co₃O₄/NEGF displayed high ORR activity during single-electrode testing, and subsequently, its potential as the cathode for a Zn-air battery (ZAB) system could be demonstrated under realistic testing conditions. The synthesis protocol involving the hydrothermal treatment followed by the freeze-drying processes is critical in achieving the desired structural and morphological features of the catalyst. The

doped nitrogen, along with its favorable contribution towards ORR, also plays a critical role in establishing the efficient dispersion of the oxide nanorods on the substrate. The catalytic activity enhancement is expected to be resulted from the regulated interplay of several favoring factors, including the high surface area, homogeneous dispersion of the active sites, better reactant distribution, high active site accessibility, and the synergistic interaction operating between the doped nitrogen and the Co_3O_4 nanorods. The 60 mV onset potential shift for ORR and the Tafel slope of 74 mV/dec recorded over $\text{Co}_3\text{O}_4/\text{NEGF}$ compared to the state-of-the-art Pt/C in the single-electrode mode are promising values expected from a non-Pt electrocatalyst. Further, the unique structural features involving the 3D architecture with the interconnected pores created by the self-assembling of the entangled graphene during the freeze-drying process is found to be assisting reactant distribution and active site utilization. The competing performance displayed by the ZAB consisting of $\text{Co}_3\text{O}_4/\text{NEGF}$ as the cathode with the counterpart system based on Pt/C cathode substantiates the structural advantages incurred by the home-made catalyst. Thus, as a cost-effective and competitive catalyst, $\text{Co}_3\text{O}_4/\text{NEGF}$ stands out as a versatile replacement for the expensive catalysts based on noble metals for the electrochemical systems involving ORR as the rate-determining electrode process.

3.5. References:

1. Cano, Z. P.; Banham, D.; Ye, S.; Hintennach, A.; Lu, J.; Fowler, M.; Chen, Z. Batteries and Fuel Cells for Emerging Electric Vehicle Markets. *Nat. Energy* **2018**, *3*, 279–289.
2. Li, Y.; Gong, M.; Liang, Y.; Feng, J.; Kim, J. E.; Wang, H.; Hong,.; Zhang, B.; Dai, H. Advanced Zinc-Air Batteries Based on High-Performance Hybrid Electrocatalysts. *Nat. Comm* **2013**, *4*, 1–7.
3. Wang, Y.; Li, J.; Wei, Z. Transition-Metal-Oxide-Based Catalysts for the Oxygen Reduction Reaction. *J. Mater Chem. A* **2018**, *6*, 8194–8209.
4. Jukk, K.; Kongi, N.; Rauwel, P.; Matisen, L.; Tammeveski, K. Platinum Nanoparticles Supported on Nitrogen-Doped Graphene Nanosheets as Electrocatalysts for Oxygen Reduction Reaction. *Electrocatalysis* **2016**, *7*, 428–440.
5. Yuan, Y.; Wang, J.; Adimi, S.; Shen, H.; Thomas, T.; Ma, R.; At field, J. P.; Yang, M. Zirconium Nitride Catalysts Surpass Platinum for Oxygen Reduction. *Nat. Mater.* **2020**, *19*, 282–286.
6. Yu, H.; Baricci, A.; Roller, J.; Wang, Y.; Casalegno, A.; Mustain, W.E.; Maric, R. Ultra-Low Pt Loading Catalyst Layers for PEMFC Using Reactive Spray Deposition Technology. *ECS Trans.* **2015**, *69*, 487–496.

7. Dhavale, V. M.; Singh, S. K.; Nadeema, A.; Gaikwad, S. S.; Kurungot, S. Nanocrystalline Fe-Fe₂O₃ Particle-Deposited N-Doped Graphene as an Activity-Modulated Pt-Free Electrocatalyst for Oxygen Reduction Reaction. *Nanoscale* **2015**, *7*, 20117–20125.
8. Liu, J.; Li, E.; Ruan, M.; Song, P.; Xu, W. Recent Progress on Fe/N/C Electrocatalysts for the Oxygen Reduction Reaction in Fuel Cells. *Catalysts* **2015**, *5*, 1167–1192.
9. Tian, L.; Zhu, J. L.; Chen, L.; An, B.; Liu, Q. Q.; Huang, K. L. Synthesis and Characterization of α -Cobalt Hydroxide Nanobelts. *J. Nanoparticle Res.* **2011**, *13*, 3483–3488.
10. Abroshan, H.; Bothra, P.; Back, S.; Kulkarni, A.; Nørskov, J. K.; Sahrostami, S. Ultrathin Cobalt Oxide Overlayer Promotes Catalytic Activity of Cobalt Nitride for the Oxygen Reduction Reaction. *J. Phys. Chem. C* **2018**, *122*, 4783–4791.
11. Mosa, I. M.; Biswas, S.; El-Sawy, A. M.; Botu, V.; Guild, C.; Song, W.; Ramprasad, R.; Rusling, J. F.; Suib, S. L. Tunable Mesoporous Manganese Oxide for High Performance Oxygen Reduction and Evolution Reactions. *J. Mater. Chem. A* **2015**, *4*, 620–631.
12. Wang, Y.; Yang, Y.; Jia, S.; Wang, X.; Lyu, K.; Peng, Y.; Zheng, H.; Wei, X.; Ren, H.; Xiao, L.; Wang, J.; Muller, D. A.; Abruña, H. D.; Hwang, B. J.; Lu, J.; Zhuang, L. Synergistic Mn-Co Catalyst Outperforms Pt on High-rate Oxygen Reduction for Alkaline Polymer Electrolyte Fuel Cells. *Nat. Commun.* **2019**, *10*, 6–13.
13. Wang, Z.; Wei, G.; Du, K.; Zhao, X.; Liu, M.; Wang, S.; Zhou, Y.; An, C.; Zhang, J. Ni Foam-Supported Carbon-Sheathed NiMoO₄ Nanowires as Integrated Electrode for High-Performance Hybrid Supercapacitors. *ACS Sustain Chem Eng* **2017**, *5*, 5964–5971.
14. Singh, S. K.; Dhavale, V. M.; Kurungot, S. Surface-Tuned Co₃O₄ Nanoparticles Dispersed on Nitrogen-Doped Graphene as an Efficient Cathode Electrocatalyst for Mechanical Rechargeable Zinc–Air Battery Application. *ACS Appl. Mater. Interfaces* **2015**, *7*, 21138–21149.
15. Singh, S. K.; Dhavale, V. M.; Kurungot, S. Low Surface Energy Plane Exposed Co₃O₄ Nanocubes Supported on Nitrogen-Doped Graphene as an Electrocatalyst for Efficient Water Oxidation. *ACS Appl. Mater. Interfaces* **2015**, *7*, 442–451.
16. Zang, M.; Xu, N.; Cao, G.; Chen, Z.; Cui, J.; Gan, L.; Dai, H.; Yang, X.; Wang, P. Cobalt Molybdenum Oxide Derived High-Performance Electrocatalyst for the Hydrogen Evolution Reaction. *ACS Catal.* **2018**, *8*, 5062–5069.
17. Gao, D.; Luo, S.; Zhang, Y.; Liu, J.; Wu, H.; Wang, S.; He, P. Mn₃O₄/Carbon Nanotubes Nanocomposites as Improved Anode Materials for Lithium-Ion Batteries. *J. Solid State Electrochem.* **2018**, *22*, 3409–3417.
18. Shen, H.; Liu, Y. PT Graphical Abstract SC. *Chin. J. Chem. Eng* **2018**, *23*, 225–232
19. Wang, B.; Li, F.; Wang, X.; Wang, G.; Wang, H.; Bai, J. Mn₃O₄ Nanotubes Encapsulated by Porous Graphene Sheets with Enhanced Electrochemical Properties for Lithium/Sodium-Ion Batteries. *Chem. Eng. J.* **2019**, *364*, 57–69.

20. Han, X.; He, G.; Yu He, Jinfeng Zhang, Xuerong Zheng, Lanlan Li, Cheng Zhong, Wenbin Hu, Yida Deng, and Tian-Yi Ma Engineering Catalytic Active Sites on Cobalt Oxide Surface for Enhanced Oxygen Electrocatalysis. *Adv. Energy Mater.* **2018**, *8*, 1702222.
21. Ling, T.; Yan, D. Yang.; Jiao, Y.; Wang, H.; Zheng, Y.; Zheng, X.; Mao, J.; Du, X. W.; Hu, Z.; Jaroniec M.; & Qiao S. Z. Activating cobalt(II) oxide nanorods for efficient electrocatalysis by strain engineering. *Nat. Commun.* **2016**, *7*, 12876.
22. Shao, L.; Zhao, Q.; Chen, J. MnOOH Nanorods as High Performance Anodes for Sodium Ion Batteries. *Chem. Commun.* **2017**, *53*, 2435–2438.
23. Zhou, Y.; Xi, S.; Wang, J.; Sun, S.; Wei, C.; Feng, Z.; Du, Y.; Xu, Z. J. Revealing the Dominant Chemistry for Oxygen Reduction Reaction on Small Oxide Nanoparticles. *ACS Catal.* **2018**, *8*, 673–677.
24. Zhao, C.; Peng, B. Synthesis of Porous Fiber-like CoMn₂O₄ Derived from Cotton Template as Lithium Ion Battery Anodes. *Int. J. Electrochem. Sci.* **2018**, *13*, 1505–1514.
25. Wang, Z. L.; Xu, D.; Xu, J. J.; Zhang, X. B. Oxygen Electrocatalysts in Metal-Air Batteries: From Aqueous to Nonaqueous Electrolytes. *Chem. Soc. Rev.* **2014**, *43*, 7746–7786.
26. Okelly, C.; Jung, S. J.; Bell, A. P.; Boland, J. J. Single Crystal Iron Nanocube Synthesis via the Surface Energy Driven Growth Method. *Nanotechnology* **2012**, *23*, 0957-4484.
27. Ishihara, A.; Ohgi, Y.; Matsuzawa, K.; Mitsushima, S.; Ota, K. I. Progress in Non-Precious Metal Oxide-Based Cathode for Polymer Electrolyte Fuel Cells. *Electrochim. Acta.* **2010**, *55*, 8005–8012.
28. Fu, X.; Choi, J. Y.; Zamani, P.; Jiang, G.; Hoque, M. A.; Hassan, F. M.; Chen, Z. Co-N Decorated Hierarchically Porous Graphene Aerogel for Efficient Oxygen Reduction Reaction in Acid. *ACS Appl. Mater. Interfaces* **2016**, *8*, 6488–6495.
29. Benson, J.; Xu, Q.; Wang, P.; Shen, Y.; Sun, L.; Wang, T.; Li, M.; Papakonstantinou, P. Tuning the Catalytic Activity of Graphene Nanosheets for Oxygen Reduction Reaction via Size and Thickness Reduction. *ACS Appl. Mater. Interfaces* **2014**, *6*, 19726-19736.
30. Galeano, C.; Meier, J. C.; Peinecke, V.; Bongard, H.; Katsounaros, I.; Topalov, A. A.; Lu, A.; Mayrhofer, K. J. J.; Schüth, F. Toward Highly Stable Electrocatalysts via Nanoparticle Pore Confinement. *J. Am. Chem. Soc.* **2012**, *134*, 20457–20465.
31. Li, W.; Liu, J.; Zhao, D. Mesoporous Materials for Energy Conversion and Storage Devices. *Nat. Rev. Mater.* **2016**, *1*, 53-65.
32. Manna, N.; Ayasha, N.; Singh, S. K.; Kurungot, S. A NiFe Layered Double Hydroxide-Decorated N-Doped Entangled-Graphene Framework: A Robust Water Oxidation Electrocatalyst. *Nanoscale Adv.* **2020**, *2*, 1709–1717.

33. Singh, S. K.; Kashyap, V.; Manna, N.; Bhange, S. N.; Soni, R.; Bo kherroub, R.; Szunerits, S.; Kurungot, S. Efficient and Durable Oxygen Reduction Electrocatalyst Based on CoMn Alloy Oxide Nanoparticles Supported over N-Doped Porous Graphene. *ACS Catal.* **2017**, *7*, 6700–6710.
34. Zhou, M.; Wang, H. L.; Guo, S. Towards High-Efficiency Nano-electrocatalysts for Oxygen Reduction through Engineering Advanced Carbon Nanomaterials. *Chem. Soc. Rev.* **2016**, *45*, 1273–1307.
35. Yang, S.; Zhang, L.; Yang, Q.; Zhang, Z.; Chen, B.; Lv, P.; Zhu, W.; Wang, G. Graphene Aerogel Prepared by Thermal Evaporation of Graphene Oxide Suspension Containing Sodium Bicarbonate. *J. Mater. Chem. A* **2015**, *3*, 7950–7958.
36. Cao, Y.; Mao, S.; Li, M.; Chen, Y.; Wang, Y. Metal/Porous Carbon Composites for Heterogeneous Catalysis: Old Catalysts with Improved Performance Promoted by N-Doping. *ACS Catal.* **2017**, *7*, 56–62.
37. Wang, J.; Wu, H.; Gao, D.; Miao, S. High-Density Iron Nanoparticles Encapsulated within Nitrogen-Doped Carbon Nanoshell as Efficient Oxygen Electrocatalyst for Zinc–Air Battery. *Materials* **2019**, *243*, 63–69.
38. Kashyap, V.; Singh, S. K.; Kurungot, S. Cobalt Ferrite Bearing Nitrogen-Doped Reduced Graphene Oxide Layers Spatially Separated with Microporous Carbon as Efficient Oxygen Reduction Electrocatalyst. *ACS Appl. Mater. Interfaces* **2016**, *8*, 20730–20740.
39. Kashyap, V.; Kurungot, S. Zirconium-Substituted Cobalt Ferrite Nanoparticle Supported N-Doped Reduced Graphene Oxide as an Efficient Bifunctional Electrocatalyst for Rechargeable Zn-Air Battery. *ACS Catal.* **2018**, *8*, 3715–3726.
40. Yang, Z.; Ren, J.; Zhang, Z.; Chen, X.; Guan, G.; Qiu, L.; Zhang, Y.; Peng, H. Recent Advancement of Nanostructured Carbon for Energy Applications. *Chem. Rev.* **2015**, *115*, 5159–5223.
41. Dai, L.; Chang, D. W.; Baek, J. B.; Lu, W. Carbon Nanomaterials for Advanced Energy Conversion and Storage. *Small* **2012**, *8*, 1130–1166.
42. Zitolo, A.; Sahraie, N. R.; Mineva, T.; Li, Jingkun.; Jia, Q.; Stamatina, Serban.; Harrington, G. F.; Lyth, S. M.; Krtil, P.; Mukerjee, S.; Fonda1, E.; & Jaouen, F.; Identification of Catalytic Sites in Cobalt-nitrogen-carbon Materials for the Oxygen Reduction Reaction. *Nat. Commun.* **2017**, *8*, 957.
43. Babar, P.T.; Lokhande, A.C.; Pawar, B.S.; Gang, M.G.; Jo, Eunjin.; Go, Changsik.; Suryawanshi, M.P.; Pawar, S.M.; Kim, J. H.; Electrocatalytic Performance Evaluation of Cobalt Hydroxide and Cobalt Oxide Thin Films for Oxygen Evolution Reaction. *Appl. Surf. Sci.* **2018**, *427*, 253–259.
44. Li, H.; Ma, L.; Han, C.; Wang, Z.; Liu, Z.; Tang, Z.; Zhi, C. Nano Energy Advanced Rechargeable Zinc-Based Batteries : Recent Progress and Future Perspectives. *Nano Energy* **2019**, *62*, 550–587.
45. Su, C.; Cheng, H.; Li, W.; Liu, Z.; Li, N.; Hou, Z. Atomic Modulation of FeCo–Nitrogen–Carbon Bifunctional Oxygen Electrodes for Rechargeable and Flexible All-Solid-State Zinc–Air Battery. *Adv. Funct. Mater.* **2017**, *20*, 1–12.

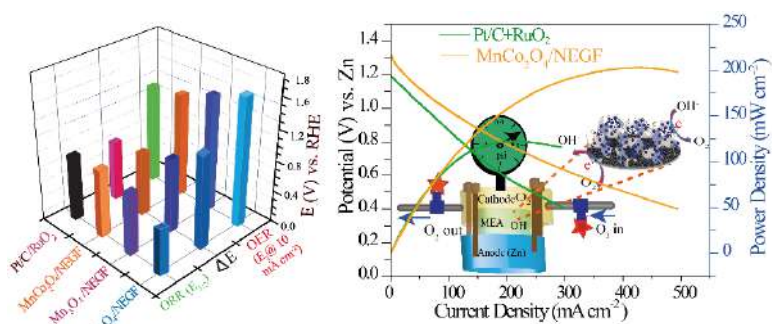
46. Bhang, S. N.; Unni, S. M.; Kurungot, S. Graphene with Fe and S Coordinated Active Centers: An Active Competitor for the Fe-N-C Active Center for Oxygen Reduction Reaction in Acidic and Basic PH Conditions. *ACS Appl. Mater. Interfaces* **2018**, *1*, 368–376.
47. Si, Y.; Guo, C.; Xie, C.; and Xiong, Z.; An Ultrasonication-Assisted Cobalt Hydroxide Composite with Enhanced Electrocatalytic Activity toward Oxygen Evolution Reaction; *Materials* **2018**, *11*, 1912
48. Yang, J.; Liu, H.; Martens, W. N. and L. Ray.; Frost Synthesis and Characterization of Cobalt Hydroxide, Cobalt Oxyhydroxide, and Cobalt Oxide Nanodiscs; *J. Phys. Chem. C* **2010**, *114*, 111–119
49. Chen, L.; Zhang, Y.; Wang, H.; Wang, Y.; Li, D. and Duan, C.; Cobalt Layered Double Hydroxides Derived CoP/Co₂P Hybrids for Electrocatalytic Overall Water Splitting. *Nanoscale*, **2018**, *10*, 21019
50. Lee, D.G.; Gwon, O.; Park, H. S; Kim, S. H; Yang, J.; Kwak, S. K.; Kim, G.; and Song, H. K.; Conductivity-Dependent Completion of Oxygen Reduction on Oxide Catalysts. *Angew. Chem. Int. Ed.* **2015**, *54*, 15730–1573
51. Weng, C. C.; Ren, J. T.; Hu, Z. P.; and Yuan, Z. Y.; Nitrogen-Doped Defect-Rich Graphitic Carbon Nanorings with CoO_x Nanoparticles as Highly Efficient Electrocatalyst for Oxygen Electrochemistry. *ACS Sustain. Chem. Eng.* **2018**, *6*, 15811–1582.

Chapter-4

Air-Cathode Interface-Engineered Electrocatalyst for Solid-State Rechargeable Zinc-Air Battery

Solid-state rechargeable zinc-air batteries (ZABs) are gaining interest as a new class of portable clean energy technology due to their advantages such as high theoretical energy density, intrinsic safety, and low cost. It is expected that an appropriately triple-phase boundary (TPB) engineered, bifunctional oxygen reaction (OER and ORR) electrocatalyst at the air-cathode of ZABs can redefine

the performance characteristics of these systems. To explore this possibility, an electrode material consisting of manganese-cobalt-based bimetallic spinel oxide (MnCo_2O_4)-supported nitrogen-doped entangled graphene ($\text{MnCo}_2\text{O}_4/\text{NEGF}$) with multiple active sites responsible for facilitating both OER and ORR has been prepared. The porous 3D graphitic support significantly affects the bifunctional oxygen reaction kinetics and helps the system to display a remarkable catalytic performance. The air-electrode consisting of the $\text{MnCo}_2\text{O}_4/\text{NEGF}$ coated over the gas diffusion layer (GDL) ensures the effective TPB and this feature works in favour of the rechargeable ZAB system under the charging and discharging modes. As an important structural and functional attribute of the electrocatalyst, the porosity and nitrogen doping in the 3D conducting support play an important role in controlling the surface wettability (hydrophilicity/hydrophobicity) of the air electrode. The fabricated solid-state rechargeable ZAB device with the developed electrode displayed a maximum peak power density of 202 mW cm^{-2} , which is significantly higher as compared to the one based on the state-of-the-art Pt/C + RuO_2 catalyst (124 mW cm^{-2}). The solid-state device which displayed an initial charge-discharge voltage gap of only 0.7 V at 10 mA cm^{-2} showed only a small increment of 86 mV after 50 h.



Content of this chapter is published in the following article: DOI: 10.1021/acsaem.2c01266

ACS Appl. Energy Mater. 2022, 5, 8756–8768.

Reproduced with permission from American Chemical Society.

4.1. Introduction:

To address the future energy and environmental challenges, economically viable energy storage technologies with improved performance characteristics are necessary.¹ Among such charge storage devices, solid-state rechargeable zinc-air batteries (ZABs) have gained appreciable interest for large-scale applications in portable electronic devices.^{2,3} Compared to the existing metal-air batteries, these systems have several advantages such as high theoretical energy density (1086 Wh kg^{-1}), involvement of safe aqueous electrolytes, and sufficient zinc metal resources.³ However, the practical applications of ZABs are impoverished by their low power density, deficient charge-discharge voltage, and overall lower output energy efficiency.⁴ These limitations are mainly attributed to the slow kinetics of oxygen reduction reaction (ORR) and oxygen evolution reaction (OER) on the air electrode.² Conventionally, the spherical-shaped platinum nanoparticle-supported carbon (Pt/C) and RuO_2 are mostly used as the electrocatalysts for ORR and OER processes, respectively.⁵ However, the lower bifunctional activity of the individual catalysts, their less availability as well as lower durability in the harsh conditions of ZABs hinder the practical prospects of the real-time application of the rechargeable ZABs.⁶ As a result, there has been a growing interest in developing efficient bi-functional oxygen electrocatalysts.⁷ Another important obstacle with the air-cathode of ZABs is the restricted mass transport of the reactant/products gas molecules and electrolytes due to the comparatively lower access of the active sites and imbalanced hydrophilicity/hydrophobicity of the electrocatalyst coated GDL interface.^{8,9} These issues necessitate a strategic design approach for building the air-electrode with improved triple-phase boundary (TPB) for effectively dealing the existing issues related to the kinetics and mass transport.¹⁰⁻¹²

As cost-effective solutions to the air-electrodes for ZABs, a series of non-noble metal-based electrodes with excellent intrinsic activities were reported (e.g., transition metal oxides/hydroxides/chalcogenides/heteroatom doped carbon-based materials and hybrids of these materials).^{5,13} Among them, the transition metal oxides (Fe, Co, Mn, and Ni) received enormous attention as the ORR/OER bifunctional electrocatalysts due to their ease of synthesis, stability, and structural flexibility.¹³ Spinel oxides ($\text{A}^{\text{II}}\text{B}^{\text{II}}\text{B}^{\text{III}}\text{O}_4$) are mostly being explored as the ORR/OER bi-functional electrocatalysts owing to the distribution of the mixed-valence metal ions in the octahedral and tetrahedral sites.¹⁴ The mixed valency metal ions in a spinel oxide crystal structure provide a preferable electron transport channel with a favorable impact in improving the electrochemical activity.¹⁵ The intrinsic bifunctional activity of the spinel oxides could be improved by morphology and compositional tuning.^{16,17} Recently, we reported the nanorod-shaped spinel cobalt oxides with promising ORR performance.¹⁶

Binary or ternary transition metal spinel oxides possess better bi-functional oxygen activity due to the involvement of the multiple catalytically active centers.^{13, 18} The presence of a second metal with different charges alters the d-band centers and changes the electronic properties of the spinel oxides.^{17, 19, 20} This contributes favorably toward the bifunctional oxygen redox activity of the system. Among the various bimetallic spinel oxides, MnCo_2O_4 is considered as a mixed-valence metal oxide with a spinel structure.^{18, 21} However, the potential applications of the spinel oxide catalysts are restricted by their poor electronic conductivity.²² This could be addressed by the incorporation of a conducting support with active sites, which simultaneously prevents the aggregation of the nanoparticles.⁵ Most of the conducting carbon supports used for dispersing the spinel oxides are 1D and 2D materials, which possess morphological limitations for efficiently establishing the active electrochemical interface.^{23, 24} In this context, the 3D porous support materials as the substrates for interlinking the bifunctional active centers are becoming more promising.^{25, 26}

Considering the importance of the active triple-phase boundary (TPB) in the electrodes of ZABs, appropriate interfacial engineering strategies to develop better air-electrodes are necessary.^{27, 28} Significant research has been done on developing the air-cathodes by depositing various metal oxide-carbon composite-derived bifunctional catalysts directly on the surface of the hydrophobic GDLs.²⁹ However, such air-electrode structures provide an almost 2D multiphase interface that is confined to the limited space between the porous GDL and the electrocatalyst layer. In this configuration, the electrolyte and gaseous reactants cannot effectively reach out to the catalytic sites.³⁰ Thus, the traditional air-cathode structure in ZAB inevitably gives rise to sluggish reaction kinetics for ORR and OER, which significantly reduces the ZAB battery performance. In this context, the 3D reactive interface can substantially increase the number of the active sites and accelerate the mass transport owing to its interconnected interfacial structure.³¹ During the catalytic process, if some electrocatalytic sites migrate within the 3D interface region, they will still be able to participate in the electrochemical process.^{8, 32, 33} This unique interface structure also allows simultaneous electrolyte permeation and oxygen diffusion within the conductive 3D multiphase interface region, offering considerable advantages for the cathode kinetics.⁸ Simultaneously, the air-cathode interface engineering by maintaining a good balance between the hydrophobicity and hydrophilicity is vital for ensuring better mass transport.³⁴

To best accommodate the abovementioned structural attributes, an ORR/OER bifunctional electrocatalyst with favorably modulated performance characteristics based on self-assembled nitrogen-doped porous 3D entangled graphene supported MnCo_2O_4 catalyst has been developed ($\text{MnCo}_2\text{O}_4/\text{NEGF}$). The nitrogen-

doped graphene acts as a better nucleation site for the nanoparticle growth over the asymmetric graphene substrate with improved hydrophobicity. This nitrogen-doped carbon microstructure retains sufficient hydrophobicity/hydrophilicity, which in turn could provide robust mass transport channels to the active sites without getting flooded with the electrolyte solution. The ORR/OER bifunctional characteristics of the catalyst are found to be competing well with that of the state-of-the-art Pt/C + RuO₂ standard pair for tackling respective single electrode processes. Finally, a realistic validation of a rechargeable ZAB system based on MnCo₂O₄/NEGF as the air-electrode reveals that the catalyst system with its favorable structural and functional attributes is capable of delivering better power density and stable cyclic stability. On these aspects, the homemade system is found to have a clear upper hand compared to the similar system based on the conventional air-cathode compositions.

4.2. Experimental Section:

4.2.1. Materials: Graphite, potassium permanganate (KMnO₄), manganese acetate tetrahydrate [Mn(OAc)₂.4H₂O], cobalt acetate tetrahydrate [Co(OAc)₂.4H₂O], zinc acetate and potassium hydroxides were purchased from Sigma-Aldrich. Ammonium hydroxide (NH₄OH), sulphuric acid (H₂SO₄) and phosphoric acid (H₃PO₄) were acquired from Thomas Baker. All the chemicals were used as such without any further purification.

4.2.2. Synthesis of Graphene Oxide (GO): Improved Hummer's method was employed to synthesize graphene oxide (GO). Firstly, (1:6) graphite powder and KMnO₄ were well mixed using a mortar and pestle. The resulting solid mixture was slowly added to the round bottom flask containing a mixture of H₃PO₄:H₂SO₄ (1:9) solution kept in the ice bath. After complete transfer of solid mixture, the reaction solution was kept on stirring for 12 h at a constant temperature of 60 °C. After the reaction was completed, the mixture was allowed to cool to room temperature. The resultant product was slowly poured into ice-cold water containing 3% H₂O₂ resulting in a yellowish solution. The resulting solution was then rinsed several times with a copious amount of distilled water followed by centrifugation at 10000 rpm. The collected solid residue was washed with 30 % HCl to remove any metal impurities; this was subsequently washed with plenty of water to neutralize the acidic pH and wash away the impurities. Finally, the dark chocolate-colored, highly viscous solution was collected and cleaned with ethanol and diethyl ether before drying at 40 °C to produce the GO powder.

4.2.3. Synthesis of MnCo₂O₄-Supported N-doped Entangled 3D Graphene (MnCo₂O₄/NEGF): To synthesize the MnCo₂O₄/NEGF, the as-prepared GO was dispersed in water (3 mg/ml) *via* overnight

stirring and water-bath sonication. After the complete dispersion of GO in water, ammonia solution (30 % v/v) was added and kept for constant stirring. After the formation of highly viscous graphene oxide solution, $\text{Mn}(\text{OAc})_2 \cdot 4\text{H}_2\text{O}$ and $\text{Co}(\text{OAc})_2 \cdot 4\text{H}_2\text{O}$ were added to the solution with a 1:2 ratio and kept under stirring for another 6 h followed by sonication by using probe sonication. After the metal ions had been thoroughly mixed, the reaction mixture was transferred to a Teflon-lined autoclave and heated at 180 °C for 12 h. After that, the autoclave was allowed to cool and the sample was washed with water 5-6 times to remove the excess ammonia. The resulting reaction mixture was then freeze-dried for 10 h at -52° C under high vacuum pressure. The sample was taken after the freeze-drying procedure was completed, and it had a black colored flaky structure. The obtained sample was named as $\text{MnCo}_2\text{O}_4/\text{NEGF}$. For comparison, the control samples such as N-doped entangled graphene (NEGF), Mn_3O_4 supported N-doped entangled 3D graphene ($\text{Mn}_3\text{O}_4/\text{NEGF}$), and Co_3O_4 supported N-doped entangled 3D graphene ($\text{Co}_3\text{O}_4/\text{NEGF}$) were also synthesized. The NEGF, $\text{Mn}_3\text{O}_4/\text{NEGF}$, $\text{Co}_3\text{O}_4/\text{NEGF}$ were prepared by using the same methods without adding any metal precursor and graphene oxide, with addition $\text{Co}(\text{OAc})_2 \cdot 4\text{H}_2\text{O}$, $\text{Mn}(\text{OAc})_2 \cdot 4\text{H}_2\text{O}$ respectively, keeping all the other parameters as such.

4.2.4. Physical Characterization: The structure, morphology, surface composition, surface properties, thermal stability, and physical interactions between the metal oxide nanoparticles and the support of the synthesized catalysts were investigated with the help of FESEM, X-ray Tomography, ESEM, TEM, HRTEM, Raman spectroscopy, XPS, XRD, TGA and BET measurements. The FESEM analyses were carried out by FEI Nova Nano SEM 450 FESEM microscopes. The samples for FESEM were prepared by the thin coating of isopropyl alcohol (IPA) dispersed sample (5 mg of the sample in 5 mg IPA) on a silicon wafer. Furthermore, the samples were dried for 1 h under an IR lamp. The three-dimensional structure of the catalyst was imaged by using X-ray microtomography (Xradia 510 Versa X-ray Microscope, Zeiss, Pleasanton, CA, USA) to study their internal structure and morphology. Dragonfly Pro (Version 3.6) was used as an image processing software to generate the volume-rendered three-dimensional (3D) images of the samples. The elemental inspection was done by using SEM-EDS with a Quanta 200 3D FEI instrument connected with the TEAM™ EDS analysis system. TEM images were recorded on a Tecnai T-20 instrument at an accelerating voltage of 200 kV. The HRTEM images were recorded using a JEOL JEM F-200 HRTEM instrument with a point-to-point resolution of 0.19 nm. The samples for TEM and HRTEM were prepared by drop-coating the well-dispersed sample in isopropyl alcohol (1.0 mg of the sample in 5 mL solvent) on a carbon-coated 200 mesh copper grid. The sample-coated TEM grid was dried for 1 h under an IR lamp. To check the crystal structure of the as-synthesized

samples, Powder X-ray diffraction (PXRD) analysis was done. Nitrogen (N₂) adsorption-desorption isotherm experiments were performed on a Quantachrome-Quadrasorb automatic volumetric instrument to analyze the surface area and pore volume of the samples. The thermal stability of the carbon support and the loading of the active catalytic center over the carbon was measured using an SDT Q600 DSC-TDA thermo-gravimetric (TG) instrument in the temperature range of room temperature to 900 °C at a constant heating rate of 10 °C min⁻¹ under an oxygen atmosphere. The XRD investigation was carried out on a Rigaku Smart Lab diffractometer with Cu K α radiation ($\lambda = 1.5406 \text{ \AA}$) in the 2θ range of 10 to 80° with a scan rate of 5° min⁻¹. Raman spectral interpretation was carried out using a 632 nm green laser (NRS 1500W) on an HR 800 RAMAN spectrometer. The XPS measurement was performed using a fully integrated, monochromatic small spot XPS system. It is specified with an X-ray monochromator source by the 180° double-focusing hemispherical analyzer-128-channel detector and micro-focused Al K α .

4.2.5. Rotating Ring Disk Electrode Study: The electrochemical analysis was done by a couple of electrochemical techniques such as voltammetry. Cyclic voltammetry (CV), linear sweep voltammetry (LSV) and impedance techniques were adopted. A rotating disc electrode (RDE) set-up (Pine Instrument) was employed for the LSV measurements. The electrochemical cell was made of a set-up of a three-electrode used with an SP-300 model BioLogic potentiostat. A graphite rod (Alfa Aesar, 99.99%) as a counter electrode and Hg/HgO as a reference electrode were employed for the electrochemical analyses. For the comparison of the ORR and OER performance of the prepared electrocatalyst in the half-cell studies, we included the ORR activity of 20% Pt/C and the OER activity of RuO₂. The catalyst slurry was prepared by mixing the catalyst (5 mg) in 1 mL isopropyl alcohol-water (3:2) solution and 40 μ L of Nafion solution (5 wt%, Sigma-Aldrich) using approximately 1 h water-bath sonication. After that, 10 μ L of the catalysts slurry was drop-coated on the surface of the working electrode, which was polished with 0.3 μ m alumina slurry in DI water followed by cleaning with DI water and acetone. The electrode was then dried under an IR-lamp for 1 h. The experiment was carried out in an aqueous solution of 0.1 M KOH for ORR and 1 M KOH for OER performance measurements to check the electrochemical performance. All the experimental electrode potentials were converted into the reversible hydrogen electrode (RHE) through an RHE calibration experiment with the previously reported procedure (ACS Catal. 2017, 7, 6700–6710)

4.2.6. The Hg/HgO Reference Electrode Calibration and Conversion to RHE:

The Hg/HgO electrode was calibrated by using the same method as reported in our previous report (ACS Catal. 2017, 7, 6700-6710) using a conventional 3-electrode system employing a platinum RDE electrode

as the working electrode (WE), graphite rod as the counter electrode (CE), and Hg/HgO as the reference electrode (RE) under H₂-saturated 0.1M KOH solution as an electrolyte. The linear sweep voltammogram (LSV) was recorded at a scan rate of 0.50 mV/s. The potential when the current crossed the zero point during the LSV measurement was taken as the thermodynamic potential for the hydrogen electrode reactions. The potential at the zero current was found to be at -0.8722 V. Hence, for the conversion of the voltage recorded with respect to Hg/HgO to the RHE scale, the following equation is used:

$$E (\text{RHE}) = E (\text{Hg/HgO}) + 0.8722 \text{ V} \dots\dots\dots 1$$

4.2.7. Preparation of the Gel Electrolytes: 2 g of the PVA powder (MW205000, Sigma-Aldrich) was typically dissolved in 16 mL ultrapure water at 90 °C with vigorous agitation. When a translucent gel solution was formed, 4 mL of 9 M KOH solution was added drop wise and stirred for 20 min. at 90 °C. The gel solution was put into a petri dish (2 cm in diameter), and then stored in the refrigerator at -20°C for 1 h and then at 0°C for another 1 h. After that, a thin sheet structure of the gel electrolyte was formed, which was used for the solid-state ZAB device fabrication.

4.2.8. Assembly and Testing of the Solid-state ZAB Device: The solid-state rechargeable ZAB was assembled by utilizing Zn powder as the anode, MnCo₂O₄/NEGF-coated GDL as the air-cathode, and PVA/KOH gel as the electrolyte in an electrochemical ZAB device set up (MTI Corporation). For the preparation of the catalyst slurry, MnCo₂O₄/NEGF was added to the 1: 4 ratio mixture of isopropyl alcohol and water followed by keeping for sonication for 1 h. To the resulting dispersion, 10 wt% Fumion solutions was added, and the mixture was sonicated for an additional 1 h. After the complete dispersion, the catalysts slurry was brush-coated over a gas diffusion layer (GDL) and was dried at 60 °C for 12 h to achieve a catalyst loading of 1.0 mg cm⁻² (electrode area = 1.0 cm²). A multichannel VMP-3 model Bio-Logic Potentiostat/Galvanostat was used to evaluate the ZAB set-up at room temperature. The ZAB was analyzed by steady-state polarization at a scan rate of 5 mV/s. The polarization analysis and EIS studies were performed at a constant voltage of 1.0 V with an amplitude of 20 mV; the galvanostatic discharge and discharge-charge cycling (5 min discharge followed by 5 min charge) tests were carried out by a Bio-Logic potentiostat.

4.3. Results and Discussion:

A schematic representation of the stages involved in the stepwise synthesis of MnCo₂O₄/NEGF as an ORR/OER bifunctional electrocatalyst and demonstration of its application as the air-electrode material

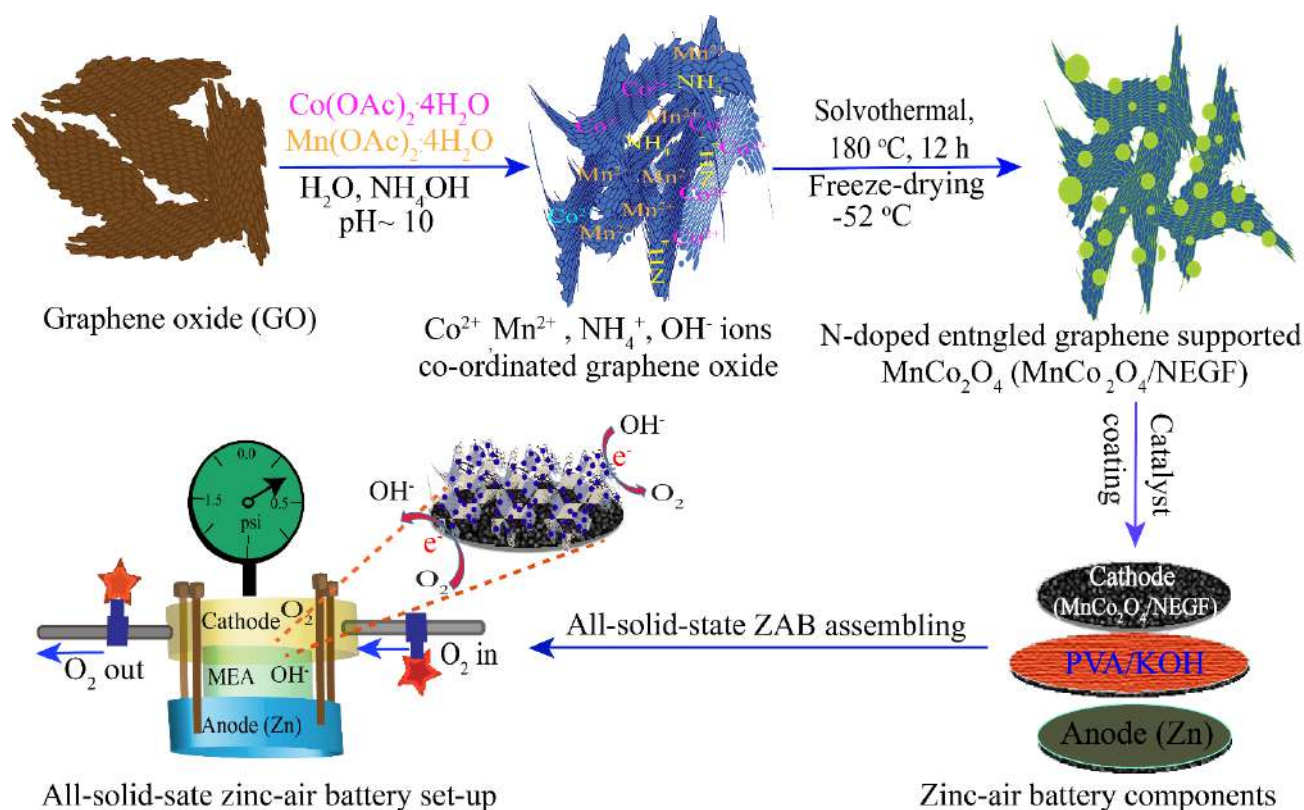


Figure 4.1. The schematic illustration of the stages involved in the stepwise synthesis of MnCo₂O₄/NEGF ORR/OER bifunctional electrocatalyst and demonstration of its application as the air-cathode for the solid-state rechargeable Zn-air battery.

for the rechargeable ZAB is presented in **Figure 4.1**. In brevity, the aqueous solution of the graphene oxide (GO) synthesized *via* the improved Hummer's method was mixed well with Co²⁺ and Mn²⁺ metal precursors (2:1) at constant stirring for 6 h. The positively charged metal ions get anchored over the negatively charged functional groups of GO through electrostatic interactions during the mixing process. Ammonium hydroxide (~30 % v/v) was added to the metal ion-anchored GO solution with continuous stirring for 6 h, followed by probe sonication for 10 min. The color of the solution was found to be changed at a certain concentration when the pH of the solution reached to ~10 due to the formation of the metal hydroxides and adsorption of the NH₄⁺ ions over the negatively charged GO surface. During the hydrothermal treatment, the decomposition of NH₄⁺ moieties occur in the beginning, followed by the doping of nitrogen into the carbon skeleton with the creation of the asymmetric metal nucleation centers. As the hydrothermal process proceeds at high temperature and pressure, the metal hydroxides gradually

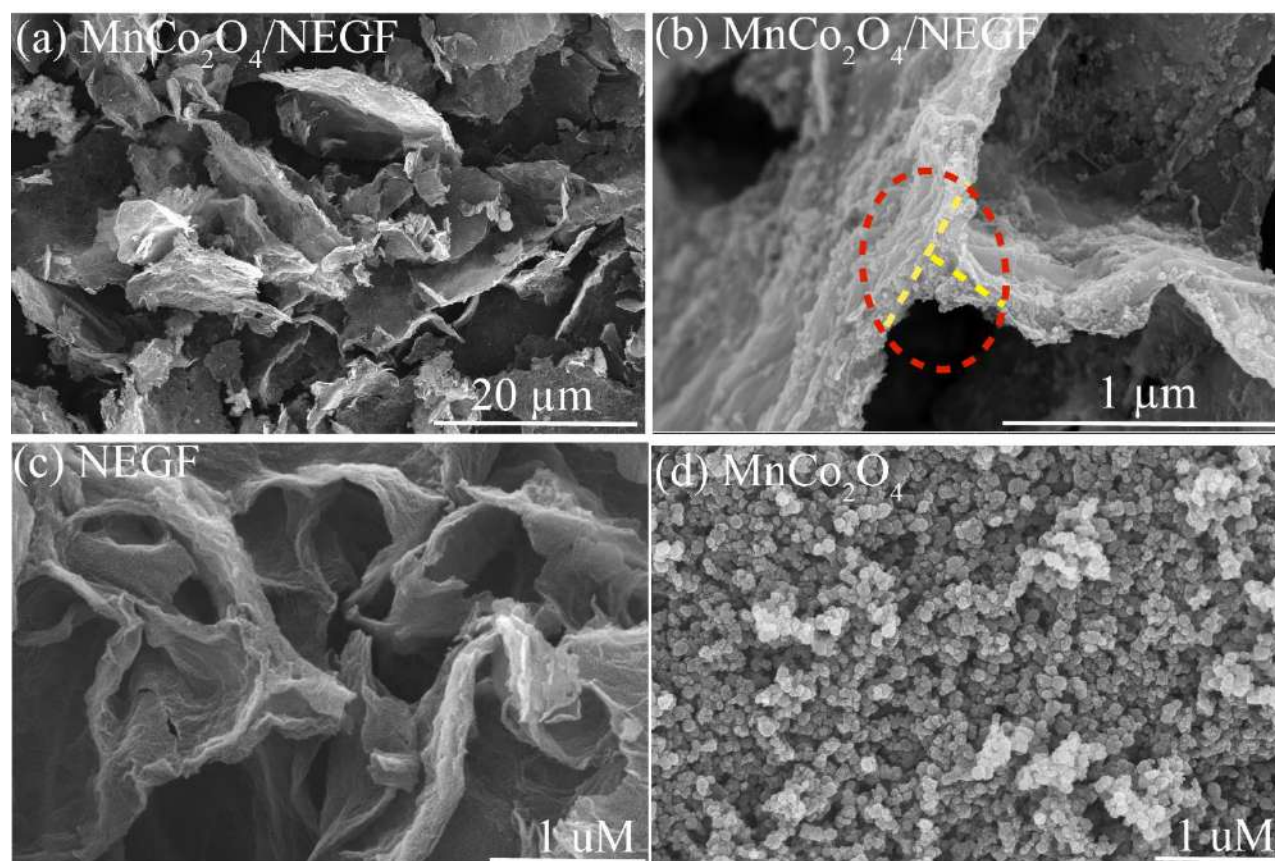


Figure 4.2. Field emission scanning electron microscopy (FESEM) images: (a)-(b) MnCo₂O₄/NEGF showing the interconnected areas and the 2D sheet structures in the 3D assembly; (c) NEGF showing the porous architecture of the entangled 3D graphene sheets; (d) the spherically shaped MnCo₂O₄ particles in the unsupported system.

decompose and nucleate at the asymmetric carbon centers, resulting in the formation of the spherically shaped spinel oxide (MnCo₂O₄) nanoparticles anchored over the surface of the N-doped reduced graphene oxide. The hydrothermal reaction is followed by the freeze-drying process, which plays a critical role in establishing the 3D geometrical orientation and re-structuring of the graphene sheets bearing the bimetallic spinel oxide nanoparticles. This electrocatalyst consisting of the entangled graphene framework with homogeneously dispersed Co-Mn spinel oxide nanoparticles (MnCo₂O₄/NEGF) possesses high surface area and accessible porous architecture to the catalytic sites. The resulting catalyst was coated over a porous carbon gas diffusion layer (GDL) in combination with PVA-KOH gel electrolyte and a solid-state rechargeable ZAB device was fabricated and demonstrated.

4.3.1. FESEM Analysis:

The morphological analysis of NEGF and the distribution of the bimetallic spinel oxide nanoparticles was investigated by field emission scanning electron microscopy (FESEM). The freeze-drying induced structural alignment leading to the establishment of homogeneous porosity to the assembly of the N-doped reduced graphene oxide layers in $\text{MnCo}_2\text{O}_4/\text{NEGF}$ is clearly evidenced in the FESEM images presented in **Figures 4.2a** and **4.2b**. **Figure 4.2a** shows the self-assembly structure of $\text{MnCo}_2\text{O}_4/\text{NEGF}$ consisting of the nitrogen-doped 3D oriented graphene sheets whereas the magnified image of the catalyst shown in **Figure 4.2b** highlights the interconnection of the sheets leading to the formation of the porous architecture of the matrix. The formation of the self-assembled 3D structured bare NEGF can be visualized in the FESEM image presented in **Figure 4.2c**. In the absence of the support, under the similar experimental conditions, the particles of MnCo_2O_4 are appeared to be formed with bigger and agglomerated structures as shown in **Figure 4.2d**. The NEGF support with its nitrogen-doped anchoring sites appeared to be creating a fertile environment for the nucleation of the MnCo_2O_4 nanoparticles, which enables homogeneous and more size-controlled dispersion.

4.3.2. Micro-Computed Tomography Analysis:

Furthermore, to gain more clarity on the dimensionally oriented 3D microstructures of the $\text{MnCo}_2\text{O}_4/\text{NEGF}$ electrocatalyst, X-ray micro-computed tomography (micro-CT) imaging was employed. Volume-rendered 3D micro-CT images of GO, NEGF and $\text{MnCo}_2\text{O}_4/\text{NEGF}$ are presented in **Figure 4.3**. These images clearly point towards the existence of the well-defined porous architecture of the system which has been originated by connecting the edges of the graphene sheets. Compared to NEGF (**Figure 4.3a**) and $\text{MnCo}_2\text{O}_4/\text{NEGF}$ (**Figure 4.3b**), the micro-CT image presented in **Figure 4.3c** for GO shows a non-separated stacked layer of the sheets. The features of $\text{MnCo}_2\text{O}_4/\text{NEGF}$ with respect to the layer-separated 3D structure with interconnection and inter-layer spacing of the graphene sheets is in agreement with the textural characteristics of the system as revealed through the FESEM images. The porous microstructure of NEGF helps the system to attain higher surface area as compared to its precursor (GO). The spatial distribution of the MnCo_2O_4 particles over the NEGF sheets is shown in **Figure 4.3d**, which displays the distribution of the closely similar-sized nanoparticles of MnCo_2O_4 in the catalyst matrix.

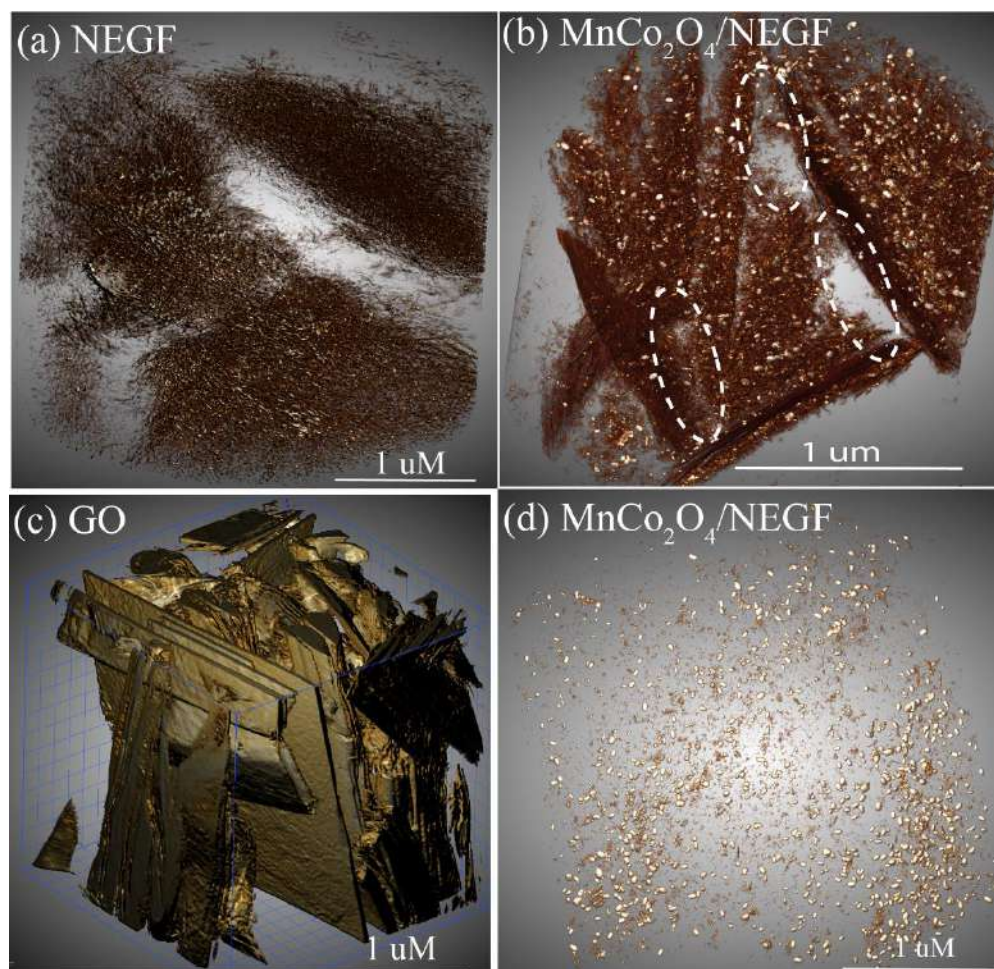


Figure 4.3. Volume-rendered 3D micro-computed tomography (CT) images; (a) NEGF showing the microporous 3D structure of the entangled graphene; (b) the 3D micro-CT image of MnCo₂O₄/NEGF, showing the porous structure of the matrix formed by the interconnection of the 2D sheets of GO; (c) GO showing the randomly oriented GO sheets; (d) 3D spatial visualization image of MnCo₂O₄ over the NEGF sheets.

4.3.3. TEM and HRTEM Analyses:

The distribution of the MnCo₂O₄ nanoparticles on NEGF could be mapped with the help of transmission electron microscopy (TEM) imaging (**Figure 4.4a**). The image points towards the homogenous distribution of the spherically shaped MnCo₂O₄ nanocrystals with size in the range of 15 to 30 nm over the individual sheets of the N-doped graphene. As mentioned previously, the controlled distribution of the metal oxide nanoparticles is mediated by the intervention of the asymmetric carbon centers present in the N-doped graphene framework, which serve as homogeneous nucleation sites for the growth of the MnCo₂O₄ nanoparticles. The contrast difference of the particles in the TEM image suggests that a fraction

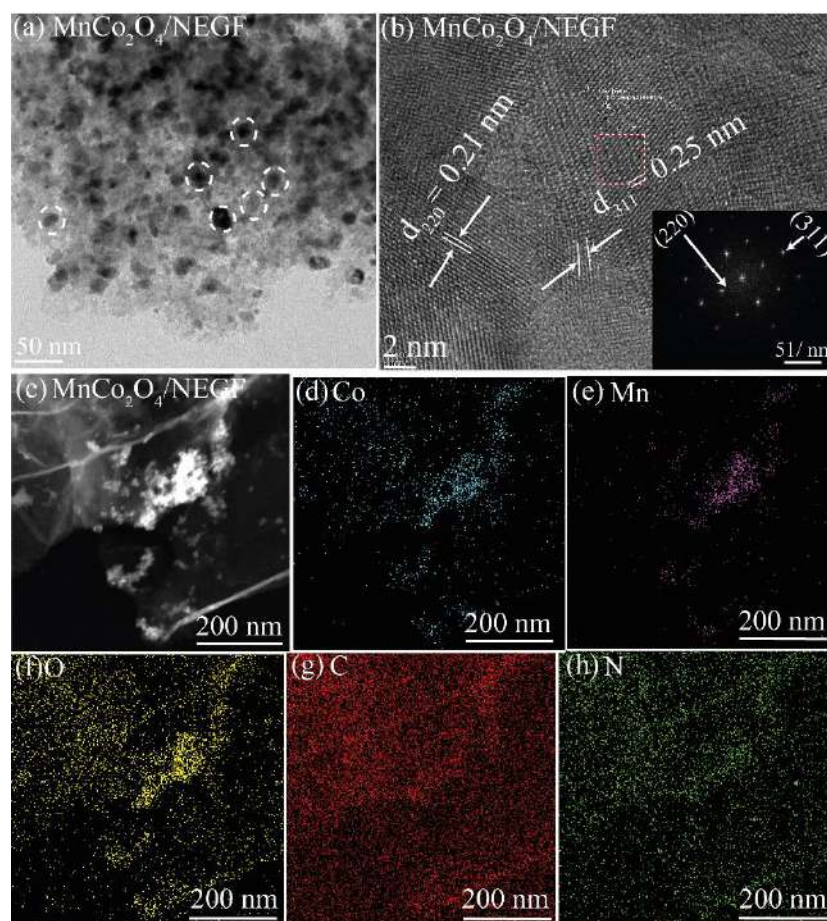


Figure 4.4. (a) The TEM image of $\text{MnCo}_2\text{O}_4/\text{NEGF}$, displaying the uniform distribution of MnCo_2O_4 over NEGF; (b) the HRTEM image of $\text{MnCo}_2\text{O}_4/\text{NEGF}$, clearly displaying the d-spacing for MnCo_2O_4 with the inset image representing the crystalline nature of MnCo_2O_4 ; (c-h) the HRTEM image and the elemental mapping corresponding to Co, Mn, N, O and C, respectively, done on $\text{MnCo}_2\text{O}_4/\text{NEGF}$.

of metal oxide nanoparticles is distributed at the inner surface of the 3D graphene, which are protected by the thin layers of the graphene sheets.³⁵ This controlled distribution of the MnCo_2O_4 nanoparticles on the either side of the graphene sheets is beneficial for providing better stability to the system by reducing the chances of self-agglomeration of the nanoparticles.³⁶ **Figure 4.4b** shows the high-resolution transmission electron microscopy (HRTEM) image of $\text{MnCo}_2\text{O}_4/\text{NEGF}$, elucidating that the metal oxides are crystalline in nature. The metal oxide nanoparticles are having lattice fringe widths (d-spacing) of 0.25 and 0.21 nm, which are ascribed to the (311) and (211) facets suggesting the formation of the cubic MnCo_2O_4 spinel phase.³⁷ The selected area electron diffraction (SAED) pattern shown as the inset image in **Figure 4.4b** displays the characteristic diffraction ring corresponding to the polycrystalline nature of

the MnCo_2O_4 spinel oxides, which again confirms the (311) and (211) planes of MnCo_2O_4 .³⁷ Using the HRTEM image shown in **Figure 4.4c**, the elemental mapping corresponding to the location has been done and the respective images are presented in **Figure 4.4d-h**. The images represent the presence and distribution of Co, Mn, O, C and Ni, which is in line with the chosen composition of the catalyst. The presence of Co and Mn in the same position with almost double intensity of Co clearly supports the bimetallic structure of the spinel oxide.

4.3.4. Surface Area Analysis:

Figure 4.5a shows the comparative pore size distribution profile of NEGF, MnCo_2O_4 , and $\text{MnCo}_2\text{O}_4/\text{NEGF}$, where the a major fraction of the pores is found to be distributed in the region of 2-30 nm for NEGF and 2-20 nm for $\text{MnCo}_2\text{O}_4/\text{NEGF}$. MnCo_2O_4 on the other hand, is found to be less porous. Hence, the dispersion of MnCo_2O_4 on NEGF slightly lowers the porosity of the composite, and this accounts the observed trend in the pore size distribution profile of $\text{MnCo}_2\text{O}_4/\text{NEGF}$ with the major portion of the pores falling in the range of 16-20 nm. This difference in the nature of the pore size distribution between the samples is also reflected in terms of their BET surface area. The surface area of $450 \text{ m}^2 \text{ g}^{-1}$ measured on NEGF has been dropped to $300 \text{ m}^2 \text{ g}^{-1}$ in the case of $\text{MnCo}_2\text{O}_4/\text{NEGF}$. Also, both NEGF and $\text{MnCo}_2\text{O}_4/\text{NEGF}$ display Type-IV isotherms (**Figure 4.5b**). The large surface area possessed by $\text{MnCo}_2\text{O}_4/\text{NEGF}$ along with its highly porous texture is a distinct advantage of the system as an electrocatalyst with the effective utilization of the active sites by establishing the interface with the electrolyte and reactants. This type of active ‘triple-phase boundary’ (TPB) formation is an important requirement for realizing the final application of the electrocatalyst as an efficient air-electrode for the rechargeable ZABs.

4.3.5. Thermogravimetric Analysis:

The total loading of the spinel oxide nanoparticles in $\text{MnCo}_2\text{O}_4/\text{NEGF}$ has been determined by thermogravimetric analysis (TGA). The TGA profiling was done under oxygen atmosphere in the temperature range of 25 to 900 °C at a scan rate of 10 °C per min. **Figure 4.5c**, displays the TGA weight loss profile for $\text{MnCo}_2\text{O}_4/\text{NEGF}$, which indicates from the residue content that the total loading of MnCo_2O_4 in the system is ~45 wt. %.

4.3.6. XRD Analysis:

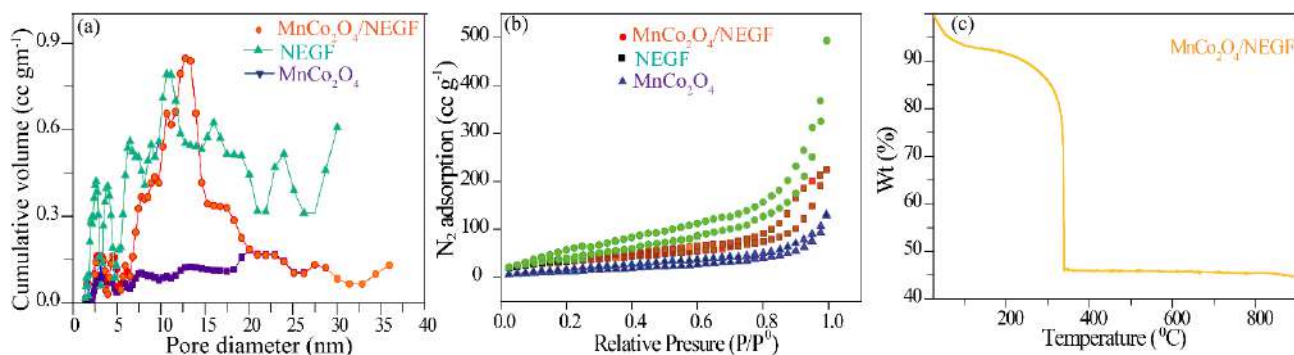


Figure 4.5. (a) The pore size distribution profiles of NEGF, MnCo_2O_4 and $\text{MnCo}_2\text{O}_4/\text{NEGF}$, suggesting that the pores are mostly distributed in 10 to 15 nm range; (b) comparative BET adsorption and desorption isotherms of NEGF, and $\text{MnCo}_2\text{O}_4/\text{NEGF}$, showing Type-IV characteristics; (c) TGA profile recorded for $\text{MnCo}_2\text{O}_4/\text{NEGF}$.

The X-ray diffraction (XRD) pattern of NEGF shown in **Figure 4.6a** displays broad diffraction peaks at the 2θ values of 26° and 43° , which are attributed to the (002) and (100) graphitic diffraction planes, respectively.³⁸ The XRD profile of $\text{Co}_3\text{O}_4/\text{NEGF}$ shows a comparatively intense peak corresponding to the (311) plane of Co_3O_4 at the 2θ values of 35° .¹⁶ However, after the incorporation of Mn into the spinel structure of Co_3O_4 , the resulting $\text{MnCo}_2\text{O}_4/\text{NEGF}$ showed almost similar peak intensities of the major phases with a small shift in the peak positions.^{39, 40} As depicted in **Figure 4.6a**, the XRD pattern of $\text{MnCo}_2\text{O}_4/\text{NEGF}$ confirmed a series of peaks at $2\theta = 18.3, 30.2, 35.6, 37.0, 43.2, 53.8, 57.2, 62.7$ and 74.0° , which are ascribed to the (111), (220), (311), (400), (422), (511), (440) and (533) planes, respectively, for the MnCo_2O_4 spinel structure (JCPDS No. 23-1237).⁴¹ Also, after incorporating the MnCo_2O_4 nanoparticles over NEGF, the (002) graphitic plane is found to be shifted towards a lower diffraction angle (25°) compared to that in NEGF (26°). This shift is expected to be originated by the expansion of the d-spacing of the nitrogen-doped graphene sheets due to the incorporation of the MnCo_2O_4 nanoparticles between the layers.

4.3.7. XPS Analysis:

Furthermore, a more focused investigation on the chemical nature of the prepared catalysts has been performed with the help of X-ray photoelectron spectroscopy (XPS); the corresponding data are presented in **Figure 4.6b-f**. The survey scan spectra of NEGF, $\text{Co}_3\text{O}_4/\text{NEGF}$, and $\text{MnCo}_2\text{O}_4/\text{NEGF}$ shown in **Figure 4.6b**, confirm the presence of Mn, Co, O, N, and C in the respective materials. The characteristic Co 2p XPS peaks corresponding to $\text{Co}_3\text{O}_4/\text{NEGF}$ and $\text{MnCo}_2\text{O}_4/\text{NEGF}$ are appearing at the B.E. values of 784.2, 795.5 eV and 783.5 eV, 796.5 eV, respectively (**Figure 4.6c**).³⁸ The characteristic peak separation (~ 15.84

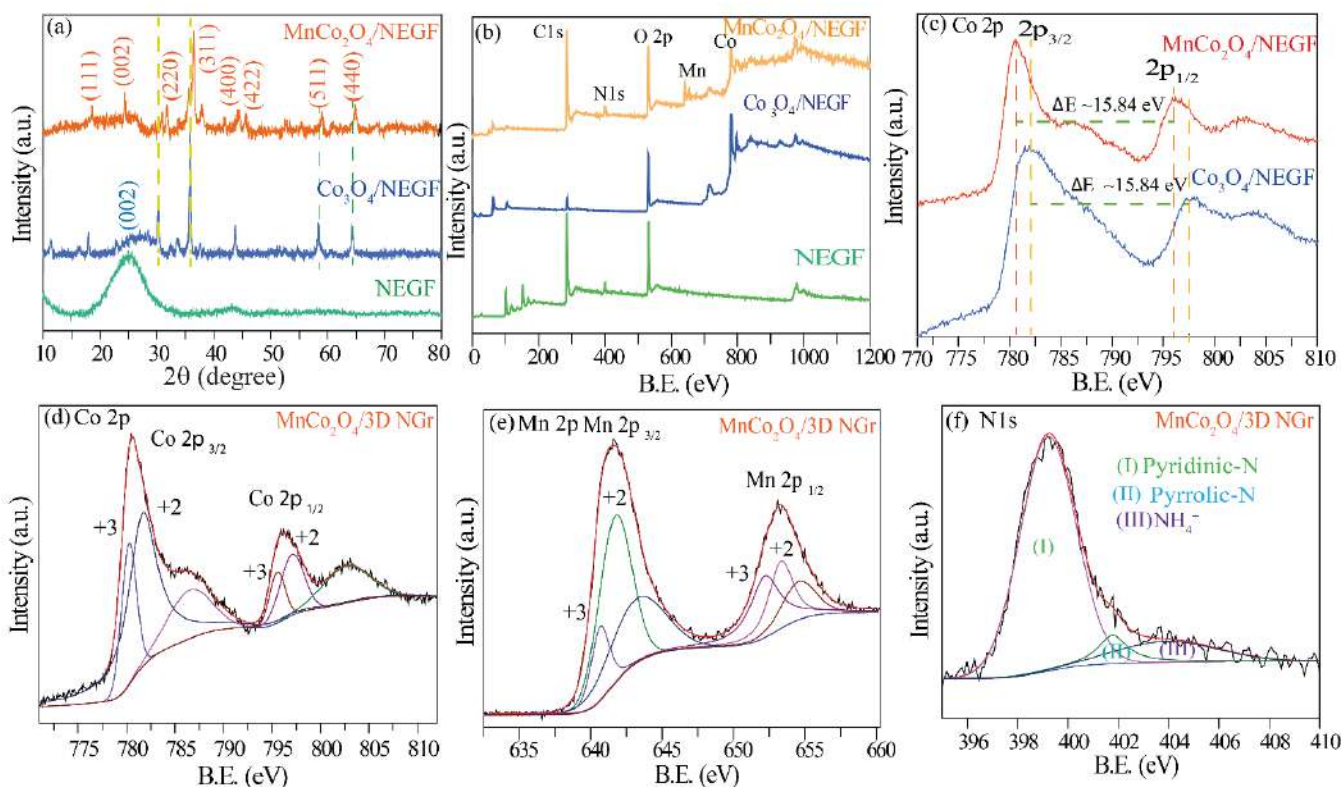


Figure 4.6. (a) The XRD profiles recorded for NEGF, Co₃O₄/NEGF, and MnCo₂O₄/NEGF; (b) the comparative survey scan spectra of NEGF, Co₃O₄/NEGF, and MnCo₂O₄/NEGF, showing the presence of C, N, O, Co, and Mn in the respective catalysts; (c) the Co 2p XPS spectra of Co₃O₄/NEGF, and MnCo₂O₄/NEGF, revealing the peak shift after the incorporation of Mn into the Co₃O₄ matrix; (d) the deconvoluted spectra of Co 2p showing the presence of two spin-spin splitting peaks revealing the +2 and +3 oxidation states of Co in MnCo₂O₄/NEGF; (e) the deconvoluted Mn spectra, showing the presence of the two peaks corresponding to the spin splitting, confirming the presence of the two oxidation states of Mn, *viz.*, +2 and +3; (f) the deconvoluted N 1s spectra, confirming the presence of the four types of nitrogen.

eV) between the two peaks remains the same for the spinel oxides. However, the shift in the B.E after incorporating Mn into the spinel lattice of Co₃O₄ provides supplementary evidence on the formation of the bimetallic (MnCo₂O₄) spinel oxide. The observed negative shift in the B.E of MnCo₂O₄ compared to Co₃O₄ might be due to the charge transfer from Co to Mn.⁴³ Furthermore, the deconvoluted XPS spectra of Co 2p in MnCo₂O₄/NEGF show two doublets (**Figure 4.6d**) at the B.E. values of 783.1 and 798.8 eV with a band separation of ~15.7 eV, pointing towards the existence of the +2 and +3 oxidation states of Co.^{16, 44} In addition, the deconvoluted Mn spectra (**Figure 4.6e**) show two spin-spin coupling peaks at the B.E. values of 783.1 and 798.8 eV, corresponding to the Mn 2p_{3/2} and Mn 2p_{1/2} states of Mn.^{5, 45}

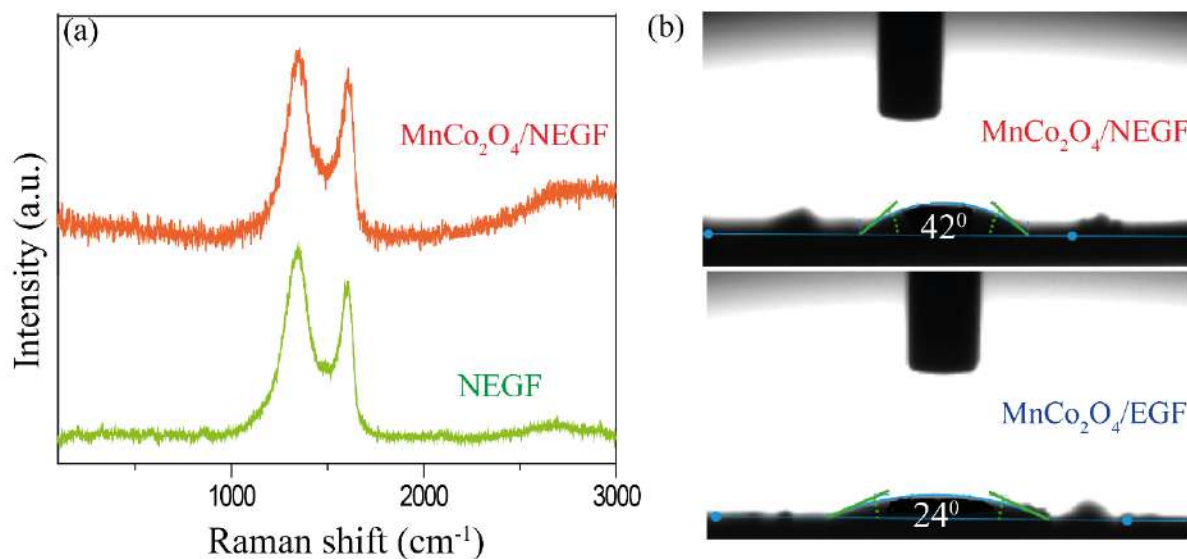


Figure 4.7. (a) The Raman spectra recorded for NEGF and $\text{MnCo}_2\text{O}_4/\text{NEGF}$; (b) the contact angle images of $\text{MnCo}_2\text{O}_4/\text{NEGF}$ and its counterpart without nitrogen doping, *i.e.* $\text{MnCo}_2\text{O}_4/\text{EGF}$, showing the dissimilarity in the wettability characteristics.

This confirms the existence of Mn in the +2 and +3 oxidation states in the system. Moreover, the deconvoluted N 1s spectra of the $\text{MnCo}_2\text{O}_4/\text{NEGF}$ (shown in **Figure 4.6f**) display the peaks of the pyridinic-N at 398.6 eV and the pyrrolic-N at 399.7 eV as the major moieties along with smaller proportions from the graphitic-N at 400.5 eV and NH_4^+ at 405.5 eV.¹⁶

4.3.8. Raman Analysis:

The extent of the defects imparted in the graphene frameworks of NEGF has been determined by calculating the I_D/I_G ratio using Raman spectroscopy. In the Raman spectra, the D-band typically expresses the defects whereas the G band represents the orderliness in the graphene lattice. The comparative Raman spectra recorded for NEGF and $\text{MnCo}_2\text{O}_4/\text{NEGF}$ are presented in **Figure 4.7a**. The D-band peak that appeared at 1350 cm^{-1} is attributed to the graphitic lattice vibration mode with the A_{1g} symmetry, while the G-band peak that appeared at 1590 cm^{-1} is credited to the graphitic lattice vibration mode with the E_{2g} symmetry.²⁷ In the case of NEGF and $\text{MnCo}_2\text{O}_4/\text{NEGF}$, the measured I_D/I_G ratios are 1.25, and 1.31, respectively. The increased I_D/I_G value reported for GO (~ 1.0) to NEGF in the present case clearly points towards the creation of new defect sites with the introduction of the doped nitrogen into the graphitic lattice structure during the solvothermal treatment at $180\text{ }^\circ\text{C}$. Such introduced defective sites in the N-doped graphene sheets are helpful for seeding the nucleation of the metal oxide

nanoparticles.⁴² The defective sites are higher in MnCo₂O₄/NEGF ($I_D/I_G = 1.31$) compared to its counterpart NEGF support ($I_D/I_G = 1.25$), which must have been introduced due to the lattice stress created during the *in-situ* growth of the metal oxide nanoparticles.⁵¹ The presence of nitrogen doping in the conducting support can modulate the surface wettability of the electrocatalysts, which is an important deciding factor in improving the activity of the catalyst by enhancing the extent of the interface formation with the electrolyte.²⁷ The contact angle (CA) measurement was performed to check the surface wettability of MnCo₂O₄/EGF and MnCo₂O₄/NEGF (**Figure 4.7b**). The lower CA value of 24° measured for MnCo₂O₄/EGF confirms the higher hydrophilicity of the enabling catalyst, which can easily wet the surface, resulting in water flooding. Therefore, the mass transfer can be hindered by the excessive wetting of the surface. After the N doping into the 3D structure of graphene, the CA value for MnCo₂O₄/NEGF reached an optimal value of 42°. This optimum hydrophilicity of the catalytic material is more conducive to forming the gas-liquid-solid TPBs during the electrochemical reactions.⁴⁶

4.3.9. Electrochemical Analysis:

The electrochemical bifunctional feature of the designed catalyst was evaluated by monitoring the ORR and OER characteristics with the help of a set of electrochemical probing methods. A 3-electrode electrochemical cell was employed to evaluate the activity of the catalyst. The catalyst-coated glassy carbon electrode (GCE) was used as the working electrode (WE), whereas an Hg/HgO and a graphite rod were used as the reference and counter electrodes, respectively. The bifunctional ORR/OER characteristics of the electrocatalyst were evaluated by the rotating disk electrode (RDE) analysis by employing 0.1 M KOH and 1 M KOH electrolytes for ORR and OER, respectively. The linear sweep voltammograms (LSVs) corresponding to ORR were recorded in 0.1 M KOH at the voltage scan rate of 10 mV sec⁻¹ under O₂ atmosphere while maintaining the working electrode rotation at 1600 RPM. The comparative LSV profiles presented in **Figure 4.8a** point towards the superior ORR performance displayed in terms of the onset potential by MnCo₂O₄/NEGF (0.93 V) compared to the control samples, *i.e.*, NEGF (0.86 V), Co₃O₄/NEGF (0.89 V), and Mn₃O₄/NEGF (0.85 V). In addition, the onset potential of 0.93 V recorded by MnCo₂O₄/NEGF is coming very close to that displayed by the state-of-the-art Pt/C catalyst (0.98 V). The observed half-wave potentials ($E_{1/2}$) recorded on the catalysts corresponding to ORR are MnCo₂O₄/NEGF (0.81 V), NEGF (0.75 V), Co₃O₄/NEGF (0.77 V), Mn₃O₄/NEGF (0.76 V) and

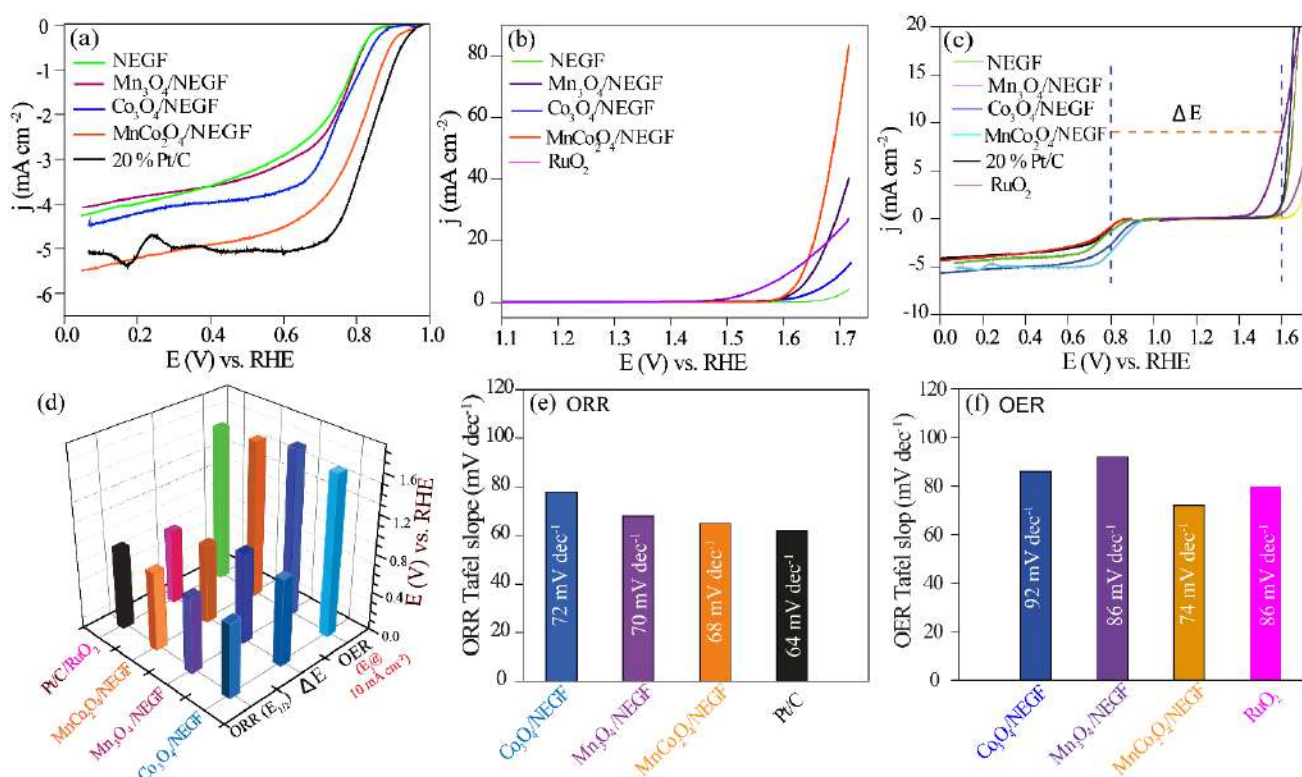


Figure 4.8. (a) The comparative LSV profiles recorded for NEGF, Co₃O₄/NEGF, MnCo₂O₄/NEGF, and Pt/C towards ORR in O₂ saturated 0.1 M KOH at 1600 rpm of the working electrode; (b) the comparative LSV profiles recorded for NEGF, Co₃O₄/NEGF, MnCo₂O₄/NEGF, and Pt/C towards OER in N₂ saturated 1 M KOH at 1600 rpm of the working electrode; (c) the LSV profiles comparing the ORR/OER bifunctional activity of NEGF, Co₃O₄/NEGF, Mn₃O₄/NEGF, and MnCo₂O₄/NEGF; (d) the graph comparing the half-wave potential ($E_{1/2}$) for ORR, the onset potential for OER ($E_j @ 10 \text{ mA cm}^{-2}$), and ΔE , *i.e.*, ORR ($E_{1/2}$)-OER ($E_j @ 10 \text{ mA cm}^{-2}$) for the catalysts; (e) the comparison of the Tafel slopes extracted from the LSV profiles recorded by the systems towards ORR; (f) comparison of the Tafel slopes extracted from the LSV profiles recorded by the systems towards OER.

Pt/C (0.84 V). Similarly, the OER activity has also been evaluated for NEGF, Co₃O₄/NEGF, Mn₃O₄/NEGF, MnCo₂O₄/NEGF, and RuO₂ in 1 M KOH at a voltage scan rate of 10 mV sec⁻¹ under N₂ atmosphere (**Figure 4.8b**). The synthesized catalysts have displayed the OER activity ($E_j @ 10 \text{ mA cm}^{-2}$) as Co₃O₄/NEGF (1.72 V), Mn₃O₄/NEGF (1.65 V), MnCo₂O₄/NEGF (1.63 V) and RuO₂ (1.61 V), respectively. Clearly, among all the homemade systems, the LSV traced for MnCo₂O₄/NEGF outperforms the other systems in terms of the OER activity. Thus, in terms of both the oxygen reactions (ORR/OER),

MnCo₂O₄/NEGF is observed to be a versatile catalyst with its unique bifunctional feature to facilitate both the reactions. Moreover, the difference between the OER potential (E_j @ 10 mA cm⁻²) and ORR half-wave potential ($E_{1/2}$) is generally being used to rate the performance of a bifunctional catalyst (**Figure 4.8c**).⁴⁷ The bar chart presented in **Figure 4.8d** compares extracted values of $E_{1/2}$ for ORR, E_j @ 10 mA cm⁻² for OER and the difference between these two values (ORR-OER) for the respective electrocatalysts. Based on the ORR-OER parameter, which is an indicative of the overall bifunctional activity of the system, MnCo₂O₄/NEGF with the difference of 0.82 V (**Figure 4.8d**) is found to be comparable to or better than the previously reported various bifunctional electrocatalysts (**Table 4.1**). The Tafel slope,

Table 4.1. Comparison of the bifunctional oxygen activity of some of the recently reported non-noble metal-based electrocatalysts vs. our catalyst.

Electrocatalysts	Half Wave Potential $E_{1/2}$ (V) vs. RHE	E_j @10 mA cm ⁻² (V vs. RHE)	Bifunctional activity, ΔE (mV)	References
Co ₃ O ₄ /NPGC	0.84	1.68	0.84	3
Co/N-C-800	0.74	1.60	0.86	4
Co ₃ O ₄ /CNW	0.76	1.57	0.83	5
MnCo ₂ O ₄ /NEGF	0.81	1.63	0.82	This Work

which is a key performance indicator representing the intrinsic activity of the catalyst, has been extracted from the LSVs recorded for ORR and the corresponding values measured for NEGF, Co₃O₄/NEGF, Mn₃O₄/NEGF, MnCo₂O₄/NEGF, and Pt/C are shown in **Figure 4.8e**. MnCo₂O₄/NEGF with its Tafel slope value of 68 mV dec⁻¹ is found to be nearly comparable to Pt/C (64 mV dec⁻¹). A similar exercise has been done to evaluate the kinetics towards OER, and the corresponding Tafel plots for the catalysts with the slopes marked are presented in **Figure 4.8f**. The measured Tafel slope value for MnCo₂O₄/NEGF and RuO₂ are 74 and 86 mV dec⁻¹, respectively. The higher Tafel slope values of Co₃O₄/NEGF (92 mV dec⁻¹) and Mn₃O₄/NEGF (86 mV dec⁻¹) compared to MnCo₂O₄/NEGF suggest better activity of the later system towards OER. Clearly, the incorporation of Mn into the Co₃O₄ lattice is playing a critical role in building the bifunctional feature in the system to enable the catalyst to perform effectively for both the ORR and OER processes.

The electrochemical durability of the catalysts has been investigated by subjecting 5000 cycling under oxygen saturated 0.1 M KOH at a scan rate of 100 mVs⁻¹ in the potential range of 1.2 and 0.8 V with

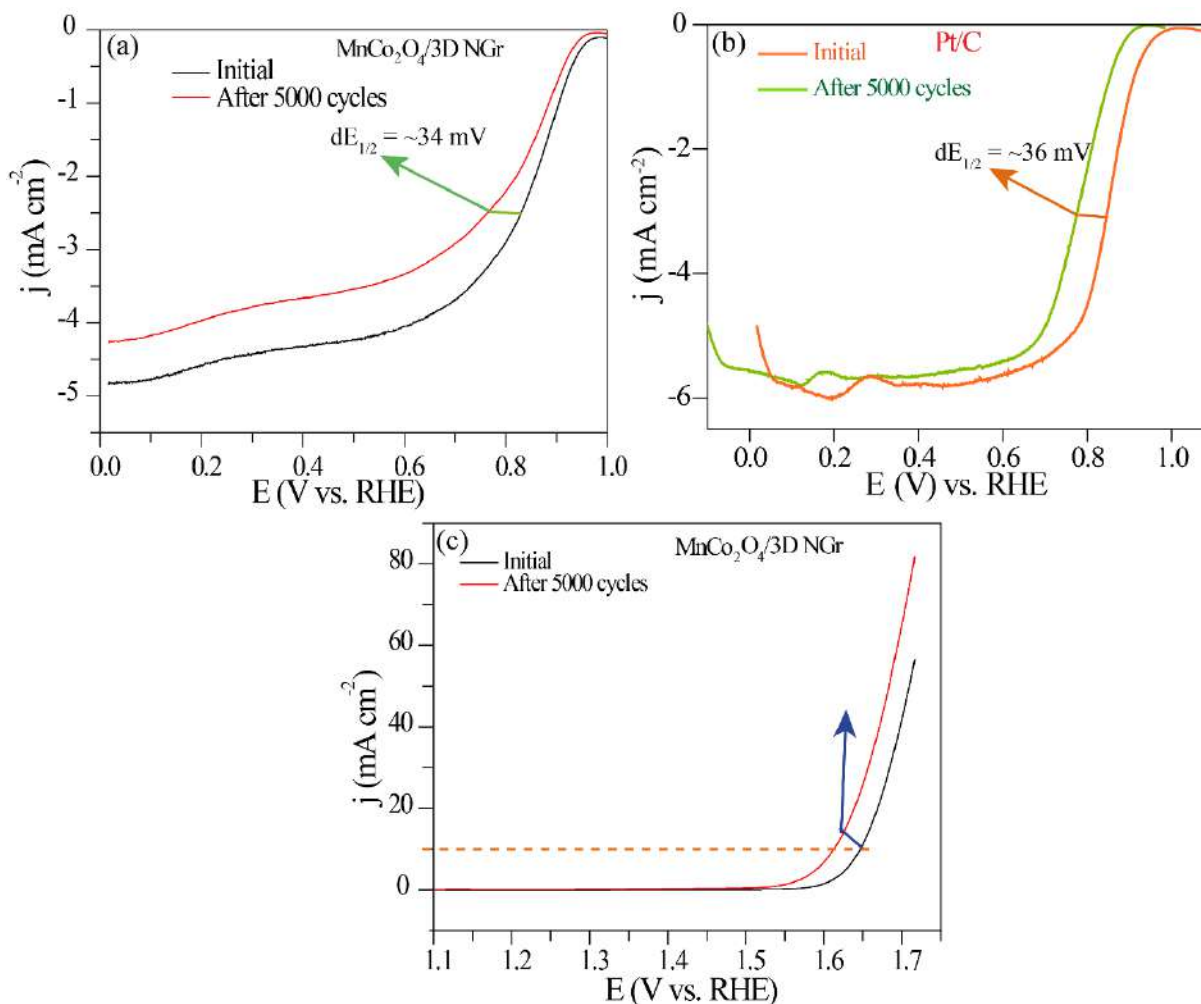


Figure 4.9. Electrochemical durability measurement of the electrocatalyst: (a) and (b) comparative LSV profiles of MnCo₂O₄/NEGF and state-of-the-art Pt/C, respectively, toward ORR recorded before and after completion of the 5000 cycles in 0.1 M KOH at 1600 rpm of the working electrode; (c) comparative LSV profiles of MnCo₂O₄/NEGF corresponding to OER recorded before and after the 5000 cycles in 1 M KOH at 1600 rpm of the working electrode.

respect to RHE, followed by recording the LSV in the oxygen reduction region. A comparison of the LSVs recorded before and after the potential cycling process showed a negative shift in the $E_{1/2}$ value with a drop of 34 mV for MnCo₂O₄/NEGF (**Figure 4.9a**). This drop is lower than that of the state-of-the-art Pt/C catalyst (36 mV) (**Figure 4.9b**) recorded under identical conditions. In a similar way, the durability analysis was performed by cycling the potential for 5000 times under N₂ saturated 1 M KOH at a voltage scan rate of 50 mV sec⁻¹ (**Figure 4.9c**). The change in the OER potential ($E_{j@10}$ mA cm⁻²) for

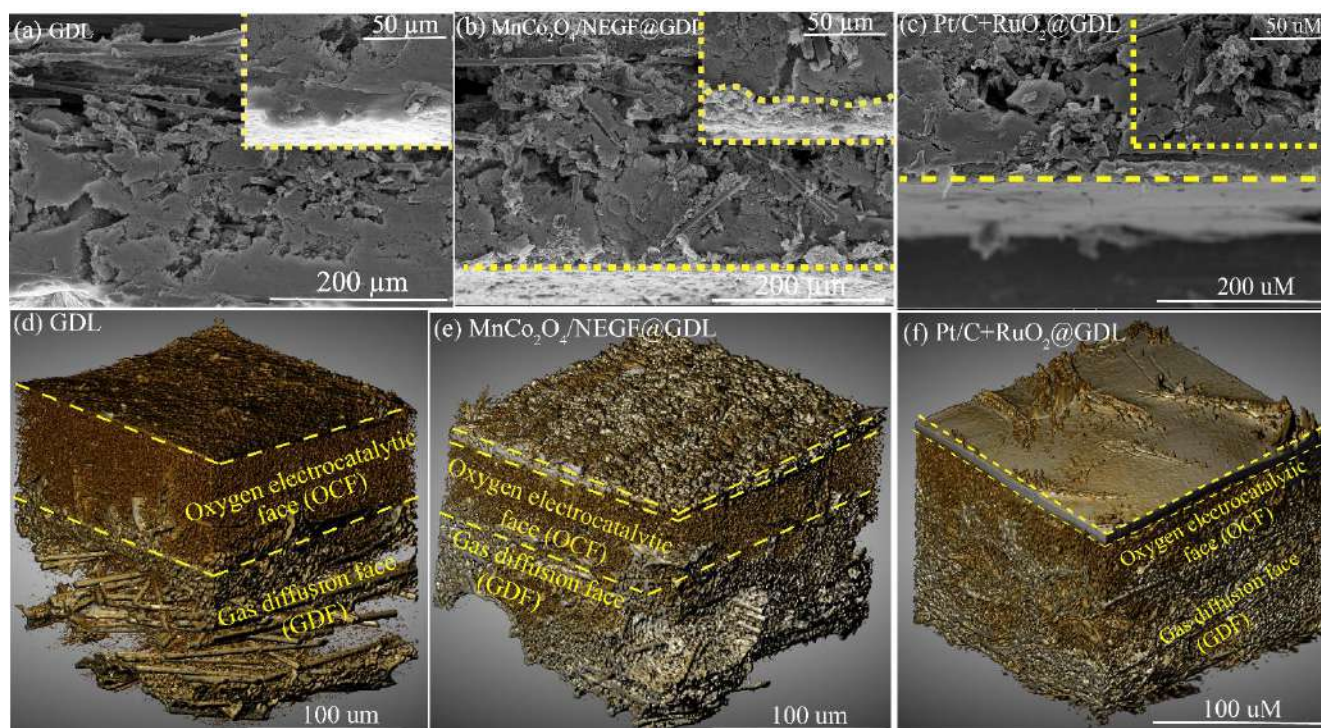


Figure 4.10. (a) The cross-sectional FESEM image of the GDL showing the plain surface boundary with the higher magnified inset image highlighting its bright plain surface; (b) the cross-sectional FESEM image of $\text{MnCo}_2\text{O}_4/\text{NEGF}$ -coated GDL demonstrating the heterojunction interface formed after coating the catalyst with the interface marked with the dotted lines, including as an inset image for better clarity; (c) the cross-sectional FESEM images of $\text{Pt/C} + \text{RuO}_2$ -coated GDL demonstrating the plain surface boundary (Inset: the higher magnified image showing the focused view of the bright part of the plain surface); (d) and (e) the 3D CT tomogram images recorded for the GDL and $\text{MnCo}_2\text{O}_4/\text{NEGF}@GDL$ along the cross-section where the bare GDL is showing the two distinct phases of OCF and GDF, whereas $\text{MnCo}_2\text{O}_4/\text{NEGF}@GDL$ displays a rough surface of the coated catalysts layer; (f) the CT 3D tomogram image recorded along the cross-section for $\text{Pt/C} + \text{RuO}_2$ -coated GDL showing the two different phase of the OCF and the GDF.

$\text{MnCo}_2\text{O}_4/\text{NEGF}$ is only 15 mV. These results reveal the better structural endurance and corrosion resistance of $\text{MnCo}_2\text{O}_4/\text{NEGF}$ as a bifunctional catalyst for OER and ORR applications.

The application of $\text{MnCo}_2\text{O}_4/\text{NEGF}$ as an air electrode to function in the discharging (ORR) and charging (OER) modes for a solid-state ZAB was demonstrated by employing the catalyst-coated gas diffusion electrode (GDE) as the cathode. Prior to the fabrication of the cell and its testing, the catalyst-coated GDL surface was characterized by using FESEM and X-ray CT mapping to check the 3D microstructure of the

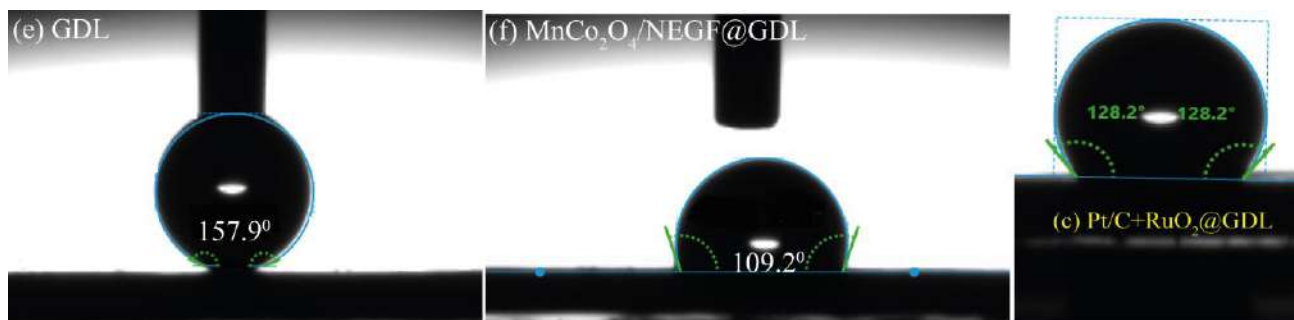


Figure 4.11. (a) and (b) the contact angle images recorded on the bare GDL and $\text{MnCo}_2\text{O}_4/\text{NEGF}$, showing the surface wettability characteristics; (c) the contact angle measurement on the $\text{Pt/C} + \text{RuO}_2$ -coated GDL.

resulting electrodes (**Figure 4.10**). **Figure 4.10a** and the inset image show the cross-sectional FESEM image of the bare GDL, revealing the mostly flat structure of the surface. However, in the case of the GDL coated with $\text{MnCo}_2\text{O}_4/\text{NEGF}$, a thick layer with 3D structure (indicated by the dotted yellow lines) is observed (**Figure 4.10b**). The inset of **Figure 4.10b** gives better clarity of the surface containing the 3D self-assembled structure of the coated layer of $\text{MnCo}_2\text{O}_4/\text{NEGF}$. This 3D microstructured catalyst layer over the GDL has a significant advantage for achieving improved TPB with better active interface and mass transfer characteristics. Compared to the highly porous nature of the $\text{MnCo}_2\text{O}_4/\text{NEGF}$ layer on the GDL, the catalyst layer of $\text{Pt/C} + \text{RuO}_2$ is found to be significantly less porous (**Figure 4.10c**). The 3D CT tomogram imaging was performed to gain further information about the nature of multiphase reactive the gas diffusion face (GDF) towards the inner and outer sides of the air-electrode, respectively. At OCF, the carbon fibers are coated with the hydrophobic PTFE, which prevents the flooding of the microporous surface of the GDL. **Figure 4.10d** and **4.10e** show the 3D tomogram cross-section images of the bare GDL and the $\text{MnCo}_2\text{O}_4/\text{NEGF}$ -coated GDL, respectively. The tomography images in **Figure 4.10d** and **4.10e** show the two distinct phases of OCF and GDF (marked with the dotted yellow lines) of the GDL. On the other hand, in the case of the 3D CT image of the catalyst-coated GDL (**Figure 4.10e**), the 3D microstructure formation of the layer of $\text{MnCo}_2\text{O}_4/\text{NEGF}$ is clearly evident, and is demarcated with the dotted yellow line. However, this type of porous 3D microstructure of the catalyst layer is not evident in the 3D CT image recorded for the $\text{Pt/C} + \text{RuO}_2$ catalyst-coated GDL (**Figure 4.10f**).

Of course, the 3D porous morphology of the $\text{MnCo}_2\text{O}_4/\text{NEGF}$ layer in the electrode is beneficial for improving the electrode-electrolyte interface formation. However, to realize this advantage significantly, the porous layer also should retain the optimum intrinsic wettability of the electrocatalyst even after it

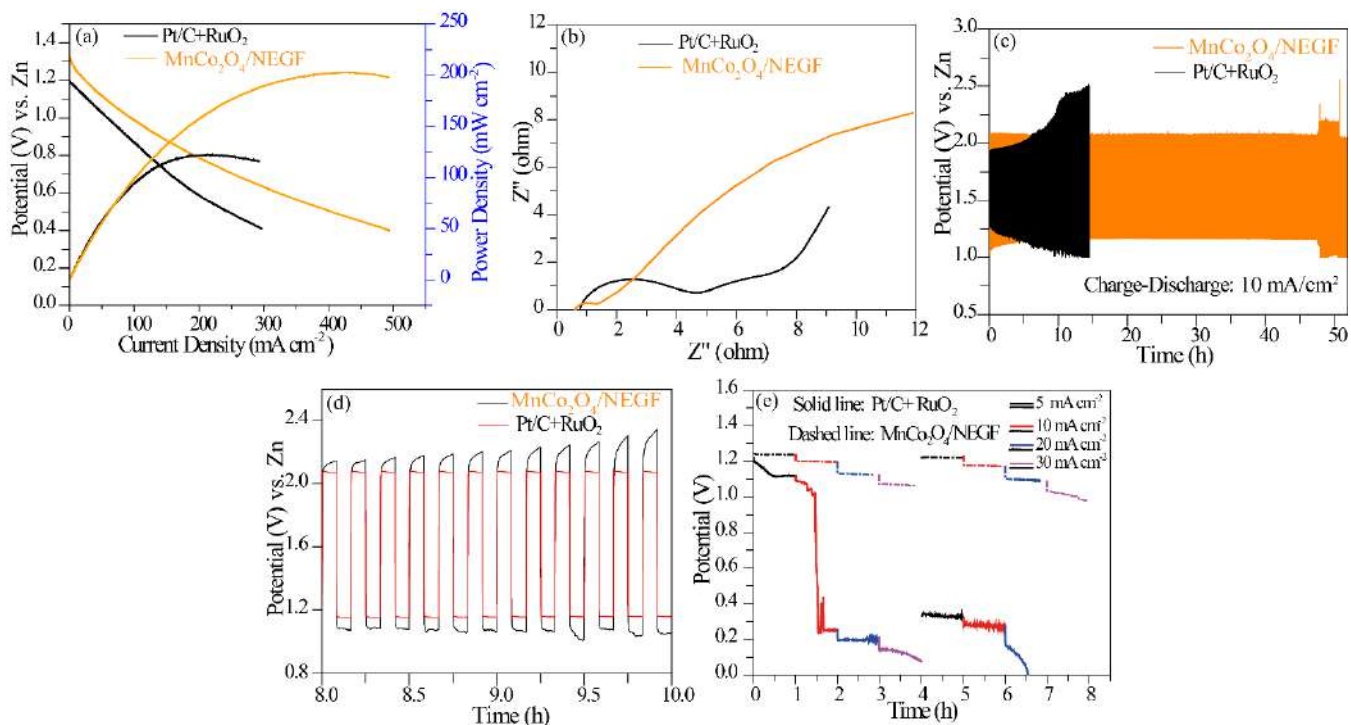


Figure 4.12. The solid-state rechargeable zinc-air battery (ZAB) performance evaluation for the systems based on $\text{MnCo}_2\text{O}_4/\text{NEGF}$ and $\text{Pt/C}+\text{RuO}_2$ as the air-electrodes: (a) the comparative polarization plots; (b) comparative impedance plots; (c) the comparative galvanostatic charge-discharge plots recorded at 10 mA cm^{-2} displaying the higher overpotential incurred by the system based on the $\text{Pt/C}+\text{RuO}_2$ air-electrode; (d) the focused view of the galvanostatic charge-discharge cycling curves recorded at 10 mA cm^{-2} between 8 to 10 h of the test, showing the asymmetric nature of the charge discharge plateau in the case of the ZAB based on the $\text{Pt/C}+\text{RuO}_2$ standard pair air-cathode compared to the perfect symmetric nature of the charge-discharge profiles traced with the system based on the $\text{MnCo}_2\text{O}_4/\text{NEGF}$ air-electrode; (e) the assessment of the galvanostatic discharge capacity of the fabricated ZABs performed at the various discharge current densities of 5, 10, 20, 30 mA cm^{-2} .

was subjected to the coating protocol during the electrode fabrication process. Interestingly, the $\text{MnCo}_2\text{O}_4/\text{NEGF}$ -coated surface of the GDL shows a water contact angle of 109.2° (**Figure 4.11a**), compared to 157.9° recorded on the CA measured on the $\text{Pt/C}+\text{RuO}_2$ -coated surface of the GDL is 128.2° (**Figure 4.11b**). From these results, it can be readily inferred that while an aqueous electrolyte can hardly wet the bare GDL, the GDL based on the $\text{MnCo}_2\text{O}_4/\text{NEGF}$ coating possesses a balanced hydrophilic/hydrophobic characteristic, which is expected to result in optimum wettability at the interface. In terms of this advantage, coupled with the 3D interconnected porous nature of the catalyst texture, the electrode based on $\text{MnCo}_2\text{O}_4/\text{NEGF}$ catalyst layer has a distinct advantage over its counterpart system based on the $\text{Pt/C}+\text{RuO}_2$ -coated electrode (**Figure 4.11c**).

Table 4.2. The comparison of the performance of some of the previously reported solid-state ZAB systems based on the non-precious metal-based electrocatalysts and the present system.

Electrocatalyst	Electrolyte	OCV (V)	Power density (mW cm ⁻²)	Stability	References
Co ₃ O _{4-x} HoNPs@HPNCS	PVA-KOH (Solid)	1.46	94.1	50 cycles for 18 h @ 3 mA cm ⁻²	6
Co/CoO/NWC	PVA-KOH (Solid)	1.32	28	36h @ 2 mA cm ⁻²	7
CoN ₄ /NG	PVA-KOH (Solid)	-	28	6 h @ 1 mA cm ⁻²	8
MnOx-GCC	PVA-KOH (Solid)	1.42	18	30 h @ 0.7 mA cm ⁻²	9
CoSx/Co-NC-800	PVA-KOH (Solid)	1.34	-	16 h @ 1 mA cm ⁻²	10
MnCo ₂ O ₄ /NEGF	PVA-KOH (Solid)	1.31	202	51 h	This work

A full-featured demonstration of the prepared catalyst in a solid-state rechargeable ZAB device was conducted by fabricating a device by employing MnCo₂O₄/NEGF-coated GDL as the air-electrode, a zinc powder-coated GDL as the anode, and PVA soaked with KOH as the electrolyte (**Figure 4.1**). A similar device by employing Pt/C + RuO₂ standard pair catalyst-coated GDL as the air-electrode was also made for the comparison purpose. The cell polarization plots presented in **Figure 4.12a** clearly demonstrate the superiority of the system based on the homemade cathode in the entire I-V region traced during the study. The ZABs based on MnCo₂O₄/NEGF and Pt/C + RuO₂ cathodes display the OCV values of 1.31 and 1.20 V, respectively. The comparative steady-state cell polarization leads to the maximum power densities (P_{\max}) of 110 and 200 mW cm⁻², respectively, for these two systems. Here, the catalyst layer in the case of the MnCo₂O₄/NEGF, with its 3D inter-connected porous structure and optimum wettability, is found to be more accommodative for the KOH soaked PVA gel electrolyte. The previous discussions based on the FESEM, CT Tomography, and water contact angle data provided adequate information towards these advantageous structural and functional attributes of the in-house system. The advantage of MnCo₂O₄/NEGF to form a more process-friendly cathode is further reflected from the substantially reduced charge transfer resistance (CTR) displayed by the cell compared to the one based on Pt/C + RuO₂ standard pair cathode (**Figure 4.12b**).

Furthermore, the galvanostatic charge/discharge curves recorded for the cells at 10 mA cm^{-2} are shown in **Figure 4.12c**. The observed difference between the charging and discharging voltages of the ZAB based on $\text{MnCo}_2\text{O}_4/\text{NEGF}$ during the initial process is 0.84 V , which is lower than (0.91 V) that observed in the case of its counterpart system based on the $\text{Pt/C} + \text{RuO}_2$ standard pair. After 50 h of continuous charge-discharge cycles, a nominal increase in the voltage difference by 0.10 V has been observed in the case $\text{MnCo}_2\text{O}_4/\text{NEGF}$ -based cell. However, in the case of the $\text{Pt/C} + \text{RuO}_2$ -based system, the voltage difference is found to be increased to 0.15 V just after 15 h of the continuous charge-discharge cycles and the test had to be terminated. Moreover, the magnified image of the charge-discharge profile in the 8 to 10 h duration, presented in **Figure 4.12d**, reveals the symmetric nature of the charge-discharge plateau in the case of the $\text{MnCo}_2\text{O}_4/\text{NEGF}$ cell. Contrary to this, the cell based on $\text{Pt/C} + \text{RuO}_2$ has asymmetric behavior in its charge-discharge profile. This difference in the feature of the charge-discharge characteristics points toward the better bifunctional activity at the air-cathode of the ZAB based on $\text{MnCo}_2\text{O}_4/\text{NEGF}$.

In the case of the rechargeable metal-air batteries, the ORR process is more sensitive to the active triple-phase interface during the discharge process compared to the OER process in the charging mode. To unravel the advantages of $\text{MnCo}_2\text{O}_4/\text{NEGF}$ due to its structural and functional attributes towards ORR in the battery configuration, the discharge curve at various current densities of 5, 10, 20, and 30 mA cm^{-2} are recorded for 1h and the comparative plots are presented in **Figure 4.12e**. It can be seen from the figure that, under each step of the discharging process, the voltage drop incurred by the $\text{MnCo}_2\text{O}_4/\text{NEGF}$ -based system is much lower compared to the one based on $\text{Pt/C} + \text{RuO}_2$. The ZAB based on $\text{MnCo}_2\text{O}_4/\text{NEGF}$ has a relatively small voltage gap of 0.11, 0.12, 0.13, and 0.15 V at 5.0, 10.0, 20.0, and 30.0 mA cm^{-2} compared to 1.05, 0.14, 0.15, and 0.60 V , respectively, recorded under the same discharging conditions for the counterpart system based on $\text{Pt/C} + \text{RuO}_2$. This distinct advantage of the $\text{MnCo}_2\text{O}_4/\text{NEGF}$ system could be credited to the favorable morphology of the catalyst in terms of better oxygen gas transport and efficient active interface formation. The presented results clearly demonstrate that these kinds of air-electrodes with nano-engineered morphological and functional features have greater prospects of ensuring better system-level performance under different current dragging conditions.

After the long cycle of the galvanostatic charge-discharge analysis, the catalysts and the air-electrode interface structure were analyzed by FESEM. The FESEM images of $\text{MnCo}_2\text{O}_4/\text{NEGF}$ and $\text{MnCo}_2\text{O}_4/\text{NEGF}$ -coated ZAB air cathode interface are shown in **Figure 4.13**. **Figure 4.13a** displays the 3D structure of NEGF retained even after the long charge-discharge cycles. The magnified image presented in **Figure 4.13b** clearly shows that the catalyst structure is more or less unaffected even after

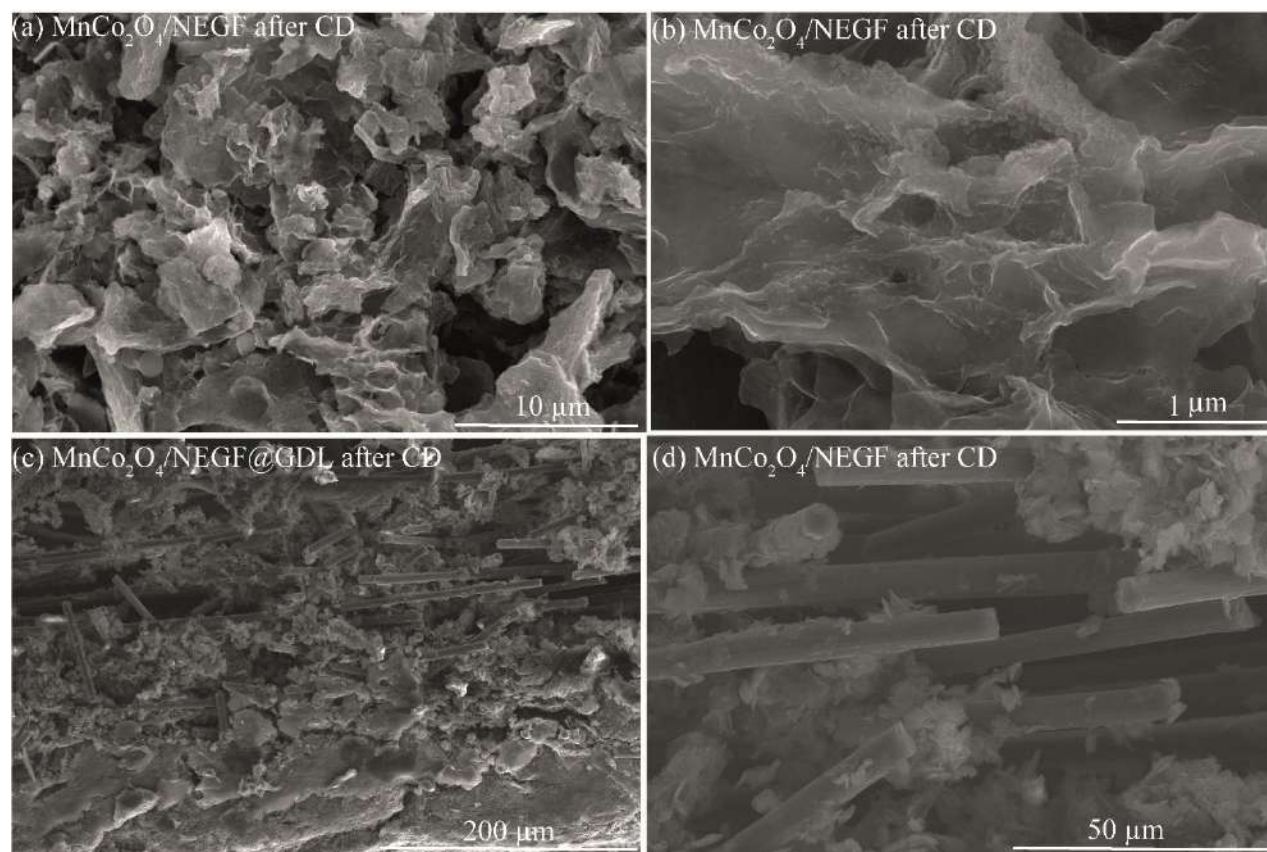


Figure 4.13. The FESEM images of the $\text{MnCo}_2\text{O}_4/\text{NEGF}$ air-cathode recorded after the continuous charge-discharge cycles: (a) $\text{MnCo}_2\text{O}_4/\text{NEGF}$ displaying its 3D structure retained after the test; (b) the magnified image clearly showing that the catalyst structure is more or less unaffected even after subjecting the system under the corrosive environment of the testing conditions; (c) and (d) the cross-sectional images indicating the detachment of a portion of the catalyst from the GDL surface after the long-term cycling.

subjecting the system to the corrosive environment of the testing conditions. The cross-sectional image analysis of the ZAB air cathode (**Figure 4.13c** and **4.13d**) shows that a portion of the catalyst gets detached from the GDL surface after the long-term charge-discharge cycling. Still, the inherent porosity of the conducting support is maintained nearly unaffected.

4.4. Conclusions:

A 3D structured electrode material, designated as $\text{MnCo}_2\text{O}_4/\text{NEGF}$, consisting of the manganese-cobalt-based bimetallic spinel oxide (MnCo_2O_4)-supported nitrogen-doped entangled graphene (NEGF) has been prepared as a versatile OER/ORR bifunctional electrocatalyst for rechargeable zinc-air battery (ZAB) application. The features like the porous 3D architecture of the catalyst, balanced

hydrophilic/hydrophobic characteristics and optimal ORR/OER activity are found to be favorably helping the system as an air-cathode for the rechargeable ZAB application. The 3D structure of the catalyst greatly helps the system for the mass transfer and active site accessibility in the electrode. At the same time, the optimal hydrophilicity originated from the functional attributes of the support surface is found to be playing a critical role in establishing the effective interface of the catalyst and the electrolyte. The study reveals the existence of synergistic interactions operating between the MnCo_2O_4 nanoparticles and the N-doped porous graphene substrate. This benefits the system in terms of its bifunctional characteristics to perform as an effective electrocatalyst for facilitating both ORR and OER processes. In terms of the activity of $\text{MnCo}_2\text{O}_4/\text{NEGF}$ towards these reactions, the overpotential values are found to be closely comparable to the respective state-of-the-art systems (*i.e.*, Pt/C for ORR and RuO_2 for OER). The demonstration of a solid-state rechargeable ZAB device with $\text{MnCo}_2\text{O}_4/\text{NEGF}$ as the air-electrode delivered a maximum peak power density of 200 mW cm^{-2} , with good stability during the charge-discharge cycling process. In terms of the performance and charge-discharge cyclability, the system based on the homemade catalyst is found to have a clear upper hand compared to a system consisting of the state-of-the-art ORR/OER catalyst combination of Pt/C+ RuO_2 .

4.5. References:

1. Sun, W.; Wang, F.; Zhang, B.; Zhang, M.; Kupers, V.; Ji, X.; Theile, C.; Bieker, P.; Xu, K.; Wang, C.; Winter, M., A rechargeable zinc-air battery based on zinc peroxide chemistry. *Science* 2021, 371 (6524), 46-51.
2. Li, Y.; Gong, M.; Liang, Y.; Feng, J.; Kim, J. E.; Wang, H.; Hong, G.; Zhang, B.; Dai, H., Advanced zinc-air batteries based on high-performance hybrid electrocatalysts. *Nat Commun* 2013, 4, 1805.
3. Cheng, F.; Chen, J., Metal-air batteries: from oxygen reduction electrochemistry to cathode catalysts. *Chem Soc Rev* 2012, 41 (6), 2172-92.
4. Lee, J.-S.; Tai Kim, S.; Cao, R.; Choi, N.-S.; Liu, M.; Lee, K. T.; Cho, J., Metal-Air Batteries with High Energy Density: Li-Air versus Zn-Air. *Advanced Energy Materials* 2011, 1 (1), 34-50.
5. Su, H.; Wang, X.-T.; Hu, J.-X.; Ouyang, T.; Xiao, K.; Liu, Z.-Q., Co-Mn spinel supported self-catalysis induced N-doped carbon nanotubes with high efficiency electron transport channels for zinc-air batteries. *Journal of Materials Chemistry A* 2019, 7 (39), 22307-22313.
6. Gu, P.; Zheng, M.; Zhao, Q.; Xiao, X.; Xue, H.; Pang, H., Rechargeable zinc-air batteries: a promising way to green energy. *Journal of Materials Chemistry A* 2017, 5 (17), 7651-7666.

7. Gangadharan, P. K.; Bhang, S. N.; Kabeer, N.; Illathvalappil, R.; Kurungot, S., NiCo₂O₄ nanoarray on CNT sponge: a bifunctional oxygen electrode material for rechargeable Zn–air batteries. *Nanoscale Advances* 2019, 1 (8), 3243-3251.
8. Yu, J.; Li, B. Q.; Zhao, C. X.; Liu, J. N.; Zhang, Q., Asymmetric Air Cathode Design for Enhanced Interfacial Electrocatalytic Reactions in High-Performance Zinc-Air Batteries. *Adv Mater* 2020, 32 (12), e1908488.
9. Wang, X. X.; Yang, X.; Liu, H.; Han, T.; Hu, J.; Li, H.; Wu, G., Air Electrodes for Flexible and Rechargeable Zn–Air Batteries. *Small Structures* 2021, 3 (1).
10. Pan, J.; Xu, Y. Y.; Yang, H.; Dong, Z.; Liu, H.; Xia, B. Y., Advanced Architectures and Relatives of Air Electrodes in Zn-Air Batteries. *Adv Sci (Weinh)* 2018, 5 (4), 1700691.
11. Wu, M.; Zhang, G.; Du, L.; Yang, D.; Yang, H.; Sun, S., Defect Electrocatalysts and Alkaline Electrolyte Membranes in Solid-State Zinc-Air Batteries: Recent Advances, Challenges, and Future Perspectives. *Small Methods* 2021, 5 (1), e2000868.
12. Chai, G.-L.; Qiu, K.; Qiao, M.; Titirici, M.-M.; Shang, C.; Guo, Z., Active sites engineering leads to exceptional ORR and OER bifunctionality in P,N Co-doped graphene frameworks. *Energy & Environmental Science* 2017, 10 (5), 1186-1195.
13. Han, C.; Li, W.; Liu, H.-K.; Dou, S.; Wang, J., Design strategies for developing non-precious metal based bi-functional catalysts for alkaline electrolyte based zinc–air batteries. *Materials Horizons* 2019, 6 (9), 1812-1827.
14. Zhao, Q.; Yan, Z.; Chen, C.; Chen, J., Spinel: Controlled Preparation, Oxygen Reduction/Evolution Reaction Application, and Beyond. *Chem Rev* 2017, 117 (15), 10121-10211.
15. Song, Z.; Liu, Q., Tolerance Factor and Phase Stability of the Normal Spinel Structure. *Crystal Growth & Design* 2020, 20 (3), 2014-2018.
16. Manna, N.; Singh, S. K.; Kharabe, G. P.; Torris, A.; Kurungot, S., Zinc–Air Batteries Catalyzed Using Co₃O₄ Nanorod-Supported N-Doped Entangled Graphene for Oxygen Reduction Reaction. *ACS Applied Energy Materials* 2021, 4 (5), 4570-4580.
17. Li, C.; Han, X.; Cheng, F.; Hu, Y.; Chen, C.; Chen, J., Phase and composition controllable synthesis of cobalt manganese spinel nanoparticles towards efficient oxygen electrocatalysis. *Nat Commun* 2015, 6, 7345.
18. Janani, G.; Surendran, S.; Choi, H.; Han, M. K.; Sim, U., In Situ Grown CoMn₂O₄ 3D-Tetragons on Carbon Cloth: Flexible Electrodes for Efficient Rechargeable Zinc-Air Battery Powered Water Splitting Systems. *Small* 2021, 17 (47), e2103613.

19. Yang, Y.; Xiong, Y.; Holtz, M. E.; Feng, X.; Zeng, R.; Chen, G.; DiSalvo, F. J.; Muller, D. A.; Abruna, H. D., Octahedral spinel electrocatalysts for alkaline fuel cells. *Proc Natl Acad Sci U S A* 2019, 116 (49), 24425-24432.
20. Zhou, Y.; Zhou, Z.; Shen, R.; Ma, R.; Liu, Q.; Cao, G.; Wang, J., Correlating electrocatalytic oxygen reduction activity with d-band centers of metallic nanoparticles. *Energy Storage Materials* 2018, 13, 189-198.
21. Gonçalves, J. M.; Silva, M. N. T.; Naik, K. K.; Martins, P. R.; Rocha, D. P.; Nossol, E.; Munoz, R. A. A.; Angnes, L.; Rout, C. S., Multifunctional spinel MnCo_2O_4 based materials for energy storage and conversion: a review on emerging trends, recent developments and future perspectives. *Journal of Materials Chemistry A* 2021, 9 (6), 3095-3124.
22. Lu, X. F.; Chen, Y.; Wang, S.; Gao, S.; Lou, X. W. D., Interfacing Manganese Oxide and Cobalt in Porous Graphitic Carbon Polyhedrons Boosts Oxygen Electrocatalysis for Zn-Air Batteries. *Adv Mater* 2019, 31 (39), e1902339.
23. Zhu, H.; Gu, L.; Yu, D.; Sun, Y.; Wan, M.; Zhang, M.; Wang, L.; Wang, L.; Wu, W.; Yao, J.; Du, M.; Guo, S., The marriage and integration of nanostructures with different dimensions for synergistic electrocatalysis. *Energy & Environmental Science* 2017, 10 (1), 321-330.
24. Dai, L.; Chang, D. W.; Baek, J. B.; Lu, W., Carbon nanomaterials for advanced energy conversion and storage. *Small* 2012, 8 (8), 1130-66.
25. Li, Y.; Zhao, M.; Zhao, Y.; Song, L.; Zhang, Z., FeNi Layered Double-Hydroxide Nanosheets on a 3D Carbon Network as an Efficient Electrocatalyst for the Oxygen Evolution Reaction. *Particle & Particle Systems Characterization* 2016, 33 (3), 158-166.
26. Mo, R.; Rooney, D.; Sun, K.; Yang, H. Y., 3D nitrogen-doped graphene foam with encapsulated germanium/nitrogen-doped graphene yolk-shell nanoarchitecture for high-performance flexible Li-ion battery. *Nat Commun* 2017, 8, 13949.
27. Cui, X.; Liu, Y.; Han, G.; Cao, M.; Han, L.; Zhou, B.; Mehdi, S.; Wu, X.; Li, B.; Jiang, J., Wood-Derived Integral Air Electrode for Enhanced Interfacial Electrocatalysis in Rechargeable Zinc-Air Battery. *Small* 2021, 17 (38), e2101607.
28. Wang, Y.-C.; Huang, L.; Zhang, P.; Qiu, Y.-T.; Sheng, T.; Zhou, Z.-Y.; Wang, G.; Liu, J.-G.; Rauf, M.; Gu, Z.-Q.; Wu, W.-T.; Sun, S.-G., Constructing a Triple-Phase Interface in Micropores to Boost Performance of Fe/N/C Catalysts for Direct Methanol Fuel Cells. *ACS Energy Letters* 2017, 2 (3), 645-650.

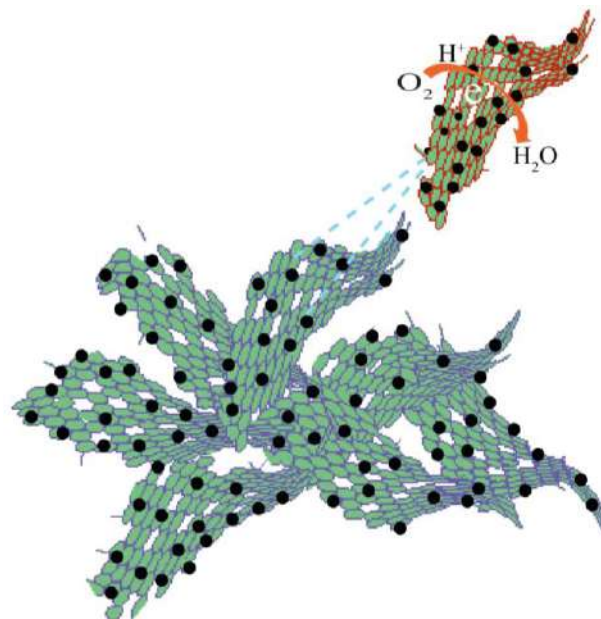
29. Li, S.; Zhou, X.; Fang, G.; Xie, G.; Liu, X.; Lin, X.; Qiu, H.-J., Multicomponent Spinel Metal Oxide Nanocomposites as High-Performance Bifunctional Catalysts in Zn–Air Batteries. *ACS Applied Energy Materials* 2020, 3 (8), 7710-7718.
30. Choi, S.; Jeon, J.; Chae, J.; Yuk, S.; Lee, D.-H.; Doo, G.; Lee, D. W.; Hyun, J.; Kwen, J.; Choi, S. Q.; Kim, H.-T., Single-Step Fabrication of a Multiscale Porous Catalyst Layer by the Emulsion Template Method for Low Pt-Loaded Proton Exchange Membrane Fuel Cells. *ACS Applied Energy Materials* 2021, 4 (4), 4012-4020.
31. Wu, Z. S.; Yang, S.; Sun, Y.; Parvez, K.; Feng, X.; Mullen, K., 3D nitrogen-doped graphene aerogel-supported Fe₃O₄ nanoparticles as efficient electrocatalysts for the oxygen reduction reaction. *J Am Chem Soc* 2012, 134 (22), 9082-5.
32. Zenyuk, I. V.; Parkinson, D. Y.; Connolly, L. G.; Weber, A. Z., Gas-diffusion-layer structural properties under compression via X-ray tomography. *Journal of Power Sources* 2016, 328, 364-376.
33. Tötzke, C.; Gaiselmann, G.; Osenberg, M.; Bohner, J.; Arlt, T.; Markötter, H.; Hilger, A.; Wieder, F.; Kupsch, A.; Müller, B. R.; Hentschel, M. P.; Banhart, J.; Schmidt, V.; Lehnert, W.; Manke, I., Three-dimensional study of compressed gas diffusion layers using synchrotron X-ray imaging. *Journal of Power Sources* 2014, 253, 123-131.
34. Jang, S.; Kim, S.; Kim, S. M.; Choi, J.; Yeon, J.; Bang, K.; Ahn, C.-Y.; Hwang, W.; Her, M.; Cho, Y.-H.; Sung, Y.-E.; Choi, M., Interface engineering for high-performance direct methanol fuel cells using multiscale patterned membranes and guided metal cracked layers. *Nano Energy* 2018, 43, 149-158.
35. Manna, N.; Ayasha, N.; Singh, S. K.; Kurungot, S., A NiFe layered double hydroxide-decorated N-doped entangled-graphene framework: a robust water oxidation electrocatalyst. *Nanoscale Advances* 2020, 2 (4), 1709-1717.
36. Li, M.; Liu, T.; Bo, X.; Zhou, M.; Guo, L., A novel flower-like architecture of FeCo@NC-functionalized ultra-thin carbon nanosheets as a highly efficient 3D bifunctional electrocatalyst for full water splitting. *Journal of Materials Chemistry A* 2017, 5 (11), 5413-5425.
37. Liang, Y.; Wang, H.; Zhou, J.; Li, Y.; Wang, J.; Regier, T.; Dai, H., Covalent hybrid of spinel manganese-cobalt oxide and graphene as advanced oxygen reduction electrocatalysts. *J Am Chem Soc* 2012, 134 (7), 3517-23.
38. Zhang, Z.; Dou, M.; Liu, H.; Dai, L.; Wang, F., A Facile Route to Bimetal and Nitrogen-Codoped 3D Porous Graphitic Carbon Networks for Efficient Oxygen Reduction. *Small* 2016, 12 (31), 4193-9.

39. Xiong, Y.; Yang, Y.; Feng, X.; DiSalvo, F. J.; Abruna, H. D., A Strategy for Increasing the Efficiency of the Oxygen Reduction Reaction in Mn-Doped Cobalt Ferrites. *J Am Chem Soc* 2019, 141 (10), 4412-4421.
40. Amirzhanova, A.; Akmanşen, N.; Karakaya, I.; Dag, Ö., Mesoporous MnCo_2O_4 , NiCo_2O_4 , and ZnCo_2O_4 Thin-Film Electrodes as Electrocatalysts for the Oxygen Evolution Reaction in Alkaline Solutions. *ACS Applied Energy Materials* 2021, 4 (3), 2769-2785.
41. Wang, Y.; Yang, Y.; Jia, S.; Wang, X.; Lyu, K.; Peng, Y.; Zheng, H.; Wei, X.; Ren, H.; Xiao, L.; Wang, J.; Muller, D. A.; Abruna, H. D.; Hwang, B. J.; Lu, J.; Zhuang, L., Synergistic Mn-Co catalyst outperforms Pt on high-rate oxygen reduction for alkaline polymer electrolyte fuel cells. *Nat Commun* 2019, 10 (1), 1506.
42. Unni, S. M.; Bhange, S. N.; Illathvalappil, R.; Mutneja, N.; Patil, K. R.; Kurungot, S., Nitrogen-induced surface area and conductivity modulation of carbon nanohorn and its function as an efficient metal-free oxygen reduction electrocatalyst for anion-exchange membrane fuel cells. *Small* 2015, 11 (3), 352-60.
43. Priamushko, T.; Guillet-Nicolas, R.; Yu, M.; Doyle, M.; Weidenthaler, C.; Tüysüz, H.; Kleitz, F., Nanocast Mixed Ni-Co-Mn Oxides with Controlled Surface and Pore Structure for Electrochemical Oxygen Evolution Reaction. *ACS Applied Energy Materials* 2020, 3 (6), 5597-5609.
44. Singh, S. K.; Dhavale, V. M.; Kurungot, S., Surface-Tuned Co_3O_4 Nanoparticles Dispersed on Nitrogen-Doped Graphene as an Efficient Cathode Electrocatalyst for Mechanical Rechargeable Zinc-Air Battery Application. *ACS Appl Mater Interfaces* 2015, 7 (38), 21138-49.
45. Akhtar, M. S.; Bui, P. T. M.; Li, Z.-Y.; Yang, O. B.; Paul, B. J.; Kim, S.; Kim, J.; Rai, A. K., Impact of porous Mn_3O_4 nanostructures on the performance of rechargeable lithium ion battery: Excellent capacity and cyclability. *Solid State Ionics* 2019, 336, 31-38.
46. Yan, X.; Jia, Y.; Chen, J.; Zhu, Z.; Yao, X., Defective-Activated-Carbon-Supported Mn-Co Nanoparticles as a Highly Efficient Electrocatalyst for Oxygen Reduction. *Adv Mater* 2016, 28 (39), 8771-8778.
47. Deng, Y. P.; Jiang, Y.; Liang, R.; Zhang, S. J.; Luo, D.; Hu, Y.; Wang, X.; Li, J. T.; Yu, A.; Chen, Z., Dynamic electrocatalyst with current-driven oxyhydroxide shell for rechargeable zinc-air battery. *Nat Commun* 2020, 11 (1), 1952.

Chapter-5

Microwave-Induced Microporous Graphene-Supported Pt₃Co Alloy Catalyst for ORR with better Process-Friendly Features

To improve the oxygen reduction reaction (ORR) performance in a PEMFC cathode with respect to the mass activity and durability, a suitable electrocatalyst design strategy is essentially needed. Here, we have prepared a sub-three nm-sized platinum (Pt)-cobalt (Co) alloy (Pt₃Co)-supported nitrogen-doped microporous 3D graphene (Pt₃Co/pNEGF) by using the polyol synthesis method. The supported alloy nanoparticles with a specific composition of Pt and Co (Pt₃Co) showed improved ORR activity compared to the Pt-supported pNEGF. A microwave-assisted synthesis method was employed to prepare the catalyst based on the 3D porous carbon support with a large pore volume and dense micro/mesoporous surfaces. Simultaneously, the doped nitrogen in the carbon framework helps in achieving the uniform distribution of the sub-nm-sized Pt₃Co nanoparticles over the nitrogen-doped porous graphene. The ORR performance of Pt₃Co/pNEGF closely matches with the *state-of-the-art* commercial Pt/C catalyst in 0.1 M HClO₄, with a small overpotential of 10 mV. The 3D microporous structure of the N-doped graphene significantly improves the mass transport of the reactant and thus the overall ORR performance. As a result of the lower loading of Pt in Pt₃Co/pNEGF as compared to Pt/C, the alloy catalyst achieved 1.5 times higher mass activity than Pt/C. The presence of the N-doped graphitic carbon support in Pt₃Co/pNEGF offers significantly improved durability. After 10000 cycles, the difference in the electrochemically active surface area (ECSA) and half-wave potential ($E_{1/2}$) of Pt₃Co/pNEGF are found to be 5 m² g_{Pt}⁻¹ (Δ ECSA) and 24 mV (Δ $E_{1/2}$), whereas for Pt/C, these values are 9 m² g_{Pt}⁻¹ and 32 mV, respectively.



The content of this chapter is under publication.

5.1. Introduction:

Efficient and durable catalysts are in continual exploration to reduce the electrochemical activation overpotentials for ORR in the proton-exchange membrane fuel cell (PEMFC) cathode.¹ The Pt nanoparticles supported on spherical-shaped carbon substrates are currently recognized as the most effective electrocatalysts for ORR.² However, due to the high cost of Pt, drop in the electrochemical surface area and the concerns associated with the overall catalytic performance over the long-term operation, meeting the technical challenges with respect to the commercial deployment of PEMFCs has become a challenge.^{3,4} The restricted mass transport in the Pt-supported conventional carbon catalysts is an important limitation that builds overpotential for ORR in PEMFCs.⁵ These issues necessitate a strategic design approach for developing a cost-effective and durable catalyst with inbuilt features for better tackling the electrode processes.⁷ These features mainly include provisions for dealing with the ORR mass transport, water management, and effective “triple-phase boundary (TPB)” formation. The TPB is the region where the gas (reactant), ions (electrolyte), and active sites (solid surface) are in seamless contact with each other. Various methods have been implemented to improve the activity and durability of the ORR catalysts.⁸

Last few decades of research efforts focused mostly on the Pt-based bimetallic alloys catalysts, in which a portion of the Pt is partially replaced by the low-cost transition metals, such as Fe, Co, and Ni. Alloying Pt with another non-noble transition metal reduces the Pt metal loading without affecting the ORR activity. In addition, the presence of an early transition metal to Pt could alter the Pt-Pt interatomic distance, resulting in a down-shift of the d-band center with a change in the electronic structures of the Pt active sites.⁸ Therefore, it introduces the Pt 5d band vacancy in an alloy structure of Pt.⁹ The increased d-band vacancy in the Pt atoms leads to the increased ability to accept the 2p electron donation from the O₂ resulting in improved Pt surface adsorption.¹⁰ As a result, the binding energy of the Pt-O bond becomes stronger while the O-O bond becomes weaker.¹⁰ Therefore, the lattice re-construction in the alloy structure provides preferable sites for oxygen adsorption, which significantly accelerates the ORR reaction kinetics.¹¹ Among the Pt alloy systems with various transition metals (Fe, Co, and Ni), Pt-Co has previously been observed with higher ORR activity.¹² Compared to the other compositions of the Pt-Co alloy structures, the Pt₃Co stoichiometry is primarily suitable for ORR.¹² The active site of Pt in the Pt₃Co alloys experiences a significant amount of ligand and strain effects, which are known to suppress the adsorption energy of the O₂ reduction intermediate species, resulting in increased ORR kinetics.

Moreover, the distribution of the controlled size and uniformity of the alloyed Pt₃Co nanoparticles over conducting support would increase the overall ORR activity and durability under the operating conditions.¹² As noted earlier, the controlled particle size and distribution of a nano-alloy have advantages in increasing the ECSA of the catalysts.¹³ Recently, the alloy structures with sub-nanometer particle sizes are considered as high-performing ORR catalysts.¹⁴ However, the introduction of the non-noble transition metal atoms in the Pt alloys with sub-nanometer particle size has limitations as they can easily segregate due to the charge effect resulting from the lattice mismatch. Therefore, incorporating suitable conducting support with uniform nucleation sites for the alloy nanoparticle growth is considered as one of the finest strategies to improve the ORR performance.⁵

In this context, most of the conducting carbon supports utilized to disperse the bimetallic Pt alloys are 1D and 2D carbon-based materials. The morphological restriction of these carbon supports imparts poor mass transport activity during the ORR process in acidic conditions.¹⁴ In addition, these carbon support experiences restacking issues, which significantly suppresses the ECSA of the electrocatalysts.¹⁵ Incorporation of 3D porous conducting support materials, such as those based on 3D structured graphenes, as the substrates for interlinking the ORR active catalytic centers is considered a promising approach.¹⁶ The porous structure of the self-assembled 3D supports helps in better distribution of the Pt-alloy particles, reduces the ionomer coverage ratio, and lowers the local O₂ transport resistance.⁸ Aside from this, the presence of the graphitic carbon support with homogeneously doped-N creates metal anchoring sites and improves the metal-support interaction. This helps for achieving better durability in the harsh electrochemical conditions of the PEMFC operation. Furthermore, in the self-assembled 3D graphene support, the pores are mostly distributed in the meso/macroporous region, which has less access to the sub-nm-sized Pt-alloy particles.¹⁰ Therefore, the carbon support porosity within the range of microporosity and mesoporosity has a significant impact on the distribution of the small-sized alloy nanoparticle as well as on achieving efficient mass transfer. Various strategies were developed to create the microporous carbon structures, and many of them involve energy-consuming processes.¹⁷ Recently, the microwave irradiation has been found to be very effective for the fast formation of the micropores in the carbon substrate.¹⁸ The microwave irradiation results in uniform heat generation within a very short time to reach a high temperature by selective energy transferring to the microwave-active polar substrates.

To best accommodate the aforementioned structural characteristics of the conducting support, in this project, an ORR electrocatalyst based on N-doped porous 3D graphene-supported sub-3 nm Pt₃Co alloy

catalyst (Pt₃Co/NEGF) has been developed. The doped-N in the graphene framework serves as the nucleation-cum-anchoring sites for the Pt₃Co nanoparticles on the asymmetric graphene substrate. Finally, the sub-nanometer-sized Pt alloy (Pt₃Co/pNEGF)-supported microporous electrocatalyst is found to compete well with those of the *state-of-the-art* (Pt/C) catalyst due to its accessible active components (Pt₃Co) and preferable mass transport channel support. With these aspects, Pt₃Co/pNEGF catalyst outperforms the conventional catalyst in terms of the key performance indicators related to the ORR activity.

5.2. Experimental Section:

5.2.1. Materials: Platinum acetylacetonate [Pt(acac)₂], cobalt acetylacetonate [Co(acac)₃], graphite, and potassium permanganate (KMnO₄) were procured from Sigma Aldrich. Phosphoric acid (H₃PO₄), sulphuric acid (H₂SO₄), perchloric acid (HClO₄), and ammonium hydroxide (NH₄OH) were acquired from Thomas Baker. Without any further purification, all the chemicals were used as such.⁶

5.2.2. Synthesis of Graphene Oxide (GO): Graphene oxide (GO) was synthesized following the Improved Hummer's method. First, the graphite powder and KMnO₄ were well mixed in a ratio of 1:6 with the help of a mortar and pestle. The obtained homogeneous solid mixture was slowly transformed into the round bottle (RB) flask kept under the ice bath environment containing the H₃PO₄:H₂SO₄ (1:9) solution mixture. The temperature of the reaction mixture was then increased to 60 °C and, under this condition, the mixture was kept for stirring for 12 h. After the complete reaction, the resulting solution was kept to cool at room temperature. The resultant viscous product was slowly poured into a beaker containing 3% H₂O₂ mixed with ice-cold water. A yellowish solution was formed, which was rinsed with distilled water several times and centrifuged at 10000 rpm for 10 min. After the centrifugation multiple times, the obtained solid residue was mixed with 30 % HCl to dissolve any metal impurities, followed by washing with water multiple times to minimize the acidic pH and also to remove any impurities present in the final product. The finally obtained dark chocolate-colored highly viscous residue was rinsed with ethanol followed by diethyl ether, and kept at 40 °C to produce the GO flakes.

5.2.3. Synthesis of Nitrogen-Doped Entangled Graphene (NEGF): To synthesize NEGF, 90 mg of GO was added to 30 ml of aqueous ammonia solution (30 % v/v) with the help of water-bath sonication followed by 12 h constant stirring. The obtained GO suspension was transformed into a Teflon-lined autoclave and kept for solvothermal treatment at 180 °C for 12 h followed by naturally cooling down to room temperature. The autoclave was opened and the obtained product was washed with DI water for 5-

6 times to discard any unreacted ammonia present; the residue was freeze-dried at $-52\text{ }^{\circ}\text{C}$ under high vacuum conditions. The applied vacuum slowly removes the water content in the system; thus formed solid residue is named as N-doped entangled graphene framework (NEGF).

5.2.4. Synthesis of Nitrogen-Doped Porous Entangled Graphene (pNEGF): To synthesize pNEGF, the as-synthesized NEGF powder was microwave (600 W) treated for 3 min. with 6 cycles of 30 sec. ON and 2 min. OFF. The obtained product possesses a different texture from the NEGF and has been named as pNEGF.

5.2.5. Synthesis of Pt₃Co Supported N-doped Entangled 3D Graphene (Pt₃Co/pNEGF): For the synthesis of Pt₃Co/NEGF, pNEGF was dispersed in ethylene glycol and kept the mixture for stirring at room temperature ($30\text{ }^{\circ}\text{C}$) for 12 h. After the complete dispersion of pNEGF, the solution becomes a black-colored suspension. The acetate salts of Pt and Co, *i.e.*, Pt(acac)₂.4H₂O and Co(acac)₂.4H₂O, in (3:1) ratio were added in the above suspension and kept in the mixture for constant stirring for another 12 h. After the complete mixing of the metal ions over pNEGF, the reaction temperature was raised to $180\text{ }^{\circ}\text{C}$ and kept under reflux for 10 h. Subsequently, the residue was filtered out and dried at $60\text{ }^{\circ}\text{C}$ in the oven for 12 h. The black-colored flaky structure of the material obtained after the drying is named as Pt₃Co/pNEGF. For the comparison purpose, Pt/pNEGF has also been prepared as a control sample by following the same method but without adding Co to the reaction mixture. Also, to check the contributions of only the mesoporous support system, Pt₃Co/NEGF was synthesized using the same method as used for Pt₃Co/pNEGF by replacing pNEGF with NEGF as the support.

5.2.6. Physical Characterization: The microstructure of the catalysts was investigated with the help of FESEM and X-ray tomography. The FESEM analyses were carried out by the FEI Nova Nano SEM 450 FESEM microscope. The samples for FESEM were prepared by the thin coating of the isopropyl alcohol (IPA) dispersed sample (5 mg of the sample in 5 mg IPA) on a silicon wafer. Furthermore, the samples were dried for 1 h under an IR lamp to remove IPA. The 3D carbon structures of the prepared catalysts were imaged by X-ray microtomography (Xradia 510 Versa X-ray Microscope, Zeiss, Pleasanton, CA, USA) to study their porous structure and morphology. The samples were filled into the sample holder and kept in between the detector and X-ray source. To generate the volume-rendered 3D images of the samples, the image processing software Dragonfly Pro (Version 3.6) was used.² The HRTEM images were recorded using a JEOL JEM F-200 HRTEM instrument with a point-to-point resolution of 0.19 nm. The samples for HRTEM were prepared by drop coating the well-dispersed sample in isopropyl alcohol

(1.0 mg of the sample in 5 mL solvent) on a carbon-coated 200 mesh copper grid. The sample-coated TEM and HRTEM grid were dried for 1 h under an IR lamp. To check the crystal structure of the as-synthesized samples, powder X-ray diffraction (PXRD) analysis was done. The XRD investigation was carried out on a Rigaku Smart Lab diffractometer with Cu K α radiation ($\lambda = 1.5406 \text{ \AA}$) in the 2θ range of 10 to 80° with a scan rate of 5° min⁻¹. The nitrogen (N₂) adsorption-desorption isotherm experiments were performed on a Quantachrome-Quadrasorb automatic volumetric instrument to analyze the surface area and pore volume of the samples. The XPS measurement was performed using a fully integrated, monochromatic small spot XPS system. It is specified with an X-ray monochromator source by the 180° double-focusing hemispherical analyzer-128-channel detector and micro-focused Al K α . Raman spectral interpretation was carried out using a 632 nm green laser (NRS 1500W) on an HR 800 RAMAN spectrometer. The thermal stability of the carbon support and the loading of the active component over the carbon were measured using an SDT Q600 DSC-TDA thermo-gravimetric (TG) instrument at room temperature to 900 °C at a constant heating rate of 10 °C min⁻¹ under an oxygen atmosphere.

5.2.7. Rotating Disk Electrode Study (RDE): The electrochemical experiments were performed with the help of the hydrodynamic technique method such as a rotating disc electrode (RDE) made of glassy carbon (0.196 cm²) connected with a Pine Instrument for the rotation of the electrodes. A three-electrode electrochemical cell was used for the electrochemical measurements with the catalyst-coated glassy carbon as the working electrode, a graphite rod (Alfa Aesar, 99.99%), and Hg/HgSO₄ as the counter and reference electrodes, respectively. The electrochemical cell was connected with an SP-300 model BioLogic potentiostat. The working electrode was polished with 0.3 μm alumina slurry and washed with DI-water, followed by the final cleaning with DI-water and acetone. Subsequently, 10 μL of the catalyst slurry was drop-casted on the surface of the working electrode, which was then dried under an IR-lamp for 1 h. The electrochemical ORR performance was measured in an aqueous solution of 0.1 M HClO₄. All the experimental electrode potentials obtained using the Ag/AgCl reference electrode were converted into the reversible hydrogen electrode (RHE) through a calibration experiment, which was previously done in our lab.

5.2.8. Rotating Ring-Disk Electrode Study (RRDE): For the RRDE analysis, the catalyst-coated disc electrode was scanned at a scan rate of 10 mV s⁻¹ by maintaining the electrode at a rotation rate of 1600 RPM. The potential of the electrode was kept fixed at 0.40 V vs. Ag/AgCl. A K₃Fe(CN)₆ solution was used to evaluate the H₂O₂ collection efficiency (N) at the ring electrode, which was 0.37.²³ The calculation

of H₂O₂ % and the number of electron transfer (n) during ORR was carried out by following the equations below:

$$\% \text{ peroxide} = (200 \times I_R \times N) / (I_D + I_R / N)$$

$$n = 4 \times I_D / (I_D + I_R / N)$$

where,

N = H₂O₂ collection efficiency of the ring electrode

I_D = Faradaic current at the disk electrode

I_R = Faradaic current at the ring electrode

All the experiments were carried out at room temperature.

5.2.9. The Ag/AgCl reference electrode calibration and conversion to RHE:

The Ag/AgCl electrode was calibrated by using using a conventional 3-electrode system employing an RDE electrode as the working electrode (WE), a graphite rod as the counter electrode (CE), and as the reference electrode (RE). The Ag/AgCl was used under an H₂-saturated 0.1 M HClO₄ electrolyte solution.⁴ Hence, for the conversion of the voltage recorded with respect to Ag/AgCl to the RHE scale, the following equation is used:

$$E \text{ (RHE)} = E \text{ (Ag/AgCl)} + 0.3 \text{ V} \dots\dots\dots 1$$

5.3. Results and Discussion:

Figure 5.1 illustrates schematically the synthesis procedure of the Pt₃Co/pNEGF catalyst. The N-doped microporous graphene (pNEGF) was synthesized by microwave irradiation of NEGF. The microwave irradiation of NEGF in the air atmosphere involves quick oxidation of the carbon to CO₂ with concomitant oxidation of some of the doped nitrogen to NO_x. These processes create nanopores in the NEGF framework. The generated pNEGF was employed as a support for the growth of the Pt₃Co nanoparticles. The presence of the fine porosity and uniformly doped nitrogen in the microwave-induced 3D graphene helps the homogeneous dispersion of the positively charged metal ions through electrostatic interactions during the mixing process. During the polyol synthesis process at 160 °C, the Pt and Co ions nucleate on the doped-N and the defective carbon centers mainly at the pore openings, resulting in the uniform growth

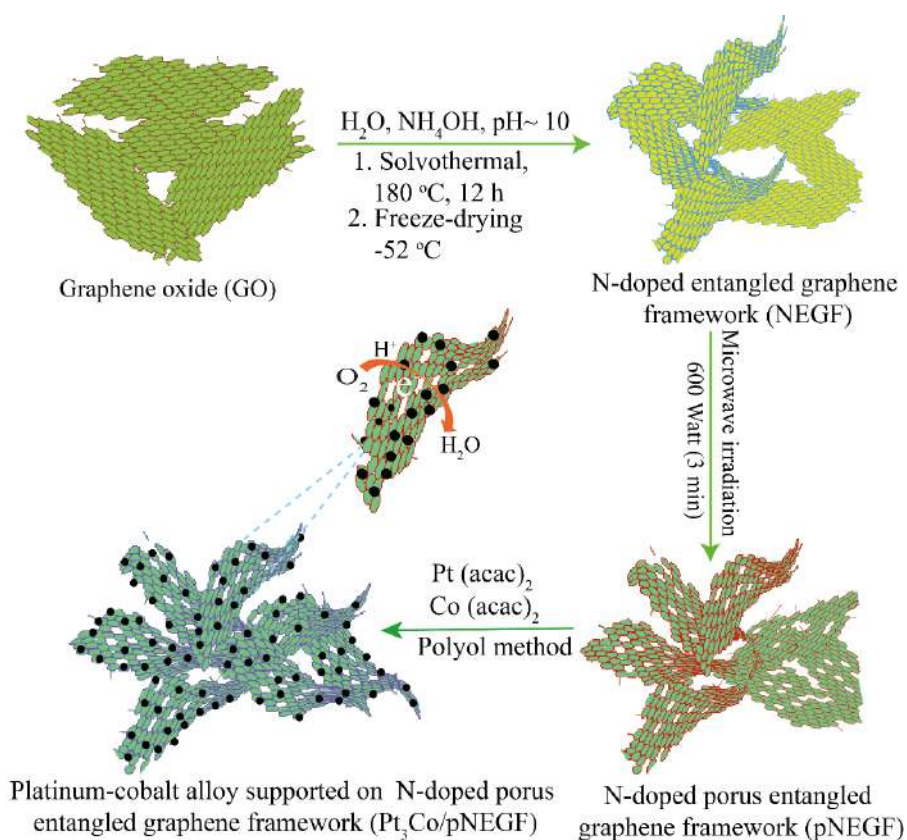


Figure 5.1. A schematic representation illustrating the synthesis of the nitrogen-doped 3D entangled graphene (NEGF) followed by the microwave-assisted synthesis of nitrogen-doped 3D porous graphene (pNEGF) and subsequently the Pt₃Co-dispersed catalyst, Pt₃Co/pNEGF, by the polyol method.

of the small-sized and spherically shaped alloy (Pt₃Co) nanoparticles over the surface of pNEGF (designated as Pt₃Co/pNEGF). The pNEGF with its well-defined structure, porosity, and composition served as an active substrate, which induces favorable electronic structural modulations of the sub-nanometer-sized Pt₃Co particles. In addition, the 3D porous architectures of the conducting support (pNEGF) in the catalyst offer an open and exposed morphology that provides high surface area and accessible porous architecture to the catalytic sites.

5.3.1. FESEM Analysis:

The morphological analysis of NEGF, pNEGF, and Pt₃Co/pNEGF has been performed by field emission scanning electron microscopy (FESEM). **Figure 5.2a** shows a 3D self-assembly structure of NEGF, formed by the interconnected sheet of the graphene during the hydrothermal treatment of GO followed by the freeze-drying. The freeze-drying method played an important role in establishing the 3D structure

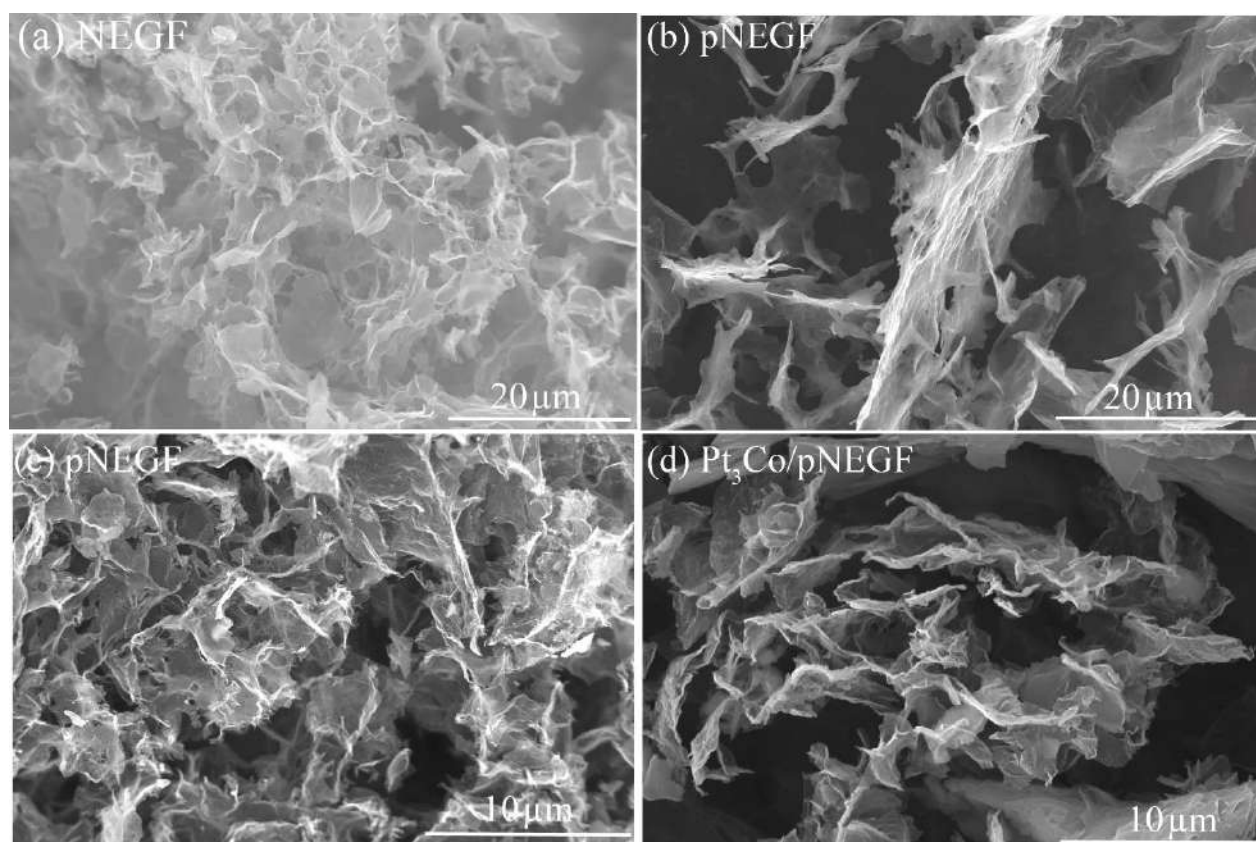


Figure 5.2. (a) The FESEM image of NEGF, demonstrating the 3D porous self-assembly architecture of the graphene sheets; (b) and (c) the FESEM images of the microwave-assistant synthesis of pNEGF, representing the exfoliated 3D porous architecture of the graphene sheets; (d) the FESEM image of Pt₃Co/pNEGF, displaying the porous structure of the catalyst originated by the exfoliated and interconnected morphology of the pNEGF substrate.

of NEGF. After the microwave irradiation of NEGF, the morphological image presented in **Figures 5.2b**, and **c** shows the exfoliated structure of the nitrogen-doped 3D graphene (pNEGF). The generated exfoliated structure formed by microwave treatment and the modified texture of the pNEGF is expected to improve the mass transport properties as compared to NEGF. The incorporation of Pt₃Co over pNEGF was performed through the polyol method, which resulted in Pt₃Co/pNEGF and retaining the same structural alignment as the bare pNEGF with its porous architecture, as shown in **Figure 5.3d**.

5.3.2. Micro-Computed Tomography Analysis:

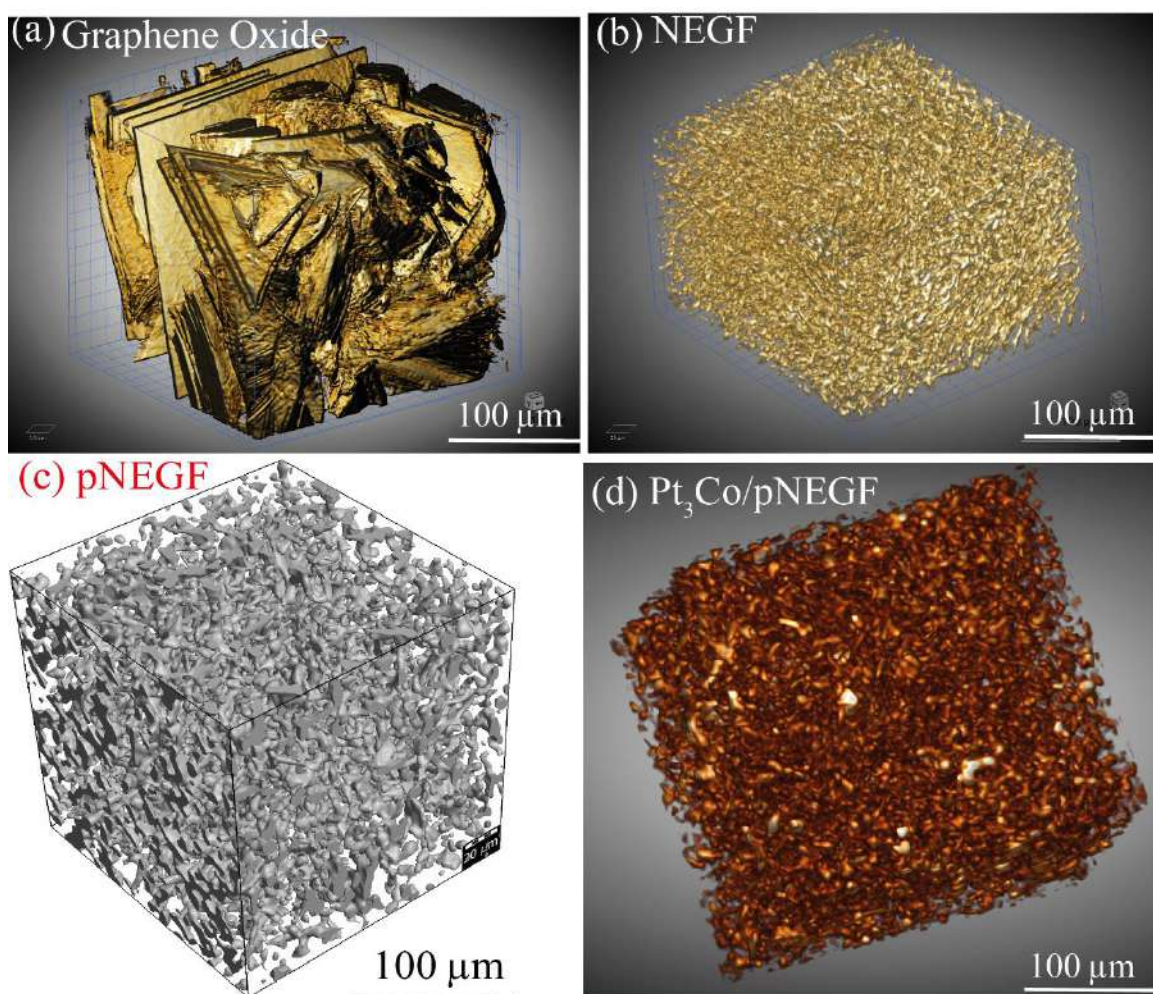


Figure 5.3. (a) The tomography image of GO represents the randomly distributed and stacked structure of the graphene sheets; (b) the tomography image of NEGF reveals the self-assembly porous structure of the graphene; (c) the 3D micro-CT image of pNEGF, displaying the existence of the well-defined porous architecture of pNEGF, after the microwave heat treatment; (d) the 3D micro-CT image of Pt₃Co/pNEGF, displaying the existence of the well-defined porous architecture of the 3D pNEGF.

The X-ray micro-CT imaging was performed to understand the 3D microstructural details of the substrate and the final electrocatalyst. The volume-rendered 3D micro-computed tomography (CT) images are presented in **Figure 5.3**. The micro-CT images displayed in **Figure 5.3a** clearly show the stacked structure of the randomly distributed GO sheets. **Figure 5.3b** represents the image of NEGF synthesized by the hydrothermal treatment followed by the freeze-drying process, which clearly reveals the presence of the well-defined porous architecture of the self-assembled graphene. The microwave irradiated NEGF shows

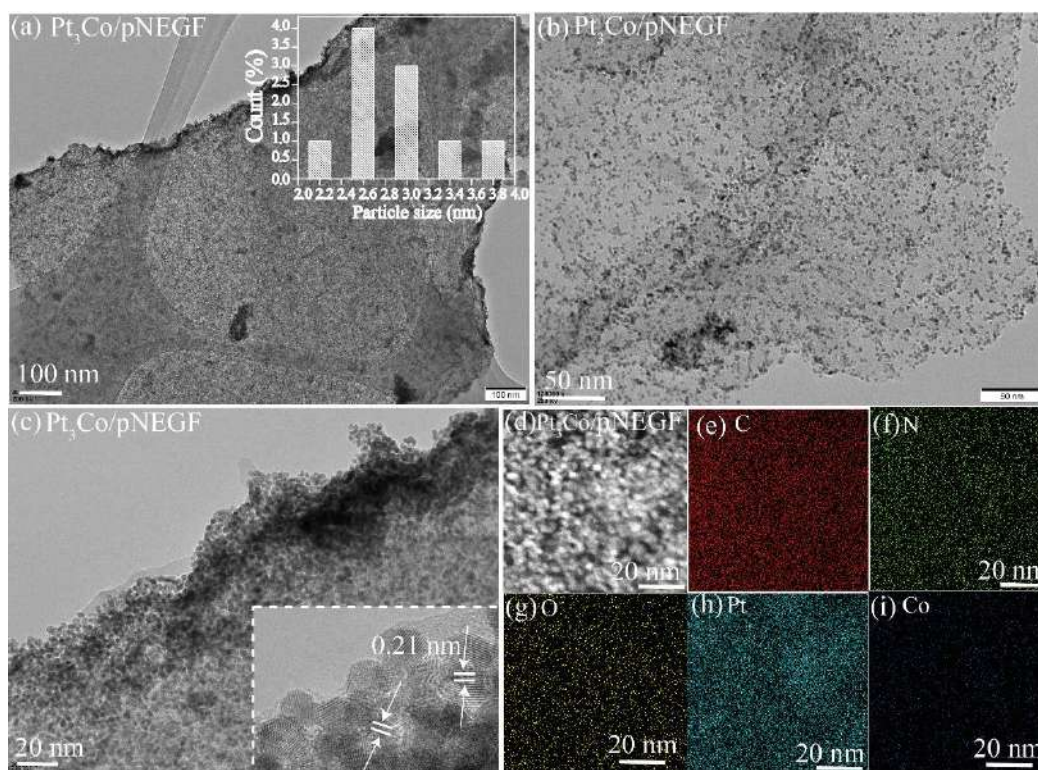


Figure 5.4. (a) HRTEM image of $\text{Pt}_3\text{Co}/\text{pNEGF}$, displaying the uniform distribution of Pt_3Co over 3D pNEGF (inset of (a) representing the size distribution histogram of the Pt_3Co nanoparticles); (b) and (c) the magnified HRTEM images of $\text{Pt}_3\text{Co}/\text{pNEGF}$ recorded at the surface and edge (inset of (c) representing the d-spacing for the Pt_3Co crystal structure); (d) the 3D structure of the graphene displaying the uniform dispersion of the Pt_3Co nanoparticles (the inset image in (c) clearly displays the d-spacing for Pt_3Co along with its crystalline nature; the HRTEM image of $\text{Pt}_3\text{Co}/\text{pNEGF}$ (d), and the corresponding elemental mapping of C (e), N (f), O (g), Pt (h), N and Co (i) done on $\text{Pt}_3\text{Co}/3\text{D pNEGF}$.

the retention of a similar porous structure as shown in **Figure 5.3c**. **Figure 5.3d** shows the similar observed structural features after incorporating Pt_3Co over pNEGF.

5.3.3. HRTEM Analyses:

A more insightful information on the nature of the distribution profile of Pt_3Co on pNEGF has been gained with the help of the high-resolution transmission electron microscopy (HR-TEM). The image presented in **Figure 5.4a** shows the fine distribution of the Pt_3Co nanoparticles on pNEGF. The inset image presented in **Figure 5.4a** represents the size distribution histogram of the Pt_3Co nanoparticles, indicating the dominant size distribution in the range of 2-3 nm. The controlled size distribution of the Pt_3Co

nanoparticles without agglomeration shows the advantage of the developed synthesis strategy. The magnified images shown in **Figures 5.4b** (on the surface) and **c** (along the edge) of the 3D graphene substantiate the previous observation that the Pt₃Co nanoparticles are uniformly distributed throughout the substrate, including its surface and the edges. These results highlight that the microwave irradiation of NEGF plays an effective role in creating the uniform nucleation sites on the substrate, leading to the controlled dispersion and distribution of the Pt₃Co nanoparticles within a size range predominantly of 2 to 3 nm. This controlled distribution of the Pt₃Co nanoparticles over the surface and the edge of the graphene mediated by the defect sites and the doped sites of the heteroatom (N) is an important structural benefit to the system as this can reduce the chances of self-agglomeration of the nanoparticles under the triggered conditions of the electrochemical environments.³⁶ In addition, the fine distribution of the active sites at the edges of the graphene layers of its 3D framework is expected to provide better reactant accessibility due to their relatively exposed nature in the catalyst framework.²⁶ The inset image in **Figure 5.4c** shows that the lattice fringe widths (d-spacing) of the Pt₃Co nanocrystal are 0.21 and 0.20 nm, which are attributed to the (111) and (200) facets, respectively, implying the formation of the fcc structure of the Pt₃Co crystal.³⁷ **Figure 5.4d** displays the HRTEM image of Pt₃Co/pNEGF, and the corresponding elemental mapping data for the respective elements are presented in **Figure 5.4e-i**. The elemental mapping images show the presence and distribution of Pt, Co, O, C, and N, corresponding to the selected composition of the catalyst. Additionally, the Pt₃Co stoichiometric composition is evidenced by the existence of Pt and Co together in the same position, as well as the observed close triple intensity of the Pt with respect to Co.

5.3.4. Surface Area and Pore Size Analyses:

The comparative pore size distribution profiles of NEGF, pNEGF, and Pt₃Co/pNEGF shown in **Figure 5.5a** suggest that the porosity for NEGF is mostly distributed in the region of 2-20 nm, indicating the presence of mesoporosity. However, after the microwave irradiation over NEGF, the transformed pNEGF shows the distribution of the pores in the range of 0-20 nm, which is ascribed to the micro-mesoporous nature of the material. Similarly, after the decoration of the 2-3 nm-sized Pt₃Co nanoparticles (Pt₃Co/pNEGF), a more or less similar porosity distribution profile (0-20 nm) is observed for the sample in **Figure 5.5a**. The retention of the porosity after the Pt₃Co dispersion is reflected in the BET surface area as well and these observations are in well-agreement with the tomography porosity distribution analysis data. The surface areas of NEGF and pNEGF are found to be 550 and 680 m² g⁻¹, respectively. The higher surface area of pNEGF is ascribed to the increased contribution of the micropores present in

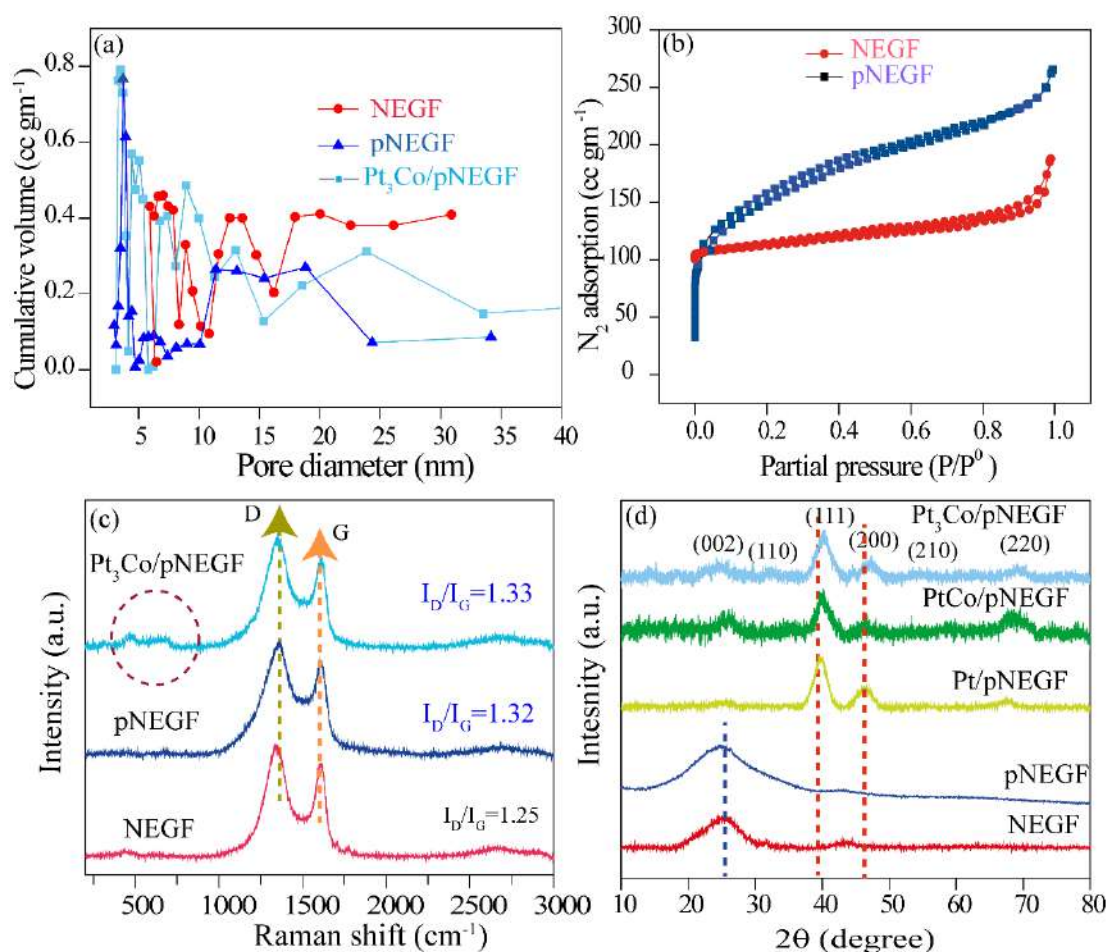


Figure 5.5. (a) The comparative pore size distribution profiles of NEGF, pNEGF, and Pt₃Co/pNEGF, indicating the mesoporous nature of NEGF and the presence of micro- and mesoporous regions for pNEGF (2-20 nm) and Pt₃Co/pNEGF (0 to 20 nm); (b) comparative BET adsorption isotherms for NEGF and pNEGF; (c) comparative Raman spectra recorded for NEGF, pNEGF, and Pt₃Co/pNEGF; (d) the XRD profiles recorded for NEGF, pNEGF, Pt/pNEGF, PtCo/pNEGF, and Pt₃Co/pNEGF.

the system. Both the systems (NEGF and pNEGF) displayed Type-IV isotherms (**Figure 5.5b**). Interestingly, **Figure 5.5b** reveals the higher N₂ uptake capacity of pNEGF compared to NEGF, which supports the presence of extra porosity in the system. The higher surface area of pNEGF, combined with its significant porous structure, is a distinguishing benefit of the system as an electrocatalyst, allowing for effective utilization of the active sites by establishing better active triple-phase-boundary (TPB) during the electrochemical ORR process.

5.3.5. Raman Analysis:

The Raman spectroscopic investigation has been performed to understand the extent of the graphitic and defective nature in the porous carbon systems. The intensity of the defective and graphitic peak (I_D/I_G) ratio points toward the extent of the defects created or present in the carbon systems. **Figure 5.5c** shows the comparative Raman spectra of NEGF, pNEGF, and Pt₃Co/pNEGF. The peaks that appeared at 1350 and 1590 cm^{-1} are credited to the G and D bands, respectively.²⁷ In the case of NEGF and pNEGF, the measured I_D/I_G ratios are 1.25, and 1.32, respectively. The increased I_D/I_G value reported for pNEGF points toward the creation of new defect sites during the microwave irradiation. During the microwave heat treatment, some of the carbon and nitrogen species are oxidized to CO_2 , and NO_x respectively, and create additional porosity in NEGF which is evidenced as defects in the Raman spectrum. After incorporating Pt₃Co over pNEGF, the I_D/I_G ratio becomes 1.33, which is almost comparable to its counterpart pNEGF. A small change in the I_D/I_G ratio for Pt₃Co/pNEGF is expected to be due to the lattice stress created during the growth of the metal alloy particles over the N-doped graphene during the polyol method at 180 °C.⁵¹

5.3.6. XRD Analysis:

The comparative X-ray diffraction (XRD) profiles of NEGF, pNEGF, Pt/pNEGF, PtCo/pNEGF, and Pt₃Co/pNEGF are shown in **Figure 5.5d**. The XRD spectrum of NEGF displays broad diffraction peaks at the 2θ values of 26 and 43°, which are attributed to the (002) and (100) graphitic diffraction planes, respectively.³⁸ Similar peak features are observed in the case of the microwave irradiated sample, *i.e.* pNEGF, with a more broad appearance and negative shift in the 2θ value. The shift in the 2θ value is ascribed to the change in the d-spacing created by the microwave exfoliation of the graphene sheets. The XRD profile of Pt/pNEGF displays three diffraction peaks at the 2θ values of 39.76°, 46.24°, and 67.45°, corresponding to the (111), (200), and (220) planes of the Pt metal with an fcc structure. However, with the Co incorporation into Pt, the resulting PtCo/pNEGF and Pt₃Co/pNEGF show a shift in the positions of the (111) and (200) peaks.^{39, 40} The observed XRD peak shift for PtCo/pNEGF and Pt₃Co/pNEGF (39.8°) is due to the contraction of the Pt lattice after the alloy formation.³⁸ Moreover, the alloy structure has been confirmed with the standard JCPDS cards of the Pt₃Co alloy phase (JSPDS No: 29-0499).⁴¹ The formation of the alloy structure with a significant change in the 2θ value alters the fcc crystal structure and the binding energy with oxygen as an intermediate species during the ORR process.

5.3.7. XPS Analysis:

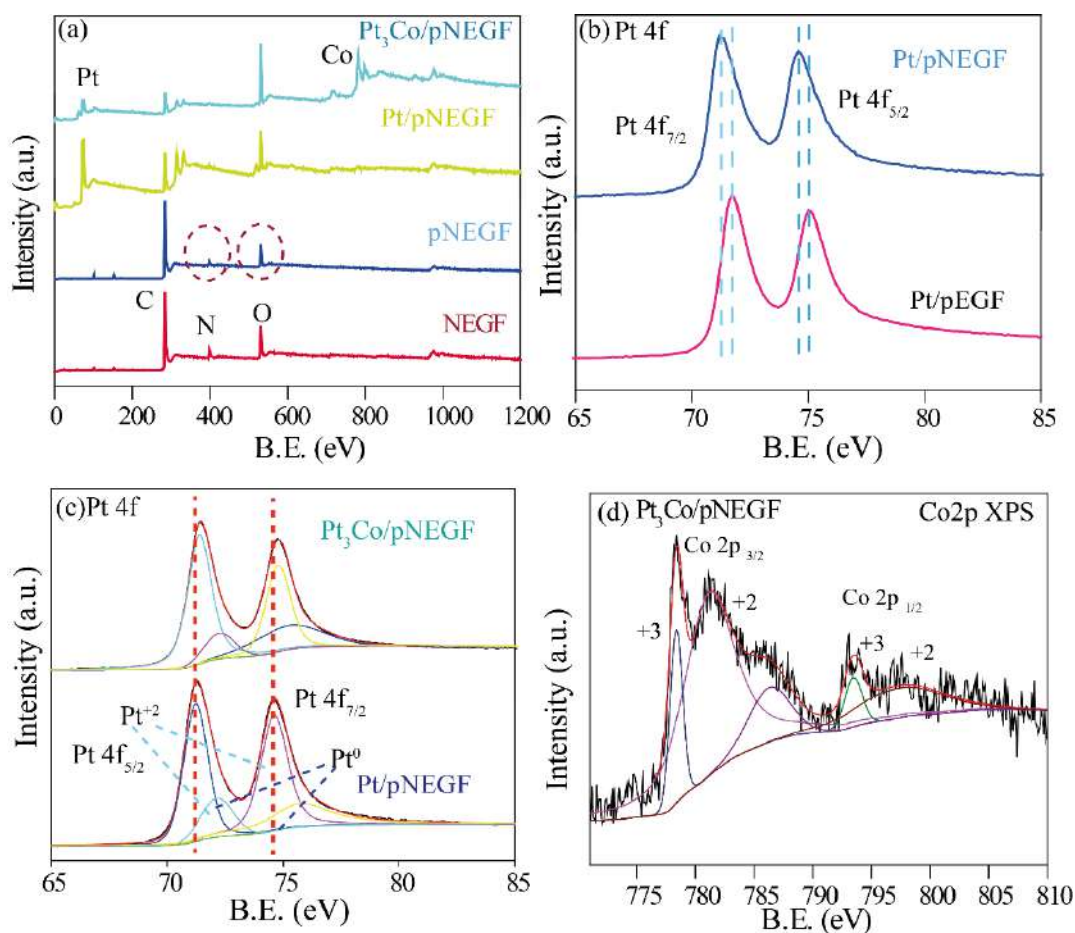


Figure 5.6. (a) The XPS survey spectra of NEGF, pNEGF, Pt/pNEGF, and Pt₃Co/pNEGF; (b) the comparative Pt 4f XPS spectra of Pt/pEGF and Pt/pNEGF, revealing the peak shift after the incorporation of N into the porous graphene support system; (c) the comparative Pt 4f spectra of Pt/pNEGF, and Pt₃Co/pNEGF, suggesting the binding energy shift after the Co incorporating into the Pt; (d) the deconvoluted Co 2p spectra of Pt₃Co/pNEGF revealing the presence of Co in +2 and +3 oxidation states.

The X-ray photoelectron spectral (XPS) analysis has been performed to analyze the elements and the chemical nature of the prepared catalysts; the corresponding data are presented in **Figure 5.6**. The comparative XPS survey scan spectra of NEGF, pNEGF, Pt/pEGF (entangled graphene framework, without nitrogen-doped), Pt/pNEGF, PtCo/pNEGF, and Pt₃Co/pNEGF are presented in **Figure 5.6a**, confirm the presence of Pt, Co, O, N, and C in the respective materials. The survey scan spectrum of pNEGF obtained through the microwave irradiation shows that the peak intensity of N 1s and O 1s has been suppressed as compared to NEGF. The comparative Pt 4f XPS peaks for the nitrogen-doped and without nitrogen-doped porous graphene supported Pt system are shown in **Figure 5.6b**. **Figure 5.6b** displays two doublet peaks of Pt 4f_{7/2} and Pt 4f_{5/2} for the Pt 4f spectrum at 72.6 and 74.3 eV for Pt/pEGF

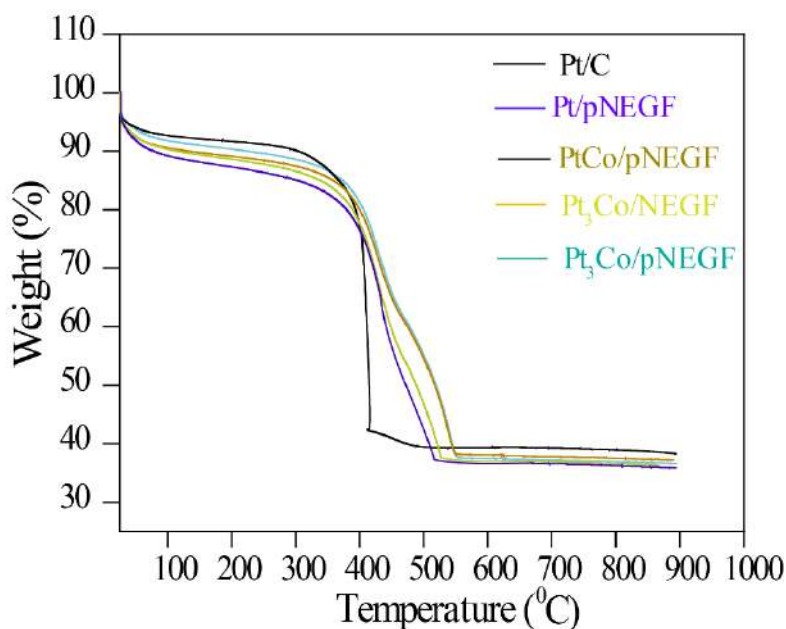


Figure 5.7. The TGA profiles recorded for Pt/pNEGF, PtCo/pNEGF, Pt₃Co/NEGF, Pt₃Co/pNEGF, and Pt/C.

and at 72.4 and 74.1 eV for Pt/pNEGF. The observed Pt 4f peak shift for Pt/pNEGF towards the negative value compared to Pt/pEGF points towards the role of the doped-N towards the anchoring of the Pt₃Co resulting from the electronic interaction between them. The shift in the binding energy value is ascribed to the charge transfer from the nitrogen to platinum, which improves the interaction between Pt₃Co and the doped-N of pNEGF.¹⁶ Furthermore, the deconvoluted spectra of Pt₃Co/pNGr suggest the two spin-orbit split doublets of Pt 4f_{7/2} and 4f_{5/2} present in the zero-valent metallic state, which produces the two main peaks with binding energies of 71.12 and 74.58 eV, respectively. The peaks at 72.16 and 75.55 eV reveal the existence of Pt in the +2 oxidation state.^{16, 44} The binding energy comparison (**Figure 5.6c**) of the Pt 4f peaks ensures the positive shift in the B.E of Pt₃Co/pNEGF compared to Pt/NEGF due to the charge transfer from Pt to Co.⁴³ This shift in B.E after the Co incorporation into the Pt lattice structure supports the formation of the bimetallic (Pt₃Co) alloy structure. Investigation of the Co 2p deconvoluted spectra shown in **Figure 5.6d** evidenced the two spin-spin coupling peaks at the B.E. of 784.2 and 795.5 eV, for Co 2p_{3/2} and 783.5 and 796.5 eV for Co 2p_{1/2}.^{5, 45} This confirms the existence of Co in +2 and +3 oxidation states in the system. The higher oxidation state of Co in Pt₃Co/pNEGF supports the previous finding of the charge transfer from the Pt to the Co metal.²⁶

5.3.7. TGA Analysis:

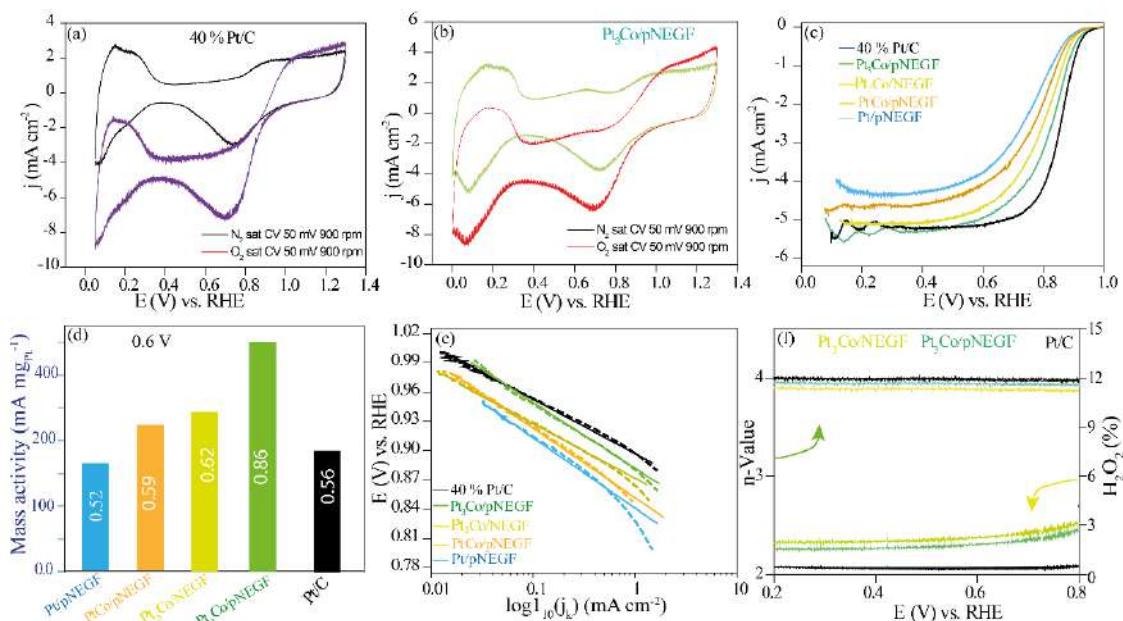


Figure 5.8. (a)-(b) The comparative CV profiles recorded for Pt₃Co/pNEGF, and Pt/C in O₂ and N₂ saturated 0.1 M HClO₄ solution at 900 rpm of the WE; (c) the comparative LSV profiles recorded for Pt/pNEGF, PtCo/pNEGF, Pt₃Co/NEGF, Pt₃Co/pNEGF and Pt/C towards ORR in O₂ saturated 0.1 M HClO₄ at 1600 rpm of the WE; (d) the bar chart comparing the mass activities as extracted from the limiting current density of the LSV profile for Pt/pNEGF, PtCo/pNEGF, Pt₃Co/NEGF, Pt₃Co/pNEGF, and Pt/C; (e) the comparison of the Tafel slopes extracted from the LSV profiles recorded by the systems towards ORR; (f) the amount of H₂O₂ formed (%) and the corresponding electron transfer number (n-value) calculated for Pt/pNEGF, PtCo/pNEGF, Pt₃Co/NEGF, Pt₃Co/pNEGF, and Pt/C.

The weight % of the loaded metal catalytic active centers over the carbon has been determined by the thermogravimetric analysis (TGA). **Figure 5.7**, shows the comparative TGA weight loss profile for Pt/pNEGF, PtCo/pNEGF, Pt₃Co/NEGF, Pt₃Co/pNEGF, and Pt/C. After the complete oxidation of the carbon and nitrogen from the N-doped carbon support (pNEGF) in the system (Pt₃Co/NEGF), the residue content is found to be ~40 wt. % for all the catalyst systems.

5.3.8. Electrochemical Analysis:

The ORR performance of the synthesized catalysts has been probed with the help of a set of electrochemical techniques. A three-electrode electrochemical cell, with the catalyst slurry-coated glassy carbon electrode (GCE) as a working electrode (WE), graphite rod, and Ag/AgCl as the counter electrode (CE) and reference electrode (RE), respectively, was employed for performing the single-electrode

studies. The recorded potential against Ag/AgCl was converted to the RHE scale with the conventional method. The electrochemical ORR performance of all the prepared and the *state-of-the-art* catalysts has been evaluated by rotating disk electrode (RDE) studies in 0.1 M HClO₄ solution. **Figures 5.8a** and **b** show the cyclic voltammograms recorded for Pt₃Co/pNEGF and Pt/C, respectively, in the N₂ and O₂ saturated atmosphere. A similar redox peak feature has been observed in both the cases. The redox peaks that appeared between the potential ranges of 0.0 to 0.20 V correspond to the hydrogen adsorption and desorption happening at the Pt surface. The ECSA was calculated in the hydrogen adsorption and desorption region from the N₂ saturated CVs of the samples. Pt₃Co/pNEGF and Pt/C show the ECSA value of 52, and 69 m² gPt⁻¹, respectively.

The intrinsic ORR activity characteristics of the catalysts have been investigated by recording the LSV profiles in N₂/O₂ saturated 0.1 M HClO₄ at the voltage scan rate of 10 mV sec⁻¹ by maintaining the working electrode rotation at 1600 RPM. The comparative linear sweep voltammograms presented in **Figure 5.8c** show a significantly improved onset potential (0.93 V) for Pt₃Co/pNEGF compared to the other control samples, *i.e.*, Pt/pNEGF (0.88 V), PtCo/pNEGF (0.89), and Pt₃Co/NEGF (0.90 V). The onset potential for Pt₃Co/pNEGF is comparable to that of Pt/C (0.94 V) and higher than that of Pt/pNEGF (0.89 V), signifying the importance of the bimetallic alloy of Pt and Co. Furthermore, a higher onset potential for Pt₃Co/pNEGF as compared to PtCo/pNEGF suggests the importance of maintaining the stoichiometric composition of the catalysts with distinct alloy phases. A well-defined stoichiometry of Pt and Co is creating strain in the Pt₃Co lattice structure during the alloy phase formation with a concomitant electronic modulation favoring the surface oxygen and intermediate adsorption energy during the ORR process. In addition, the half-wave (E_{1/2}) potential for the catalysts has been calculated for all the catalysts from the respective LSV profiles. The observed E_{1/2} values for Pt/pNEGF, PtCo/pNEGF, Pt₃Co/NEGF, Pt₃Co/pNEGF, and Pt/C are 0.71, 0.73, 0.76, 0.77 and 0.81 V, respectively. The significantly improved E_{1/2} value for Pt₃Co/pNEGF compared to Pt₃Co/NEGF is expected to be originated from the structural advantage of having the better porous texture of the microwave irradiated substrate in the case of Pt₃Co/pNEGF.

The comparative mass activity plot presented in **Figure 5.8d** shows that Pt₃Co/pNEGF has 1.5 times higher mass activity compared to 40% Pt/C, based on the quantification made at 0.60 V. This higher mass activity of Pt₃Co/pNEGF suggests the better synergistic interaction between Pt₃Co and the N-doped microporous 3D support. Further insight into the ORR kinetics has been achieved from the Tafel slope data presented in **Figure 5.8e**. The measured Tafel slope values of the catalysts follow the order:

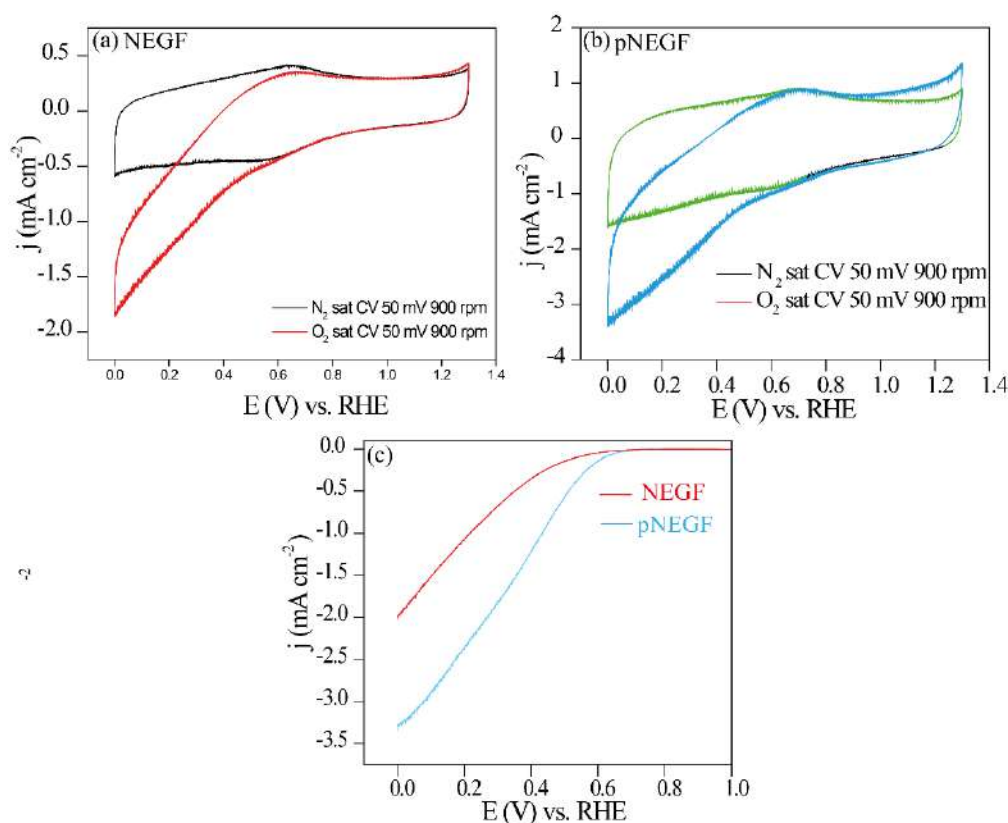


Figure 5.9. (a) - (b) The comparative CV profiles recorded for NEGF and pNEGF in O_2 and N_2 saturated 0.1 M HClO_4 at 900 rpm of the WE; (c) the comparative LSV profiles recorded for NEGF and pNEGF in O_2 saturated 0.1 M HClO_4 at 1600 rpm of the WE.

Pt/pNEGF (72 mV dec^{-1}) > PtCo/pNEGF (68 mV dec^{-1}) > $\text{Pt}_3\text{Co/NEGF}$ (67 mV dec^{-1}) > $\text{Pt}_3\text{Co/pNEGF}$ (64 mV dec^{-1}) > Pt/C (62 mV dec^{-1}). The lower Tafel slope values for $\text{Pt}_3\text{Co/pNEGF}$ as compared to Pt/pNEGF and PtCo/pNEGF suggest better feasibility of ORR on this system. The observed trend of the Tafel slope also suggests the role played by the Co incorporation into the Pt lattices by enabling the catalyst to perform more effectively towards the ORR process.

To know the mechanism of the electrochemical ORR process, RRDE analysis was performed in 0.1 M HClO_4 . The obtained H_2O_2 % generated during the ORR cycle was investigated and quantified as shown in **Figure 5.8f**. The recorded amount of H_2O_2 during the catalytic ORR process is found to be less than 4% for $\text{Pt}_3\text{Co/pNEGF}$, which is comparable to that recorded on Pt/C (~2 %). The result reveals that, like Pt/C , $\text{Pt}_3\text{Co/pNEGF}$ also promotes the direct 4e- transfer process for the reduction of oxygen. The amount of H_2O_2 calculated for $\text{Pt}_3\text{Co/NEGF}$ is 6 %, which is slightly higher than that of $\text{Pt}_3\text{Co/pNEGF}$. Further, the number of electrons involved (n-value) in the reduction process has also been estimated, and the values

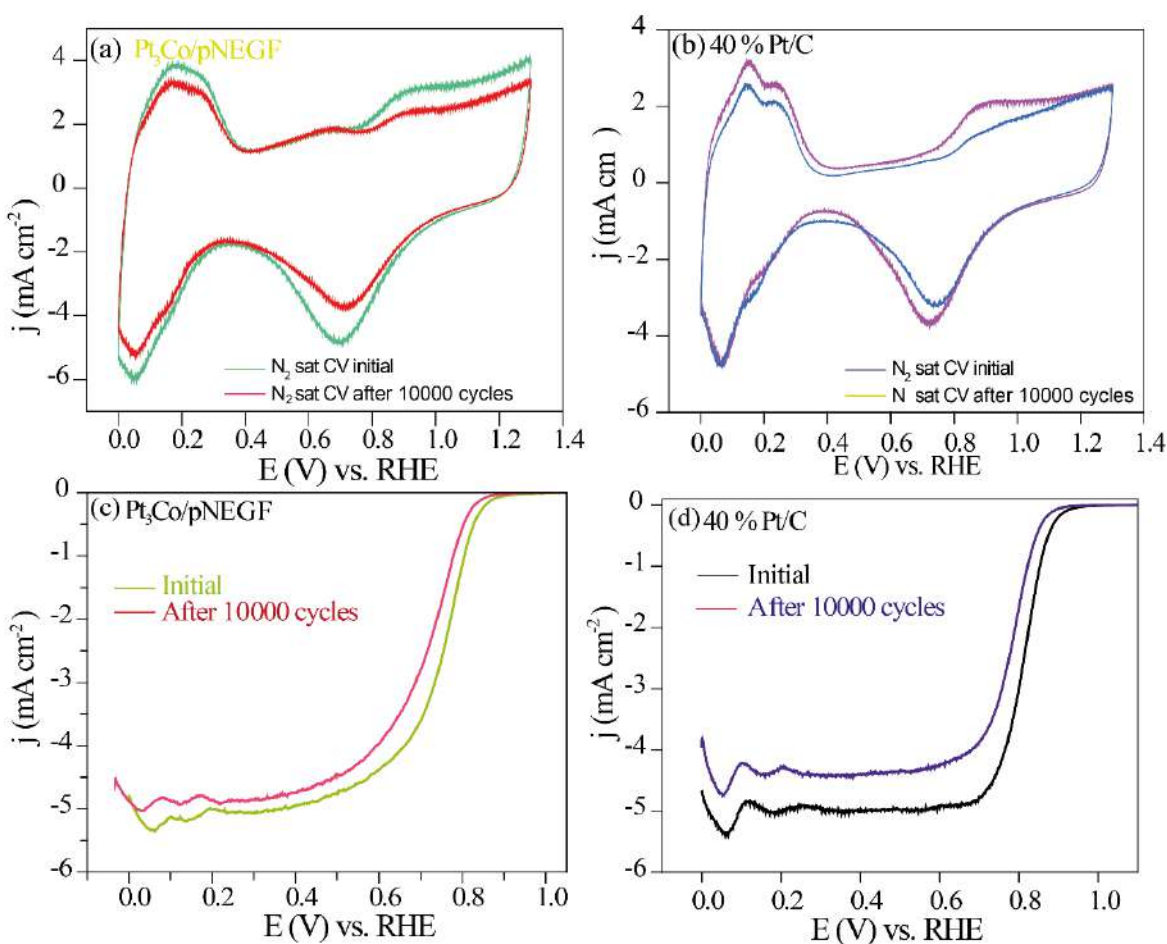


Figure-5.10. The comparative CV profiles recorded for Pt₃Co/pNEGF (a), and Pt/C (b) towards ORR in O₂ saturated 0.1 M HClO₄ at 1600 rpm of the WE before and after the 10000 cycles; the comparative LSV profiles recorded for Pt₃Co/NEGF (c), and Pt/C (d) towards ORR in O₂ saturated 0.1 M HClO₄ recorded before after the 10000 CV cycles.

are as PtCo/pNEGF (3.8), Pt₃Co/pNEGF (3.9), and Pt/C (4.0). The lower percentage of H₂O₂, as well as the n-value close to 4 for Pt₃Co/pNEGF, suggest that the system is fairly free from the parasitic 2-electron reduction process, which was expected to be a possible process due to the presence of the Co and N-doped carbon in the catalyst composition.

The comparative CV profiles presented in **Figures 5.9a**, and **b**, show the improved limiting current density of pNEGF after the microwave treatment of NEGF. The higher percentage of the microporosity helps for more charge accumulation on the porous substrate than the NEGF having only mesoporosity. Similar behavior is observed in the comparative LSV performance measurement in **Figure 5.9c**.

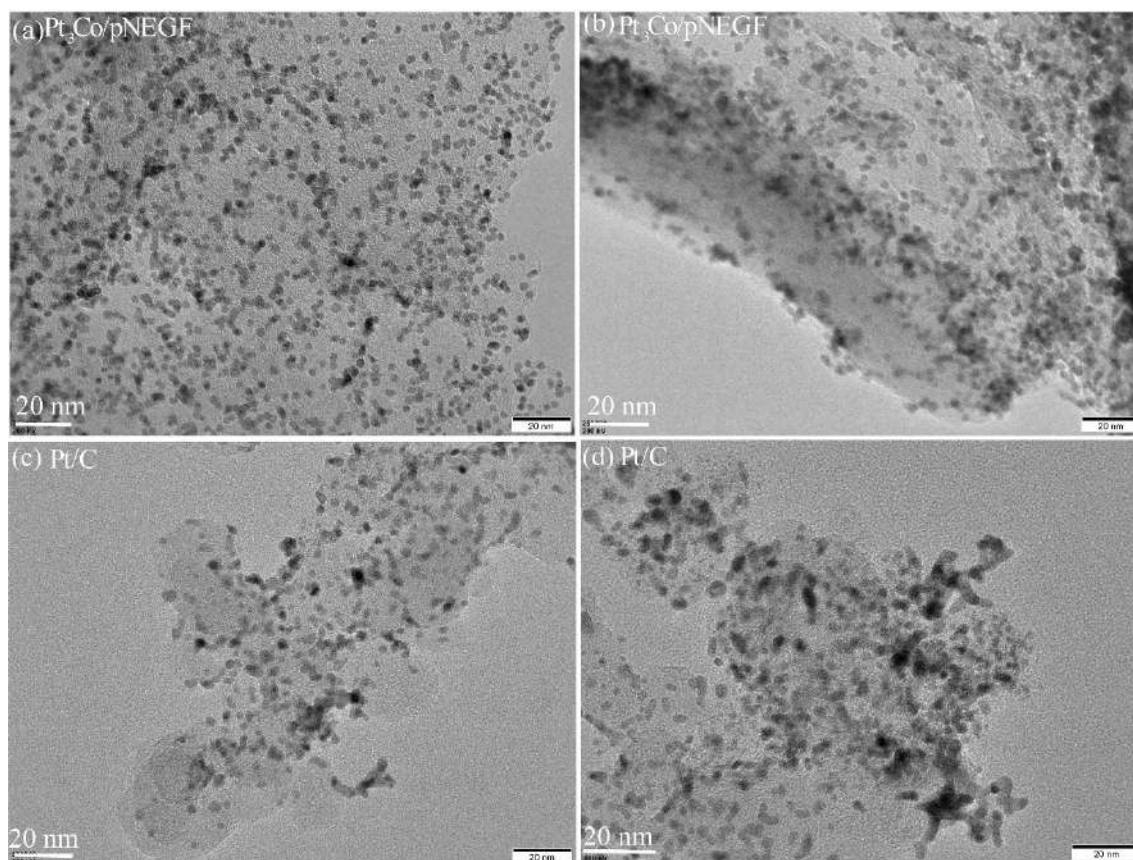


Figure 5.11. The HRTEM images of the $\text{Pt}_3\text{Co}/\text{pNEGF}$ recorded before (a) and after (b) the 10000 CV cycles show that the particle distribution is unaffected after the test; the HRTEM images of Pt/C before (c) and after (d) the cycling test, displaying the Pt particle aggregation at some locations subsequent to the test.

The electrochemical accelerated durability test (ADT) of the catalyst has been performed by recording 10000 cycles under oxygen saturated 0.1 M HClO_4 at a scan rate of 100 mVs^{-1} in the potential range of 0.80 and 1.2 V with respect to RHE. After the durability cycling, the CV and LSV were recorded on $\text{Pt}_3\text{Co}/\text{pNEGF}$ and Pt/C) and compared the status with respect to the corresponding initial cycles as shown in **Figure 5.10a** and **b**, respectively. The CV profiles recorded before and after the 10000 cycles (**Figure 5.10a**) for $\text{Pt}_3\text{Co}/\text{pNEGF}$ show nearly similar peak features of the hydrogen adsorption and desorption. After the 10000 cycles, the ECSA change for $\text{Pt}_3\text{Co}/\text{pNEGF}$ ($\Delta\text{ECSA} = 5 \text{ m}^2 \text{ gPt}^{-1}$) is lower than the value obtained for Pt/C ($\Delta\text{ECSA} = 9 \text{ m}^2 \text{ gPt}^{-1}$) (**Figure 5.10b**). Furthermore, the LSVs recorded before and after the CV cycling showed a negative shift in the $E_{1/2}$ value with a drop of 24 mV for $\text{Pt}_3\text{Co}/\text{pNEGF}$ (**Figure 5.10c**). The observed change in $E_{1/2}$ value for $\text{Pt}_3\text{Co}/\text{pNEGF}$ is lower than that of Pt/C (32 mV) (**Figure 5.10d**) recorded under the identical conditions. This indicates the better stability of the homemade

catalyst under the operating conditions and is attributed to the less corrosive nature of the graphitic carbon support. Furthermore, the strong interaction between the doped-N and Pt₃Co nanoparticles is also expected to be playing a major role in enhancing the electrochemical stability of the catalyst.

After the long cycle of the accelerated durability test (ADT) analysis, the structure of the catalyst was analyzed by HRETEM and compared with pre-cycled samples. The HRTEM images of Pt₃Co/pNEGF and Pt/C recorded before and after ADT are shown in **Figure 5.11**. **Figures 5.11a** and **b**, display respectively the HRTEM images of Pt₃Co/pNEGF taken before and after ADT. Apparently, the triggered condition did not make any visual changes in the nature of dispersion of the Pt₃Co nanoparticles and the overall morphology of the catalyst system. The result thus validates the promising structural endurance possessed by the catalyst. On the other hand, the HRTEM images of Pt/C recorded before and after cycling test, **Figure 5.11c**, and **d**, respectively, show indications of Pt particle aggregation.

5.4. Conclusion:

A unique 3D structured ORR electrocatalyst based on the nitrogen-doped porous graphene-supported Pt₃Co nanoparticles (Pt₃Co/pNEGF) could be prepared by employing a sequential preparation process involving freeze drying, microwave treatment, and polyol reduction. The introduction of the microporosity into the 3D micro-mesoporous conducting support system has great advantages over those carbons which display only mesoporosity. It is found that the surface adsorption properties of the Pt are getting considerably modified by the stoichiometric addition of Co into the system. Furthermore, a well-suited stoichiometric composition of Pt and Co (*i.e.* Pt₃Co in the present case) along with the controlled interplay of the other contributing factors such as the doped nitrogen, microporosity, and 3D architecture of the catalyst unit are favorably modulating the catalyst towards the oxygen adsorption and subsequently the ORR performance. The 3D structure of the support favors mass transfer and effective formation of the active “triple-phase boundary” and, as a result, Pt₃Co/pNEGF shows an ORR activity that is nearly comparable to that of the *state-of-the-art* (Pt/C) catalyst. The synergistic interactions operating in the system between the Pt₃Co nanoparticles and the N-doped porous graphene are primarily responsible for the higher catalytic activity and durability displayed by Pt₃Co/pNEGF. The presence of the microporosity in the carbon system enhances the available reaction sites for the gas and electrolyte interface formation and contributes significantly to improving the mass activity of the catalyst. Pt₃Co/pNEGF also displays high structural endurance and corrosion resistance and the dispersion characteristics of the Pt₃Co

nanoparticles and the textural features of the catalyst are found to be unaffected even after the system was subjected to the electrochemical potential cycling stability tests that lasted for 10 K cycles.

5.5. References

1. Stacy, J.; Regmi, Y. N.; Leonard, B.; Fan, M. The Recent Progress and Future of Oxygen Reduction Reaction Catalysis; *Renewable Sustainable Energy Rev.* 2017, 69, 401–414.
2. Van Spronsen, M. A.; Frenken, J. W. M.; Groot, I. M. N. Surface Science under Reaction Conditions: CO Oxidation on Pt and Pd Model Catalysts. *Chem. Soc. Rev.* 2017, 46, 4347.
3. Deutschmann, O.; Knözinger, H.; Kochloefl, K.; Turek, T. Heterogeneous Catalysis and Solid Catalysts. *Ullmann's Encyclopedia of Industrial Chemistry* 2009, 1, 5–6.
4. Quaino, P.; Juarez, F.; Santos, E.; Schmickler, W. Volcano Plots in Hydrogen Electrocatalysis-Uses and Abuses. *Beilstein J. Nanotechnol.* 2014, 5, 846–854.
5. Pomerantseva, E.; Resini, C.; Kovnir, K.; Kolen'ko, Y. V. Emerging Nanostructured Electrode Materials for Water Electrolysis and Rechargeable beyond Li-Ion Batteries. *Advances in Physics: X.* 2017, 2, 211–253.
6. Stephens, I. E. L.; Bondarenko, A. S.; Grønbjerg, U.; Rossmeisl, J.; Chorkendorff, I. Understanding the Electrocatalysis of Oxygen Reduction on Platinum and Its Alloys. *Energy Environ. Sci.* 2012, 5, 6744–6762.
7. Greeley, J.; Stephens, I. E. L.; Bondarenko, A. S.; Johansson, T. P.; Hansen, H. A.; Jaramillo, T. F.; Rossmeisl, J.; Chorkendorff, I.; Nørskov, J. K. Alloys of Platinum and Early Transition Metals as Oxygen Reduction Electrocatalysts. *Nat. Chem.* 2009, 1, 552–556.
8. Gutic, S. J.; Dobrota, A. S.; Fako, E.; Skorodumova, N. V.; López, N.; Pasti, I. A. Hydrogen Evolution Reaction-From Single Crystal to Single Atom Catalysts. *Catalysts* 2020, 10, 290.
9. Sheng, W.; Myint, M.; Chen, J. G.; Yan, Y. Correlating the Hydrogen Evolution Reaction Activity in Alkaline Electrolytes with the Hydrogen Binding Energy on Monometallic Surfaces. *Energy Environ. Sci.* 2013, 6, 1509–1512.

10. Xia, W.; Mahmood, A.; Liang, Z.; Zou, R.; Guo, S. Earth Abundant Nanomaterials for Oxygen Reduction. *Angew. Chem., Int. Ed.* 2016, 55, 2650–2676.
11. Xu, D.; Bliznakov, S.; Liu, Z.; Fang, J.; Dimitrov, N. Composition-Dependent Electrocatalytic Activity of Pt-Cu Nanocube Catalysts for Formic Acid Oxidation. *Angew. Chem., Int. Ed.* 2010, 49, 1282–1285.
12. Koh, S.; Strasser, P. Electrocatalysis on Bimetallic Surfaces: Modifying Catalytic Reactivity for Oxygen Reduction by Voltammetric Surface Dealloying. *J. Am. Chem. Soc.* 2007, 129, 12624–12625.
13. Xu, D.; Liu, Z.; Yang, H.; Liu, Q.; Zhang, J.; Fang, J.; Zou, S.; Sun, K. Solution-Based Evolution and Enhanced Methanol Oxidation Activity of Monodisperse Platinum-Copper Nanocubes. *Angew. Chem., Int. Ed.* 2009, 48, 4217–4221.
14. Zhou, S.; Varughese, B.; Eichhorn, B.; Jackson, G.; McIlwrath, K. Pt–Cu Core–Shell and Alloy Nanoparticles for Heterogeneous NO_x Reduction: Anomalous Stability and Reactivity of a Core–Shell Nanostructure. *Angew. Chem., Int. Ed.* 2005, 44, 4539–4543.
15. Kodama, K.; Nagai, T.; Kuwaki, A.; Jinnouchi, R.; Morimoto, Y. Challenges in Applying Highly Active Pt-Based Nanostructured Catalysts for Oxygen Reduction Reactions to Fuel Cell Vehicles. *Nat. Nanotechnol.* 2021, 16, 140–147.
16. Manna, N.; Singh, S. K.; Kharabe, G. P.; Torris, A.; Kurungot, S., Zinc–Air Batteries Catalyzed Using Pt Nanorod-Supported N-Doped Entangled Graphene for Oxygen Reduction Reaction. *ACS Applied Energy Materials* 2021, 4 (5), 4570-4580.
17. Li, C.; Han, X.; Cheng, F.; Hu, Y.; Chen, C.; Chen, J., Phase and composition controllable synthesis of cobalt manganese spinel nanoparticles towards efficient oxygen electrocatalysis. *Nat Commun* 2015, 6, 7345.
18. Singh, S. K.; Kashyap, V.; Manna, N.; Bhange, S. N.; Soni, R.; Bo kherroub, R.; Szunerits, S.; Kurungot, S. Efficient and Durable Oxygen Reduction Electrocatalyst Based on CoMn Alloy Oxide Nanoparticles Supported over N-Doped Porous Graphene. *ACS Catal.* 2017, 7, 6700–6710.

-
19. Yang, Y.; Xiong, Y.; Holtz, M. E.; Feng, X.; Zeng, R.; Chen, G.; DiSalvo, F. J.; Muller, D. A.; Abruna, H. D., Octahedral spinel electrocatalysts for alkaline fuel cells. *Proc Natl Acad Sci U S A* 2019, 116 (49), 24425-24432.
20. Zhou, Y.; Zhou, Z.; Shen, R.; Ma, R.; Liu, Q.; Cao, G.; Wang, J., Correlating electrocatalytic oxygen reduction activity with d-band centers of metallic nanoparticles. *Energy Storage Materials* 2018, 13, 189-198.
21. Gonçalves, J. M.; Silva, M. N. T.; Naik, K. K.; Martins, P. R.; Rocha, D. P.; Nossol, E.; Munoz, R. A. A.; Angnes, L.; Rout, C. S., Multifunctional spinel Pt₃Co based materials for energy storage and conversion: a review on emerging trends, recent developments and future perspectives. *Journal of Materials Chemistry A* 2021, 9 (6), 3095-3124.
22. Lu, X. F.; Chen, Y.; Wang, S.; Gao, S.; Lou, X. W. D., Interfacing Manganese Oxide and Cobalt in Porous Graphitic Carbon Polyhedrons Boosts Oxygen Electrocatalysis for Zn-Air Batteries. *Adv Mater* 2019, 31 (39), e1902339.
23. Zhu, H.; Gu, L.; Yu, D.; Sun, Y.; Wan, M.; Zhang, M.; Wang, L.; Wang, L.; Wu, W.; Yao, J.; Du, M.; Guo, S., The marriage and integration of nanostructures with different dimensions for synergistic electrocatalysis. *Energy & Environmental Science* 2017, 10 (1), 321-330.
24. Dai, L.; Chang, D. W.; Baek, J. B.; Lu, W., Carbon nanomaterials for advanced energy conversion and storage. *Small* 2012, 8 (8), 1130-66.
25. Li, Y.; Zhao, M.; Zhao, Y.; Song, L.; Zhang, Z., FeNi Layered Double-Hydroxide Nanosheets on a 3D Carbon Network as an Efficient Electrocatalyst for the Oxygen Evolution Reaction. *Particle & Particle Systems Characterization* 2016, 33 (3), 158-166.
26. Mo, R.; Rooney, D.; Sun, K.; Yang, H. Y., 3D nitrogen-doped graphene foam with encapsulated germanium/nitrogen-doped graphene yolk-shell nanoarchitecture for high-performance flexible Li-ion battery. *Nat Commun* 2017, 8, 13949.
27. Cao, S.; Tao, F.; Tang, Y.; Li, Y.; Yu, J. Size- and Shape-Dependent Catalytic Performances of Oxidation and Reduction Reactions on Nanocatalysts. *Chem. Soc. Rev.* 2016, 45, 4747.

28. Wang, Y.-C.; Huang, L.; Zhang, P.; Qiu, Y.-T.; Sheng, T.; Zhou, Z.-Y.; Wang, G.; Liu, J.-G.; Rauf, M.; Gu, Z.-Q.; Wu, W.-T.; Sun, S.-G., Constructing a Triple-Phase Interface in Micropores to Boost Performance of Fe/N/C Catalysts for Direct Methanol Fuel Cells. *ACS Energy Letters* 2017, 2 (3), 645-650.
29. Liu, H.; Li, C.; Chen, D.; Cui, P.; Ye, F.; Yang, J. Uniformly Dispersed Platinum-Cobalt Alloy Nanoparticles with Stable Compositions on Carbon Substrates for Methanol Oxidation Reaction. *Sci. Rep.* 2017, 7, 1–8
30. Choi, S.; Jeon, J.; Chae, J.; Yuk, S.; Lee, D.-H.; Doo, G.; Lee, D. W.; Hyun, J.; Kwen, J.; Choi, S. Q.; Kim, H.-T., Single-Step Fabrication of a Multiscale Porous Catalyst Layer by the Emulsion Template Method for Low Pt-Loaded Proton Exchange Membrane Fuel Cells. *ACS Applied Energy Materials* 2021, 4 (4), 4012-4020.
31. Wu, Z. S.; Yang, S.; Sun, Y.; Parvez, K.; Feng, X.; Mullen, K., 3D nitrogen-doped graphene aerogel-supported Fe₃O₄ nanoparticles as efficient electrocatalysts for the oxygen reduction reaction. *J Am Chem Soc* 2012, 134 (22), 9082-5.
32. Zenyuk, I. V.; Parkinson, D. Y.; Connolly, L. G.; Weber, A. Z., Gas-diffusion-layer structural properties under compression via X-ray tomography. *Journal of Power Sources* 2016, 328, 364-376.
33. Tötzke, C.; Gaiselmann, G.; Osenberg, M.; Bohner, J.; Arlt, T.; Markötter, H.; Hilger, A.; Wieder, F.; Kupsch, A.; Müller, B. R.; Hentschel, M. P.; Banhart, J.; Schmidt, V.; Lehnert, W.; Manke, I., Three-dimensional study of compressed gas diffusion layers using synchrotron X-ray imaging. *Journal of Power Sources* 2014, 253, 123-131.
34. Jang, S.; Kim, S.; Kim, S. M.; Choi, J.; Yeon, J.; Bang, K.; Ahn, C.-Y.; Hwang, W.; Her, M.; Cho, Y.-H.; Sung, Y.-E.; Choi, M., Interface engineering for high-performance direct methanol fuel cells using multiscale patterned membranes and guided metal cracked layers. *Nano Energy* 2018, 43, 149-158.
35. Manna, N.; Ayasha, N.; Singh, S. K.; Kurungot, S., A NiFe layered double hydroxide-decorated N-doped en-tangled-graphene framework: a robust water oxidation electrocatalyst. *Nanoscale Advances* 2020, 2 (4), 1709-1717.

36. Lee, J. D.; Jishkariani, D.; Zhao, Y.; Najmr, S.; Rosen, D.; Kikkawa, J. M.; Stach, E. A.; Murray, C. B. Tuning the Electrocatalytic Oxygen Reduction Reaction Activity of Pt-Co Nanocrystals by Cobalt Concentration with Atomic-Scale Understanding. *ACS Appl. Mater. Interfaces* 2019, 11, 26789–26797.
37. Jung, N.; Bhattacharjee, S.; Gautam, S.; Park, H.-Y.; Ryu, J.; Chung, Y.-H.; Lee, S.-Y.; Jang, I.; Jang, J. H.; Park, S. H.; Chung, D. Y.; Sung, Y.-E.; Chae, K.-H.; Waghmare, U. V.; Lee, S.-C.; Yoo, S. J. Organic-Inorganic Hybrid PtCo Nanoparticle with High Electrocatalytic Activity and Durability for Oxygen Reduction. *NPG Asia Mater.* 2016, 8, 237.
38. Wang, Y.-J.; Zhao, N.; Fang, B.; Li, H.; Bi, X. T.; Wang, H. A Highly Efficient PtCo/C Electrocatalyst for the Oxygen Reduction Reaction. *RSC Adv.* 2016, 6, 34484–34491.
39. Myint, M. N. Z.; Yan, B.; Wan, J.; Zhao, S.; Chen, J. G. Reforming and Oxidative Dehydrogenation of Ethane with CO₂ as a Soft Oxidant over Bimetallic Catalysts. *J. Catal.* 2016, 343, 168–177.
40. Jia, Q.; Caldwell, K.; Strickland, K.; Ziegelbauer, J. M.; Liu, Z.; Yu, Z.; Ramaker, D. E.; Mukerjee, S. Improved Oxygen Reduction Activity and Durability of Dealloyed PtCo_x Catalysts for Proton Exchange Membrane Fuel Cells: Strain, Ligand, and Particle Size Effects. *ACS Catal.* 2015, 5, 176–186.
41. Boyaci San, F. G.; Dursun, S.; Yazici, M. S. PtCo on Continuous-Phase Graphene as PEM Fuel Cell Catalyst. *Int. J. Energy Res.* 2021, 45, 1673–1684.
42. Lee, H.; Lim, J.; Lee, C.; Back, S.; An, K.; Shin, J. W.; Ryoo, R.; Jung, Y.; Park, J. Y. Boosting Hot Electron Flux and Catalytic Activity at Metal–Oxide Interfaces of PtCo Bimetallic Nanoparticles. *Nat. Commun.* 2018, 9, 1–8.
43. Farkas, B.; Perry, C. B.; Jones, G.; De Leeuw, N. H. Adsorbate-Induced Segregation of Cobalt from PtCo Nanoparticles: Modeling Au Doping and Core AuCo Alloying for the Improvement of Fuel Cell Cathode Catalysts. *J. Phys. Chem. C* 2020, 124, 18321–18334.
44. Yu, Z.; Zhang, J.; Liu, Z.; Ziegelbauer, J. M.; Xin, H.; Muller, D. A.; Wagner, F. T. Comparison between Dealloyed PtCo₃ and PtCu₃ Cathode Catalysts for Proton Exchange Membrane Fuel Cells. *J. Phys. Chem. C* 2012, 116, 19877–19885.
45. Liu, Z.; Lei, Y.; Wang, G. First-Principles Computation of Surface Segregation in L10 CoPt Magnetic Nanoparticles. *J. Phys.: Condens. Matter* 2016, 28, 266002.

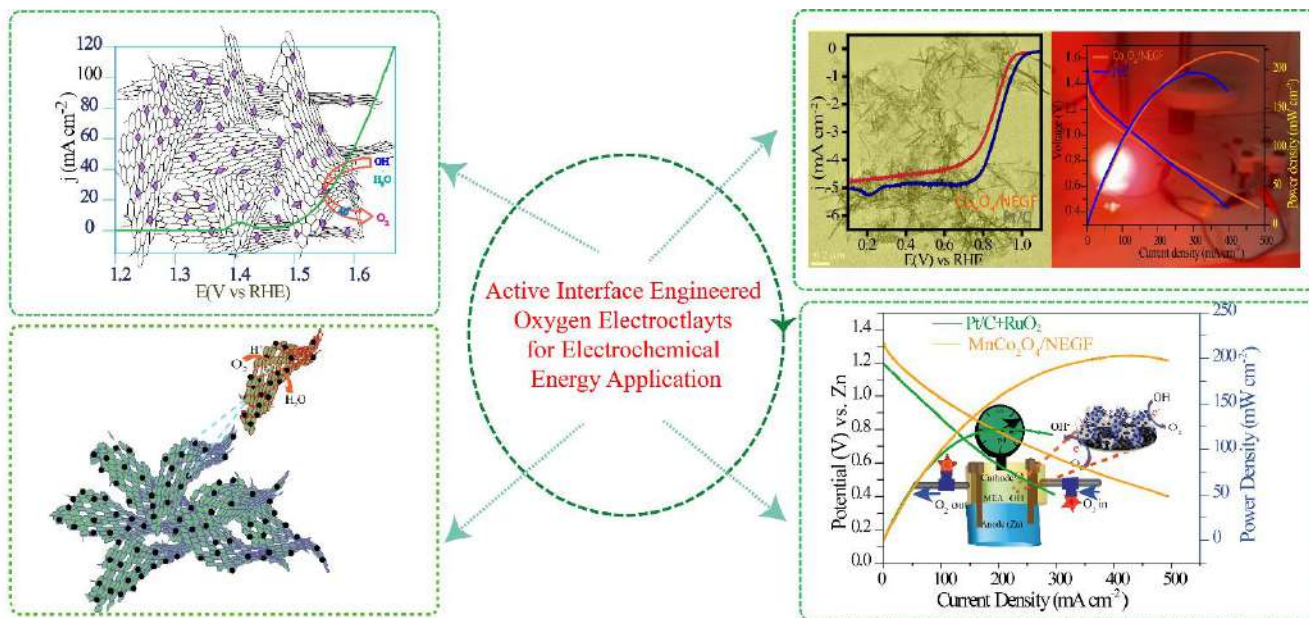
46. Sun, X.; Jia, Z. Y.; Huang, Y. H.; Harrell, J. W.; Nikles, D. E.; Sun, K.; Wang, L. M. Synthesis and Magnetic Properties of CoPt Nanoparticles. *J. Appl. Phys.* 2004, 95, 6747.

47. Karipoth, P.; Joseyphus, R. J. Evolution of High Coercivity in CoPt Nanoparticles Through Nitrogen Assisted Annealing. *J. Supercond. Novel Magn.* 2014, 27, 2123–2130

Summary & Future Perspectives

6.1. Summary:

This chapter summarizes the outcomes of the research works discussed in the preceding chapters based on the strategies adopted for designing the various electrocatalysts by using the 3D graphene support for both oxygen reduction reaction (ORR) and oxygen evolution reaction (OER) applications. The working principles of the electrochemical energy devices such as water electrolyzers, polymer electrolyte membrane fuel cells (PEMFCs), and rechargeable metal-air batteries (RZABs) along with their advantages and system-level limitations are discussed in the introductory chapter (**Chapter 1**). To overcome the existing limitations related to the oxygen electrokinetics in the electrochemical energy devices such as water electrolyzer (OER), PEMFCs (ORR), and RZAB (ORR and OER), more cost-effective and durable catalysts are required. Therefore, strategic modulation of the required active sites and structural fine-tuning of the catalyst morphologies and functionalities are necessary to effectively overcome many of these existing challenges. The size, shape, and compositional tuning of the active centers are promising ways to improve the catalyst performance. In addition, the support morphology plays an important role in effectively meeting the various critical activity deciding factors such as mass transport and active site accessibility. Apart from the morphology, the selected support should have electronic conductivity for better



electron transport, structural rigidity, and corrosion resistance for enabling the system to withstand harsh electrochemical conditions. Along with these, considering the cost as well as performance deciding factors, the development of low-Pt, and Pt-free electrocatalysts for ORR and OER applications is also becoming an important thrust area. Moreover, compared to the conventional 1D and 2D structured support materials, the less explored 3D structured supports have the unique advantages of providing better accessible active sites, which results in improved electrocatalytic performance.

In the context of the abovementioned technical challenges, a focused effort has been made, as detailed in the various working chapters of this thesis, to develop a series of new classes of the graphene-based 3D structured electrocatalysts for the oxygen electrochemistry applications. The synthesized catalysts show significantly improved performance compared to the *state-of-the-art catalysts* for the respective reactions. The relevant morphology of the 3D graphene also provides unique structural integrity. In addition, the doping of nitrogen into the 3D framework of the graphene sheets provides efficient anchoring sites for the uniform and well-anchored dispersion of the desired active sites. Furthermore, the stable morphology of the 3D support with its N-doped centers improves the metal-support interaction and thus the designed systems are found to be surviving well under the harsh electrochemical conditions. The 3D morphological features of the catalysts are also helpful for achieving better electrode-electrolyte interface formation and, thereby, improved active site utilization. Further, the creation of additional porosity on the 3D support matrix within the range of micro to meso shows another significant advantage of achieving the formation and dispersion of nanometer-sized alloy nanoparticles on the support surface. The details of the works carried out as part of meeting the key objectives of the dissertation are presented in the four working chapters of the thesis (**Chapter 2**, **Chapter 3**, **Chapter 4**, and **Chapter 5**).

The significant achievements of this thesis as they appear in different working chapters are listed as follows:

6.1. NiFe Layered double hydroxide-Decorated N-Doped Entangled-Graphene Framework: A Robust Water Oxidation Electrocatalyst (Chapter 2)

This work deals with the development of a low-cost OER electrocatalyst based on the NiFe-LDH (Layered Double Hydroxide) nanostructures supported by the N-doped entangled graphene framework (NiFe-LDH/NEGF). The use of an aqueous solution of ammonium hydroxide acted not only as a nitrogen source but also helped in maintaining the pH of the solution for the formation of the self-assembled graphene as well as the NiFe-LDH nanostructures. The freeze-drying method further helped in the formation of a stable entangled structure of NiFe-

LDH/NEGF. With its porous and open morphology, the designed catalyst assisted towards better electrolyte diffusion as well as releasing of the gaseous products during the electrochemical reaction conditions.

The key highlights of the present work are:

- A simple, two-step synthesis procedure was adopted to design a robust NiFe-LDH-supported NEGF electrocatalyst (NiFe-LDH/NEGF) *via* the low-temperature hydrothermal treatment in the presence of ammonium hydroxide and graphene oxide.
- The acquired porosity in the catalyst due to the distribution of the graphene layers in the framework helped to improve the hydroxyl ion diffusion and gaseous product release during the electrochemical oxygen evolution reaction.
- The higher surface area of NiFe-LDH/NEGF provides a larger number of adsorption positions for the reactants and intermediates, leading to better electrocatalytic activity.
- In the presence of Fe, in the NiFe-LDH supported NEGF system, the hydroxide crystallinity and orders have been improved, which helped in achieving better electrocatalytic activity.
- The N-doping over the carbon substrate support facilitated better electronic coupling between the N-doped entangled graphene and the NiFe-LDH moieties, which resulted in lowering the overpotential to 290 mV to reach the oxygen evolution current density of 10 mA cm^{-2} .
- The reasons for the high performance achieved are the coexisting factors such as the uniformly distributed and exposed active sites of LDH, the plentiful hydrated LDH channels for the reaction species transportation, and the 3D porous structure of the graphene to facilitate the electrolyte infiltrations and the product gas transport.
- Most importantly, the designed catalyst offers long-term catalytic ability and is found to be performing quite efficiently even after the 20 h of the continuous operation by retaining up to ~80 % of its original performance.

6.2. Zinc-Air Battery Catalyzed by Co_3O_4 Nanorod-Supported N-doped Entangled Graphene for Oxygen Reduction Reaction (Chapter 3)

Chapter 3 deals with the development of Co_3O_4 nanorod bearing NEGF ($\text{Co}_3\text{O}_4/\text{NEGF}$) as a versatile noble metal-free ORR electrocatalyst and its application as an air-electrode in the primary zinc-air battery (ZAB). The spinel structure of the oxide with the nanorod morphology shows significant advantages for the electrochemical oxygen reduction reaction (ORR). An aqueous ammonia solution was used as the nitrogen source, which simultaneously

helped in maintaining the pH of the solution required for the formation of the self-assembled N-doped 3D graphene as well as the Co_3O_4 nanorod structure growth.

The key highlights of the present work are:

- A non-Pt electrocatalyst for ORR could be developed through a sequential pathway involving hydrothermal treatment followed by freeze-drying to build the desired structural architecture of the catalyst. The designed catalyst ($\text{Co}_3\text{O}_4/\text{NEGF}$), which contains the Co_3O_4 nanorods anchored on the surface of the 3D structured N-doped graphene, was found to be displaying higher ORR activity during the single-electrode testing and demonstration of a Zn-air battery (ZAB) system.
- The hydrothermal treatment and freeze-drying processes are found to be playing vital roles in tuning the structural and morphological features of the catalyst. The doped nitrogen, apart from its favorable contribution towards ORR, helps to facilitate efficient dispersion of the oxide nanorods on the graphene.
- The 60 mV onset potential shift for ORR and the Tafel slope of 74 mV/dec recorded over $\text{Co}_3\text{O}_4/\text{NEGF}$ compared to the *state-of-the-art* Pt/C in the single-electrode mode are promising values expected from a non-Pt electrocatalyst.
- A realistic system level validation of the catalyst also could be successfully performed by constructing and testing a ZAB consisting of $\text{Co}_3\text{O}_4/\text{NEGF}$ as the cathode catalyst and comparing the performance characteristics of a similar cell constructed with the Pt/C cathode.
- This high performance has been credited to the controlled interplay of the governing factors such as the interfacial interactions leading to the efficient dispersion of the metal oxide nanorods, increased catalyst surface area, the cooperative effect arising from the defects present in the N-doped porous 3D-graphene, and the synergetic interactions operating in the system.

6.3. Air-Cathode Interface Engineered Electrocatalyst for the All-Solid-State Rechargeable Zinc-Air Battery (Chapter 4)

Aiming at the rechargeability of the ZAB systems, this chapter introduces a bimetallic manganese-cobalt-based spinel oxide (MnCo_2O_4) supported NEGF ($\text{MnCo}_2\text{O}_4/\text{NEGF}$) as an efficient bifunctional electrocatalyst for facilitating both ORR and OER, and, thereby, as a versatile air-electrode material for the rechargeable zinc-air battery (RZAB) application. Followed by the single-electrode studies targeted the validation of the ORR and OER activities of the system, an all-solid-state RZAB could be demonstrated by employing $\text{MnCo}_2\text{O}_4/\text{NEGF}$ as the air-cathode since the 3D morphology of the catalyst helped to

achieve an effective interface with the electrolyte. The chapter covers the interesting aspects of this material as the air-electrode for the solid-state device.

The key highlights of the present work are:

- A cost-effective bifunctional electrocatalyst possessing rationally designed structural and functional attributes for facilitating both ORR and OER and favoring the effective formation of the active “triple-phase boundary (TPB)” at the air cathode of the RZAB has been prepared. This has been achieved by homogeneously dispersing manganese-cobalt bimetallic spinel oxide (MnCo_2O_4) nanoparticles over a 3D structured nitrogen-doped entangled graphene framework ($\text{MnCo}_2\text{O}_4/\text{NEGF}$).
- The hydrothermal treatment and freeze-drying processes are found to be playing vital roles in tuning the structural and morphological features of the catalyst. Apart from its favorable contribution towards ORR and OER, the doped nitrogen helps as a nucleating site for the efficient dispersion of the bimetallic spinel oxide on the graphene layers of the 3D structured NEGF and also brings in the optimal surface wettability to the catalyst.
- The study reveals the existence of synergistic interactions operating between the MnCo_2O_4 nanoparticles and the N-doped porous graphene substrate. This benefits the system in terms of its bifunctional activity of $\text{MnCo}_2\text{O}_4/\text{NEGF}$ towards these reactions; the overpotential values are found to be closely comparable to the respective *state-of-the-art* systems (*i.e.*, Pt/C for ORR and RuO_2 for OER).
- The air-electrode consisting of the $\text{MnCo}_2\text{O}_4/\text{NEGF}$ -coated gas diffusion layer (GDL) ensures the effective formation of the active ‘triple-phase boundary’ even in the presence of the OH^- ion conducting gel electrolyte due to the porous 3D morphology of the catalyst layer. These structural and functional advantages of the electrocatalyst are found to be working in favor during the demonstration of the ZAB in its solid-state mode under charging and discharging conditions.
- The optimal hydrophilicity originated from the functional attributes of the support surface is found to be playing a significant role in constructing the effective interface of the catalyst and the electrolyte.
- The demonstration of a solid-state rechargeable ZAB device with $\text{MnCo}_2\text{O}_4/\text{NEGF}$ as the air-electrode delivered a maximum peak power density of 200 mW cm^{-2} , with good stability during the charge-discharge cycling process. In terms of the performance and charge-discharge cyclability, the system based

on the homemade catalyst is found to have a clear upper hand compared to a system consisting of the state-of-the-art ORR/OER standard catalyst pair of Pt/C+RuO₂.

6.4. Microwave-Induced Micro-Porous Graphene Supported Pt₃Co Alloy as an Improved Mass Active and Durable ORR Catalyst (Chapter 5)

The catalytic materials based on the non-noble metal-supported NEGF assemblies developed as per the details given in **Chapters 2, 3, and 4** displayed high electrocatalytic ORR and OER activities under the basic conditions with long term durability. Considering the interesting stable morphology of the mesoporous structure of the NEGF system, further incorporation of the microporosity in the system (pNEGF) has the benefit of further tuning the electrode requirements. Furthermore, the non-noble metal-based active sites are ORR active and stable in the basic conditions but they registered significant overpotentials and stability issues under the acidic conditions. Accordingly, **Chapter 5** deals with the results pertaining to the development and demonstration of the 3D graphene-supported Pt-Co alloy system (Pt₃Co/pNEGF) with the *in-situ* created microporosity as an ORR electrocatalyst with the ability to function better under the acidic conditions. The incorporation of the microporosity helps to achieve uniform dispersion of the sub-nm-sized Pt-Co alloy (Pt₃Co) nanoparticles with improved mass activity.

The key aspects of the work are listed below:

- A microwave-assisted synthesis method was employed to create the 3D porous carbon support with a large pore volume and dense micro/mesoporous surface. Simultaneously, the doped nitrogen in the carbon framework helps in achieving the uniform distribution of the sub-nm-sized Pt₃Co nanoparticles over the 3D graphene substrate during the polyol method.
- Alloying Pt with Co slightly reduces the Pt metal loading without affecting the ORR activity. In addition, the presence of an early transition metal to the Pt could alter the Pt-Pt interatomic distance, resulting in a down-shift of the d-band center and a change in the electronic structures of the active Pt sites for ORR. These factors along with the small size of the Pt₃Co nanoparticles and their homogeneous dispersion resulted in high ORR activity of the system with more process-friendly nature.
- The ORR performance of Pt₃Co/pNEGF closely matches with the *state-of-the-art* commercial Pt/C catalyst in 0.1 M HClO₄, with a small overpotential of 10 mV. The 3D framework of the substrate with

the microporous texture of the N-doped graphene significantly improves the mass transfer characteristics and contributes favorably to the overall ORR performance.

- Pt₃Co/pNEGF and 40 % Pt/C in 0.1 M HClO₄ display the ORR onset potentials of 0.99 and 1.0 V vs. RHE, respectively. The mass activities calculated from the ORR polarization curves reveal 1.5 times higher activity for Pt₃Co/pNEGF compared to its counterpart Pt/C system.
- Pt₃Co/pNEGF also displays high structural endurance and corrosion resistance compared to its carbon-based counterpart system. The presence of the N-doped graphitic carbon support offers strong coordination sites for the Pt₃Co nanoparticles and prevents particle aggregation under the testing conditions. Even after the 10000 potential cycles, which have been performed as part of the accelerated durability test protocol, the drop in the electrochemically active surface area (ECSA) and the half-wave potential ($E_{1/2}$) of Pt₃Co/pNEGF is found to be less ($\Delta\text{ECSA} = 5 \text{ m}^2 \text{ g}_{\text{Pt}}^{-1}$, $\Delta E_{1/2} = 24 \text{ mV}$) compared to that of Pt/C ($\Delta\text{ECSA} = 9 \text{ m}^2 \text{ g}_{\text{Pt}}^{-1}$, $\Delta E_{1/2} = 32 \text{ mV}$).

6.2. Future Perspectives:

The results presented in this thesis demonstrate how one can effectively utilize the graphene framework for building new classes of 3D structured electrocatalysts for ORR and OER applications by strategically tuning the morphological features. The demonstrations in this thesis are focused on PEMFCs, electrolyzers, and metal-air batteries. The transformation of a catalyst to the electrode requires different process protocols and the fabrication strategies often spoil the favorable structural attributes of the designed catalysts. This limitation is common in most of the electrochemical devices. Hence, to make the electrodes more process friendly, a real “bottom-up” designing strategy is required and the present thesis is a humble attempt in this direction. The concepts like 3D structuring, creation of mass-transfer channels, and exposed active sites are based on the consideration of minimizing the issues that we normally face during the electrode fabrications. From a broader perspective, the findings of the thesis, even though at present are restricted to electrolyzers, PEMFCs, and metal-air batteries, have significant implications in the relative areas such as the other types of batteries, supercapacitors, sensors, etc, where the effective utilization of the active sites and interface formation is challenging and tricky. For example, by effectively tweaking the process demonstrated for developing the catalyst for the electrolyzer or the metal-air battery applications in this thesis, one can explore the possibilities of making better systems for building solid-state supercapacitors by utilizing the 3D structure of the catalyst and by adjusting the active sites in the desired way. In the case of the metal-ion batteries, the electrochemical sensors, and the other types of electrochemical

processes such as electrochemical ammonia synthesis, nitrogen reduction, and direct methanol fuel cells, the strategies proposed in this thesis have great prospects for further exploration. The finding of this dissertation also can get attention in the areas other than the electrochemical systems where the active site utilization and mass transfer issues are the major activity limiting factors. One such area is the heterogeneous and homogeneous catalysis, where activities are often limited by the poor accessibility of the active sites, their low stability, and the tendency for aggregation. All these can be effectively addressed by adopting appropriate 3D architecting strategies as detailed in this thesis. Since graphene is still in the limelight as an effective substrate material for different active sites for the targeted applications, the findings of the thesis will help for value addition for graphene as a material for those who are working in the areas of electrochemistry and catalysis.

ABSTRACT

Name of the Candidate: Mr. Narugopal Manna**Registration No: 10CC16A26001****Faculty of Study: Chemical Sciences****Year of Submission: 2022****AcSIR academic centre/CSIR Lab:
CSIR-National Chemical Laboratory****Name of the Supervisor: Dr. Sreekumar
Kurungot****Title of the thesis: Active Interface Engineered Oxygen Electrocatalysts for Electrochemical Energy Applications**

This thesis deals with the development of 3D structured oxygen electrocatalysts possessing enhanced active interfaces that can better handle the electrode processes. The working principles of the electrochemical energy devices such as water electrolyzers, polymer electrolyte membrane fuel cells (PEMFCs), and rechargeable metal-air batteries (RZABs) along with their advantages and system-level limitations are discussed in **Chapter 1**. This chapter discussed the strategies adopted for designing the various electrocatalysts by using the 3D graphene support for both oxygen reduction reaction (ORR) and oxygen evolution reaction (OER) for the energy applications. **Chapter 2** discussed the development of a low-cost OER electrocatalyst based on the NiFe-LDH (Layered Double Hydroxide) nanostructures supported by the N-doped entangled graphene framework (NiFe-LDH/NEGF). **Chapter 3** deals with the development of Co_3O_4 nanorod bearing NEGF ($\text{Co}_3\text{O}_4/\text{NEGF}$) as a versatile noble metal-free ORR electrocatalyst and its application as an air-electrode in the primary zinc-air battery (ZAB). **Chapter 4** introduces a bimetallic manganese-cobalt-based spinel oxide (MnCo_2O_4) supported NEGF ($\text{MnCo}_2\text{O}_4/\text{NEGF}$) as an efficient bifunctional electrocatalyst for facilitating both ORR and OER, and, thereby, as a versatile air-electrode material for the rechargeable zinc-air battery (RZAB) application. Followed by the single-electrode studies targeted the validation of the ORR and OER activities of the system, an all-solid-state RZAB could be demonstrated by employing $\text{MnCo}_2\text{O}_4/\text{NEGF}$ as the air-cathode since the 3D morphology of the catalyst helped to achieve an effective interface with the electrolyte. **Chapter 5** deals with the results pertaining to the development and demonstration of the microporous 3D graphene-supported Pt-Co alloy system ($\text{Pt}_3\text{Co}/\text{pNEGF}$) as an ORR electrocatalyst with the ability to function under the acidic conditions. The incorporation of the microporosity into the 3D graphene support helps to achieve uniform dispersion of the sub-nm-sized Pt-Co alloy (Pt_3Co) nanoparticles with improved mass activity in the ORR performance measurement in 0.1 M HClO_4 solution. **Chapter 6** summarizes the key findings presented in each working chapter of this thesis and provides future directives on the prepared catalysts for performance improvement in the electrochemical energy devices.

1) DETAILS OF THE PUBLICATIONS EMANATING FROM THE THESIS WORK

List of publication(s) in SCI Journal(s) (published & accepted) emanating from the thesis work, with complete bibliographic details

1. NiFe layered double hydroxide decorated N-doped entangled-graphene framework: a robust water oxidation electrocatalyst, Manna, N.; Ayasha, N.; Singh, S. K.; Kurungot, S. *Nanoscale Adv.*, **2020**, 2, 1709-1717.

2) DETAILS OF OTHER PUBLICATIONS NOT RELATED TO THESIS WORK

Research articles

1. An Efficient and Durable Oxygen Reduction Electrocatalyst Based on CoMn Alloy Oxide Nanoparticles Supported Over N-Doped Porous Graphene, Singh, K. S.; Kashyap, V.; Manna, N.; Bhanage, S. N.; Sony, R.; B. Rabah; S, Sabine.; Kurungot, S. *ACS Catalysis*, **2017**, 7, 6700-6710.

2. Zinc-Air Batteries Catalyzed Using Co₃O₄ Nanorod-Supported N-Doped Entangled Graphene for Oxygen Reduction Reaction, Manna, N.; Singh, S. K.; Kharabe, P. G.; Torris, A.; Kurungot, S. *ACS Appl. Energy Mater.* **2021**, 45, 4570-4580.

3. Synergistic Electronic Coupling/Cross-talk between the Isolated Metal Halide Units of Zero Dimensional Heterometallic (Sb, Mn) Halide Hybrid with Enhanced Emission Biswas, A.; Bakthavatsalam, R.; Das, D.; Sam, J.; Mali, B.; Biswas, C.; Manna, N.; Thomson, S.; Raavi, S, S. Kumar, Kurungot, S.; Gonnade, R.; Dutta, S.; Kundu, J. J. *Mater. Chem. C*, **2022**, 10, 360-370.

4. Pseudo-Boehmite AlOOH supported NGr Composite-Based Air Electrode for Mechanically Rechargeable Zn-Air Battery Applications, Kharabe P. G; Manna, N.; Ayasha, N.; Singh, S. K.;, Mehta, S; Nair, A; Joshi, K; Kurungot, S. *Journal of Materials Chemistry A.*, **2022**, 10, 10014–10025

Patents filed:

1. **AlOOH/NGr Composite-Based Air Electrode for Primary Zn-Air Battery Applications**, Kharabe P. G; Ayasha, N.; Manna, N.; Singh, S. K.; Kurungot, S. (Invention Disclosure: 2021-INV-0019).

2. **Electrocatalyst for All-Solid-State Rechargeable Zinc-Air Battery**, Manna, N.; Kurungot, S. (Invention Disclosure: 2021-INV-0018).

3) LIST OF PAPERS WITH ABSTRACT PRESENTED (ORAL/POSTER) AT NATIONAL/INTERNATIONAL CONFERENCES/SEMINARS WITH COMPLETE DETAILS

1. Poster presentation entitled “**NiFe Layered double hydroxide-Decorated N-Doped Entangled-Graphene Framework: A Robust Water Oxidation Electrocatalyst**” in Institute for Complex Adaptive Matter (ICAM), International Workshop (2017) on Electrochemistry, JNCASR, Bangalore, India.

Achievements & Publications

Abstract: Three Dimensional (3D) porous carbon materials are highly desirable for electrochemical applications owing to their high surface area and porosity. Uniform distributed porosity in the 3D architecture of the carbon support materials allows the reactant molecules to access more numbers of electrochemical active centres and simultaneously facilitate the removal of the product formed during the electrochemical reactions. Herein, we have prepared a nitrogen-doped entangled graphene framework (NEGF), decorated with the NiFe-LDH nanostructures by the in-situ solvothermal method followed by freeze-drying at high vacuum pressure and low-temperature conditions. The freeze-drying method helped to prevent the restacking of the graphene sheets, and the formation of high surface area nitrogen-doped entangled graphene (NEGF) supported NiFe-LDH. The incorporation of NEGF has significantly reduced the overpotential for the electrochemical oxygen evolution reaction (OER) in 1 M KOH solution. This corresponds to an overpotential reduction from 340 mV for NiFe-LDH to 290 mV for NiFe-LDH/NEGF to reach the benchmark current density of 10 mA cm⁻². The preparation of the catalyst is conceived through a low-temperature scalable process.

2. Presented a poster entitled “**Zinc-Air Battery Catalyzed by Co₃O₄ Nanorod-Supported N-doped Entangled Graphene for Oxygen Reduction Reaction**” in KPIT Conference on Energy & Mobility (2019) organized by the Indian Institute of Science Education and Research (IISER) Pune and KPIT, India.

Abstract: The work reported here deals with the development of an efficient non-Pt electrocatalyst for electrochemical oxygen reduction reaction (ORR) through a sequential pathway involving hydrothermal treatment followed by freeze-drying to build the desired structural architecture of the catalyst. The designed catalyst (Co₃O₄/NEGF), which contains the Co₃O₄ nanorods anchored on the surface of the 3D structured N-doped graphene, was found to be displaying higher ORR activity during single-electrode testing and demonstration of a Zn-air battery (ZAB) system. Under the hydrothermal treatment at 180 °C in the presence of ammonia, nitrogen got doped into the carbon framework of the graphene, which subsequently formed a self-assembled entangled 3D structure of graphene after freeze-drying. The hydrothermal treatment and freeze-drying processes are found to be playing vital roles in tuning the morphological and structural features of the catalyst. The doped nitrogen, apart from its favorable contribution towards ORR, helps to facilitate efficient dispersion of the oxide nanorods on graphene. Co₃O₄/NEGF displayed remarkable ORR activity in 0.1 M KOH solution, as evident from the 60 mV onset potential shift compared to the state-of-the-art Pt/C catalyst and the Tafel slope value of 74 mV dec⁻¹ vs. 68 mV dec⁻¹ for Pt/C. The ZAB fabricated by employing Co₃O₄/NEGF as the cathode catalyst was found to be an efficient competitor for the system based on the Pt/C cathode. This high performance has been credited to the controlled interplay of the governing factors such as the interfacial interactions leading to the efficient dispersion of the metal oxide nanorods, increased catalyst surface area, the cooperative effect arising from the defects present in the N-doped porous 3D-graphene, and the synergetic Interactions operating in the system.

3. Oral presentation entitled **Air-Cathode Interface-Engineered Electrocatalyst for Solid-State Rechargeable Zinc-Air Battery** in Global Webinar on Materials Science and Engineering conference organized by Global Scientific Guild, Bangalore, India.

Achievements & Publications

ABSTRACT: Solid-state rechargeable zinc-air batteries (ZABs) are gaining interest as a new class of portable clean energy technology due to their advantages such as high theoretical energy density, intrinsic safety, and low cost. It is expected that an appropriately triple-phase boundary (TPB) engineered, bifunctional oxygen reaction (OER and ORR) electrocatalyst at the air-electrode of ZABs can redefine the performance characteristics of these systems. To explore this possibility, an electrode material consisting of manganese-cobalt-based bimetallic spinel oxide (MnCo_2O_4)-supported nitrogen-doped entangled graphene ($\text{MnCo}_2\text{O}_4/\text{NEGF}$) with multiple active sites responsible for facilitating both OER and ORR has been prepared. The porous 3D graphitic support significantly affects the bifunctional oxygen reaction kinetics and helps the system to display a remarkable catalytic performance. The air-electrode consisting of the $\text{MnCo}_2\text{O}_4/\text{NEGF}$ catalyst coated over the gas diffusion layer (GDL) ensures the effective TPB and this feature works in favor of the rechargeable ZAB system under the charging and discharging modes. As an important structural and functional attribute of the electrocatalyst, the porosity and nitrogen doping in the 3D conducting support play a decisive aspect in controlling the surface wettability (hydrophilicity/hydrophobicity) of the air electrode. The fabricated solid-state rechargeable ZAB device with the developed electrode displayed a maximum peak power density of 202 mW cm^{-2} , which is significantly improved as compared to the one based on the Pt/C+ RuO_2 standard catalyst pair (124 mW cm^{-2}). The solid-state device which displayed an initial charge-discharge voltage gap of only 0.7 V at 10 mA cm^{-2} showed only a small increment of 86 mV after 50 h.

4) AWARDS & RECOGNITIONS

1. Best poster presentation award at National Chemical Laboratory, Pune on Science day 2019.
2. Received best oral presentation award, NCL Research Foundation (NCL RF), 2021.
3. CSIR-UGC NET and Junior Research Fellowship (JRF) with an all India rank of 42 (December 2015)
4. West Bengal “Swami Vivekananda Merit-Cum-Means” SCHOLARSHIP” for Higher Education (2010-2013)

5) A COPY OF ALL SCI PUBLICATION(S), EMANATING FROM THE THESIS ARE ATTACHED AT THE END OF THE THESIS.

Erratum

Cite this: *Nanoscale Adv.*, 2020, 2, 1709

A NiFe layered double hydroxide-decorated N-doped entangled-graphene framework: a robust water oxidation electrocatalyst†

Narugopal Manna,^{ab} Nadeema Ayasha,^{ab} Santosh K. Singh^c and Sreekumar Kurungot^{id}*^{ab}

Three dimensional (3D) porous carbon materials are highly desirable for electrochemical applications owing to their high surface area and porosity. Uniformly distributed porosity in the 3D architecture of carbon support materials allows reactant molecules to access more electrochemically active centres and simultaneously facilitate removal of the product formed during electrochemical reactions. Herein, we have prepared a nitrogen-doped entangled graphene framework (NEGF), decorated with NiFe-LDH nanostructures by an *in situ* solvothermal method followed by freeze-drying at high vacuum pressure and low temperature. The freeze-drying method helped to prevent the restacking of the graphene sheets and the formation of a high surface area nitrogen-doped entangled graphene framework (NEGF) supported NiFe-LDHs. The incorporation of the NEGF has significantly reduced the overpotential for the electrochemical oxygen evolution reaction (OER) in 1 M KOH solution. This corresponds to an overpotential reduction from 340 mV for NiFe-LDHs to 290 mV for NiFe-LDH/NEGF to reach the benchmark current density of 10 mA cm⁻². The preparation of the catalyst is conceived through a low-temperature scalable process.

Received 29th December 2019
Accepted 2nd March 2020

DOI: 10.1039/c9na00808j

rsc.li/nanoscale-advances

Introduction

Owing to the increased energy demand and environmental concerns, there is an urgent need to focus on alternative carbon-free fuels.¹ In this respect, fuel cells have emerged as a promising alternative technology to conventional heat engines.² However, being an electrochemical energy conversion device, their sustainability, as well as eco-friendly nature, is directly dependent on the source of the fuel, *e.g.*, H₂ (having the highest gravimetric energy density, *i.e.*, 140 MJ kg⁻¹).³ Among the various ways of H₂ generation, water splitting can be the sustainable resource of H₂.⁴ Electrochemical water splitting involves two half-cell reactions, *i.e.*, the cathodic hydrogen evolution reaction (HER) and the anodic oxygen evolution reaction (OER). However, owing to four proton-coupled four electron-transfer reactions, the OER is thermodynamically unfavourable, limiting the overall energy efficiency of these vital electrochemical areas.⁵ Currently, precious-group metal-based, *i.e.*, IrO₂- and RuO₂-based, catalysts

are the benchmark in both the acidic and alkaline medium for the OER.⁶ However, their high cost and scarcity have triggered research toward the development of low-cost and readily available active materials for scale-up utilizations.⁷ In the last few years, various earth-abundant transition metal (Mn, Fe, Co, and Ni)-based oxides, hydroxides, and alloys have been explored as promising alternatives to catalyze the OER in the alkaline medium.⁸⁻¹⁰ For instance, Sumboja *et al.*⁸ designed NiMn layered double hydroxides as an efficient oxygen evolution reaction electrocatalyst. In another report, Kang *et al.*¹¹ demonstrated the activity of NiFe-oxide toward the water oxidation reaction. Despite satisfactory performances, these support-free catalysts suffer from active centre agglomeration and poor electronic conductivity issues, affecting their long-term stability.¹¹⁻¹⁴ A solution for the conductivity issue is to modulate the electronic structure by *in situ* anchoring these transition metal oxides/hydroxides over cost-effective conducting supports.^{15,16} Among various cost-effective conducting supports, carbon-based materials with electrochemically favourable characteristics, *i.e.*, high electronic conductivity and surface area, have emerged as universal choices in the electrocatalysis field.^{15,16} For instance, in a recent report, Zhan *et al.*¹⁷ achieved improved activity and stability by anchoring the OER-active NiFe layered double hydroxides over nitrogen-doped graphene. Similarly, Chandrasekaran *et al.*¹⁸ also reported improved OER performance by anchoring NiFe layer double hydroxides over reduced graphene oxide.

^aPhysical & Materials Chemistry Division, CSIR-National Chemical Laboratory, Pune, Maharashtra, India. E-mail: k.sreekumar@ncl.res.in; Fax: +91-20-25902636

^bAcademy of Scientific and Innovative Research, Postal Staff College, Nehru Nagar, Ghaziabad, Uttar Pradesh-201002, India

^cFaculty of Pure and Applied Sciences, University of Tsukuba, 1-1-1 Tennodai, Tsukuba, Ibaraki 305-8573, Japan

† Electronic supplementary information (ESI) available. See DOI: 10.1039/c9na00808j



Though two-dimensional graphene and one-dimensional carbon nanotubes have emerged as convincing OER-catalyst supports, their in-depth micro-architecture has turned out to be the proficiency-limiting factor.¹⁶ For instance, theoretically, graphene provides a surface area as high as $\sim 2630 \text{ m}^2 \text{ g}^{-1}$ as well as outstanding electrical conductivity.^{19,20} However, practically, the well-known restacking issue of graphene layers affects their surface area and electronic conductivity to a large extent.²¹ Besides, CNTs suffer from low surface area, restricting sufficient active material loading, and detachment during the reaction.^{20,21} Hence, tuning the micro-architectural characteristics of the catalyst support is a key contributor to increase the active centre loading as well as its accessibility to tune the overall performance.²² Among several potential candidates, three-dimensional entangled-graphene frameworks (3D-EGFs), having a high surface area as well as electronic conductivity, are gaining enormous attention as a conducting support.^{22,23} In spite of this, 3D-EGFs with a hierarchical porous structure also serve as a promising substrate to accommodate a huge number of exposed active materials to facilitate the seamless diffusion of the electrocatalytic reaction species.^{24–26} Recently, several methods have been adopted for the designing of 3D graphene including hard and soft-template-based methods,²⁷ freeze-drying methods,³⁰ a microporous template-based CVD method^{28,30,31} and a nonporous metal-based CVD method.^{28,29}

Among all these methods, freeze-drying is found to be quite appealing as it generates plenty of homogeneous pores, and the process leads to the higher mechanical strength of the interconnected graphene network.^{27,32,33} Here, we focussed on alleviating the current performance-constraining issues of the low-cost best-performing-system. The primary activity degradation factors include insufficient electronic conductivity, poor active centre exposure, and hindered reaction species transport. By keeping all these performance-constraining factors in mind, herein, we introduce the anchoring of the nano-sized NiFe-layered double hydroxide (NiFe-LDH) over a N-doped entangled graphene framework (NEGF) to further improve the performance. The rationally designed NEGF acted as a useful active substrate to tune the electronic structure and the NiFe-LDH distribution, along with providing an architecture comprised of an open and exposed catalytic system.

Experimental section

Synthesis of the nitrogen doped entangled graphene framework (NEGF)

60 mg of graphene oxide (GO) was dispersed in a 20 ml (3 : 1) aqueous solution of ammonia (30% v/v), *via* water-bath sonication and overnight stirring. The complete solution was transferred into a Teflon-lined autoclave and kept for 12 h at 180 °C. After complete cooling to room temperature, the sample was washed with water 5–6 times to remove the excess ammonia, followed by freeze-drying to prepare the nitrogen-doped entangled graphene framework (NEGF).

Synthesis of the NiFe-LDH supported nitrogen-doped entangled graphene framework (NiFe-LDH/NEGF)

60 mg of the as-prepared GO was added to a 20 ml (3 : 1) aqueous solution of ammonia (30% v/v), *via* water-bath sonication and overnight stirring. After the complete dispersion of GO, Ni(OAc)₂·4H₂O and Fe(OAc)₂·4H₂O were added to the solution and kept stirring for another 6 h. After complete mixing of the metal ions, the reaction mixture was transferred into a Teflon-lined autoclave and heated at 180 °C for 12 h; afterward the autoclave was allowed to cool down naturally, and the sample was washed with water 5–6 times to remove the excess ammonia. This was further subjected to freeze-drying for 10 h at –52 °C under high vacuum pressure. After the completion of the freeze-drying process, the sample was collected, which adopted a flaky kind of structure.

Synthesis of unsupported NiFe-LDHs

Synthesis of NiFe-LDHs was done by adding nickel acetate and iron acetate salt into a 20 ml (3 : 1) aqueous solution of ammonia (30% v/v), and it was kept for 6 h with constant stirring. After complete mixing, the solution was transferred into a Teflon-lined autoclave and kept for 12 h at 180 °C. After complete cooling to room temperature, the sample was washed with water 5–6 times to remove the excess ammonia. The final samples were dried in an oven at 60 °C and collected.

Synthesis of Ni(OH)₂/NEGF

Synthesis of Ni(OH)₂/NEGF is the same as that of NiFe-LDH/NEGF, except for addition of iron acetate; 60 mg of graphene oxide (GO) was dispersed in a 20 ml (3 : 1) aqueous solution of ammonia (30% v/v), *via* water-bath sonication and overnight stirring.

After complete dispersion of graphene oxide, nickel acetate was added to the solution and kept for 6 h with constant stirring. After complete mixing, the solution was transferred into a Teflon-lined autoclave and kept for 12 h at 180 °C. After complete cooling to room temperature, the sample was washed with water 5–6 times to remove the excess ammonia, followed by freeze-drying to prepare the Ni(OH)₂/NEGF.

Synthesis of NiFe-LDH/NEGF (w/o)

To comparatively study the effect of freeze-drying and nitrogen atom doping on the carbon support, we have synthesized NiFe-LDHs over the nitrogen-doped graphene without freeze-drying, which is named NiFe-LDH/NGF (w/o). Synthesis of NiFe-LDH/NEGF (w/o) is the same as that of NiFe-LDH/NEGF, except that here instead of using freeze-drying, the sample was dried by filtration after hydrothermal treatment for 12 h at 180 °C.

Synthesis of NiFe-LDH/EGF

Instead of ammonia, only water is used to study the effect of nitrogen-doping, and the sample is named NiFe-LDH/EGF. Synthesis of NiFe-LDH/EGF is the same as that of NiFe-LDH/NEGF, except that here instead of using ammonia solution only



water is used as the solvent, followed by solvothermal treatment for 12 h at 180 °C and applying the freeze-drying method.

Results and discussion

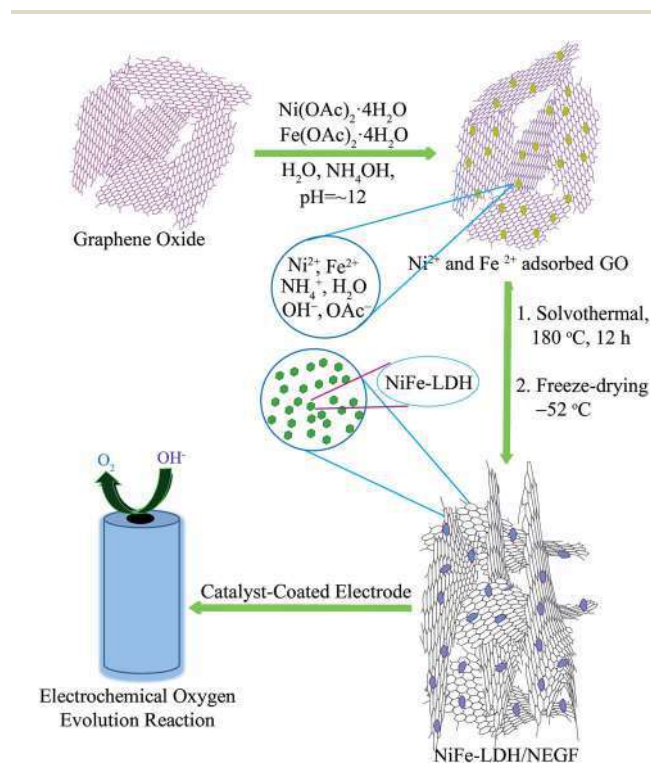
The preparation procedure for the homogeneously distributed NiFe-LDH over the NEGF involves two steps, as illustrated in Scheme 1. The reaction mixture was first treated solvothermally followed by lyophilization under high vacuum and low temperature (−52 °C) conditions. The adopted lyophilization process helped to prevent the graphene sheet-restacking under these experimental conditions, generating an entangled graphene framework by the crosslinking of the graphene sheets.²⁹ The interesting role played by ammonium ions is that they help in the strengthening of the graphene hydrogel along with nitrogen doping at a temperature as low as just 180 °C under the solvothermal conditions.³⁴ Ammonium hydroxide enhances the interaction between two graphene sheets with its alkaline hydroxyl groups and ammonium ions.

Formation of the hierarchical NEGF was first examined through field-emission scanning electron microscopy (FESEM). Fig. 1a presents the FESEM image of the NEGF, showing the 3D entangled network, formulated with randomly oriented graphene nanosheets. Such an entangled 3D framework not only prevented the agglomeration of the graphene nanosheets but it also provided high surface area as well as the porosity to the matrix. It, henceforth, facilitated the easy migration of reactants and gaseous products released during the electrochemical

reactions.^{24,25} Such a type of interconnected graphene framework is also retained during the *in situ* loading of the active material, *i.e.*, NiFe-LDHs, as shown in Fig. 1b. Fig. 1c shows the FESEM image of the NiFe-LDH-anchored nitrogen-doped graphene without the freeze-drying step, presenting a well-defined agglomerated morphology with thick and stacked graphene patches. Hence, FESEM analyses support the role of lyophilization to prevent the restacking of the graphene nanosheets, assisted by the water removal under the high vacuum and low-temperature conditions.

Next to FESEM, transmission electron microscopy (TEM) analysis was performed to find out the size and distribution of the decorated NiFe-LDH over the graphene sheets. Fig. 1d and e present the TEM images of NiFe-LDH/NEGF at different magnifications. The TEM analyses revealed a homogeneous distribution of the layered double hydroxide nanostructures over the NEGF. The further magnified TEM image in Fig. 1f shows that the anchored LDH nanostructures are well-resolved and amorphous in nature. The amorphous nature of the anchored NiFe-LDH is further supported by the diffused ring pattern in selected area electron diffraction (SAED) analysis (inset of Fig. 1f). The role of N-doping toward facilitating the homogeneous distribution of the metal hydroxides over the NEGF is also studied by comparatively analyzing the TEM images of NiFe-LDH-anchored N-doped and un-doped entangled graphene frameworks (EGFs). Fig. S1a and b† present the TEM image of the NiFe-LDH-supported un-doped EGF, showing the larger agglomerates of NiFe-LDHs over the support sheets. This finding shows the crucial role played by N-doping in creating plenty of metal anchoring sites along with the tuning of the size of LDH nanostructures as well as in avoiding their agglomeration.^{34,35} Furthermore, to study the need for supports for decorating discrete active LDH nanostructures, TEM analysis was extended to a support-free NiFe-LDH system. The comparative study showed that in the absence of any substrate, LDHs show more chances of agglomeration and acquiring a bulky morphology (Fig. S2a and b†). We have further extracted the weight % and atomic % of various species present in the sample and the corresponding data are presented in Fig. S3,† a table for respective elements shown in Table S1.†

To further understand the role of freeze-drying in improving the surface area as well as increasing the number of porous channels, specific surface area and pore size distribution were evaluated by nitrogen adsorption–desorption isotherm analysis. A BET surface area value of 547 m² g^{−1} (Fig. S4†) obtained for the NEGF confirms the highly open and porous structure of the NEGF, supporting the FESEM findings. The BET surface area measurement was also carried out to find out the benefit of freeze-drying over the without freeze-drying (w/o) sample. Both NiFe-LDH/NEGF and NiFe-LDH/NG (w/o) show type-IV isotherms (Fig. S5†). However, the BET analysis of NiFe-LDH/NEGF evidenced the essential role played by freeze-drying in maintaining a highly porous and exposed surface of the catalyst. It is reflected both through the surface area obtained, *i.e.*, 328 m² g^{−1}, and porosity from the pore size distribution profile, giving the distribution of pores in the range of 2 to 5 nm (Fig. 2a). These results further guarantee the individual



Scheme 1 Schematic representation of the synthesis of the NiFe-LDH-anchored N-doped 3D entangled graphene framework (NiFe-LDH/NEGF) and its application as an efficient OER electrocatalyst.



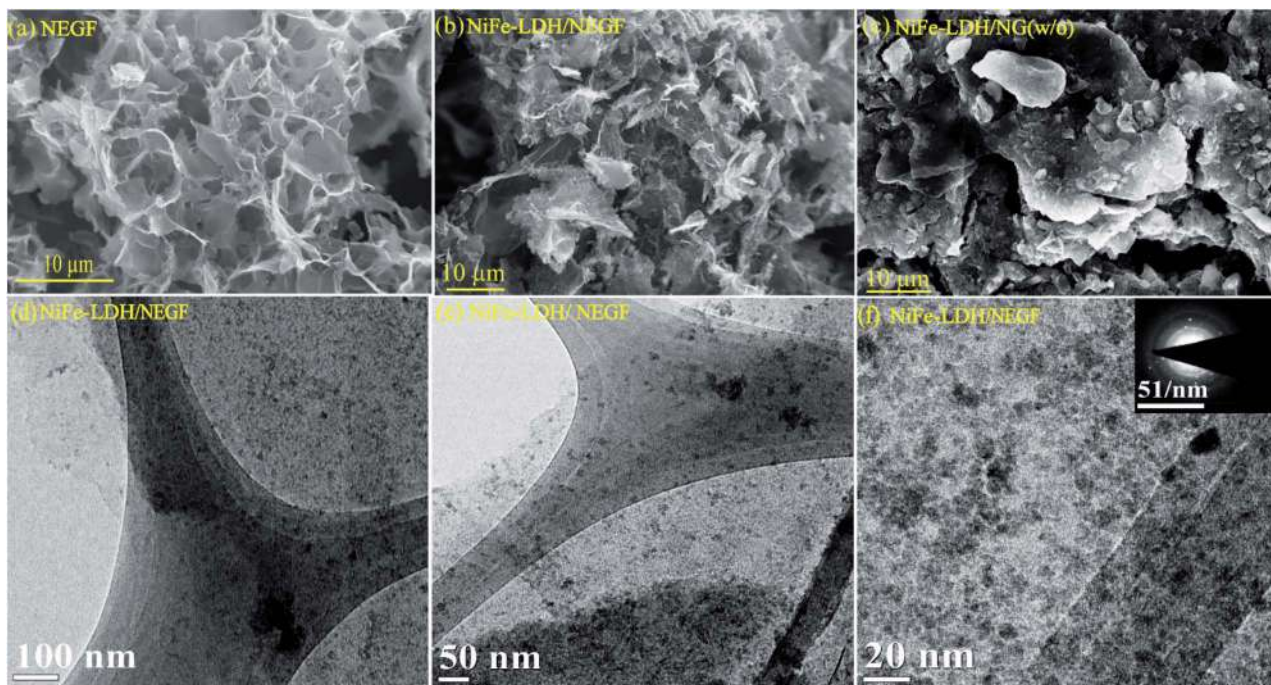


Fig. 1 FESEM images of (a) NEGF; (b) NiFe-LDH/NEGF; (c) NiFe-LDH/NEGF (w/o); (d), (e), and (f) the TEM images of NiFe-LDH/NEGF at different magnifications.

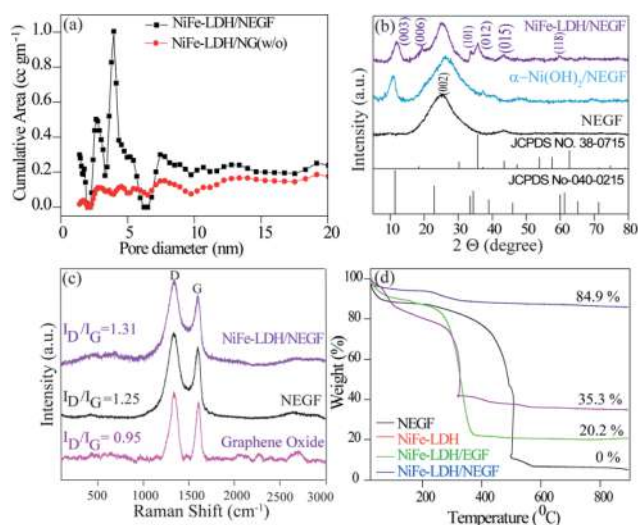


Fig. 2 Comparative physical characterization of the as-prepared catalysts: (a) pore-size distribution profiles of the NEGF and NiFe-LDH/NEGF, (b) PXRD patterns of the NEGF, α -Ni(OH)₂, and NiFe-LDH/NEGF, (c) Raman spectra of GO, the NEGF and NiFe-LDH/NEGF and (d) TGA profiles.

graphene sheets into the bulk structure. Notably, the surface area of the NEGF is found to be higher than that of NiFe-LDH/NEGF ($547 \text{ m}^2 \text{ g}^{-1}$ vs. $328 \text{ m}^2 \text{ g}^{-1}$), which is obvious owing to the blockage and covering of some of the pores of the NEGF through the as-grown NiFe-LDH nanostructures. As shown in Fig. 2a, NiFe-LDH/NEGF shows the higher cumulative area in the pore size range of 2 to 5 nm, suggesting the mesoporous

nature of NiFe-LDH/NEGF. However, the pore-size distribution profile of NiFe-LDH/NEGF (w/o) showed decreased intensity in the above-mentioned pore-size region, supporting the role of freeze-drying in making open and exposed catalyst frameworks. Pore size distribution analysis is also extended on the NEGF, presenting a pore size distribution profile similar to that of NiFe-LDH/NEGF (Fig. S4b[†]). To make a better understanding of the contribution of different parameters towards catalytic performance, the catalyst BET surface area measurement results of all the samples are presented in Fig. S6[†] and the corresponding data are presented in Table S2.[†]

To identify the phase and crystallinity of the as-synthesized samples, X-ray diffraction (XRD) analysis was performed. Fig. 2b consists of the comparative XRD pattern for the NEGF and NiFe-LDH/NEGF. The PXRD pattern for the NEGF shows an intense peak at a 2θ value of 26° , corresponding to the (002) diffraction peak of the reduced graphene oxide.²⁶ The PXRD pattern of NiFe-LDH/NEGF shows a comparatively intense and prominent (001) plane, matching well with the JCPDS Card no. 040-0215. NiFe-LDH/NEGF also shows a broad and intense (002) plane of the NEGF, attributing to the anchoring of NiFe-LDHs over the NEGF. To study the role of Fe incorporation in the Ni-hydroxide crystal structure, the growth of nickel hydroxide over the nitrogen-doped entangled graphene framework (NEGF) has been realized under the same reaction conditions and abbreviated as α -Ni(OH)₂/NEGF. Comparative PXRD patterns of α -Ni(OH)₂/NEGF and NiFe-LDH/NEGF suggested the increased orderness of the hydroxide layers after the Fe incorporation into the α -Ni(OH)₂ crystal structure owing to the poor intensity of hydroxide peaks in the former case.^{36,37}



Next to the crystal phase identification, Raman analysis was conducted to investigate the graphitization and defect extent in the microstructure of the synthesized graphene-based material. Fig. 2c comprises the comparative Raman spectra of graphene oxide (GO), the NEGF, and NiFe-LDH/NEGF. The spectra show that the typical peaks for all the samples are located in the range of 1300 and 1600 cm^{-1} , which is due to the stock phonon interaction of the carbon materials created by the laser excitation.³⁶ In all the comparative samples, the intense peak at 1320 cm^{-1} is due to the defective (D) nature of the carbon, including disorders in bonding, heteroatom doping and vacancies in the carbon lattice.³⁷ As shown in Fig. 2c, another intense peak which appeared in the range of 1580 to 1600 cm^{-1} is attributed to the graphitic nature of the carbon,³⁸ indicating the ordered lattice structure from the vibration of the Csp^2 in the plane.³⁹ The intensity ratio of the defective carbon peak to the graphitic carbon peak, *i.e.*, the I_D/I_G ratio, helps to find out the extent of defects/disorderness and graphitization extent in carbon-based materials.^{34,39} The I_D/I_G values for the NEGF (1.31) and NiFe-LDH/NEGF (1.25) are higher than those of GO (0.95), suggesting the GO reduction to reduced graphene oxide during the hydrothermal treatment. Besides, higher intensity of the defective carbon for the NEGF and NiFe-LDH/NEGF shows a decrease in the average size of the sp^2 domains due to the removal of the oxygen-containing functional groups and doping of nitrogen (N) atoms over the carbon atom.^{34,41} Higher defects and disorders over the carbon support help to generate plenty of nucleation sites for the nanoparticle growth, their controlled homogeneity, and size distribution.⁴¹

After confirming the highly open and entangled graphene framework characteristics of the NEGF along with the good active material dispersion over the NEGF, thermogravimetric analysis (TGA) was employed to determine total active material loading over the NEGF. TGA was carried out by annealing the sample from 25 to 900 $^{\circ}\text{C}$ with a scan rate of 5 $^{\circ}\text{C}$ per minute in an oxygen atmosphere. Fig. 2d presents the TGA curves for the NEGF, NiFe-LDH, NiFe-LDH/NEGF, and NiFe-LDH/EGF. For all the compared samples, an initial weight loss was observed at around 100–150 $^{\circ}\text{C}$, owing to the evaporation of physisorbed water molecules. The NEGF contains only a composite of nitrogen and oxygen and major content of carbon, which starts burning at around 400 $^{\circ}\text{C}$, and near 500 $^{\circ}\text{C}$ complete calcination is observed in an oxygen atmosphere. This complete conversion of carbon and nitrogen to mixed oxide products drawn away in the form of gas, so the rest of the sample weight becomes zero. In the case of NiFe-LDHs, no such major weight loss was observed. However, in the other two supported systems, *i.e.*, NiFe-LDH/NEGF and NiFe-LDH/EGF, reasonable water loss is encountered owing to the presence of LDHs and porous carbon having larger accessibility for a physisorbed water molecule. In the two later samples, major weight loss in the temperature region of 350 to 500 $^{\circ}\text{C}$ might be due to the oxidation of carbon. As it is already illustrated in the Raman analysis section, nitrogen doping over the carbon surface helps to create plenty of metal-binding sites, which increases the metal support interactions.⁴⁴ This can be further supported by the TGA data. As seen from Fig. 2d, NiFe-LDH/NEGF shows comparatively

higher active material loading ($\sim 35\%$) than NiFe-LDH/EGF ($\sim 20\%$). This strongly anchored and higher active material loading may help in improving the electrocatalytic activity and durability.⁴²

The electronic structure tuning of all the surface elements, *i.e.*, N-doping over the carbon support, binding energy change due to the catalyst support interactions and formation of NiFe-LDHs, is thoroughly analyzed by employing X-ray photoelectron spectroscopy (XPS) measurements. Fig. 3a presents the survey spectra of the NEGF and NiFe-LDH/NEGF, confirming the presence of Ni, Fe, O, N, and C in NiFe-LDH/NEGF and N, O and C in the NEGF. In both cases, common elements are C, O, and N, having binding energy located at around ~ 284.8 , ~ 531.5 and ~ 400.5 eV, respectively.^{43–45} In the case of NiFe-LDH/NEGF, two new peaks are present at ~ 710.8 and ~ 855.6 eV corresponding to the elements Fe and Ni, respectively.^{46–48} From Fig. 3a, it is apparent that the surface composition of carbon and nitrogen is decreased in NiFe-LDH/NEGF, which is due to the coverage of NiFe-LDHs over the nitrogen-doped carbon. However, the O 1s peak is found to intensify after the NiFe-LDH loading, basically coming from the hydroxide moieties as well as intercalated carbonate and water species.^{40–42}

Furthermore, by high-resolution XPS, the NEGF and NiFe-LDH/NEGF are comparatively analyzed in the C 1s, N 1s, and O 1s core regions. Various chemical states of carbon, *i.e.*, C–C, C=C (284), C–O (286), and C–N/C=N (400), with different binding energy values owing to the unique chemical environment of carbon are marked in the respective figures (Fig. S7a and b†).^{43,44} The C 1s spectrum of NiFe-LDH/NEGF showed an additional CO_3^{2-} anion peak at 289.8 eV, indirectly illustrating the growth of layer double hydroxides over the NEGF.^{46–48} Subsequently, a deconvoluted O 1s core level spectrum was comparatively examined for both the NEGF and NiFe-LDH/

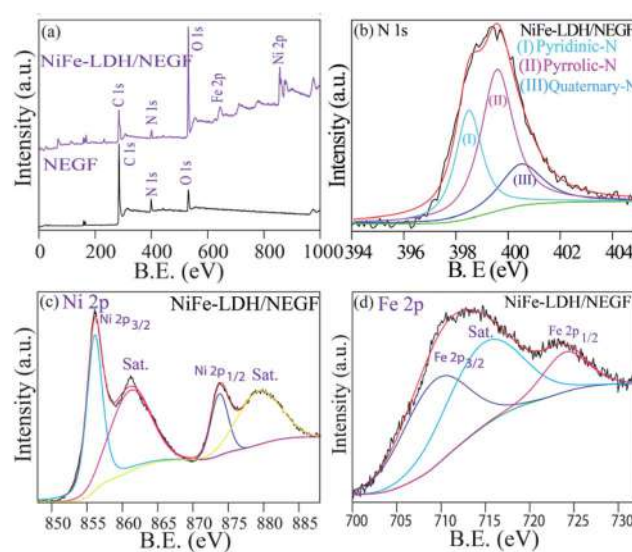


Fig. 3 XPS analysis: (a) XPS survey scan spectra of the NEGF and NiFe-LDH/NEGF. Panels (b), (c) and (d) show the high-resolution deconvoluted spectra of N 1s, Ni 2p and Fe 2p of NiFe-LDH/NEGF, respectively.



NEGF, as given in Fig. S5c and d.† In the NEGF, oxygen binds with carbon in the form of C–O and C=O, and by epoxy group formation. However, in the case of NiFe-LDH/NEGF, O 1s spectra show quite good disparity owing to the surface rich layer double hydroxide (LDH), having oxygen coordinated in the form of Ni(OOH), Fe–OH, and Ni–OH and in the carbonate or lattice H₂O form. Deconvoluted N 1s spectra of the NEGF and NiFe-LDH/NEGF are also examined to know the types of nitrogen present in the graphene matrix along with their total percentage. The N 1s spectrum of the NEGF in the ESI (Fig. S7e†) shows a higher percentage (42.4%) of pyrrolic-N (399.7 eV) and almost similar percentage (41.6%) of pyridinic-N (398.6 eV) nitrogen along with a lower quantity (15.9%) of quaternary-N (400.5 eV); furthermore, the N 1s spectrum of NiFe-LDH/NEGF is also deconvoluted to find out any change in the XPS spectrum after the NiFe-LDH loading over the NEGF. Fig. 3b shows the deconvoluted N 1s spectrum locating all the deconvoluted peaks which are present in the NEGF, suggesting that N-doping in the graphene matrix remains the same during the *in situ* loading of NiFe-LDHs. For comparison, along with the obtained data we have presented the previously reported data in Table S3 in the ESI.† Thus, deconvoluted XPS spectra of C 1s, O 1s, and N 1s clearly show the solvothermal-assisted reduced graphene oxide formation as well as layer double hydroxide growth. The survey spectrum of NiFe-LDH/NEGF also shows two extra peaks corresponding to the Ni 2p and Fe 2p core level (Fig. 3a). These core level spectra were deconvoluted to study their chemical state in the LDH system. Fig. 3c presents the deconvoluted Ni 2p spectrum of NiFe-LDH/NEGF, showing the two main spin–orbit doublets of Ni, *i.e.*, Ni 2p_{3/2} (873.3 eV) and Ni 2p_{1/2} (855.6 eV) along with two bands. The binding energy value of these two doublets suggests the +2 oxidation state of Ni in the NiFe-LDH system.^{48,49}

There is a strong interaction between the supported NiFe-LDH and the N dopant of the graphene. Due to the electronegativity difference between the N dopant and NiFe, there will be electron transfer between these two entities. The comparable XPS spectra of NiFe-LDH and NiFe-LDH/NEGF shown in Fig. S8† clearly show a shift in the binding energy of the metals evidencing the electron transfer from the nitrogen dopant to the metal, which is responsible for the reduction in B.E. Fig. 3d presents the deconvoluted XPS spectra of NiFe-LDH/NEGF in the Fe 2p core level. It exhibits two prominent spin–orbit doublets located at 710.9 and 725.1 eV corresponding to Fe 2p_{3/2} and Fe 2p_{1/2}, splitting for the Fe³⁺ oxidation state, respectively.^{50,51} Hence, deconvolution, as well as binding energy assignment of the different spin states of Ni and Fe core-level spectra, has helped to find out the oxidation states of the two elements in LDHs.

Electrochemical oxygen evolution reaction

All the employed physical characterization techniques conclude the formation and favorable characteristics of NiFe-LDH/NEGF in catalyzing the water oxidation; half-cell electrochemical analyses were carried out by employing various techniques, *e.g.*, electrochemical surface area (ECSA) measurement, linear sweep

voltammetry (LSV) and chronoamperometry. All the analyses were carried out using Hg/HgO as a reference electrode in 1 M KOH, which was further calibrated to RHE using a standard calibration method.⁴⁹ All the polarization curves were recorded after an ohmic potential drop (*iR*-drop) compensation by 65%. Comparative ECSA values were first examined to find out the accessible active center density of the various employed catalysts. For platinum-free systems, double-layer capacitance (C_{dl}) in the non-faradaic region is the reasonable parameter to measure the ECSA.⁵⁰ Fig. 4a and S9† show the higher double-layer capacitance (C_{dl}) values possessed by NiFe-LDH/NEGF (7.9 mF cm⁻²), as compared to those of the other two samples, *i.e.*, for NiFe-LDH/NG (w/o) (3.7 mF cm⁻²) and NiFe-LDH (1.0 mF cm⁻²). This suggests higher charge accumulation as well as electrolyte infiltration on the highly exposed and open texture of the catalyst system (NiFe-LDH/NEGF). Fig. 4b presents the polarization curves recorded for the oxygen evolution reaction (OER). The overpotential observed at a current density of 10 mA cm⁻² for NiFe-LDH/NEGF (290 mV) is lower than that of NiFe-LDHs (350 mV), NiFe-LDH/NG (w/o) (340 mV), and 20% RuO₂/C (310 mV). The higher electrocatalytic activity of NiFe-LDH/NEGF toward the OER, as compared to that of NiFe-LDHs clearly reveals the effect of the NEGF support on distributing the active NiFe-LDH homogeneously and also alleviates the active center agglomeration. Moreover, the effect of freeze-drying is also reflected from the polarization plots, representing poor activity of the without freeze-drying sample (*i.e.*, NiFe-LDH/NG (w/o)). All the catalysts composed of Ni has a characteristic oxidation peak just before starting the OER process but due to higher OER current in LSV these peaks are not prominently visible. However, after zooming the oxidative region these peaks can be visualized prominently as shown in Fig. S11.† The oxidation peak at 1.4 V is derived from the oxy hydroxyl formation of the NiFe active sites. This peak appears mostly in the Ni based systems. When Ni is mixed with Fe, the intensity of the peak is enhanced by the redox active metal centers. As the conductivity and activity of the NiFe system become low, during oxy hydroxyl ion formation, current generated will not be much significant. In the case of the carbon supported systems *viz.* NiFe-LDH/NG (w/o) and NiFe-LDH/NEGF, intense peaks should appear. In the case of the without freeze drying system, NiFe-LDH/NG (w/o), activity is too low compared to NiFe-LDH/NEGF. Hence, the peak at 1.4 V for the NiFe-LDH/NG (w/o) system is not a prominent one. On the other hand, in the case of NiFe-LDH/NEGF, the activity is high and so is the intensity of the peak at 1.4 V when all the synergy works well for this system. Hence, in the case of NiFe-LDH/NG (w/o), the self-assembly texture gets collapsed, restricting the active center accessibility. Further, the role of N-doping in designing a robust catalyst can also be studied by comparatively analyzing the OER activity for NiFe-LDH/NEGF and NiFe-LDH/EGF (w/o) (without N-doping in the carbon support matrix). Fig. S10† presents the lower performance of NiFe-LDH/EGF (370 mV) as compared to that of NiFe-LDH/NEGF (290 mV). The reason for such a performance variation substantiates the role of nitrogen doping, which provides better interaction of the active material with the support as well as its better active



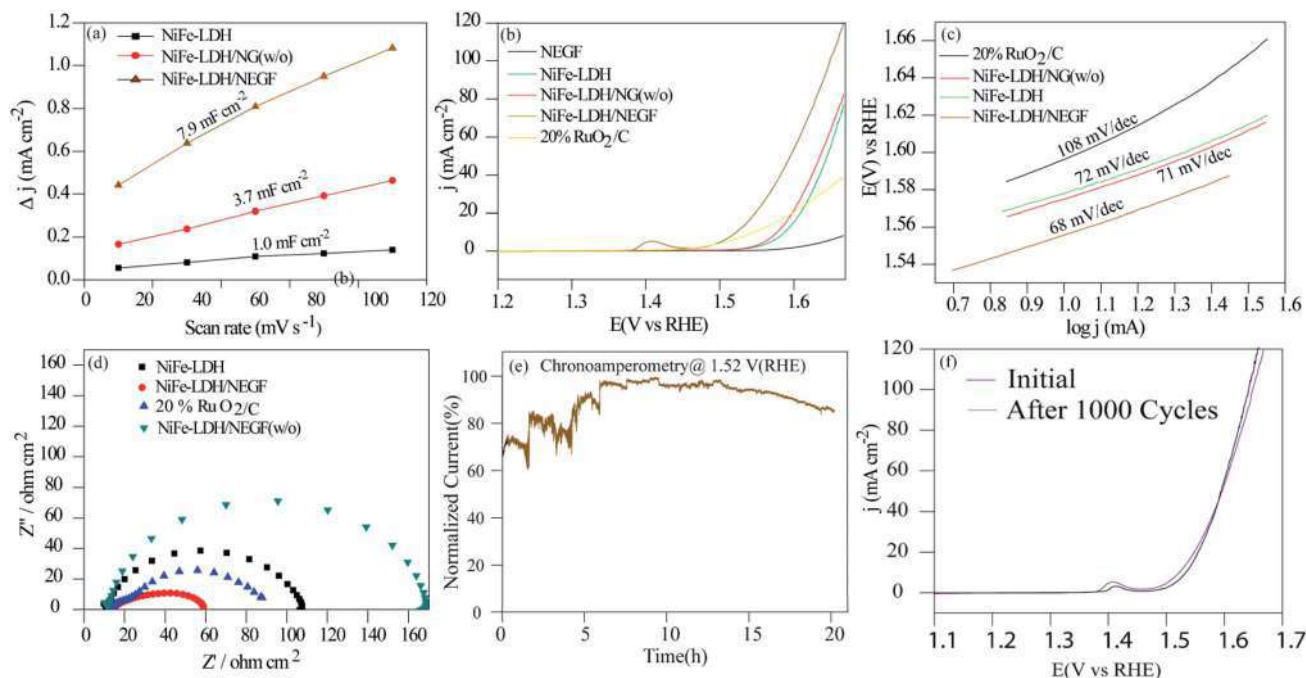


Fig. 4 Electrochemical analysis of the as-synthesized catalysts in 1 M KOH: (a) comparative plots of the scan rate dependent double layer capacitive current density (C_{dl}) at 0.91 V vs. RHE; (b) the OER polarization curves recorded at the 10 mV s^{-1} scan rate and 1600 rpm of the working electrode; (c) Tafel plots; (d) Nyquist plots recorded for NiFe-LDH, NiFe-LDH/NEGF, 20% RuO_2/C and NiFe-LDH/NEGF (w/o) at an applied potential of 1.57 V in the AC frequency range between 100 kHz and 0.1 Hz; (e) chronoamperometric stability test for NiFe-LDH/NEGF; (f) LSV plots recorded over NiFe-LDH/NEGF before and after the 1000 CV cycles.

material dispersion properties. Hence, N-doping helps to improve the electrocatalytic activity by controlling the particle size as well as facilitating a higher catalytically active center loading. Table S3 in the ESI† summarizes the performance of the various employed catalysts.

Kinetics for the adsorption of the reactant and intermediates as well as desorption of the product, *i.e.*, O_2 over the catalytic site, can be examined by Tafel analysis. A lower Tafel slope defines faster reaction kinetics, low overpotential, and higher kinetic current density.^{51,52} The Tafel slope was obtained by plotting the log of current density ($\log j$) vs. potential (V) in the OER potential range. The comparative Tafel plots for NiFe-LDH/NEGF (68 mV dec^{-1}), NiFe-LDH (72 mV dec^{-1}), NiFe-LDH/NEGF (w/o) (72 mV dec^{-1}) and 20% RuO_2/C (68 mV dec^{-1}) have been shown in Fig. 4c. The lower Tafel value for NiFe-LDH/NEGF indicates better OER kinetics as compared to that of the other catalysts. To further determine the kinetics of the electron transport in various employed catalysts, the faradaic impedance analysis at a particular potential (1.57 V) was performed. N-doping in the graphitic carbon matrix is expected to give better electrochemical activity compared to the system without nitrogen doping due to electronic structure modulation of the catalysts. In the revised manuscript, we have included the electrochemical impedance measurement data in Fig. S12 in the revised ESI,† which clearly shows a smaller charge transfer resistance (RCT) for N-rGO. This result stands out as direct evidence of faster charge transfer during the catalytic OER process. The comparative Nyquist plots given in Fig. 4d show the lowest charge-transfer resistance ($R_{ct} = 46 \text{ ohm cm}^2$) in the

case of NiFe-LDH/NEGF as compared to other catalysts, RuO_2 ($R_{ct} = 86 \text{ ohm cm}^2$), NiFe-LDH ($R_{ct} = 107 \text{ ohm cm}^2$), and NiFe-LDH/NEGF ($R_{ct} = 159 \text{ ohm cm}^2$). The lower R_{ct} value indicated better electronic transport throughout the catalyst system owing to a better interaction of NiFe-LDHs with the N-doped entangled framework of graphene.

The durability of the catalyst is another vital parameter to define its robustness, basically its lifetime. The durability of the catalyst was measured by performing chronoamperometry and cycling durability. The chronoamperometric test was performed at a constant potential (a potential needed to achieve a current density of 10 mA cm^{-2}) with a continuous rotation of the working electrode as 1600 rpm. Fig. 4e presents quite good stability of the designed catalyst and shows nearly 80% performance retention even after 20 h of continuous performance. Fig. 4f shows the LSV plots before and after the 1000 CV stability cycles, further supporting the higher durability of the designed catalyst. A slight increment in the current density after the cycle durability is basically due to the exposure of more and more catalytic active centers during the electrochemical cycling. Such good durability of the catalyst is attributed to the better interaction of the N-doped entangled graphene with NiFe-LDHs.

Conclusions

In this work, a solvothermal treatment followed by the freeze-drying method is proposed for the synthesis of NiFe-LDHs on the surface of the nitrogen-doped entangled graphene framework (NEGF). In the presence of ammonium hydroxide, the



formation of layered double hydroxides and nitrogen doping on the graphitic carbon skeleton are realized in a single step. Furthermore, freeze-drying helped to maintain the stable, interconnected structure of the graphene sheets, leading to the formation of the entangled structure of graphene. Establishment of high surface area N-doped entangled graphene supported NiFe-LDH has been confirmed by FESEM, TEM, XRD and BET surface area measurements. High surface area and well-maintained porous graphene has shown higher accessibility of gaseous reactants and electrolytes. Homogeneously distributed NiFe-LDH over nitrogen-doped graphene exhibited excellent performance for the oxygen evolution reaction. This promising OER catalytic activity can be ascribed to the following reasons: (1) the uniform distribution of the NiFe-LDH nanostructure in the presence of the anchoring sites on the NEGF, (2) the synergistic effect of the bimetallic double hydroxide layer and N-doped graphene and (3) homogeneous distribution of the pores over the N-doped graphene. The catalyst also exhibited outstanding catalytic stability even after 20 h of continuous operation.

Conflicts of interest

There are no conflicts to declare.

Acknowledgements

NM acknowledges the Council of Scientific and Industrial Research (CSIR), New Delhi, India, for Research Fellowship. KS acknowledges the CSIR, New Delhi, for project funding (TLP003526).

References

- 1 S. Chu and A. Majumdar, *Nature*, 2012, **488**, 294–303.
- 2 S. Chu, Y. Cui and N. Liu, *Nat. Mater.*, 2016, **16**, 16–22.
- 3 J. O. M. Bockris, *Science*, 1972, **176**, 1323.
- 4 T. E. Mallouk, *Nat. Chem.*, 2013, **5**, 362–363.
- 5 M. Görlin, P. Chernev, J. F. d. Araújo, T. Reier, S. Dresp, B. Paul, R. Krahnert, H. Dau and P. Strasser, *J. Am. Chem. Soc.*, 2016, **138**, 5603–5614.
- 6 Y. Lee, J. Suntivich, K. J. May, E. E. Perry and Y. Shao-Horn, *J. Phys. Chem. Lett.*, 2012, **3**, 399–404.
- 7 C. C. McCrory, S. Jung, J. C. Peters and T. F. Jaramillo, *J. Am. Chem. Soc.*, 2013, **135**, 16977–16987.
- 8 A. Sumboja, J. Chen, Y. Zong, P. S. Lee and Z. Liu, *Nanoscale*, 2017, **9**, 774–780.
- 9 S. K. Singh, D. Kumar, V. M. Dhavale, S. Pal and S. Kurungot, *Adv. Mater. Interfaces*, 2016, **3**, 1600532.
- 10 Q. Wang, L. Shang, R. Shi, X. Zhang, Y. Zhao, G. I. N. Waterhouse, L. Z. Wu, C. H. Tung and T. Zhang, *Adv. Energy Mater.*, 2017, 1700467.
- 11 B. K. Kang, M. H. Woo, J. Lee, Y. H. Song, Z. Wang, Y. Guo and D. H. Yoon, *J. Mater. Chem. A*, 2017, **5**, 4320–4324.
- 12 X. Li, X. Hao, A. Abudula and G. Guan, *J. Mater. Chem. A*, 2016, 11973–12000.
- 13 F. Dionigi and P. Strasser, *Adv. Energy Mater.*, 2016, **6**, 1600621.
- 14 S. Chen, S. S. Thind and A. Chen, *Electrochem. Commun.*, 2016, **63**, 10–17.
- 15 N. Chandrasekaran and S. Muthusamy, *Langmuir*, 2017, **33**, 2–10.
- 16 Y. Li, H. He, W. Fu, C. Mu, X. Z. Tang, Z. Liu, D. Chi and X. Hu, *Chem. Commun.*, 2016, **52**, 1439–1442.
- 17 T. Zhan, X. Liu, S. Lu and W. Hou, *Appl. Catal., B*, 2017, **205**, 551–558.
- 18 N. Chandrasekaran and S. Muthusamy, *Langmuir*, 2017, **3**, 2–10.
- 19 Q. Quan, X. Lin, N. Zhang and Y. J. Xu, *Nanoscale*, 2017, **9**, 2398–2416.
- 20 Y. Zhu, S. Murali, W. Cai, X. Li, J. W. Suk, J. R. Potts and R. S. Ruoff, *Adv. Mater.*, 2010, **22**, 3906–3924.
- 21 W. Ng, Y. Yang, K. van der Veen, G. Rothenberg and N. Yan, *Carbon*, 2018, **129**, 293–300.
- 22 X. Tang, Y. Zeng, L. Cao, L. Yang, Z. Wang, D. Fang, Y. Gao, Z. Shao and B. Yi, *J. Mater. Chem. A*, 2018, **6**, 15074–15082.
- 23 S. Chen, J. Duan, M. Jaroniec and S. Z. Qiao, *Angew. Chem.*, 2013, **52**, 13567–13570.
- 24 Z. S. Wu, S. Yang, Y. Sun, K. Parvez, X. Feng and K. Mullen, *J. Am. Chem. Soc.*, 2012, **134**, 9082–9085.
- 25 C. Zhu, H. Li, S. Fu, D. Du and Y. Lin, *Chem. Soc. Rev.*, 2016, **45**, 517–531.
- 26 Y. Ma, L. Sun, W. Huang, L. Zhang, J. Zhao, Q. Fan and W. Huang, *J. Phys. Chem. C*, 2011, **115**, 24592–24597.
- 27 Y. Ito, Y. Tanabe, K. Sugawara, M. Koshino, T. Takahashi, K. Tanigaki, H. Aoki and M. Chen, *Phys. Chem. Chem. Phys.*, 2018, **20**, 6024–6033.
- 28 Q. Shi, Y. Cha, Y. Song, J. Lee, I. Zhu, C. Li, X. Song, M. K. Du, D. Lin and Y. Lin, *Nanoscale*, 2016, **8**, 15414–15447.
- 29 L. Zhang, T. Wu, H. Na, C. Pan, X. Xu, G. Huang, Y. Liu, J. Gao and L. Zhang, *Ind. Eng. Chem. Res.*, 2016, **55**, 6553–6562.
- 30 A. Kong, A. Kong, X. Zhu, Z. Han, Y. Yu, Y. Zhang, B. Dong and Y. Shan, *ACS Catal.*, 2014, **4**, 1793–1800.
- 31 L. Jiang and Z. Fan, *Nanoscale*, 2014, **6**, 1922–1945.
- 32 X. Zhang, Z. Sui, B. Xu, S. Yue, Y. Luo, W. Zhan and B. Liu, *J. Mater. Chem.*, 2011, **21**, 6494.
- 33 S. H. Lee, H. W. Kim, J. O. Hwang, W. J. Lee, J. Kwon, C. W. Bielawski, R. S. Ruoff, S. O. Kim and S. H. Lee, *Angew. Chem., Int. Ed.*, 2010, **49**, 10084–10088.
- 34 S. Kabir, K. Artyushkova, A. Serov, P. Atanassov and S. Kabir, *ACS Appl. Mater. Interfaces*, 2018, **10**, 11623–11632.
- 35 R. Karunagaran, C. Coghlan, C. Shearer, D. Tran, K. Gulat, T. T. Tung, C. Doonan and D. Losic, *Materials*, 2018, **11**, 205.
- 36 N. Ayasha, V. M. Dhavale and S. Kurungot, *Nanoscale*, 2017, **9**, 12590.
- 37 M. Gao, W. Sheng, Z. Zhuang, Q. Fang, S. Gu, J. Jiang and Y. Yan, *J. Am. Chem. Soc.*, 2014, **136**, 7077–7084.
- 38 S. K. Singh, V. M. Dhavale and S. Kurungot, *ACS Appl. Mater. Interfaces*, 2015, **7**, 442–451.
- 39 I. S. Amiin, J. Zhang, Z. Kou, X. Liu, O. K. Asare, H. Zhou, K. Cheng, H. Zhang, L. Mai, M. Pan and S. Mu, *ACS Appl. Mater. Interfaces*, 2016, **8**, 29408–29418.



- 40 A. Nadeema, S. Walko Priyanka, D. R. Nandini and K. Sreekumar, *ACS Appl. Energy Mater.*, 2018, **1**, 5500–5510.
- 41 Y. Cao, S. Mao, M. Li, Y. Chen and Y. Wang, *ACS Catal.*, 2017, **7**, 8090–8112.
- 42 S. K. Singh, V. M. Dhavale and S. Kurungot, *ACS Appl. Mater. Interfaces*, 2015, **7**, 21138–21149.
- 43 S. K. Singh, V. Kashyap, N. Manna, S. N. Bhange, R. Soni, R. Boukherroub, S. Szunerits and S. Kurungot, *ACS Catal.*, 2017, **7**, 6700–6710.
- 44 Q. Xiang, Y. Liu, X. Zou, B. Hu, Y. Qiang, D. Yu, W. Yin and C. Chen, *ACS Appl. Mater. Interfaces*, 2018, **10**, 10842–10850.
- 45 S. N. Bhange, S. M. Unni and S. Kurungot, *J. Mater. Chem. A*, 2016, **4**, 6014–6020.
- 46 C. Xie, Y. Wang, K. Hu, L. Tao, X. Huang, J. Huo and S. Wang, *J. Mater. Chem. A*, 2017, **5**, 87–91.
- 47 S. K. Singh, V. M. Dhavale and S. Kurungot, *ACS Appl. Mater. Interfaces*, 2015, **7**, 442–451.
- 48 D. Mullangi, V. Dhavale, S. Shalini, S. Nandi, S. Collins, T. Woo, S. Kurungot and R. Vaidhyanathan, *Adv. Energy Mater.*, 2016, **6**, 1600110.
- 49 P. K. Gangadharan, S. M. Unni, N. Kumar, P. Ghosh and S. Kurungot, *ChemElectroChem*, 2017, **4**, 2643–2652.
- 50 V. A. Alves, L. A. da Silva and J. F. C. Boodts, *Electrochim. Acta*, 1998, **44**, 1525–1534.
- 51 V. Kashyap and S. Kurungot, *ACS Catal.*, 2018, **8**, 3715–3726.
- 52 V. M. Dhavale, S. S. Gaikwad, L. George, R. N. Devi and S. Kurungot, *Nanoscale*, 2014, **6**, 13179–13187.



Zinc–Air Batteries Catalyzed Using Co_3O_4 Nanorod-Supported N-Doped Entangled Graphene for Oxygen Reduction Reaction

Narugopal Manna, Santosh K. Singh, Geeta Pandurang Kharabe, Arun Torris, and Sreekumar Kurungot*

Cite This: *ACS Appl. Energy Mater.* 2021, 4, 4570–4580

Read Online

ACCESS |



Metrics & More



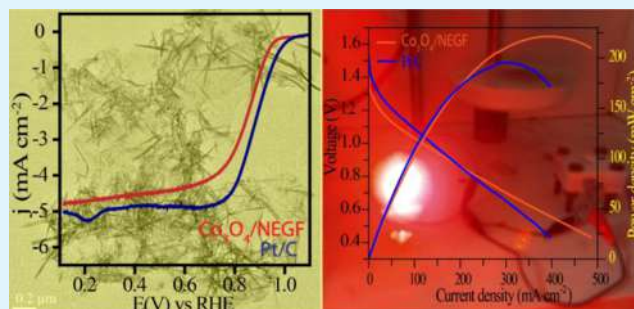
Article Recommendations



Supporting Information

ABSTRACT: The work reported here deals with the development of an efficient non-platinum electrocatalyst for electrochemical oxygen reduction reaction (ORR) through a sequential pathway involving hydrothermal treatment followed by freeze-drying to build the desired structural architecture of the catalyst. The designed catalyst (Co_3O_4 / nitrogen-doped entangled porous 3D graphene (NEGF)), which contains Co_3O_4 nanorods anchored on the surface of three-dimensional (3D)-structured N-doped graphene, was found to display higher ORR activity during single-electrode testing and demonstrate a Zn–air battery (ZAB) system. Under the hydrothermal treatment at 180 °C, in the presence of ammonia, nitrogen was doped into the carbon framework of graphene, which subsequently formed a self-assembled entangled 3D structure of graphene after freeze-drying. The hydrothermal treatment and freeze-drying processes were found to play vital roles in tuning the morphological and structural features of the catalyst. The doped nitrogen, apart from its favorable contribution toward ORR, helped facilitate efficient dispersion of oxide nanorods on graphene. Co_3O_4 /NEGF displayed remarkable ORR activity in 0.1 M KOH solution, as evident from the 60 mV onset potential shift compared to the state-of-the-art Pt/C catalyst and the Tafel slope value of 74 mV dec^{-1} vs 68 mV dec^{-1} for Pt/C. The ZAB fabricated by employing Co_3O_4 /NEGF as the cathode catalyst was found to be an efficient competitor for the system based on the Pt/C cathode. This high performance has been credited to the controlled interplay of the governing factors such as the interfacial interactions leading to the efficient dispersion of metal oxide nanorods, increased catalyst surface area, the cooperative effect arising from the defects present in the N-doped porous 3D graphene, and the synergetic interactions operating in the system.

KEYWORDS: cobalt-oxide nanorod, N-doped entangled graphene, freeze-drying, hydrothermal, oxygen reduction reaction, zinc–air battery



1. INTRODUCTION

The strategic designing of cost-effective advanced electrocatalysts with better electrocatalytic performance for the oxygen reduction reaction (ORR) has become immensely important for realizing alkaline electrolyte membrane fuel cells (AEMFCs) and metal–air batteries (MABs) as competitive candidates in the energy market.^{1,2} However, the sluggish ORR kinetics at the cathode is considered as a significant limiting factor in achieving the enhanced efficiency of energy conversion from these classes of energy devices.³ Platinum nanoparticle-supported carbon (Pt/C) materials are primarily used as electrocatalysts for promoting ORR in real systems, which are still suffering from high-cost and low stability under operating conditions.⁴ Normally, the ORR process is known to be slow; even though the ORR kinetics can be improved by increasing the Pt/C catalyst loading, this cannot be taken as a practical solution owing to the exorbitant cost of Pt catalysts.⁴ In addition, the less availability of Pt (37 ppb in Earth's crust) and its expensiveness (US\$32.4 g^{-1} as 2019 average price)

have triggered the scientific community to perform progressive work on increasing the efficiency of Pt-based catalysts or the development of highly efficient low-Pt/Pt-free catalysts.^{5,6} However, most of the reported low-Pt/Pt-free systems are unable to evolve as viable alternatives to the state-of-the-art Pt systems owing to reasons such as complicated synthesis chemistry, stability issues, and unreliable performance characteristics.^{6,7} Therefore, industries are still compelled to depend on Pt catalysts all the while indulging in active research and development efforts for developing reliable and high-performance low-cost Pt-free ORR catalysts.⁸

Received: January 20, 2021

Accepted: April 7, 2021

Published: April 20, 2021



Among the various non-Pt systems explored for ORR, extensive studies have been carried out in the last few decades focused on the nonprecious transition-metal-based oxides and hydroxides.⁹ Among the various transition-metal (Fe, Co, Mn, and Ni) systems, the oxides of cobalt received enormous attention as ORR electrocatalysts because of their favorable electronic structure.^{10–13} Based on the current advances in cobalt oxides, spinel and perovskite structures of cobalt oxides are being explored for electrochemical device applications in recent times.³ Among these, the spinel-structured cobalt oxides have gained particular interest toward electrocatalytic applications.³ The spinel structure mixed valency of Co in Co₃O₄ (i.e., Co²⁺ and Co³⁺) plays a vital role in the face-centered cubic (fcc) crystal structure.^{14,15} Moreover, in the normal spinel structure (AB₂O₄) of Co₃O₄, the mixed-valency cations are distributed in the octahedral and tetrahedral sites. In Co₃O₄, 1/8 of the tetrahedral A sites and 1/2 of the octahedral sites are occupied by Co²⁺ and Co³⁺ ions, respectively.^{14,15} The mixed valency of cobalt helps in establishing a better electron-transport mechanism and thereby toward preferable electrochemical activity.¹⁶ Furthermore, as a means to improve the intrinsic ORR characteristics, recently, shape- and size-controlled designing of metal-oxide-based catalysts has also been executed as a strategy, and interesting performance fine-tuning could be realized.^{12–14,22} Considering the fact, the shape- and size-controlled modifications of cobalt oxide nanoparticles help in achieving promising electronic enhancement, which assists to realize improved catalytic performance and durability.^{17–19} Previously, various shape- and size-controlled cobalt oxide morphologies (cubic,²⁰ truncated octahedron,²⁰ polyhedron,²⁰ and nanorod²¹) have been reported for electrocatalytic ORR processes.⁵ Among them, the nanorods of cobalt oxide have become an interesting class of the one-dimensional (1D) morphology that helps facilitate rapid charge transport and also assures adequate diffusion of the reactants.^{22,21} However, cobalt oxide-based electrodes suffer from the limitation of poor electronic conductivity, which detrimentally affects their prospects to serve as potential electrocatalysts.^{24,25} The incorporation of conducting carbon support to cobalt oxides has been adopted as a viable strategy to overcome the conductivity-related limitations of these classes of systems.^{23,25,26}

Despite promises the nanorods of Co₃O₄ offer as an effective ORR catalyst, these morphologies need to be dispersed on a carbon substrate to tackle the issues related to conductivity and aggregation simultaneously.²⁵ Among the various carbon supports, graphitic carbons show optimum activity as well as durability. There are few previous reports suggesting the synthesis of different cobalt oxide nanoparticle-based systems supported over nitrogen-doped graphitic carbon formed through various high-/low-temperature in-situ/ex-situ methods. Jasinski, et al⁴² reported the ORR activity of a cobalt-based metal–N–C catalyst prepared by the pyrolysis of cobalt phthalocyanine along with separate metal, nitrogen, and carbon precursors. Although the activity and durability of such catalysts have been improved with time, identifying the active-site structure still lagged because of the lack of the crystallographic order of metal atoms and the simultaneous presence of crystalline metal phases.⁴² Hence, high-temperature methods that control the structural and morphological features of metal centers and carbon substrates are not preferably feasible.⁴² Considering the low-temperature meth-

od, the anchoring of active catalytic sites (metal oxides) on two-dimensional (2D) graphene (Gr) has emerged as a promising strategy because of the interesting features of Gr and the desirable morphological features of Gr-based composites. For example, Gr offers a theoretical surface area as high as $\sim 2630 \text{ m}^2 \text{ g}^{-1}$ as well as excellent electrical conductivity.^{26–28,40,41} However, practically, their electrocatalytic surface area (ECSA) is affected by the Gr layers because of a well-known restacking issue.²⁹ Conventional approaches for constructing interfaces between the two different components have followed the method of epitaxial growth under solution conditions in which the substrate's crystal surface and the epitaxial interfaces should be precisely controlled.^{30,31} Nevertheless, these approaches suffer from tedious multistage processes, substantial waste of metal species, and low yields, which ultimately hinder the large-scale production of the systems.³¹

Hence, looking at the difficulties in the synthesis of Co₃O₄ nanorods along with their proper dispersion on the Gr support, we, here, report an easy and scalable procedure involving the dispersion of Co₃O₄ nanorods on nitrogen-doped entangled porous 3D graphene (NEGF) by utilizing the electronegativity difference of doped N to act as efficient anchoring sites for the metal oxide nanoparticles.³² The rationally designed NEGF functioned as an anchoring-cum-active substrate, which ensured both the homogeneous distribution of Co₃O₄ nanorods and favorable modulation toward ORR. We have introduced a sequential pathway involving hydrothermal treatment followed by freeze-drying to build the desired structural architecture of the catalyst containing a Co₃O₄ nanorod anchored on NEGF (Co₃O₄/NEGF). The realistic validation of the catalyst as a versatile cathode for Zn–air batteries (ZABs) could be subsequently performed, which is found to be competing well with a similar system based on the Pt/C catalyst.

2. EXPERIMENTAL SECTION

2.1. Materials. Cobalt acetate tetrahydrate [Co(OAc)₂·4H₂O], potassium permanganate (KMnO₄), graphite, and ammonium hydroxide (NH₄OH) were purchased from Sigma-Aldrich. Phosphoric acid (H₃PO₄) and sulphuric acid (H₂SO₄) were procured from Thomas Baker. All the chemicals were used as such without any further purification.

2.2. Synthesis of Graphene Oxide. For the synthesis of graphene oxide (GO), improved Hummer's method was employed.³³ In brevity, 3 g of graphite powder and 18 g of KMnO₄ were mixed well using a mortar and pestle. After proper mixing, the resulting powder was slowly added to the flask containing a solution of H₃PO₄:H₂SO₄ (1:9) under an ice bath environment. After complete transfer of the solid combination, the temperature of the reaction mixture was increased slowly up to 60 °C, and the mixture was continuously stirred for 12 h at a constant temperature. After completing the reaction, the mixture was held for a few hours with continuous rotation to cool to room temperature. The resulting reaction mixture was slowly poured into ice-cooled water containing 3% H₂O₂, which became a yellowish solution. Furthermore, the obtained solution was washed several times with copious amount of distilled water, followed by centrifugation at 10,000 rpm. The obtained solid residue was further washed with 30% HCl to remove any metal impurities, followed by washing with plenty of water to neutralize the acidic pH and wash off the impurities. Finally, the collected dark chocolate-colored, highly viscous solution was washed with ethanol and diethyl ether and kept in an oven for drying at 40 °C to obtain the GO powder.

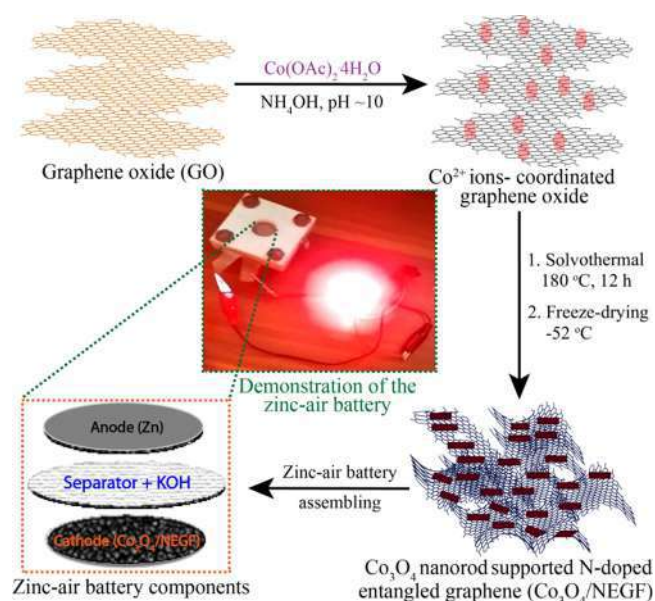
2.3. Synthesis of Co₃O₄/NEGF. For the synthesis of the active catalytic material, 90 mg of the as-prepared GO was added to 30 mL

of an aqueous solution of ammonia (30% v/v) by maintaining the ratio of 3:1 via overnight stirring and water-bath sonication. $\text{Co}(\text{OAc})_2 \cdot 4\text{H}_2\text{O}$ was added to the solution after the full dispersion of GO, and the mixture was kept on stirring for another 6 h. Initially, at a low concentration of ammonia, cobalt ions reacted with ammonia and formed $\text{Co}(\text{NH}_3)_6^{2+}$, which led to the change of the color of the solution from pink to green (see the color change of the solution in the Supporting Information, Figure S1). Further changing the pH of the solution in the presence of air causes the oxidation of $\text{Co}(\text{NH}_4)_6^{2+}$ to $\text{Co}(\text{NH}_4)_6^{3+}$. However, when the concentration of hydroxyl ions increases, Co^{3+} ions react with hydroxyl ions (as the solubility product of $\text{Co}(\text{OH})_3 = 1 \times 10^{-43}$), resulting in the formation of $\text{Co}(\text{OH})_3$.²⁰ The well-mixed reaction mixture was transferred into a Teflon-lined autoclave, and the system was kept for 12 h at 180 °C. $\text{Co}(\text{OH})_3$ facilitates the growth of the nanorod structure of Co_3O_4 during the hydrothermal treatment.²⁰ After completing the reaction, the mixture was allowed to cool to room temperature naturally, followed by washing the obtained materials with copious amount of water to eliminate the excess ammonia. The resulting sample was also vacuum freeze-dried at -52 °C for 10 h. After the freeze-drying process, the powder sample was collected, which adopted a flaky and light texture, and the sample was designated as $\text{Co}_3\text{O}_4/\text{NEGF}$. The employed method is a simple and fast process that is promising for scaling up to larger applications. For comparing the catalytic activity during electrochemical investigations, controlled samples like NEGF and Co_3O_4 nanorods were synthesized using the same methods without adding any metal precursor and graphene oxide. The detailed physical and electrochemical characterization techniques adopted for investigating the systems are mentioned in the Supporting Information (Experimental Section I.1, I.2, and I.3).

3. RESULTS AND DISCUSSION

The stepwise procedure involved in the synthesis of $\text{Co}_3\text{O}_4/\text{NEGF}$ and its applications as the cathode material for ZAB fabrication is presented in Scheme 1. The hydrothermal treatment was performed after facilitating the anchoring of cobalt (Co^{2+}) and ammonium (NH_4^+) ions on the surface of GO. The adsorption of the positively charged ions over GO is enabled because of the electronegativity difference of the oxy/

Scheme 1. Schematic Presentation of the Stepwise Synthesis Strategy Developed to Obtain the $\text{Co}_3\text{O}_4/\text{NEGF}$ Catalyst Followed by the Fabrication and Demonstration of the Zn–Air Battery



carboxy functional groups present on the GO. The GO anchored with the Co^{2+} ions was subjected to the hydrothermal treatment at 180 °C, which facilitates the in-situ formation and the dispersion of Co_3O_4 nanorods on N-doped reduced GO. This was followed by freeze-drying to establish the self-assembled structure of the metal oxide nanorods bearing NEGF. In the process, the negatively charged GO surface interacts with the positively charged metal ions and thus mobilizes their adsorption during continuous stirring at room temperature. As the hydrothermal process proceeds at high temperature and pressure, the metal ions gradually become nucleated, resulting in the formation of Co_3O_4 nanorods anchored over the N-doped reduced GO. The crucial freeze-drying step adopted subsequent to the hydrothermal process helps establish the 3D-interconnected morphology ($\text{Co}_3\text{O}_4/\text{NEGF}$), ensuring a high surface area and accessible porous architecture to the catalyst. With the help of field-emission scanning electron microscopy (FESEM), X-ray micro-CT, high-resolution transmission electron microscopy (HRTEM), and electron energy loss spectroscopy (EELS) studies, a detailed structural analysis of the prepared catalyst was carried out. As mentioned before, the freeze-drying step induces porosity in the entangled reduced GO, which could be evidenced in the FESEM images presented in Figure 1. Figure 1a represents the FESEM images of the pristine GO, which exhibits the presence of stacked graphene sheets. However, the role of the adopted freeze-drying process to accomplish the 3D interconnected nature of NEGF in bare NEGF and $\text{Co}_3\text{O}_4/\text{NEGF}$ is evident in the FESEM images presented in Figure 1b,c, respectively. The distribution of the Co_3O_4 nanorods is visible in the more focused view of the FESEM image presented in Figure S2a, ESI. This surface aligned growth points toward the influence of the oxy-functional groups of GO for facilitating the metal-ion adsorption followed by the nucleation process to accomplish the well-distributed growth of the Co_3O_4 nanorods during the hydrothermal treatment. In addition, FESEM imaging revealed the formation of a well-connected network of the nitrogen-doped graphene sheets, which originated from the self-assembling process under the reaction conditions.

To unveil the 3D microstructures of GO, NEGF, and $\text{Co}_3\text{O}_4/\text{NEGF}$, an X-ray micro-CT imaging technique has been employed (Figure 1d–f, Section S2b, ESI). The 3D micro-CT image of GO presented in Figure 1d shows randomly oriented GO sheets, which also support the findings in the FESEM image of GO (Figure 1a), validating the presence of the stacked graphene sheets in pristine GO. On the other hand, the 3D micro-CT image of NEGF (Figure 1e) shows a haystack-like structure. This points toward the vital effect of the freeze-drying method toward the formation of a porous 3D structure. Furthermore, advanced segmentation-based image analysis showed a significant amount of porosity (approximately 58%) in NEGF. The porous microstructure of NEGF has resulted in a higher surface area as compared to its precursor (GO). The 3D micro-CT image of $\text{Co}_3\text{O}_4/\text{NEGF}$ (Figure 1f) also shows the 3D spatial distribution of the Co_3O_4 particles (Figure 1f, highlighted with blue circles) over the NEGF sheets. With the aid of a gray-scale histogram and mean intensity projection (MIP), the Co_3O_4 particles present in the 3D micro-CT image of $\text{Co}_3\text{O}_4/\text{NEGF}$ are visualized separately in Figure S2b, ESI. The observed 3D micro-CT image shows the true spatial distribution of the Co_3O_4 particles over the NEGF sheets. Because of the limitations induced by the micro-

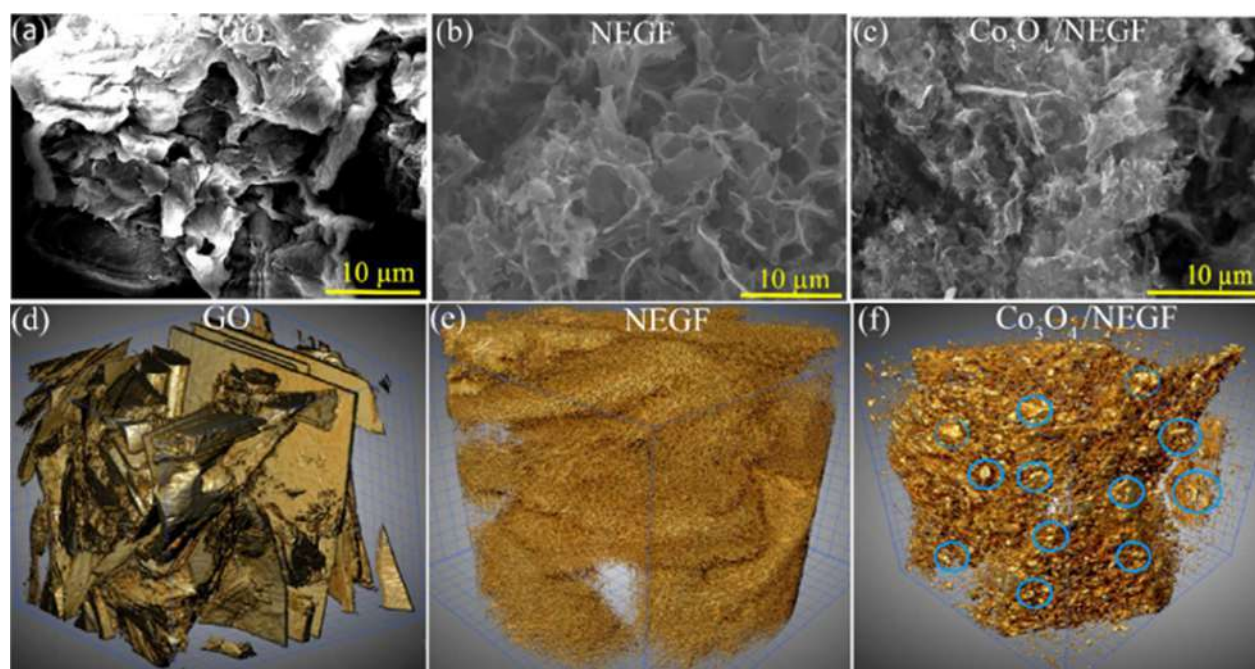


Figure 1. Field-emission scanning electron microscopy (FESEM) and the corresponding volume-rendered 3D micro-computed tomography (CT) images: (a) FESEM images of GO showing the stacked nature of the sheets in their pristine form; (b, c) FESEM images of NEGF and $\text{Co}_3\text{O}_4/\text{NEGF}$, respectively, displaying the porous architecture of the entangled 3D graphene sheets; (d) 3D micro-CT images of GO showing the randomly oriented stacks of individual GO sheets; (e) NEGF showing the microporous 3D structure of the entangled graphene; (f) Co_3O_4 with bright dots in the image representing the distribution of Co_3O_4 over the NEGF sheets, where few such dots are circled for easy recognition (grid size is 100 microns).

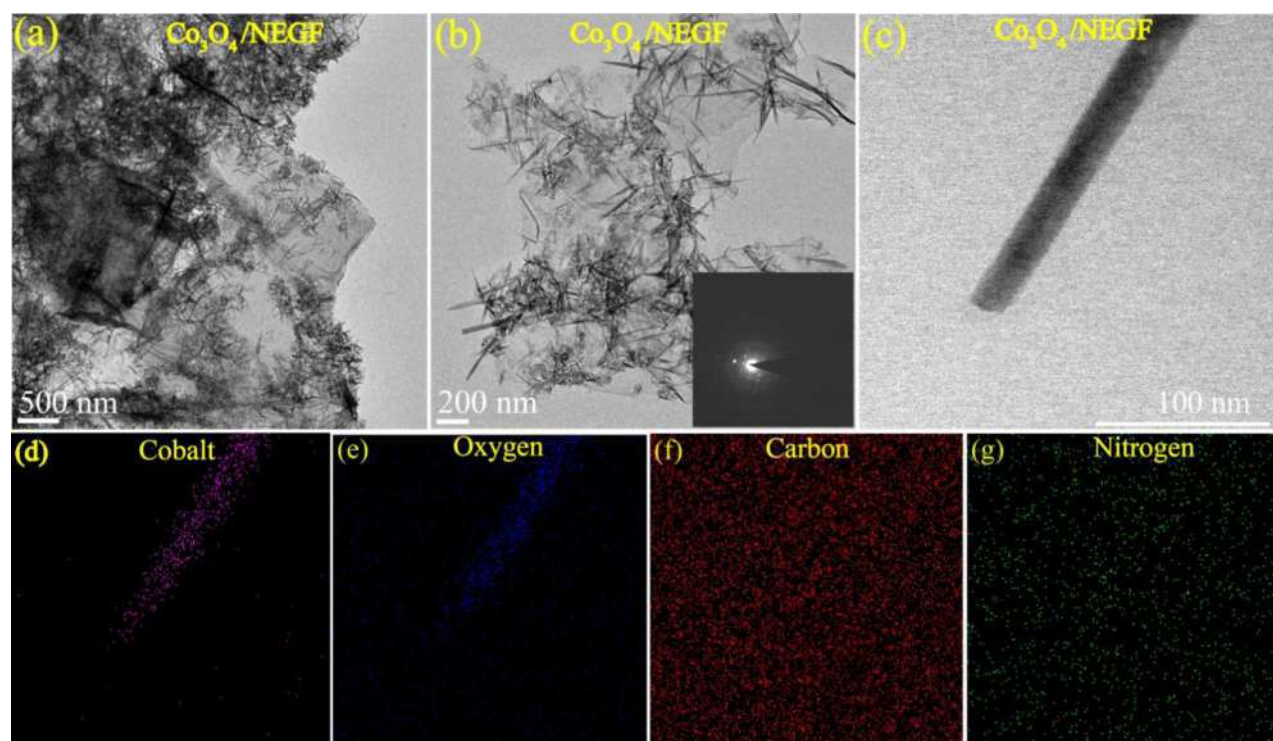


Figure 2. Transmission electron microscopy (TEM) images and the elemental mapping of $\text{Co}_3\text{O}_4/\text{NEGF}$: (a, b) TEM image of $\text{Co}_3\text{O}_4/\text{NEGF}$ displaying the distribution of Co_3O_4 nanorods over the surface of the transparent sheets of NEGF (Inset of (b): SAED pattern showing the crystalline nature of Co_3O_4); (c) focused image of a single Co_3O_4 nanorod recorded for performing elemental mapping; (d-g) elemental analysis of $\text{Co}_3\text{O}_4/\text{NEGF}$ displaying the distribution of cobalt along the focused nanorod and oxygen, carbon, and nitrogen in the system.

CT resolution (1 micron), the shape of the Co_3O_4 particles is not resolved. $\text{Co}_3\text{O}_4/\text{NEGF}$ has approximately 48% porosity,

which is 10% lower than its precursor (NEGF), and this reduction is attributed to the distribution of the metal oxide

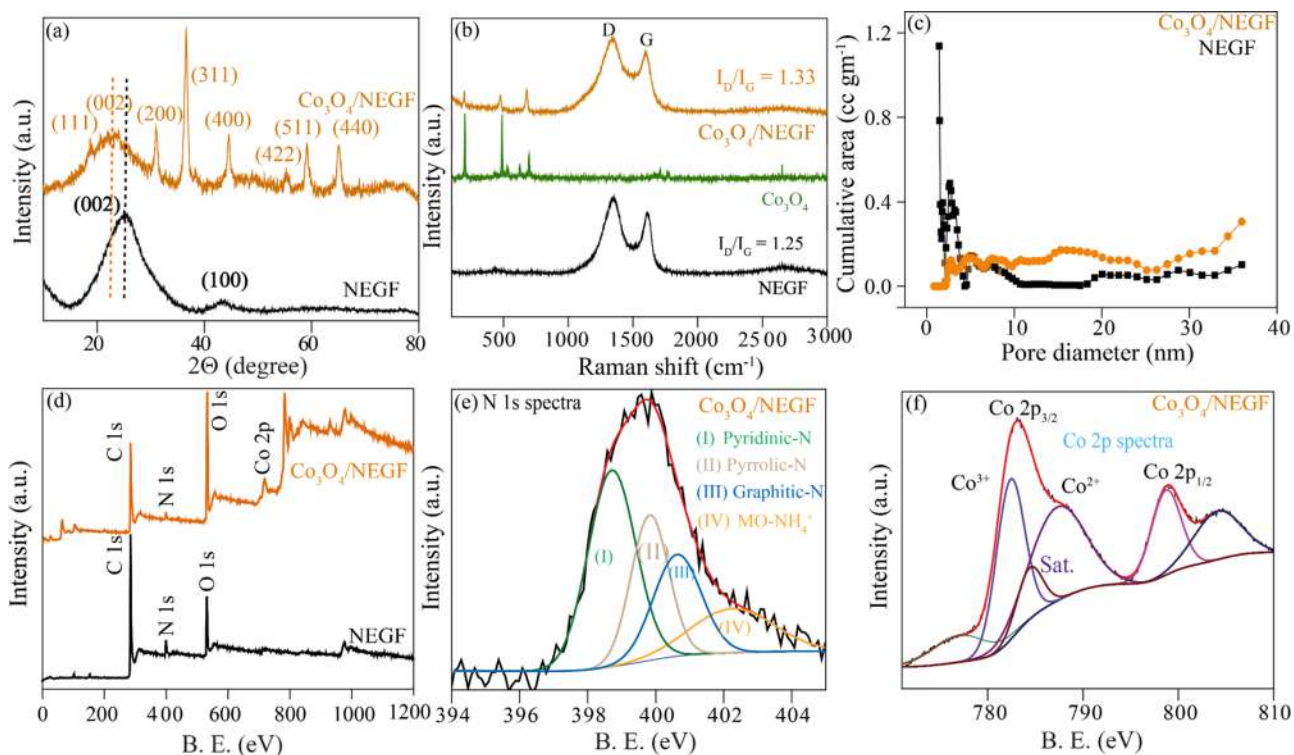


Figure 3. (a) Comparative powdered X-ray diffraction (PXRD) patterns of NEGF and $\text{Co}_3\text{O}_4/\text{NEGF}$ showing diffraction planes corresponding to the spinel lattice of the Co_3O_4 nanorods; (b) Raman spectra of NEGF, Co_3O_4 , and $\text{Co}_3\text{O}_4/\text{NEGF}$; (c) comparative pore-size distribution profiles of NEGF and $\text{Co}_3\text{O}_4/\text{NEGF}$ showing the mesoporous nature of the prepared catalyst; (d) survey scan XPS spectra of NEGF and $\text{Co}_3\text{O}_4/\text{NEGF}$ confirming the presence of C, N, O, and Co in the respective systems; (e, f) high-resolution deconvoluted XPS spectra of Co 2p and N 1s states of $\text{Co}_3\text{O}_4/\text{NEGF}$.

nanoparticles over NEGF. GO and $\text{Co}_3\text{O}_4/\text{NEGF}$ sheets showed an aspect ratio of 2:1 (length to width), as measured from their 2D micro-CT to their precursors (GO). Overall, the micro-CT images point towards the versatility of the catalyst synthesis steps in retaining the 3D structure of the products. The TEM images of $\text{Co}_3\text{O}_4/\text{NEGF}$ are shown in Figure 2a,b and Figure S3, ESI. These images clearly depict the aligned distribution of the Co_3O_4 nanorods along the surface of NEGF. It should be noted that while some rods are clearly visible on the graphene surface (Figure 2a,b), few others have a hazy appearance. The possible reason for the ambiguity in the visibility is that while the nanorods are distributed in the self-assembly structure of the entangled graphene, a significant amount would be lying toward the inner side of the graphene sheets, thereby partially masking them. The high-magnification TEM image presented in Figure 2c clearly shows the nanorod structure of Co_3O_4 . The nanorods are found to possess a length of ~ 120 nm and a radius of ~ 5 nm. The selected-area electron diffraction (SAED) pattern is shown in the inset of Figure 2b; the pattern displays a well-characterized diffraction ring corresponding to the polycrystalline nature of the Co_3O_4 nanorods.^{22,23} The observed diffraction rings are ascribed to the (002), (220), (400), (511), and (440) planes of the Co_3O_4 nanorods.^{22,23} Figure 2c, Figure S4a and b, ESI, represent the focused HRTEM images of a single Co_3O_4 nanorod recorded to perform elemental mapping. The corresponding data presented in Figure 2d–g exhibit the presence and distribution of Co, O, C, and N, and this goes well with the expected composition of the catalyst.

The X-ray diffraction (XRD) profile of NEGF (Figure 3a) displays broad diffraction peaks at the 2θ values of 26 and 43°

corresponding to the (002) and (100) graphitic diffraction planes of the reduced GO.³⁷ The presence of metal impurities could be ruled out from the absence of any other diffraction peaks in the sample. The PXRD profile of $\text{Co}_3\text{O}_4/\text{NEGF}$ shows comparatively intense and prominent peaks corresponding to the (311) plane of Co_3O_4 , which matches well with the data in JCPDS card no: 00–042–1467.^{25,22,23} The presence of these phases confirms the spinel structure possessed by the Co_3O_4 nanorods. As expected, $\text{Co}_3\text{O}_4/\text{NEGF}$ also shows the peak corresponding to the (002) plane of the NEGF substrate, which appears as a broad peak at the 2θ value of 24.5° . A small shift of the graphitic peak corresponding to the (002) plane in $\text{Co}_3\text{O}_4/\text{NEGF}$ toward a lower diffraction angle (Figure 3a) in comparison to the pristine NEGF has been observed. This is ascribed to the increased d-spacing of the graphene layers because of the insertion of Co_3O_4 nanorods in between the graphene layer.³⁴ The introduced defects in the porous N-doped 3D graphene support were further explored by Raman spectroscopy (Figure 3b). The D-band peak appeared to resemble the graphitic lattice vibration mode with the A_{1g} symmetry at a wavenumber of 1350 cm^{-1} , while the G-band peak at 1590 cm^{-1} corresponds to the E_{2g} symmetry graphitic lattice vibration mode.³⁵ It should be noted that the D-band in the Raman spectra stands out as an indication of the introduced defects in the graphene framework, whereas the G-band describes the orderliness in the graphene.³⁵ In order to check the extent of the defects in the supported conducting carbon materials, the I_D/I_G ratio of the samples has been calculated, which was found to be 1.25 for NEGF and 1.33 for $\text{Co}_3\text{O}_4/\text{NEGF}$. A more graphitic structure would be helpful for ensuring better electrocatalytic activity as well as durability.

Furthermore, the incorporation of defects creates nucleation sites for metal oxide growth, leading to improved dispersion of the active sites and concomitantly high performance.²⁹ However, a considerable higher extent of defects can affect the stability of the carbon support. This points toward the need of an optimized level of graphitization and defects in the conducting support for ensuring improved overall catalytic performance as well as durability. The observed defect to the graphitic peak ratio in the case of NEGF ($I_D/I_G = 1.25$) is higher than that in the case of GO ($I_D/I_G = 1.0$). This shows that the defective sites are predominant in the case of NEGF as compared to GO. Furthermore, the Raman spectra analysis of Co_3O_4 (Figure 3b) shows the presence of peaks at 400–600 cm^{-1} , corresponding to the vibrations of the Co–O bond in a different plane of Co_3O_4 .¹⁴ A similar peak is observed in the case of $\text{Co}_3\text{O}_4/\text{NEGF}$; however, in this case, the peak intensity is slightly lower compared to the pristine Co_3O_4 presumably because of the carbon support effect. However, the defective peak intensity is more prominent in $\text{Co}_3\text{O}_4/\text{NEGF}$ as compared to NEGF. The introduced higher defects in $\text{Co}_3\text{O}_4/\text{NEGF}$ compared to NEGF are due to metal oxide growth during the in-situ conditions.⁵¹ The observed higher I_D/I_G ratio in the case of the metal oxide-supported catalyst stands out as substantiating evidence toward the presence of the comparatively high density of the defective sites in the system, which is found to assist the system in enhancing its catalytic activity.³⁶

For further understanding of the role of freeze-drying toward improving the surface area of the catalyst as well as increasing the number of porous channels, BET surface area, and pore size distribution analyses have been performed (Figure 3c, and Figure S5, ESI). The comparative pore size distribution profiles of NEGF and $\text{Co}_3\text{O}_4/\text{NEGF}$ are shown in Figure 3c. The pore size distribution analysis shows pore distribution in the range of 2 to 5 nm in both NEGF and $\text{Co}_3\text{O}_4/\text{NEGF}$, but the former clearly showed high-intensity pore distribution in the mesoporous size range of 2–7 nm. Additionally, NEGF shows a higher BET surface area of 450 $\text{m}^2 \text{g}^{-1}$, confirming the remarkably accessible and porous structure of the material, as visualized from the FESEM images. However, the BET surface area of $\text{Co}_3\text{O}_4/\text{NEGF}$ is found to be decreased substantially to 95 $\text{m}^2 \text{g}^{-1}$, suggesting the blockage of the pores and the masking of the surface of the substrate in the presence of dispersed metal oxide moieties. Both NEGF and $\text{Co}_3\text{O}_4/\text{NEGF}$ showed type-IV isotherms (Figure S5, ESI).³⁷ The prepared $\text{Co}_3\text{O}_4/\text{NEGF}$ catalyst contains almost 35% of the cobalt oxide nanorods of dimensions 120 nm in length and 12 nm in width responsible for lowering the overall BET surface area. In this case, most of the porous carbon surfaces are covered with metal oxide nanorods which have a lower surface area ($\sim 45 \text{ m}^2 \text{g}^{-1}$), as shown in Figure S6, ESI. In this case, the carbon surfaces loaded with Co_3O_4 entities are not exposed completely to the adsorption of gas molecules, which affect the total cumulative volume of $\text{Co}_3\text{O}_4/\text{NEGF}$ (Figure 3c). The defective sites and high porosity of the prepared catalyst are expected to allow seamless and fast diffusion of the reactants and electrolytes during electrocatalysis. This advantage is a determining factor in accomplishing the obtained higher electrocatalytic activity in the present case, as can be seen in a later section.

The total metal oxide active-site loading in $\text{Co}_3\text{O}_4/\text{NEGF}$ was determined by performing thermogravimetric analysis (TGA). The measurement was performed by sampling from 25

to 900 °C at a scan rate of 5 °C per minute in the oxygen atmosphere. Figure S7, ESI displays the TGA weight loss profiles for NEGF and $\text{Co}_3\text{O}_4/\text{NEGF}$, indicating a cobalt oxide loading of $\sim 35.4\%$ in the latter case.⁶

The insightful information on the nature of the surface moieties and the characteristics of electronic interactions operating in the prepared system has been gained by employing X-ray photoelectron spectroscopy (XPS) measurements. Figure 3d shows the survey scan spectra of NEGF and $\text{Co}_3\text{O}_4/\text{NEGF}$, which confirm the presence of Co, O, N, and C in the systems from the characteristic binding energy peaks. In both the systems, C, O, and N appear as the common elements in the binding energy (BE) values at 284.8, 531.5, and 400.5 eV, respectively. The XPS peaks that appear between 0 and 200 eV correspond to Si because silicon wafer was employed as the support to the samples during the analysis. The observed two peaks at 100 and 150 eV correspond to the Si 2s and Si 2p states. The characteristic peak corresponding to Co in the case of $\text{Co}_3\text{O}_4/\text{NEGF}$ appeared at the BE value of 784.2 eV.³⁸ The C and N peak intensities in $\text{Co}_3\text{O}_4/\text{NEGF}$ are found to be decreased because of the Co_3O_4 coverage over NEGF. The comparative deconvoluted XPS spectra of NEGF and $\text{Co}_3\text{O}_4/\text{NEGF}$ are studied for gaining insightful information of C 1s, N 1s, O 1s, and Co 2p. The deconvoluted C1s spectra of NEGF displayed various peaks corresponding to C–C (283.5 eV), C=C (284 eV), C–N/C=N (287.5 eV), and C–O (291.5 eV), with different BE values because of the particular chemical environment of carbon, as shown in Figure S8a, ESI.³⁸ Similarly, the deconvoluted C1s spectra of $\text{Co}_3\text{O}_4/\text{NEGF}$ displayed peaks corresponding to C–C (283.5), C=C (284), C–N/C=N (287.5 eV), and C–O (291.5), with similar BE and small change in intensities because of the presence of Co_3O_4 , as shown in Figure S8b, ESI. The peak intensities of the C–C and C–O bonds are higher than those of the C=C and C=N bonds in the case of $\text{Co}_3\text{O}_4/\text{NEGF}$ compared to NEGF because of the lower extent of graphitization in the presence of Co_3O_4 nanorods. This observation is in accordance with the information gained from the Raman analysis.

The deconvoluted N 1s spectra of NEGF, as shown in Figure S8c, ESI, displayed pyridinic-N at 398.6 eV (32.9%) and pyrrolic-N at 399.7 eV (41.6%) as the major moieties along with smaller proportions from the graphitic-N at 400.5 eV (19.3%) and NH_4^+ at 405.5 eV (15.9%). Furthermore, Figure 3e shows the deconvoluted N 1s spectra of $\text{Co}_3\text{O}_4/\text{NEGF}$. The deconvoluted peaks of $\text{Co}_3\text{O}_4/\text{NEGF}$ suggest that the N-doping in the graphene matrix remains the same during the in-situ loading of Co_3O_4 along with the presence of pyridinic-N at 398.6 eV (41.6%), pyrrolic-N at 399.7 eV (32.9%), graphitic-N at 400.5 eV (19.3%), and NH_4^+ at 402.5 eV (15.9%). The doped nitrogen in the graphene framework regulates metal oxide nanorod growth kinetics during the catalyst synthesis process. The Co 2p spectra of $\text{Co}_3\text{O}_4/\text{NEGF}$ showed two peaks (Figure 3f) at the BE values of 783.1 and 798.8 eV with a band separation of ~ 15.7 eV. The peak separation of 15.7 eV is the characteristic feature of Co_3O_4 . These deconvoluted spectra show the two spin–spin coupling peaks for peaks corresponding to the Co 2p_{3/2} and Co 2p_{1/2} states of Co, thus pointing toward the existence of the +2 and +3 oxidation states, respectively, in the system.^{38,39,48}

The obtained catalyst was further explored for the electrochemical ORR performance by adopting a set of electrochemical techniques. The measurements were first

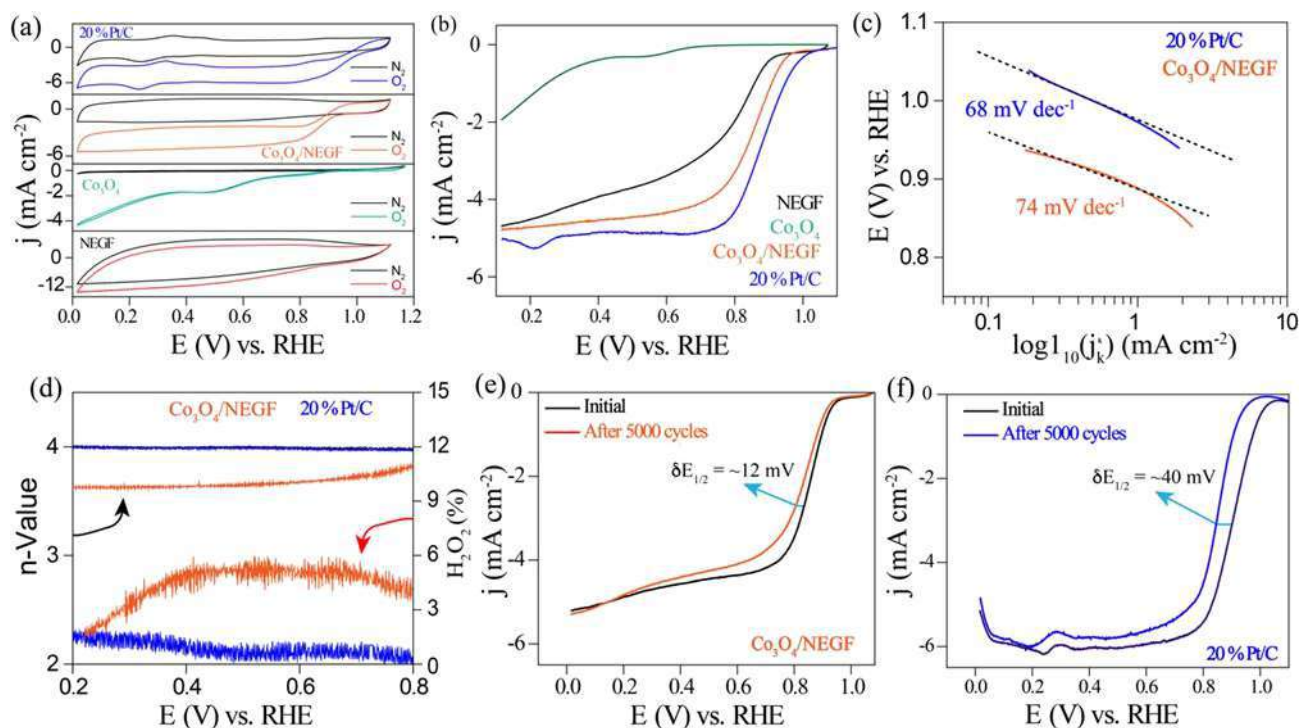


Figure 4. Electrocatalytic performance evaluation of $\text{Co}_3\text{O}_4/\text{NEGF}$ and the control samples (Co_3O_4 and NEGF) toward ORR in comparison to the state-of-the-art (Pt/C) catalyst: (a) comparative cyclic voltammetry (CV) profiles recorded for NEGF, Co_3O_4 , $\text{Co}_3\text{O}_4/\text{NEGF}$, and Pt/C in N_2/O_2 saturated 0.1 M KOH at 900 rpm of the working electrode (WE); (b) linear sweep voltammetry (LSV) profiles of Pt/C, $\text{Co}_3\text{O}_4/\text{NEGF}$, Co_3O_4 , and NEGF recorded at an rpm of 1600 of the WE displaying onset potentials at 1.00, 0.94, 0.80, and 0.65 V, respectively, with respect to RHE; (c) Tafel plots constructed for $\text{Co}_3\text{O}_4/\text{NEGF}$ and Pt/C with the measured slopes of 74 and 68 mV dec^{-1} , respectively; (d) Rotating ring disc electrode (RRDE) analysis of Pt/C and $\text{Co}_3\text{O}_4/\text{NEGF}$ displaying the amount of H_2O_2 generated and the electron transfer number (n -value) corresponding to the ORR process; (e, f) accelerated durability test (ADT) data of $\text{Co}_3\text{O}_4/\text{NEGF}$ and Pt/C.

recorded using Hg/HgO as the reference electrode, and potentials were converted to the reversible hydrogen electrode (RHE) scale based on the methodology discussed in Section 1.4, ESI. The cyclic voltammogram recorded for $\text{Co}_3\text{O}_4/\text{NEGF}$ under the O_2 -saturated 0.1 M KOH electrolyte at a WE rotation speed of 900 rpm displays an ORR onset potential at 0.94 V vs RHE, which is found to be only 60 mV lower compared to the onset potential of 1.00 V vs RHE recorded for the state-of-the-art Pt/C catalyst (Figure 4a). On the other hand, a much large shift of the onset potentials toward a higher overpotential has been observed for NEGF (0.80 V vs RHE) and Co_3O_4 (0.65 V vs RHE), as shown in Figure 4a. The CV profile of NEGF (Figure 4a) follows a notable capacitive nature, which results from the high surface area acquired by the 3D graphene morphology resulting from the freeze-drying process.⁵⁰ Furthermore, to distinguish the effect of working electrode rotation toward exposing the greater number of active sites, we have carried out CV experiments with (w) and without (w/o) the rotation of the catalyst-coated rotating disc electrode (RDE). Figure S9, ESI shows the CV profiles of Co_3O_4 , NEGF, $\text{Co}_3\text{O}_4/\text{NEGF}$, and 20% Pt/C recorded at the conditions w and w/o the rotation of the working electrode in the oxygen-saturated 0.1 M KOH solution at the scan rate of 50 mV/sec . In both the cases, $\text{Co}_3\text{O}_4/\text{NEGF}$ displays an ORR onset potential of 0.60 V vs RHE. However, in the case of the experiment with the rotation of the electrode at 900 rpm, the change in the limiting current density reveals the improved mass transport of the reactant to the active sites. This points toward the enrichment of the catalyst sites with the higher concentration of surface O_2 during the hydrodynamic

movement of the electrolyte as a result of the rotation of the electrode. To gain more precise information on the intrinsic activity characteristics of the systems toward ORR, the linear sweep voltammograms (LSVs) were recorded in the RDE mode. The LSVs were recorded under O_2 -saturated conditions for $\text{Co}_3\text{O}_4/\text{NEGF}$, Co_3O_4 , NEGF, and Pt/C (Figure 4b) by maintaining the rotation speed of the WE at 1600 rpm and performing the voltage scan at the rate of 10 mV s^{-1} . The comparative LSV profiles presented in Figure 4b clearly display the superior ORR performance achieved using $\text{Co}_3\text{O}_4/\text{NEGF}$ in comparison to the control samples, viz., Co_3O_4 and NEGF. With an onset potential of 0.94 V vs RHE (accounting only 60 mV overpotential compared to Pt/C) and a well-featured LSV profile, $\text{Co}_3\text{O}_4/\text{NEGF}$ could emerge as a potential contender as a non-Pt electrocatalyst for ORR. The half-wave potential ($E_{1/2}$) of $\text{Co}_3\text{O}_4/\text{NEGF}$ (0.80 V vs RHE) is also found to be very close to that of Pt/C (0.90 V), which stands out as a quantitative indicator pointing toward the efficacy of the system to perform under more demanding conditions of reasonable current dragging. Table S1, ESI summarizes the values of the onset potential and $E_{1/2}$ for all the systems compared in this study. Associating the drastic difference in the ORR performance characteristics of Co_3O_4 and $\text{Co}_3\text{O}_4/\text{NEGF}$ toward ORR, it can be clearly understood the huge advantage incurred by the supported system through the cooperative and synergistic effects originated from the metal oxide–support interactions. The controlled interplay originated from factors like the rough surface and nanorod morphology of Co_3O_4 , the 3D-morphology of the substrate with its ability for ensuring seamless mass transport, and the modulations incurred through

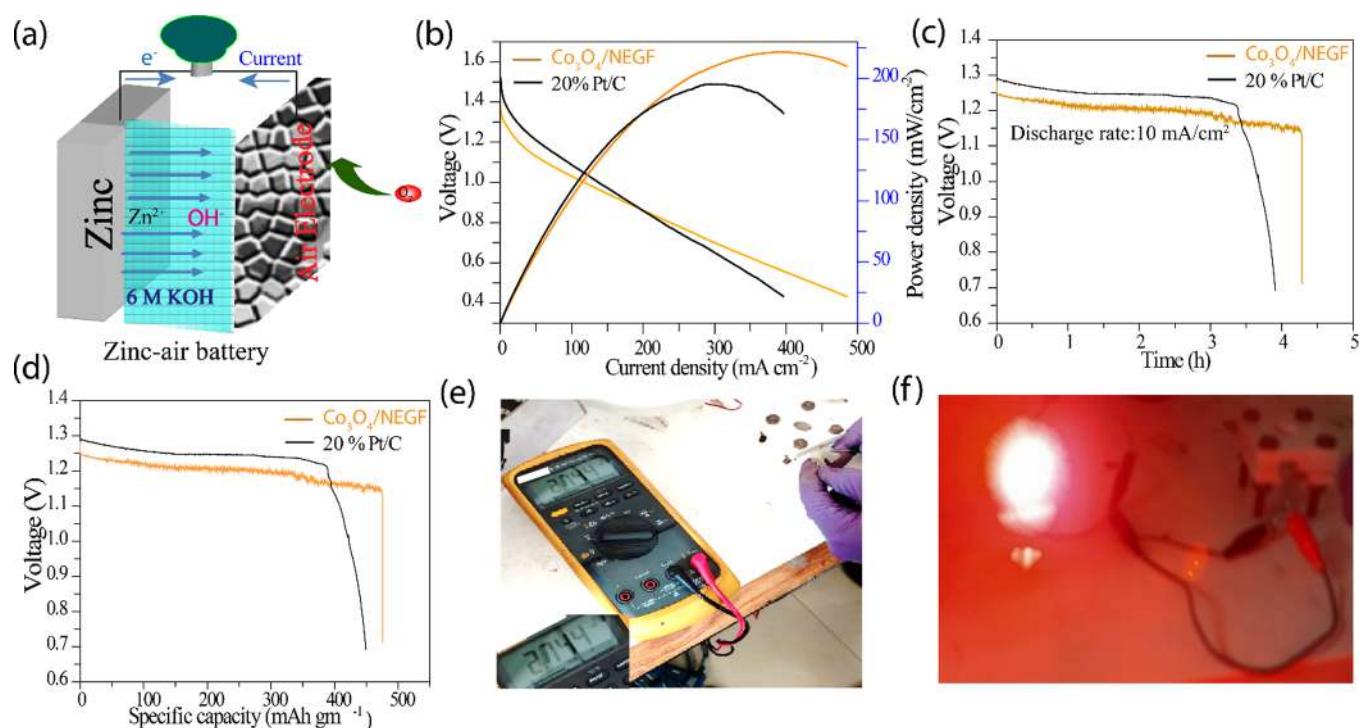


Figure 5. ZAB fabrication, performance evaluation, and demonstration: (a) schematic representation of the fabricated ZAB (cathode catalyst loading: 1.0 mg/cm^2 ; anode: zinc powder; separator: Celgard membrane soaked with 6 M KOH); (b) polarization plots recorded on the ZABs fabricated by employing $\text{Co}_3\text{O}_4/\text{NEGF}$ and Pt/C as the air electrodes; (c) long-term galvanostatic discharge curves of the ZABs with $\text{Co}_3\text{O}_4/\text{NEGF}$ and Pt/C as the cathode catalysts until complete consumption of the anodic zinc powder; (d) galvanostatic discharge capacity of the battery after normalizing with the consumed amount of zinc powder used for the fabrication of the ZABs; (e) demonstration of the assembled ZAB displaying the voltage of the two cells connected in series showing the voltage of 2.744 V, as measured using a multimeter; (f) digital photograph of the LED illuminated using the ZAB containing $\text{Co}_3\text{O}_4/\text{NEGF}$ as the cathode catalyst.

the electronic interactions in the dispersed state is emerging as the beneficial factor for $\text{Co}_3\text{O}_4/\text{NEGF}$. To understand the morphological effect of Co_3O_4 toward the ORR activity, the prepared catalyst performance was compared with that of the previously reported catalysts (Table S2, ESI). Comparative studies show that $\text{Co}_3\text{O}_4/\text{NEGF}$ exhibits comparable activity and even higher activity in some cases.

Tafel slope is another important quantifiable parameter to understand the ORR kinetics. Tafel analysis has been performed for $\text{Co}_3\text{O}_4/\text{NEGF}$ and Pt/C by following the standard procedure (Figure 4c). $\text{Co}_3\text{O}_4/\text{NEGF}$ displays a Tafel slope of approximately 74 mV dec^{-1} , nearly comparable to 68 mV dec^{-1} measured for Pt/C. The observed Tafel slope values for NEGF and Co_3O_4 are 92 and 108 mV dec^{-1} , respectively (Figure S10, ESI). The higher Tafel slope values of NEGF and Co_3O_4 compared to $\text{Co}_3\text{O}_4/\text{NEGF}$ suggest the slower ORR kinetics involved in the catalytic process over these systems. A critical issue with the existing several non-Pt electrocatalysts for ORR is the parallel involvement of the parasitic 2e- reduction process leading to the formation of H_2O_2 along with the desired 4e- reduction, resulting in the formation of H_2O . The limitation of this possibility has been ruled out in the present case by performing a rotating ring disc electrode (RRDE) analysis, which indicated an H_2O_2 yield of less than 6%. In the RRDE data presented in Figure 4d and Figure S11, ESI, the peroxide species (HO_2^-) generated during the ORR cycle was investigated and quantified. From Figure 4d and Figure S12, ESI, $\text{H}_2\text{O}_2\%$ is found to be remaining below 6% with only marginal variations across the potential window. The percentage of H_2O_2 generated in the case NEGF is around

3%, and that on Co_3O_4 is around 28% at 0.60 V with respect to RHE. (Figures S13, S14 ESI). Although the percentage of H_2O_2 formation is higher in the individual electrocatalysts compared to the composite ($\text{Co}_3\text{O}_4/\text{NEGF}$), the relatively higher percentage of H_2O_2 formation in Co_3O_4 is due to the hindered electronic transport because of the lower conductivity of the metal oxide.⁵⁰ The obtained low H_2O_2 generation in the case of $\text{Co}_3\text{O}_4/\text{NEGF}$ has been further substantiated from the calculated number of electrons (represented as 'n-value' in Figure 4d) of 3.75 in the case of $\text{Co}_3\text{O}_4/\text{NEGF}$ (compared to 3.98 for Pt/C), which indicates the dominance of the water-formation pathway (4e- transfer) in the reduction process. An accelerated durability test (ADT) of $\text{Co}_3\text{O}_4/\text{NEGF}$ in comparison with Pt/C has been performed by subjecting the system under potential cycling between 1.2 and 0.80 V (RHE) at 100 mV s^{-1} in the O_2 -saturated 0.1 M KOH condition. The purpose of this study was to understand the electrochemical stability of the system under corrosion-induced conditions, which can lead to a catastrophic failure of the morphological features and result in concomitant variations in the key performance indicators. The ADT data corresponding to $\text{Co}_3\text{O}_4/\text{NEGF}$ and Pt/C are presented in Figure 4e,f. As can be seen from the ADT profiles, $\text{Co}_3\text{O}_4/\text{NEGF}$ could survive better under the triggered condition compared to its Pt/C counterpart, inferring better structural endurance possessed by the former.

This can be quantitatively evaluated from the $E_{1/2}$ value change of the systems subsequent to ADT, where the drop observed in the case of $\text{Co}_3\text{O}_4/\text{NEGF}$ is only 12.2 mV compared to 40.5 mV incurred by Pt/C. It is known that

conventional carbon is prone to corrosion under the ORR conditions, which can lead to catalyst fouling, particle aggregation, and dissolution. While replacing carbon with NEGF, the process enhances the binding interactions between the metal nanoparticles and graphene with the help of its functionalized and heteroatom-incorporated binding centers.²⁸ The observed differences in the chemical and physical properties of the Co₃O₄/NEGF catalyst before and after ADT are responsible for the minimal variation in the E_{1/2} of 12 mV, which is very less in comparison to that of the Pt/C catalyst (40 mV) (Figure 4e,f). The post durability analysis of the Co₃O₄/NEGF catalyst has been performed by the physical characterization of the precycled sample. The TEM analysis of the pretreated sample clearly shows the intact distribution of the Co₃O₄ nanorod as similar to the pristine Co₃O₄/NEGF case. However, surface roughness along with the thin-layer formation over Co₃O₄ nanorods (Figure S15a,b ESI) was evidenced, revealing textural changes in the supported Co₃O₄ nanorods. The changes in the crystalline phase of Co₃O₄/NEGF after ADT were observed by the XRD analysis (Figure S15c, ESI). The XRD analysis revealed that the surface is covered with a thin layer of Co(OH)₂, which was verified by the presence of the mixed phase of Co₃O₄ and Co(OH)₂ peaks.⁴⁶ The observed diffraction peaks are ascribed to the (002), (220), (400), (511), and (440) planes of the Co₃O₄ nanorods.^{20,46} It is suppressing the more active (311) peak of Co₃O₄ after 5000 cycles with the concomitant formation of a more active (100) peak for Co(OH)₂.^{46,47} In addition, the XPS analysis of the sample further supported the presence of Co(OH)₂ (Figure S15d,e, ESI).^{43,48,49} After the durability test, further deconvoluted Co 2p spectra analysis suggested the change in the electronic state, as evidenced from the change in the Co peak position (Figure S15e, ESI).^{48,49} The deconvoluted XPS spectra of Co₃O₄ after ADT evidenced the presence of three different forms of Co ions. Furthermore, to evaluate the dissolution of Co₃O₄ during the catalytic performance, the inductively coupled plasma (ICP) analysis (Table S3, ESI) of post ADT Co₃O₄/NEGF was performed. The amount of cobalt present in the post ADT sample is close to that in the as-prepared Co₃O₄/NEGF catalyst with a minute change in Co (~1%). Hence, in the longer run, the in-house catalyst is expected to outperform the Pt/C system both in terms of performance and durability under a realistic system-level demonstration. The high intrinsic ORR activity displayed by Co₃O₄/NEGF in the single-electrode mode could be further translated in terms of performance in the device level in a ZAB. As shown in Figure 5a, the ZAB consists of the ORR catalyst-coated gas-carbon diffusion layer (GDL) as the cathode, zinc powder as the anode, and 6 M KOH as the electrolyte. During the operation of the ZABs, diffused oxygen through the porous air cathode reduces to OH⁻, which subsequently travels toward the anode through the electrolyte to facilitate the oxidation of Zn to form its hydroxide and oxide. The released electron during the oxidation process of Zn flows through the outer circuit and establishes the flow of electric current.^{2,44,41} In the present case, the cells based on Co₃O₄/NEGF and Pt/C are found to display the open-circuit voltage (OCV) values of 1.31 and 1.40 V, respectively, which is in good agreement with the performance recorded during the half-cell mode of operation (Figure 5b). The performance of the demonstrated system is comparable to that of the ZAB systems reported in the literature (Table S4, ESI). The comparative steady-state cell polarization (Figure 5b) leads to

maximum power densities (P_{\max}) of 190 and 210 mW cm⁻², respectively, for the ZABs based on Pt/C and Co₃O₄/NEGF as the cathode catalysts. It is interesting to note that although the OCV for the cell based on Co₃O₄/NEGF is lower as compared to the counterpart system based on Pt/C, the performance of the former gradually improves and outperforms the later. This is expected to be realized from the intrinsic advantage of Co₃O₄/NEGF as the ORR catalyst in terms of mass transport governed by the porous 3D architecture of NEGF.

Furthermore, the galvanostatic discharge curve recorded at 10 mA cm⁻² (Figure 5c) points toward the robustness of the in-house ZAB system. The discharge time for the ZABs based on Co₃O₄/NEGF and Pt/C is found to be nearly 4.5 and 4 h, respectively. The voltage drop in the plateau region concerning the operation time is expected to result from the side reactions taking place over the surface of the Zn powder.^{22,45,46} The estimated specific capacity (Figure 5d) of the assembled ZAB based on Co₃O₄/NEGF is about 474 mAh/g_{Zn} compared to 445 mAh/g_{Zn} measured for the system based on Pt/C. For the real-time demonstration of fabricated ZAB, two ZAB devices based on the Co₃O₄/NEGF cathode were connected in series, which result in an overall voltage of 2.744 V, as measured using a multimeter device (Figure 5e). Long-term galvanostatic discharge curves of the ZAB (two cells connected together) with Co₃O₄/NEGF as the air electrode until full consumption of the anode catalyst (Figure S16, ESI). This device was subsequently employed to light an LED of 2 V, which resulted in steady illumination for a long time without any interruption (Figure 5f and Video VS1, ESI). Thus, overall, a close matching and promising performance could be ensured during the demonstration of the ZAB based on the in-house catalyst for facilitating ORR in the cathode, which justified our findings of the performance mapping of the material-specific intrinsic activity of Co₃O₄/NEGF through the single-electrode studies.

4. CONCLUSIONS

In summary, a prospective non-noble metal-based ORR electrocatalyst derived by the dispersion of Co₃O₄ nanorods on 3D-structured NEGF, designated as Co₃O₄/NEGF, was achieved by employing a simple and scalable hydrothermal method followed by freeze-drying. As a catalyst, Co₃O₄/NEGF displayed high ORR activity during single-electrode testing, and subsequently, its potential as the cathode for a ZAB system could be demonstrated under realistic testing conditions. The synthesis protocol involving the hydrothermal treatment followed by freeze-drying is critical for achieving the desired structural and morphological features of the catalyst. The doped nitrogen, along with its favorable contribution toward ORR, also plays a critical role in establishing efficient dispersion of the oxide nanorods on the substrate. The catalytic activity enhancement is expected to be resulted from the regulated interplay of several favoring factors, including high surface area, homogeneous dispersion of the active sites, better reactant distribution, high active-site accessibility, and the synergistic interaction operating between the doped nitrogen and the Co₃O₄ nanorods. The 60 mV onset potential shift for ORR and the Tafel slope of 74 mV/dec recorded over Co₃O₄/NEGF compared to the state-of-the-art Pt/C in the single-electrode mode are promising values expected from a non-Pt electrocatalyst. Furthermore, the unique structural features involving the 3D architecture with the interconnected pores created by the self-assembling of the entangled graphene during the freeze-drying process is found to assist reactant

distribution and active-site utilization. The competing performance displayed by the ZAB consisting of $\text{Co}_3\text{O}_4/\text{NEGF}$ as the cathode with the counterpart system based on Pt/C cathode substantiates the structural advantages incurred by the homemade catalyst. Thus, as a cost-effective and competitive catalyst, $\text{Co}_3\text{O}_4/\text{NEGF}$ stands out as a versatile replacement for the expensive catalysts based on noble metals for the electrochemical systems involving ORR as the rate-determining electrode process.⁴²

■ ASSOCIATED CONTENT

Supporting Information

The Supporting Information is available free of charge at <https://pubs.acs.org/doi/10.1021/acsaem.1c00210>.

Experimental section; digital photographs, FESEM, TEM and HRTEM images, BET analysis, TGA profiles, cyclic voltammograms, Tafel plots, RRDE study, post-electrochemical analysis and long-term galvanostatic discharge curves, ICP-OES data, and comparison of ZAB performance (PDF)

Steady illumination without any interruption (MP4)

■ AUTHOR INFORMATION

Corresponding Author

Sreekumar Kurungot – Physical and Materials Chemistry Division, CSIR-National Chemical Laboratory, Pune, Maharashtra 411008, India; Academy of Scientific and Innovative Research (AcSIR), New Delhi 110001, India; orcid.org/0000-0001-5446-7923; Email: k.sreekumar@ncl.res.in

Authors

Narugopal Manna – Physical and Materials Chemistry Division, CSIR-National Chemical Laboratory, Pune, Maharashtra 411008, India; Academy of Scientific and Innovative Research (AcSIR), New Delhi 110001, India

Santosh K. Singh – Faculty of Pure and Applied Sciences, University of Tsukuba, Tsukuba, Ibaraki 305-8573, Japan

Geeta Pandurang Kharabe – Physical and Materials Chemistry Division, CSIR-National Chemical Laboratory, Pune, Maharashtra 411008, India; Academy of Scientific and Innovative Research (AcSIR), New Delhi 110001, India

Arun Torris – Polymer Science and Engineering Division, CSIR-National Chemical Laboratory, Pune, Maharashtra 411008, India; orcid.org/0000-0003-4487-2604

Complete contact information is available at: <https://pubs.acs.org/doi/10.1021/acsaem.1c00210>

Author Contributions

The manuscript was written through contributions of all authors. All authors have given approval to the final version of the manuscript.

Notes

The authors declare no competing financial interest.

■ ACKNOWLEDGMENTS

N.M. acknowledges the Council of Scientific and Industrial Research (CSIR), New Delhi, India, for Research Fellowship. K.S. acknowledges the Department of Science & Technology (DST), New Delhi, India, for the project funding (GAP328726).

■ REFERENCES

- (1) Cano, Z. P.; Banham, D.; Ye, S.; Hintennach, A.; Lu, J.; Fowler, M.; Chen, Z. Batteries and Fuel Cells for Emerging Electric Vehicle Markets. *Nat. Energy* **2018**, *3*, 279–289.
- (2) Li, Y.; Gong, M.; Liang, Y.; Feng, J.; Kim, J. E.; Wang, H.; Hong, Zhang, B.; Dai, H. Advanced Zinc-Air Batteries Based on High-Performance Hybrid Electrocatalysts. *Nat. Commun.* **2013**, *4*, 1–7.
- (3) Wang, Y.; Li, J.; Wei, Z. Transition-Metal-Oxide-Based Catalysts for the Oxygen Reduction Reaction. *J. Mater. Chem. A* **2018**, *6*, 8194–8209.
- (4) Jukk, K.; Kongi, N.; Rauwel, P.; Matisen, L.; Tammeveski, K. Platinum Nanoparticles Supported on Nitrogen-Doped Graphene Nanosheets as Electrocatalysts for Oxygen Reduction Reaction. *Electrocatalysis* **2016**, *7*, 428–440.
- (5) Yuan, Y.; Wang, J.; Adimi, S.; Shen, H.; Thomas, T.; Ma, R.; Atfield, J. P.; Yang, M. Zirconium Nitride Catalysts Surpass Platinum for Oxygen Reduction. *Nat. Mater.* **2020**, *19*, 282–286.
- (6) Yu, H.; Baricci, A.; Roller, J.; Wang, Y.; Casalegno, A.; Mustain, W. E.; Maric, R. Ultra-Low Pt Loading Catalyst Layers for PEMFC Using Reactive Spray Deposition Technology. *ECS Trans.* **2015**, *69*, 487–496.
- (7) Dhavale, V. M.; Singh, S. K.; Nadeema, A.; Gaikwad, S. S.; Kurungot, S. Nanocrystalline Fe-Fe₂O₃ Particle-Deposited N-Doped Graphene as an Activity-Modulated Pt-Free Electrocatalyst for Oxygen Reduction Reaction. *Nanoscale* **2015**, *7*, 20117–20125.
- (8) Liu, J.; Li, E.; Ruan, M.; Song, P.; Xu, W. Recent Progress on Fe/N/C Electrocatalysts for the Oxygen Reduction Reaction in Fuel Cells. *Catalysts* **2015**, *5*, 1167–1192.
- (9) Tian, L.; Zhu, J. L.; Chen, L.; An, B.; Liu, Q. Q.; Huang, K. L. Synthesis and Characterization of α -Cobalt Hydroxide Nanobelts. *J. Nanopart. Res.* **2011**, *13*, 3483–3488.
- (10) Abroshan, H.; Bothra, P.; Back, S.; Kulkarni, A.; Nørskov, J. K.; Sahrostami, S. Ultrathin Cobalt Oxide Overlayer Promotes Catalytic Activity of Cobalt Nitride for the Oxygen Reduction Reaction. *J. Phys. Chem. C* **2018**, *122*, 4783–4791.
- (11) Mosa, I. M.; Biswas, S.; El-Sawy, A. M.; Botu, V.; Guild, C.; Song, W.; Ramprasad, R.; Rusling, J. F.; Suib, S. L. Tunable Mesoporous Manganese Oxide for High Performance Oxygen Reduction and Evolution Reactions. *J. Mater. Chem. A* **2016**, *4*, 620–631.
- (12) Wang, Y.; Yang, Y.; Jia, S.; Wang, X.; Lyu, K.; Peng, Y.; Zheng, H.; Wei, X.; Ren, H.; Xiao, L.; Wang, J.; Muller, D. A.; Abruña, H. D.; Hwang, B. J.; Lu, J.; Zhuang, L. Synergistic Mn-Co Catalyst Outperforms Pt on High-rate Oxygen Reduction for Alkaline Polymer Electrolyte Fuel Cells. *Nat. Commun.* **2019**, *10*, 6–13.
- (13) Wang, Z.; Wei, G.; Du, K.; Zhao, X.; Liu, M.; Wang, S.; Zhou, Y.; An, C.; Zhang, J. Ni Foam-Supported Carbon-Sheathed NiMoO₄ Nanowires as Integrated Electrode for High-Performance Hybrid Super capacitors. *ACS Sustainable Chem. Eng.* **2017**, *5*, 5964–5971.
- (14) Singh, S. K.; Dhavale, V. M.; Kurungot, S. Surface-Tuned Co₃O₄ Nanoparticles Dispersed on Nitrogen-Doped Graphene as an Efficient Cathode Electrocatalyst for Mechanical Rechargeable Zinc-Air Battery Application. *ACS Appl. Mater. Interfaces* **2015**, *7*, 21138–21149.
- (15) Singh, S. K.; Dhavale, V. M.; Kurungot, S. Low Surface Energy Plane Exposed Co₃O₄ Nanocubes Supported on Nitrogen-Doped Graphene as an Electrocatalyst for Efficient Water Oxidation. *ACS Appl. Mater. Interfaces* **2015**, *7*, 442–451.
- (16) Zang, M.; Xu, N.; Cao, G.; Chen, Z.; Cui, J.; Gan, L.; Dai, H.; Yang, X.; Wang, P. Cobalt Molybdenum Oxide Derived High-Performance Electrocatalyst for the Hydrogen Evolution Reaction. *ACS Catal.* **2018**, *8*, 5062–5069.
- (17) Gao, D.; Luo, S.; Zhang, Y.; Liu, J.; Wu, H.; Wang, S.; He, P. Mn₃O₄/Carbon Nanotubes Nanocomposites as Improved Anode Materials for Lithium-Ion Batteries. *J. Solid State Electrochem.* **2018**, *22*, 3409–3417.
- (18) Shen, H.; Liu, Y. PT Graphical Abstract SC. *Chin. J. Chem. Eng.* **2018**, *23*, 225–232.

- (19) Wang, B.; Li, F.; Wang, X.; Wang, G.; Wang, H.; Bai, J. Mn_3O_4 Nanotubes Encapsulated by Porous Graphene Sheets with Enhanced Electrochemical Properties for Lithium/Sodium-Ion Batteries. *Chem. Eng. J.* **2019**, *364*, 57–69.
- (20) Han, X.; He, G.; He, Y.; Zhang, J.; Zheng, X.; Li, L.; Zhong, C.; Hu, W.; Deng, Y.; Ma, T.-Y. Engineering Catalytic Active Sites on Cobalt Oxide Surface for Enhanced Oxygen Electrocatalysis. *Adv. Energy Mater.* **2018**, *8*, 1702222.
- (21) Ling, T.; Yan, D. Y.; Jiao, Y.; Wang, H.; Zheng, Y.; Zheng, X.; Mao, J.; Du, X. W.; Hu, Z.; Jaroniec, M.; Qiao, S. Z. Activating cobalt(II) oxide nanorods for efficient electrocatalysis by strain engineering. *Nat. Commun.* **2016**, *8*, 12876.
- (22) Shao, L.; Zhao, Q.; Chen, J. MnOOH Nanorods as High Performance Anodes for Sodium Ion Batteries. *Chem. Commun.* **2017**, *53*, 2435–2438.
- (23) Zhou, Y.; Xi, S.; Wang, J.; Sun, S.; Wei, C.; Feng, Z.; Du, Y.; Xu, Z. J. Revealing the Dominant Chemistry for Oxygen Reduction Reaction on Small Oxide Nanoparticles. *ACS Catal.* **2018**, *8*, 673–677.
- (24) Zhao, C.; Peng, B. Synthesis of Porous Fiber-like CoMn_2O_4 Derived from Cotton Template as Lithium Ion Battery Anodes. *Int. J. Electrochem. Sci.* **2018**, *13*, 1505–1514.
- (25) Wang, Z. L.; Xu, D.; Xu, J. J.; Zhang, X. B. Oxygen Electrocatalysts in Metal-Air Batteries: From Aqueous to Nonaqueous Electrolytes. *Chem. Soc. Rev.* **2014**, *43*, 7746–7786.
- (26) Okelly, C.; Jung, S. J.; Bell, A. P.; Boland, J. J. Single Crystal Iron Nanocube Synthesis via the Surface Energy Driven Growth Method. *Nanotechnology* **2012**, *23*, 0957–4484.
- (27) Ishihara, A.; Ohgi, Y.; Matsuzawa, K.; Mitsushima, S.; Ota, K. I. Progress in Non-Precious Metal Oxide-Based Cathode for Polymer Electrolyte Fuel Cells. *Electrochim. Acta* **2010**, *55*, 8005–8012.
- (28) Fu, X.; Choi, J. Y.; Zamani, P.; Jiang, G.; Hoque, M. A.; Hassan, F. M.; Chen, Z. Co-N Decorated Hierarchically Porous Graphene Aerogel for Efficient Oxygen Reduction Reaction in Acid. *ACS Appl. Mater. Interfaces* **2016**, *8*, 6488–6495.
- (29) Benson, J.; Xu, Q.; Wang, P.; Shen, Y.; Sun, L.; Wang, T.; Li, M.; Papakonstantinou, P. Tuning the Catalytic Activity of Graphene Nanosheets for Oxygen Reduction Reaction via Size and Thickness Reduction. *ACS Appl. Mater. Interfaces* **2014**, *6*, 19726–19736.
- (30) Galeano, C.; Meier, J. C.; Peinecke, V.; Bongard, H.; Katsounaros, I.; Topalov, A. A.; Lu, A.; Mayrhofer, K. J. J.; Schüth, F. Toward Highly Stable Electrocatalysts via Nanoparticle Pore Confinement. *J. Am. Chem. Soc.* **2012**, *134*, 20457–20465.
- (31) Li, W.; Liu, J.; Zhao, D. Mesoporous Materials for Energy Conversion and Storage Devices. *Nat. Rev. Mater.* **2016**, *1*, 53–65.
- (32) Manna, N.; Ayasha, N.; Singh, S. K.; Kurungot, S. A NiFe Layered Double Hydroxide-Decorated N-Doped Entangled-Graphene Framework: A Robust Water Oxidation Electrocatalyst. *Nanoscale Adv.* **2020**, *2*, 1709–1717.
- (33) Singh, S. K.; Kashyap, V.; Manna, N.; Bhang, S. N.; Soni, R.; Bo kherroub, R.; Szunerits, S.; Kurungot, S. Efficient and Durable Oxygen Reduction Electrocatalyst Based on CoMn Alloy Oxide Nanoparticles Supported over N-Doped Porous Graphene. *ACS Catal.* **2017**, *7*, 6700–6710.
- (34) Zhou, M.; Wang, H. L.; Guo, S. Towards High-Efficiency Nanoelectrocatalysts for Oxygen Reduction through Engineering Advanced Carbon Nanomaterials. *Chem. Soc. Rev.* **2016**, *45*, 1273–1307.
- (35) Yang, S.; Zhang, L.; Yang, Q.; Zhang, Z.; Chen, B.; Lv, P.; Zhu, W.; Wang, G. Graphene Aerogel Prepared by Thermal Evaporation of Graphene Oxide Suspension Containing Sodium Bicarbonate. *J. Mater. Chem. A* **2015**, *3*, 7950–7958.
- (36) Cao, Y.; Mao, S.; Li, M.; Chen, Y.; Wang, Y. Metal/Porous Carbon Composites for Heterogeneous Catalysis: Old Catalysts with Improved Performance Promoted by N-Doping. *ACS Catal.* **2017**, *7*, 8090–8112.
- (37) Wang, J.; Wu, H.; Gao, D.; Miao, S. High-Density Iron Nanoparticles Encapsulated within Nitrogen-Doped Carbon Nano-shell as Efficient Oxygen Electrocatalyst for Zinc–Air Battery. *Materials* **2019**, *13*, 63–396.
- (38) Kashyap, V.; Singh, S. K.; Kurungot, S. Cobalt Ferrite Bearing Nitrogen-Doped Reduced Graphene Oxide Layers Spatially Separated with Microporous Carbon as Efficient Oxygen Reduction Electrocatalyst. *ACS Appl. Mater. Interfaces* **2016**, *8*, 20730–20740.
- (39) Kashyap, V.; Kurungot, S. Zirconium-Substituted Cobalt Ferrite Nanoparticle Supported N-Doped Reduced Graphene Oxide as an Efficient Bifunctional Electrocatalyst for Rechargeable Zn-Air Battery. *ACS Catal.* **2018**, *8*, 3715–3726.
- (40) Yang, Z.; Ren, J.; Zhang, Z.; Chen, X.; Guan, G.; Qiu, L.; Zhang, Y.; Peng, H. Recent Advancement of Nanostructured Carbon for Energy Applications. *Chem. Rev.* **2015**, *115*, 5159–5223.
- (41) Dai, L.; Chang, D. W.; Baek, J. B.; Lu, W. Carbon Nanomaterials for Advanced Energy Conversion and Storage. *Small* **2012**, *8*, 1130–1166.
- (42) Zitolo, A.; Sahraie, N. R.; Mineva, T.; Li, J.; Jia, Q.; Stamatina, S.; Harrington, G. F.; Lyth, S. M.; Krttil, P.; Mukerjee, S.; Fonda, E.; Jaouen, F. Identification of Catalytic Sites in Cobalt–nitrogen–carbon Materials for the Oxygen Reduction Reaction. *Nat. Commun.* **2017**, *8*, 957.
- (43) Babar, P. T.; Lokhande, A. C.; Pawar, B. S.; Gang, M. G.; Jo, E.; Go, C.; Suryawanshi, M. P.; Pawar, S. M.; Kim, J. H. Electrocatalytic Performance Evaluation of Cobalt Hydroxide and Cobalt Oxide Thin Films for Oxygen Evolution Reaction. *Appl. Surf. Sci.* **2018**, *427*, 253–259.
- (44) Li, H.; Ma, L.; Han, C.; Wang, Z.; Liu, Z.; Tang, Z.; Zhi, C. Nano Energy Advanced Rechargeable Zinc-Based Batteries : Recent Progress and Future Perspectives. *Nano Energy* **2019**, *62*, 550–587.
- (45) Su, C.; Cheng, H.; Li, W.; Liu, Z.; Li, N.; Hou, Z. Atomic Modulation of FeCo–Nitrogen–Carbon Bifunctional Oxygen Electrodes for Rechargeable and Flexible All-Solid-State Zinc–Air Battery. *Adv. Funct. Mater.* **2017**, *7*, 1–12.
- (46) Bhang, S. N.; Unni, S. M.; Kurungot, S. Graphene with Fe and S Coordinated Active Centers: An Active Competitor for the Fe-N-C Active Center for Oxygen Reduction Reaction in Acidic and Basic PH Conditions. *ACS Appl. Mater. Interfaces* **2018**, *1*, 368–376.
- (47) Si, Y.; Guo, C.; Xie, C.; Xiong, Z. An Ultrasonication-Assisted Cobalt Hydroxide Composite with Enhanced Electrocatalytic Activity toward Oxygen Evolution Reaction. *Materials* **2018**, *11*, 1912.
- (48) Yang, J.; Liu, H.; Martens, W. N.; Frost, R. L. Synthesis and Characterization of Cobalt Hydroxide, Cobalt Oxyhydroxide, and Cobalt Oxide Nanodiscs. *J. Phys. Chem. C* **2010**, *114*, 111–119.
- (49) Chen, L.; Zhang, Y.; Wang, H.; Wang, Y.; Li, D.; Duan, C. Cobalt Layered Double Hydroxides Derived CoP/Co₂P Hybrids for Electrocatalytic Overall Water Splitting. *Nanoscale* **2018**, *10*, 21019.
- (50) Lee, D. G.; Gwon, O.; Park, H. S.; Kim, S. H.; Yang, J.; Kwak, S. K.; Kim, G.; Song, H. K. Conductivity-Dependent Completion of Oxygen Reduction on Oxide Catalysts. *Angew. Chem., Int. Ed.* **2015**, *54*, 15730–15733.
- (51) Weng, C. C.; Ren, J. T.; Hu, Z. P.; Yuan, Z. Y. Nitrogen-Doped Defect-Rich Graphitic Carbon Nanorings with CoOx Nanoparticles as Highly Efficient Electrocatalyst for Oxygen Electrochemistry. *ACS Sustainable Chem. Eng.* **2018**, *6*, 15811–15821.

Air–Cathode Interface-Engineered Electrocatalyst for Solid-State Rechargeable Zinc–Air Batteries

Narugopal Manna, Santosh K. Singh, Maria Kurian, Arun Torris, and Sreekumar Kurungot*

Cite This: *ACS Appl. Energy Mater.* 2022, 5, 8756–8768

Read Online

ACCESS |



Metrics & More



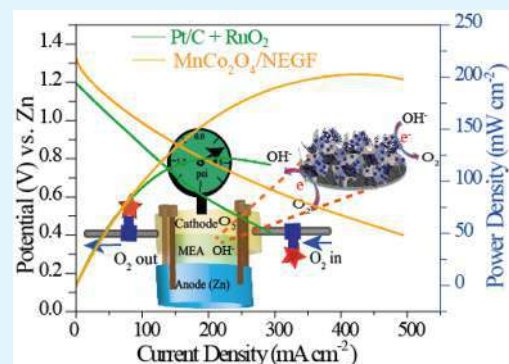
Article Recommendations



Supporting Information

ABSTRACT: Solid-state rechargeable zinc–air batteries (ZABs) are gaining interest as a class of portable clean energy technology due to their advantages such as high theoretical energy density, intrinsic safety, and low cost. It is expected that an appropriately triple-phase boundary (TPB) engineered, bifunctional oxygen reaction (OER and ORR) electrocatalyst at the air–electrode of ZABs can redefine the performance characteristics of these systems. To explore this possibility, an electrode material consisting of manganese–cobalt-based bimetallic spinel oxide (MnCo_2O_4)-supported nitrogen-doped entangled graphene ($\text{MnCo}_2\text{O}_4/\text{NEGF}$) with multiple active sites responsible for facilitating both OER and ORR has been prepared. The porous 3D graphitic support significantly affects the bifunctional oxygen reaction kinetics and helps the system display a remarkable catalytic performance. The air electrode consisting of the $\text{MnCo}_2\text{O}_4/\text{NEGF}$ catalyst coated over the gas diffusion layer (GDL) ensures the effective TPB, and this feature works in favor of the rechargeable ZAB system under the charging and discharging modes. As an important structural and functional attribute of the electrocatalyst, the porosity and nitrogen doping in the 3D conducting support play a decisive aspect in controlling the surface wettability (hydrophilicity/hydrophobicity) of the air electrode. The fabricated solid-state rechargeable ZAB device with the developed electrode displayed a maximum peak power density of 202 mW cm^{-2} , which is significantly improved as compared to the one based on the Pt/C + RuO_2 standard catalyst pair (124 mW cm^{-2}). The solid-state device which displayed an initial charge–discharge voltage gap of only 0.7 V at 10 mA cm^{-2} showed only a small increment of 86 mV after 50 h.

KEYWORDS: spinel oxides, N-doped entangled graphene, bifunctional oxygen catalyst, air–cathode interface, solid-state zinc–air battery



1. INTRODUCTION

To address future energy and environmental challenges, economically viable energy storage technologies with improved performance characteristics are necessary.¹ Among such charge storage devices, solid-state rechargeable zinc–air batteries (ZABs) have gained appreciable interest for large-scale applications in portable electronic devices.^{2,4} Compared to the existing metal–air batteries, these systems have several advantages such as high theoretical energy density (1086 W h kg^{-1}), involvement of safe aqueous electrolytes, and sufficient zinc metal resources.³ However, the practical applications of ZABs are impoverished by their low power density, deficient charge–discharge voltage, and overall lower output energy efficiency.⁴ These limitations are mainly attributed to the slow kinetics of oxygen reduction reaction (ORR) and oxygen evolution reaction (OER) on the air electrode.^{2,3} Conventionally, the spherical-shaped platinum nanoparticles supported carbon (Pt/C) and RuO_2 are mostly used as the electrocatalysts for ORR and OER processes, respectively.⁷ However, the lower bifunctional activity of the individual catalysts,⁸ their less availability as well as lower durability in the harsh conditions of ZABs hinder the practical prospects of the real-

time application of the rechargeable ZABs.⁷ As a result, there is a growing interest in the development of efficient bifunctional oxygen electrocatalysts.⁷ Another important obstacle with the air-cathode of ZABs is the restricted mass transport of the reactant/products gas molecules and electrolytes due to the comparatively lower access of the active sites and imbalanced hydrophilicity/hydrophobicity of the electrocatalyst-coated GDL interface.^{9,10} These issues necessitate a strategic design approach for building the air-electrode with improved triple-phase boundary (TPB) for effectively dealing with the existing issues related to kinetics and mass transport.^{11–13}

As cost-effective solutions to the air-electrodes for ZABs, a series of non-noble metal-based electrodes with excellent intrinsic activities were reported (e.g., transition metal oxides/hydroxides/chalcogenides/heteroatom doped carbon-based

Received: April 27, 2022

Accepted: June 29, 2022

Published: July 12, 2022



Scheme 1. Schematic Illustration of the Stages Involved in the Stepwise Synthesis of $\text{MnCo}_2\text{O}_4/\text{NEGF}$ as an ORR/OER Bifunctional Electrocatalyst and Demonstration of Its Application as the Air-Electrode for the Solid-State Rechargeable Zn–Air Battery



materials and hybrids of these materials).^{5,13,14} Among them, the transition metal oxides (Fe, Co, Mn, and Ni) received immense consideration as the ORR/OER bifunctional electrocatalysts due to their ease of synthesis, stability, and structural flexibility.^{15,16} Spinel oxides ($\text{A}^{\text{II}}\text{B}^{\text{III}}\text{B}^{\text{III}}\text{O}_4$) are mostly being marked as the ORR/OER bi-functional electrocatalysts owing to the distribution of the mixed-valence metal ions in the octahedral and tetrahedral positions.^{17,18} The mixed valency metal ions in a spinel oxide crystal structure provide a preferable electron transport channel with a favorable impact on improving the electrochemical activity.¹⁹ The intrinsic bifunctional activity of the spinel oxides could be improved by morphological and compositional tuning.²¹ Recently, we reported the nanorod-shaped spinel cobalt oxides with promising ORR performance.²⁰ Binary or ternary transition metal spinel oxides possess better bifunctional oxygen activity due to the involvement of the multiple catalytically active centers.^{15,22} The presence of a second metal with different charges alters the d-band centers and changes the electronic properties of the spinel oxides.^{21,23–25} This contributes favorably toward the bifunctional oxygen redox activity of the system. Among the various bimetallic spinel oxides, MnCo_2O_4 is recognized as a mixed-valence metal oxide with a spinel structure.^{22,25,26} However, the potential applications of the spinel oxide catalysts are restricted by their poor electronic conductivity.²⁷ This could be addressed by the incorporation of a conducting support with active sites, which simultaneously prevents the aggregation of the nanoparticles.⁶ Most of the conducting carbon supports used for dispersing the spinel oxides are 1D and 2D materials, which possess morphological limitations for efficiently establishing the active electrochemical interface.^{28,29} In this context, the 3D porous support materials as the substrates for interlinking the bifunctional active centers are becoming more promising.^{30,31}

Considering the importance of the active TPB in the electrodes of ZABs, appropriate interfacial engineering strategies to develop better air electrodes are necessary.^{32,33} Significant research has been done on developing the air cathodes by depositing various metal oxide–carbon composite-derived bifunctional catalysts directly on the surface of the hydrophobic GDLs.³⁴ However, such air-electrode structures

provide an almost 2D multiphase interface that is restricted to the limited space between the porous GDL and the electrocatalyst layer. In this configuration, the electrolyte and gaseous reactants cannot effectively reach out to the catalytic sites.³⁵ Thus, the traditional air-electrode structure in ZAB evidently gives rise to sluggish reaction kinetics for ORR and OER, which significantly reduces the ZAB battery performance. In this context, the 3D active interface can substantially improve the number of active catalytic sites and accelerate mass transport because of its interconnected interfacial structure.³⁶ During the catalytic process, if some electrocatalytic sites immigrate within the 3D interface region, they will still be able to participate in the electrochemical process.^{9,37,38} This unique type of interface structure also allows for simultaneous oxygen diffusion and electrolyte permeation within the interface region of the conductive 3D multiphase, which has significant implications for cathode kinetics.⁹ Simultaneously, the air-cathode interface engineering by maintaining a good balance between the hydrophobicity and hydrophilicity is vital for ensuring better mass transport.³⁹

To best accommodate the abovementioned structural attributes, an ORR/OER bifunctional electrocatalyst with favorably modulated performance characteristics based on self-assembled nitrogen-doped porous 3D entangled graphene-supported MnCo_2O_4 catalyst has been developed ($\text{MnCo}_2\text{O}_4/\text{NEGF}$). The nitrogen-doped graphene acts as a better nucleation site for the nanoparticles' growth over the asymmetric graphene substrate with improved hydrophobicity. This nitrogen-doped carbon microstructure retains sufficient hydrophobicity/hydrophilicity, which in turn could provide efficient mass transport routes to the active sites without getting flooded with the electrolyte solution. The ORR/OER bifunctional characteristics of the catalyst are found to be competing well with that of the state-of-the-art Pt/C + RuO_2 standard pair for tackling respective single electrode processes. Finally, a realistic validation of a rechargeable ZAB system based on $\text{MnCo}_2\text{O}_4/\text{NEGF}$ as the air-electrode reveals that the catalyst system with its favorable structural and functional attributes is capable of delivering better power density and stable cyclic stability. In these aspects, the homemade system is

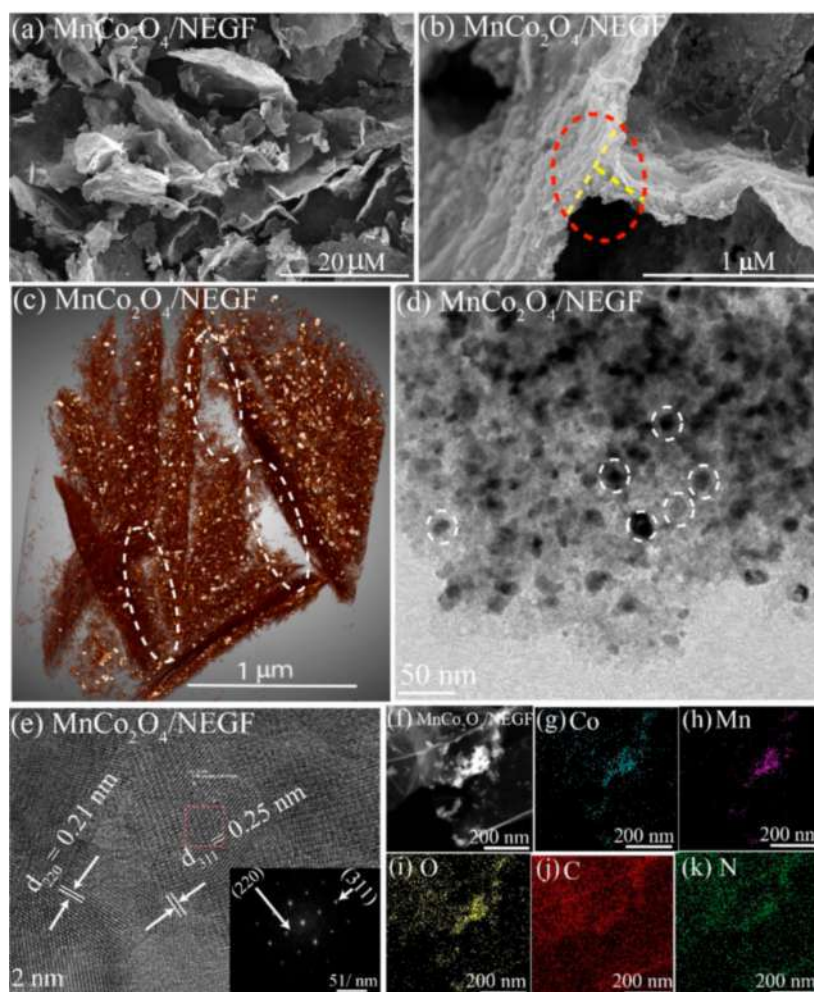


Figure 1. (a) FESEM images of $\text{MnCo}_2\text{O}_4/\text{NEGF}$, demonstrating the 3D porous self-assembly architecture of the graphene sheets; (b) magnified FESEM image of $\text{MnCo}_2\text{O}_4/\text{NEGF}$, showing the interconnected network of the 3D structure; (c) 3D micro-CT image of $\text{MnCo}_2\text{O}_4/\text{NEGF}$, displaying the porous structure of the matrix formed by the interconnection of the 2D GO sheets; (d) TEM image of $\text{MnCo}_2\text{O}_4/\text{NEGF}$, displaying the uniform distribution of MnCo_2O_4 over NEGF; (e) HRTEM image of $\text{MnCo}_2\text{O}_4/\text{NEGF}$, clearly displaying the d -spacing for MnCo_2O_4 with the inset image representing the crystalline nature of MnCo_2O_4 ; (f–k) elemental mapping corresponding to Co, Mn, N, O, and C, respectively, done on $\text{MnCo}_2\text{O}_4/\text{NEGF}$.

found to have a clear upper hand compared to a similar system based on the conventional air–cathode compositions.

2. RESULTS AND DISCUSSION

Scheme 1 depicts a simplified illustration of the stages involved in the stepwise synthesis of $\text{MnCo}_2\text{O}_4/\text{NEGF}$ as an ORR/OER bifunctional electrocatalyst and demonstration of its application as the air-electrode material for the rechargeable ZAB. The experimental details for the synthesis of the catalyst are presented in the Experimental Section, **Supporting Information**. In brevity, the aqueous solution of the graphene oxide (GO) synthesized *via* the improved Hummer's method was mixed well with Co^{2+} and Mn^{2+} metal precursors (2:1) at constant stirring for 6 h. The positively charged metal ions get anchored over the negatively charged functional groups of GO through electrostatic interactions during the mixing process. Ammonium hydroxide ($\sim 30\%$ v/v) was added to the metal ion-anchored GO solution with continuous stirring for 6 h, followed by probe sonication for 10 min. The color of the solution was found to be changed at a certain concentration when the pH of the solution reached ~ 10 due to the formation of the metal hydroxides and adsorption of the NH_4^+ ions over

the negatively charged GO surface. During the hydrothermal treatment, the decomposition of NH_4^+ moieties occurs in the beginning, followed by the doping of nitrogen into the carbon skeleton. Graphene oxide layers are connected with various functional groups such as epoxy, OH, and COOH groups. Depending on the nature of the functional groups and the binding strength of carbon–carbon bonds, the doped nitrogen exists in various forms such as pyrrolic, pyridine, graphitic, and quaternary states. This creates asymmetric carbon centers with some differences in the electronegativity in the system. At high temperatures and pressure of the solvothermal treatment, the metal hydroxides gradually decompose and nucleate at the asymmetric carbon centers, resulting in the formation of the spherically shaped spinel oxide (MnCo_2O_4) nanoparticles anchored over the N-doped reduced graphene oxide's surface. The solvothermal reaction is followed by the freeze-drying process, which plays an important aspect in establishing the 3D geometrical orientation and restructuring of the graphene sheets bearing the bimetallic spinel oxide nanoparticles. This electrocatalyst consisting of the entangled graphene framework with homogeneously dispersed Co–Mn spinel oxide nanoparticles ($\text{MnCo}_2\text{O}_4/\text{NEGF}$) possesses a high surface area and

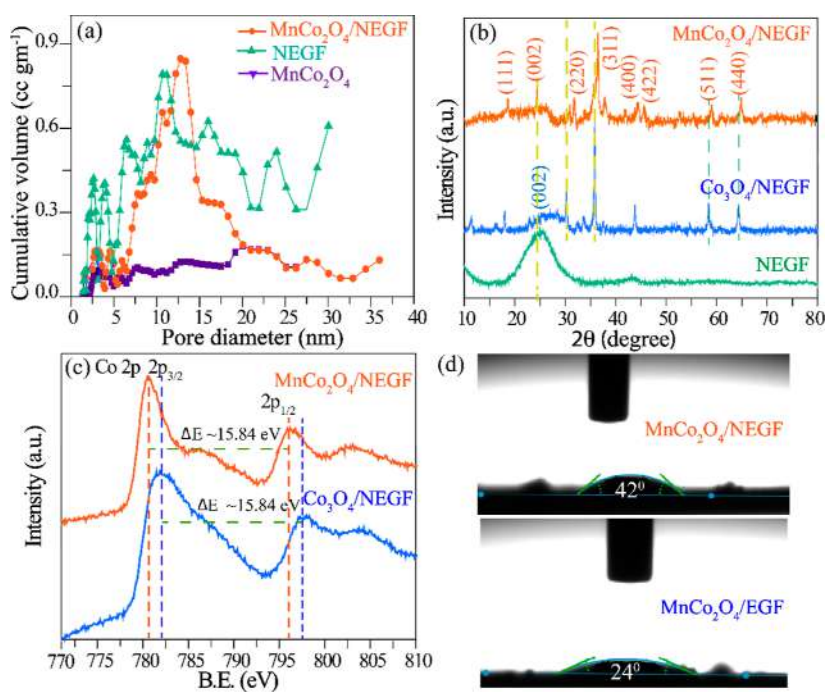


Figure 2. (a) Pore size distribution profiles of NEGF, MnCo_2O_4 , and $\text{MnCo}_2\text{O}_4/\text{NEGF}$, suggesting that the pores are mostly distributed in the 10 to 15 nm range; (b) XRD profiles recorded for NEGF, $\text{Co}_3\text{O}_4/\text{NEGF}$, and $\text{MnCo}_2\text{O}_4/\text{NEGF}$; (c) Co 2p XPS spectra of $\text{Co}_3\text{O}_4/\text{NEGF}$, and $\text{MnCo}_2\text{O}_4/\text{NEGF}$, revealing the peak shift after the incorporation of Mn into the Co_3O_4 matrix; (d) contact angle images of $\text{MnCo}_2\text{O}_4/\text{NEGF}$ and its counterpart without nitrogen doping, that is $\text{MnCo}_2\text{O}_4/\text{EGF}$, showing the dissimilarity in the wettability characteristics.

catalytic site-accessible porous architecture. The resulting catalyst was coated over a porous carbon gas diffusion layer (GDL) in combination with PVA-KOH gel electrolyte, and a solid-state rechargeable ZAB device was fabricated and demonstrated. The details of the catalyst synthesis and ZAB device fabrication are given in [Supporting Information](#).

The morphological analysis of the N-doped 3D graphene and distribution of the bimetallic spinel oxide nanoparticles were investigated by field emission scanning electron microscopy (FESEM). The freeze-drying induced structural alignment, leading to the establishment of homogeneous porosity to the assembly of the N-doped reduced graphene oxide layers in $\text{MnCo}_2\text{O}_4/\text{NEGF}$, is clearly evidenced in the FESEM images presented in [Figures 1a,b](#), and [S1](#), [Supporting Information](#). [Figure 1a](#) shows the self-assembly structure of $\text{MnCo}_2\text{O}_4/\text{NEGF}$ consisting of the nitrogen-doped 3D oriented graphene sheets, whereas the magnified image of the catalyst shown in [Figure 1b](#) highlights the interconnection of the sheets that lead to the formation of the porous architecture of the matrix. The formation of the self-assembled 3D structured bare NEGF can be visualized in the FESEM image presented in [Figure S1a](#), [Supporting Information](#), whereas the images of the support bearing the MnCo_2O_4 nanoparticles ($\text{MnCo}_2\text{O}_4/\text{NEGF}$), which retains the same structural attributes anchoring sites appeared to be creating a fertile environment for the nucleation of the MnCo_2O_4 nanoparticles, which enables homogeneous and more size-controlled dispersion.

Furthermore, to gain more clarity on the dimensionally oriented 3D microstructures of the $\text{MnCo}_2\text{O}_4/\text{NEGF}$ electrocatalyst, X-ray micro-computed tomography (micro-CT) imaging was employed. The volume-rendered 3D micro-CT images of GO, NEGF, and $\text{MnCo}_2\text{O}_4/\text{NEGF}$ are presented in [Figures 1c](#) and [S2](#) ([Figure S2a–d](#), [Supporting Information](#)).

These images clearly point toward the existence of the well-defined porous architecture of the system which has been originated by connecting the edges of the graphene sheets. Compared to NEGF ([Figure S2b](#), [Supporting Information](#)) and $\text{MnCo}_2\text{O}_4/\text{NEGF}$ ([Figures 1c](#) and [S2c](#), [Supporting Information](#)), the micro-CT image presented in [Figure S2a](#), [Supporting Information](#), for GO shows a nonseparated stacked layer of the sheets. The features of $\text{MnCo}_2\text{O}_4/\text{NEGF}$ with respect to the layer-separated 3D structure with interconnection and interlayer spacing of the graphene sheets are in agreement with the textural characteristics of the system as revealed through the FESEM images. The porous microstructure of NEGF allows the system to have a larger surface area than its precursor (GO). The spatial distribution of the MnCo_2O_4 particles over the NEGF sheets is shown in [Figure S2d](#), which displays the distribution of the closely similar-sized nanoparticles of MnCo_2O_4 in the catalyst matrix.

The distribution of the MnCo_2O_4 nanoparticles on 3D NEGF could be mapped with the help of transmission electron microscopy (TEM) imaging ([Figure 1d](#)). The image points toward the homogenous distribution of the spherically shaped MnCo_2O_4 nanocrystals with sizes in the range of 15 to 30 nm over the individual sheets of the N-doped graphene. As mentioned previously, the controlled distribution of the metal oxide nanoparticles is mediated by the intervention of the asymmetric carbon centers present in the N-doped graphene framework, which serve as homogeneous nucleation sites for the growth of the MnCo_2O_4 nanoparticles. The contrast difference of the particles in the TEM image suggests that a fraction of metal oxide nanoparticles is distributed at the inner surface of the 3D graphene, which is protected by the thin layers of the graphene sheets.⁴⁰ This controlled distribution of the MnCo_2O_4 nanoparticles on either side of the graphene sheets is beneficial for providing better stability to the system

by reducing the chances of self-agglomeration of the nanoparticles.⁴¹ Figure 1e shows the high-resolution transmission electron microscopy (HRTEM) image of MnCo₂O₄/NEGF, elucidating that the metal oxides are crystalline in nature. The metal oxide nanoparticles are having lattice fringe widths (*d*-spacing) of 0.25 and 0.21 nm, which are ascribed to the (311) and (211) facets suggesting the formation of the cubic MnCo₂O₄ spinel phase.⁴² The selected area electron diffraction (SAED) pattern presented as an inset image in Figure 1e shows the characteristic diffraction ring corresponding to the polycrystalline nature of the MnCo₂O₄ spinel oxide, confirming the (311) and (211) planes of MnCo₂O₄.³⁷ Using the HRTEM image shown in Figure 1f, the elemental mapping corresponding to the location has been done and the respective images are presented in Figure 1g–k. To validate the synergistic effect of MnCo₂O₄ and the 3D conducting support (NEGF), a physically mixed composite catalyst (MnCo₂O₄@NEGF) was also prepared by mixing the MnCo₂O₄ nanoparticles with NEGF and grounding well by using a mortar and pestle. Figure S3a, Supporting Information, shows the HRTEM image of the physically mixed catalyst (MnCo₂O₄@NEGF), which reveals that the particles are nonuniformly distributed over the NEGF surface. This redefines the important role of the chemically synthesized catalyst systems where the process of the nucleation and growth of the nanoparticles over the nucleating sites plays the most important role in simultaneously achieving the distribution and size control. Furthermore, to understand the role played by the doped-N in the conducting support, the catalyst without the nitrogen-doped conducting support, that is, the entangled graphene framework (EGF), was also synthesized (MnCo₂O₄/EGF). The HRTEM image of MnCo₂O₄@EGF shown in Figure S3b, Supporting Information reveals that particles are less uniformly distributed, ascribed to the poor interaction of EGF and MnCo₂O₄ when the conducting support is lacking the doped-N as nucleation sites. Because of the absence of the doped-N in the conducting support (EGF), the MnCo₂O₄ nanoparticles are self-agglomerated at the time of nucleation during the hydrothermal treatment. Hence, the support with nitrogen doping has a significant role in attaining uniform particle distribution.

The images represent the presence and distribution of Co, Mn, O, C, and Ni, which is in line with the chosen composition of the catalyst. The presence of Co and Mn in the same position with an almost double intensity of Co clearly supports the bimetallic structure of the spinel oxide. Further, the energy dispersive X-ray (EDX) analysis of the samples also provides similar evidence of the elemental composition (Figure S4, Supporting Information).

Figure 2a shows the comparative pore size distribution profile of NEGF, MnCo₂O₄, and MnCo₂O₄/NEGF, where a major fraction of the pores is found to be distributed in the region of 2–30 nm for NEGF and 2–20 nm for MnCo₂O₄/NEGF. MnCo₂O₄ on the other hand is found to be less porous. Hence, the dispersion of MnCo₂O₄ on NEGF slightly lowers the porosity of the composite, and this accounts for the observed trend in the pore size distribution profile of MnCo₂O₄/NEGF with the major portion of the pores falling in the range of 16–20 nm. This difference in the nature of the pore size distribution between the samples is also reflected in terms of their BET surface area. The surface area of 450 m² g⁻¹ measured on NEGF has been dropped to 300 m² g⁻¹ in the case of MnCo₂O₄/NEGF. Also, both NEGF and MnCo₂O₄/

NEGF display type-IV isotherms (Figure S5, Supporting Information). The large surface area possessed by MnCo₂O₄/NEGF along with its highly porous texture is a distinct advantage of the system as an electrocatalyst with the efficient usage of the active sites by establishing the interface with the electrolyte and reactants. This type of active “triple-phase boundary” (TPB) formation is an important requirement for realizing the final application of the electrocatalyst as an efficient air-electrode for rechargeable ZABs. The total loading of the spinel oxide nanoparticles in MnCo₂O₄/NEGF has been determined by thermogravimetric analysis (TGA). The TGA profiling was done under an oxygen atmosphere in the temperature range of 25 to 900 °C with a scan rate of 10 °C per min. The TGA weight loss profile for MnCo₂O₄/NEGF is shown in Figure S6, Supporting Information, and the residue content indicates that the total loading of MnCo₂O₄ in the system is 45 wt. %.

Figure 2b shows the X-ray diffraction (XRD) pattern of NEGF, which shows broad diffraction peaks at the 2θ values of 26 and 43°, which are attributed to the (002) and (100) graphitic diffraction planes, respectively.⁴³ The XRD profile of Co₃O₄/NEGF shows a comparatively intense peak for the (311) plane of Co₃O₄ at the 2θ values of 35°. The spinel structure of Co₃O₄ (Co^{II}Co^{III}O₄) with a cubic spinel structure has an intense peak of the (311) plane, matching well with the JCPDS Card No: 00-042-1467.⁴⁰ However, after the incorporation of Mn into the spinel structure of Co₃O₄, the resulting MnCo₂O₄/NEGF showed almost similar peak intensities of the major phases with a small shift in the peak positions.^{44,45} As depicted in Figure 2b, the XRD pattern of MnCo₂O₄/NEGF confirmed a series of peaks at 2θ = 18.3, 30.2, 35.6, 37.0, 43.2, 53.8, 57.2, 62.7, and 74.0°, which are attributable to the (111), (220), (311), (400), (422), (511), (440), and (533) planes, respectively, for the MnCo₂O₄ spinel structure (JCPDS no. 23-1237).⁴⁶ In Co₃O₄, the Co ions are present in the octahedral and tetrahedral sites.⁴⁰ After the Mn incorporation, the Co present in one of the tetrahedral sites gets occupied by the Mn and forms a normal spinel structure (Co^{III}Mn^{II}Co^{III}O₄).⁴⁶ However, the larger ionic radius of the Mn causes the lattice contraction, resulting in a change in the *d*-spacing value. The formation of MnCo₂O₄ spinel oxide peaks is well-matched with the JCPDS Card no. 23-1237. Therefore, the MnCo₂O₄ spinel oxides, like Co₃O₄ spinel oxides, are found to be cubic structures. Also, after incorporating the MnCo₂O₄ nanoparticles over NEGF, the (002) graphitic plane is found to be shifted toward a lower diffraction angle (25°) compared to that in NEGF (26°). This shift is expected to be originated from the expansion of the *d*-spacing of the N-doped graphene sheets due to the incorporation of the MnCo₂O₄ nanocrystals between the layers.

The extent of the defects imparted in the graphene frameworks of NEGF has been determined by calculating the I_D/I_G ratio using Raman spectroscopy. In the Raman spectra, the D-band typically expresses the defects, whereas the G band represents the order structure in the graphene lattice. The comparative Raman spectra recorded for NEGF and MnCo₂O₄/NEGF are presented in Figure S7, Supporting Information. The D-band peak at 1350 cm⁻¹ and the G-band peak at 1590 cm⁻¹ are attributed to the A_{1g} symmetry and E_{2g} symmetry of graphitic lattice vibration mode, respectively.²⁷ In the case of NEGF and MnCo₂O₄/NEGF, the measured I_D/I_G ratios are 1.25 and 1.31, respectively. The increased I_D/I_G value reported for GO (~1.0) to NEGF in the present case clearly

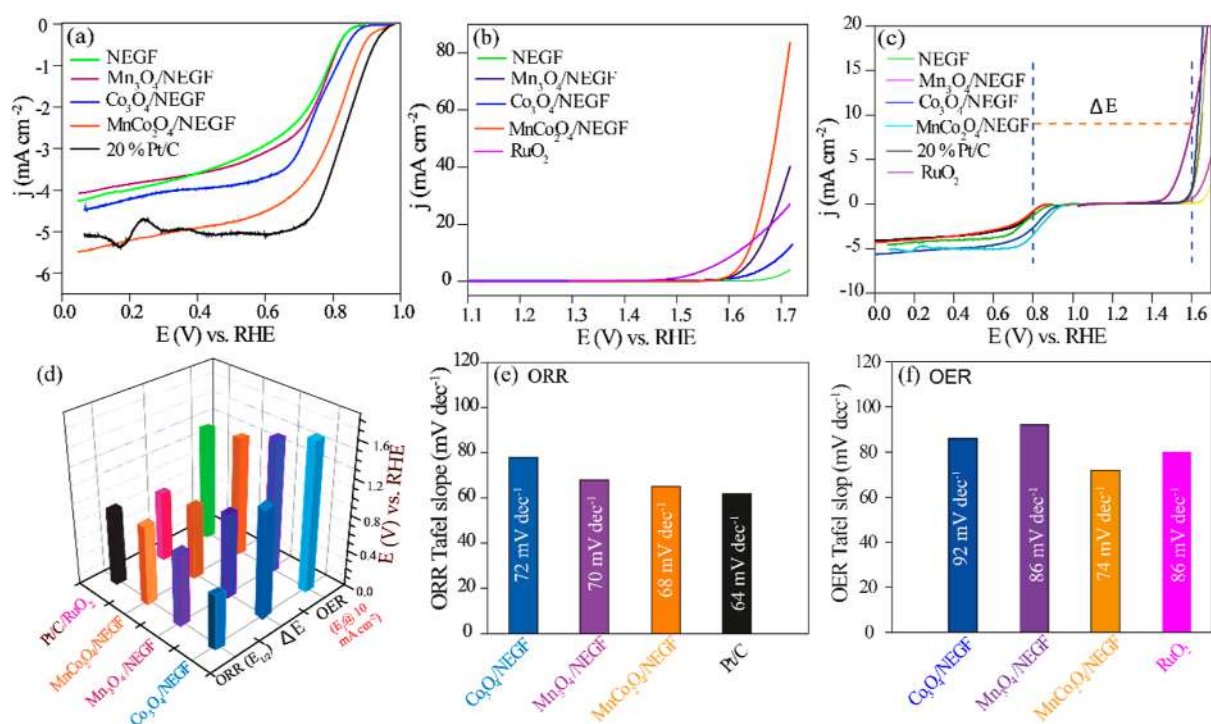


Figure 3. (a) Comparative LSV profiles recorded for NEGF, Co₃O₄/NEGF, MnCo₂O₄/NEGF, and Pt/C toward ORR in O₂ saturated 0.1 M KOH with the rotation of the working electrode at 1600 rpm; (b) comparative LSV profiles recorded for NEGF, Co₃O₄/NEGF, MnCo₂O₄/NEGF, and Pt/C toward OER in N₂ saturated 1 M KOH with rotation of the working electrode at 1600 rpm; (c) LSV profiles comparing the ORR/OER bifunctional activity of NEGF, Co₃O₄/NEGF, Mn₃O₄/NEGF, and MnCo₂O₄/NEGF; (d) graph comparing the onset potential for OER (E_j @ 10 mA cm⁻²), half-wave potential ($E_{1/2}$) for ORR, and ΔE , that is, ORR ($E_{1/2}$)—OER (E_j @ 10 mA cm⁻²) for the catalysts; (e) the comparison of the Tafel slopes extracted from the LSV profiles recorded by the systems toward ORR; (f) comparison of the Tafel slopes extracted from the LSV profiles recorded by the systems toward OER.

points toward the creation of new defect sites with the introduction of the doped nitrogen into the graphitic lattice structure during the solvothermal treatment at 180 °C. Such introduced defective sites in the N-doped graphene sheets are helpful for seeding the nucleation of the metal oxide nanoparticles.⁴⁷ The defective sites are higher in MnCo₂O₄/NEGF ($I_D/I_G = 1.31$) compared to its counterpart NEGF support ($I_D/I_G = 1.25$), which must have been introduced due to the lattice stress created during the *in situ* growth of the metal oxide nanoparticles.⁵¹

Furthermore, a more focused investigation on the chemical nature of the prepared catalysts has been performed with the help of X-ray photoelectron spectroscopy (XPS); the corresponding data are presented in Figures 2c and S8, Supporting Information. Figure S8a, Supporting Information displays the survey scan spectra of NEGF, Co₃O₄/NEGF, and MnCo₂O₄/NEGF, which confirm the presence of the Mn, Co, O, N, and C in the respective materials.

The characteristic Co 2p XPS peaks corresponding to Co₃O₄/NEGF and MnCo₂O₄/NEGF are appearing at the B.E. values of 784.2 and 795.5 eV and 783.5 and 796.5 eV, respectively (Figure 2c).⁴³ The characteristic peak separation (~15.84 eV) between the two peaks remains the same for the spinel oxides. However, the shift in the B.E after incorporating Mn into the spinel lattice of Co₃O₄ provides supplementary evidence of the formation of the bimetallic (MnCo₂O₄) spinel oxide. The observed negative shift in the B.E of MnCo₂O₄ compared to Co₃O₄ might be due to the charge transfer from Co to Mn.⁴⁸ The deconvoluted XPS spectra of Co 2p in Co₃O₄/NEGF (Figure S8b) show two doublet peaks at the

B.E. values of 783.4 and 799.2 eV for Co²⁺ and 783.8 and 799.6 eV for Co³⁺. Furthermore, the deconvoluted XPS spectra of Co 2p in MnCo₂O₄/NEGF presented two doublets (Figure S8c Supporting Information) at B.E. values of 783.1 and 798.8 eV with a peak gap of 15.7 eV, indicating the presence of the +2 and +3 oxidation states of Co.^{20,49} Moreover, the deconvoluted Mn spectra (Figure S8d) show two spin–spin coupling peaks at the B.E. values of 640.1 and 651.3 eV and 642.2 and 653.3 eV corresponding to the Mn 2p_{3/2} and Mn 2p_{1/2} states, respectively.^{6,50} This confirms the presence of Mn in the system having +2 and +3 oxidation states. Furthermore, the deconvoluted N 1s spectra of Co₃O₄/NEGF and MnCo₂O₄/NEGF (Figure S9a,b, Supporting Information) show the major proportion of the XPS peaks for pyridinic-N at 398.6 eV, and pyrrolic-N at 399.7 eV, with a smaller fraction of the graphitic-N at 400.5 eV and NH₄⁺ at 405.5 eV.²⁰ Furthermore, the Co 2p and Mn 2p spectra of MnCo₂O₄/EGF (graphene without the doping of the nitrogen) and MnCo₂O₄/NEGF are compared to know the role of doped nitrogen in the support (Figure S9c,d). The presence of a higher portion of the pyridinic-N, and pyrrolic-N can help for the direct coordination with the Co and Mn in MnCo₂O₄/NEGF, and this is responsible for the observed binding energy shift.

The presence of nitrogen doping in the conducting support can modulate the surface wettability of the electrocatalysts, which is an important deciding factor in improving the activity of the catalyst by enhancing the extent of the interface formation with the electrolyte.³² The contact angle (CA) measurement was performed to check the surface wettability of MnCo₂O₄/EGF and MnCo₂O₄/NEGF (Figure 2d). The lower

CA value of 24° measured for $\text{MnCo}_2\text{O}_4/\text{EGF}$ confirms the higher hydrophilicity of the enabling catalyst, which can easily wet the surface, resulting in water flooding. Therefore, the mass transfer can be hindered by the excessive wetting of the surface. After the N doping into the 3D structure of graphene, the CA value for $\text{MnCo}_2\text{O}_4/\text{NEGF}$ reached an optimal value of 42° . This optimal hydrophilicity of the catalytic material promotes the formation of the gas–liquid–solid TPBs during the electrochemical reactions.⁵¹

The electrochemical bifunctional feature of the designed catalyst was evaluated by monitoring the ORR and OER characteristics with the help of a set of electrochemical probing methods. The activity of the catalyst was evaluated using a three-electrode electrochemical cell. The working electrode (WE) was a catalyst-coated glassy carbon electrode (GCE), while the reference and counter electrodes were Hg/HgO and a graphite rod, respectively. The applied potential was converted into the RHE scale with the standard process as explained in the experimental section in the [Supporting Information](#) (Section S3.2.). The bifunctional ORR/OER characteristics of the electrocatalyst were evaluated by the rotating disk electrode (RDE) analysis by employing 0.1 M KOH and 1 M KOH electrolytes for ORR and OER, respectively. The linear sweep voltammograms (LSVs) corresponding to ORR were recorded in 0.1 M KOH at the voltage scan rate of 10 mV s^{-1} under an O_2 atmosphere while maintaining the working electrode rotation at 1600 rpm. The comparative LSV profiles shown in [Figure 3a](#) indicate that $\text{MnCo}_2\text{O}_4/\text{NEGF}$ (0.93 V) exhibits superior ORR performance in terms of the onset potential when compared to the control samples NEGF (0.86 V), $\text{Co}_3\text{O}_4/\text{NEGF}$ (0.89 V), and $\text{Mn}_3\text{O}_4/\text{NEGF}$ (0.85 V). In addition, the onset potential of 0.93 V recorded by $\text{MnCo}_2\text{O}_4/\text{NEGF}$ is coming very close to that displayed by the *state-of-the-art* Pt/C catalyst (0.98 V). The observed half-wave potentials ($E_{1/2}$) recorded on the catalysts corresponding to ORR are $\text{MnCo}_2\text{O}_4/\text{NEGF}$ (0.81 V), NEGF (0.75 V), $\text{Co}_3\text{O}_4/\text{NEGF}$ (0.77 V), $\text{Mn}_3\text{O}_4/\text{NEGF}$ (0.76 V), and Pt/C (0.84 V). Similarly, the OER activity has also been evaluated for NEGF, $\text{Co}_3\text{O}_4/\text{NEGF}$, $\text{Mn}_3\text{O}_4/\text{NEGF}$, $\text{MnCo}_2\text{O}_4/\text{NEGF}$, and RuO_2 in 1 M KOH at a voltage scan rate of 10 mV s^{-1} under a N_2 atmosphere ([Figure 3b](#)). The synthesized catalysts have displayed the OER activity (E_j @ 10 mA cm^{-2}) as $\text{Co}_3\text{O}_4/\text{NEGF}$ (1.72 V), $\text{Mn}_3\text{O}_4/\text{NEGF}$ (1.65 V), $\text{MnCo}_2\text{O}_4/\text{NEGF}$ (1.63 V) and RuO_2 (1.61 V), respectively. Clearly, among all the homemade systems, the LSV traced for $\text{MnCo}_2\text{O}_4/\text{NEGF}$ outperforms the other systems in terms of the OER activity. Thus, in terms of both oxygen reactions (ORR/OER), $\text{MnCo}_2\text{O}_4/\text{NEGF}$ is observed to be a versatile catalyst with its unique bifunctional feature to facilitate both reactions. The improved electrochemical ORR/OER performance of $\text{MnCo}_2\text{O}_4/\text{NEGF}$ is mainly attributed to the synergistic interaction of NEGF and MnCo_2O_4 prepared *via* the hydrothermal treatment. [Figure S10a](#) shows the comparative ORR LSV profiles for MnCo_2O_4 , $\text{MnCo}_2\text{O}_4/\text{EGF}$ (without N-doped), and $\text{MnCo}_2\text{O}_4/\text{NEGF}$ (physical mixture). Although after the incorporation of the support, the ORR onset potential is found to be improved in the case of $\text{MnCo}_2\text{O}_4/\text{EGF}$ (0.89 V) compared to MnCo_2O_4 (0.82 V), which reveals the important role played by the support. The ORR onset potential of the catalyst shows similar performance in the presence of the N-doped support. Similarly, the OER performance ([Figure S10b](#)) of the catalysts shows the order as $\text{MnCo}_2\text{O}_4/\text{NEGF} \approx \text{MnCo}_2\text{O}_4/\text{EGF} > \text{MnCo}_2\text{O}_4$. Impor-

tantly, the ORR/OER performance of $\text{MnCo}_2\text{O}_4/\text{NEGF}$ (physically mixed) is significantly lower than that of the catalyst prepared *via* the hydrothermal treatment. These results suggest the role of the chemical dispersion process in establishing better interactions of the active sites and the support, leading to more effective synergistic interactions in the system. Hence, the support with the doped nitrogen has a significant role in favorably modulating the ORR/OER activity in the case of the chemically synthesized catalyst ($\text{MnCo}_2\text{O}_4/\text{NEGF}$) compared to its physically mixed counterpart ($\text{MnCo}_2\text{O}_4/\text{NEGF}$). Furthermore, the difference in the OER potential (E_j @ 10 mA cm^{-2}) and the ORR half-wave potential ($E_{1/2}$) is commonly used to evaluate the bifunctional electrocatalyst performance ([Figure 3c](#)).⁵² The bar chart presented in [Figure 3d](#) compares the extracted values of $E_{1/2}$ for ORR, E_j @ 10 mA cm^{-2} for OER, and the difference between these two values (ORR–OER) for the respective electrocatalysts. Based on the ORR–OER parameter, which is indicative of the overall bifunctional activity of the system, $\text{MnCo}_2\text{O}_4/\text{NEGF}$ with the difference of 0.82 V ([Figure 3d](#)) is found to be comparable to or better than the previously reported various bifunctional electrocatalysts ([Table S1](#), [Supporting Information](#)). To validate the concentration effect of the electrolyte on the catalyst performance, the ORR and OER activities of $\text{MnCo}_2\text{O}_4/\text{NEGF}$ have been measured in 0.1 M KOH solution ([Figure S11](#)). The OER activity of $\text{MnCo}_2\text{O}_4/\text{NEGF}$ in the 0.1 M KOH solution is significantly low due to the low hydroxyl ion concentration.³¹ Here, the potential difference corresponding to the bifunctional characteristics of $\text{MnCo}_2\text{O}_4/\text{NEGF}$ is 0.86 V, which is higher compared to the difference estimated based on the ORR activity measured in 0.1 M KOH and OER activity in 1 M KOH solutions. This study indicates the need for the KOH electrolyte with two different concentrations in each half-cell reaction for the effective functioning of the system.

The Tafel slope, which is a key performance indicator representing the intrinsic activity of the catalyst, has been extracted from the LSVs recorded for ORR and the corresponding values measured for NEGF, $\text{Co}_3\text{O}_4/\text{NEGF}$, $\text{Mn}_3\text{O}_4/\text{NEGF}$, $\text{MnCo}_2\text{O}_4/\text{NEGF}$, and Pt/C are shown in [Figure 3e](#). $\text{MnCo}_2\text{O}_4/\text{NEGF}$ with its Tafel slope value of 68 mV dec^{-1} is found to be nearly comparable to Pt/C (64 mV dec^{-1}). A similar exercise has been done to evaluate the kinetics toward OER, and the corresponding Tafel plots for the catalysts with the slopes marked are presented in [Figure 3f](#). The measured Tafel slope value for $\text{MnCo}_2\text{O}_4/\text{NEGF}$ and RuO_2 are 74 and 86 mV dec^{-1} , respectively. The higher Tafel slope values of $\text{Co}_3\text{O}_4/\text{NEGF}$ (92 mV dec^{-1}) and $\text{Mn}_3\text{O}_4/\text{NEGF}$ (86 mV dec^{-1}) compared to $\text{MnCo}_2\text{O}_4/\text{NEGF}$ suggest better activity of the latter system toward OER. The incorporation of Mn into the Co_3O_4 lattice plays a critical role in building the bifunctional feature in the system, enabling the catalyst to perform effectively for both the ORR and OER processes.

The electrochemical durability of the catalysts has been investigated by cycling it 5000 times under oxygen saturated 0.1 M KOH at a scan rate of 100 mV s^{-1} in the potential range of 1.2 and 0.8 V with respect to RHE, followed by recording the LSV in the oxygen reduction region. A comparison of the LSVs recorded before and after the potential cycling process showed a negative shift in the $E_{1/2}$ value with a drop of 34 mV for $\text{MnCo}_2\text{O}_4/\text{NEGF}$ ([Figure S12a](#), [Supporting Information](#)). This drop is lower than that of the *state-of-the-art* Pt/C catalyst

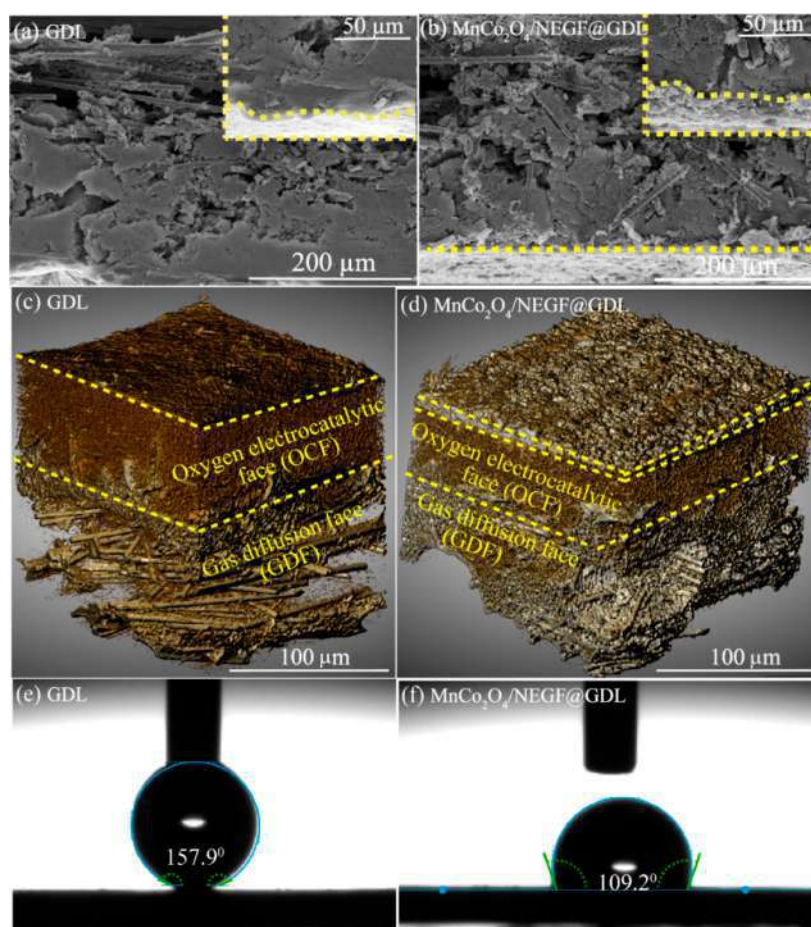


Figure 4. (a) Cross-sectional FESEM image of the GDL showing the plain surface boundary with the higher magnified inset image highlighting its bright plain surface; (b) cross-sectional FESEM image of $\text{MnCo}_2\text{O}_4/\text{NEGF}$ -coated GDL demonstrating the heterojunction interface formed after coating the catalyst with the interface marked with the dotted lines, including as an inset image for better clarity; (c,d) 3D CT tomogram images recorded for the GDL and $\text{MnCo}_2\text{O}_4/\text{NEGF}@GDL$ along the cross-section where the bare GDL is showing the two distinct phases of OCF and GDF, whereas $\text{MnCo}_2\text{O}_4/\text{NEGF}@GDL$ displays a rough surface of the coated catalysts layer; (e,f) contact angle images recorded on the bare GDL and $\text{MnCo}_2\text{O}_4/\text{NEGF}$, showing the surface wettability characteristics.

(36 mV) (Figure S12b, Supporting Information) recorded under identical conditions. In a similar way, the durability analysis was performed by cycling the potential 5000 times under N_2 saturated 1 M KOH at a voltage scan rate of 50 mV s^{-1} (Figure S12c, Supporting Information). The change in the OER potential (E_j @10 mA cm^{-2}) for $\text{MnCo}_2\text{O}_4/\text{NEGF}$ is only 15 mV. These results reveal the better structural endurance and corrosion resistance of $\text{MnCo}_2\text{O}_4/\text{NEGF}$ as a bifunctional catalyst for OER and ORR applications.

To check the structural changes of the electrocatalysts and the support after the accelerated durability test (ADT), the $\text{MnCo}_2\text{O}_4/\text{NEGF}$ -coated GDL was subjected to electrocatalytic cycling. The catalyst-coated GDL was analyzed after the 5000 cycles in O_2 saturated 0.1 M KOH solution. The sample was subjected to FESEM analysis, and Figure S13a, Supporting Information, represents the corresponding image. The figure shows that the self-assembled 3D structure of the graphene in $\text{MnCo}_2\text{O}_4/\text{NEGF}$ is retained almost perfectly after the 5000 ADT cycles. Additionally, the magnified image presented in Figure S13b reveals that the uniform distribution of the MnCo_2O_4 particles on the support in the pristine sample is unaffected under the triggered condition, suggesting the structural integrity of the system. For the phase comparison after ADT, XRD analysis has been performed for the bare

GDL, the GDL-coated catalyst ($\text{MnCo}_2\text{O}_4/\text{NEGF}@GDL$), and the catalyst after ADT. As the materials are coated over the GDL, a higher intense (002) peak at 26° for the GDL carbon is noticed in the catalysts. The XRD profile of $\text{MnCo}_2\text{O}_4/\text{NEGF}@GDL$, shown in Figure S13c, exhibits the peaks for the (111), (220), (311), (400), (422), (511), (440), and (533) planes. After ADT, the intensity of the peak corresponding to the (311) plane of MnCo_2O_4 is found to be suppressed, which is ascribed to the formation of the thin oxide layers of $\text{Mn}(\text{OH})_2$ and $\text{Co}(\text{OH})_2$. The formation of the metal hydroxide peaks is well justified as the reaction is carried out under an alkaline solution. Further, XPS analysis has been performed to confirm the changes in the chemical nature of the samples. Figure S13d represents the comparative XPS survey spectra of the catalyst before and after the 5000 ADT cycles. The increase in the intensity of the O 1s peak suggests the formation of the surface oxide layer. Furthermore, the deconvoluted Co 2p XPS spectra in Figure S13e show two doublet peaks at the B.E. values of 782.9 and 798.6 eV for Co^{2+} and 783.1 and 798.8 eV for Co^{3+} . The change in the XPS binding energy reveals the formation of $\text{Co}(\text{OH})_2$ and the B.E. peaks are corresponding to the Co–OH bond. Furthermore, the deconvoluted XPS peaks of Mn 2p presented in Figure S13f show two doublet peaks at the B.E. values of 639.9 and

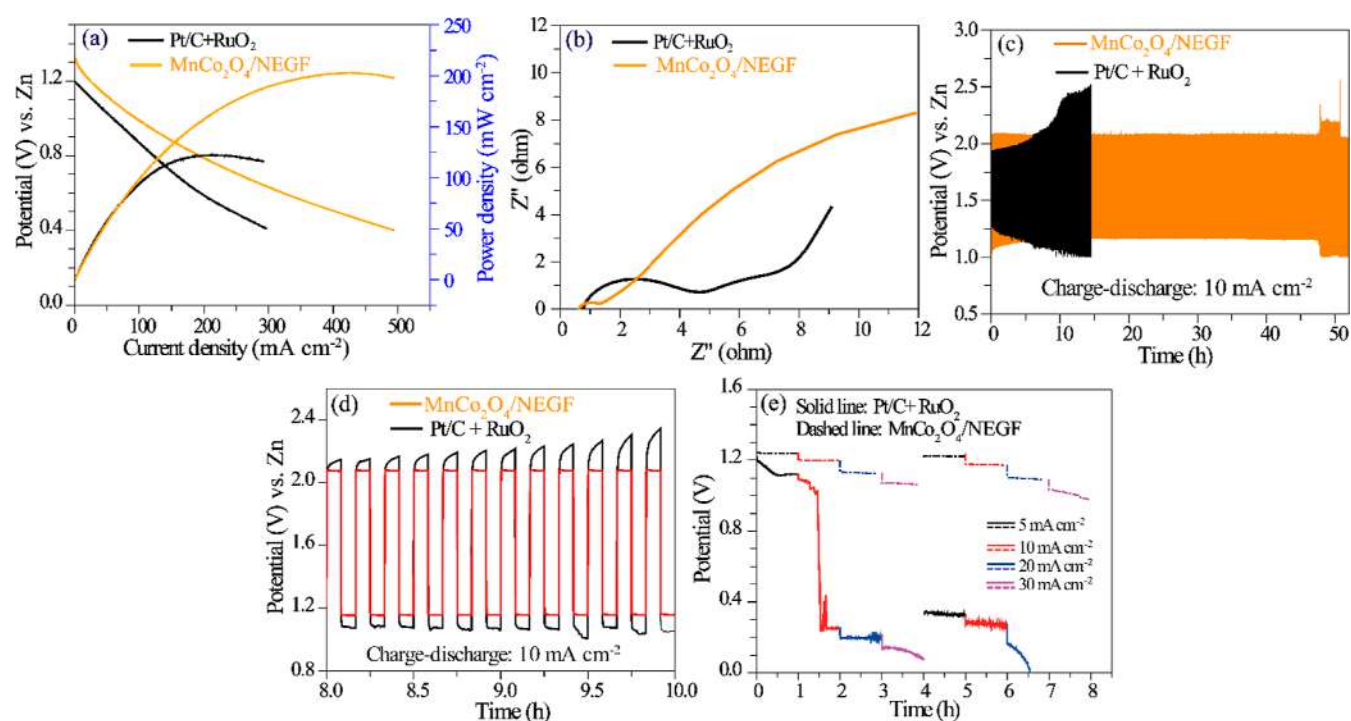


Figure 5. Solid-state rechargeable zinc–air battery (ZAB) performance evaluation for the systems based on $\text{MnCo}_2\text{O}_4/\text{NEGF}$ and $\text{Pt/C} + \text{RuO}_2$ as the air-electrodes: (a) comparative polarization plots; (b) comparative impedance plots; (c) comparative galvanostatic charge–discharge plots recorded at 10 mA cm^{-2} displaying the higher overpotential incurred by the system based on the $\text{Pt/C} + \text{RuO}_2$ air-electrode; (d) focused view of the galvanostatic charge–discharge cycling curves recorded at 10 mA cm^{-2} between 8 and 10 h of the test, showing the asymmetric nature of the charge–discharge plate in the case of the ZAB based on the $\text{Pt/C} + \text{RuO}_2$ standard pair air–cathode compared to the perfect symmetric nature of the charge–discharge profiles traced with the system based on the $\text{MnCo}_2\text{O}_4/\text{NEGF}$ air–electrode; (e) assessment of the galvanostatic discharge capacity of the fabricated ZABs performed at the various discharge current densities of 5, 10, 20, and 30 mA cm^{-2} .

651.2 eV for Mn^{2+} and 642.0 and 653.1 eV for Mn^{3+} . The change in the binding energy, in this case, is attributed to the presence of $\text{Mn}(\text{OH})_3$.

The application of $\text{MnCo}_2\text{O}_4/\text{NEGF}$ as an air electrode to function in the discharging (ORR) and charging (OER) modes for a solid-state ZAB was demonstrated by employing the catalyst-coated gas diffusion electrode (GDE) as the cathode. Prior to the fabrication of the cell and its testing, the catalyst-coated GDL surface was characterized by using FESEM and X-ray CT mapping to check the 3D microstructure of the resulting electrodes (Figure 4a–d). Figure 4a and the inset image show the cross-sectional FESEM image of the bare GDL, revealing the mostly flat structure of the surface. However, in the case of GDL coated with $\text{MnCo}_2\text{O}_4/\text{NEGF}$, a thick layer with a 3D structure (indicated by the dotted yellow lines) is observed (Figure 4b). The inset of Figure 4b gives better clarity of the surface of the GDL containing the 3D self-assembled structure of the coated layer of $\text{MnCo}_2\text{O}_4/\text{NEGF}$. This 3D microstructured catalyst layer over the GDL has a significant advantage for achieving improved TPB with better active interface and mass transfer characteristics. Compared to the highly porous nature of the $\text{MnCo}_2\text{O}_4/\text{NEGF}$ layer on the GDL, the catalyst layer of $\text{Pt/C} + \text{RuO}_2$ is found to be significantly less porous (Figure S14a, Supporting Information). The 3D CT tomogram imaging was performed to gain further information about the nature of the multiphase reactive interface of the air electrode. The commercial bare GDL consists of two parts (indicated by the dotted yellow lines in Figure 4c,d, i.e., the oxygen catalytic face (OCF) and the gas diffusion face (GDF) toward the inner and outer side of the

air-electrode, respectively. At OCF, the carbon fibers are coated with the hydrophobic PTFE, which prevents the flooding of the microporous surface of the GDL. Figure 4c,d shows the 3D tomogram cross-section images of the bare GDL and the $\text{MnCo}_2\text{O}_4/\text{NEGF}$ -coated GDL, respectively. Animated representations of the 3D CT images are shown in Movie S1 (Supporting Information). The tomography image in Figure 4c shows the two distinct phases of OCF and GDF (marked with the dotted yellow lines) of the GDL, as already indicated in the FESEM image of the corresponding sample presented in Figure 4a. On the other hand, in the case of the 3D CT image of the catalyst-coated GDL (Figure 4d), the 3D microstructure formation of the layer of $\text{MnCo}_2\text{O}_4/\text{NEGF}$ is evident and is demarcated with the dotted yellow line. However, this type of porous 3D microstructure of the catalyst layer is not evident in the 3D CT image recorded for the $\text{Pt/C} + \text{RuO}_2$ standard pair catalyst-coated GDL (Figure S14b, Supporting Information).

Of course, the 3D porous morphology of the $\text{MnCo}_2\text{O}_4/\text{NEGF}$ layer in the electrode is beneficial for improving the electrode–electrolyte interface formation. However, to realize this advantage significantly, the porous layer also should retain the optimum intrinsic wettability of the electrocatalyst even after it was subjected to the coating protocol during the electrode fabrication process. Interestingly, the $\text{MnCo}_2\text{O}_4/\text{NEGF}$ -coated surface of the GDL shows a water contact angle of 109.2° (Figure 4f), compared to 157.9° recorded on the CA measured on the $\text{Pt/C} + \text{RuO}_2$ -coated surface of the GDL is 128.2° (Figure S14c). The CA data corresponding to the bare GDL is presented in Figure 4e. From these results, it can be readily inferred that while an aqueous electrolyte can hardly

wet the bare GDL, the GDL based on the $\text{MnCo}_2\text{O}_4/\text{NEGF}$ coating possesses a balanced hydrophilic/hydrophobic characteristic, which is expected to result in optimum wettability at the interface.

To demonstrate a liquid-state ZAB, the $\text{MnCo}_2\text{O}_4/\text{NEGF}$ -coated GDL was used as the air electrode, a Zn foil as the anode, and 6 M KOH as the electrolyte. The details of the liquid-state ZAB fabrication are included in the Experimental section presented in [Supporting Information](#). The current (I)–voltage (V) polarization plots corresponding to the ZAB with the $\text{MnCo}_2\text{O}_4/\text{NEGF}$ cathode and its counterpart system with the Pt/C + RuO_2 standard pair cathode ([Figure S15a](#)) display the open-circuit voltage (OCV) values of 1.35 and 1.33 V, respectively. This trend in the polarization plot goes well in line with the intrinsic activity of the catalysts toward ORR, where Pt/C performs better compared to $\text{MnCo}_2\text{O}_4/\text{NEGF}$ in terms of the ORR onset potential and $E_{1/2}$ values. The maximum power densities (P_{max}) recorded on the ZABs based on $\text{MnCo}_2\text{O}_4/\text{NEGF}$ and Pt/C + RuO_2 cathodes are 52 and 43 mW cm^{-2} , respectively. Additionally, both systems display nearly similar charge transfer resistance characteristics as indicated by the Nyquist plots presented in [Figure S15b](#). Furthermore, the galvanostatic charge–discharge curves recorded for the cells at 10 mA cm^{-2} are shown in [Figure S15c](#). The potential difference between the charging and discharging of the liquid-state ZAB based on $\text{MnCo}_2\text{O}_4/\text{NEGF}$ air cathode is 1.1 V, which is higher than that observed in the case of its counterpart system based on the Pt/C + RuO_2 standard pair (0.65 V). After the 48 h of continuous charge–discharge cycles, the Pt/C + RuO_2 system shows a significant increase in the voltage difference by 0.65 V and the cell is completely dead. However, in the case of the $\text{MnCo}_2\text{O}_4/\text{NEGF}$ system, the voltage difference almost remains steady for 62 h.

In terms of this advantage, coupled with the 3D interconnected porous nature of the catalyst texture, the electrode based on the $\text{MnCo}_2\text{O}_4/\text{NEGF}$ catalyst layer has a distinct advantage over its counterpart system based on the Pt/C + RuO_2 -coated electrode. A full-featured demonstration of the prepared catalyst in a solid-state rechargeable ZAB device was conducted by fabricating a device by employing the $\text{MnCo}_2\text{O}_4/\text{NEGF}$ -coated GDL as the air-electrode, a zinc powder-coated GDL as the anode, and PVA soaked with KOH as the electrolyte (refer [Scheme 1](#), and Experimental Section S3.3, [Supporting Information](#)). A similar device employing Pt/C + RuO_2 standard pair catalyst-coated GDL as the air-electrode was also made for comparison purposes. The cell polarization plots presented in [Figure 5a](#) demonstrate the superiority of the system based on the homemade cathode in the entire I – V region traced during the study. The OCV values for the ZABs based on $\text{MnCo}_2\text{O}_4/\text{NEGF}$ and Pt/C + RuO_2 cathodes are 1.31 and 1.20 V, respectively. For these two systems, the comparative steady-state cell polarisation results in the maximum power densities (P_{max}) of 110 and 200 mW cm^{-2} , respectively. Here, the catalyst layer in the case of the $\text{MnCo}_2\text{O}_4/\text{NEGF}$, with its 3D interconnected porous structure and optimum wettability, is found to be more accommodative for the KOH-soaked PVA gel electrolyte. The previous discussions based on the FESEM, CT Tomography, and water contact angle data provided adequate information on these advantageous structural and functional attributes of the in-house system. The performance of the fabricated solid-state ZAB is found to be comparable and even superior to some of

the reported solid-state ZABs in the literature ([Table S2](#), [Supporting Information](#)). The advantage of $\text{MnCo}_2\text{O}_4/\text{NEGF}$ to form a more process-friendly cathode is further reflected in the substantially reduced charge transfer resistance (CTR) displayed by the cell compared to the one based on the Pt/C + RuO_2 standard pair cathode ([Figure 5b](#)). Furthermore, the galvanostatic charge–discharge curves recorded for the cells at 10 mA cm^{-2} are shown in [Figure 5c](#). The observed difference between the charging and discharging voltages of the ZAB based on $\text{MnCo}_2\text{O}_4/\text{NEGF}$ during the initial process is 0.84 V, which is lower than (0.91 V) that observed in the case of its counterpart system based on the Pt/C + RuO_2 standard pair. After 50 h of continuous charge–discharge cycles, a nominal increase in the voltage difference by 0.10 V has been observed in the case of the $\text{MnCo}_2\text{O}_4/\text{NEGF}$ -based cell. However, in the case of the Pt/C + RuO_2 -based system, the voltage difference is found to be increased to 0.15 V just after 15 h of the continuous charge–discharge cycles, and the test had to be terminated. Moreover, the magnified image of the charge–discharge profile in the 8 to 10 h duration, presented in [Figure 5d](#), reveals the symmetric nature of the charge–discharge plateau in the case of the $\text{MnCo}_2\text{O}_4/\text{NEGF}$ cell. Contrary to this, the cell based on Pt/C + RuO_2 has asymmetric behavior in its charge–discharge profile. This difference in the feature of the charge–discharge characteristics points toward the better bifunctional activity at the air-cathode of the ZAB based on $\text{MnCo}_2\text{O}_4/\text{NEGF}$.

In the case of rechargeable metal–air batteries, the ORR process is more sensitive to the active triple-phase interface during the discharge process compared to the OER process in the charging mode. To unravel the advantages of $\text{MnCo}_2\text{O}_4/\text{NEGF}$ due to its structural and functional attributes toward ORR in the battery configuration, the discharge curve at various current densities of 5, 10, 20, and 30 mA cm^{-2} are recorded for 1 h, and the comparative plots are presented in [Figure 5e](#). [Figure 5e](#) represents that, under each step of the discharging process, the voltage drop incurred by the $\text{MnCo}_2\text{O}_4/\text{NEGF}$ -based system is much lower compared to the one based on Pt/C + RuO_2 . The ZAB based on $\text{MnCo}_2\text{O}_4/\text{NEGF}$ has a relatively small voltage gap of 0.11, 0.12, 0.13, and 0.15 V at 5.0, 10.0, 20.0, and 30.0 mA cm^{-2} compared to 1.05, 0.14, 0.15, and 0.60 V, respectively, recorded under the same discharging conditions for the counterpart system based on Pt/C + RuO_2 . This distinct advantage of the $\text{MnCo}_2\text{O}_4/\text{NEGF}$ system could be credited to the favorable morphology of the catalyst in terms of better oxygen gas transport and efficient active interface formation. The presented results demonstrate that these kinds of air-electrodes with nano-engineered morphological and functional features have greater prospects of ensuring better system-level performance under different current dragging conditions. The comparative galvanostatic discharge curves ([Figure S16](#), [Supporting Information](#)) were recorded for the solid-state ZAB systems based on $\text{MnCo}_2\text{O}_4/\text{NEGF}$ and Pt/C + RuO_2 catalysts. The discharge profiles recorded at a current density of 5 mA cm^{-2} show almost 48 and 40 h of flat discharge curve for the systems based on $\text{MnCo}_2\text{O}_4/\text{NEGF}$ and Pt/C + RuO_2 , respectively. The obtained comparatively long discharge curve for the homemade system represents the stability and structural integrity of the catalyst under operating conditions.

After the long cycle of the galvanostatic charge–discharge analysis, the catalysts and the air-electrode interface structure were investigated by FESEM. The FESEM images of

MnCo₂O₄/NEGF and MnCo₂O₄/NEGF-coated ZAB air cathode interface are shown in Figure S17, Supporting Information. Figure S17a, Supporting Information, displays the 3D structure of NEGF retained even after the long charge–discharge cycles. The magnified image presented in Figure S17b, Supporting Information, clearly shows that the catalyst structure is more or less unaffected even after subjecting the system to the corrosive environment of the testing conditions. The cross-sectional image analysis of the ZAB air cathode (Figure S17c,d) shows that a portion of the catalyst gets detached from the GDL surface after the long-term charge–discharge cycling. Still, the inherent porosity of the conducting support is nearly unaffected.

3. CONCLUSIONS

A 3D structured electrode material, designated as MnCo₂O₄/NEGF, consisting of the manganese–cobalt-based bimetallic spinel oxide (MnCo₂O₄)-supported nitrogen-doped entangled graphene (NEGF) has been prepared as a versatile OER/ORR bifunctional electrocatalyst for rechargeable zinc–air battery (ZAB) application. Features like the porous 3D architecture of the catalyst, balanced hydrophilic/hydrophobic characteristics, and optimal ORR/OER activity are found to be favorably helping the system as an air-electrode for the rechargeable ZAB application. The 3D structure of the catalyst greatly helps the system in mass transfer and active site accessibility in the electrode. At the same time, the optimal hydrophilicity, originating from the functional attributes of the support surface, is found to play a significant role in constructing an effective interface for the catalyst and the electrolyte. The study reveals the existence of synergistic interactions operating between the MnCo₂O₄ nanoparticles and the N-doped porous graphene substrate. This benefits the system in terms of its bifunctional characteristics to perform as an effective electrocatalyst for facilitating both ORR and OER processes. In terms of the activity of MnCo₂O₄/NEGF toward these reactions, the overpotential values are found to be closely comparable to the respective *state-of-the-art* systems (i.e., Pt/C for ORR and RuO₂ for OER). The demonstration of a solid-state rechargeable ZAB device with MnCo₂O₄/NEGF as the air-electrode delivered a maximum peak power density of 200 mW cm⁻², with good stability at the time of the charge–discharge cycling process. In terms of performance and charge–discharge cyclability, the system based on the homemade catalyst is found to have a clear upper hand compared to a system consisting of the *state-of-the-art* ORR/OER catalyst combination of Pt/C + RuO₂.

■ ASSOCIATED CONTENT

SI Supporting Information

The Supporting Information is available free of charge at <https://pubs.acs.org/doi/10.1021/acsaem.2c01266>.

Experimental section, FESEM, CT-Tomography, BET analysis, TGA profiles, post electrochemical analysis, and long-term galvanostatic discharge curves (PDF)

Animated representations of the 3D CT images of the ZAB air electrode interface (AVI)

■ AUTHOR INFORMATION

Corresponding Author

Sreekumar Kurungot – Physical and Materials Chemistry Division, CSIR-National Chemical Laboratory, Pune

411008, India; Academy of Scientific and Innovative Research (AcSIR), CSIR-Human Resource Development Centre, Ghaziabad 201 002 Uttar Pradesh, India; orcid.org/0000-0001-5446-7923; Email: k.sreekumar@ncl.res.in

Authors

Narugopal Manna – Physical and Materials Chemistry Division, CSIR-National Chemical Laboratory, Pune 411008, India; Academy of Scientific and Innovative Research (AcSIR), CSIR-Human Resource Development Centre, Ghaziabad 201 002 Uttar Pradesh, India; orcid.org/0000-0001-6343-1746

Santosh K. Singh – Department of Chemistry, School of Natural Sciences, Shiv Nadar University, Uttar Pradesh 201314, India

Maria Kurian – Physical and Materials Chemistry Division, CSIR-National Chemical Laboratory, Pune 411008, India; Academy of Scientific and Innovative Research (AcSIR), CSIR-Human Resource Development Centre, Ghaziabad 201 002 Uttar Pradesh, India

Arun Torris – Polymer Science and Engineering Division, CSIR-National Chemical Laboratory, Pune 411008, India; orcid.org/0000-0003-4487-2604

Complete contact information is available at: <https://pubs.acs.org/doi/10.1021/acsaem.2c01266>

Author Contributions

The manuscript was written through the contributions of all authors. All authors have given approval to the final version of the manuscript.

Notes

The authors declare no competing financial interest.

■ ACKNOWLEDGMENTS

N.M. acknowledges the Council of Scientific and Industrial Research (CSIR), New Delhi, India, for a Research Fellowship. S.K. and M.K. acknowledge the Science & Engineering Research Board (SERB), Department of Science & Technology (DST), New Delhi, for funding through the project GAP328726 (SERB Sanction Order: CRG/2019/000277).

■ REFERENCES

- (1) Sun, W.; Wang, F.; Zhang, B.; Zhang, M.; Küpers, V.; Ji, X.; Theile, C.; Bieker, P.; Xu, K.; Wang, C.; Winter, M. A rechargeable zinc-air battery based on zinc peroxide chemistry. *Science* **2021**, *371*, 46–51.
- (2) Li, Y.; Gong, M.; Liang, Y.; Feng, J.; Kim, J.-E.; Wang, H.; Hong, G.; Zhang, B.; Dai, H. Advanced zinc-air batteries based on high-performance hybrid electrocatalysts. *Nat. Commun.* **2013**, *4*, 1805.
- (3) Liu, J.; Shen, X.; Zhou, J.; Wang, M.; Niu, C.; Qian, T.; Yan, C. Nonflammable and High-Voltage-Tolerated Polymer Electrolyte Achieving High Stability and Safety in 4.9 V-Class Lithium Metal Battery. *ACS Appl. Mater. Interfaces* **2019**, *11*, 45048–45056.
- (4) Cheng, F.; Chen, J. Metal-air batteries: from oxygen reduction electrochemistry to cathode catalysts. *Chem. Soc. Rev.* **2012**, *41*, 2172–2192.
- (5) Lee, J.-S.; Tai Kim, S.; Cao, R.; Choi, N.-S.; Liu, M.; Lee, K. T.; Cho, J. Metal-Air Batteries with High Energy Density: Li-Air versus Zn-Air. *Adv. Energy Mater.* **2011**, *1*, 34–50.
- (6) Su, H.; Wang, X.-T.; Hu, J.-X.; Ouyang, T.; Xiao, K.; Liu, Z.-Q. Co–Mn spinel supported self-catalysis induced N-doped carbon nanotubes with high efficiency electron transport channels for zinc-air batteries. *J. Mater. Chem. A* **2019**, *7*, 22307–22313.

- (7) Gu, P.; Zheng, M.; Zhao, Q.; Xiao, X.; Xue, H.; Pang, H. Rechargeable zinc-air batteries: a promising way to green energy. *J. Mater. Chem. A* **2017**, *5*, 7651–7666.
- (8) Gangadharan, P. K.; Bhanghe, S. N.; Kabeer, N.; Illathvalappil, R.; Kurungot, S. NiCo₂O₄ nanoarray on CNT sponge: a bifunctional oxygen electrode material for rechargeable Zn–air batteries. *Nanoscale Adv.* **2019**, *1*, 3243–3251.
- (9) Yu, J.; Li, B.-Q.; Zhao, C.-X.; Liu, J.-N.; Zhang, Q. Asymmetric Air Cathode Design for Enhanced Interfacial Electrocatalytic Reactions in High-Performance Zinc-Air Batteries. *Adv. Mater.* **2020**, *32*, 1908488.
- (10) Wang, X. X.; Yang, X.; Liu, H.; Han, T.; Hu, J.; Li, H.; Wu, G. Air Electrodes for Flexible and Rechargeable Zn–Air Batteries. *Small Struct.* **2022**, *3*, 2100103.
- (11) Pan, J.; Xu, Y. Y.; Yang, H.; Dong, Z.; Liu, H.; Xia, B. Y. Advanced Architectures and Relatives of Air Electrodes in Zn–Air Batteries. *Adv. Sci.* **2018**, *5*, 1700691.
- (12) Wu, M.; Zhang, G.; Du, L.; Yang, D.; Yang, H.; Sun, S. Defect Electrocatalysts and Alkaline Electrolyte Membranes in Solid-State Zinc-Air Batteries: Recent Advances, Challenges, and Future Perspectives. *Small Methods* **2021**, *5*, 2000868.
- (13) Chai, G.-L.; Qiu, K.; Qiao, M.; Titirici, M.-M.; Shang, C.; Guo, Z. Active sites engineering leads to exceptional ORR and OER bifunctionality in P,N Co-doped graphene frameworks. *Energy Environ. Sci.* **2017**, *10*, 1186–1195.
- (14) Wang, M.; Ji, H.; Liu, S.; Sun, H.; Liu, J.; Yan, C.; Qian, T. Single-atom scale metal vacancy engineering in heteroatom-doped carbon for rechargeable zinc-air battery with reduced overpotential. *Chem. Eng. J.* **2020**, *393*, 124702.
- (15) Han, C.; Li, W.; Liu, H.-K.; Dou, S.; Wang, J. Design strategies for developing non-precious metal based bi-functional catalysts for alkaline electrolyte based zinc–air batteries. *Mater. Horiz.* **2019**, *6*, 1812–1827.
- (16) Ji, H.; Wang, M.; Liu, S.; Sun, H.; Liu, J.; Qian, T.; Yan, C. In-situ observation as activity descriptor enables rational design of oxygen reduction catalyst for zinc-air battery. *Energy Storage Mater.* **2020**, *27*, 226–231.
- (17) Zhao, Q.; Yan, Z.; Chen, C.; Chen, J. Spinels: Controlled Preparation, Oxygen Reduction/Evolution Reaction Application, and Beyond. *Chem. Rev.* **2017**, *117*, 10121–10211.
- (18) Wang, X. T.; Ouyang, T.; Wang, L.; Zhong, J.-H.; Liu, Z.-Q. Surface Reorganization on Electrochemically-Induced Zn–Ni–Co Spinel Oxides for Enhanced Oxygen Electrocatalysis. *Angew. Chem. Int. Ed.* **2020**, *59*, 6492–6499.
- (19) Song, Z.; Liu, Q. Tolerance Factor and Phase Stability of the Normal Spinel Structure. *Cryst. Growth Des.* **2020**, *20*, 2014–2018.
- (20) Manna, N.; Singh, S. K.; Kharabe, G. P.; Torris, A.; Kurungot, S. Zinc–Air Batteries Catalyzed Using Co₃O₄ Nanorod-Supported N-Doped Entangled Graphene for Oxygen Reduction Reaction. *ACS Appl. Energy Mater.* **2021**, *4*, 4570–4580.
- (21) Li, C.; Han, X.; Cheng, F.; Hu, Y.; Chen, C.; Chen, J. Phase and composition controllable synthesis of cobalt manganese spinel nanoparticles towards efficient oxygen electrocatalysis. *Nat. Commun.* **2015**, *6*, 7345.
- (22) Janani, G.; Surendran, S.; Choi, H.; Han, M.-K.; Sim, U. In Situ Grown CoMn₂O₄ 3D-Tetragons on Carbon Cloth: Flexible Electrodes for Efficient Rechargeable Zinc-Air Battery Powered Water Splitting Systems. *Small* **2021**, *17*, 2103613.
- (23) Yang, Y.; Xiong, Y.; Holtz, M. E.; Feng, X.; Zeng, R.; Chen, G.; DiSalvo, F. J.; Muller, D. A.; Abruña, H. D. Octahedral spinel electrocatalysts for alkaline fuel cells. *Proc. Natl. Acad. Sci. U. S. A.* **2019**, *116*, 24425–24432.
- (24) Liu, Z. Q.; Cheng, H.; Li, N.; Ma, T. Y.; Su, Y. Z. ZnCo₂O₄ Quantum Dots Anchored on Nitrogen-Doped Carbon Nanotubes as Reversible Oxygen Reduction/Evolution Electrocatalysts. *Adv. Mater.* **2016**, *28*, 3777–3784.
- (25) Chen, C.; Wang, X. T.; Zhong, J. H.; Liu, J.; Waterhouse, G. I. N.; Liu, Z. Q. Epitaxially Grown Heterostructured SrMn₃O₆@xSrMnO₃ with HighValence Mn^{3+/4+} for Improved Oxygen Reduction Catalysis. *Angew. Chem., Int. Ed.* **2021**, *60*, 22043–22050.
- (26) Wang, Z.; Huang, J.; Wang, L.; Liu, Y.; Liu, W.; Zhao, S.; Liu, Z.-Q. Cation-Tuning Induced d-Band Center Modulation on Co-Based Spinel Oxide for Oxygen Reduction/Evolution Reaction. *Angew. Chem. Int. Ed.* **2022**, *61*, No. e202114696.
- (27) Lu, X. F.; Chen, Y.; Wang, S.; Gao, S.; Lou, X. W. Interfacing Manganese Oxide and Cobalt in Porous Graphitic Carbon Polyhedrons Boosts Oxygen Electrocatalysis for Zn-Air Batteries. *Adv. Mater.* **2019**, *31*, 1902339.
- (28) Zhu, H.; Gu, L.; Yu, D.; Sun, Y.; Wan, M.; Zhang, M.; Wang, L.; Wang, L.; Wu, W.; Yao, J.; Du, M.; Guo, S. The marriage and integration of nanostructures with different dimensions for synergistic electrocatalysis. *Energy Environ. Sci.* **2017**, *10*, 321–330.
- (29) Dai, L.; Chang, D. W.; Baek, J.-B.; Lu, W. Carbon nanomaterials for advanced energy conversion and storage. *Small* **2012**, *8*, 1130–1166.
- (30) Li, Y.; Zhao, M.; Zhao, Y.; Song, L.; Zhang, Z. FeNi Layered Double-Hydroxide Nanosheets on a 3D Carbon Network as an Efficient Electrocatalyst for the Oxygen Evolution Reaction. *Part. Part. Syst. Char.* **2016**, *33*, 158–166.
- (31) Mo, R.; Rooney, D.; Sun, K.; Yang, H. Y. 3D nitrogen-doped graphene foam with encapsulated germanium/nitrogen-doped graphene yolk-shell nanoarchitecture for high-performance flexible Li-ion battery. *Nat. Commun.* **2017**, *8*, 13949.
- (32) Cui, X.; Liu, Y.; Han, G.; Cao, M.; Han, L.; Zhou, B.; Mehdi, S.; Wu, X.; Li, B.; Jiang, J. Wood-Derived Integral Air Electrode for Enhanced Interfacial Electrocatalysis in Rechargeable Zinc-Air Battery. *Small* **2021**, *17*, 2101607.
- (33) Wang, Y.-C.; Huang, L.; Zhang, P.; Qiu, Y.-T.; Sheng, T.; Zhou, Z.-Y.; Wang, G.; Liu, J.-G.; Rauf, M.; Gu, Z.-Q.; Wu, W.-T.; Sun, S.-G. Constructing a Triple-Phase Interface in Micropores to Boost Performance of Fe/N/C Catalysts for Direct Methanol Fuel Cells. *ACS Energy Lett.* **2017**, *2*, 645–650.
- (34) Li, S.; Zhou, X.; Fang, G.; Xie, G.; Liu, X.; Lin, X.; Qiu, H.-J. Multicomponent Spinel Metal Oxide Nanocomposites as High-Performance Bifunctional Catalysts in Zn–Air Batteries. *ACS Appl. Energy Mater.* **2020**, *3*, 7710–7718.
- (35) Choi, S.; Jeon, J.; Chae, J.; Yuk, S.; Lee, D.-H.; Doo, G.; Lee, D. W.; Hyun, J.; Kwen, J.; Choi, S. Q.; Kim, H.-T. Single-Step Fabrication of a Multiscale Porous Catalyst Layer by the Emulsion Template Method for Low Pt-Loaded Proton Exchange Membrane Fuel Cells. *ACS Appl. Energy Mater.* **2021**, *4*, 4012–4020.
- (36) Wu, Z.-S.; Yang, S.; Sun, Y.; Parvez, K.; Feng, X.; Müllen, K. 3D nitrogen-doped graphene aerogel-supported Fe₃O₄ nanoparticles as efficient electrocatalysts for the oxygen reduction reaction. *J. Am. Chem. Soc.* **2012**, *134*, 9082–9085.
- (37) Zenyuk, I. V.; Parkinson, D. Y.; Connolly, L. G.; Weber, A. Z. Gas-diffusion-layer structural properties under compression via X-ray tomography. *J. Power Sources* **2016**, *328*, 364–376.
- (38) Tötze, C.; Gaiselmann, G.; Osenberg, M.; Bohner, J.; Arlt, T.; Markötter, H.; Hilger, A.; Wieder, F.; Kupsch, A.; Müller, B. R.; Hentschel, M. P.; Banhart, J.; Schmidt, V.; Lehnert, W.; Manke, I. Three-dimensional study of compressed gas diffusion layers using synchrotron X-ray imaging. *J. Power Sources* **2014**, *253*, 123–131.
- (39) Jang, S.; Kim, S.; Kim, S. M.; Choi, J.; Yeon, J.; Bang, K.; Ahn, C.-Y.; Hwang, W.; Her, M.; Cho, Y.-H.; Sung, Y.-E.; Choi, M. Interface engineering for high-performance direct methanol fuel cells using multiscale patterned membranes and guided metal cracked layers. *Nano Energy* **2018**, *43*, 149–158.
- (40) Manna, N.; Ayasha, N.; Singh, S. K.; Kurungot, S. A NiFe layered double hydroxide-decorated N-doped entangled-graphene framework: a robust water oxidation electrocatalyst. *Nanoscale Adv.* **2020**, *2*, 1709–1717.
- (41) Li, M.; Liu, T.; Bo, X.; Zhou, M.; Guo, L. A novel flower-like architecture of FeCo@NC-functionalized ultra-thin carbon nanosheets as a highly efficient 3D bifunctional electrocatalyst for full water splitting. *J. Mater. Chem. A* **2017**, *5*, 5413–5425.

(42) Liang, Y.; Wang, H.; Zhou, J.; Li, Y.; Wang, J.; Regier, T.; Dai, H. Covalent hybrid of spinel manganese-cobalt oxide and graphene as advanced oxygen reduction electrocatalysts. *J. Am. Chem. Soc.* **2012**, *134*, 3517–3523.

(43) Zhang, Z.; Dou, M.; Liu, H.; Dai, L.; Wang, F. A Facile Route to Bimetal and Nitrogen-Codoped 3D Porous Graphitic Carbon Networks for Efficient Oxygen Reduction. *Small* **2016**, *12*, 4193–4199.

(44) Xiong, Y.; Yang, Y.; Feng, X.; DiSalvo, F. J.; Abruña, H. D. A Strategy for Increasing the Efficiency of the Oxygen Reduction Reaction in Mn-Doped Cobalt Ferrites. *J. Am. Chem. Soc.* **2019**, *141*, 4412–4421.

(45) Amirzhanova, A.; Akmanşen, N.; Karakaya, I.; Dag, Ö. Mesoporous MnCo_2O_4 , NiCo_2O_4 , and ZnCo_2O_4 Thin-Film Electrodes as Electrocatalysts for the Oxygen Evolution Reaction in Alkaline Solutions. *ACS Appl. Energy Mater.* **2021**, *4*, 2769–2785.

(46) Wang, Y.; Yang, Y.; Jia, S.; Wang, X.; Lyu, K.; Peng, Y.; Zheng, H.; Wei, X.; Ren, H.; Xiao, L.; Wang, J.; Muller, D. A.; Abruña, H. D.; Hwang, B. J.; Lu, J.; Zhuang, L. Synergistic Mn-Co catalyst outperforms Pt on high-rate oxygen reduction for alkaline polymer electrolyte fuel cells. *Nat. Commun.* **2019**, *10*, 1506.

(47) Unni, S. M.; Bhang, S. N.; Illathvalappil, R.; Mutneja, N.; Patil, K. R.; Kurungot, S. Nitrogen-induced surface area and conductivity modulation of carbon nanohorn and its function as an efficient metal-free oxygen reduction electrocatalyst for anion-exchange membrane fuel cells. *Small* **2015**, *11*, 352–360.

(48) Priamushko, T.; Guillet-Nicolas, R.; Yu, M.; Doyle, M.; Weidenthaler, C.; Tüysüz, H.; Kleitz, F. Nanocast Mixed Ni–Co–Mn Oxides with Controlled Surface and Pore Structure for Electrochemical Oxygen Evolution Reaction. *ACS Appl. Energy Mater.* **2020**, *3*, 5597–5609.

(49) Singh, S. K.; Dhavale, V. M.; Kurungot, S. Surface-Tuned Co_3O_4 Nanoparticles Dispersed on Nitrogen-Doped Graphene as an Efficient Cathode Electrocatalyst for Mechanical Rechargeable Zinc-Air Battery Application. *ACS Appl. Mater. Interfaces* **2015**, *7*, 21138–21149.

(50) Akhtar, M. S.; Bui, P. T. M.; Li, Z.-Y.; Yang, O.-B.; Paul, B. J.; Kim, S.; Kim, J.; Rai, A. K. Impact of porous Mn_3O_4 nanostructures on the performance of rechargeable lithium ion battery: Excellent capacity and cyclability. *Solid State Ionics* **2019**, *336*, 31–38.

(51) Yan, X.; Jia, Y.; Chen, J.; Zhu, Z.; Yao, X. Defective-Activated-Carbon-Supported Mn-Co Nanoparticles as a Highly Efficient Electrocatalyst for Oxygen Reduction. *Adv. Mater.* **2016**, *28*, 8771–8778.

(52) Deng, Y.-P.; Jiang, Y.; Liang, R.; Zhang, S.-J.; Luo, D.; Hu, Y.; Wang, X.; Li, J.-T.; Yu, A.; Chen, Z. Dynamic electrocatalyst with current-driven oxyhydroxide shell for rechargeable zinc-air battery. *Nat. Commun.* **2020**, *11*, 1952.

Recommended by ACS

Regulating the Catalytically Active Sites in Low-Cost and Earth-Abundant 3d Transition-Metal-Based Electrode Materials for High-Performance Zinc–Air...

Jiajun Wang, Wenbin Hu, *et al.*

MARCH 29, 2021
ENERGY & FUELS

READ 

Cobalt Nanoparticles Dispersed Nitrogen-Doped Graphitic Nanospheres-Based Rechargeable High Performance Zinc–Air Batteries

Pallavi Thakur, Tharangattu N. Narayanan, *et al.*

JULY 27, 2020
ACS APPLIED ENERGY MATERIALS

READ 

Three-Dimensional Nitrogen-Doped Graphitic Carbon-Encapsulated MnO-Co Heterostructure: A Bifunctional Energy Storage Material for Zn-Ion and Zn–Air Batte...

Arpan Samanta, C. Retna Raj, *et al.*

SEPTEMBER 22, 2020
ACS APPLIED ENERGY MATERIALS

READ 

Boosting the Oxygen Reduction Reaction in Zn–Air Batteries via a Uniform Trace N-Doped Carbon-Based Pore Structure

Qi Yang, Shupeng Zhang, *et al.*

JANUARY 04, 2022
ACS APPLIED ENERGY MATERIALS

READ 

Get More Suggestions >

Microporous 3D-Structured Hierarchically Entangled Graphene-Supported Pt₃Co Alloy Catalyst for PEMFC Application with Process-Friendly Features

Narugopal Manna, Mayank Singh, and Sreekumar Kurungot*



Cite This: *ACS Appl. Mater. Interfaces* 2023, 15, 28023–28035



Read Online

ACCESS |



Metrics & More



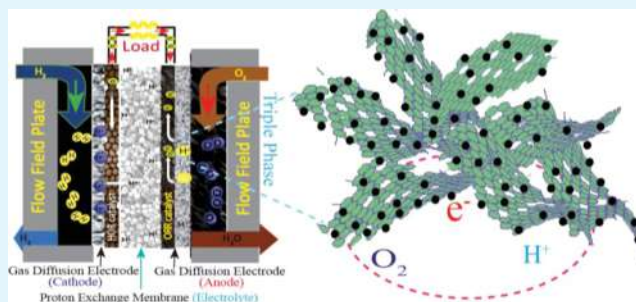
Article Recommendations



Supporting Information

ABSTRACT: To improve the oxygen reduction reaction (ORR) performance in a proton-exchange membrane fuel cell (PEMFC) cathode with respect to mass activity and durability, a suitable electrocatalyst design strategy is essentially needed. Here, we have prepared a sub-three nm-sized platinum (Pt)–cobalt (Co) alloy (Pt₃Co)-supported N-doped microporous 3D graphene (Pt₃Co/pNEGF) by using the polyol synthesis method. A microwave-assisted synthesis method was employed to prepare the catalyst based on the 3D porous carbon support with a large pore volume and dense micro-/mesoporous surfaces. The ORR performance of Pt₃Co/pNEGF closely matches with the *state-of-the-art* commercial Pt/C catalyst in 0.1 M HClO₄, with a small overpotential of 10 mV. The 3D microporous structure of the N-doped graphene significantly improves the mass transport of the reactant and thus the overall ORR performance. As a result of the lower loading of Pt in Pt₃Co/pNEGF as compared to that in Pt/C, the alloy catalyst achieved 1.5 times higher mass activity than Pt/C. After 10,000 cycles, the difference in the electrochemically active surface area (ECSA) and half-wave potential ($E_{1/2}$) of Pt₃Co/pNEGF is found to be 5 m² g_{Pt}⁻¹ (Δ ECSA) and 24 mV (Δ $E_{1/2}$), whereas, for Pt/C, these values are 9 m² g_{Pt}⁻¹ and 32 mV, respectively. Finally, in a realistic perspective, single-cell testing of a membrane electrode assembly (MEA) was made by sandwiching the Pt₃Co/pNEGF-coated gas diffusion layers as the cathode displayed a maximum power density of 800 mW cm⁻² under H₂–O₂ feed conditions with a clear indication of helping the system in the mass-transfer region (i.e., the high current dragging condition). The nature of the *I*–*V* polarization shows a progressively lower slope in this region of the polarization plot compared to a similar system made from its Pt/C counterpart and a significantly improved performance throughout the polarization region in the case of the system made from the Pt₃Co/NEGF catalyst (without the microwave treatment) counterpart. These results validate the better process friendliness of Pt₃Co/pNEGF as a PEMFC electrode-specific catalyst owing to its unique texture with 3D architecture and well-defined porosity with better structural endurance.

KEYWORDS: Pt₃Co alloy, N-doped porous 3D graphene, microwave synthesis, polyol synthesis, ORR, PEMFC



1. INTRODUCTION

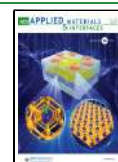
Efficient and durable catalysts are in continual exploration to reduce the cathodic electrochemical activation overpotential for the oxygen reduction reaction (ORR) in proton-exchange membrane fuel cells (PEMFCs).¹ Platinum (Pt) nanoparticles supported on conventional carbon substrates like Ketjen black and Vulcan XC-72 are currently recognized as the most effective electrocatalysts for ORR.² However, issues like the high cost of Pt, the drop in the electrochemical surface area (ECSA) during electrode processing, and the concerns associated with the long-term durability are the limitations of the *state-of-the-art* catalysts.^{3,4} The restricted mass transport in the electrodes derived from the Pt-supported conventional carbon catalysts is an inherent problem created during the multiple stages involved in the conversion of the catalyst to the ink and finally to the electrode by adopting various coating techniques.⁵ The overpotentials created due to such limitations

create a significant gap between the intrinsic ORR activity of the catalysts and the practically attainable performance during the single-cell evaluations of the membrane electrode assemblies (MEAs) derived from the cathodes of these catalysts.^{6,7} These issues necessitate a strategic design approach for developing a cost-effective and durable catalyst with inbuilt features for better tackling the electrode processes.⁸ These features mainly include provisions for dealing with the ORR mass transport, water management, and effective “triple-phase

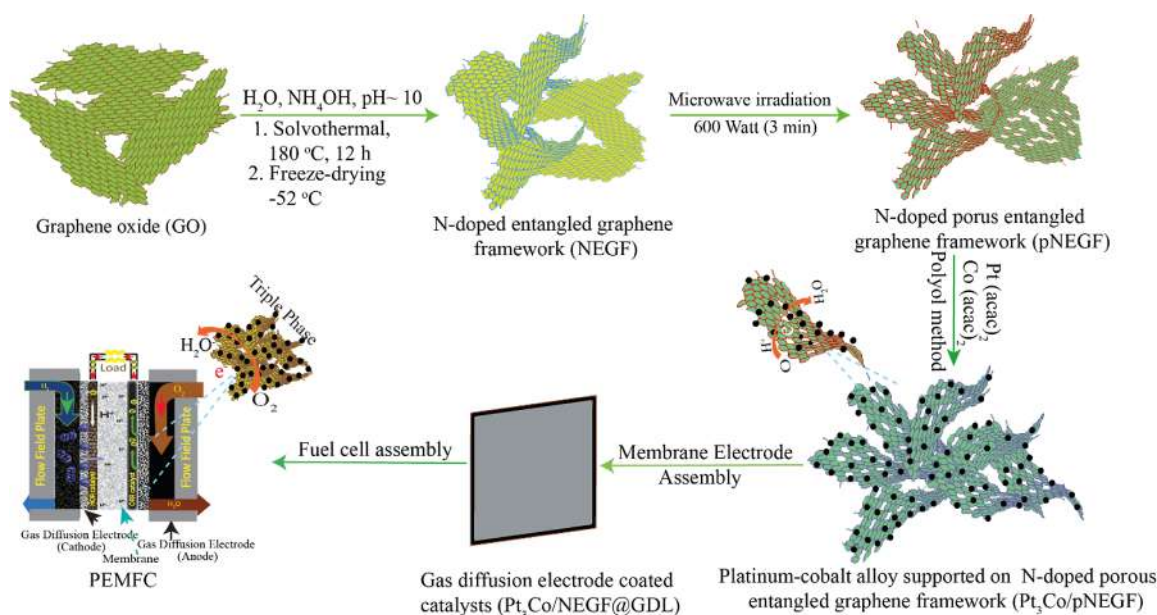
Received: March 8, 2023

Accepted: May 19, 2023

Published: June 2, 2023



Scheme 1. Schematic Representation Illustrating the Synthesis of the NEGF and the Microwave-Assisted Synthesis of the pNEGF and Subsequently the Pt₃Co-Dispersed Catalyst, Pt₃Co/pNEGF, by the Polyol Method, Followed by the Demonstration of the PEMFC Based on the Electrodes Derived from This Catalyst (Pt₃Co/NEGF@GDL)



boundary (TPB)” formation. The TPB is the region where the gas (reactant), ions (electrolyte), and active sites (solid surface) are in seamless contact with each other. Various methods have been implemented to improve the activity and durability of the ORR catalysts.^{8,9}

As better alternatives to the conventional Pt catalysts, Pt-based alloy catalysts in which Pt is partially replaced by low-cost transition metals such as Fe, Co, and Ni are being proposed in recent times.^{10,11} Alloying Pt with another non-noble transition metal reduces the Pt metal loading without affecting the ORR activity.¹² In addition, the presence of an early transition metal to Pt could alter the Pt–Pt interatomic distance, resulting in a downshift of the d-band center with a change in the electronic structures of the Pt active sites.^{13,14} Therefore, it introduces the Pt 5d band vacancy in an alloy structure of Pt.¹⁴ The increased d-band vacancy in the Pt atoms leads to the increased ability to accept the 2p electron donation from O₂, resulting in improved Pt surface adsorption.¹⁵ As a result, the binding energy of the Pt–O bond becomes stronger, while the O–O bond becomes weaker.^{14,15} Therefore, the lattice reconstruction in the alloy structure provides preferable sites for oxygen adsorption, which significantly accelerates the ORR kinetics.^{14,15} Among the Pt alloy systems with various transition metals (Fe, Co, and Ni), Pt–Co alloys have previously been recognized with their higher ORR activity.^{16–21} Compared to the other compositions of the Pt–Co alloy structures, the Pt₃Co stoichiometry is primarily suitable for the ORR.^{22–24} The active site of Pt in the Pt₃Co alloys experiences a significant amount of ligand and strain effects, which are known to suppress the adsorption energy of the O₂ reduction intermediate species, resulting in increased ORR kinetics.^{25,26} Moreover, the distribution of the controlled size and uniformity of the alloyed Pt₃Co nanoparticles over the conducting support would increase the overall ORR activity and durability under the operating conditions.^{27,28} As noted earlier, the controlled particle size and distribution of a nanoalloy phase have advantages in

increasing the ECSA of the catalysts.²⁹ The alloy structures with sub-nanometer particle sizes are reported to be high-performing toward the ORR as per the recent studies.³⁰ However, the introduction of non-noble transition-metal atoms in Pt alloys with sub-nanometer particle size has limitations as they can easily segregate due to the charge effect resulting from the lattice mismatch.³⁰ Therefore, incorporating suitable conducting support with uniform nucleation sites that can facilitate the seamless growth of the sub-nanometer-sized alloy nanoparticles over the surface is being considered as one of the finest strategies to improve the ORR performance of the fuel-cell catalysts.^{18,19}

In this context, it is important to revisit the fact that most of the conducting carbon supports utilized to disperse the bimetallic Pt alloys are 1D and 2D carbon-based materials.^{31–33} While at one end, when more active ORR sites are being generated with the nanoalloy particles, there must be a complementary strategy in place for developing a better support structure to effectively tackle the final electrode-specific challenges.³⁴ The morphological restriction of the conventional carbon supports imparts poor mass transport activity during the ORR process in acidic conditions.³⁵ In addition, these carbon supports experience restacking issues, which significantly suppress the ECSA of the electrocatalysts.^{31,36} Incorporation of the 3D porous conducting support materials, such as those based on 3D structured graphenes, as the substrates for interlinking the ORR active catalytic centers is considered a promising approach.^{37,38} The porous structure of the self-assembled 3D supports helps in better distribution of the Pt alloy particles, reducing the ionomer coverage ratio and lowering the local O₂ transport resistance.³⁸ Aside from these, the presence of the graphitic carbon support with homogeneously doped nitrogen centers (N-doped sites) creates metal anchoring sites and improves the metal–support interaction.^{39,40} This helps in achieving better durability in the harsh electrochemical conditions of the PEMFC operation.⁴¹ Furthermore, in the self-assembled 3D

graphene support, the pores are mostly distributed in the meso-/macroporous region, which has less access to the sub-nanometer-sized Pt alloy particles.^{42,43} Therefore, the carbon support porosity within the range of microporosity and mesoporosity has a significant impact on the distribution of the small-sized alloy nanoparticle as well as on ensuring efficient mass transfer.^{44,45} In this direction, even though various strategies have been developed to create microporous carbon structures, many of them involve energy-consuming processes.⁴⁶

Recently, microwave irradiation has been very effective for the fast formation of micropores in the carbon substrate.⁴⁷ The microwave irradiation results in uniform heat generation within a very short time to reach a high temperature by selective energy transfer to the microwave-active polar substrates.⁴⁷ To best accommodate the aforementioned structural characteristics of the conducting support, with the help of microwave irradiation, here, we report the development of an efficient ORR electrocatalyst based on N-doped porous 3D graphene-supported sub-3 nm Pt₃Co alloy particles (Pt₃Co/pNEGF, i.e., the porous nitrogen-doped entangled graphene framework). The doped-N in the graphene framework serves as the nucleation-cum-anchoring sites for the Pt₃Co nanoparticles on the asymmetric graphene substrate. Pt₃Co/pNEGF is found to compete well with those of the *state-of-the-art* Pt/C catalyst in terms of its mass activity due to its accessible active components (Pt₃Co) and preferable mass transport channel support.

2. RESULTS AND DISCUSSION

Scheme 1 illustrates the stages involved in the synthesis of the Pt₃Co/pNEGF catalyst and its application as a cathode catalyst in PEMFCs. The experimental details on the synthesis of the various samples prepared for the present work are given in the **Supporting Information**. N-doped microporous graphene (pNEGF) was synthesized by microwave irradiation of the NEGF. The microwave irradiation of the NEGF in the air atmosphere involves quick oxidation of carbon to CO₂ with concomitant oxidation of some of the doped nitrogen to NO_x. These processes create micropores in the NEGF. The generated pNEGF was employed as a support for the growth of the Pt₃Co nanoparticles. The presence of fine porosity and uniformly doped nitrogen in the microwave-induced 3D graphene helps the homogeneous dispersion of the positively charged metal ions through electrostatic interactions during the mixing process. During the polyol synthesis process at 160 °C, the Pt and Co ions nucleate on the doped-N and the defective carbon centers mainly at the pore openings, resulting in the uniform growth of the small-sized and spherically shaped alloy (Pt₃Co) nanoparticles over the surface of pNEGF (designated as Pt₃Co/pNEGF). The pNEGF with its well-defined structure, porosity, and composition served as an active substrate, which induces favorable electronic structural modulations of the sub-nanometer-sized Pt₃Co particles. In addition, the 3D porous architectures of the conducting support (pNEGF) in the catalyst offer an open and exposed morphology that provides high surface area and accessible porous architecture to the catalytic sites.

The morphological analysis of the NEGF, pNEGF, and Pt₃Co/pNEGF has been performed initially by field emission scanning electron microscopy (FESEM). **Figure 1a** shows a 3D self-assembly structure of the NEGF, formed by the interconnected sheet of graphene during the hydrothermal

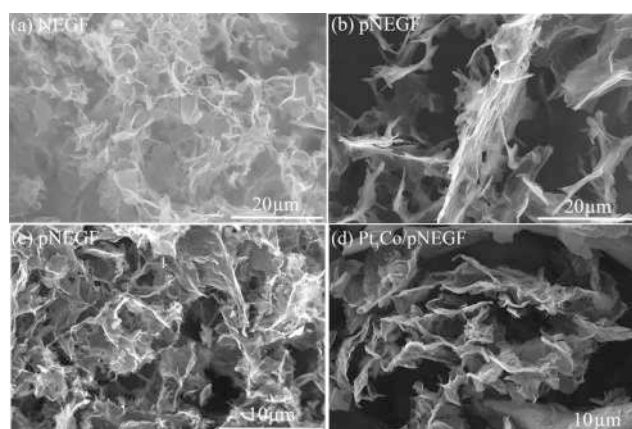


Figure 1. (a) FESEM image of the NEGF showing the 3D porous architecture of the graphene sheets; (b,c) FESEM images of the porous NEGF (pNEGF) formed through the microwave irradiation route, representing the exfoliated 3D porous structure of the graphene sheets; (d) FESEM image of the Pt₃Co/pNEGF representing the porous structure of the catalyst originating from the exfoliated and interconnected morphology of the pNEGF substrate.

treatment of GO followed by freeze drying. The freeze-drying method played an important role in establishing the 3D structure of the NEGF. After the microwave irradiation of the NEGF, the morphological images presented in **Figure 1b,c** show the exfoliated structure of the pNEGF. The generated exfoliated structure formed by microwave treatment and the modified texture of the pNEGF are expected to improve the mass transport properties as compared to the NEGF. The incorporation of Pt₃Co over the pNEGF was performed through the polyol method, which resulted in Pt₃Co/pNEGF, retaining the same structural alignment as the bare pNEGF with its porous architecture, as shown in **Figure 1d**.

More insightful information on the nature of the distribution profile of Pt₃Co on the pNEGF has been gained with the help of high-resolution transmission electron microscopy (HR-TEM). The image presented in **Figure 2a** shows the fine distribution of the Pt₃Co nanoparticles on the pNEGF. The inset image presented in **Figure 2a** shows the size distribution histogram of the Pt₃Co nanoparticles, indicating the dominant size distribution in the range of 2–3 nm. The controlled size distribution of the Pt₃Co nanoparticles without agglomeration shows the advantage of the developed synthesis strategy. The magnified images shown in **Figure 2b** (on the surface) and **2c** (along the edge) of the 3D graphene substantiate the previous observation that the Pt₃Co nanoparticles are uniformly distributed throughout the substrate, including its surface and the edges. These results highlight that the microwave irradiation of the NEGF plays an effective role in creating uniform nucleation sites on the substrate, leading to the controlled dispersion and distribution of the Pt₃Co nanoparticles within a size range predominantly of 2 to 3 nm. This controlled distribution of the Pt₃Co nanoparticles over the surface and the edge of the graphene mediated by the defect sites and the doped sites of the heteroatom (N) is an important structural benefit to the system as this can suppress the self-agglomeration possibility of the nanoparticles under the triggered conditions of the electrochemical environments.⁴⁰ In addition, the fine distribution of the active sites at the edges of the graphene layers of its 3D framework is expected to provide better reactant accessibility due to their

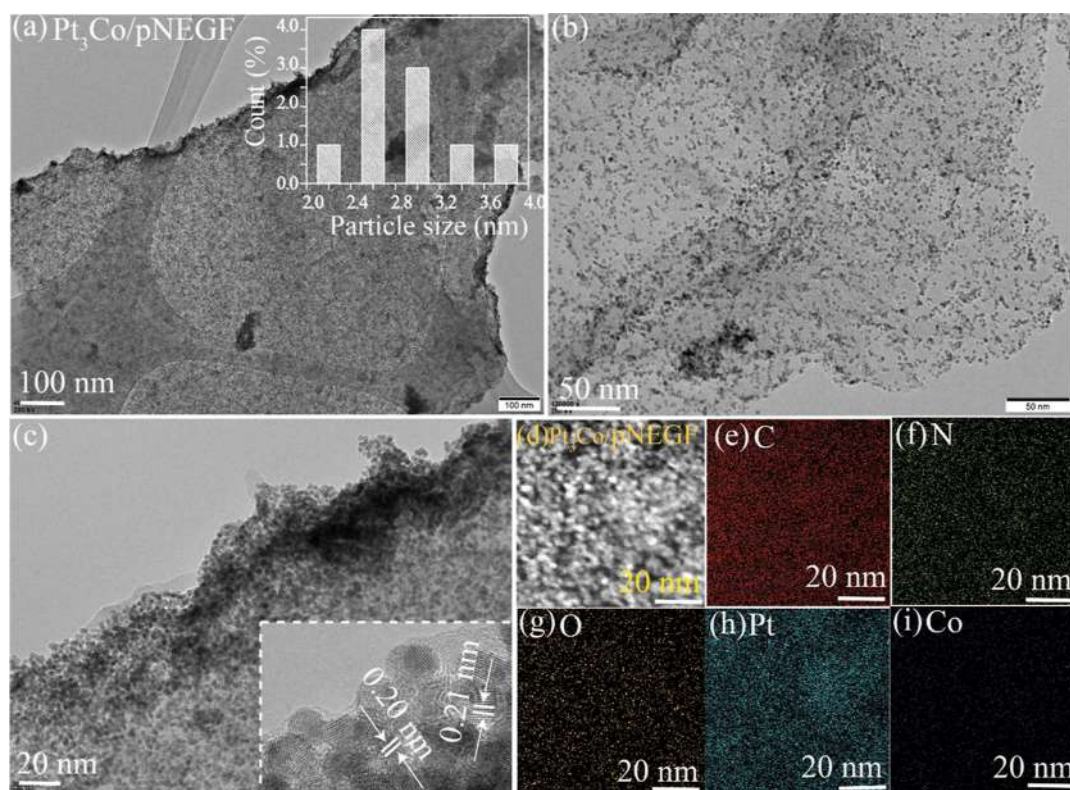


Figure 2. (a) HRTEM image of the $\text{Pt}_3\text{Co}/\text{pNEGF}$ displaying the uniform distribution of Pt_3Co over 3D pNEGF (the inset image represents the size distribution histogram of the Pt_3Co nanoparticles); (b,c) magnified HRTEM images of $\text{Pt}_3\text{Co}/\text{pNEGF}$ recorded at the surface and edge of the graphene sheet (the inset image of (c) represents the d -spacing for the Pt_3Co crystal structure); (d) 3D structure of graphene displaying the uniform dispersion of the Pt_3Co nanoparticles and the respective elemental mapping of C (e), N (f), O (g), Pt (h), and N and Co (i) done on $\text{Pt}_3\text{Co}/3\text{D pNEGF}$.

relatively exposed nature in the catalyst framework.⁴² The inset image in Figure 2c shows that the Pt_3Co nanocrystal lattice fringe widths (d -spacing) are 0.21 and 0.20 nm, which are attributed to the (111) and (200) facets, respectively, implying the formation of the fcc structure of the Pt_3Co crystal.³⁷ Figure S2, Supporting Information, presents the HRTEM images of the Pt/pNEGF and PtCo/pNEGF. Figure S2a,b, Supporting Information, shows the HRTEM image of the Pt/pNEGF, where the Pt particles are uniformly distributed. Similarly, the HRTEM images of the PtCo/pNEGF given in Figure S2c,d, Supporting Information, show the uniformity in the distribution of the particles. Figure 2d displays the HRTEM image of the $\text{Pt}_3\text{Co}/\text{pNEGF}$, and the corresponding elemental mapping data for the respective elements are presented in Figure 2e–i. The elemental mapping images show the existence and distribution of Pt, Co, O, C, and N, corresponding to the selected composition of the catalyst. Additionally, the Pt_3Co stoichiometric composition is evidenced by the existence of Pt and Co together in the same position, as well as the observed close triple intensity of Pt with respect to Co.

To investigate the exact composition of the catalysts, inductively coupled plasma (ICP) experiments were conducted. Table 1, Supporting Information, presents the ICP analysis data, indicating that the Pt and Co ratios in the composite catalysts match well with the precursor ratios used during the synthesis. The atomic percentages of Pt are 98.905% in 40% Pt/C, 99.301% in Pt/NEGF, 54.915% in PtCo/pNEGF, 73.103% in $\text{Pt}_3\text{Co}/\text{NEGF}$, and 72.115% in $\text{Pt}_3\text{Co}/\text{pNEGF}$. The weight percentage of Pt is 39.56, 39.72,

21.96, 29.24, and 28.84% in 40% Pt/C, Pt/NEGF, PtCo/pNEGF, $\text{Pt}_3\text{Co}/\text{NEGF}$, and $\text{Pt}_3\text{Co}/\text{pNEGF}$, respectively.

The pore size distribution comparison profiles using the DFT method of the NEGF, pNEGF, and $\text{Pt}_3\text{Co}/\text{pNEGF}$ shown in Figure 3a suggest that the porosity of the NEGF mostly resides in the region of 5–20 nm, indicating the presence of mesoporosity. However, after the microwave irradiation of the NEGF, the transformed pNEGF shows that the pores are distributed in the range of 1–20 nm, which is ascribed to the micro–mesoporous nature of the material. Similarly, after the decoration of the 2–3 nm-sized Pt_3Co nanoparticles ($\text{Pt}_3\text{Co}/\text{pNEGF}$), a more or less similar porosity distribution profile (1–20 nm) is observed for the sample in Figure 3a. The retention of the porosity after the Pt_3Co dispersion is reflected in the BET surface area as well. The surface areas of the NEGF and pNEGF are found to be 550 and 780 $\text{m}^2 \text{g}^{-1}$, respectively. The higher surface area of the pNEGF is ascribed to the increased contribution of the micropores present in the system. Both the systems (NEGF and pNEGF) displayed type-IV isotherms (Figure S3, Supporting Information). Interestingly, it reveals the higher N_2 uptake capacity of the pNEGF compared to the NEGF, which supports the presence of extra porosity in the system. The higher surface area of the pNEGF, combined with its significant porous structure, is a distinguishing benefit of the electrocatalyst support, allowing for efficient utilization of the electrochemically active sites by establishing a better active TPB during the electrochemical ORR process.

The Raman spectroscopic investigation has been performed to understand the extent of the graphitic and defective nature

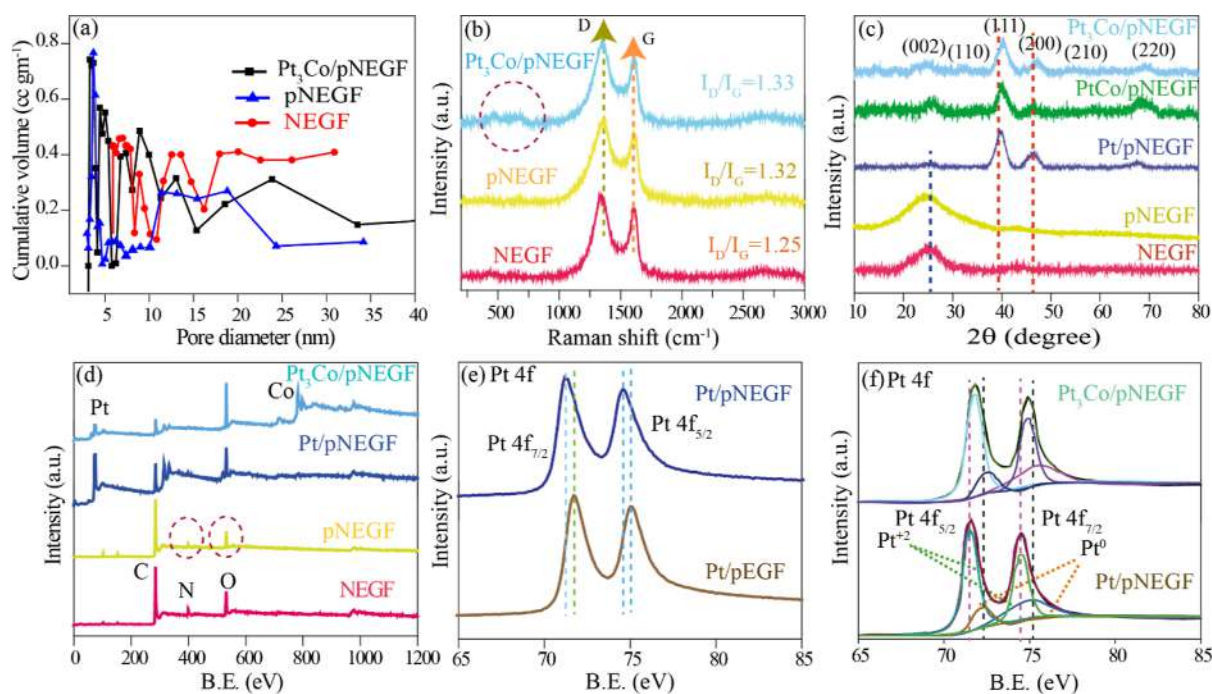


Figure 3. (a) Relative pore size distribution profiles of the NEGF, pNEGF, and Pt₃Co/pNEGF, indicating the mesoporous nature of the NEGF and the presence of micro- and mesoporous regions for the pNEGF (2–20 nm) and Pt₃Co/pNEGF (1 to 20 nm); (b) Raman spectra reported for the NEGF, pNEGF, and Pt₃Co/pNEGF; (c) XRD profiles recorded for the NEGF, pNEGF, Pt/pNEGF, PtCo/pNEGF, and Pt₃Co/pNEGF; (d) XPS survey spectra of the NEGF, pNEGF, Pt/pNEGF, and Pt₃Co/pNEGF; (e) comparative Pt 4f XPS spectra of Pt/pEGF and Pt/pNEGF shows the shift in the peak after the N incorporation into the porous graphene support system; (f) comparative Pt 4f spectra of Pt/pNEGF and Pt₃Co/pNEGF, suggesting the binding energy shift after Co incorporation into Pt.

in the porous carbon systems. The intensity of the defective and graphitic peak (I_D/I_G) ratio points toward the extent of the defects created or present in the carbon systems. Figure 3b shows the comparative Raman spectra of the NEGF, pNEGF, and Pt₃Co/pNEGF. The peaks that appeared at 1350 and 1590 cm^{-1} are credited to the G and D bands, respectively.⁴⁰ In the case of the NEGF and pNEGF, the measured I_D/I_G ratios are 1.25 and 1.32, respectively. The increased I_D/I_G value reported for the pNEGF points toward new defect site creation during the microwave irradiation. During the microwave heat treatment, some of the carbon and nitrogen species are oxidized to CO_2 and NO_x , respectively, and create additional porosity in the NEGF which is evidenced as defects in the Raman spectrum. After incorporating Pt₃Co over the pNEGF, the I_D/I_G ratio becomes 1.33, which is almost comparable to its counterpart pNEGF. A small change in the I_D/I_G ratio for the Pt₃Co/pNEGF is expected to be due to the lattice stress created at the growth time of the metal alloy particles over the N-doped graphene during the polyol method at 180 °C.³⁰ Moreover, the analysis of the Raman spectra for Pt₃Co (Figure S4, Supporting Information) indicates the existence of peaks in the range of 400–600 cm^{-1} , which correspond to the vibrations of the Pt–Co bond in a distinct plane of the Pt₃Co alloy.⁴⁸ Similarly, a comparable peak can be observed in the Pt₃Co/pNEGF, but its intensity is somewhat lower than that of the pristine Pt₃Co, which is likely due to the influence of the carbon support.

The comparative X-ray diffraction (XRD) profiles of the NEGF, pNEGF, Pt/pNEGF, PtCo/pNEGF, and Pt₃Co/pNEGF are shown in Figure 3c. For the NEGF, the two XRD peaks that appeared at the 2θ values of 26 and 43° correspond to the graphitic diffraction planes (002) and (100),

respectively.³⁸ Similar peak features are observed in the case of the microwave-irradiated sample, i.e., pNEGF, with a broad appearance and a shift in the 2θ value in the negative direction. The shift in the 2θ value is ascribed to the change in the d -spacing created by the microwave exfoliation of the graphene sheets. The XRD profile of Pt/pNEGF displays three diffraction peaks at the 2θ values of 39.78, 46.26, and 67.55°, corresponding to the (111), (200), and (220) planes of the Pt metal with an fcc structure. However, with the Co incorporation into Pt, the resulting PtCo/pNEGF and Pt₃Co/pNEGF show a shift in the positions of the (111) and (200) peaks.^{39,40} The observed XRD peak shifts for PtCo/pNEGF and Pt₃Co/pNEGF (39.8°) are due to the contraction of the Pt lattice after the alloy formation.³⁸ Moreover, the alloy structure has been confirmed with the standard JCPDS cards of the Pt₃Co alloy phase (JCPDS no.: 29-0499).⁴¹ The formation of the alloy structure with a significant change in the 2θ value alters the fcc crystal structure and the binding energy with oxygen as an intermediate species during the ORR process.

The X-ray photoelectron spectroscopy (XPS) analysis has been done to analyze the elements and the corresponding chemical nature of the prepared catalysts, which are presented in Figure 3d. The comparative XPS survey scan spectra of the NEGF, pNEGF, Pt/pEGF (without N-doping), Pt/pNEGF, PtCo/pNEGF, and Pt₃Co/pNEGF are presented in Figure 3d, which shows the presence of Pt, Co, C, N, and O in the respective catalyst materials. The survey scan spectrum of the pNEGF obtained through microwave irradiation shows that the peak intensity of N 1s and O 1s has been suppressed as compared to that of the NEGF. The comparative Pt 4f XPS peaks for the N-doped and without N-doped porous graphene-

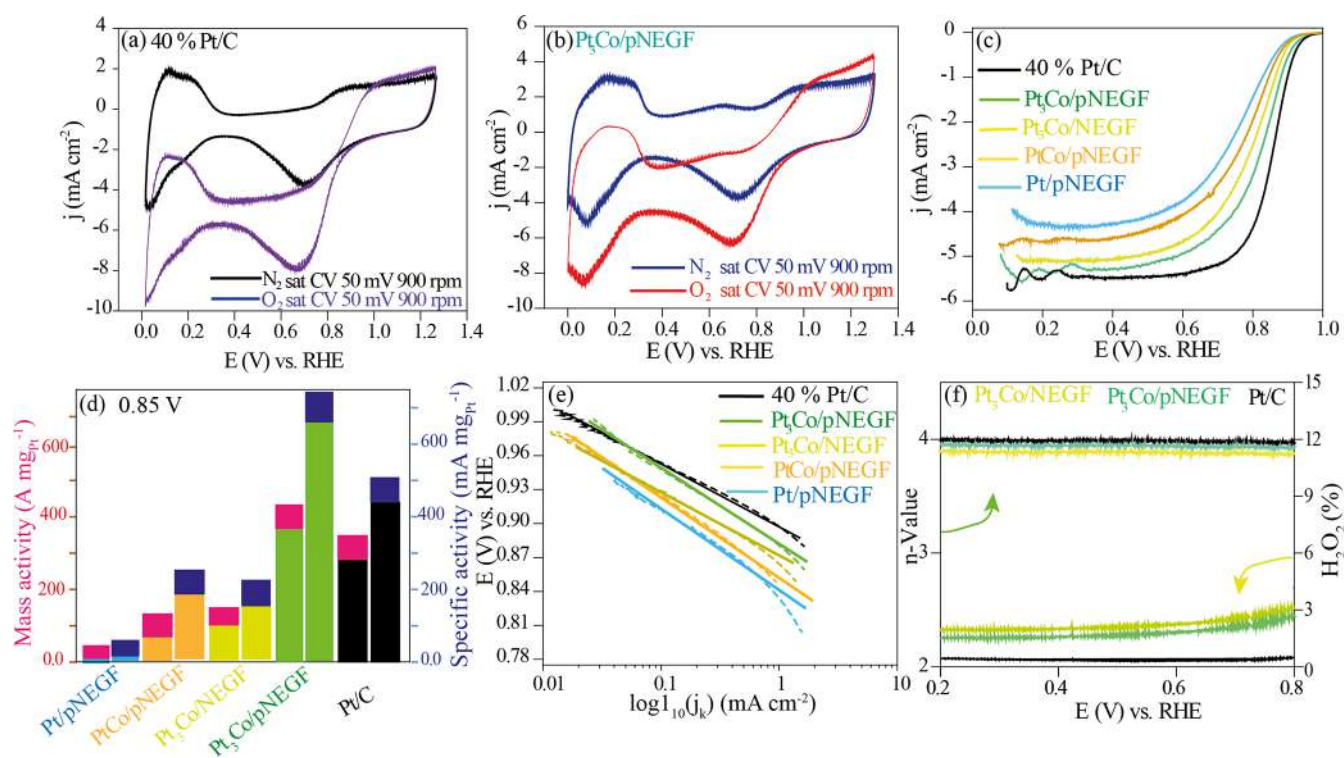


Figure 4. (a,b) Comparative CV curves recorded for Pt₃Co/pNEGF and Pt/C in O₂- and N₂-saturated 0.1 M HClO₄ solutions with a scan rate of 50 mV/s at 900 rpm of the WE; (c) comparative LSV plots recorded for Pt/pNEGF, PtCo/pNEGF, Pt₃Co/NEGF, Pt₃Co/pNEGF, and Pt/C toward ORR activity in O₂-saturated 0.1 M HClO₄ with a scan rate of 10 mV/s at 1600 rpm of the WE; (d) bar chart comparing the mass activities and specific activity for Pt/pNEGF, PtCo/pNEGF, Pt₃Co/NEGF, Pt₃Co/pNEGF, and Pt/C with respect to the measured mass loading of Pt; (e) comparable Tafel slopes analyzed from the ORR LSV profiles; (f) amount of H₂O₂ formed (%) and the corresponding electron transfer number (*n*-value) calculated for Pt/pNEGF, PtCo/pNEGF, Pt₃Co/NEGF, Pt₃Co/pNEGF, and Pt/C.

supported Pt system are shown in Figure 3e. The figure displays two doublet peaks of Pt 4f_{7/2} and Pt 4f_{5/2} for the Pt 4f spectrum at 71.6 and 74.9 eV for Pt/pEGF and at 71.4 and 74.7 eV for Pt/pNEGF. The observed Pt 4f peak shift for Pt/pNEGF points toward the role of the doped-N toward the anchoring of Pt₃Co resulting from the electronic interaction between them. The shift in the binding energy value is ascribed to the charge transfer from N to Pt, which improves the interaction between Pt₃Co and the doped-N of the pNEGF.¹⁶ Moreover, the deconvoluted N 1s spectra of Pt/pNEGF shown in Figure S5a, Supporting Information, state the presence of four types of nitrogen for pyrrolic-N at 399.7 eV and pyridinic-N at 398.6 eV, with a smaller fraction of NH₄⁺ at 405.5 eV and graphitic-N at 400.5 eV. Furthermore, the deconvoluted spectra of Pt/pNEGF (Figure 3f) suggest the two spin-orbit split doublets of Pt 4f_{7/2} and 4f_{5/2}. The observed binding energy (BE) value at 71.7 and 75.1 eV for the +2 oxidation state of Pt and BE values of 71.9 and 75.3 eV, respectively, reveal the existence of the zero-valent metallic state of Pt in the Pt/pNEGF.^{16,44} The binding energy comparison (Figure 3f) of the Pt 4f peaks ensures the positive shift in the BE at 71.8 and 75.2 eV for the +2 and 72.0 and 75.4 eV for the zero oxidation state for Pt₃Co/pNEGF compared to Pt/NEGF due to the inclusion of Co in the Pt structure and the resulting lattice contraction.⁴³ This shift in the BE after the Co incorporation into the Pt lattice structure supports the formation of the bimetallic (Pt₃Co) alloy phase. Investigation of the Co 2p deconvoluted spectra shown in Figure S5b, Supporting Information, evidenced the two spin-spin coupling peaks at the BEs of

780.2 and 795.5 eV for Co 2p_{3/2} and 781.0 and 796.3 eV for Co 2p_{1/2}.^{5,45} This confirms the existence of Co in +2 and zero oxidation states in the system.⁴⁹ The higher oxidation state of Co in Pt₃Co/pNEGF supports the previous finding of the charge transfer from the Co to the Pt metal.⁵⁰ In the alloy structure of Pt₃Co, due to the lower electronegativity of Co (1.9) compared to that of Pt (2.2), an electron transfer from Co to Pt is expected.⁴⁹ The electronic structure of Co gets modified by Pt in the Pt₃Co alloy, which claims that the transfer of charge from Co to Pt leads to a higher oxidation state of Co.⁵⁰

The weight % of the loaded metal catalytic active centers over carbon has been determined by thermogravimetric analysis (TGA). Figure S6, Supporting Information, shows the comparative TGA weight loss profile for Pt/pNEGF, PtCo/pNEGF, Pt₃Co/NEGF, Pt₃Co/pNEGF, and Pt/C. After the complete oxidation of carbon and nitrogen from the N-doped carbon support (pNEGF) in the system (Pt₃Co/NEGF), the residue content is found to be ~40 wt % for all the catalyst systems.

The ORR performance of the synthesized catalysts has been probed with the help of electroanalytical techniques. A three-electrode electrochemical cell consisting of the catalyst-coated glassy carbon electrode as a working electrode (WE) and graphite carbon rod and Ag/AgCl as the counter electrode and reference electrode (RE), respectively, was employed for performing the single-electrode studies. The recorded potential against Ag/AgCl was converted to the RHE scale with the conventional method (for details, refer to the corresponding discussion in Figure S1, Supporting Information). The

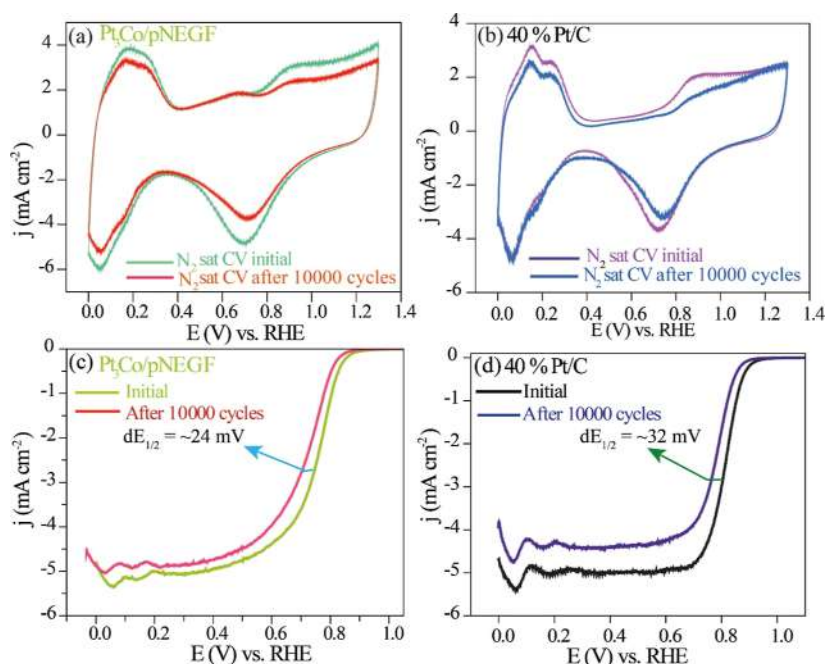


Figure 5. Comparative CV profiles recorded for Pt₃Co/pNEGF (a) and Pt/C; (b) toward the ORR in O₂-saturated 0.1 M HClO₄ at 1600 rpm of the WE before and after 10,000 cycles with a scan rate of 50 mV s⁻¹; comparative LSV profiles recorded for Pt₃Co/pNEGF (c) and Pt/C; (d) toward the ORR in O₂-saturated 0.1 M HClO₄ recorded before and after 10,000 CV cycles at 1600 rpm of the WE before and after 10,000 cycles with a scan rate of 50 mV s⁻¹.

electrochemical ORR performance of all the prepared and *state-of-the-art* catalysts has been evaluated by rotating disk electrode studies in a 0.1 M HClO₄ solution. The comparative CV profiles presented in Figure S7a,b, [Supporting Information](#), show the improved limiting current density of the pNEGF after the microwave treatment of NEGF. The higher percentage of microporosity helps in more charge accumulation on the porous substrate than the NEGF having only mesoporosity. Similar behavior is observed in the comparative LSV performance measurement in Figure S7c, [Supporting Information](#).

Figure 4a,b shows the recorded cyclic voltammograms for Pt₃Co/pNEGF and Pt/C, respectively, in the N₂- and O₂-saturated atmosphere. A similar redox peak feature has been observed in both cases. The redox peaks that appeared between the potential ranges of 0.0 to 0.20 V correspond to the hydrogen adsorption and desorption happening at the Pt surface. The ECSA was calculated in the hydrogen adsorption and desorption region from the N₂-saturated cyclic voltammograms of the samples. Pt₃Co/pNEGF and Pt/C show the ECSA values of 52 and 69 m² g_{Pt}⁻¹, respectively. The intrinsic ORR activity of the catalysts has been investigated by recording the LSV profiles in N₂-/O₂-saturated 0.1 M HClO₄ at a voltage scan rate of 10 mV s⁻¹ by maintaining the WE rotation at 1600 rpm. The comparative linear sweep voltammograms presented in Figure 4c show a significantly improved onset potential (0.93 V) for Pt₃Co/pNEGF with respect to the other control samples prepared, i.e., Pt/pNEGF (0.88 V), PtCo/pNEGF (0.89 V), and Pt₃Co/NEGF (0.93 V). The onset potential for Pt₃Co/pNEGF is comparable to that of Pt/C (0.94 V) and higher than that of Pt/pNEGF (0.89 V), signifying the importance of the bimetallic alloy of Pt and Co. Furthermore, a higher onset potential for Pt₃Co/pNEGF as compared to that for PtCo/pNEGF suggests the importance of maintaining the stoichiometric composition of the catalysts

with distinct alloy phases. In addition, the half-wave ($E_{1/2}$) potential for the catalysts has been calculated for all the catalysts from the respective LSV profiles. The observed $E_{1/2}$ values for Pt/pNEGF, PtCo/pNEGF, Pt₃Co/NEGF, Pt₃Co/pNEGF, and Pt/C are 0.71, 0.73, 0.76, 0.77, and 0.83 V, respectively. The significantly improved $E_{1/2}$ value for Pt₃Co/pNEGF compared to that for Pt₃Co/NEGF is expected to originate from the structural advantage of having the better porous texture of the microwave-irradiated substrate in the case of Pt₃Co/pNEGF. To expand the analytical range, the ORR data from a commercially available 20% Pt/C catalyst is compared with that of 40% Pt/C and Pt₃Co/pNEGF (Figure S8, [Supporting Information](#)). The results indicate that the onset potential values for both catalysts are similar; however, the half-wave potential and limiting current densities for the 20% Pt/C catalyst are lower in comparison to those for the 40% Pt/C catalyst. The limiting current value for 20% Pt/C is also found to be slightly lower than that for Pt₃Co/pNEGF. This could be due to the lower loading of the Pt active sites (20%) in the catalyst compared to the relatively higher loading of Pt of 40 and 30 wt %, respectively, in 40 wt % Pt/C and Pt₃Co/pNEGF. The comparative mass activity and specific activity plot (calculated using eqs 2–4, [Supporting Information](#)) with respect to Pt are presented in Figure 4d in the double Y-axis format (the color pink is utilized to represent the mass activity, whereas the color blue is used to represent the specific activity). The mass activity for Pt is 386.2 A mg⁻¹ in Pt/C, 63 A mg⁻¹ in Pt/NEGF, 114 A mg⁻¹ in PtCo/pNEGF, 145 A mg⁻¹ in Pt₃Co/NEGF, and 403 A mg⁻¹ in Pt₃Co/pNEGF. The specific activity for Pt is 559 mA mg⁻¹ in Pt/C, 151 mA mg⁻¹ in Pt/NEGF, 248 mA mg⁻¹ in PtCo/pNEGF, 295 mA mg⁻¹ in Pt₃Co/NEGF, and 775 mA mg⁻¹ in Pt₃Co/pNEGF. This means that Pt₃Co/pNEGF has 1.5 times higher mass activity compared to 40% Pt/C based on the quantification made at 0.085 V. Figure S9, [Supporting](#)

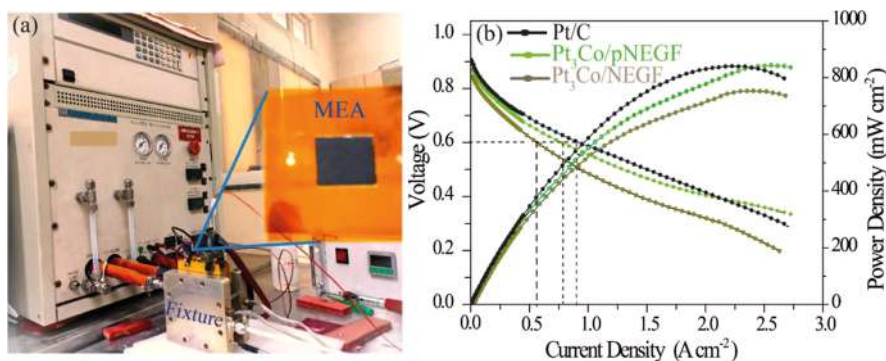


Figure 6. (a) Digital photograph showing the testing arrangement with a $3 \times 3 \text{ cm}^2$ fixture connected to the fuel-cell test station (an inset image showing the digital photograph of the MEA); (b) comparative I - V polarization plots for the single-cell testing of the PEMFC using the three configurations as (i) $\text{Pt}_3\text{Co}/\text{pNEGF}$ (cathode) + Pt/C (anode), (ii) $\text{Pt}_3\text{Co}/\text{NEGF}$ (cathode) + Pt/C (anode), and (iii) Pt/C as the cathode and anode by sandwiching with the Nafion 212 membrane. The testing was carried out under H_2/O_2 conditions for the MEA.

Information, shows the comparative LSV profiles, indicating the mass activities with respect to Pt for Pt/pNEGF , PtCo/pNEGF , $\text{Pt}_3\text{Co}/\text{NEGF}$, $\text{Pt}_3\text{Co}/\text{pNEGF}$, and Pt/C . This higher mass activity of $\text{Pt}_3\text{Co}/\text{pNEGF}$ suggests a better synergistic interaction operating between Pt_3Co and the N-doped microporous 3D support.

Further insight into the ORR kinetics has been achieved from the Tafel slope data shown in Figure 4e. The measured Tafel slope values of the catalysts follow the order: Pt/pNEGF (72 mV dec^{-1}) > PtCo/pNEGF (68 mV dec^{-1}) > $\text{Pt}_3\text{Co}/\text{NEGF}$ (67 mV dec^{-1}) > $\text{Pt}_3\text{Co}/\text{pNEGF}$ (64 mV dec^{-1}) > Pt/C (62 mV dec^{-1}). The lower Tafel slope value for $\text{Pt}_3\text{Co}/\text{pNEGF}$ as compared to that for Pt/pNEGF and PtCo/pNEGF suggests better feasibility of the ORR on this system. The observed trend of the Tafel slope also suggests the role played by Co incorporation into the Pt lattices by supporting the catalyst to perform more effectively toward the ORR process.

To know the mechanism of the electrochemical ORR process, RRDE analysis was done in 0.1 M HClO_4 . The obtained $\text{H}_2\text{O}_2\%$ generated during the ORR cycle was investigated and quantified as shown in Figure 4f. The recorded amount of H_2O_2 during the catalytic ORR process was found to be less than 4% for $\text{Pt}_3\text{Co}/\text{pNEGF}$, which is close to that recorded on Pt/C ($\sim 2\%$). The result reveals that, like Pt/C , $\text{Pt}_3\text{Co}/\text{pNEGF}$ also promotes the direct 4e-transfer process for the reduction of oxygen. The amount of H_2O_2 calculated for $\text{Pt}_3\text{Co}/\text{NEGF}$ is 6%, which is slightly higher than that for $\text{Pt}_3\text{Co}/\text{pNEGF}$. Furthermore, the number of electrons involved (n -value) in the oxygen reduction process has also been estimated, and the values are as follows: $\text{Pt}_3\text{Co}/\text{NEGF}$ (3.8), $\text{Pt}_3\text{Co}/\text{pNEGF}$ (3.9), and Pt/C (4.0). The lower percentage of H_2O_2 , as well as the n -value close to 4 for $\text{Pt}_3\text{Co}/\text{pNEGF}$, suggest that the system is fairly free from the parasitic two-electron reduction process, which was expected to be a possible process due to the presence of Co- and N-doped carbon in the catalyst composition.

The electrochemical accelerated durability test (ADT) of the catalyst has been performed by recording 10,000 cycles in oxygen-saturated 0.1 M HClO_4 at a scan rate of 100 mV s^{-1} within the potential range of 0.80 and 1.2 V with respect to the RHE. After the durability cycling, the CV and LSV results were recorded on $\text{Pt}_3\text{Co}/\text{pNEGF}$ and Pt/C which were compared against the corresponding initial cycles as shown in Figure 5a,b, respectively. The CV profiles recorded before and after the 10,000 cycles (Figure 5a) for $\text{Pt}_3\text{Co}/\text{pNEGF}$ show nearly

similar peak features of hydrogen adsorption and desorption. After 10,000 cycles, the ECSA change for $\text{Pt}_3\text{Co}/\text{pNEGF}$ ($\Delta\text{ECSA} = 5 \text{ m}^2 \text{ g}_{\text{Pt}}^{-1}$) is lower than the value obtained for Pt/C ($\Delta\text{ECSA} = 9 \text{ m}^2 \text{ g}_{\text{Pt}}^{-1}$) (Figure 5b). Furthermore, the LSV curve recorded before and after the ADT CV cycling showed a shift in the $E_{1/2}$ value in a negative direction with a drop of 24 mV for $\text{Pt}_3\text{Co}/\text{pNEGF}$ (Figure 5c). The observed change in the $E_{1/2}$ value for $\text{Pt}_3\text{Co}/\text{pNEGF}$ is lower than that for Pt/C (32 mV) (Figure 5d) recorded under identical conditions. This indicates the better stability of the homemade catalyst under operating conditions and is attributed to the less corrosive nature of the graphitic carbon support. Furthermore, the strong interaction between the doped-N and Pt_3Co nanoparticles is also expected to play a major role in enhancing the electrochemical stability of the catalyst. The ADT result has another major implication because, even though Pt/C appears to be a better catalyst than $\text{Pt}_3\text{Co}/\text{pNEGF}$ based on the initial key performance indicators such as the $E_{1/2}$ value and Tafel slope, in the long run, $\text{Pt}_3\text{Co}/\text{pNEGF}$ is expected to beat the performance of Pt/C . The conventional carbon-based catalysts are vulnerable to electrochemical corrosion, which has been considered as a major drawback particularly when the PEMFC is expected to be subjected to periodic on-off cyclings. The ADT reveals that the $\text{Pt}_3\text{Co}/\text{pNEGF}$ is electrochemically more enduring and can warrant better dividends in terms of performance in the long run. This will be further complemented by its porous structure based on the entangled network of the graphene layers, ensuring a greater ability to prevent particle aggregation and the associated issues related to mass transfer and water management during the operation of the PEMFCs.

The structural analysis of the post-ADT samples by HRTEM points toward the structural endurance of the $\text{Pt}_3\text{Co}/\text{pNEGF}$ (Figure S10, Supporting Information). Figure S6a,b displays, respectively, the HRTEM images of $\text{Pt}_3\text{Co}/\text{pNEGF}$ taken before and after ADT. Apparently, the triggered condition did not reveal any visual changes in the nature of the dispersion of the Pt_3Co nanoparticles and the overall morphology of the catalyst system. On the other hand, a similar analysis of Pt/C (Figure S10c,d, Supporting Information) reveals the issue of the aggregation of the Pt nanoparticles subsequent to ADT. The more stable graphitic nature of the pNEGF and strong interaction of the Pt_3Co nanoparticles assisted by the nanoporous texture of the substrate and its N-doped anchoring sites could be the major contributing factors that bring the

improved stability of the dispersion state of the active sites in the case of Pt₃Co/pNEGF. These findings are in accordance with the results of XPS and the morphological studies as detailed in the previous sections.

Since Pt₃Co/3D pNEGF shows significantly improved ORR activity and durability in acidic conditions, the catalyst was tested by employing it as the cathode for PEMFCs by fabricating the MEA followed by single-cell testing. For comparison purposes, the MEAs made from the *state-of-the-art* Pt/C (Johnson Matthey) and Pt₃Co/NEGF (without microwave treatment) were also tested under identical conditions. The MEAs based on Pt₃Co/pNEGF and Pt₃Co/NEGF were made by sandwiching the respective catalyst-coated porous gas diffusion layer (GDL and SGL carbon) as the cathode (0.50 mg cm⁻²), Pt/C catalysts-coated GDL as the anode (0.50 mg cm⁻²) on either side of a Nafion 212 (DuPont, USA) proton conducting membrane. In the case of the MEA based on Pt/C, the catalyst-coated GDL was employed for both the anode and cathode (0.50 mg cm⁻²) in the MEA. The active area of the MEA was maintained at 9 cm² in all the cases. The testing was performed by mounting the hot-pressed MEA in a single-cell test fixture (Fuel Cell Technologies Inc, USA) and connecting it to a fuel-cell test station (Fuel Cell Technologies Inc., USA). The testing was performed by following the standard operating protocols under H₂-O₂ feed conditions, initially by activating the MEA under humidified conditions till the cell reached a condition to deliver its maximum optimized active sites in the case of the electrode based on Pt₃Co/pNEGF, which is expected to improve the active TPB performance at 60 °C. The photograph of the single-cell fixture connected to the fuel cell test station and the image of the magnified view of the MEA used are presented in Figure 6a.

Once the system attains steady open-circuit voltage (OCV), the test station drags current as per the preset standard program, and the current (*I*)-voltage (*V*) polarization plots are generated. The thus-obtained comparative *I*-*V* polarization plots for the three MEAs are presented in Figure 6b. It is interesting to note that both Pt₃Co/pNEGF and Pt/C cathode-based MEAs have only a slight difference in terms of their *I*-*V* polarization characteristics even though the difference in their ORR activity as validated from the single-electrode LSV profiling is comparatively more significant (Figure 4c). The performance of the Pt₃Co/NEGF (without the nanopores)-based MEA is the least among the three MEAs tested. The OCV values for the MEA with the Pt₃Co/pNEGF cathode and its counterpart system with the Pt/C cathode are 0.89 and 0.91 V, respectively. This trend in the OCV values is consistent with the intrinsic ORR activity of the catalysts, which slightly favors Pt/C over Pt₃Co/pNEGF in terms of the ORR onset potential and *E*_{1/2} values. The OCV value for the Pt₃Co/NEGF (0.86 V) is lower than that for the Pt₃Co/pNEGF, which is ascribed to the favorable role played by the microporous structure of the 3D graphene in the latter case. Furthermore, the *I*-*V* polarization plots of the MEA based on the Pt/C, Pt₃Co/pNEGF, and Pt₃Co/pNEGF as the cathode catalysts are compared with respect to the performance at 0.60 V, which is a commonly used metric for evaluating the performance of PEMFCs. The current densities measured at 0.60 V for the Pt₃Co/NEGF, Pt₃Co/pNEGF, and Pt/C-based cells are 850, 790, and 600 mA/cm², respectively. The better performance of the cell based on Pt₃Co/pNEGF compared to its counterpart system (Pt₃Co/NEGF) is credited to the

improved microporous texture of the catalyst which helps to attain a favorable active interface in the electrode. Furthermore, the higher performance of the system based on Pt/C is in agreement with the higher catalytic activity of Pt/C as reflected in the LSV profiling during the ORR performance mapping. Also, it is interesting to note that the difference in the performance of the Pt₃Co/pNEGF- and Pt/C-based MEAs gradually narrows down as the current dragging increases, and finally, at around 2.25 A cm⁻², the performance of both the MEAs reaches the same level, registering a maximum power density of 800 mW cm⁻². This gradually improved performance of the MEA based on the homemade catalyst with the current dragging is a clear indication of the better mass transport and water management offered by the electrode made from this catalyst due to its more process-friendly texture. The porous texture has an exposed and better accessible nature of formation with the Nafion ionomer without compromising its porosity.

The TPB is created when the catalyst, ionomer, and reactant gases are combined efficiently, which balances the oxygen transport and water management at the catalyst layer (CL) interface. Hence, it is crucial to promote the formation of an improved interface within CL. Thus, the CL plays an important role in the TPB formation, maintaining suitable interface creation with the GDL and electrolytes. Therefore, prior to the assembly of the MEA, the catalyst-coated GDL was analyzed to evaluate the contribution of the CL in the TPB formation. The 3D microstructure of the cross-section of the GDL and catalyst-coated GDL was examined using FESEM. Figure S11, Supporting Information, shows the cross-sectional FESEM images of the GDL, Pt-supported carbon-coated GDL (Pt/C@GDL), Pt₃Co/NEGF-coated GDL (Pt₃Co/NEGF@GDL), and Pt₃Co/pNEGF-coated GDL (Pt₃Co/pNEGF@GDL). Figure S11a and the inset image show the cross-sectional FESEM image of the bare GDL which represents a flat surface, whereas a thick layer of the catalyst was observed when the GDL was coated with Pt/C as shown in Figure S11b and its inset image. Furthermore, the cross-sectional FESEM image of Pt₃Co/NEGF@GDL (Figure S11c) represents a thick layer of the catalyst with a rough surface. The magnified FESEM image analysis of the Pt₃Co/NEGF@GDL shown in the inset image of Figure S11c displayed the porous structure of the CL. In addition, the yellow dotted line in the inset image of Figure S11c shows the self-assembled structure of the 3D graphene. The microwave treatment of the 3D graphene (pNEGF)-supported alloy-coated GDL (Pt₃Co/pNEGF@GDL) (Figure S11d) displayed a thick layer of the 3D self-assembled structure of the catalyst over the GDL. Moreover, the marked yellow dotted line in the magnified image of Figure S11d shows a crumbled porous structure for the microwave-treated support. The porous self-assembly structure obtained after the microwave treatment is beneficial to form an asymmetric CL that helps the TPB formation by providing better active interface formation with the membrane and GDL, thereby enhancing the oxygen and proton transfer mechanisms of the MEA during the PEMFC operation.

Water management plays an important role in efficient TPB formation that affects the performance and durability of the MEA. Specifically, the water management in the CL and the interface of CL, membrane, and GDL is crucial to balance the proton and oxygen transport to the TPB during the MEA operation. Therefore, CL requires a proper hydration balance to avoid excessive liquid water, which can impede gas flow to

the reaction sites and dry conditions and hinder proton transfer. To evaluate the wetting (hydrophobicity/hydrophilicity) properties of the CL, contact angle (CA) measurements were performed for the GDL, Pt/C@GDL, Pt₃Co/NEGF@GDL, and Pt₃Co/pNEGF@GDL (Figure S12, Supporting Information). Figure S12a shows the CA value for the blank GDL, which is almost 180°; this is due to the superhydrophobic nature of the PTFE-coated microporous layer of the GDL, and the resulting surface has no affinity for water. Additionally, the Pt/C-coated surface of the GDL (Pt/C@GDL) shown in Figure S12b had a CA of 138°, indicating comparatively higher hydrophilicity and improved affinity for water. Similarly, the Pt₃Co/NEGF-coated GDL (Pt₃Co/NEGF@GDL) exhibited a CA value of 135.7° (Figure S12c), which indicates further higher hydrophilicity compared to that of Pt/C@GDL. After the microwave treatment of the NEGF, the formed pNEGF-supported Pt₃Co alloy-coated GDL (Pt₃Co/pNEGF@GDL) had a more rough and porous surface, which led to more water accumulation and a lower CA value of 109.2° (Figure S12d). A CA of close to 90° can help to balance the hydrophilicity and hydrophobicity at the CL interface, thereby improving the water management on the catalyst surface, which is an important criterion to design the suitable TPB formation unit.

In the membrane/CL/GDL interface, the CL consisting of the catalyst and ionomer interaction plays an important role in the effective TPB formation. The efficient combination of the catalyst and the ionomer facilitates proton transfer and balanced interaction with the reactant oxygen at the TPB. The polarization plots were generated for various Nafion/carbon (N/C) ratios of 0.20, 0.30, and 0.40 to evaluate their impact on the power density and current density characteristics for the different MEAs fabricated with the Pt₃Co/pNEGF catalyst. The *I*–*V* plots in Figure S13 show that when the N/C value is 0.20, the OCV value is around 0.82 V, and the power density is 765 mW cm⁻². By changing the N/C value to 0.30, the OCV (0.89 V) and the power density (800 mW cm⁻²) values are found to be significantly improved. Furthermore, while increasing the N/C to 0.40, a drop in the OCV (0.80) and the power density (790 mW cm⁻²) is observed as shown in Figure S13. The best performance for the MEA was observed at N/C = 0.30, which is attributed to the appropriate ionomer-to-carbon ratio for the Pt₃Co/pNEGF catalyst, facilitating better TPB formation. These results emphasize the importance of the ionomer concentration for a particular catalyst.

To gain a further insightful understanding of the effects of the membrane/CL/GDL interface along with the mass transport and water management in the MEA performance during the fuel cell testing condition, the electrochemical impedance spectroscopy (EIS) analysis has been performed and the data are presented in Figure S14. This study employed the EIS analysis to assess the MEAs containing different catalysts, namely, Pt/C, Pt₃Co/NEGF, and Pt₃Co/pNEGF, in the cathode. The EIS measurement has been performed at the OCV, 0.60, and 0.20 V. Figure S14a shows the Nyquist plots recorded at the OCV, which reveals that both Pt/C and Pt₃Co/pNEGF have almost the same charge transfer resistance, whereas the Pt₃Co/NEGF-based MEA shows higher charge transfer resistance. Additionally, the comparative Nyquist plots (Figure S14b) recorded at 0.60 V show a lower intercept for Pt₃Co/pNEGF compared to those for Pt/C and Pt₃Co/pNEGF due to the better interface formation with the

membrane and GDL, which suppresses the ohmic resistance. However, the charge transfer resistance for Pt₃Co/pNEGF is found to be higher than that of Pt/C due to the slow ORR kinetics of the former compared to the latter. Furthermore, a significant change in the ohmic resistance is observed in the Nyquist plots recorded at 0.20 V. As the 0.20 V is the higher current density region with the possibility of more water formation, the EIS spectra (Figure S14c) show that there is a significantly favorable change in the ohmic resistance for the MEA based on Pt₃Co/pNEGF compared to that of the Pt/C-based MEA. At 0.20 V, a lower charge transfer resistance has been noticed for the Pt₃Co/pNEGF-based MEA compared to the counterpart systems based on Pt/C and Pt₃Co/NEGF. This is ascribed to the presence of the microporous layer of the pNEGF, which helps to attain better interface formation and thereby improve mass transfer and water management at higher current densities.

Hence, the electrode offers better oxidant distribution and water dissipation, which are expected to be more sluggish under high current dragging conditions in the case of the normal electrodes. This is the region where the electrodes based on conventional carbon-based catalysts struggle and fail to deliver good performance. It also should be noted that the microwave treatment creates a greater contribution of smaller pores in the case of Pt₃Co/pNEGF compared to that in Pt₃Co/NEGF. The significant performance difference between the MEAs based on these two catalysts as the cathode implies that the greater extent of the nanopores has a significant role in favorably tuning the cell performance. The nanopores play a critical role as oxygen nanoreservoirs and help to increase the local oxygen concentration, thus aiding the Pt₃Co/pNEGF system to work in a comparatively better mode during the polarization conditions. The advantage of the Pt₃Co/pNEGF-based MEA over its counterpart based on Pt/C in the high current dragging condition, even though it looks less significant in a small area single-cell polarization data, will have stronger implications in larger MEAs and even prominently as we go from the single cells to the stacks of PEMFCs. In this context, the interesting trend obtained in the *I*–*V* polarization plot of the MEA based on the Pt₃Co/pNEGF cathode with its process-friendly nature has greater technological significance and prospects apart from its another important advantage of having better corrosion resistance as confirmed from the ADT (Figure 5).

3. CONCLUSIONS

A unique 3D structured ORR electrocatalyst based on the nitrogen-doped porous graphene-supported Pt₃Co nanoparticles (Pt₃Co/pNEGF) was prepared by employing a sequential preparation process involving freeze drying, microwave treatment, and polyol reduction. The introduction of nano-/microporosity into the 3D micro-mesoporous conducting support system has great advantages over those carbons which display only mesoporosity. It is found that the surface adsorption properties of the Pt are considerably modified by the stoichiometric addition of Co into the system. Furthermore, a well-suited stoichiometric composition of Pt and Co (i.e., Pt₃Co in the present case) along with the controlled interplay of the other contributing factors such as the doped nitrogen, microporosity, and 3D architecture of the catalyst unit favorably modulates the catalyst toward the oxygen adsorption and subsequently the ORR performance. The 3D structure of the support favors mass transfer and

effective formation of the active “TPB”, and as a result, Pt₃Co/pNEGF shows an ORR activity that differs only slightly from that of the *state-of-the-art* (Pt/C) catalyst. The synergistic interactions operating in the system between the Pt₃Co nanoparticles and the N-doped porous graphene are primarily responsible for the higher catalytic activity and durability displayed by Pt₃Co/pNEGF. The presence of nano-/microporosity in the carbon system enhances the available reaction sites for the gas and electrolyte interface formation and contributes significantly to improving the mass activity of the catalyst. Pt₃Co/pNEGF also displays high structural endurance and corrosion resistance, and the dispersion characteristics of the Pt₃Co nanoparticles and the textural features of the catalyst are found to be unaffected even after the system is subjected to the electrochemical potential cycling stability tests that last for 10 K cycles. Finally, PEMFC testing in a single-cell mode by fabricating an MEA, with Pt₃Co/pNEGF as the cathode and Pt/C as the anode using Nafion 211 membrane, displayed the better ability of the MEA based on the homemade catalyst to perform under high current dragging conditions. This is an important advantage that has a significant impact on dealing with the mass transfer and water management issues in the case of the larger MEAs and PEMFC stacks. This advantage in the *I*–*V* polarization profiling of the MEA made from Pt₃Co/pNEGF is a result of the attained more process-friendly texture of the electrode that is better suited to dealing with the mass transfer, reactant distribution, active site utilization, and water management. This is an important technological advantage of the electrode, apart from the improved corrosion resistance of the catalyst, as proven by the accelerated durability studies.

■ ASSOCIATED CONTENT

SI Supporting Information

The Supporting Information is available free of charge at <https://pubs.acs.org/doi/10.1021/acsami.3c03372>.

Experimental section, HRTEM images, BET analysis, XPS, and TGA profiles (PDF)

■ AUTHOR INFORMATION

Corresponding Author

Sreekumar Kurungot – *Physical and Materials Chemistry Division, CSIR-National Chemical Laboratory, Pune 411008, India; Academy of Scientific and Innovative Research (AcSIR), Ghaziabad, Uttar Pradesh 201002, India; orcid.org/0000-0001-5446-7923; Email: k.sreekumar@ncl.res.in*

Authors

Narugopal Manna – *Physical and Materials Chemistry Division, CSIR-National Chemical Laboratory, Pune 411008, India; Academy of Scientific and Innovative Research (AcSIR), Ghaziabad, Uttar Pradesh 201002, India; orcid.org/0000-0001-6343-1746*

Mayank Singh – *Physical and Materials Chemistry Division, CSIR-National Chemical Laboratory, Pune 411008, India; Academy of Scientific and Innovative Research (AcSIR), Ghaziabad, Uttar Pradesh 201002, India*

Complete contact information is available at: <https://pubs.acs.org/doi/10.1021/acsami.3c03372>

Author Contributions

The manuscript was written through the contributions of all authors. All authors have given approval to the final version of the manuscript.

Notes

The authors declare no competing financial interest.

■ ACKNOWLEDGMENTS

N.M. acknowledges the Council of Scientific and Industrial Research (CSIR), New Delhi, India, for the Senior Research Fellowship. S.K. acknowledges the research funding (HCP44-07) from the CSIR, New Delhi, through the Hydrogen Mission Program.

■ REFERENCES

- (1) Stacy, J.; Regmi, Y. N.; Leonard, B.; Fan, M. The recent progress and future of oxygen reduction reaction catalysis: a review. *Renew. Sustain. Energy Rev.* **2017**, *69*, 401–414.
- (2) Van Spronsen, M. A.; Frenken, J. W. M.; Groot, I. M. N. Surface Science under Reaction Conditions: CO Oxidation on Pt and Pd Model Catalysts. *Chem. Soc. Rev.* **2017**, *46*, 4347–4374.
- (3) Deutschmann, O.; Knözinger, H.; Kochloefl, K.; Turek, T. Heterogeneous Catalysis and Solid Catalysts. *Ullmann's Encyclopedia of Industrial Chemistry*, 2009; Vol. 1; pp 5–6.
- (4) Quaino, P.; Juarez, F.; Santos, E.; Schmickler, W. Volcano Plots in Hydrogen Electrocatalysis-Uses and Abuses. *Beilstein J. Nanotechnol.* **2014**, *5*, 846–854.
- (5) Lin, X.; Zalitis, C. M.; Sharman, J.; Kucernak, A. Electrocatalyst Performance at the Gas/Electrolyte Interface under High-Mass-Transport Conditions: Optimization of the “Floating Electrode” Method. *ACS Appl. Mater. Interfaces* **2020**, *12*, 47467–47481.
- (6) Schröder, J.; Mints, V. A.; Bornet, A.; Berner, E.; Fathi Tovini, M.; Quinson, J.; Wiberg, G. K. H.; Bizzotto, F.; El-Sayed, H. A.; Arenz, M. The Gas Diffusion Electrode Setup as Straightforward Testing Device for Proton Exchange Membrane Water Electrolyzer Catalysts. *JACS Au* **2021**, *1*, 247–251.
- (7) Meier, J. C.; Galeano, C.; Katsounaros, I.; Witte, J.; Bongard, H. J.; Topalov, A. A.; Baldizzone, C.; Mezzavilla, S.; Schüth, F.; Mayrhofer, K. J. J. Design Criteria for Stable Pt/C Fuel Cell Catalysts. *Beilstein J. Nanotechnol.* **2014**, *5*, 44–67.
- (8) Suter, A. M.; Smith, K.; Hack, J.; Rasha, L.; Rana, Z.; Angel, G. M. A.; Shearing, P. R.; Miller, T. S.; Brett, D. J. L. Engineering Catalyst Layers for Next-Generation Polymer Electrolyte Fuel Cells: A Review of Design, Materials, and Methods. *Adv. Energy Mater.* **2021**, *11*, 2101025.
- (9) Ehelebe, K.; Schmitt, N.; Sievers, G.; Jensen, A. W.; Hrnjić, A.; Collantes Jiménez, P.; Kaiser, P.; Geuß, M.; Ku, Y. P.; Jovanovic, P.; Mayrhofer, K. J. J.; Etzold, B.; Hodnik, N.; Escudero-Escribano, M.; Arenz, M.; Cherevko, S. Benchmarking Fuel Cell Electrocatalysts Using Gas Diffusion Electrodes: Inter-Lab Comparison and Best Practices. *ACS Energy Lett.* **2022**, *7*, 816–826.
- (10) Stephens, I. E. L.; Bondarenko, A. S.; Grønbjerg, U.; Rossmeisl, J.; Chorkendorff, I. Understanding the Electrocatalysis of Oxygen Reduction on Platinum and Its Alloys. *Energy Environ. Sci.* **2012**, *5*, 6744–6762.
- (11) Greeley, J.; Stephens, I. E. L.; Bondarenko, A. S.; Johansson, T. P.; Hansen, H. A.; Jaramillo, T. F.; Rossmeisl, J.; Chorkendorff, I.; Nørskov, J. K. Alloys of Platinum and Early Transition Metals as Oxygen Reduction Electrocatalysts. *Nat. Chem.* **2009**, *1*, 552–556.
- (12) Xu, D.; Bliznakov, S.; Liu, Z.; Fang, J.; Dimitrov, N. Composition-Dependent Electrocatalytic Activity of Pt-Cu Nanocube Catalysts for Formic Acid Oxidation. *Angew. Chem., Int. Ed.* **2010**, *49*, 1282–1285.
- (13) Koh, S.; Strasser, P. Electrocatalysis on Bimetallic Surfaces: Modifying Catalytic Reactivity for Oxygen Reduction by Voltammetric Surface Dealloying. *J. Am. Chem. Soc.* **2007**, *129*, 12624–12625.

- (14) Zhou, Y.; Zhou, Z.; Shen, R.; Ma, R.; Liu, Q.; Cao, G.; Wang, J. Correlating Electrocatalytic Oxygen Reduction Activity with d-band Centers of Metallic Nanoparticles. *Energy Storage Mater.* **2018**, *13*, 189–198.
- (15) Zhou, S.; Varughese, B.; Eichhorn, B.; Jackson, G.; McIlwrath, K. Pt–Cu Core–Shell and Alloy Nanoparticles for Heterogeneous NO_x Reduction: Anomalous Stability and Reactivity of a Core–Shell Nanostructure. *Angew. Chem., Int. Ed.* **2005**, *44*, 4539–4543.
- (16) Kodama, K.; Nagai, T.; Kuwaki, A.; Jinnouchi, R.; Morimoto, Y. Challenges in Applying Highly Active Pt-Based Nanostructured Catalysts for Oxygen Reduction Reactions to Fuel Cell Vehicles. *Nat. Nanotechnol.* **2021**, *16*, 140–147.
- (17) Gonçalves, J. M.; Silva, M. N. T.; Naik, K. K.; Martins, P. R.; Rocha, D. P.; Nossol, E.; Munoz, R. A. A.; Angnes, L.; Rout, C. S. Multifunctional Spinel Pt₃Co Based Materials for Energy Storage and Conversion: a Review on Emerging Trends, Recent Developments and Future Perspectives. *J. Mater. Chem. A* **2021**, *9*, 3095–3124.
- (18) Liu, H.; Li, C.; Chen, D.; Cui, P.; Ye, F.; Yang, J. Uniformly Dispersed Platinum–Cobalt Alloy Nanoparticles with Stable Compositions on Carbon Substrates for Methanol Oxidation Reaction. *Sci. Rep.* **2017**, *7*, 11421–11428.
- (19) Choi, S.; Jeon, J.; Chae, J.; Yuk, S.; Lee, D.-H.; Doo, G.; Lee, D. W.; Hyun, J.; Kwen, J.; Choi, S. Q.; Kim, H.-T. Single-Step Fabrication of a Multiscale Porous Catalyst Layer by the Emulsion Template Method for Low Pt-Loaded Proton Exchange Membrane Fuel Cells. *ACS Appl. Energy Mater.* **2021**, *4*, 4012–4020.
- (20) Lee, J. D.; Jishkariani, D.; Zhao, Y.; Najmr, S.; Rosen, D.; Kikkawa, J. M.; Stach, E. A.; Murray, C. B. Tuning the Electrocatalytic Oxygen Reduction Reaction Activity of Pt–Co Nanocrystals by Cobalt Concentration with Atomic-Scale Understanding. *ACS Appl. Mater. Interfaces* **2019**, *11*, 26789–26797.
- (21) Jung, N.; Bhattacharjee, S.; Gautam, S.; Park, H.-Y.; Ryu, J.; Chung, Y.-H.; Lee, S.-Y.; Jang, I.; Jang, J. H.; Park, S. H.; Chung, D. Y.; Sung, Y.-E.; Chae, K.-H.; Waghamare, U. V.; Lee, S.-C.; Yoo, S. J. Organic–Inorganic Hybrid PtCo Nanoparticle with High Electrocatalytic Activity and Durability for Oxygen Reduction. *NPG Asia Mater.* **2016**, *8*, 237.
- (22) Wang, Y.-J.; Zhao, N.; Fang, B.; Li, H.; Bi, X. T.; Wang, H. A Highly Efficient PtCo/C Electrocatalyst for the Oxygen Reduction Reaction. *RSC Adv.* **2016**, *6*, 34484–34491.
- (23) Jia, Q.; Caldwell, K.; Strickland, K.; Ziegelbauer, J. M.; Liu, Z.; Yu, Z.; Ramaker, D. E.; Mukerjee, S. Improved Oxygen Reduction Activity and Durability of Dealloyed PtCo_x Catalysts for Proton Exchange Membrane Fuel Cells: Strain, Ligand, and Particle Size Effects. *ACS Catal.* **2015**, *5*, 176–186.
- (24) Boyaci San, F. G.; Dursun, S.; Yazici, M. S. PtCo on Continuous-Phase Graphene as PEM Fuel Cell Catalyst. *Int. J. Energy Res.* **2021**, *45*, 1673–1684.
- (25) Lee, H.; Lim, J.; Lee, C.; Back, S.; An, K.; Shin, J. W.; Ryoo, R.; Jung, Y.; Park, J. Y. Boosting Hot Electron Flux and Catalytic Activity at Metal–Oxide Interfaces of PtCo Bimetallic Nanoparticles. *Nat. Commun.* **2018**, *9*, 2235–2238.
- (26) Farkas, B.; Perry, C. B.; Jones, G.; De Leeuw, N. H. Adsorbate-Induced Segregation of Cobalt from PtCo Nanoparticles: Modeling Au Doping and Core AuCo Alloying for the Improvement of Fuel Cell Cathode Catalysts. *J. Phys. Chem. C* **2020**, *124*, 18321–18334.
- (27) Yu, Z.; Zhang, J.; Liu, Z.; Ziegelbauer, J. M.; Xin, H.; Dutta, L.; Muller, D. A.; Wagner, F. T. Comparison between Dealloyed PtCo₃ and PtCu₃ Cathode Catalysts for Proton Exchange Membrane Fuel Cells. *J. Phys. Chem. C* **2012**, *116*, 19877–19885.
- (28) Liu, Z.; Lei, Y.; Wang, G. First-Principles Computation of Surface Segregation in L10 CoPt Magnetic Nanoparticles. *J. Phys.: Condens. Matter* **2016**, *28*, 266002.
- (29) Sun, X.; Jia, Z. Y.; Huang, Y. H.; Harrell, J. W.; Nikles, D. E.; Sun, K.; Wang, L. M. Synthesis and Magnetic Properties of CoPt Nanoparticles. *J. Appl. Phys.* **2004**, *95*, 6747–6749.
- (30) Karipoth, P.; Joseyphus, R. J. Evolution of High Coercivity in CoPt Nanoparticles Through Nitrogen Assisted Annealing. *J. Supercond. Novel Magn.* **2014**, *27*, 2123–2130.
- (31) Manna, N.; Singh, S. K.; Kharabe, G. P.; Torris, A.; Kurungot, S. Zinc–Air Batteries Catalyzed Using Co₃O₄ Nanorod-Supported N-Doped Entangled Graphene for Oxygen Reduction Reaction. *ACS Appl. Energy Mater.* **2021**, *4*, 4570–4580.
- (32) Zhu, H.; Gu, L.; Yu, D.; Sun, Y.; Wan, M.; Zhang, M.; Wang, L.; Wang, L.; Wu, W.; Yao, J.; Du, M.; Guo, S. The Marriage and Integration of Nanostructures with Different Dimensions for Synergistic Electrocatalysis. *Energy Environ. Sci.* **2017**, *10*, 321–330.
- (33) Dai, L.; Chang, D. W.; Baek, J. B.; Lu, W. Carbon NanoMaterials for Advanced Energy Conversion and Storage. *Small* **2012**, *8*, 1130–1166.
- (34) Fan, F.; Hui, Y.; Devasenathipathy, R.; Peng, X.; Huang, Q.; Xu, W.; Yang, F.; Liu, X.; Wang, L.; Chen, D. H.; Fan, Y.; Chen, W. Composition-adjustable Mo₆Co₆C₇/Co@carbon nanocage for enhanced oxygen reduction and evolution reactions. *J. Colloid Interface Sci.* **2023**, *636*, 450–458.
- (35) Fan, F.; Huang, Q.; Devasenathipathy, R.; Peng, X.; Yang, F.; Liu, X.-a.; Wang, L.; Chen, D.-H.; Fan, Y.; Chen, W. Composite-Structure-Defined Nitrogen-Doped Carbon Nanocage Embedded Co/Co_xP for Enhanced Oxygen Reduction and Evolution Reactions. *Electrochim. Acta* **2023**, *437*, 141514.
- (36) Zhong, J.-P.; Hou, C.; Sun, M.-L.; Yang, Z.-Y.; Chen, Du.-H.; Fan, Y.-J.; Chen, W.; Liao, H.-G.; Sun, S.-G. A Superior Electro-Catalyst Toward the Oxygen Reduction Reaction Obtained by Atomically Dispersing Copper on N, F co-doped Graphene Through Atomic Interface Engineering. *J. Mater. Chem. A* **2022**, *10*, 13876–13883.
- (37) Huang, K.; Zhang, W.; Li, J.; Fan, Y.; Yang, B.; Rong, C.; Qi, J.; Chen, W.; Yang, J. In Situ Anchoring of Zeolite Imidazole Framework-Derived Co, N-Doped Porous Carbon on Multiwalled Carbon Nanotubes toward Efficient Electrocatalytic Oxygen Reduction. *ACS Sustainable Chem. Eng.* **2020**, *8*, 478–485.
- (38) Li, Y.; Zhao, M.; Zhao, Y.; Song, L.; Zhang, Z. FeNi Layered Double-Hydroxide Nanosheets on a 3D Carbon Network as an Efficient Electrocatalyst for the Oxygen Evolution Reaction. *Part. Part. Syst. Char.* **2016**, *33*, 158–166.
- (39) Mo, R.; Rooney, D.; Sun, K.; Yang, H. Y. 3D Nitrogen-Doped Graphene Foam with Encapsulated Germanium/nitrogen-doped Graphene Yolk-shell Nanoarchitecture for High-Performance Flexible Li-ion battery. *Nat. Commun.* **2017**, *8*, 13949.
- (40) Manna, N.; Singh, S. K.; Kurian, M.; Torris, A.; Kurungot, S. Air-Cathode Interface-Engineered Electro-catalyst for Solid-State Rechargeable Zinc–Air Batteries. *ACS Appl. Energy Mater.* **2022**, *5*, 8756–8768.
- (41) Wang, Y.-C.; Huang, L.; Zhang, P.; Qiu, Y.-T.; Sheng, T.; Zhou, Z.-Y.; Wang, G.; Liu, J.-G.; Rauf, M.; Gu, Z.-Q.; Wu, W.-T.; Sun, S.-G. Constructing a Triple-Phase Interface in Micropores to Boost Performance of Fe/N/C Catalysts for Direct Methanol Fuel Cells. *ACS Energy Lett.* **2017**, *2*, 645–650.
- (42) Manna, N.; Ayasha, N.; Singh, S. K.; Kurungot, S. A NiFe Layered Double Hydroxide-decorated N-doped Entangled-graphene Framework: A Robust Water Oxidation Electrocatalyst. *Nanoscale Adv.* **2020**, *2*, 1709–1717.
- (43) Wu, Z. S.; Yang, S.; Sun, Y.; Parvez, K.; Feng, X.; Mullen, K. 3D Nitrogen-doped Graphene Aerogel-supported Fe₃O₄ Nanoparticles as Efficient Electrocatalysts for the Oxygen Reduction Reaction. *J. Am. Chem. Soc.* **2012**, *134*, 9082–9085.
- (44) Zenyuk, I. V.; Parkinson, D. Y.; Connolly, L. G.; Weber, A. Z. Gas-diffusion-layer Structural Properties Under Compression via X-ray Tomography. *J. Power Sources* **2016**, *328*, 364–376.
- (45) Tötzke, C.; Gaiselmann, G.; Osenberg, M.; Bohner, J.; Arlt, T.; Markötter, H.; Hilger, A.; Wieder, F.; Kupsch, A.; Müller, B. R.; Hentschel, M. P.; Banhart, J.; Schmidt, V.; Lehnert, W.; Manke, I. Three-dimensional Study of Compressed Gas Diffusion Layers Using Synchrotron X-ray Imaging. *J. Power Sources* **2014**, *253*, 123–131.
- (46) Jang, S.; Kim, S.; Kim, S. M.; Choi, J.; Yeon, J.; Bang, K.; Ahn, C.-Y.; Hwang, W.; Her, M.; Cho, Y.-H.; Sung, Y.-E.; Choi, M. Interface Engineering for High-performance Direct Methanol Fuel

Cells Using Multiscale Patterned Membranes and Guided Metal Cracked Layers. *Nano Energy* **2018**, *43*, 149–158.

(47) Singh, S. K.; Kashyap, V.; Manna, N.; Bhange, S. N.; Soni, R.; Boukherroub, R.; Szunerits, S.; Kurungot, S. Efficient and Durable Oxygen Reduction Electrocatalyst Based on CoMn Alloy Oxide Nanoparticles Supported over N-Doped Porous Graphene. *ACS Catal.* **2017**, *7*, 6700–6710.

(48) Wang, Y. H.; Le, J. B.; Li, W. Q.; Wei, J.; Radjenovic, P. M.; Zhang, H.; Zhou, X. S.; Cheng, J.; Tian, Z. Q.; Li, J. F. In situ Spectroscopic Insight into the Origin of the Enhanced Performance of Bimetallic Nanocatalysts towards the Oxygen Reduction Reaction (ORR). *Angew. Chem.* **2019**, *131*, 16208–16212.

(49) Xu, L.; Lv, Y.; Li, X. N-doped carbon-stabilized Pt₃Co nanoparticles as an efficient catalyst for methanol electro-oxidation. *Colloids Surf, A* **2021**, *617*, 126411.

(50) Han, X. F.; Batool, N.; Wang, W. T.; Teng, H. T.; Zhang, L.; Yang, R.; Tian, J. H. Templated-Assisted Synthesis of Structurally Ordered Intermetallic Pt₃Co with Ultralow Loading Supported on 3D Porous Carbon for Oxygen Reduction Reaction. *ACS Appl. Mater. Interfaces* **2021**, *13*, 37133–37141.